DEVELOPMENT OF A MODEL FOR PREDICTING

WAVE-CURRENT INTERACTIONS AND SEDIMENT

TRANSPORT PROCESSES IN NEARSHORE COASTAL WATERS

A thesis submitted to the Cardiff University
In candidature for the degree of
Doctor of Philosophy

by

Umme Kulsum Navera

B.Sc., M.Eng.

Division of Civil Engineering, Cardiff School of Engineering
Cardiff University

February 2004

UMI Number: U584643

Dissertation Publishing

ProQuest LLC
789 East Eisenhower Parkway
P.O. Box 1346
Ann Arbor, MI 48106-1346

DECLARATION

This work has not previously been accepted in substance for any degree and is not being concurrently submitted in candidature for any degree.

Signed.. (candidate)

Date....................27/02/04...................

STATEMENT 1

This thesis is the result of my own investigations, except where otherwise stated.
Other sources are acknowledged by footnotes giving explicit references. A bibliography is appended.

Signed.. (candidate)

Date....................27/02/04...................

SATATEMENT 2

I hereby give consent for my thesis, if accepted, to be available for photocopying and for inter-library loan, and for the title and summary to made available to outside organisations.

Signed.. (candidate)

Date....................27/02/04...................

ABSTRACT

A two-dimensional numerical model has been developed to simulate wave-current induced nearshore circulation patterns in beaches and surf zones. The wave model is based on the parabolic wave equation for mild slope beaches. The parabolic equation method has been chosen because it is a viable means of predicting the characteristics of surface waves in slowly varying domains and in its present form dissipation and wave breaking are also included. The two dimensional parabolic mild slope equation was discretised and solved in a fully implicit manner, so stability did not create a major problem. This wave model was then embedded into the existing numerical model DIVAST. The sediment transport formulae from Van Rijn was used to calculate the nearshore sediment transport rate.

The estuarine model DIVAST has been refined and first used to simulate different tidal scenarios in the Bristol Channel, the agreement between field data and model predictions was good. Residual erosion after various tidal cycles was highlighted, which give rise to long-time effect predictions for the estuarine behaviour. The newly developed wave model was then introduced in to the estuarine model and the combined model has been verified against various laboratory data. At first, the model was applied to a sinusoidal beach with different beach orientations. Then the model was compared against a three-cusp beach. In both cases, model results showed that the model was capable of simulating the wave generated velocity field with a high level of accuracy. Then the model was applied to published laboratory data. The comparison between the laboratory data with model predictions confirmed the model's capability of simulating wave heights, cross-shore and longshore velocity profiles and water level variations. An acceptable level of accuracy was obtained.

Finally, the model was applied to a recent laboratory investigation by the research group. Various scenarios were simulated for the sensitivity test of the main model parameters and some of the parameters have been investigated to obtain the best comparable results. It was found that the velocity field was sensitive to changes in the bed resistance, friction co-efficient and wave breaking index. The nearshore sediment transport rate predicted by the model was verified against other existing numerical model results, with very close agreement being obtained. Also the morphological parameters and bed level changes were calculated and compared with laboratory results and again giving good agreement.

A combined wave-current model which can be applied to both estuarine and nearshore circulation predictions has been established, and the agreement between the predicted numerical model results and laboratory data have been very encouraging for all of the model applications considered. The numerical results confirm that the new wave-current model is stable, accurate and economical in terms of computational resources.

Keywords: estuarine transport; wave-current interaction; parabolic wave equation; numerical modelling; nearshore circulation; Finite Difference Method.

ACKNOWLEDGEMENTS

To my parents

and

my husband

TABLE OF CONTENTS

Chapter 1   *INTRODUCTION*

Chapter 2   *LITERATURE REVIEW*

Chapter 3   *GOVERNING EQUATIONS OF FLUID FLOW*

Chapter 4   NUMERICAL MODELLING

Chapter 5   TIDAL MODEL APPLICATION

Chapter 8   *CONCLUSIONS AND RECOMMENDATIONS FOR FURTHER STUDY*

LIST OF FIGURES

LIST OF TABLES

NOTATION

a	wave amplitude
a_x, a_y	local fluid acceleration
a, b	parameters to find breaker index
C	phase velocity or wave celerity
C_b	bed load concentration
C_D	drag co-efficient
C_f	Courant number
C_g	group velocity
d	total depth of water
D_*	dimensionless particle parameter
D_{50}, D_{90}	particle size
D_{xx}, D_{yy}	depth averaged dispersion-diffusion co-efficients in x and y direction respectively (m /s)
E	total energy
$\bar{e}$	horizontal unit vector
$\bar{F}$	resultant forces acting on a mass
f	Coriolis coefficient
F_*	entrained function
g	gravitational acceleration
h	water depth below mean water level
H	wave height
H_b,h_b	breaking wave height and breaking water depth
i	imaginary operator
i, j	grid point location in x,y direction respectively
J	Jacobian of transformation
k	wave number
k_l	longitudinal depth average dispersion constant
k_t	depth average turbulent diffusion constant
l_x	mixing length

L	wave length
m	mass
n	time step number
P, p	hydrostatic pressure
P'	subsurface pressure under wave
q_s	sediment flux per unit width
q_b	transport rate of the bed load
R_*	shear Reynolds number
S	depth average suspended sediment concentration (section 3.6)
S_{ij}	radiation stress tensor
s	sediment specific gravity
T	wave period
u,v,w	time average velocity in the x,y,z direction respectively
$\overline{u},\overline{v},\overline{w}$	instantaneous velocity in the x,y,z direction respectively
u',v',w'	fluctuating turbulence part of the instant velocity $\overline{u},\overline{v},\overline{w}$ in the x,y,z direction respectively
u_b	particle velocity
u_η, v_η, w_η	velocity at the free surface
u_{-h}, v_{-h}, w_{-h}	velocity at the bed
u_{*cr}	critical bed shear velocity
U, V	depth average velocity component in x,y drection
w_s	particle settling velocity
W	weight of any element
z	reference datum
Z_0	effective roughness height of the surface
$\Delta x, \Delta y, \Delta z$	control volume, unit spacing
Δt	infinitesimal time increment
ρ	fluid density or mass/unit volume of fluid
ρ_a	density of air
τ_b	bed shear stress component
τ_c	critical shear stress

τ_{yz}, τ_{zx}	shear stress component
τ_w	surface wind stress
$\bar{\sigma}$	trace of the stress tensor in a state of motion
σ	angular frequency of wave
σ_{xx}	normal stress component (tensile fluid stress)
μ	coefficient of viscosity
ν	kinemetic viscosity
β	momentum correction factor
η'	absolute eddy viscosity
ε	kinematic eddy viscosity
$\bar{\varepsilon}$	depth average eddy viscosity
ω	angular or radian frequency
ω	angular speed of earth's rotation
φ	angle of latitude of domain
φ	velocity potential
η	height of water surface above mean water level
κ	von Karman's constant (0.4)
γ_a	air/water resistance coefficient
θ	phase angle
θ_{cr}	critical mibility parameter
ψ	stress function or stream function
ϕ	a variable coefficient for Helmholtz equation
Φ^+, Φ^-	forward and backward scattered waves
ϕ_m	a variable
λ	a variable
γ_b	breaker depth index
$\tan\beta$, m	slope of the bottom
δ_{ij}	Kronekar delta
ρ_s	sediment density
δ_b	saltation height

CHAPTER 1

INTRODUCTION

1.1   Background of the Study

Coastal areas and estuaries are constantly exposed to different meteorological and hydrological conditions. In recent years, these areas have been subjected to serious development considerations with an increase in population, more use of water bodies such as rivers, lakes and estuaries in water supply, flood control, irrigation and navigation systems. Environmental awareness has also risen sharply due to more and more use of these areas for commercial and recreational purposes. There are lots of artificial as well as natural changes taking place along the land and sea interface which effect the ecosystem seriously.

Coastal areas can be characterised by complex flow patterns with tidal effects, complex bathymetries and continuously changing wind-wave behaviour. All of these factors can result in significant changes in the sediment transport processes. The ever changing sediment transport gives rise to one of the most severe problems in coastal engineering, which is 'coastal erosion'. In estuarine waters, sediment transport is a very complicated process as river water meets the ocean water in regular tidal intervals. These processes become more complicated as the river water carrying sediment particles, along with its flow, travels through sedimentary land. The ever changing tidal flow pattern changes the sediment motion, which gives a

new complicated flow pattern within the estuary. To understand this estuarine flow system, different scientists have undertaken various studies. However, there is no unique solution to describe estuarine sediment transport processes completely.

The sediment particles are in constant change, both in size and shape, in estuarine waters. These changes occur due to natural causes, changes due to hydrodynamic condition and also due to human activities. Among all other factors (like tidal variation, salinity and river flow) the main factors are the upstream river sediment capacity, sea-level change and the different seasons of the year. The construction of coastal structures, resulting in changes in the flow characteristics, also leads to changes in sediment transport processes and in the long term the hydrodynamic characteristics of the estuary. The problems associated with estuarine erosion and deposition are one of the main challenges for engineers and scientists to address for the benefit of mankind. To find out the long term erosional and depositional characteristics of the flow pattern in an estuary, the sediment transport and tidal influence has to be well understood to make accurate future predictions.

Another important coastal areas are the beaches, which is the line of division between land and sea. The beaches are in a constant state of change due to the supply of sediment and natural forces of erosion due to wave attack. An understanding of the nearshore processes, such as wave-climate, interaction of waves with shallow water, wind induced shear stresses, nearshore circulation of refracted and reflected waves are all very important to visualise the changes in shorelines and beach profiles with time.

The nearshore circulation due to wave induced forces result from complex processes based on gravity water waves. While approaching the coastline or coastal structures, waves undergoes shoaling, reflection, refraction, diffraction, dissipation and wave-current interaction; after these processes have occurred, nearshore currents are produced by the excess momentum flux due to the breaking of waves, with thus is called the radiation stresses. In this highly dynamic system the nearshore currents are then modified by the bottom friction and mixing processes in the surf zone. The mean water level will also change due to the presence of waves. The numerical

model developed during this study is capable of computing the wave field resulting from the transformation of an incident, linear, monochromatic wave over a region of arbitrary extent and bathymetry. The solution technique described herein uses the finite difference technique so that the wave climate, in terms of wave height, period and direction, can be specified at every single computational point.

During the last three decades extensive analyse have been undertaken to characterise the sediment transport process in the estuarine waters and nearshore regions and numerical models have become a popular tool to do so. The rapid developments in numerical modelling have enabled researchers to pursue research in a cost effective way and in a relatively short time, which is not generally possible using physical models. A standard numerical model can simulate different physical problems by changing the hydrodynamic and physical variables. Numerical models are flexible, transportable and economical and fast computers are cheap nowadays. The estuarine and nearshore region processes can be accurately predicted using well-developed numerical models.

The difficulty of the prediction of sediment transport by numerical model (resulting in erosion and deposition) in estuaries and nearshore coastal zones is mainly the lack of understanding of the physical processes involved, although many researchers have devoted much time establishing exact solutions. There is no exact set of solutions up to the present time to describe sediment transport process perfectly as there are so many parameters affecting the processes, which are also often difficult to measure. Still upto now researches have always depended upon empirical formulae that have to be adopted for different situations based on the specific assumptions.

The study of estuarine sediment transport processes resulting in erosion and deposition are long term processes. By using numerical models for estuarine transport, the governing processes are described mathematically via a set of differential equations. For the case of nearshore processes, sediment transport primarily occurs due to wave induced currents in nearshore zones. The current system arises for either normal or oblique incident waves. It is very important to

observe and describe the nearshore flow due to breaking, resulting in nearshore sediment transport. In this study a mathematical model has been developed which can simulate estuarine sediment transport processes and as well as the characteristics of nearshore circulation processes.

1.2   Scope of the Study

Coastal engineering is a part of Water Resources Engineering and is a vast field of academic and practical research. It is still a field of considerable uncertainty, with a lot of unanswered questions. The basic scope of this research work was to study sediment transport process in estuarine waters effected by tidal fluctuations and using a numerical modelling approach. The same numerical model with the addition of wave sub-model has been applied to predict the nearshore velocity due to breaking waves and the corresponding sediment transport rates in the nearshore zone. In both cases the major factors influencing the sediment transport processes have been highlighted.

It is very important to understand the hydraulic behaviour of the estuaries and nearshore coastal zones (or surf zones) before undertaking any numerical modelling process. In the area of shallow water (or estuarine area where horizontal flow is dominant), there is a significant tidal fluctuation, it can often be assumed that the flow is well mixed vertically (Falconer and Owens, 1990). Based on this assumption the flow and sediment transport processes in shallow water can be accurately predicted by two-dimensional models. The two-dimensional model DIVAST (Depth Integrated Velocities And Solute Transport) was chosen for refinement and for predicting the shallow water flows by numerical predictions. The hydrodynamic part of the model was developed by solving the three dimensional mass and momentum equations and integrating them vertically to obtain the depth averaged flow parameters. The accuracy of prediction of the long-term sediment transport processes mainly depends nearly upon solving these basic governing equations as

accurately as possible. In DIVAST, the advection-diffusion equation has been solved using the highly accurate ULTIMATE QUICKEST scheme.

The breaking of waves is one of the dominant forces for nearshore circulation, which results in increase in turbulence level and sediment suspension. Over the past three decades there have been considerable developments in the understanding of nearshore circulation induced by waves. Several wave models have been developed, which include more physical parameters like bottom friction, lateral mixing and mixing processes. The recently developed models have the ability to predict many of the nearshore processes, but a comprehensive model which can take care of all of physical conditions in the nearshore zone could not yet be developed.

A numerical model for wave simulation or nearshore wave circulation should be able to predict:- (i) the nearshore velocity component, (ii) the location and magnitude of breaking waves, (iii) the longshore and cross shore sediment rate, (iv) the areas of erosion and accretion due to wave attack, (v) the effects of any new constructed coastal structures on the nearshore zone, (vi) the flood inundation levels due to extreme events such as tides, surges, cyclones etc. The wave model in this study has been established from a parabolic mild slope equation and based on the theory of Booij (1981). The model has been be calibrated against different sets of laboratory results to test its applicability for nearshore circulation predictions.

1.3   Study Objectives

The fundamental need for any research work arises due to various reasons such as academic interests, practical conditions, theoretical enhancement of social and cultural circumstances, human development and so on. The objective of this research study is to observe and understand the estuarine sediment transport patterns due to tidal effects and also the nearshore flow and velocity field due to normal and oblique wave attack.   The need is particularly relevant in countries such as Bangladesh, where coastal areas are exposed to extreme hydrological (i.e. cyclones, tidal surges,

coastal erosion etc.) conditions. The proper fulfilment of the objectives of this research work will enhance the understanding of the natural forces that shape the physical properties of the coastal areas for countries such as Bangladesh, which largely determine the potential for human settlement and development.

The development of two-dimensional parabolic wave equations has been outlined and applied to nearshore field studies to observe the velocity field. The wave model has been incorporated in a widely used shallow water model, namely DIVAST, to predict the nearshore flow due to breaking waves. The model was also refined to establish the characteristics of sediment movement under normal and oblique incident waves. DIVAST is a two dimensional depth integrated numerical model, originally developed by Falconer (1980) and then modified for sediment transport by Owens (1986) and Lin and Falconer (1997) for shallow water flows in estuaries. Until recent times DIVAST has been modified by several researchers (Kashefipour et al., 2002) for introducing new techniques (for water quality, mangrove estuarine flow pattern etc.) so the model was appropriate for application to natural shallow flow domains for large estuarine areas.

The purpose of any numerical model to predict sediment transport rate in estuarine and nearshore waters is to obtain the closest possible solution to the governing equations, which can represent the hydrodynamic part accurately. The governing equations for estuarine shallow water flows are based on flow variables, tidal simulation and sediment transport parameters. At the time, when the wave part was included in the shallow water model, there was another set of variables mainly the wave parameters to be included. So the shallow water model reported herein comprises three sub-models namely: the hydrodynamic, the sediment transport and the wave sub-models.

The basic governing equations for the hydrodynamic sub-model were derived from the shallow water flow three-dimensional form of the equations. The two-dimensional depth integrated form of the equations was adapted for the numerical model to represent the shallow water flows. The sediment transport sub-model is included through the advective-diffusion equation to determine the depth integrated

two dimensional sediment load fluxes. The wave sub-model comprises the two-dimensional parabolic mild slope equations. The governing equation have been discretised to calculate or predict the wave height (H), wave period (T) and wave angle (θ) after any simulation time. So the three sub-models were connected together to set up a network for the two-dimensional depth integrated numerical model for predicting sediment transport processes in shallow waters (or estuaries) and nearshore flow fields or wave climates in the surf zone. The finite difference method has been used here to discretise the governing differential equations with a Cartesian co-ordinate system. The Alternating Direction Implicit (ADI) scheme was used to solve the hydrodynamic equations. The advective-diffusion equation was used to discretise solute transport with the highly accurate ULTIMATE QUICKEST scheme being used for the advective terms. The parabolic mild slope wave equations were set up for large angles according to Berkhoff (1972), Noda (1974), Radder (1979) and Booij (1981).

The shallow water model DIVAST, including the new wave model, needed to be verified and validated, like any other numerical model. Some field data and laboratory experimental results, together with some test cases which has already been in established literature, have been chosen for model verification. The models (i.e. for shallow water estuarine flow, due to tidal effects and nearshore circulation due to wave effects) has been tested against field (data from Bristol Channel to validate the tidal model) and laboratory data (data from Lima, 1981 for test case II in Chapter 6 and Antoniadis, 2003 for the comparison in Chapter 7 to validate wave model) to ascertain its accuracy and efficiency.

The principle objectives of this research study have therefore been to:

(i)   develop an integral wave-current model,

(ii)   validate the DIVAST model against field data,

(iii)   extend and incorporate the wave model into DIVAST, and

(iv)   verify and validate the new integrated model against comprehensive data.

1.4   Structure of the Thesis

The study undertaken in this research thesis includes eight chapters (including this one), which can be summarised as follows:

Chapter 1 represents the basis against which the need for this study arises. The fundamental scope and objectives to undertake this study has been defined. Also the structure of the thesis has been laid out.

Chapter 2 deals with reviewing the vast field of estuarine processes and nearshore wave circulation processes. In this chapter the main aim has been to review recent developments in two broad divisions of estuary and wave processes and modelling. The study of previous works already undertaken in both fields was categorised as: field studies, laboratory experiments, theoretical studies, sediment transport processes and numerical modelling techniques. These reviews could give an overall idea of the research done in this field and also outline the basis for the current research work.

Chapter 3 consists of the derivation of the governing equations for shallow water flow processes, which includes the equations for the hydrodynamic part, the sediment transport processes and the parabolic wave generation processes. The different assumptions and conditions applied in deriving the two-dimensional depth integrated shallow water flow equations were also described, thereby enabling an understanding of the methodology adopted in this research work.

Chapter 4 provides a brief description of the fundamentals of the finite difference method, which have been used by outlining the discretisation of the different components of the shallow water and wave models. The solution procedure and the stability criteria for the numerical scheme have been discussed. The different boundary conditions were also outlined which were applied in the model.

Chapter 5 describes the application of tidal model DIVAST to a physical estuary, namely the Bristol Channel. A detailed analysis has been undertaken. The model has

been calibrated and verified against two different sets of field data. Also the model has been applied against a new set of field data from 2001. The sediment transport phenomena with tidal cycle and the residual erosion and deposition after different tidal cycle were also discussed.

Chapter 6 evolved with the application of the wave model to published experimental work. The wave model was applied to laboratory data. Three test cases were discussed and the results were plotted and compared for the predicted and measured data. For test case III, the predicted velocity field, wave height and water levels were compared with the laboratory data.

Chapter 7 presents the details of the validation of the numerical wave model predictions against the laboratory data. These extensive experimental data were compared with the wave model predictions and helped to show the establishment of the wave model. Sediment transport rate and bed level changes were also predicted by the model and compared with laboratory data.

Chapter 8 provides the conclusion of the findings from the research work, and concluding remarks on the tidal model and the wave model. This was followed citing some recommendations from this study for further study to follow on.

CHAPTER 2

LITERATURE REVIEW

2.1 Introduction

The success of any research study depends on the true identification of the problem for any research field. The procedure of problem identification is very delicate and time consuming process. To find out about a new topic or a gap in previous scientific research, the best way is to perform a rigorous scrutinisation of the work already undertaken in the field. The different exposures of problems and the view expressed by the respective researchers provide the basis for new questions which need to be answered and thus initiate the scope of new horizons for exploration. The research interest for this study focused on estuarine sediment transport due to tidal currents and nearshore circulation processes due to wave-current interaction. Both of these processes are mainly based on shallow water hydrodynamics. Estuarine sediment transport arises due to tidal asymmetry and the tidal influence on the estuary determines the magnitude and direction of the sediment movement. Whereas in the case of nearshore processes waves are the dominating factor. The wave height, wave period and incident wave angle, together with the bed slope and bottom friction, create an environment for wave breaking and the resulting nearshore transport process.

This chapter has been organised to underline the necessity for the current research. Section 2.2 will illustrate the definition and classification of estuaries and beaches

based on different geological, hydrodynamic and environmental factors. The different hydrodynamic processes taking place in the estuaries and beaches are described in section 2.3, which provides a foundation of the underlying problems in the field. While searching for previous scientific work in the field, the basic work has been divided into two categories namely: estuary and nearshore zone. To distinguish between the respective problems, each category has been divided into sub categories as field work, laboratory experiments, theoretical investigations, sediment transport (as sediment transport is one of the focus of this study for coastal and estuarine flow) and numerical modelling. The division of categories has been done to focus on the different aspect of the problems and their corresponding solutions.

2.2   Classification of Estuaries and Beaches

Estuaries are areas of interaction between fresh and salt water. Among many different definitions one of the most widely cited was given by Pritchard (1967) as "An estuary is a semi-enclosed coastal body which has free connection to the open sea, extending into the river as far as the limit of tidal influence and within which sea water is measurably diluted with fresh water derived from land discharge". Topography, river flow and tidal action are the most important factors that influence the rate and extent of the mixing of the salt and fresh water. **Pritchard (1967)** has divided estuaries into two groups; a positive estuary is one where the fresh water flow derived from river discharge and precipitation exceeds the evaporation, and a negative estuary is the one where evaporation exceeds river flow plus precipitation.

Davies (1964) classified estuaries in the tidal context and described them by their tidal range (TR), which are: (a) Microtidal estuary, TR < 2m (b) Mesotidal estuary, 2m < TR < 4m (c) Macrotidal estuary, 4m < TR< 6m and (d) Hypertidal estuary, TR > 6m. Depending on the convergence of the estuary sides and the friction in the shallower waters three types of estuary may be found including: (a) Hypersynchronous estuaries where convergence exceeds friction mainly due to the

funnel shaped of the estuary, (b) Synchronous estuaries where convergence and friction have roughly equal and opposite effects on the tide, and (c) Hyposynchronous estuaries where friction exceeds convergence and the tidal range diminishes throughout the estuary.

Based on topography there are three types of estuaries: (a) Coastal plain estuaries, formed by the floods of previously incised valleys, (b) Fjords, which were formed in areas covered by pliestones ice sheets, and (c) Bar-built estuaries, or the drowned river valleys. Based on the interplay between the river, waves and tidal currents there are two types of estuaries: (a) Wave dominated estuaries where waves are significant at the mouth and sediments eroded from the coastline are transported alongshore to form a spit, and (b) Tide dominated estuaries, where the tidal currents are large relative to the wave effects. The mouth area generally contains sandbanks which are aligned with the current flow and around which sediments circulate.

Based on the salinity distribution estuaries may be classified into: (a) a highly stratified estuary of the salt wedge type, (b) a highly stratified Fjord type estuary, and (c) a partially mixed estuary. Based on the fact that the tidal range may be large relative to the water depth and the turbulence produced by the velocity shear on the bottom may be large enough to mix the water column completely and make the estuary vertically homogeneous, there are two types of estuaries in another context, i.e.: (a) laterally inhomogeneous, and (b) laterally homogeneous.

Natural beaches and the shoreline are the line of demarcation between land and water. Beach and shallow water sediments are continuously responding to direct wave action, wave-induced littoral currents, wind and tidal currents. The stability of a section of sedimentary shoreline depends on the balance between the volume of sediment available over the section and the net onshore-offshore and alongshore sediment transport capacity of waves, wind and currents along the section **(Sorenson, 1978)**. The shoreline may thus be eroding, accreting or remain in equilibrium.

Based on the sediment composition of the beach material the beaches may be classified as: (a) muddy coasts (5-10% of the world's coast) where the coast consists of predominantly inorganic sediment of median size less than 63 micron (0.063mm) and are known as chenier or chenier plain coasts, (b) sandy coasts (10-15% of world's coast) where wave dominated depositional materials is deposited i.e. sediment grains range from 0.063 to 2mm, the sand accumulated is generally deposited through processes of wave action and wave induced currents, rather than through tide or wind induced currents, (c) gravel/shingle coasts, which consist of gravel (2 to 64 mm), pebbles and cobbles (64 to 256 mm) and are generally known as coarse clastic beaches, and (d) rock and cliff coasts (75-85%) which are high and steep faced coasts without a noticeable beach, granite and basalt to sandstone and mudstone are the materials of these type of coasts.

Based on typical coastal features (phenomenological or morphological) six types of beaches may exists including: (a) barrier island coasts, (b) delta coasts, (c) dune coasts, (d) coral reef coasts, (e) mangrove coasts, and (f) marsh grass coasts. Based on the river-sediment discharge (water and sediment, wave climate and relative strength of tide-induced forces (tidal range, TR) and wave-induced forces (H=annual mean nearshore wave height), the following classification can also be given: (a) riverine dominated coast, (b) wave energy-dominated coast (TR/H = 0.5-1.0), (c) mixed energy coast (TR/H = 1.0-3.0), and (d) tide energy-dominated coast (TR/H > 3.0). According to genetic controls as given by genetic classification methods, beaches are effected by: land configuration, relative vertical movement of land and sea (emergence or submergence with time) and physical processes modifying the coast line (erosion and deposition with time in relation to emergence or submergence).

2.3   Hydrodynamic (Tidal and Wave) Processes

In the shallower water of estuaries two main processes affect the tidal wave. The first is that even in a frictionless estuary, when the tidal variation relative to the water depth is large, the wave crest will move more quickly than the trough **(Dyer,**

1997). The crest of the tide may partially overtake the trough, resulting in a shorter flood and longer ebb. The second is the effect of bottom friction, which is non-linear process and depends on the square of the current to produce greater friction in shallow water. The combined effects of these two processes produce a short duration of flood phase of tide called flood dominance. Ebb dominance can be produced within estuaries essentially by interactions between the deep channel and the shallow water areas and the varying distribution of friction during the tide.

Mixing in an estuary is a combination of internally generated and boundary generated turbulence, which varies in relative magnitude in space and time. Turbulence is difficult to measure and explains why a means of parameterizing can be more easily measured. The coefficients are eddy diffusion coefficients and eddy viscosity. Dispersion is considered as a gradient process like diffusion and its magnitude depends on the shear in the horizontal velocity, combined with the vertical turbulent diffusion. The physical processes active in the coastal zone are: (a) aerodynamic such as air-sea interaction, aeolian transport, (b) hydrodynamic processes such as waves, currents and water levels, (c) morphodynamic, such as sediment transport and bed evaluation, (d) geodynamic, such as subsidence, uplift, earth-quakes, sliding, and (e) eco-dynamic such as organisms, plants, nutrients, chemical reactions etc.

Coastal evolution is a highly non-linear, three dimensional and time dependent product of morphodynamic processes that occur in response to the external (partly stochastic) hydrodynamic and aerodynamic (wind blown sand) conditions. The most basic hydrodynamic forces in the coastal zone are: (a) breaking waves and wave-induced currents in the surf zone and varying over the seasons, under calm conditions the surf zone may be reduced to a narrow swash zone, but under storm conditions it may extend offshore to depths of 8 to 10 m, where the waves first begin to break, and (b) non-breaking irregular waves combined with tide, density and wind-induced currents in the shoreface zone, seawards of the surf zone.

Mass transport in the near water surface region is considerably enhanced in breaking wave conditions. When oblique incident waves break in the nearshore zone, a

complicated current pattern is generated in the surf zone, which consists of longshore currents and offshore return currents the near bed region (undertow). The mean currents interact with the instantaneous wave orbital motions, yielding a complicated time dependent 3-D pattern. The generation of the longshore and cross-shore mean currents can be explained by the radiation stress concept **(Longuet-Higgins and Stewart, 1962)** which describes the momentum flux associated with waves. The gradient of the onshore radiation stress component is balanced by the pressure gradient related to the water surface set up in the surf zone. As a result of the onshore mass transport in the near surface region and the mean water surface set up, an offshore return current is generated below the trough level.

The longshore current is largely confined to the surf zone **[Longuet-Higgins (1970), Komar (1971), Sonu (1972), Noda (1972)]** and rapidly decreases in velocity seawards of the breaker line. The longshore velocity is found to be strongly related to the wave height decay in the surf zone and the orientation of the wave crests. The beach slope appears to be of less importance. In nature wave induced longshore currents are often enhanced by wind induced currents. Analysis of fluid data has shown that **(Church and Thornton, 1992)** the cross-shore distribution of the longshore currents is rather insignificant to the contributions of individual waves in a random wave field. Reasonable agreement between measured and computed longshore velocities can only be obtained **(Van Rijn and Wijnberg, 1994)** by introducing a longshore water surface gradient in the inner surf zone.

The main hydrodynamic parameters in the coastal zone are: (a) wind induced waves, (b) tide induced waves and currents, (c) wind induced currents, (d) density induced currents and (e) wave induced currents.

(a) <u>Wind induced waves:</u> Wind induced waves with typical wave periods of 5 to 15 seconds propagate into shallow water and are affected by reflection, refraction, bottom friction and shoaling phenomena and finally by wave breaking in the surf zone. The wave climate factor is expressed by: (i) low wave energy [H_S<0.6m], (ii) moderate wave energy [H_S=0.6-1.5 m], and (iii) high wave energy [H_S>1.5m], where H_S is the annual mean significant wave height at the edge of the surf zone.

Low frequency wave motions with periods of 15 to 100sec are present inside and outside the surf zone, especially during rough weather conditions. Incident waves coming from the sea to the shore line can be categorised as wind waves and swell, bound long waves, which travel with a group velocity of wind waves, and free long waves. Waves moving in a wind field will be propagated in the main wind direction and may move out of the wind field to become more regular and symmetric, with long crests and swell waves.

(b) <u>Tide induced waves and currents:</u> The generation of the astronomical tide is the result of the gravitational interaction between the sun, the earth and the moon. The tidal range is a maximum (spring tide) when the sun and the moon are in a line, and a minimum (neap tide) when the sun and the moon are at right angles. Tidal waves have typical periods in the range of 12 to 24 hours. The propagation of tidal waves is affected due to geometrical effects of the nearshore area, by damping due to bottom friction, by reflection against boundaries and by deformation due to differences of propagation velocities under wave crests and wave troughs. The rotation of the Earth introduces an apparent force (Coriolis force) acting on the fluid which is directed perpendicular to the direction of the fluid where (h>20m). Tidal currents are controlled by pressure gradients (mean surface slope, fluid density variation), bottom friction (dominant in depths smaller than 10m) and Coriolis forces.

(c) <u>Wind induced currents:</u> There are two types of wind induced currents, one is wind drift currents of relatively short duration generated by local storm winds and the other is large scale circulation systems generated by long duration effects, such as zonal winds and atmospheric pressure systems. When the wind is blowing in a certain direction in deep water, current velocities will be induced in that direction and due to Coriolis forces also in various other directions. In shallower water near the coast (h<10m) the current responds rapidly to wind stresses and the surface current tends to be aligned with the wind direction. Storm surges of several metres high in the neashore zone can be generated by the direct effect of onshore wind forces, the action of Coriolis forces and by inverted barometric effects of low atmospheric pressure.

(d) <u>Density induced currents:</u> Density induced currents are related to spatial density gradients of the fluid sediment mixture due to variations of temperature, salinity and sediment concentration. The density gradient effect is most pronounced in the near bed region yielding relative large on-shore near bed velocities during flood tides and relatively small offshore velocities during ebb tide. As a result a near bed residual current is generated, which may cause a net landward transport of sediments, with the process being reversed and yielding a residual seaward flow near the water surface.

(e) <u>Wave induced currents:</u> The wave and current fields interact mutually through a number of mechanisms which are: (i) refraction of waves by horizontal currents, (ii) generation of near bed streaming by waves, (iii) generation of longshore currents by breaking waves, (iv) modification of wave kinematics by the currents, (v) enhancement of the bottom friction experienced by the currents due to interaction with the wave boundary layer, and (vi) enhancement of the bed shear stresses and energy dissipation of the waves due to interaction with the current boundary layer.

There has been much research undertaken in both estuarine and nearshore dynamics and the rest of this chapter will focus on previous investigations undertaken by several researchers. The studies on estuarine and nearshore hydrodynamics will be categorised into different sections as field work, laboratory experiments, theoretical investigations, sediment transport and numerical modelling. The intention is to provide a clear picture of the nature and complexity of the coastal zone and the diversity of the research in each of the individual fields described above.

2.4   Tidal Effects in Estuarine Waters

In recent years there has been an increasing interest in understanding the flow mechanisms associated with tidal fluctuations, river discharges, pollutant distributions, water quality monitoring and seasonal effects, particularly since the prediction of flow fields and transport processes in coastal and offshore waters are being increasingly determined by numerical model solutions. There have been

numerous field studies undertaken to understand the mechanisms of shallow water flows, which in turn helps to solve environmental and civil engineering problems. It is very difficult to study an estuary using physical models due to scale problems with such large domains. However, some work has been done which focuses on specific parameters in laboratory model investigations. Also there has been much research undertaken on developing different theoretical formulations for estuarine hydrodynamics. The different studies undertaken for the above three categories will be reviewed in the following sections.

2.4.1 Field Work

A semi-enclosed water body located at the Gulf of Kutch was numerically modelled with the help of information on tides and currents by **Unnikrishnan et al. (1999).** There were regular tidal measurements at different locations and the important tidal constituents were developed for documentation, which showed that the semidiurnal tides were amplified more than the diurnal tides. **Jones (2000)** examined wave observations at two shallow water sites in the UK, which showed significant variations at semi-diurnal frequencies, period, amplitude and direction for semi-diurnal tides. The interaction between tides and waves was studied using linear wave theory refraction, with emphasis being focussed on slowly varying currents and depths. A study of tidal mixing through two constrictions at the entrance of an estuary in Canada undertaken by **Isachsen and Pond (2000).** Observations were taken during spring tides with small floods bringing external water into the basin, and with large flood resulting in intrusions of highly mixed water, of lower density. During neap tides the density decreased slowly and turbulent vertical diffusion was the dominant process along the estuary.

A field study was undertaken by **Wolanski et al. (1984)** in Australia to observe the large-scale eddy structure in the lee of Rattray Island. Separation occurred at the tip of the headland. A detailed field study was undertaken using current meters and they showed the positive effect of using Landsat imagery and aerial photographs for visual observations, which helps researchers a lot. **Lessa (2000)** measured the monthly tide and current velocities in two shallow macrotidal estuaries in Australia

and showed that the hydrodynamics were controlled by the depth of the channel bed across the ebb tidal delta and the elevation of the mangrove banks. It was possible to analyse this dynamic behaviour, as there were large differences between spring and neap tidal ranges.

Process modelling was believed to give better insight into the respective roles of tides and waves in driving long-term morphological changes. The coastal morphodynamic processes around tidal inlets in mixed energy environments are very complex, as observed by **Cayocca (2001)** for Archachon Lagoon, France. Several tide and wave conditions produced significant bathymetry changes as time scales varied from hours to decades or centuries. **Tonis et al. (2002)** studied from 1970 to 1999 the closure of Harlingvliet estuary by the construction of a dam with sluices. The structure had a profound effect on the hydrodynamics and morphology of the area. Morphological adaptation processes of an estuary after major human intervention are very complex and long-term bathymetric analysis might reveal the key parameters. **Van Rijn et al. (2003)** showed the prediction of coastal processes like beach and coastal profile modelling during the EU-COAST3D project. Deterministic and probabilistic profile models have been compared with hydrodynamic and morphodynamic data of laboratory and field experiments which provided the in-depth characteristics of these kind of modelling.

Field tests were carried out through a tidal cycle in a tide dominated shallow water reach of the English channel by **Chapalain and Thais (2001).** The purpose was to test a new sand trapping system, that enabled measurements of horizontal transport rate of suspended sand in the boundary layer in multi-directional unsteady currents. The amounts of sediment trapped in different directions were compared with theoretical studies and the trap appeared to be a promising tool for future measurement. **Hossain et al. (2001)** investigated suspended sediment transport and sediment dynamics in a sub-tropical estuary in Australia. The estuary received net sediment input from the continental shelf during low flow months and exported sediment to the shelf during high flows, and depending on the magnitude of the flood. The net accumulation of sediment in the estuary for all post flood recovery stages was observed.

2.4.2 Laboratory Experiments

Tidal circulation, tidal current patterns, sediment movement and wave action are all very important phenomena in estuaries and which can be understood through laboratory flume studies. However, it is very difficult to replicate a prototype estuary in a physical model in a laboratory due to scaling problems. Though scientists and hydraulic engineers have tried to construct prototypes from as early as 1885. Tidal circulation and tide induced depth averaged velocity distributions were studied using both physical and numerical models for square and rectangular harbours by **Nece and Falconer (1989)**. Velocity distributions of the complex tidal eddies within the harbour were compared for different distortion ratios to investigate the influence of distortion and results showed little variation in velocity distributions for both flood and ebb tides.

Price and Thorn (1994) described the history of the development and importance of physical models and postulated that a properly designed physical hydraulic model could reproduce accurately tidal wave propagation and tidal currents, including secondary flows. The principal disadvantages were cost and relative inflexibility. **McAnally and Mehta (2002)** examined the aggregation process by which the properties of suspended fine sediment particles changed during transport, for the simple case of deposition of estuarine sediments in a flume. A multi-class model for aggregation was combined with a one-dimensional, unsteady multi class sediment transport model to calculate the deposition rate for two flume experiments. The results suggest that multi class fine sediment aggregation plus deposition calculations can produce more realistic results than the single class calculations for estuaries.

2.4.3 Theoretical Investigations

Tidal motion is an important challenge to coastal engineers and to describe tidal phenomena qualitatively different tidal theories have been proposed by researchers from as early as the seventeenth century. **Kalkwijk and Booij (1986)** implemented an approximate method for convection of momentum of the secondary flow to solve

the generation and decay of secondary flow in steady or quasi-steady nearly horizontal flow models. The method included both the Coriolis acceleration and curvature and showed that their effects were almost equivalent. Results for secondary flows were verified by comparison with flume results and satisfactory answers were obtained. **Dalrymple (1994)** developed the water wave theory in the context of the current digital computer. He showed that the classical linear wave theory by Airy was the simplest, with drawbacks, but despite these assumptions it still had a wide range of applications. Airy theory is useful for a first estimate of wave properties but for design purposes non-linear wave theory should be used.

One of the important parameters in shallow water wave motion is the presence of turbulence as discussed by **Rodi (1994)**. Turbulence is responsible for carrying sediments, governs the bed of coastal and estuarial regions, diffuses and disperses effluents from industry, urban pollutants and agricultural waste. He emphasises the importance of the development of turbulence modelling for practical applications. **Kuo et al. (1996)** formulated the bottom shear stress boundary condition for an unsteady tidal flow model. Numerical experiments for a hypothetical homogeneous estuary indicated that the error in the calculated bottom stress increased with the vertical grid spacing when a logarithmic profile was used to relate the bottom stress to the velocity. The use of this formulation, which included a correction term, significantly reduced the error for a wide range of vertical grid spacings.

Accurate predictions of tides can only be possible for a long period of measurement (>1 month), but **Yen et al. (1996)** proposed a method of harmonic tidal analysis which enables tides to be predicted for short lengths of measurement. The main parameters, such as amplitude and harmonic components were estimated by the Kalman filtering technique using a few days of tidal records and the assumption of a known angular frequency. **Flick et al. (2003)** suggested that studies concerned with present and future water levels should take into account more tidal datum statistics than just mean sea level (MSL). He showed that in SanFrancisco the diurnal tidal range increased by 64 mm from 1900 to 1998. Several stations in the USA showed rates of increase of mean high water (MHW) that were about twice those of mean

sea level (MSL). Hence for long term coastal planning these changes should be taken into account.

2.5   Wave Effects in Coastal Waters

Waves play a dominant role in the nearshore zone, which is often in a constant state of change. Wave processes are responsible for large oscillatory fluid motions, which generally drive currents and as a result sediment transport occurs and the bed level changes. During their propagation to the shore, the relatively well organised motion of offshore waves are transformed into several motions of different types and scales and are subjected to: shoaling, refraction, reflection, diffraction and breaking. Wave breaking occurs when the fluid velocities of the wave crest tend to become equal to the wave propagation velocity. Wave breaking mainly occurs in the surf zone and the main types of breaking are dependent upon beach slope and the wave steepness.

2.5.1   Field work

Field investigations of short period waves are inherently difficult to undertake, with difficulties including the uncertainties about some aspects of incident waves, the bathymetry and boundary conditions. The effective reflection coefficient can rarely be estimated with precision. Despite the impossibility of getting highly accurate and controlled field data, these are extremely valuable for rough validation to ensure that the chosen parameter values within the range can provide reasonable results. **Thomson et al. (1996)** verified their numerical model HARBD against field data for Kaumalapau Harbour, Hawaii, to demonstrate the effects of input parameters on model results and provide guidelines about the choice of parameter values in further modelling studies.

In recent years, there have been numerous studies on nearshore waves and currents and various theories have been proposed by different researchers. These theories are not always validated because of the lack of precise field data and also sometimes the accuracy of numerical models cannot be established due to a scarcity of precise field

data. The main difficulties for field exploration are the spatial distribution, rough waves and currents in the surf zone and time dependency. **Sasaki et al. (1976)** made a significant development with regard to establishing a new field observation system called STEREO-BACS, which consisted of a pair of balloons. The aim was to achieve simultaneous measurements of spatial distributions of nearshore waves and currents over a relatively broad area. **Dingemans et al. (1984)** showed the accuracy of CREDIZ, a wave propagation model used in a field study in south-western part of the Netherlands. The authors emphasised choosing the input parameters carefully for better results, such as the breaking criteria and friction coefficient. Field data of fluid motion presented by **Guza and Thornton (1985)** might be useful for the evaluation and construction of sediment transport models, they also reviewed some sediment transport models from their field velocity data relevant to nearshore transport. Recent advances in current meter technology have made possible the gathering of large sets velocity field data. These observed field values from Torry Pine Beach, California showed good accuracy with low order normalised moments and with theoretical assumptions.

It is very important to evaluate the wave field with good accuracy to predict properly the beach evolution due to construction of a coastal structure or due to severe wave conditions. Many researchers have pursued research to verify the field applicabilities of both the parabolic models and energy flux models against field data. Much research has been based on practical field observations. **Antia (1989), Frihy et al. (1991), Shimizu et al. (1992), Kumar et al. (2001)** showed the importance and significance of field validation. **Antia (1989)** made investigations along a 3km long high energy sandy beach in Nigeria to find out the volumetric beach change under the existence and extinction phases for beach cusps. The author suggested that the results of systematically obtained field data on beach changes under different cusp phases over a prolonged period of time were very beneficial to coastal engineering practise. **Frihy et al. (1991)** studied coastal processes along the Nile Delta, Egypt, and showed the response of beaches due to offshore construction, geomorphological shoreline features and large scale changes in shoreline orientation due to erosion and accretion. He drew multiple indicators from sand blockage to grain size variation to understand the sediment transport pathways. **Shimizu et al. (1992)** verified the field

applicability of the parabolic equation model (PEM) and energy flux equation model (EFEM) with field data from Tamioka fishery harbour facing directly towards the Pacific Ocean and with a complex bathymetry. These kinds of field data have enabled the establishment of numerical models which can use for practical applications. According to **Kumar et al. (2001)**, accurate estimates of wave height and direction at the breaker line are required to predict the longshore current and sediment transport rates. The longshore sediment transport rate was estimated along a beach in India and a comparative study was undertaken for theoretical and measured rates.

Some field studies have been undertaken directly to establish the beach dynamics and in recent times these studies have increased significantly because of its importance for the design of beach nourishment projects and coastal structures. The wave climate within a coastal bight is spatially complex as it consists of several offshore islands, shallow banks and submarine canyons. The field data obtained from this kind of area is very important to validate the numerical model which can be applied to other similar areas. **O'Reilly and Guza (1993)** used a spectral refraction model (R-model) and a refraction-diffraction model (RD model) to simulate the propagation of surface gravity waves across the southern California Bight with good result predicted.

There has been a lot of field work undertaken to observe the nearshore dynamics and results obtained can provide new methods of erosion control for severely eroding beaches, exact location of offshore structures to prevent wave overtopping and tidal surge, water quality monitoring for safer beaches etc. An extensive field experiment was undertaken by **Kirk (1992)** in New Zealand to provide a solution for a severely eroded and inundated hazard complex. The experiment was monitored for combined beach reconstruction and re-nourishment for 5 years for the extensive analysis of coastal hazards. Field experiments have shown that difference in beach erosion between steep slopes and gentle sloping beaches, based on the theory of generating gravity waves. **Katoh (1994)** had studied the physical difference of beach erosion in experimental flume and field and conclude that the incident wave was predominant

in the wave run up phenomena on the steeper beach while the infragravity waves were predominant on the gentler beach.

Schoonees and Theron (1993) showed that the accuracy of formulae for predicting longshore sediment transport in the surf zone depended on a limited number of field measurements which exhibit scatter. The author suggested that high quality measurements were needed to improve the accuracy of predictive empirical formulae and to understand their range of applicability. **Wang and Kraus (1999)** undertaken the measurement of longshore sediment transport using different methods, such as sand tracer, impoundment and sediment traps, and discussed the various processes and their merits. **Nordstrom et al. (2003)** discussed the difficulty of predicting longshore sediment transport due to a lack of field data, especially for low energy beaches. Most studies have been undertaken for beaches with well developed and gently sloping surf zones, which make it difficult to apply the results for estuarine beaches.

2.5.2 Laboratory Experiments

The prediction of shoreline evolution is one of the main challenges in coastal engineering owing to the important social and economic developments often being undertaken in the coastal zone. It is a difficult to undertake laboratory experiments of a prototype of nearshore circulation and transport patterns, but laboratory experiments provide some very useful knowledge about wave breaking patterns, breaking criteria, direction of waves and sediment transport patterns. **Führböter (1986)** explored the wave impacts and wave runup in a prototype tank. To design a navigation channel and breakwaters, information about the wave fields between the breakwater for different incident waves were needed. **Liu and Boisservain (1988)** presented a numerical model for computing wave propagation between two breakwaters and numerical results were compared with data measured during two laboratory experiments. Laboratory data sometimes provide the essential basis for any theoretical or numerical model study. A small scale experimental study was undertaken by **Dulou et al. (2002)** for sand bar formation under breaking waves, based on accurate and simultaneous analysis for spatial variations of wave height

and bathymetric profiles. This type of experiment helps to deal with hydrodynamic forcing developed by sand bars and to observe the corresponding pattern.

Theories of longshore currents have progressed much after the introduction of the radiation stress by **Longuet-Higgins (1972).** The theoretical achievements obtained have been considerable, but some assumptions were still crude and have needed comparison with accurate experimental data to evaluate the theoretical results and to establish guidelines for improving the theory. **Visser (1991)** undertake a detailed experimental study on longshore currents in a wave basin, with a pumped recirculation system and minimal return flows in the offshore region, with the currents being accompanied with longshore currents. The experimental results were presented for different wave fields, beach slopes and beach roughness. The wave-induced currents associated with cusped beaches are important for large scale horizontal mixing process. **Borthwick et al. (1997)** observed nearshore currents in a sinusoidal multicusped beach. Horizontal spatial patterns of the currents were determined by digital image analysis to show stable meandering longshore current.

The morphological behaviour of nearshore bars and the associated net sediment transport rates under the influence of wave action, wave and tide induced currents are poorly understood. **Grasmeijer and Van Rijn (1999)** showed that the physical processes related to sand transport under breaking waves over a nearshore bar and a series of flume experiments with an artificial sand bar, exhibited the importance of the mean and oscillatory sand transport along a barred profile and highlighted that the processes were very difficult to measure. **Mizuguchi and Horikawa (1976)** performed several laboratory experiments to observe the current system by changing parameters like d, T, H_0/L_0, H_i and showed that outside the breaker line the offshore current velocity decreased so that it might be reasonable to neglect the radiation stress in this region. The experimental results suggested that the wave current interaction had two aspects, one was the wave number interaction and the other was the energy coupling, which contributed to modifying the wave height distribution.

Beach profile evolution was examined in a Large-Scale Sediment Transport Facility (LSTF) by **Wang et al. (2003).** Unidirectional irregular waves were generated over

a fine sand beach and measurements of the waves, currents and sediment transport under spilling and plunging breakers were taken. This experiment demonstrated the mechanism of beach evolution and the process for shoreface equilibrium, which provided very useful information for other researchers.

2.5.3   Theoretical Investigations

The interaction between gravity waves and currents have attained increasing attention over the past three decades. A general understanding of mechanisms and processes governing the flow field in water waves in the surf zone is still an outstanding problem in fluid mechanics. Several theories have been proposed to make it possible to identify the characteristics of the flow. The works by **Longuet-Higgins and Stewart (1960)** showed the mechanism of radiation stress, which made it possible for proper theoretical determination of wave thrust, mean energy flux and energy dissipation.

A new qualitative picture of the breaking process was developed by **Basco (1985)**, presenting major features and patterns of motion of water waves just after breaking. He observed the patterns of spilling and plunger type breakers, where the overturning jets created a second surface disturbance distinctly separate from the original breaking wave. **Wu and Thornton (1986)** showed a direct method of solution for wave numbers of linear progressive waves with an explicit solution which had an accuracy better than 0.05%. Numerical examples proved that for a desired accuracy this method could save significant amounts of computing time.

Bishop et al. (1992) compared the empirical steady-state wave prediction method given in the Shore Protection Manual (1984) with measured wave data and with three other wave prediction formulae proposed by Sverdrup-Munk-Bretschneider, Jonswap and Donela and the 1977 SPM version. Results showed that the 1984 formula overpredicted the wave height and period and was the poorest predictor. Hence, the authors suggested modifications and revision to the original version. A coastal profile under combined action of cross-shore and longshore transport processes for oblique wave incidence was studied by **Elfrink and Deigaard (2000)**.

The bed shear stress and turbulence associated with longshore wave-driven currents was important for cross-shore circulatory flow and sediment transport and by including this interaction, the modelling of profile development and distribution of longshore currents was found to be more consistent.

Boussinesq-type equations have been commonly used to describe weakly nonlinear and dispersive wave propagation in shallow water. **Chen and Liu (1995)** re-derived the modified Boussinesq equations by Nwogu(1993a), as the major limitation was that this equation was only applicable to relatively shallow waters. They assumed the weak nonlinearity represented by the ratio of the wave amplitude to the water depth was of the same order of magnitude as the frequency dispersion, denoted by the square of the ratio of the water depth to wavelength. To investigate the interactions between current and non-linear shallow water wave, **Yoon and Liu (1986)** used the Boussinesq equations to derive the evolution equation for spectral wave components. The current intensity was assumed to be larger than the leading wave orbital velocity and smaller than the group velocity. **Schaffer et al. (1993)** solved the Boussinesq equations in a one dimensional model and extended their solution to describe conditions in the surf zone. This solution can represent the initiation and cessation of wave breaking over a bar, breaking point, wave setup etc.

Another type of wave equation has been derived by several authors which can take care of refraction and diffraction, but both factors together were first taken care of by **Berkhoff (1972)**. He derived a two-dimensional differential equation for combined refraction-diffraction for simple harmonic waves and also a method for solving this equation. The theory was restricted to irrotational linear harmonic waves and loss of energy due to friction or wave breaking was not accounted for. **Panchang et al. (1988)** obtained a method of solution for the combined refraction-diffraction equation over a large domain. This equation was modified to the reduced wave equation and the elliptic boundary value problem was solved by the marching or 'Error Vector Propagation' [EVF] method. The solution method was direct and eliminated computer storage problems associated with large matrices obtained in standard methods.

The propagation of periodic, small amplitude surface gravity waves over mild-slope can be described by the solution of the reduced wave equation with appropriate boundary conditions. **Radder (1979)** derived a parabolic equation in shoaling waters, with the approximation being made of splitting the wave field into transmitted and reflected components and the solution of this equation was undertaken using a finite difference algorithm. This parabolic equation can be applied to short period wave propagation in large coastal areas with complex bottom topographies. **Kirby and Dalrymple (1984)** verified that a parabolic equation for weakly non-linear waves based on the Stokes expansion, was capable of predicting accurate results for cusped caustics and there was a difference in the predictions for linear and non-linear models when applied to laboratory data.

The parabolic method for wave propagation proved to be very effective and a rapid method for calculation of the surface wave field for water of varying depths, including refraction and diffraction. **Dalrymple and Kirby (1988)** developed a wide-angle parabolic model to describe the diffraction of linear water waves for a bathymetry of parallel bottom contours by using the Fourier transform. **Kirby (1988)** applied the parabolic equation method [PEM] for surface wave propagation in a non-Cartesian co-ordinate system. The transformed governing equation led to a model whose results were in close agreement with laboratory data for the case of waves propagating into a breakwater type harbour. **Dalrymple and Kirby (1994)** examined the propagation of waves in curved channels of constant depth, which were annular in plan-form. The wave field within the channel was predicted by an analytic solution, a parabolic solution and spectral methods for a given wave height. All of the methods gave good results for narrow channels, but errors began to increase as the channel width increased.

The mild-slope equation is a vertically integrated refraction-diffraction equation used to predict wave propagation in a region with an uneven bottom and based on a mild bottom slope. **Booij (1983)** developed the mild slope equation and examined the accuracy of this equation as a function of the bottom slope. Several numerical experiments were carried out to check on the range of slopes for which the mild slope equation can be used. He found that for waves propagating parallel to the

depth contours accurate results were obtained even if the bottom slopes was of order 1, but for waves propagating normal to the depth contours the equation could only be used for a bottom inclination up to 1:3. **Madsen and Larsen (1987)** derived a differential equation where the stationary part was reduced to an elliptic mild slope equation as this approach reduce the computational effort of large model areas. The mild slope equation was preferable to use for wave induced currents in the surf zone as it reduced the computational effort involved in modelling.

Li and Anastasiou (1991) used the multigrid method to solve the elliptic form of the mild slope equation for water wave propagation over large areas and in the presence of currents. They also considered the effects of shoaling, refraction, diffraction and wave breaking. The governing equation was recast in terms of unknown variables, which varied slowly over a wavelength and thereby required fewer computational points per wavelength than full elliptic or hyperbolic solvers. **Yu et al. (1992)** extended the mild slope equation to simulate nearshore wave transformation including breaking. They summarised different boundary conditions with a physical background, and included the amplitude of the water surface elevation and its normal derivative. The set of equations were discretised using the finite element method and the computational results gave good agreement with the measured data.

2.6   Sediment Transport Processes

Most marine sediments are derived from the weathering of rock on land by the action of wind, water and ice, and under the influence of temperature, pressure and chemical reactions. The types of sediment that can be distinguished are: (a) lithogenous (quartz and clay mineral): entering the sea as discrete particles (e.g. boulders, stones, gravel, sand, silt and clay), (b) hydrogenous: sediments that are formed by precipitation from the sea-water (e.g. salt type sediments, manganese modules), and (c) biogenus: sediments that are formed by organisms (e.g. coral and shell sands).

Estuarine and coastal suspended sediment dynamics is a complex phenomenon, with the sediments in estuaries and coasts undergoing a series of processes such as erosion, deposition, advective and diffusive transport **(Lin and Falconer, 1996).** The rise and fall of the tide governs the magnitude of the oscillatory currents. During a tidal cycle the concentration of the suspended sediment in the turbidity maximum varies due to erosion and deposition, such that it is not simply the residual water circulation that causes sediment circulation **(Dyer, 1986).**

Sediment samples from beaches and shore faces exhibit different grain sized material, which may be interpreted as indicators of a certain mode of transport. Sediment can be transported by wind, wave, tide and density driven currents or by oscillatory water motion due to the deformation of short period waves under the influence of decreasing water depth and by a combination of currents and short period waves. In the surf zone sediment transport is dominated by waves, through wave breaking and wave induced currents in the longshore and cross-shore directions. The near bed oscillatory water motion and also the wave breaking processes bring large quantities of sand into suspension, which can then be transported as suspended load by tides, and wind and wave driven currents.

2.6.1 Tidal Effects on Sediment Transport Process

A conceptual model exhibiting the effects of a particular size of sediment on the transport rate of other sizes was proposed by **Misri et al. (1984)** and experimental measurements of the bed load transport rate of different fractions in a mixture were provided. The experimental data were analysed to show the accuracy of existing methods and a new proposed method for the computation of bed load transport. **Hu and Hui (1996)** showed that the mechanical characteristics of saltation of bed load transport for flowing water. Experiments had been carried out by means of high-speed photography and advanced data processing techniques to show the relation between magnitude of saltation parameters and flow intensity. **Ruhl et al. (2001)** described the spatial and temporal variations of suspended sediment concentrations (SSC) in San Francisco Bay, as affected by turbulence, semidiurnal tides, the spring-neap cycle, seasonal winds and freshwater flows. The authors produced a synthesis

of high resolution temporal SSC data, with aerial coverage of satellite imagery to provide the information needed to document the physical processes controlling the SSCs in the bay.

Teisson (1991) suggested that the prediction of movement of very fine sediments in coastal and estuarine waters was of major importance. The relative failure to gain accurate results might not come from the numerical techniques so much as the incomplete knowledge of basic processes, such as deposition, erosion and consolidation of cohesive sediments. The unsatisfactory predictions related to discrepancies between physical laws and prototype behaviour should be taken into serious consideration. **Falconer and Chen (1996)** described tidal floodplains as complex ecosystems serving as a meeting point between land and sea and an important source for coastal aquaculture, acting as a natural filter for suspended material and offer effective flood protection to low lying areas. The authors suggested that when a tidal floodplain need to be enhanced, restored or studied, it is very important to identify the most significant hydrodynamic, sediment flux and water quality processes at the site.

A theoretical and an experimental study to validate an asymptotic solution of the 2-D convection-diffusion equation for a depth integrated model of suspended sediment transport was undertaken by **Wang and Ribberink (1986)**. The theoretical study provided some parameters to validate the flow and sediment transport model and was in good agreement with experimental study. **Wang (1992a)** generalised the depth-integrated model for suspended sediment transport based on an asymptotic solution of the convection-diffusion equation, originally developed by Galappatti. The validity and applicability of the model was studied by analysing the convergence of the asymptotic solution and also the morphological behaviour of the model.

Lin and Falconer (1995) refined a boundary fitted finite-difference numerical model to predict 2-D depth-integrated tidal flows and extended this model to include sediment transport processes. The ULTIMATE QUICKEST scheme was used to solve the advective terms, the advection-diffusion equation for suspended sediment

transport. **Yoon and Kim (1995)** presented a quasi-3D hydrodynamic model capable of integrating the logarithmic velocity distribution and also incorporating the wake function by including the pressure gradient and bed roughness. The model computed the 3-D velocity field from the 2-D depth-integrated velocities.

Lin and Falconer (1996) described the development and application of a 3-D layer-integrated model to predict suspended sediment fluxes in estuarine and coastal waters. The finite difference technique was used to solve the equations of mass and momentum, and the operator-splitting technique was used to solve the transport equation for suspended sediments. **Mason et al. (1999)** presented an illustrative sediment transport measurements over a large dynamic intertidal area at a reasonable cost and for a spatio-temporal resolution. They used the waterline method, consisting of remote sensing and hydrodynamic modelling. Areas and volumes of deposition and erosion were measured in a study area in the UK for 5 years and tidal asymmetry was considered to be the dominant agent of the sediment movement, with waves being of secondary importance. **Wu and Shen (1999)** presented an in-depth study of estuarine sediment movement by applying the McLaren model in coastal areas with multiple sediment sources. This model was applied to calculate the sediment transport trends in south China and the results were in good agreement with the observed hydrodynamics.

Berg and Van (1993) tested three equilibrium sand transport formulae [Ackers and White (1973), Engelund and Hansen (1967) and Van Rijn (1984b)] to predict the suspended bed material transport rate in the Yellow River, China. The Van Rijn function produced the best results, with the Engelund-Hansen equation giving better results at low flow stages, and the Ackers-White formula overpredicting the measured values. Some modifications were proposed to the Van Rijn formula for flows over very fine sand and silt. **Patel and Ranga Raju (1996)** conducted extensive experiments on fractional bed load transport and analysed their data, as well as data available from other sources, for a wide range of flow conditions and sediment non-uniformity. An empirical relationship was proposed, incorporating several parameters which influence the bed load transport of non-uniform sediments.

The measuring techniques for coastal sediments in the field, which were categorised as total or suspension traps, tracers, optics, acoustics, impact, conductivity and radiation was investigated by **White (1998)**. The use of each method depends on different situation and reasons. Each technique had a unique history of development, theory of use, means of translating the data, advantages and limitations, problems during use and the solutions to these problems. The accuracy and cost of different methods was compared. The author showed that there was no systematic plan for correcting these measurement deficiencies which was certainly needed.

2.6.2   Wave and Current Effects on Sediment Transport Process

The ability to improve our knowledge of predicting the sediment transport rates of all physical parameters is important in coastal engineering practise. Wave induced longshore currents are assumed to be the result of a balance between a gradient of incident wave radiation stresses, a gradient of horizontal turbulent Reynold's stresses and bottom friction acting along the longshore current. These three balancing forces are parameterised in terms of easily measured macroscopic profiles of flow.

Huntly (1976) undertook experiments on a shallow beach with two component flowmeters to measure cross-shore and longshore currents along a line normal to the shoreline. The theories used to predict the longshore currents included a number of uncertainties, but mainly the parameterisation of the Reynolds stress, bottom friction and turbulence. The author suggested a new hypothesis for longshore currents with success. **Davies and Villaret (2000)** presented a model which included the 'wave related' component of the suspended sediment transport rate, the duration of transport where waves and currents were superimposed at some general angle of attack and the adaptability of the model to transport above rippled beds. The authors emphasised that the practical role of this research model was still probably to improve existing engineering formulations.

A knowledge of sediment transport due to wave action is required to understand the dynamic processes of nearshore morphology. Wave induced sediment transport is a complicated phenomenon particularly due to unsteady flow characteristics, and the presence of turbulence and interactions between the fluid flow and sediments. Progress in this study is depended upon appropriate theories. **Weggel and Perlin (1988)** highlighted a statistical method for of presenting the longshore transport environment for any coastal site in terms of six parameters. The total population was separated into two positive and negative transport processes, each of which was derived by a log-normal probability distribution. Among the six parameters, two were the mean and standard deviation that define the two log-normal distributions and fractions of time the transport was positive or negative.

Schoones and Theron (1994) investigated the accuracy and applicability of the SPM (Shore Protection Manual) formula which predicts the time averaged longshore sediment transport rate. This formula is possibly the most widely used and its accuracy is of prime importance. Several variations of this formula were tested against comprehensive data sets and guidance was given as to its use for coarse bed material. A number of methods from the SPM formula were used to compute the longshore sediment transport for waves and were then compared and correlated by **White (1994)** based on offshore wave gauges. White specified the circumstances under which an equation performed well, bad or moderate. The placement of wave gauges and the method of analysis were thought to increase the probability of obtaining good estimates of the longshore transport from directional wave data.

The ability to predict accurately longshore transport rates is essential for many coastal engineering applications. An analytical formula for longshore bed load sediment transport was derived by **Damgaard and Soulsby (1996)** based on the sediment physics and was therefore less dependent on calibration. This method was compared with the CERC 1977 formula, numerical model and field data results and a correction factor was introduced for the simplified assumptions made in the analytical formula. **Schoones and Theron (1996)** identified a universally applicable formula for longshore transport processes and tested it against a comprehensive data set. **Nakamura et al. (2000)** presented a method for evaluating nearshore waves,

currents and the cross-shore distribution of longshore sand transport rates for obliquely incident regular waves. They recommended improvements in the modelling of sediment transport processes under co-existent waves and currents.

The limited amount of high-quality field data available at present makes it difficult to introduce parameters that would be applicable to a wide range of wave and beach conditions. **Bayram et al. (2001)** evaluated the attributes of six well-known longshore sediment transport formulae against high quality hydrodynamic field data. Formulae by Bijker (1967), Engelund-Hansen (1967), Ackers-White (1973), Bailard-Inman(1981), Van Rijn (1984) and Watanabe (1992) were investigated as they were mostly widely used to calculate the time average net sediment transport rate in the surf zone. Van Rijn's formula was again found to yield the most reliable predictions over swell and storm conditions, with the Engelund-Hansen formula also being reasonably accurate.

The field investigation of longterm longshore transport rates is a complicated process. It might be useful to be able to predict the maximum rates over shorter time spans. **Seymour and Castel (1985)** measured nearshore directional waves several times a day during 1979-1982 at seven West Coasts sites in the USA. Time series of daily net longshore transport rates were estimated using the energy flux method. The evaluation of episodicity in a non-dimensional sense was found to be accurate in the study and might be useful for other studies. **Cheong et al. (1993)** showed the application of a probabilistic approach to estimating the sediment transport rate along the reclaimed shoreline of the coast of Singapore. Data were obtained by radioactive tracer experiments and it was found that the transport rate per unit transverse width of the beach was proportional to the effective depth of transport. **Ono et al. (1994)** presented a procedure to estimate the vertical diffusion coefficient and the reference concentration of the time averaged suspended sediment concentration by waves and currents based on experimental results. Few studies have been undertaken on the non-equilibrium suspended sediment concentrations due to currents superposed on waves. These studies have shown that the non-dimensional diffusion coefficient, normalised by the product of the shear velocity and the equivalent roughness, were closely related to Shield's number.

The average values for the breaker height and angle for different months of a year and the littoral drift for the Madras coast were computed by **Prasad and Reddy (1988)**. They outlined the geomorphological changes due to construction of a harbour along the coastline and the various factors for the annual and seasonal sedimentary patterns around the harbour based on surveys. **Van Rijn and Kroon (1992)** presented a mathematical and experimental sediment transport modelling process for the coastal environment. The convection-diffusion equation for suspended sediment particles was used to compute the vertical distribution of the time-averaged concentrations. They showed that the current velocity hardly affected the near bed sediment concentration when the wave motion was dominant and the sediment concentrations were maximum when the waves were directed normal to the current. **Briand and Kamphuis (1993)** presented a promising approach to sediment transport calculations in the nearshore area, in which quasi 3-D velocities and local vertical distributions of suspended sediment concentrations were combined.

A numerical investigation was presented by **Savioli (1998)** to predict sediment transport rates under combined wave-current flows. This complex mechanism was simplified into ideal cases as pure waves and pure currents. The predictions of the model showed good agreement with the experimental measurements. **Li and Shibayama (2000)** proposed a numerical method for the computation of longshore currents based on the Boussinesq equation. The method was tested against the laboratory data of longshore currents of Visser (1991) and showed good agreement. The effects of side boundary conditions on the longshore currents were discussed and a method to handle the side boundaries to obtain uniform longshore distributions was proposed.

2.7   Numerical Model Studies

A numerical model is a tool used to describe a physical process in a rational way, with the help of a series of mathematical formulations. Numerical models are used to simulate and predict the behaviour of any physical process to a certain level of

accuracy. With respect to coastal models, such tools represent the basic hydrodynamic and sediment transport processes. In recent years a range of useful numerical model concepts have been developed, which can be classified in two categories, namely: process related models and behaviour related models. The main objective of coastal morphological modelling is the large scale and long-term behaviour of morphological features and systems in relation to human interference or any physical process (such as climate change, high sediment discharges from rivers, salinity levels, or wind, wave, or tidal effects). Long term morphological changes are the result of a sequence of erosional and depositional events due to variations in some or all of these physical processes.

In predicting wave behaviour in coastal regions, numerical wave propagation models are now commonly used in engineering practise. The physical processes usually accounted for in such wave models are shoaling, refraction and diffraction. Various approximations can be derived from the well-known mild slope equation, in which refraction and diffraction effects are both modelled. Because of the elliptic nature of this equation the numerical solution is quite involved. Neglecting diffraction in the mild slope equation results in the wave ray (geometric optics) approximation. An intermediate case is obtained by neglecting diffraction in the main wave propagation direction only and maintaining it in the transverse direction; this results in the so-called parabolic approximation.

2.7.1 Modelling Tidal Currents

Falconer (1991) highlighted the limitations and restrictions of both physical and numerical hydraulic models to predict hydrodynamic parameters. **Chapalain and Thais (2000)** showed their concern while modelling fluid and suspended sediment dynamics in a tide-dominated environment and described the process as a very complex one which needs careful modelling. They used a one-dimensional vertical model driven by an oscillatory horizontal pressure gradient, which was derived from a two-dimensional vertically integrated tidal model. A series of advection-diffusion equations were used to evaluate the concentration distribution of suspended sediments of different size.

Ten methods for simulating wetting and drying in implicit 2-D shallow water flow models were tested by **Balzano (1998)**. The comparison showed that the criteria for declaring a cell wet or dry had a significant effect on the effective retention storage of the basin. By considering all of the methods it was possible to advance one grid at a time, which is a severe limitation when dealing with extremely flat areas where further research is needed. **de Vriend et al. (1993)** discussed the development of long-term coastal modelling where data reduction and empirical modelling are vital to link with real-life coastal behaviour. According to de Vriend there are two sources of knowledge in coastal dynamics, one based on physical principles, mainly short and medium term processes, and the other is based on field observations, which includes the long term behaviour.

The development of an inverse model for application to coastal problems was described by **Copeland and Bayne (1998)** because the required types of data were available from remote sensing measuring techniques. A direct minimisation solution was used to employ conjugate gradient descent and 2-D steady cases show the model's ability to accommodate different topographies. **Gorman and Neilson (1999)** described an experiment to measure wave growth in an estuary with extensive intertidal flats. The SWAN third-generation spectral model was used to simulate wave transformation with south-westerly winds, and also incorporating refraction by currents. Measured wave spectra compared with model results and showed that the bed friction and exponential growth of wind played a dominant role.

Prandle et al. (2000) monitored the dynamics of sediment distributions in the vicinity of a rapidly eroding coastline. The modelling components were tide and surge currents, wave evolution, and the vertical distribution of turbulence and the resulting spatial pattern of sediment transport in this region. Simulations of tidal currents confirmed the accuracy of such models. **Zhang and Gin (2000)** described the development and application of a 3-D multi level hydrodynamic and tidal model in Singapore's coastal waters. A two step Euler predictor-corrector approach was introduced to predict and correct the free surface water elevation. The current circulation, time history of sealevel, discharge and residual currents were all predicted.

The use of boundary fitted curvilinear grids in hydrodynamic model have been undertaken for estuarine currents, one such study was reported by **Bao et al. (2000).** This kind of grid fit to the coastline and bathymetry and makes the kinetic boundary condition simple and much more accurate. This method is effective for coastal regions where the current is usually impractical to solve for using a uniform Cartesian grid system with the shoreline and bathymetry represented by numerous stair-steps. **Lin and Falconer (2001)** outlined a three dimensional layer integrated model to predict tidal currents and water quality in coastal, estuarine and inland waters. They used a finite difference algorithm to solve the three-dimensional mass and momentum conservation equations and the advective-diffusion equation was used to describe a wide range of water quality parameters.

Modelling tides on a regional scale allows tidal propagation and interaction along the coast to be more accurately represented according to **Myers and Baptista (2001).** A regional model can act as a liaison between open ocean dynamics and physical processes more pertinent to coastal systems. **Naidu and Sarma (2001)** applied a 2-D numerical model to a funnel shaped semi-enclosed water body in India. Tide induced currents and amplitudes were observed and it was shown that at high tide the agreement in phase was good. They can show different behaviour of the estuary with this study. **Sankaranarayanana and McCay (2003)** applied a three-dimensional hydrodynamic model to the world's highest tidal range occurring in the Bay of Fundy. A very fine resolution grid and a moderate grid mesh were used and the predicted surface elevation, amplitude and phase values compared well with observations.

Ozer et al. (2000) developed a generic module tool, which combined the modelling of tides, surges and waves in shallow waters in the North Sea. The existing operational model has been adapted to account for interactions between the various processes and to implement in a coupling framework. The increasing importance of coupling when going towards shallower areas had been investigated by the author and further developments of generic models was discussed. **Mason and Garg (2001)** described the construction of a morphodynamic model for an intertidal region in England and its calibration and validation using extensive sediment volume

change data measured by remote sensing. A properly validated sediment transport model is of great importance for coastal defence, management and economic purposes. The morphodynamic model consisted of a set of linked modules to predict the 2-D depth averaged tidal currents, waves, sediment transport rates and sediment budgets. The intertidal bathymetry was updated at regular intervals and the currents, waves and sediment transport patterns were re-computed using the bathymetry.

2.7.2 Modelling Waves

In the last three decades, rapid progress has been made in modelling nearshore hydrodynamic processes using numerical techniques. The prediction of nearshore waves entered a new dimension with the introduction of the mild-slope equation by **Berkhoff (1972)** and progressed with more computational techniques by **Noda (1974), Radder (1979), Ebersole (1985), Yoo and O'Connor (1986)** and other researchers. The development and application of numerical models has been undertaken by many researchers and some of this works is described in the following paragraphs. **Lee and Wang (1992)** evaluated five numerical wave-current interaction models in a 2-D domain through mutual comparisons. The performance of each model was evaluated with respect to some bench mark cases and the compared results showed no single model clearly outperformed the others. The selection of a model for application depended totally on the intended purpose of the user and the author presented a useful guideline for model selection.

A numerical method to obtain wave patterns in a region of arbitrary shape was presented by **Ito and Tanimoto (1972)**. The linearised wave equations under given boundary conditions were solved and the model applied first to find the wave height distribution along a semi-infinite detached breakwater for wave diffraction. The model was then applied to predict wave refraction around a submerged shoal, with concentric circular contours, and with the model giving satisfactory results. **Liu and Tsay (1984)** developed a model to calculate the transformation and propagation of Stokes wave, which varied in the direction of wave propagation and with the assumptions of water depth varying slowly. The author suggested the relaxation of

the requirement of a small bottom slope compared with the wave slope and an extension of this theory for shallow water regimes.

A simple explicit numerical model suitable for personal computers was proposed by **Dalrymple (1988)** which provided the refraction and shoaling of linear and non-linear water waves over irregular bathymetries and wave current interactions. The model results were independent of the step size and the model was able to obtain wave heights and directions at grid points where Snell's law is valid. **Borthwick and Joynes (1989)** considered the relative merits between an implicit and explicit scheme to solve the mass and momentum equations governing wave-current interactions. These models were validated by data from wave basin experiments and showed that an ADI method had significant computational advantages over the explicit method.

A model for the shoaling and refraction of an incident directional spectrum over a beach topography that varied only in the on-offshore direction was developed by **Kirby (1990)**. The advantage of using this model was that there was no restriction on the angle of incidence with respect to the shore normal direction. **Briand and Kamphuis (1993)** developed a PC based quasi 3-D model to calculate the wave climate and wave induced currents. Its application was restricted to beaches without sharp bathymetric gradients in the longshore direction, as diffraction was neglected.

A horizontal 2-D numerical model to predict the time dependent free surface elevation and fluid velocities in swash and surf zones under obliquely incident waves was developed by **Kobayashi and Karjadi (1994)**. The assumption of shallow water waves with small incident angles were made to reduce computational efforts and eliminate difficulties with lateral boundary conditions. **Pechon and Teisson (1994)** presented a numerical model for time averaged 3-D currents due to breaking waves. The driving term in the momentum equations were the radiation stresses derived from organised velocity of waves and roller contributions. **Nielson and You (1996)** developed a model for the Eulerian time mean velocities in combined wave-current flows which could handle very weak currents, and where their influence on the wave motion was negligible. The measurements of stronger

currents were also obtained by modification of the Reynolds stresses, which influenced the current impact on the wave motion.

Different time dependent quasi-3D models were developed by **Karjadi and Kobayashi (1996), Kobayashi, Karjadi and Johnson (1997)** to predict the temporal and cross variations of the free surface elevation and fluid velocities in the surf and swash zones under obliquely incident waves. The former model included the dispersion due to vertical variations in the instantaneous horizontal velocities and was an extension of an earlier 2-D model developed by the same authors. The later model was for obliquely incident shallow water waves, with small incident angles to elucidate the dispersion effects due to vertical variations in the instantaneous horizontal fluid velocities. The equations for cross-shore continuity, momentum and momentum flux corrections were solved numerically to predict the water depth and cross-shore depth averaged velocities and the near bottom velocities. **Sanders (2002)** implemented non-reflecting boundary conditions in a finite-volume based shallow water model. There has been a growing interest in finite-volume based schemes in recent years and this method has proven useful in coastal applications such as long wave run-up on a beaches and tidal inundations of wetlands.

Based on different wave theories, several methods of modelling have been proposed. There are relative merits and demerits of each model but it is important to visualise the physical mechanism involved in applying the model correctly. A modelling system to generate and run predictions for short period waves of any form, with any physically realistic current field and for any bathymetry, was developed by **Abbot et al. (1978)**. The system generated model was based on the Boussinesq equations, with the vertical velocity increasing linearly from zero at the bed to a maximum at the surface, and for two independent variables in space and time. **Karambas and Koutitas (1992)** proposed a wave propagation model based on the Bossinesq equations which were valid in both the shoaling and breaking regions. A dispersion term was introduced to simulate the Reynolds stresses, which simulate the deformation in the surf zone and the turbulence dissipation conditions during breaking.

There are many wave models based on refraction-diffraction theory and one of the models for linear water waves was developed by **Lozano and Liu (1980)**, based on the parabolic approximation. The main assumption in this model was to vary the water depth very slowly so that the model equation described the forward-scattered wavefield. This model worked well against combined wave refraction and diffraction by a semi-infinite thin barrier installed on a uniformly sloping bottom, with wave convergence over a stepped bottom. **Berkhoff et al. (1982)** verified three numerical models indicated as the refraction model, the parabolic refraction-diffraction model and the full refraction-diffraction model, against measurements from a hydraulic scale model. The models were based on the theory of simple harmonic linear water waves. From the results it was shown that the physical processes of wave propagation and deformation by a shoal were best described by complete refraction-diffraction equations.

Yoo and O'Connor (1986) presented a mathematical model to describe wave induced nearshore circulation by including: refraction, diffraction, wave-induced currents, set-up and set-down, mixing processes and bottom friction effects on both waves and currents. They refined the classical ray model to include the effects of diffraction and current interaction and the new ray model was able to deal with large or small scale areas involving coastal structures. **Gao and Radder (1998)** used a numerical model for wave refraction and diffraction to compute irregular waves. The model was based on parabolic approximations but when it was combined with the perfect boundary condition it was also suitable for waves propagating with large incident angles. Irregular waves were modelled through the linear superposition of wave components.

The establishment of a parabolic approximation in water wave theory gave the opportunity to explore the wave field more clearly and several numerical models have been developed based on this approximation. A parabolic wave model for combined refraction-diffraction of monochromatic linear waves was developed by **Dalrymple et al. (1984) and** included a term for the dissipation of the wave energy. The parabolic model of Radder (1979) was modified here to include energy dissipation and the coefficient of the dissipation term was related to a number of

dissipative models. **Kirby and Dalrymple (1986)** developed a semi-empirical model for surf zone wave height decay, which was adapted to the parabolic equation method to include the effects of depth limited wave breaking. A 'thin film' model was developed to predict wave heights in the vicinity of an island without the computational necessity of including internal boundary conditions in the model.

Tsay et al. (1989) applied a parabolic approximation to the mild-slope equation with a boundary fitted curvilinear co-ordinate system to describe wave propagation. The numerical model was used to compute wave propagation near an irregular shoreline and examples demonstrated the capability of the numerical model. **Kirby et al. (1994)** provided an adequate foundation for the application of small and large angle parabolic approximations in distorted grids which were related to Cartesian space by a conformal transformation. The grids of these model types were desirable, since the scaling aspects of the resulting parabolic models were well understood.

A numerical model for wave propagation in circular jettied channels was presented by **Melo and Gobbi (1998)**. The model combined a polar co-ordinate parabolic equation with a model for wave propagation in jettied channels. The effects of the jetties on the wave field within a circular jettied channel were discussed. **Johnson and Poulin (1998)** investigated the errors in parabolic equation models (PEM) for wave refraction and diffraction by examining the case of waves propagating over a planer bathymetry, for which the analytical solution was established. The models investigated the lowest order parabolic approximation, such as Pade approximation and minimax approximation models. The errors in wave height, direction, radiation stresses and the resulting longshore current were investigated analytically and by numerical tests using the parabolic equation model MIKE 21 PMS. The results showed that the predicted wave directions were generally accurate, but that the wave height, radiation stresses and longshore currents could contain significant errors, depending on the parabolic approximation used.

Li (1994) efficiently and economically solved a linear system of the mild slope equation for pure wave propagation and using the generalised conjugate gradient

method. The model had a fast convergence rate, relatively small storage requirements and was easy to apply in complicated non-rectangular regions. **Kirby et al. (1994)** applied the time dependent form of the mild slope wave equation to the propagation of regular and irregular wave trains over variable bathymetries. Linear and non-linear versions of the model were applied to Berkhoff's shoal. The non-linear model gave better results than the linear model.

2.8 Summary

The investigation of previous work on the specific field of estuarine sediment transport and nearshore circulation has shown that this is a field of very complex natural processes, which are sensitive to changes in any hydrodynamic parameters. Several researchers have been working to solve different problems in this field and by thorough investigation of the different fields of work and their solutions outlined in this chapter, a consistent gap has been established which need to be explored. The gap is to have an interactive wave-current model which can be applied to large estuarine area for tidal condition and also can be applied to the nearshore area for wave induced flow circulation. The tidal effect in estuarine waters has been investigated and there are numerical models to predict the hydrodynamic behaviour and their corresponding sediment transport. The nearshore circulation processes due to wave current generation and wave breaking can be predicted by numerical models. The establishment of a numerical model which can be applied to predict both estuarine circulation process and nearshore circulation has therefore been highlighted as the primary objective of this research project.

CHAPTER 3

GOVERNING EQUATIONS OF FLUID FLOW

3.1 Introduction

The flow of any fluid is subject to certain fundamental laws of physics and these laws are essential in order to develop the governing equations of fluid flow. The fundamental equations of fluid dynamics are based on the laws of:

1. conservation of mass;
2. conservation of momentum;
3. conservation of energy.

The laws of fluid dynamics can be formulated in many ways. In order to predict the flow of a fluid, it is essential to develop a set of governing mathematical equations to formulate a model. The behaviour of a natural physical system (here a fluid flow system) can be thoroughly described and determined by the above conservation laws. Thus the motion of fluid and sediment particles can be described completely by the conservation laws, with the help of three basic properties of mass, momentum and energy (Hirsch, 1988). So a numerical model basically depends upon a system of governing equations, which in turn depend themselves on the conservation laws. Therefore, the governing equations of fluid flow, sediment transport, wave motion and bed level changes can be evaluated with the help of these conservation laws. The governing equations for a general hydrodynamic model which will be able to

predict the flow and sediment transport in shallow water systems, i.e. mainly estuarine and nearshore flow systems, will be derived in this chapter with the basic and appropriate approximations also being considered.

The fluid flow properties, mainly the velocity and depth, and the sediment transport and bed level changes, wave height and wave angle are the parameters which were to be predicted in this study. So at any instant of time, the velocity field, sediment concentration, wave height, wave angle and bed level changes needed to be predicted at any point within a hydrodynamic domain system. During the process of determining these parameters, correct information was required about the behaviour of the fluid and sediment particles, namely the fluid density, sediment particle density, viscosity etc.

3.2 General Form of the Conservation Laws

The principles of the conservation of fluid flow were initially developed for solid bodies and then introduced to the fluid flow system, with the basic assumptions unchanged. These principles state that the variation of a conserved flow quantity in an arbitrary volume is caused by the net effect of internal sources or sinks and the flux of the quantity crossing the boundary surface of that volume (Hirsch, 1988). For a fluid flow these quantities are mainly scalar, and vector quantities such as the mass and momentum. The different conservation laws can be described as (Chadwick and Morfett, 1998):

1. The law of conservation of matter stipulates that matter can neither be created nor destroyed, though it may be transformed by any process. Since this study of mechanics of fluids excludes chemical activity from consideration, the law reduces to the principle of conservation of mass.

   Figure 3.2.1 represents a fixed region within the flow and according to conservation of mass (Massey, 1997).

Rate at which mass enters the region = Rate at which mass leaves the region + Rate of accumulation of mass in the region
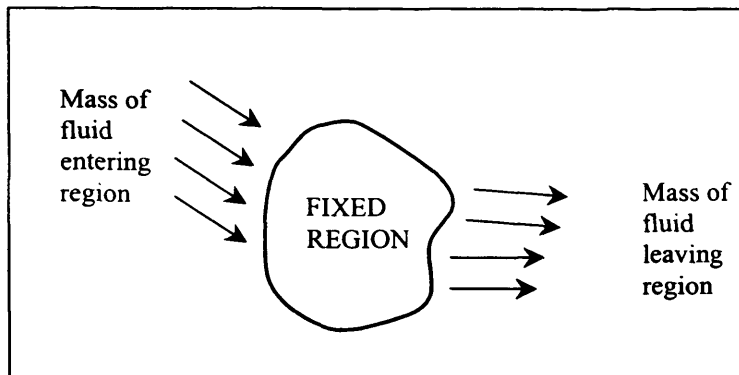
Figure 3.2.1 Representation of conservation of mass.

2. The basic equation for the law of conservation of energy may be derived from the First Law of Thermodynamics. One of the fundamental generalizations of science is that, in the absence of chemical reactions, energy can be neither created nor destroyed. Energy can be transformed from one form to another, but none is actually lost.

The principle states that, for any mass system (that is, any identified and unchanging collection of matter) the net heat supplied to system equals the increase in energy of the system plus all the energy that leaves the system as work is done (Massey, 1997).

3. The law of conservation of momentum states that a body in motion cannot gain or lose momentum unless some external force is applied. The classical statement of this law is Newton's second law of motion, which states that the net force acting on a body in any fixed direction is equal to the rate of increase of momentum of the body in that direction.

In mathematical terms, this may be expressed as:

Force = Rate of Change of Momentum.

3.3   Hydrodynamic Equations

The governing equations of fluid motion can be derived by the conservation of mass and momentum. The full derivation of the governing equations was given by Schlichting (1987) for an incompressible turbulent flow on a rotating earth. These equations are time averaged and can be depth integrated. The purpose of time averaging is to remove temporal fluctuations due to turbulence and in order respects, waves. The resultant velocity is considered as a sum of a time dependent mean flow, a wave-induced flow and an arbitrary fluctuating component.
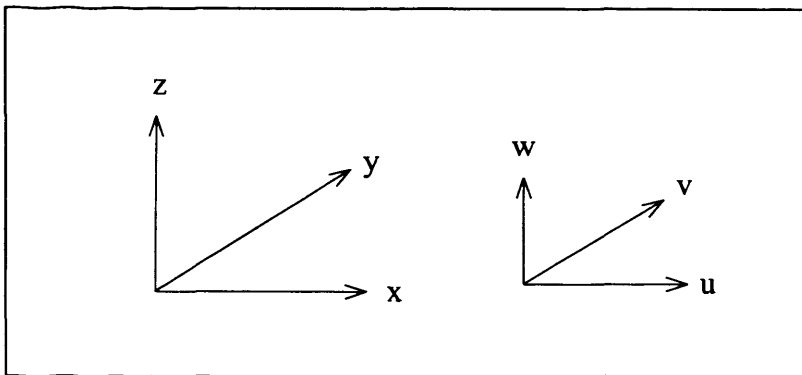
Figure 3.3.1 Cartesian co-ordinate system

The Governing Equations of fluid flow in coastal and estuarine waters, with particular reference to the flow associated with tidal force or wave propagation will be established in this chapter. The corresponding equations are based on the conservation laws of mass (continuity equation) and momentum equation (Newton's second law of motion), with the required unknown variables being the water elevation above datum η, the velocity components u, v, w as shown in Figure. 3.3.1.

3.3.1   Conservation of Mass

In deriving the continuity equation for three dimensional unsteady flow, an infinitesimal control volume of sides Δx, Δy, Δz is considered, with the velocity components being u, v, w at the centre of the control volume and with all derivatives

being assumed known at this point. The depth integrated two-dimensional continuity equation will be derived from this equation. By applying Taylor's series defined for some fluid characteristics φ (e.g. velocity, pressure etc) in the x-direction as:

$$\phi\left(x\pm\frac{\nabla x}{2}\right)=\phi(x)\pm\frac{1}{2}\left[\frac{\partial\phi(x)}{\partial x}\frac{\nabla x}{1!}\right]+\frac{1}{4}\left[\frac{\partial^2(x)}{\partial x^2}\frac{\nabla x^2}{2!}\right]\pm\frac{1}{8}\left[\frac{\partial^3(x)}{\partial x^3}\frac{\nabla x^3}{3!}\right]+\ldots\ldots \qquad (3.3.1)$$

and assuming that terms higher than third order, ie. $O(\nabla x^3)$, are small for the flow field, then the mass fluxes per unit area in the x-direction for the control volume are shown in Figure 3.3.2. The similar mass flux components can be expressed for the y and z-directions respectively.

For flow in the x-direction, the mass influx across side ABCD in the interval Δt is given as

$$M_{in_x}=\left[\rho u-\frac{\partial\rho u}{\partial x}\frac{\Delta x}{2}\right]\Delta y\Delta z\Delta t \qquad (3.3.2)$$

where ρ = fluid density or mass/unit volume of fluid, the mass afflux across side EFGH in time interval Δt is given by

$$M_{out_x}=\left[\rho u+\frac{\partial\rho u}{\partial x}\frac{\Delta x}{2}\right]\Delta y\Delta z\Delta t \qquad (3.3.3)$$

so the resulting net x-direction mass flux is given as

$$M_{net_x}=M_{in_x}-M_{out_x}=-\frac{\partial\rho u}{\partial x}\Delta x\Delta y\Delta z\Delta t \qquad (3.3.4a)$$

Similar expressions can be obtained for the y and z-directions as

$$M_{net_y}=-\frac{\partial\rho v}{\partial y}\Delta x\Delta y\Delta z\Delta t \quad\text{and}\quad M_{net_z}=-\frac{\partial\rho w}{\partial z}\Delta x\Delta y\Delta z\Delta t \qquad (3.3.4b)$$

Therefore the net mass acoss the control volume can be expressed as

$$\text{Net Mass Influx}=-\left[\frac{\partial\rho u}{\partial x}+\frac{\partial\rho v}{\partial y}+\frac{\partial\rho w}{\partial z}\right]\Delta x\Delta y\Delta z\Delta t \qquad (3.3.5)$$
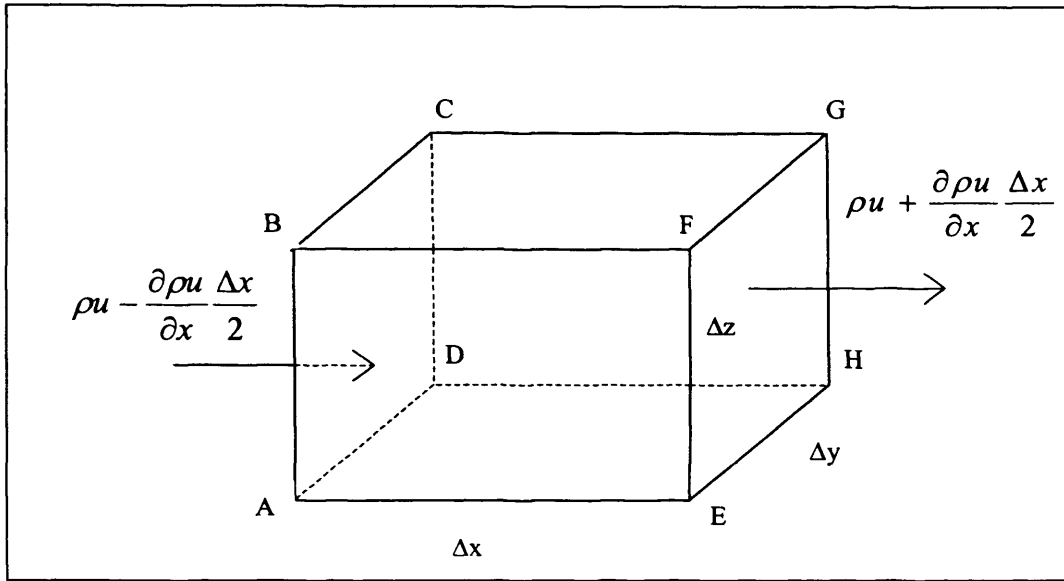
Figure 3.3.2   Flow into and out of control volume

For the corresponding change of mass within the control volume, if the fluid elemental mass at time t is given by $\rho\Delta x\Delta y\Delta z$, then Taylor's series gives for the mass at time $(t+\dfrac{\Delta t}{2})$ and $(t-\dfrac{\Delta t}{2})$ respectively

$$M_{\left(t+\frac{\Delta t}{2}\right)} = \rho\Delta x\Delta y\Delta z + \frac{\partial}{\partial t}(\rho\Delta x\Delta y\Delta z)\frac{\Delta t}{2} \qquad (3.3.6)$$

$$M_{\left(t-\frac{\Delta t}{2}\right)} = \rho\Delta x\Delta y\Delta z - \frac{\partial}{\partial t}(\rho\Delta x\Delta y\Delta z)\frac{\Delta t}{2} \qquad (3.3.7)$$

Hence the net mass increase in time Δt can be expressed as

Net Mass Increase, $M_{\Delta t} = \dfrac{\partial}{\partial t}(\rho\Delta x\Delta y\Delta z)\Delta t$ $\qquad (3.3.8)$

Equating the net mass influx (equation 3.3.5) with the net mass increase within the control volume in time Δt (equation 3.3.8) gives the three dimensional continuity equation.

$$\frac{\partial}{\partial t}(\rho\Delta x\Delta y\Delta z)\Delta t = -\left[\frac{\partial\rho u}{\partial x} + \frac{\partial\rho v}{\partial y} + \frac{\partial\rho w}{\partial z}\right]\Delta x\Delta y\Delta z\Delta t$$

The general form of the three dimensional conservation of mass equation is-

$$\frac{\partial \rho}{\partial t} + \frac{\partial \rho u}{\partial x} + \frac{\partial \rho v}{\partial y} + \frac{\partial \rho w}{\partial z} = 0 \qquad\qquad (3.3.9)$$

This equation applies for all types of flow such as steady, unsteady, laminar, turbulent compressible or incompressible flow.

Then the time averaged continuity equation for an incompressible flow of fluid in an orthogonal Cartesian co-ordinate system, equation (3.3.9) reduces to (Falconer, 1993):

$$\frac{\partial u}{\partial x} + \frac{\partial v}{\partial y} + \frac{\partial w}{\partial z} = 0 \qquad\qquad (3.3.10)$$

where $u, v, w = fn(x, y, z, t)$ and are time averaged velocity components in the x, y, and z-direction respectively. Equation (3.3.10) can be written for each fluid element in the computational domain.

3.3.2 Conservation of Momentum

In considering the momentum equations for three dimensional unsteady flow, Newton's second law of motion states that the sum of the external forces acting on a unit mass must equal the rate of change of linear momentum, that is-

$$\sum \vec{F} = \frac{d(m\vec{V})}{dt} = m\frac{d\vec{V}}{dt} + \vec{V}\frac{dm}{dt} \qquad\qquad (3.3.11)$$

where F = resultant force, m = mass and V = velocity. For incompressible flow it can be considered that the rate of change of mass with time can be neglected, therefore equation (3.3.11) reduces to:

$$\sum \vec{F} = m\frac{d\vec{V}}{dt} \qquad\qquad (3.3.12)$$

This equation can now be expanded by considering the force components illustrated for the infinitesimal control volume of sides Δx, Δy, Δz shown in Figure 3.3.3. Using the notation that the first subscript defines the plane normal to the direction indicated by the subscript and the second subscript defines the stress direction on the plane,

then the x-direction forces on the fluid element include the shear stress components τ_{yx} and τ_{zx}, the normal stress component σ_{xx} and the body force per unit mass X. If the elemental volume is assumed to remain constant, then application of Equation (3.3.12) to the control volume gives:

$$\rho\Delta x\Delta y\Delta z\frac{du}{dt} = \rho X\Delta x\Delta y\Delta z + \frac{\partial\sigma_{xx}}{\partial x}\Delta x\Delta y\Delta z + \frac{\partial\tau_{yx}}{\partial y}\Delta x\Delta y\Delta z + \frac{\partial\tau_{zx}}{\partial z}\Delta x\Delta y\Delta z \qquad (3.3.13)$$

When a fluid is at rest, there are only normal components of stress acting on the surface resulting in the internal force of:

$$\sigma_{xx} = -P_h; \qquad \sigma_{yy} = -P_h; \qquad \sigma_{zz} = -P_h \qquad (3.3.14)$$

where P_h is the pressure and the negative sign introduced to indicate that the normal components of stress are tension rather than compression. Schlicting (1987) explains that while the fluid is in motion, then viscosity causes additional components of stress. The normal stresses defined above become unequal and shear stresses develop. So for a moving fluid, the tensile fluid stress can be split into (i) a hydrostatic pressure component (P_h) that would have exist if the fluid were at rest and (ii) a part σ' due to fluid motion alone, giving:

$$\sigma_{xx} = \sigma'_{xx} - P_h; \qquad \sigma_{yy} = \sigma'_{yy} - P_h; \qquad \sigma_{zz} = \sigma'_{zz} - P_h \qquad (3.3.15)$$
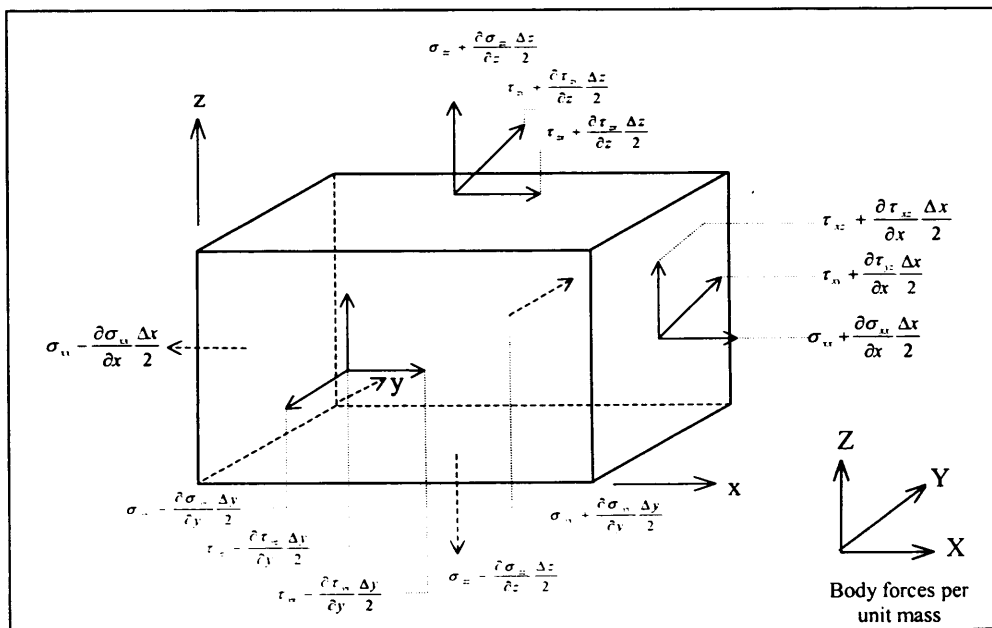
Figure 3.3.3 Forces/stresses acting on a fluid element or control volume

Substituting Equation (3.3.15) in (3.3.13) and dividing by $(\rho \Delta x \Delta y \Delta z)$ gives the momentum equation in the x-direction for laminar or turbulent flow as:

$$\frac{du}{dt} = X - \frac{1}{\rho}\frac{\partial P}{\partial x} + \frac{1}{\rho}\left[\frac{\partial \sigma_{xx}'}{\partial x} + \frac{\partial \tau_{yx}}{\partial y} + \frac{\partial \tau_{zx}}{\partial z}\right] \qquad (3.3.16)$$

However, for three dimensional unsteady flow $u = fn(x,y,z,t)$ and the total acceleration can be decomposed into its local and advective components, as follows:

$$\frac{du}{dt} = \frac{\partial u}{\partial t} + \frac{\partial u}{\partial x}\frac{dx}{dt} + \frac{\partial u}{\partial y}\frac{dy}{dt} + \frac{\partial u}{\partial z}\frac{dz}{dt} = \frac{\partial u}{\partial t} + u\frac{\partial u}{\partial x} + v\frac{\partial u}{\partial y} + w\frac{\partial u}{\partial z} \qquad (3.3.17)$$

Including the above equation (3.3.17) in equation (3.3.16) gives:

$$\left(\frac{\partial u}{\partial t} + u\frac{\partial u}{\partial x} + v\frac{\partial u}{\partial y} + w\frac{\partial u}{\partial z}\right) = X - \frac{1}{\rho}\frac{\partial P}{\partial x} + \frac{1}{\rho}\left[\frac{\partial \sigma_{xx}'}{\partial x} + \frac{\partial \tau_{yx}}{\partial y} + \frac{\partial \tau_{zx}}{\partial z}\right] \qquad (3.3.18)$$

For a Newtonian fluid, these viscous stresses (σ'_{xx}) are proportional to the rates of deformation. The three dimensional form of Newton's law of viscosity for compressible flows involves two constants of proportionality; the first viscosity is called the dynamic viscosity μ, relating stresses to linear deformations, and the second viscosity, λ, relating stresses to volumetric deformation. The effect of second viscosity λ is small in practice and can be approximated by taking $\lambda = -2/3\mu$ (from Schlichting, 1987). Hence the nine viscous stress components, of which six are independent, can now be defined as:

$$\sigma_{xx}' = 2\mu\frac{\partial u}{\partial x} + \lambda\left(\frac{\partial u}{\partial x} + \frac{\partial v}{\partial y} + \frac{\partial w}{\partial z}\right) = \mu\left[2\frac{\partial u}{\partial x} - \frac{2}{3}\left(\frac{\partial u}{\partial x} + \frac{\partial v}{\partial y} + \frac{\partial w}{\partial z}\right)\right] \qquad (3.3.19)$$

$$\sigma_{yy}' = 2\mu\frac{\partial v}{\partial y} + \lambda\left(\frac{\partial u}{\partial x} + \frac{\partial v}{\partial y} + \frac{\partial w}{\partial z}\right) = \mu\left[2\frac{\partial v}{\partial y} - \frac{2}{3}\left(\frac{\partial u}{\partial x} + \frac{\partial v}{\partial y} + \frac{\partial w}{\partial z}\right)\right] \qquad (3.3.20)$$

$$\sigma_{zz}' = 2\mu\frac{\partial w}{\partial z} + \lambda\left(\frac{\partial u}{\partial x} + \frac{\partial v}{\partial y} + \frac{\partial w}{\partial z}\right) = \mu\left[2\frac{\partial w}{\partial z} - \frac{2}{3}\left(\frac{\partial u}{\partial x} + \frac{\partial v}{\partial y} + \frac{\partial w}{\partial z}\right)\right] \qquad (3.3.21)$$

$$\tau_{xy} = \tau_{yx} = \mu\left(\frac{\partial v}{\partial x} + \frac{\partial u}{\partial y}\right) \quad ; \quad \tau_{yz} = \tau_{zz} = \mu\left(\frac{\partial v}{\partial z} + \frac{\partial w}{\partial y}\right) \quad \tau_{zx} = \tau_{zx} = \mu\left(\frac{\partial w}{\partial x} + \frac{\partial u}{\partial z}\right) \quad (3.3.22)$$

Substituting equations (3.3.19) and (3.3.22) in equation (3.3.18) gives the Navier-Stokes equation for compressible flow in the x-direction:

$$\frac{\partial u}{\partial t} + u\frac{\partial u}{\partial x} + v\frac{\partial u}{\partial y} + w\frac{\partial u}{\partial z} = X - \frac{1}{\rho}\frac{\partial P}{\partial x} + v\left[\frac{\partial^2 u}{\partial x^2} + \frac{\partial^2 u}{\partial y^2} + \frac{\partial^2 u}{\partial z^2}\right] + \frac{v}{3}\left[\frac{\partial^2 u}{\partial x^2} + \frac{\partial^2 v}{\partial x\partial y} + \frac{\partial^2 w}{\partial x\partial z}\right]$$

$$\dots\dots\dots\dots(3.3.23)$$

For incompressible flow (ρ = constant) equation (3.3.23) reduces to:

$$\frac{\partial u}{\partial t} + u\frac{\partial u}{\partial x} + v\frac{\partial u}{\partial y} + w\frac{\partial u}{\partial z} = X - \frac{1}{\rho}\frac{\partial P}{\partial x} + v\left[\frac{\partial^2 u}{\partial x^2} + \frac{\partial^2 u}{\partial y^2} + \frac{\partial^2 u}{\partial z^2}\right] \qquad (3.3.24)$$

where $v = \mu/\rho$ = kinemetic viscosity (used for diffusivities for momentum, Batchelor, 1967)

For turbulent flow conditions the Navier-Stokes equation should be modified to accommodate the turbulence of the flow. The continuity equation (3.3.10) is first multiplied by (u) giving:

$$u\frac{\partial u}{\partial x} + u\frac{\partial v}{\partial y} + u\frac{\partial w}{\partial z} = 0 \qquad (3.3.25)$$

By combining equation (3.3.25) and (3.3.24) gives:

$$\frac{\partial u}{\partial t} + \frac{\partial u^2}{\partial x} + \frac{\partial uv}{\partial y} + \frac{\partial uw}{\partial z} = X - \frac{1}{\rho}\frac{\partial P}{\partial x} + v\left[\frac{\partial^2 u}{\partial x^2} + \frac{\partial^2 u}{\partial y^2} + \frac{\partial^2 u}{\partial z^2}\right] \qquad (3.3.26)$$

For a turbulent flow, the instantaneous velocity component u can be expressed in terms of its temporal fluctuating and average components (LeMéhauté, 1976) such as:

$$u = \bar{u} + u' \qquad (3.3.27)$$

here $\bar{u}$ = time average velocity component = $\dfrac{1}{\Delta t}\displaystyle\int_{t}^{t+\Delta t} u\,dt$

u' = fluctuating velocity components where $\bar{u}' = 0$

this means that $\dfrac{1}{\Delta t}\displaystyle\int_{t}^{t+\Delta t} u'\,dt = 0$

Substituting the time average and fluctuating components in equation (3.3.24) gives:

$$\left(\frac{\partial}{\partial t}(\bar{u} + u') + \frac{\partial}{\partial x}(\bar{u} + u')(\bar{u} + u') + \frac{\partial}{\partial y}(\bar{u} + u')(\bar{v} + v') + \frac{\partial}{\partial z}(\bar{u} + u')(\bar{w} + w') \right)$$

$$= (\bar{X} + X') - \frac{1}{\rho}\frac{\partial}{\partial x}(\bar{P} + P') + \nu\left[\frac{\partial^2}{\partial x^2}(\bar{u} + u') + \frac{\partial^2}{\partial y^2}(\bar{u} + u') + \frac{\partial^2}{\partial z^2}(\bar{u} + u') \right]$$

(3.3.28)

Time averaging the whole of equation (3.3.28) gives:

$$\frac{\partial}{\partial t}\left(\overline{\bar{u} + u'}\right) + \frac{\partial}{\partial x}\left(\overline{\bar{u}\bar{u} + 2u'\bar{u} + u'^2}\right) + \frac{\partial}{\partial y}\left(\overline{\bar{u}\bar{v} + u'\bar{v} + v'\bar{u} + u'v'}\right) + \frac{\partial}{\partial z}\left(\overline{\bar{u}\bar{w} + u'\bar{w} + w'\bar{u} + u'w'}\right)$$

$$= \overline{X} + \overline{X'} - \frac{1}{\rho}\left(\overline{\bar{P} + P'}\right) + \nu\left[\frac{\partial^2}{\partial x^2}\left(\overline{\bar{u} + u'}\right) + \frac{\partial^2}{\partial y^2}\left(\overline{\bar{u} + u'}\right) + \frac{\partial^2}{\partial z^2}\left(\overline{\bar{u} + u'}\right) \right]$$

............(3.3.29)

Now $\qquad \overline{\bar{u} + u'} = \frac{1}{\Delta t}\int\limits_{t}^{t+\Delta t}(\bar{u} + u')dt = \bar{u} + \frac{1}{\Delta t}\int\limits_{t}^{t+\Delta t}u'dt = \bar{u}$ (3.3.30)

but $\dfrac{1}{\Delta t}\int\limits_{t}^{t+\Delta t}\bar{u}\,dt = \bar{u} =$ time average velocity component and $\dfrac{1}{\Delta t}\int\limits_{t}^{t+\Delta t}u'dt = 0$ (3.3.31)

and similarly all other terms in this form can be expanded and evaluated and equation (3.3.29) reduces to:

$$\frac{\partial \bar{u}}{\partial t} + \frac{\partial \bar{u}\bar{u}}{\partial x} + \frac{\partial \bar{u}\bar{v}}{\partial y} + \frac{\partial \bar{u}\bar{w}}{\partial z} = \overline{X} - \frac{1}{\rho}\frac{\partial \bar{P}}{\partial x} + \nu\left[\frac{\partial^2 \bar{u}}{\partial x^2} + \frac{\partial^2 \bar{u}}{\partial y^2} + \frac{\partial^2 \bar{u}}{\partial z^2} \right] - \left[\frac{\partial \overline{u'u'}}{\partial x} + \frac{\partial \overline{u'v'}}{\partial y} + \frac{\partial \overline{u'w'}}{\partial z} \right]$$

............(3.3.32)

Now by subtracting the continuity equation again from equation (3.3.32), this gives the Navier-Stokes equation for incompressible turbulent flow in the x-direction.

$$\frac{\partial \bar{u}}{\partial t} + \bar{u}\frac{\partial \bar{u}}{\partial x} + \bar{v}\frac{\partial \bar{u}}{\partial y} + \bar{w}\frac{\partial \bar{u}}{\partial z} = \overline{X} - \frac{1}{\rho}\frac{\partial \bar{P}}{\partial x} + \frac{1}{\rho}\frac{\partial}{\partial x}\left[\mu\frac{\partial \bar{u}}{\partial x} - \rho\overline{u'u'} \right]$$

$$+ \frac{1}{\rho}\frac{\partial}{\partial y}\left[\mu\frac{\partial \bar{u}}{\partial y} - \rho\overline{u'v'} \right] + \frac{1}{\rho}\frac{\partial}{\partial z}\left[\mu\frac{\partial \bar{u}}{\partial z} - \rho\overline{u'w'} \right]$$

(3.3.33)

Similar equations can be obtained for both the y and z-direction respectively. The expressions $\left(-\rho\overline{u'u'}\right)$, $\left(-\rho\overline{u'v'}\right)$ and $\left(-\rho\overline{u'w'}\right)$ are known as the Reynolds stresses,

with their form being similar to viscous shear stresses. These stresses arises due to the presence of turbulent flow and for laminar flow are zero. According to Boussinesq (Goldstein, 1938 and 1965) these Reynolds shear stresses can be represented in a diffusive manner as follows:

$$- \rho \overline{u'u'} = \eta' \left[\frac{\partial \overline{u}}{\partial x} + \frac{\partial \overline{u}}{\partial x} \right]; \qquad - \rho \overline{u'v'} = \eta' \left[\frac{\partial \overline{u}}{\partial y} + \frac{\partial \overline{v}}{\partial x} \right]; \qquad - \rho \overline{u'w'} = \eta' \left[\frac{\partial \overline{u}}{\partial z} + \frac{\partial \overline{w}}{\partial x} \right]$$

$$(3.3.34)$$

where η' = absolute eddy viscosity = $\rho \varepsilon$ and ε = kinematic eddy viscosity

In equations (3.3.33), $\overline{X}$ is the external force acting on the water body. Similarly $\overline{Y}$ and $\overline{Z}$ are the forces in the y and z-directions respectivey. These forces arise due to the earth's rotation (Coriolis acceleration) and gravity. In the Navier-Stokes equation the assumptions made are that: (i) the x-direction is parallel to the equator, (ii) the y-direction is from the south to north and (iii) the z-direction is upward normal to the earth's surface. So the external forces can be written in the form:

$$X = f.v = +2\overline{\omega} \sin \overline{\varphi} \; ; \quad Y = -f.u = -2u\overline{\omega} \sin \overline{\varphi} \quad \text{and} \quad Z = -g \qquad (3.3.35)$$

where f = Coriolis coefficient = $2\overline{\omega} \sin \overline{\varphi}$

$\overline{\omega}$ = anguler speed of the earth's rotation = 7.3 x 10^{-5} rad/sec.

$\overline{\varphi}$ = angle of latitude of the domain

g = gravitational acceleration = 9.807 m/sec^2

The assumption of a vertical hydrostatic pressure distribution can be made when the vertical acceleration of the fluid flow is much smaller than the pressure gradient and gravitational acceleration. The hydrostatic pressure can be described in the form:

$$P = \rho g(\eta - z) + p_a \qquad (3.3.36)$$

In which, h = water depth below mean water level (MWL)

η = height of water surface above MWL, and

z = elevation above MWL.

p_a = atmospheric pressure
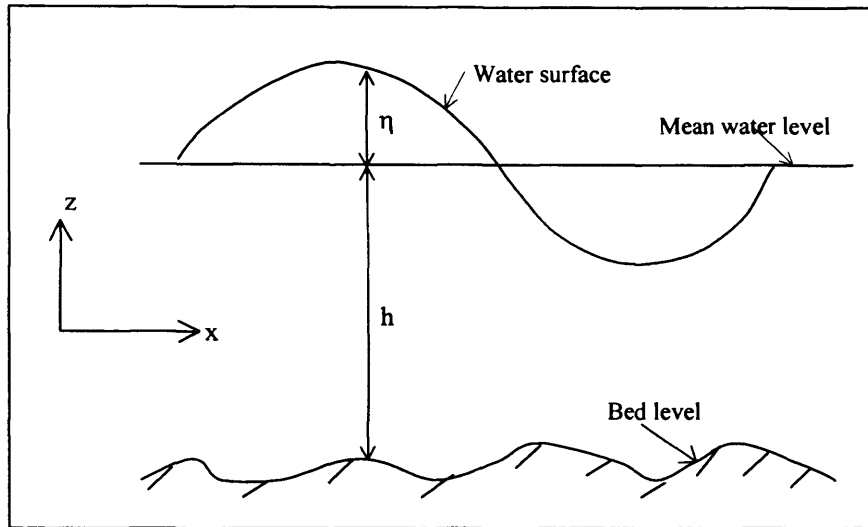
Figure 3.3.4 Hydrostaic pressure distribution

This equation can now be differentiated independently with respect to x to give an expression for the corresponding pressure gradient term in the Navier-Stokes equation for the x-direction.

$$\frac{\partial P}{\partial x} = \rho g \frac{\partial \eta}{\partial x} + g(\eta - z)\frac{\partial \rho}{\partial x} + \frac{\partial p_a}{\partial x} \tag{3.3.37}$$

For the scales being considered in this study the atmospheric pressure gradient will generally be negligible in comparison with the water surface slope (Dronkers, 1964) and can therefore be omitted from equations (3.3.37). A mean constant value for the horizontal density gradient has been assumed throughout, which means ($\delta\rho/\delta x \cong 0$). Therefore, the pressure gradient term can be expressed as:

$$\frac{\partial P}{\partial x} = \rho g \frac{\partial \eta}{\partial x} \tag{3.3.38}$$

By inserting the value of external force and the pressure gradient in equation (3.3.33) the Navier-Stokes equation becomes:

$$\frac{\partial \bar{u}}{\partial t} + \bar{u}\frac{\partial \bar{u}}{\partial x} + \bar{v}\frac{\partial \bar{u}}{\partial y} + \bar{w}\frac{\partial \bar{u}}{\partial z} = f.v - g\frac{\partial \eta}{\partial x} + \frac{1}{\rho}\frac{\partial}{\partial x}\left[\mu\frac{\partial \bar{u}}{\partial x} - \rho\overline{u'u'}\right]$$
$$+ \frac{1}{\rho}\frac{\partial}{\partial y}\left[\mu\frac{\partial \bar{u}}{\partial y} - \rho\overline{u'v'}\right] + \frac{1}{\rho}\frac{\partial}{\partial z}\left[\mu\frac{\partial \bar{u}}{\partial z} - \rho\overline{u'w'}\right] \tag{3.3.39}$$

3.3.3 Boundary Conditions

Figure 3.3.5 shows the co-ordinate system and the important parameters considered in the present model. To establish the two-dimensional depth integrated mass and momentum equations, it is necessary to specify boundary conditions governing the velocity and stress components at the surface and bed. The free surface boundary condition (FSBC) describes the vertical velocity at the free surface and the corresponding rate of change of instantaneous water surface elevation η, is given by
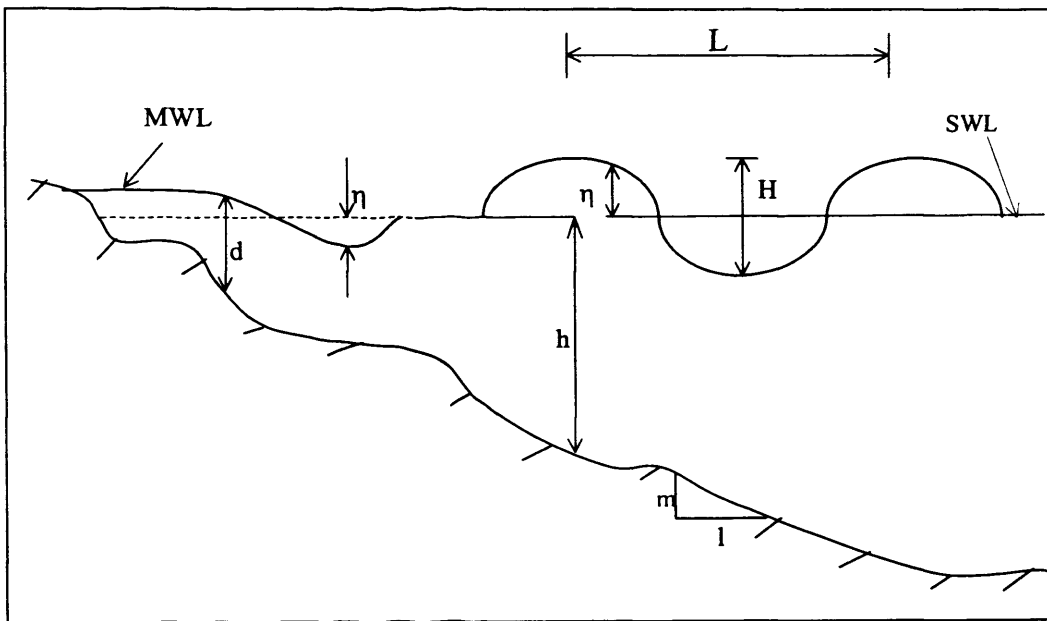
Figure 3.3.5 Section of defination sketch

$$\frac{d\eta}{dt} = \frac{\partial \eta}{\partial t} + \frac{\partial \eta}{\partial x}\frac{dx}{dt} + \frac{\partial \eta}{\partial y}\frac{dy}{dt} = \frac{\partial \eta}{\partial t} + u\frac{\partial \eta}{\partial x} + v\frac{\partial \eta}{\partial y} = w_\eta \qquad (3.3.40)$$

$$\text{or,} \quad -u_\eta \frac{\partial \eta}{\partial x} - v_\eta \frac{\partial \eta}{\partial y} + w_\eta = \frac{\partial \eta}{\partial t} \qquad (3.3.41)$$

At the bed the no slip boundary condition gives:

$$u_{-h} = v_{-h} = w_{-h} = 0 \qquad (3.3.42)$$

Further boundary conditions can be expressed in terms of components of the wind induced surface shear, τ_w, and the bed friction τ_b. These conditions are given by Vreugdenhil (1998) and take the form at the free surface of:

$$-\tau_{xx_\eta} \frac{\partial \eta}{\partial x} - \tau_{yx\eta} \frac{\partial \eta}{\partial y} + \tau_{zx_\eta} = \tau_{wx}$$

(3.3.43a)

$$-\tau_{xy_\eta} \frac{\partial \eta}{\partial x} - \tau_{yy_\eta} \frac{\partial \eta}{\partial y} + \tau_{zy\eta} = \tau_{wy}$$

(3.3.43b)

and similarly, for the bed

$$-\tau_{xx_{-h}} \frac{\partial (-h)}{\partial x} - \tau_{yx_{-h}} \frac{\partial (-h)}{\partial y} + \tau_{zx_{-h}} = \tau_{bx}$$

(3.3.44a)

$$-\tau_{xy_{-h}} \frac{\partial (-h)}{\partial x} - \tau_{yy_{-h}} \frac{\partial (-h)}{\partial y} + \tau_{zy_{-h}} = \tau_{by}$$

(3.3.44b)

where, τ_{wx}, τ_{wy} = x and y components of τ_w respectively

τ_{bx}, τ_{by} = x and y components of τ_b respectively

$\tau_{xx_\eta}, \tau_{xx_{-h}}$ ....are the components of shear stresses along three coordinates at

surface and bed respectively.

3.3.4   Two Dimensional Depth Integrated (Shallow Water) Equations

For flow fields where the vertical variation in fluid flow quantities is either small or less significant then the flow may be evenly mixed vertically and a two-dimensinal fluid model may be applicable. The three dimensional equations of continuity and momentum are integrated over the total water depth and solved numerically to give the depth averaged velocity field, which normally occurs in wide estuaries, harbours, bays etc.

Another case where the two dimensional depth integrated equations are needed is for temporally periodic, long crested, gradually varying progressive wave propagating over a small bottom slope, when superimposed on a weak nearly horizontal mean flow; that is flow in the nearshore zone. The three dimensional variation of the nearshore current in space is very complicated to examine either experimentally or theoretically, so the equations are reduced to two horizontal dimensions by depth integrating the equations of mass and momentum. The continuity equation (3.3.10) can now be integrated over the depth to form the two-dimensional partial differential continuity equation. This depth integration of the continuity equation gives:

$$\int_{-h}^{\eta}\left[\frac{\partial u}{\partial x}+\frac{\partial v}{\partial y}+\frac{\partial w}{\partial z}\right]dz = \int_{-h}^{\eta}\left[\frac{\partial u}{\partial x}+\frac{\partial v}{\partial y}\right]dz + w_{\eta} - w_{-h} = 0 \qquad (3.3.45)$$

Applying Leibnitz's rule (Sokolnikoff and Redheffex, 1966) to equation (3.3.45) gives:

$$\frac{\partial}{\partial x}\int_{-h}^{\eta}udz - u_{\eta}\frac{\partial\eta}{\partial x}\bigg|_{\eta} + u_{-h}\frac{\partial(-h)}{\partial x}\bigg|_{-h} + \frac{\partial}{\partial y}\int_{-h}^{\eta}vdz - v_{\eta}\frac{\partial\eta}{\partial y}\bigg|_{\eta} + v_{-h}\frac{\partial(-h)}{\partial y}\bigg|_{-h} + w_{\eta} - w_{-h} = 0$$

$$\ldots\ldots\ldots\ldots(3.3.46)$$

Now using the free surface boundary condition (FSBC) (Eq. 3.3.41) and bottom boundary condition (BBC) (Eq. 3.3.42), then Eq. (3.3.46) can be simplified to give:

$$\frac{\partial}{\partial x}\int_{-h}^{\eta}udz + \frac{\partial}{\partial y}\int_{-h}^{\eta}vdz + \frac{\partial\eta}{\partial t} = 0 \qquad (3.3.47)$$

If the depth averaged velocity components U and V are now defined as:

$$U = \frac{1}{H}\int_{-h}^{\eta}udz \qquad \text{and} \qquad V = \frac{1}{H}\int_{-h}^{\eta}vdz \qquad (3.3.48)$$

Then substituting the above definition and assuming that the location of the bed is constant with time, the following form of the depth averaged two dimensional continuity equation results:

$$\frac{\partial\eta}{\partial t} + \frac{\partial}{\partial x}(UH) + \frac{\partial}{\partial y}(VH) = 0 \qquad (3.3.49)$$

The two dimensional depth averaged momentum equations for incompressible turbulent flow can be obtained by depth integration of Navier-Stokes equation in the x and y-direction. These can be derived in a manner giving for the x-direction (Falconer, 1976: see Westwater, 2001) as:

$$\frac{\partial UH}{\partial t} + \frac{\partial}{\partial x}\left(\beta U^{2}H\right) + \frac{\partial}{\partial y}\left(\beta UVH\right) = fVH - gH\frac{\partial\eta}{\partial x}$$

$$\int_{-h}^{\eta}\varepsilon\left(\frac{\partial u}{\partial z}+\frac{\partial w}{\partial z}\right)dz + 2\frac{\partial}{\partial x}\left(\overline{\varepsilon}H\frac{\partial U}{\partial x}\right) + \frac{\partial}{\partial y}\left(\overline{\varepsilon}H\left(\frac{\partial U}{\partial y}+\frac{\partial V}{\partial y}\right)\right) \qquad (3.3.50)$$

where

β = momentum correction factor for non-uniformity of vertical velocity profile

= 1.016 for Seventh Power Law Velocity Distribution (Falconer and Chen, 1996 and Yin, et al., 2000).

It can be shown from the shear stress function that

$$\varepsilon\left(\frac{\partial u}{\partial z} + \frac{\partial w}{\partial z}\right) = \tau_z \qquad (3.3.51)$$

Then
$$\int_{-h}^{\eta}\varepsilon\left(\frac{\partial u}{\partial z} + \frac{\partial w}{\partial z}\right)dz = \int_{-h}^{\eta}\tau_z dz = \tau_{xw} - \tau_{xb} \qquad (3.3.52)$$

Here τ_{xw} = surface wind shear stress component, which is zero for this current study, τ_{xb} = bed shear stress component which includes bed shear stresses. So the x-direction depth averaged momentum equation becomes:

$$\frac{\partial UH}{\partial t} + \frac{\partial}{\partial x}\left(\beta U^2 H\right) + \frac{\partial}{\partial y}\left(\beta UVH\right) = fVH - gH\frac{\partial \eta}{\partial x}$$
$$+ \frac{\tau_{xw}}{\rho} - \frac{\tau_{xb}}{\rho} + 2\frac{\partial}{\partial x}\left(\bar{\varepsilon}\frac{\partial UH}{\partial x}\right) + \frac{\partial}{\partial y}\left(\bar{\varepsilon}\frac{\partial UH}{\partial y} + \bar{\varepsilon}\frac{\partial VH}{\partial x}\right) \qquad (3.3.53)$$

A similar derivation can be made for the y-direction depth averaged momentum equation to give:

$$\frac{\partial VH}{\partial t} + \frac{\partial}{\partial y}\left(\beta V^2 H\right) + \frac{\partial}{\partial x}\left(\beta VUH\right) = -fUH - gH\frac{\partial \eta}{\partial y}$$
$$+ \frac{\tau_{yw}}{\rho} - \frac{\tau_{yb}}{\rho} + 2\frac{\partial}{\partial y}\left(\bar{\varepsilon}\frac{\partial VH}{\partial y}\right) + \frac{\partial}{\partial x}\left(\bar{\varepsilon}\frac{\partial VH}{\partial x} + \bar{\varepsilon}\frac{\partial UH}{\partial y}\right) \qquad (3.3.54)$$

The depth average eddy viscosity $\bar{\varepsilon}$ for a logarithmic velocity profile can be expressed as:

$$\bar{\varepsilon} = \frac{\kappa\sqrt{g}\left(\sqrt{U^2 + V^2}\right)H}{6C} \qquad (3.3.55)$$

where $\kappa = 0.4$ (von Karman's constant) and

C = Chezy coefficient = $H^{1/6}/n$; n = Manning's coefficient

The friction between the moving air and the fluid surface elements generates a different type of shear stress called the surface shear stress. The method to determine this surface stress due to wind was formulated by Van Dorn (1953), and later was suggested in the Shore Protection Manual. The surface shear stress due to wind is normally calculated using a formula after Munk (see Dronkers, 1964) giving:

$$\tau_{xw} = \gamma \rho_a W_x \sqrt{W_x^2 + W_y^2}$$ (3.3.56)

where γ = air/water resistance constant = 0.0026

             ρ_a = air density = 1.292 kg/m^3

             W_x = wind velocity component in x-direction at 10m above surface.

The term $\sqrt{W_x^2 + W_y^2}$, is the absolute wind speed at 10m above the surface, although this is not the only recommended standard method of measurement. Wilson (1960) collected many different sets of data at different locations, obtained under various wind conditions. From the data set and by using a Karman-Prandtl velocity distribution equation, he suggested that:

$$W = 2.5 W_* \ln(\frac{z}{Z_0})$$ (3.5.57)

where W = wind speed at height z above the surface, W$_*$ = shear velocity ($W_* = \sqrt{\tau_w / \rho_a}$) and Z_0 = effective roughness height of the surface.

The bottom boundary, which is considered at the bed of a water body, a shear stress is developed called the bottom shear stress. This stress causes a frictional resistance between the fluid layer and the bottom solid layer. This shear stress can be approximated in the form of a quadratic friction law by considering steady uniform open channel flow. Longuet-Higgins (1970) assumed that the bottom friction stress due to waves and currents would be adequately represented by equation (3.3.55) where the bed shear stress is usually represented in a manner similar to that for uniform flow:

$$\tau_{xb} = \frac{\rho g U \sqrt{U^2 + V^2}}{C^2}$$ (3.3.58)

The turbulent diffusion terms in equation (3.3.51) and (3.3.52) are first simplified by neglecting the gradients of $\bar{\varepsilon}H$ and the divergence of the mean flow (Kuipers and Vreugdenhil, 1973: see Westwater, 2001), giving for the x-direction:

$$2\frac{\partial}{\partial x}\left[\bar{\varepsilon}H\frac{\partial U}{\partial x}\right] + \frac{\partial}{\partial y}\left[\bar{\varepsilon}H\left(\frac{\partial U}{\partial y} + \frac{\partial V}{\partial x}\right)\right]$$

$$= 2\bar{\varepsilon}H\frac{\partial^2 U}{\partial x^2} + \bar{\varepsilon}H\frac{\partial}{\partial y}\left[\frac{\partial U}{\partial y} + \frac{\partial V}{\partial x}\right] + 2\frac{\partial U}{\partial x}\frac{\partial \bar{\varepsilon}H}{\partial x} + \frac{\partial \bar{\varepsilon}H}{\partial y}\left[\frac{\partial U}{\partial y} + \frac{\partial V}{\partial x}\right] \qquad (3.3.59)$$

$$\cong \bar{\varepsilon}H\left[2\frac{\partial^2 U}{\partial x^2} + \frac{\partial^2 U}{\partial y^2} + \frac{\partial^2 V}{\partial x \partial y}\right]$$

and similarly for the y-direction

$$2\frac{\partial}{\partial y}\left[\bar{\varepsilon}H\frac{\partial V}{\partial x}\right] + \frac{\partial}{\partial x}\left[\bar{\varepsilon}H\left(\frac{\partial U}{\partial y} + \frac{\partial V}{\partial x}\right)\right] \cong \bar{\varepsilon}H\left[\frac{\partial^2 V}{\partial x^2} + 2\frac{\partial^2 V}{\partial y^2} + \frac{\partial^2 U}{\partial x \partial y}\right] \qquad (3.3.60)$$

For 2-D depth average flow, the depth avearge eddy viscosity $\bar{\varepsilon}$ is often dropped in literature and refered as kinemetic eddy viscosity ε. Finally, the two-dimensional depth integrated fluid flow equation with all of its components in the x and y-direction is given by:

$$\frac{\partial UH}{\partial t} + \frac{\partial \beta U^2 H}{\partial x} + \frac{\partial \beta UVH}{\partial y} = fVH - gH\frac{\partial \eta}{\partial x} + \frac{\rho_a}{\rho}C_w W_x\sqrt{W_x^2 + W_y^2}$$

$$-\frac{gU\sqrt{U^2 + V^2}}{C^2} + \varepsilon H\left(2\frac{\partial^2 U}{\partial x^2} + \frac{\partial^2 U}{\partial y^2} + \frac{\partial^2 V}{\partial x \partial y}\right) \qquad (3.3.61)$$

$$\frac{\partial VH}{\partial t} + \frac{\partial \beta UVH}{\partial x} + \frac{\partial \beta V^2 H}{\partial y} = fUH - gH\frac{\partial \eta}{\partial y} + \frac{\rho_a}{\rho}C_w W_y\sqrt{W_x^2 + W_y^2}$$

$$-\frac{gV\sqrt{U^2 + V^2}}{C^2} + \varepsilon H\left(2\frac{\partial^2 V}{\partial x^2} + \frac{\partial^2 V}{\partial y^2} + \frac{\partial^2 U}{\partial x \partial y}\right) \qquad (3.3.62)$$

These are the depth integarted momentum equations in the x and y-direction which, in conjunction with the depth integrated continuity equation (Equation 3.3.49) are used to derive the hydrodynamic module of the numerical model of this study.

3.4   Governing Equations for Shallow Water Waves

A progressive wave can be represented by the variables x(spatial) and t(temporal) or by their combination (phase), defined as $\theta = (kx - \omega t)$, values of θ vary from 0 to 2π. Other important parameters which can describe periodic waves are the wave height H, wave length L and the water depth h. The wave amplitude is defined as $a = H/2$, the wave period T is the time interval between the passage of two successive wave crests or troughs at a given point and the wavelength L is the horizontal distance between two identical points on two successive wave crests or two successive wave troughs. Further definitions include:

$\omega = \dfrac{2\pi}{T}$ is the angular or radian frequency

$k = \dfrac{2\pi}{L}$ is the wave number

$C = \dfrac{L}{T} = \dfrac{\omega}{k}$ is the phase velocity or wave celerity

H/L is the wave steepness

h/L is the relative depth and

η/h is the relative wave height.

Linear Wave Theory: The most elementary wave theory is small amplitude or linear wave theory. It was first developed by Airy, 1845 (see Sorenson, 1978). The assumptions made in developing linear wave theory are as follows:

i.   Fluid is homogeneous and incompressible, therefore density ρ is constant.

ii.   Surface tension can be neglected.

iii.   Coriolis effects due to earth's rotation can be neglected.

iv.   Pressure at the free surface is uniform and constant.

v.   The fluid is ideal or inviscid (i.e. it lacks viscosity).

vi.   The particular wave being considered does not interact with any other water motions. The flow is irrotational so that the water particles do not rotate.

vii.   The bed is horizontal, fixed and is an impermeable boundary, which implies that the vertical velocity at the bed is zero.

viii.   The wave amplitude is small and the waveform is invariant in time and space.

ix.   Waves are plane or long crested (2-D).
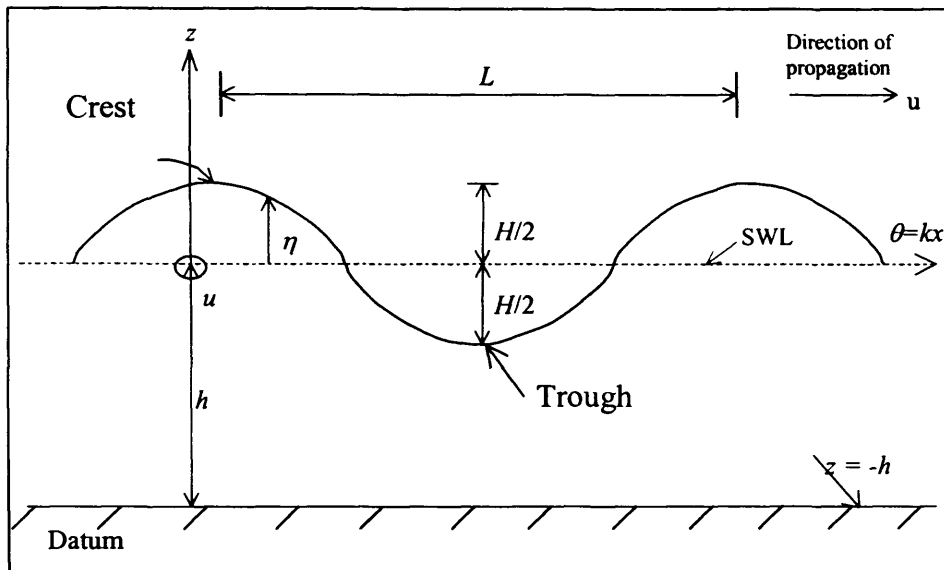
Figure 3.4.1 Definition sketch for sinusoidal progressive waves.

The use of a mathematical function termed a 'velocity potential' "φ" describes the irrotational status of a wave. The velocity potential is a scalar function whose gradient at any point in the fluid gives the velocity vector that is:

$$u = \frac{\partial \varphi}{\partial x}$$
                                                                              (3.4.1)

$$w = \frac{\partial \varphi}{\partial z}$$
                                                                              (3.4.2)

where u and w are fluid velocity in the x and z-direction respectively.

There is another mathematical function termed a 'stress function' "ψ", which is orthogonal to the potential function φ, and for an expression if φ is known then ψ can be found and vice versa using the equation

$$u = \frac{\partial \varphi}{\partial x} = \frac{\partial \psi}{\partial z}$$
                                                                              (3.4.3)

$$w = \frac{\partial \varphi}{\partial z} = -\frac{\partial \psi}{\partial x}$$
                                                                              (3.4.4)

Incompressible inviscid fluid flow usually provides an accurate description for water wave motion. Considering a Cartesian co-ordinate system, with z-upwards and the origin at free surface at rest, here the free surface is given by $z = \eta(x, y, t)$ and the rigid incompressible bottom is given by $z = - h(x,y)$. With the assumption of irrotational motion and an incompressible fluid, a velocity potential exists which should satisfy the continuity equation:

$$\nabla \cdot u = 0 \Rightarrow \nabla \cdot \nabla \phi = 0 \qquad\qquad (3.4.5)$$

The divergence of a gradient leads to the Laplace equation, which must hold throughout the fluid:

$$\nabla^2 \phi = \frac{\partial^2 \phi}{\partial x^2} + \frac{\partial^2 \phi}{\partial y^2} + \frac{\partial^2 \phi}{\partial z^2} = 0 \qquad\qquad (3.4.6)$$

Both φ and ψ satisfy the Laplace's equation, which governs the flow of an ideal fluid. The Laplace equation in two dimensions with x-horizontal and z-vertical axes in terms of velocity potential φ is given by

$$\frac{\partial^2 \varphi}{\partial x^2} + \frac{\partial^2 \varphi}{\partial z^2} = 0 \qquad\qquad (3.4.7)$$

In terms of stream function ψ, the Laplace equation becomes

$$\frac{\partial^2 \psi}{\partial x^2} + \frac{\partial^2 \psi}{\partial z^2} = 0 \qquad\qquad (3.4.8)$$

The governing equation from the continuity equation for the water waves is:

$$\frac{\partial u}{\partial x} + \frac{\partial w}{\partial z} = 0 \qquad\qquad (3.4.9)$$

where $-h(x) \leq z \leq \eta(x, t)$

3.4.1 Boundary Conditions

At any boundary, whether it is fixed - such as the bed, or free - such as the water surface, and is free to deform under the influence of forces, then certain physical conditions must be satisfied by the fluid velocity. These conditions on the water

particle kinematics are called kinematic boundary conditions. The mathematical expression for the kinematic boundary condition may be derived from the equation which describes the surface that constitutes the boundary.

The bottom boundary condition (BBC) is the lower boundary where $z = -h$. For a two dimensional case the origin is located at the still water level and h represents the below the SWL depth. For a horizontal bottom bed:

$w = 0$ on $z = -h$ *(3.4.10a)*

For a sloping bottom

$$\frac{w}{u} = -\frac{dh}{dx}$$ *(3.4.10b)*

The kinematic free surface boundary condition (KFSBC) can be described as:

$F(x, y, z, t) = z - \eta(x, y, t) = 0$

where $\eta(x, y, t)$ is the displacement of the free surface about the horizontal plane.

The KFSBC at the free surface is:

$$w = \frac{\partial \eta}{\partial t}$$ on $z = \eta$ *(3.4.11)*

The dynamic free surface boundary condition (DFSBC) states that the pressure on the free surface be uniform along the wave form. The Bernoulli equation at the surface gives the boundary condition as:

$$\frac{1}{g}\frac{\partial \phi}{\partial t} + \eta + \frac{P}{\rho g} = Const.$$ *(3.4.12)*

3.4.2   Solution of Linearized Water Wave Boundary Value Problem

The solution of the water waves that are periodic in space and time propagating over a nearly horizontal bottom can be developed by using the boundary value problem. This requires the solution of the Laplace equation. A convenient method for solving the linear partial differential equations for water waves is called the separation of variables (Dean and Dalrymple, 1994). The assumption is that the solution can be

expressed as a product term, each of which is a function of only one of the independent variables, such as:

$$\phi(x,z,t) = X(x).Z(z).T(t) \qquad\qquad (3.4.13)$$

where $X(x)$, $Z(z)$ and $T(t)$ are functions which depend only on x, z and t respectively. So ϕ must be periodic in time as given by the lateral boundary conditions, and we can specify $T(t) = \sin\sigma t$, then to find σ, the angular frequency of the wave, the periodic boundary condition gives, $\sin \sigma t = \sin \sigma(t+T) = \sin\sigma t \cos\sigma T + \cos\sigma t \sin\sigma T$ and which is true for $\sigma = 2\pi/T$. The velocity potential now takes the form

$$\phi(x,z,t) = X(x).Z(z).\sin\sigma t \qquad\qquad (3.4.14)$$

Substituting into the Laplace equation, we get

$$\frac{d^2 X(x)}{dx^2}.Z(z).\sin\sigma t + X(x).\frac{d^2 Z(z)}{dz^2}\sin\sigma t = 0 \qquad\qquad (3.4.15)$$

Dividing throughout by ϕ gives

$$\frac{1}{X}\frac{\partial^2 X}{\partial x^2} + \frac{1}{Z}\frac{\partial^2 Z}{\partial z^2} = 0 \qquad\qquad (3.4.16)$$

The first term of this equation depends on x-alone while the second term depends on z only. If there is any variation in either term then the only way that the equation can hold true is if each term is equal to the same constant, except for a sign difference, that is:

$$\frac{d^2 X(x)/dx^2}{X(x)} = -k^2 \quad and \quad \frac{d^2 Z(z)/dz^2}{Z(z)} = +k^2 \qquad\qquad (3.4.17)$$

Equation (3.4.17) is now an ordinary differential equation and each equation can be solved separately. Three possible cases can arise to this solution for the nature of k, these are for k is real, $k=0$, and for k being a pure imaginary number. If k is real and non-zero, then the solution to the Laplace equation gives the following velocity potential:

$$\phi = (A\cos kx + B\sin kx)(ce^{kz} + De^{-kz})\sin\sigma t \qquad\qquad (3.4.18)$$

Considering $\phi\ (x,t)= \phi(x+L,t)$ and $\phi\ (x,t)= \phi(x,t+T)$ explicitly, then the first part of equation (3.4.18) become $[A(coskx\ coskL\text{-}sinkx\ sinkL)+B(sinkx\ coskL+coskx\ sinkL)]$ which satisfies $coskL=1$ and $sinkL=0$. This means that $kL\ =\ 2\pi$ and the velocity potential becomes $\phi = A\cos kx(Ce^{kz} + De^{-kz})\sin \sigma t$.

The bottom boundary condition (BBC) may now be introduced, yielding:

$$w = -\frac{\partial \phi}{\partial z} = -A\cos kx(kCe^{kz} - kDe^{-kz})\sin \sigma t = 0 \qquad \text{at } z = -h \qquad (3.4.19)$$

After substitution and by taking $G=2ADe^{kh}$ the velocity potential becomes:

$$\phi = G\cos kx \cosh k(h + z)\sin \sigma t \qquad (3.4.20)$$

The dynamic free surface boundary condition (DFSBC) states that Bernoulli's equation should be satisfied everywhere at $z = \eta(x,t)$. The pressure at the surface is assumed to be gage pressure, or $P = 0$ in equation (3.4.12). Neglecting the small terms in equation (3.4.12), gives for Bernoulli's equation:

$$\left(-\frac{\partial \phi}{\partial t} + g\eta\right)_{z=0} = C(t) \text{ or, } \eta = \frac{1}{g}\frac{\partial \phi}{\partial t}\bigg|_{z=0} + \frac{C(t)}{g} \qquad (3.4.21)$$

where $C(t)$ is a constant. Substituting the velocity potential as given in equation (3.4.20) in the above equation and recalling that η will have a zero spatial and temporal mean, which gives $C(t)=0$, and by taking $G = \dfrac{Hg}{2\sigma \cosh kh}$, then η becomes

$$\eta = \frac{H}{2}\cos kx\cos \sigma t \qquad (3.4.22)$$

Finally, the velocity potential becomes

$$\phi = \frac{Hg\cosh k(h + z)}{2\sigma \cosh kh}\cos kx\sin \sigma t \qquad (3.4.23)$$

The linearized kinematic free surface boundary condition (KFSBC) gives:

$$w = \frac{\partial \eta}{\partial t}\bigg|_{z=0} \quad \text{or} \quad -\frac{\partial \phi}{\partial z}\bigg|_{z=0} = \frac{\partial \eta}{\partial t} \qquad (3.4.24)$$

Substituting for ϕ and η gives us the 'dispersion relationship'

$$\sigma^2 = gk \tanh kh \qquad (3.4.25)$$

Now $\sigma = 2\pi/T$ and $k = 2\pi/L$ and the speed of the wave propagation can be expressed by relating the wave celerity to wave length and water depth as given by

$$C = \sqrt{\frac{gL}{2\pi} \tanh(\frac{2\pi h}{L})} \qquad (3.4.26)$$

When the relative water depth becomes shallow (i.e. $2\pi h/L < 1/4$ or $h/L < 1/25$) then the wave celerity becomes:

$$C = \sqrt{gh} \qquad (3.4.27)$$

The local fluid velocities and accelerations for various values of z and t during passage of a wave can be found by the relationship of velocity potential with horizontal and vertical velocity components u and w and are given by (Dean and Dalrymple, 1994):

$$u = \frac{\partial \phi}{\partial x} = \frac{H}{2} \frac{gT}{L} \frac{\cosh[2\pi(z+h)/L]}{\cosh(2\pi/L)} \cos\theta \qquad (3.4.28a)$$

$$w = \frac{\partial \phi}{\partial z} = \frac{H}{2} \frac{gT}{L} \frac{\sinh[2\pi(z+h)/L]}{\cosh(2\pi/L)} \sin\theta \qquad (3.4.28b)$$

$$a_x = \frac{\partial u}{\partial t} = \frac{g\pi H}{L} \frac{\cosh[2\pi(z+h)/L]}{\cosh(2\pi h/L)} \sin\theta \qquad (3.4.29a)$$

$$a_z = \frac{\partial w}{\partial t} = -\frac{g\pi H}{L} \frac{\sinh[2\pi(z+h)/L]}{\sinh(2\pi h/L)} \sin\theta \qquad (3.4.29b)$$

The sub-surface pressure under a wave is the sum of two contributing components, i.e. dynamic pressure and static pressure, and is given by:

$$P' = \frac{\rho g H \cosh[\frac{2\pi(z+h)}{L}]}{2\cosh(\frac{2\pi h}{L})} \cos\theta - \rho gz + P_a \qquad (3.4.30)$$

where P' is the total or absolute pressure and P_a is the atmospheric pressure. The first term of Equation (3.4.30) represents a dynamic component due to the fluid acceleration, while the second term is the static component of pressure. Normally the pressure is usually taken as

$$P = P' - P_a = \frac{\rho g H \cosh[\frac{2\pi(z+h)}{L}]}{2\cosh(\frac{2\pi h}{L})}\cos\theta - \rho gz = \rho g \eta \frac{\cosh[\frac{2\pi(z+h)}{L}]}{2\cosh(\frac{2\pi h}{L})} - \rho gz$$

$$\dots\dots\dots\dots(3.4.31)$$

The speed of a group of waves, or a wave train, differes from the speed of individual waves within the group speed and this group celerity C_g is given by:

$$C_g = \frac{1}{2}\frac{L}{T}\left[1 + \frac{4\pi h/L}{\sinh(4\pi h/L)}\right] = nC \qquad (3.4.32)$$

where $\qquad n = \frac{1}{2}\left[1 + \frac{4\pi h/L}{\sinh(4\pi h/L)}\right] \qquad (3.4.33)$

For deep water conditions: $\qquad \dfrac{4\pi h/L}{\sinh(4\pi h/L)} \approx 0$; $\quad$ Then: $n = 1/2$

And for shallow water conditions: $\quad \sinh(\dfrac{4\pi h}{L}) \approx \dfrac{4\pi h}{L}$; $\quad$ Then $C_{gs} = \dfrac{L}{T} = C \approx \sqrt{gh}$

The total energy of a wave system is the sum of kinetic energy and potential energy. The kinetic energy per unit length of a wave crest for linear wave theory is given by:

$$\overline{E_K} = \int_x^{x+L}\int_{-h}^{\eta}\rho\frac{u^2+v^2}{2}dzdx = \frac{1}{16}\rho g H^2 L \qquad (3.4.34)$$

The potential energy is that part of the energy resulting from the part of the fluid mass being above the trough, i.e. the wave crest. The potential energy per unit length of a wave crest for linear wave conditions is given as:

$$\overline{E_P} = \int_x^{x+L}\rho g[\frac{(\eta+h)^2}{2} - \frac{h^2}{2}]dx = \frac{1}{16}\rho g H^2 L \qquad (3.4.35)$$

Thus the total wave energy over one wavelength per unit crest width is given by:

$$E = \overline{E_K} + \overline{E_P} = \frac{1}{16}\rho g H^2 L + \frac{1}{16}\rho g H^2 L = \frac{1}{8}\rho g H^2 L \qquad (3.4.36)$$

The total average wave energy per unit surface area is termed as specific energy or energy density and is given by:

$$E = \frac{E}{L} = \frac{1}{8}\rho g H^2 \qquad (3.4.37)$$

3.4.3 Principles of Wave Transformation

Processes that can affect a wave as it propagates from deep water into shallow water includes (i) refraction, (ii) shoaling, (iii) diffraction, (iv) dissipation due to friction, (v) wave breaking, (vi) additional growth due to wind, (vii) wave current interactions, and (viii) wave wave interactions. The first three effects are propagation effects because they result from the convergence or divergence of waves caused by shape of the bottom topography, which in turn influences the direction of wave travel and causes wave energy to be concentrated or spread out. Points (iv) and (v) are sink mechanisms, because they remove energy from the wave field through dissipation. The wind is a source mechanism and the presence of a large scale current field can affect wave propagation and dissipation. Wave-wave interactions results from the non-linear coupling of wave components and results in the transfer of energy from some waves to others.

Waves approaching the coast increase in steepness as the water depth decreases. At the time wave steepness (H/L) reaches its limiting value, the wave breaks. As a result energy dissipation occurs creating nearshore currents and increasing the mean water level. Waves break in water at a depth of approximately equal to the wave height. The surf zone is the region extending from the seaward boundary of the wave breaking to the limit of wave uprush. Wave breaking is the dominant hydrodynamic process within the surf zone. Hydrodynamic processes like wave set-up, setdown, wave runup and nearshore currents are all the result of waves breaking in surf zone. This zone is the most dynamic coastal region, where sediment transport and bathymetric changes are driven by breaking waves and nearshore currents.

3.4.4   Mild Slope Equation with Parabolic Approximation

The refraction-diffraction (R-D) equation developed by Berkhoff (1972), which is also known as the mild slope equation, is strictly linear and non-dissipative. For this reason, the use of the R-D equations in areas containing beaches is not possible because a linear and non-dissipative model will predict an infinite wave height at the line of a beach. Radder (1979) took care of this problem in the beach area by applying the parabolic approximation to the mild slope equation. In this model wave breaking is included as well as the influence of wave height on the propagation velocity which is a nonlinear effect. The effect of nonlinearity and energy dissipation can be included in mild slope equation theoretically, but for computational reasons the parabolic approximation deals better with nonlinear effects as the equations are solved in a step wise manner. The parabolic approximation has got some restrictions, mainly is that it can not take care of wave reflections and hence the model is only applicable to very small slopes.

The mild slope equation is able to account for the effect of dissipative forces, such as bottom friction and wave breaking. Wave driven forces are obtained from the gradient of radiation stress tensor, i.e. $F_i = - \delta S_{ij}/\delta x_j$ (Longuet-Higgins, 1972), where S_{ij} is the radiation stress and will be discussed in section 3.5.2.

The time-dependent mild slope equation can be expressed as (Li, 1994)

$$-\frac{\partial^2 \phi}{\partial t^2} + \nabla \cdot \left(CC_g \nabla \phi\right) - \left(\omega^2 - k^2 CC_g\right)\phi = 0 \qquad (3.4.38)$$

or it can be expressed in terms of free surface elevation η as

$$-\frac{\partial^2 \eta}{\partial t^2} + \nabla \cdot \left(CC_g \nabla \eta\right) - \left(\omega^2 - k^2 CC_g\right)\eta = 0 \qquad (3.4.39)$$

Equations (3.4.38) and (3.4.39) form the time dependent mild slope equation for nearly harmonic waves. The equation which is usually denoted as the 'mild-slope equation' follows on from (3.4.38) for purely harmonic motion:

$$\phi(x,t) = \text{Re}\left\{\psi(x)e^{-i\omega t}\right\} \qquad (3.4.40)$$

as [$\nabla \cdot (CC_g \nabla \psi) + k^2 CC_g \psi = 0$]; for the complex velocity potential $\psi(x)$. Again for the water surface elevation:

$$\eta(x,t) = \mathrm{Re}\{\eta(x)e^{-i\omega t}\}$$ *(3.4.41)*

And the mild slope equation becomes

$$\nabla \cdot (CC_g \nabla \eta) + k^2 CC_g \eta = 0$$ *(3.4.42)*

The solution of the mild slope equation requires a computational effort which might become too large when large areas are considered. An area is said to be large, when measured a characteristic wave length, comprises the distance of more than a couple hundred wave lengths Dingimean, 1978 (see Mei, 1989). The parabolic approximation of mild slope equation gives the oppurtunity to deal with large areas with simple solution methods as long as the slope remains mild. For milder slope the parabolic equations can provide accurate predictions for wave height. In the parabolic approximation, diffraction effects in the main wave propagation direction are neglected, but in the direction normal to main wave direction, they are formulated.

Berkhoff (1972) formulated an advanced approach for modelling wave propagation as Ray approaches turning into difficulties when the bathymetry becomes complex and at the same time when the model includes refraction, shoaling and diffraction simultaneously to incorporate structures. His mild-slope equation is given by:

$$\nabla(CC_g \phi) + \omega^2 (\frac{C_g}{C})\phi = 0$$ *(3.4.43)*

with $\phi(x,y,z) = \phi \dfrac{\cosh k(h+z)}{\cosh(kh)}$ *(3.4.44)*

where $\nabla = (\dfrac{\partial}{\partial x_i}, \dfrac{\partial}{\partial y_j})$. This provides a solution φ for amplitude and phase of the waves in the horizontal plane. Berkhoff assumed that the bottom slope was mild, with models based on the mild slope equation performing better than the ray models. Berkhoff's approach solves the velocity potential of the wave in the horizontal direction and typically requires 5-10 computational grid points per wave length. This is impractical for many cases. Radder (1979) used a parabolic approximation, which

is computationally efficient but with more limitations. The governing equations for the mild slope equation of Berkhoff (1972) involve the use of instantaneous water surface displacement $\eta(x,y)$ as the starting point giving:

$$\left(CC_g \eta_x\right) + \left(CC_g \eta_y\right) + k^2 CC_g \eta = 0 \qquad (3.4.45)$$

The subscripts here denote the derivative. The wave number k is related to the local water depth h by the dispersion relationship which was shown in equation (3.4.25). Then the mild slope equation is reduced to a variable coefficient Helmholtz equation by introducing a transformation described by Radder (1979), which is given by:

$$\Phi = \sqrt{CC_g} \qquad (3.4.46)$$

Inserting this expression for Φ into the mild slope equation gives

$$\Phi_{xx} + \Phi_{yy} + K^2\Phi = 0 \qquad (3.4.47)$$

$$\text{where} \qquad K^2 = k^2 - \frac{\left(\sqrt{CC_g}\right)_{xx} + \left(\sqrt{CC_g}\right)_{yy}}{\sqrt{CC_g}} \qquad (3.4.48)$$

For the case when considering the mapping of the variable coefficient Helmholtz equation from Cartesian (x,y) space into an alternate (u,v) space, the Jacobian of the transformation J can be expressed as (Sokolnikoff and Redheffer, 1966):

$$J = x_u y_v - x_v y_u \qquad (3.4.49)$$

In this derivation of the mild slope equation, with a parabolic approximation for a large wave angle, the orthogonal system (u,v) and the Cartesian system (x,y) represents the same co-ordinate system and the governing equation can be expressed in terms of (u,v) co-ordinates to match up with Kirby et al. (1994). For the Cartesian system J becomes unity, that is $J = 1$, (as $x_u = 1$, $y_v = 1$, $x_v = 0$ and $y_u = 0$) and equation (3.4.48) can be re written as:

$$\Phi_{uu} + \Phi_{vv} + K^2\Phi = 0 \qquad (3.4.50)$$

which gives the governing equation for the orthogonal domain.

In this section a parabolic method first proposed by Booij (1981) has been the higher order (alternatively the large angle) approximation to Booij's method has been justified in the context of a consistent multiple-scale expression by Kirby (1986). The governing Helmholz equation (3.4.50) can be split into forward and back scattered waves Φ^+ and Φ^-, where $\Phi = \Phi^+ + \Phi^-$. This approach is based on the observation (Booij, 1981) that the differential equation

$$\frac{\partial}{\partial u}\left(\frac{1}{\sigma}\frac{\partial \phi_m}{\partial u}\right) + \sigma\phi_m = 0 \qquad (3.4.51)$$

can be split exactly into an equation for the transmitted field and an equation for the reflected field giving:

$$\frac{\partial \phi_m^+}{\partial u} = i\sigma\phi_m^+ \quad \text{and} \quad \frac{\partial \phi_m^-}{\partial u} = -i\sigma\phi_m^- \qquad (3.4.52)$$

where $\Phi_m = \Phi_m{}^+ + \Phi_m{}^-$

A new variable can be introduced of the form:

$$\phi_m = \lambda\Phi \qquad (3.4.53)$$

which when substituted into equation (3.4.51) gives the equation

$$\lambda\Phi_{uu} + \left(2\lambda_u - \frac{\lambda\sigma_u}{\sigma}\right)\Phi_u + \left(\lambda_{uu} - \frac{\sigma_u\lambda_u}{\sigma}\right)\Phi + \lambda\sigma^2\Phi = 0 \qquad (3.4.54)$$

Eequation (3.4.50) can now be re-written as

$$\Phi_{uu} + \sigma^2\Phi = 0 \qquad (3.4.55)$$

where $\qquad \sigma^2\Phi = \Phi_{vv} + K^2\Phi = K^2\left(\Phi + \frac{\Phi_{vv}}{K^2}\right) \qquad (3.4.56)$

In equation (3.4.55) there is no single derivative of Φ, so we require the coefficient of Φ_u in equation (3.4.54) to be zero which gives

$$\left(2\lambda_u - \frac{\lambda\sigma_u}{\sigma}\right) = 0 \text{ which gives } \lambda = \sigma^{\frac{1}{2}} \qquad (3.4.57)$$

Hence equation (3.4.54) becomes

$$\Phi_{uu} + \lambda\left[\left(\lambda^{-2}\lambda_u\right)_u\right]\Phi + \lambda^4\Phi = 0 \qquad (3.4.58)$$

In the same way as was done by Radder, it can be assumed here that the derivatives of λ (second derivatives of λ with respect to u and terms which are quadratic in λ_u) can be neglected to recover equation (3.4.55) from equation (3.4.58). By using equation (3.4.57) in equation (3.4.52), this gives:

$$\left(\lambda\Phi^+\right)_u = i\lambda^3\Phi^+ \tag{3.4.59}$$

which gives (as $\lambda = \sigma^{1/2}$) from equation (3.4.56)

$$\left[\left(K^{1/4}\right)\left(\Phi^+ + \frac{1}{K^2}\Phi_{vv}^+\right)^{1/4}\right]_u = i\left(K^2\right)^{3/4}\left(\Phi^+ + \frac{1}{K^2}\Phi_{vv}^+\right)^{3/4} \tag{3.4.60}$$

By approximating the operators in equation (3.4.60) and using the first two terms of the binomial expansion (according to Booij, 1981) then this gives the parabolic model equation.

$$\left[\left(K^{1/4}\right)\left(\Phi^+ + \frac{1}{4K^2}\Phi_{vv}^+\right)\right]_u = i\left(K^2\right)^{3/4}\left(\Phi^+ + \frac{3}{4K^2}\Phi_{vv}^+\right) \tag{3.4.61}$$

Hence, by dropping the (+) superscript and also differentiating gives the equation

$$\Phi_u + (2K)^{-1}(K)_u\Phi - \frac{3}{8}\left(K^2\right)^{-\frac{3}{2}}\left(\left(K^2\right)^{\frac{1}{2}}\right)_u\Phi_{vv} + \left(4K^2\right)^{-1}\Phi_{uvv} = iK\Phi + \frac{3i}{4}(K)^{-1}\Phi_{vv}$$

$$.....(3.4.62)$$

Again based on parabolic approximations, it can be assumed that the wave being considered here consists of a progressive part, whose phase accumulates along lines of constant v, and which therefore has u as the preferred propagation direction. So the velocity potential Φ can be written as

$$\Phi = \mathrm{Re}\left\{Ae^{i\int K_0 J_0^{1/2}du}\right\} = \mathrm{Re}\left\{Ae^{i\int K_0 du}\right\} = \mathrm{Re}\ \{\phi\} = \mathrm{Re}\ \{AI\} \tag{3.4.63}$$

where $\phi = Ae^{i\int K_0 du}$ and $I = e^{i\int K_0 du}$ as $J_0 = 1$

Then

$$\phi_u = A_u e^{i\int K_0 du} + AiK_0 e^{i\int K_0 du} = A_u I + AiK_0 I \tag{3.4.64a}$$

$$\phi_{uu} = A_{uu}e^{i\int K_0 du} + 2A_u iK_0 e^{i\int K_0 du} + Ai(K_0)_u e^{i\int K_0 du} + A(iK_0)^2 e^{i\int K_0 du}$$

$$= A_{uu}I + 2A_u iK_0 I + Ai(K_0)_u - AK_0^2 I \qquad (3.4.64b)$$

$$\phi_v = A_v e^{i\int K_0 du} = A_v I \qquad (3.4.64c)$$

$$\phi_{vv} = A_{vv}I \qquad (3.4.64d)$$

$$\phi_{uvv} = A_{uvv}I + A_{vv}iK_0 e^{i\int K_0 du} = A_{uvv}I + A_{vv}iK_0 I \qquad (3.4.64e)$$

By substituting the value of equation (3.4.64a) to (3.4.64e) into equation (3.4.63), and cancelling I from each side and multiply by (2iK), we get

$$2iKA_u + 2K(K - K_0)A + i(K)_u A + \left[\frac{3}{2} - \frac{1}{2}\left(\frac{K_0}{K}\right)^{1/2}\right]A_{vv} - \frac{3i}{4K^2}(K)_u A_{vv} + \frac{i}{2K}A_{uvv} = 0$$

$$(3.4.65)$$

Neglecting the small term A_{uvv} the above equation becomes

$$2iKA_u + [2K(K - K_0)A + i(K)_u]A + \left[\frac{3}{2} - \frac{1}{2}\left(\frac{K_0}{K}\right)^{1/2} - \frac{3i}{4K^2}(K)_u\right]A_{vv} = 0 \qquad (3.4.66)$$

This is the governing equation for the parabolic wave model that will be used to predict the wave height after specified simualtion time. The value of the different co-efficient will be discretise in finite difference scheme (in Chapter 4). The solution of a parabolic differential equation requires the availability of initial and boundary conditions. The initial values can be derived from the incoming wave field, the conditions along the lateral boundaries are more difficult to establish. The boundary condition should be such that wave approaching a boundary are not reflected there.

3.4.5 Wave Breaking

The wave height is limited by both depth and wavelength. For a given depth and wave period, there is a maximum height limit above which the wave becomes unstable and breaks. This upper limit of wave height is called breaking wave height. In deep water it is a function of wave length only but in shallow water it is a function of both depth and wavelength. Waves propagating through shallow water

are strongly influenced by the underlying bathymetry and currents. A sloping or undulating bottom, or a bottom characterised by shoals or underwater canyons, can cause large changes in the wave height and direction of travel. Other bathymetric features can reduce wave heights. The magnitude of these changes is particularly sensitive to wave period and direction and how the wave energy is spread in frequency and direction. Wave transformation across irregular bathymetry is complex.

When a wave approaches a beach, its wave length L decreases and its height H will generally increase, causing the wave steepness H/L to increase. A wave breaks as it reaches a limiting steepness, which is a function of the relative depth h/L and the beach slope $\tan\beta$. Much research has been undertaken to develop a relationship to predict the wave height at incipient breaking, H_b. The term breaker index is often used to describe the non-dimensional breaker height, with the common index being expressed as

$$\gamma_b = \frac{H_b}{h_b} \tag{3.4.67}$$

where h_b is the depth at breaking. McCowan, 1891 (see Weggel, 1972) theoretically determine the breaker depth index as $\gamma_b = 0.78$ for a solitary wave travelling over a horizontal bottom. Later it was established that breaker indices depend on a beach slope and incident wave steepness. From laboratory data using monochromatic waves breaking on smooth plane slopes, Weggel(1972) derived the following expressions for the breaker depth index:

$$\gamma_b = b - a \frac{H_b}{gT^2} \tag{3.4.68}$$

for $\tan\beta \leq 0.1$ and $H_0{'} / L_0 \leq 0.06$; and parameters a and b can be obtained empirically giving:

$$a = 43.8(1 - e^{19\tan\beta}) \quad \text{and} \quad b = \frac{1.56}{(1 + e^{-19.5\tan\beta})} \tag{3.4.69}$$

Wave set-up is the superelevation of the mean water level caused by wave action, the total water depth is the sum of the still water depth and the setup, that is:

$d = h + \eta$

The mean water level is governed by the cross-shore balance momentum

$$\frac{d\overline{\eta}}{dx} = -\frac{1}{\rho g h}\frac{dS_{xx}}{dx}$$

                                                            (3.4.70)

3.4.6   Calculation of Wave Height and Wave Angle

When a wave enters a shallow water region, it undergoes various mechanisms before breaking. All these processes either create or dissipate energy. Based on the conservation of energy these processes can be formulated in the form of mathematical equations. The main parameters such as wave height, wave angle and wave period are given as uniform values over the model domain at the beginning of the simulation. The wave celerity, wave number and the dispersion coefficient are obtained with the initial values, then the initial wave height and wave angle are calculated by using Snell's law. These calculations can be done both with or without currents. Hence, based on equation 3.4.66, the different complex values of that equation are obtained by solving the matrix coefficients.

The calculation of the wave height and wave angle based on the conservation of energy are described in this following section. The main assumption is that the wave model first opeartes then the current model starts functioning. The equation of conservation of wave action is given as:

$$\frac{\partial \overline{k}}{\partial t} + \nabla \overline{\sigma} = 0$$

                                                            (3.4.71)

This equation states that any temporal variation in the wave number vector (k) must be balanced by spatial changes in the wave angular frequency (σ). In assuming that the wave front is moving with the current $\overline{U} = U\overline{i} + V\overline{j}$, then the frequency of the wave with respect to a stationary frame of reference (Dean and Dalrymple, 1994) is given as:

$$\overline{\sigma} = \sigma + \overline{k}\cdot\overline{U}$$

                                                            (3.4.72)

Substituting equation (3.4.72) into (3.4.71) gives:

$$\frac{\partial \vec{k}}{\partial t} + \nabla(\sigma + \vec{k} \cdot \vec{U}) = 0 \qquad\qquad (3.4.73)$$

For steady wave number field $\nabla(\sigma + \vec{k} \cdot \vec{U}) = 0$ which requires that $[\sigma + \vec{k} \cdot \vec{U} = Const.]$, and where no current is present ($\overline{U} = 0$), then $\sigma = Const. = 2\pi/T$ and:

$$\sigma + \vec{k} \cdot \vec{U} = \frac{2\pi}{T} \qquad\qquad (3.4.74)$$

By using the dispersion relationship (Eq. 3.4.25), then the wave refraction equation through wave-current interaction is given by (Longuet-Higgins and Stewart, 1962)

$$\sqrt{gk \tanh(kh)} + Uk\cos\theta + Vk\sin\theta = \frac{2\pi}{T} \qquad\qquad (3.4.75)$$

The wave number *(k)* is determined from equation (3.4.75) for a given current velocity, wave angle and water depth. The wave angle θ is calculated from the following equation (Dean and Dalrymple, 1994) to give:

$$\cos\theta\left(\frac{\partial\theta}{\partial x} - \frac{1}{k}\frac{\partial k}{\partial y}\right) + \sin\theta\left(\frac{\partial\theta}{\partial y} + \frac{1}{k}\frac{\partial k}{\partial x}\right) = 0 \qquad\qquad (3.4.76)$$

Noda et al., 1974 (see Lima, 1981) give the value for the different terms used in equation (3.4.76) as:

$$\frac{1}{k}\frac{\partial k}{\partial x} = \frac{\partial\theta}{\partial x}\left[\frac{U\sin\theta - V\cos\theta}{A}\right] + \frac{1}{k}\frac{\partial k}{\partial x} \qquad\qquad (3.4.77)$$

$$\frac{1}{k}\frac{\partial k}{\partial y} = \frac{\partial\theta}{\partial y}\left[\frac{U\sin\theta - V\cos\theta}{A}\right] + \frac{1}{k}\frac{\partial k}{\partial y} \qquad\qquad (3.4.78)$$

where $\quad A = U\cos\theta + V\sin\theta + \frac{1}{2}\left[1 + \frac{2kh}{\sinh(2kh)}\right]\left[\frac{\sigma}{k} - U\cos\theta - V\sin\theta\right] \qquad (3.4.79)$

$$\frac{1}{k}\frac{\partial k}{\partial x} = -\frac{1}{A}\left[\left(\cos\theta\frac{\partial U}{\partial x} + \sin\theta\frac{\partial V}{\partial x}\right) + \left(\frac{\sigma - Uk\cos\theta - Vk\sin\theta}{\sinh(2kh)}\right)\frac{\partial h}{\partial x}\right] \qquad (3.4.80)$$

$$\frac{1}{k}\frac{\partial k}{\partial y} = -\frac{1}{A}\left[\left(\cos\theta\frac{\partial U}{\partial y} + \sin\theta\frac{\partial V}{\partial y}\right) + \left(\frac{\sigma - Uk\cos\theta - Vk\sin\theta}{\sinh(2kh)}\right)\frac{\partial h}{\partial y}\right] \qquad (3.4.81)$$

The final form of the wave angle equation can be obtained by substituting equation (3.4.77) and (3.4.78) into (3.4.76) to give:

$$\frac{\partial\theta}{\partial x}\left[\cos\theta + \frac{\sin\theta(U\sin\theta - V\cos\theta)}{A}\right] + \frac{\partial\theta}{\partial y}\left[\sin\theta - \frac{\cos\theta(U\sin\theta - V\cos\theta)}{A}\right]$$

$$= \frac{1}{k}\frac{\partial k}{\partial x}\cos\theta - \frac{1}{k}\frac{\partial k}{\partial y}\sin\theta \qquad\qquad (3.4.82)$$

The effect of refraction and shoaling on the wave heights, due to wave-current interactions is determined by using the energy equation. The form of the energy equation was first given by Longuet-Higgins and Stewart (1960,1961) to give:

$$\frac{\partial E}{\partial t} + \frac{\partial}{\partial x}\{E(U + C_{g_x})\} + \frac{\partial}{\partial y}\{E(U + C_{g_y})\} + S_{xx}\frac{\partial U}{\partial x} + S_{xy}\frac{\partial V}{\partial x} + S_{yx}\frac{\partial U}{\partial y} + S_{yy}\frac{\partial V}{\partial y} = 0$$

$$\ldots\ldots\ldots\ldots(3.4.83)$$

Dividing equation (3.4.83) by E and expanding in Cartesian co-ordinate form gives:

$$\frac{1}{E}\frac{\partial E}{\partial t} + (U + C_g\cos\theta)\frac{1}{E}\frac{\partial E}{\partial x} + (V + C_g\sin\theta)\frac{1}{E}\frac{\partial E}{\partial y} + \frac{\partial}{\partial x}(U + C_g\cos\theta) +$$

$$\frac{\partial}{\partial y}(U + C_g\sin\theta) + \frac{1}{E}\left\{S_{xx}\frac{\partial U}{\partial x} + S_{xy}\frac{\partial V}{\partial x} + S_{yx}\frac{\partial U}{\partial y} + S_{yy}\frac{\partial V}{\partial y}\right\} = 0 \qquad (3.4.84)$$

where E is the total energy given by (3.4.37). For a direct relationship for the wave height, by differentiating equation (3.4.84), then the energy equation becomes:

$$\frac{2}{H}\frac{\partial H}{\partial t} + (U + C_g\cos\theta)\frac{2}{H}\frac{\partial H}{\partial x} + (V + C_g\sin\theta)\frac{2}{H}\frac{\partial H}{\partial y} + \frac{\partial U}{\partial x} + \frac{\partial V}{\partial y}$$

$$- C_g\sin\theta\frac{\partial\theta}{\partial x} + \cos\theta\frac{\partial C_g}{\partial x} + C_g\cos\theta\frac{\partial\theta}{\partial y} + \sin\theta\frac{\partial C_g}{\partial y} + Q = 0 \qquad (3.4.85)$$

where $Q = \frac{1}{E}\left[S_{xx}\frac{\partial U}{\partial x} + S_{xy}\frac{\partial V}{\partial x} + S_{yx}\frac{\partial U}{\partial y} + S_{yy}\frac{\partial V}{\partial y}\right]$

and the group velocity C_g is given by equation (3.4.32). The group velocity derivatives as required for equation (3.4.85) are given as:

$$\frac{\partial C_g}{\partial x} = \frac{C\left[k\dfrac{\partial h}{\partial x} + h\dfrac{\partial k}{\partial x}\right]\left[\sinh(2kh) - 2kh\cosh(2kh)\right]}{\sinh^2(2kh)} + \frac{1}{2}\left[1 + \frac{2kh}{\sinh(2kh)}\right]\frac{\partial C}{\partial x} \qquad (3.4.86)$$

$$\frac{\partial C_g}{\partial y} = \frac{C\left[k\dfrac{\partial h}{\partial y} + h\dfrac{\partial k}{\partial y}\right]\left[\sinh(2kh) - 2kh\cosh(2kh)\right]}{\sinh^2(2kh)} + \frac{1}{2}\left[1 + \frac{2kh}{\sinh(2kh)}\right]\frac{\partial C}{\partial y} \qquad (3.4.87)$$

where

$$\frac{\partial C}{\partial x} = \frac{g}{2k^2 C}\left[k\sec h^2(kh)\left(k\frac{\partial h}{\partial x} + h\frac{\partial k}{\partial x}\right) - \tanh(kh)\frac{\partial k}{\partial x}\right] \qquad (3.4.88)$$

$$\frac{\partial C}{\partial y} = \frac{g}{2k^2 C}\left[k\sec h^2(kh)\left(k\frac{\partial h}{\partial y} + h\frac{\partial k}{\partial y}\right) - \tanh(kh)\frac{\partial k}{\partial y}\right] \qquad (3.4.89)$$

The wave height can be calculated by using equation (3.4.86) to (3.4.89).

3.5 Stresses Due To Wave-Current Interaction

3.5.1 Shear Stresses

From the theory of wave kinematics the shear stress distribution can be found by using the momentum equation on the control surface shown in Figure 3.5.1. The control surface is fixed in space and has horizontal and vertical sides. Its width is dx, and it extends from the level z into the air above the wave. The momentum equation is a vector equation, which contains integral over the volume and the surface area of the control surface (see Fredsoe and Deigaard, 1994)

$$\int_V \rho\frac{\partial \vec{u}}{\partial t}dV = -\int_A \rho\vec{u}(\vec{u}.d\vec{A}) - \int_A pd\vec{A} + \int_V \rho gdV + \int_A d\vec{T} \qquad (3.5.1)$$

where dA is the area vector of surface element, directed out of the surface, and dT is the force from the shear stress acting on a surface element. Equation (3.5.1) states that the acceleration of the mass in the volume of the control surface is equal to the sum of the momentum flux through the surface, the pressure force, gravity, and the shear stress force acting on the control volume. Here the horizontal projection of

equation (3.5.1) is used, and the equation is averaged over one wave period. The control surface extends into the air and all of the terms in eqn. (3.5.1) become zero above the instantaneous level of the water surface (Fredsoe and Deigaard, 1992). The left hand side of the equation becomes zero after time averaging, because the waves are periodic, i.e. no momentum is added to the system during one wave period. Each element of equation (3.5.1), after undertaking integration and with assumptions, becomes:
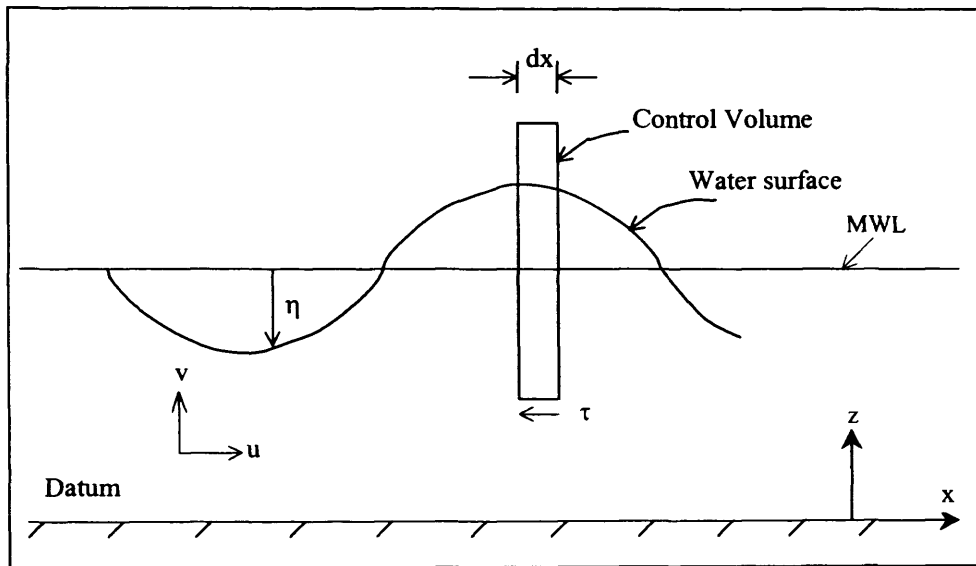
Figure 3.5.1 Control volume to which the momentum equation is applied

$$\overline{\vec{e}\int_A \rho \vec{u}(\vec{u}.d\vec{A})} = \left\{ \rho \frac{d}{dx}\left(\frac{cA}{T}\right) + \rho g H H_x{}' \left(\frac{1}{4} - \frac{1}{8}\frac{z}{D}\right) \right\} dx \qquad (3.5.2)$$

where $\overline{e}$ is a horizontal unit vector. The pressure can be found from the hydrostatic pressure distribution to give:

$$\overline{\vec{e}\int_A p d\vec{A}} = \rho g \left(\frac{H H_x{}'}{8} + S(D-z) \right) dx \qquad (3.5.3)$$

The gravity force becomes zero as a horizontal projection is used. The only shear stress force, which is non-zero, is due to shear stress acting on the horizontal bottom of the control surface giving

$$\overline{\vec{e}\int_A d\vec{T}} = -\overline{\tau}dx \qquad (3.5.4)$$

where $\bar{\tau}$ is the shear stress. The momentum equation can now be re-written as:

$$0 = \left\{ \rho \frac{d}{dx}\left(\frac{cA}{T}\right) + \rho g H H_x{}'\left(\frac{1}{4} - \frac{1}{8}\frac{z}{D}\right) \right\} dx + \rho g \left(\frac{H H_x{}'}{8} + S(D - z)\right) dx - \bar{\tau} dx \qquad (3.5.5)$$

$$\bar{\tau} = -\frac{\rho g}{8}\frac{d(H^2)}{dx}\left(1 + \frac{D - z}{2D}\right) - \frac{\rho}{T}\frac{d(cA)}{dA} - S\rho g D\frac{D - z}{D}$$

or

$$= \frac{1}{c}\frac{dE_{fw}}{dx}\left(1 + \frac{D - z}{2D}\right) - \frac{\rho}{T}\frac{d(cA)}{dA} - S\rho g D\frac{D - z}{D} \qquad (3.5.6)$$

where E is the energy flux of the wave motion. The mean shear stress in the surf zone is thus composed of three contribution including: (i) the pressure of momentum fluxes associated with the decaying wave motion in the surf zone, (ii) the change of momentum in the surface rollers which is constant over the depth, and (iii) the slope S of the mean water surface, i.e. the wave set-up. It has a triangular stress distribution well known from uniform channel flow in hydraulics. Near the mean water surface (at the wave trough level), where $z \approx D$ the shear stress becomes:

$$\bar{\tau}_s = \frac{1}{c}\frac{dE_{fw}}{dx} - \frac{\rho}{T}\frac{d(cA)}{dA} = \frac{1}{c}\bar{D} - \frac{\rho}{T}\frac{d(cA)}{dx} \qquad (3.5.7)$$

where $\bar{D}$ is the rate of loss of wave energy per unit bed area. In equation (3.5.7) the first term is due to the pressure and momentum flux of the wave motion, and the second term, which was first recognised by Svendsen (1984), is due to a change in the momentum of the surface rollers. For a uniform unsteady wave situation then the near surface mean shear stress can be written as:

$$\bar{\tau}_s = \frac{1}{c}\frac{dE}{dt} - \frac{\rho}{L}\frac{d(cA)}{dt} \qquad (3.5.8)$$

where E is the energy per unit bed area and given by $E = \frac{1}{8}\rho g H^2$.

3.5.2 Radiation Stresses

Radiation stresses are the forces per unit area that arise because of the excess momentum flux due to the pressure of waves. In simple terms, there is more momentum flow in the direction of wave advance because the velocity u is in the

direction of wave propagation under the wave crest, when the instantaneous water surface is high (crest) and in the opposite direction when the water surface is low (trough). Also the pressure stress acting under the wave crest is greater than the pressure stress under the wave trough, leading to a net stress over a wave period. Small amplitude wave theory can be used to approximate reasonably the radiation stresses.

The presence of waves will result in an excess flow of momentum, which is defined as the radiation stress (Longuet-Higgins and Stewart, 1964). This flux of momentum is formed by two contributions; first the momentum per unit volume associated with a fluid particle is ρu, and its contribution to the flux of momentum across a vertical section normal to the s-axis (the direction of wave propagation) is given as ρu^2. Hence, the total flux of momentum in the s-direction due to wave generated motion is (Fredsoe and Deigaard, 1994) given as:

$$I_m = \int_0^{h+\eta} \rho u^2 dz \qquad (3.5.9)$$

In the horizontal n-direction perpendicular to the s-axis, there is no momentum flux due to wave generated motion, as the wave-generated velocity is zero in this direction. The second contribution to the momentum flux originates from the pressure and is given by

$$I_p = \int_0^{h+\eta} p dz \qquad (3.5.10)$$
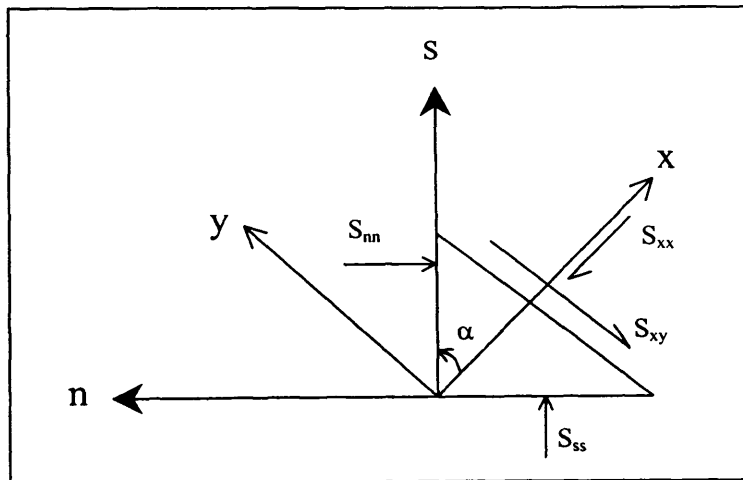
Figure 3.5.2. Radiation Stresses acting on a small triangular element

The principle component of the radiation stress in the direction of wave propagation is defined as the time averaged total momentum flux due to the presence of waves, minus the mean flux in the absence of waves, that is

$$S_{ss} = \overline{\int_0^{h+\eta} (p + \rho u^2)\,dz} - \int_0^h p_0\,dz \qquad\qquad (3.5.11)$$

where p_0 is the hydrostatic pressure. The force per unit width caused by the presence of waves can be given by equation (3.4.32) and (3.4.37) and is always directed towards the body of fluid considered, no matter whether the waves are travelling to the left or to the right. As terms of third and higher order are disregarded, then S_{SS} can be calculated from linear wave theory to give:

$$S_{ss} = \frac{1}{8}\rho g H^2 \left(1 + \frac{2kh}{\sinh(2kh)}\right) = \frac{1}{2}E(1 + G) \qquad\qquad (3.5.12)$$

Similarly the radiation stress in the n-direction is given by:

$$S_{nn} = \overline{\int_0^{h+\eta} p\,dz} - \int_0^h p_0\,dz = \frac{1}{8}\rho g H^2 \left(\frac{2kh}{\sinh(2kh)}\right) = \frac{1}{2}EG \qquad\qquad (3.5.13)$$

Hence, the radiation stress tensor becomes:

$$S = \begin{bmatrix} S_{ss} & S_{sn} \\ S_{ns} & S_{nn} \end{bmatrix} = \frac{1}{2}E \begin{bmatrix} (1+2G) & 0 \\ 0 & G \end{bmatrix} \qquad\qquad (3.5.14)$$

In the co-ordinate system where the two horizontal axes x and y do not coincide with the s and n-directions, then the radiation stress tensor can easily be calculated by considering the force balance on a small triangular vertical column as indicated in Figure 3.5.2. This gives the following radiation stress tensor:

$$[S] = \begin{bmatrix} S_{xx} & S_{xy} \\ S_{yx} & S_{yy} \end{bmatrix} = \frac{1}{2}E \begin{bmatrix} (1+G)\cos^2\alpha + G & (1+G)\sin\alpha\cos\alpha \\ (1+G)\sin\alpha\cos\alpha & (1+G)\sin^2\alpha + G \end{bmatrix} \qquad (3.5.15)$$

In complex coastal areas, obliquely incident waves are genereated from offshore deep water to shallow water beaches. Wave driven currents are produced which, in turn create the radiation stresses in the longshore and cross-shore directions. In order

to obtain the depth integrated momentum equation for wave-current driven flows, the depth integrated momentum equations in the x and y-direction (i.e. equations 3.3.61. and 3.3.62) should include the radiation stress terms (equation 3.5.15). The modified depth integrated momentum equations, including the radiation stresses for wave current driven flows can be described in the x and y-directions as:

$$\frac{\partial UH}{\partial t} + \frac{\partial \beta U^2 H}{\partial x} + \frac{\partial \beta UVH}{\partial y} = fVH - gH\frac{\partial \eta}{\partial x} + \frac{\rho_a}{\rho} C_W W_x \sqrt{W_x^2 + W_y^2}$$

$$- \frac{gU\sqrt{U^2 + V^2}}{C^2} + \varepsilon H\left(2\frac{\partial^2 U}{\partial x^2} + \frac{\partial^2 U}{\partial y^2} + \frac{\partial^2 V}{\partial x \partial y}\right) - \frac{\partial S_{xx}}{\partial x} - \frac{\partial S_{xy}}{\partial y}$$

$$(3.5.16)$$

$$\frac{\partial VH}{\partial t} + \frac{\partial \beta UVH}{\partial x} + \frac{\partial \beta V^2 H}{\partial y} = fUH - gH\frac{\partial \eta}{\partial x} + \frac{\rho_a}{\rho} C_W W_y \sqrt{W_x^2 + W_y^2}$$

$$- \frac{gV\sqrt{U^2 + V^2}}{C^2} + \varepsilon H\left(2\frac{\partial^2 V}{\partial x^2} + \frac{\partial^2 V}{\partial y^2} + \frac{\partial^2 U}{\partial x \partial y}\right) - \frac{\partial S_{yy}}{\partial y} - \frac{\partial S_{xy}}{\partial x}$$

$$(3.5.17)$$

3.5.3 Lateral Mixing

Lateral mixing is based on momentum exchange between fluid elements as they fluctuate. It was first observed by Prandtl, 1925 (see LeMéhauté, 1976) and explained by the exchange of momentum that occurs in forward direction of the turbulent flow due to the difference in speed between two fluid elements. The average distance travelled by particles before their momentum is suddenly absorbed by their new environment was called the 'mixing length', l_x. Figure 3.5.3 is a schematic representation of this exchange of momentum for lateral mixing formulation.

The flux of the momentum in translating fluid from x_1 to x_2 (Figure 3.5.3) is $\rho u'$. The momentum change per unit time in the direction of the mean flow is $(-\rho u' v')$, where $(-v')$ is the difference in velocities between the two layers. Conversely according to Newton's Second Law, the shear stress per unit area exerted by the

fluid layer at x_1 on the fluid layer at x_2 is given by $\tau = -\rho u'v'$. Using the Taylor expansion to first order, the shear stress between the fluid layers can be written as

$$\tau = -\rho u'l_x \frac{\partial V}{\partial x} \qquad (3.5.18)$$
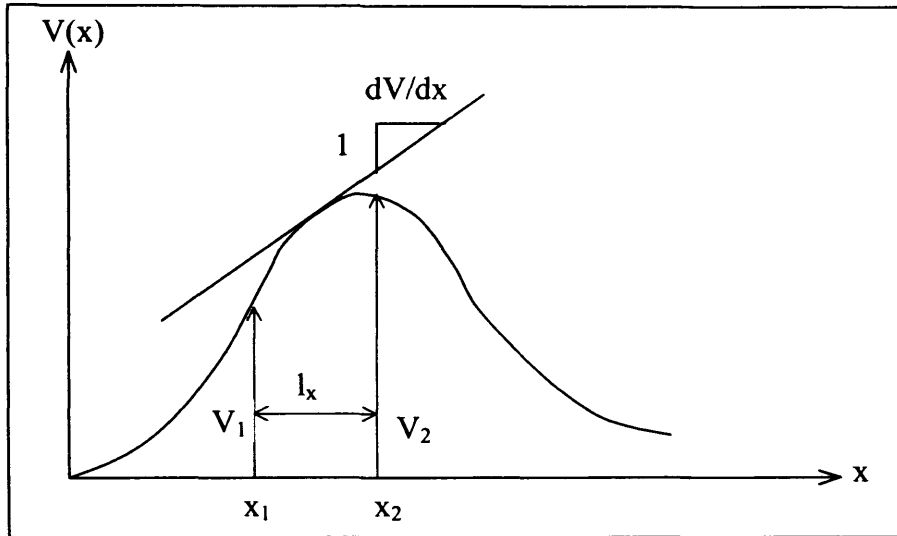
Figure 3.5.3. Lateral mixing formulation sketch

The velocity distribution could vary in two directions for an arbitrary co-ordinate system, therefore the shear stress could also include a term (Dronkers, 1964)

$$\tau = -\rho v'l_y \frac{\partial U}{\partial y} \qquad (3.5.19)$$

The shear stress will be assumed to be

$$\tau_l \propto -\rho(u'l_x \frac{\partial V}{\partial x} + v'l_y \frac{\partial U}{\partial y}) \qquad (3.5.20)$$

For a Newtonian fluid in local hydrodynamic equilibrium, the viscous shear stress can be described as:

$$\tau_{ij} = \mu(\partial_i v_j + \partial_j v_i) - \frac{2}{3}(\vec{\nabla}.\vec{v})\mu\delta_{ij} \qquad (3.5.21)$$

where δ_{ij} is the Kroneker delta: $\begin{cases} \delta_{ij} = 1 & i = j \\ \delta_{ij} = 0 & i \neq j \end{cases}$

Equation (3.5.19) can be re-written in the form: $\tau^v = (\tau_{ij}^v) = \rho v \left(\frac{\partial u_i}{\partial x_j} \right)$

In solving the turbulent Reynolds stresses, Boussinesq (1877) (see LeMéhauté, 1976) proposed that they could be represented in a diffusive manner (Falconer, 1993) as:

$$-\overline{u_i' u_j'} = \upsilon' (\partial_i u_j + \partial_j u_i) - \frac{2}{3} \lambda \delta_{i,j} \qquad (3.5.22)$$

where λ is the kinetic energy per unit mass contained in the turbulent fluctuating motion and defined as $\lambda = 1/2 * [u^2 + v^2 + w^2]$ (ASCE, 1988). So for coastal and estuarine waters the turbulent shear stress can be assumed to have the same form as the viscous shear stress (Equation 3.5.20) (McComb, 1992) and can be expressed as

$$\tau' = -\rho \overline{u_i' u_j'} = (\tau_{i,j}') = \rho \upsilon' \left(\frac{\partial u_i}{\partial x_j} \right) \qquad (3.5.23)$$

Based on the above equation, the components of equation (3.5.20) can be written as:

$$\varepsilon_x = \overline{u' l_x} \, and \varepsilon_y = \overline{v' l_y} \qquad (3.5.24)$$

The lateral shear stress can be finally written as:

$$\tau_l = -\rho (\varepsilon_x \frac{\partial V}{\partial x} + \varepsilon_y \frac{\partial U}{\partial y}) \qquad (3.5.25)$$

3.6   Sediment Transport

The mechanism of sediment transport is still not fully understood, especially in complex areas like estuaries and surf zone regions where so many interacting processes are occuring at the same time. Researchers have for some times been trying to find a unique sediment transport formula which can be applied to any cases. The complexity of the mechanisms and the difficulty of getting accurate physical data are another obstruction. The sediment transport flux is dependent on many parameters including, for example:

$$q_s = f(u_*, U, V, H, d, h, w_s, s, \upsilon, \rho, \ldots \ldots) \qquad (3.6.1)$$

where q_s =sediment flux per unit width; d= sediment mean size; w_s = particle settling velocity; s = sediment specific gravity = ρ_s / ρ; and ρ_s = sediment density.

Sediment Size: The most common measure of sediment size is the sieve diameter, because of the different particle shapes in nature. The sieve diameter is the length of a side of a square sieve opening through which a particle will just pass. Different sizes of representative diameter must be chosen when dealing with natural sediments. Most of the time the median diameter d_{50}, is used (where the subscript d denotes the percentage by weight of sediment finer than that diameter). Some authors have used different values in their respective formulae. Ackers and White (1973) recommended d_{35}, Einstein (1942) (see Graf, 1971) favoured splitting the sediment into different size fractions and analysing them independently.

Settling Velocity: The settling velocity is the terminal velocity of a particle falling in clear still fluid. This is a very important parameter, since it express the hydraulic properties of a sediment particle, mainly the size, shape, density and chemical properties. Owen (1976) recommended measuring the fall velocity in situ. This is not often used and the settling velocity is generally calculated from the measured diameter. By definition of the settling velocity the particle is in equilibrium and the submerged weight can be equated to the drag force giving, for a sphere:

$$(\rho_s - \rho)g\pi d^3 / 6 = C_D \rho w_S \pi d^2 / 8 \qquad (3.6.2)$$

where C_D = Drag coefficient. Since C_D varies in a complicated manner with sediment size, different formulae have been proposed for various ranges of particle size. For coarser particles van Rijn (1984b) proposed a relationship of the form:

$$w_S = 1.1\sqrt{(s-1)gd} \qquad (3.6.3)$$

These formulae can only be considered as an approximation to the settling velocity, since they rely on many assumption.

Initiation of Motion: The importance of the bed shear stress as the governing mechanism causing sediment motion was first recognised by Du Buat (1786) (See Owens, 1986). The concept of critical shear stress τ_c, which is just sufficient to cause incipient motion, was first introduced in this century and much work is still on-going in this field. The concept of initiation of motion can be explained by

Shield's diagram, in which a relationship for the initiation of motion was first developed. The relationship is between two dimensionless parameter called the shear Reynold's number R_*, and an entrained function F_*, given as

$$R_* = \frac{u_* d}{\upsilon}$$ (3.6.4)

$$F_* = \frac{u_*^2}{(s-1)gd}$$ (3.6.5)

The Shield's diagram is sketched in Figure 3.6.1. This curve represents the relationship between the sediment size and the thickness of the laminar sublayer of the flow. The entrainment function is proportional to the ratio of the lift force to the submerged weight of a particle. Shield's curve is widely used in sediment transport formulae, but one disadvantage is the use of u_* in both dimensional parameters R_* and F_*. To overcome this problem u_* can be eliminated from equation (3.6.4) and (3.6.5) to give the dimensionless particle parameter, D_*
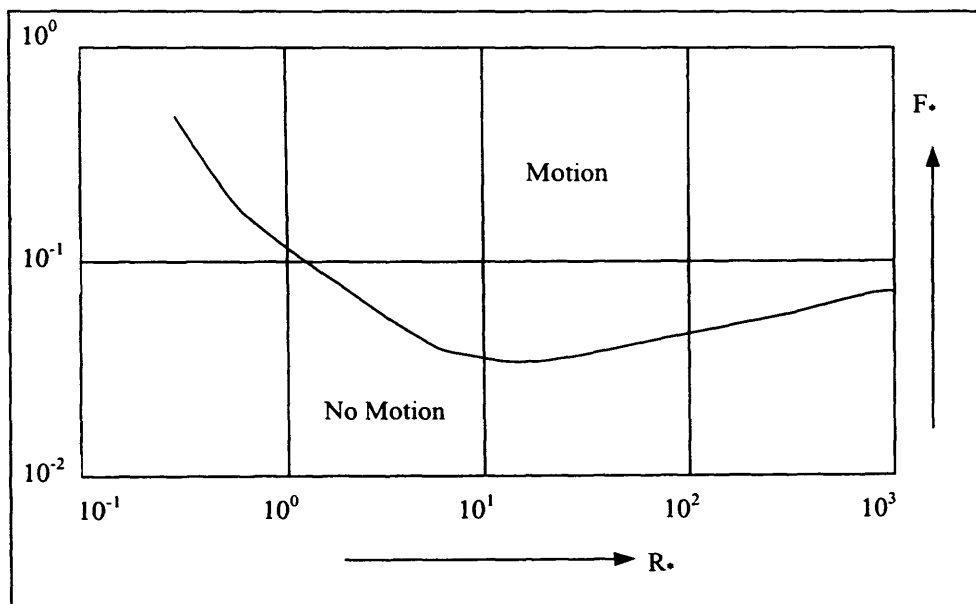

Figure 3.6.1: Shield's diagram

where $$D_* = d\left[\frac{(s-1)g}{\upsilon^2}\right]^{1/3}$$ (3.6.6)

D_* was used by Van Rijn (1984a) as an axis for Shield's curve.

3.6.1   Two Dimensional Depth Averaged Sediment Transport Equation

For the sediment transport model, two widely used equations are considered in the formulation of DIVAST for predicting both suspended and bed load sediment fluxes. These two well known formulae are those proposed by Engelund-Hansen (1967) (see Graf, 1971) and Van Rijn (1984). Owens (1986) did some detailed comparison of several sediment transport formulation for extensive laboratory flume data and sediment flux measurements and found that the Engelund-Hansen formulation apppeared to be more accurate than most of the other schemes considered and it was also computationally more efficient. Again in the recent times Van Rijn's formulation is more widely used by researchers and practising engineers in sediment transport modelling because it is based more on physical reasoning, and backed up by field measurements, rather than being based on empirical formulations relating to the specific data.

For a horizontal or quasi-horizontal flow, the three-dimensional solute mass balance equation can be integrated over the water depth to give the two-dimensional depth integrated advective-diffusion equation according to Fischer (1979) as :

$$\frac{\partial HS}{\partial t} + \frac{\partial HUS}{\partial x} + \frac{\partial HVS}{\partial y} - \frac{\partial}{\partial x}\left[HD_{xx}\frac{\partial S}{\partial x} + HD_{xy}\frac{\partial S}{\partial y}\right] + \frac{\partial}{\partial y}\left[HD_{yx}\frac{\partial S}{\partial x} + HD_{yy}\frac{\partial S}{\partial y}\right] = E$$

$$\dots\dots\dots(3.6.7)$$

where

S = Depth averaged suspended sediment concentration (unit/volume).

D_{xx}, D_{xy}, D_{yx}, D_{yy} = Depth averaged dispersion-diffusion coefficients in the x,y directions (m^2/s), For the dispersion-diffusion terms, the coefficients can be of the following form in two-dimensions according to Falconer et al. (1996). In which, k_l is the longitudinal depth averaged dispersion constant (dimensionless), k_t is the depth averaged lateral turbulent diffusion constant (dimensionless). For values of k_l and k_t these can be set to minimum values assuming a logarithmic velocity distribution. The value of k_l = 5.93 and k_t = 0.15 were proposed by Elder (1959).

$$D_{xx} = \frac{\left(k_l U^2 + k_t V^2\right) H \sqrt{g}}{C\sqrt{U^2 + V^2}}$$ (3.6.8)

$$D_{xy} = D_{yx} = \frac{\left(k_l - k_t\right) U V H \sqrt{g}}{C\sqrt{U^2 + V^2}}$$ (3.6.9)

$$D_{yy} = \frac{\left(k_l V^2 + k_t U^2\right) H \sqrt{g}}{C\sqrt{U^2 + V^2}}$$ (3.6.10)

E = net erosion or deposition per unit area of the bed. It can be shown (Owens, 1986) that the depth averaged erosion or deposition can be expressed as:

$$E = \gamma w_s \left(S_e - S\right)$$ (3.6.11)

where

S_e = depth averaged equilibrium concentration

γ = a profile factor given by the ratio of the bed concentration S_a to the depth averaged concentration S.

3.6.2 Estuarine Sediment Transport

(i)   Bed-load transport (Van Rijn, 1984a)

The transport of particles by rolling, sliding and saltation is called the bed load transport and Van Rijn, (1984a) formulae is described here. Bed load transport can be calculated from a number of different methods as given by Meyer-Peter et al. 1948 (see Graf, 1971); Bagnold 1966 (see Graf, 1971) and Van Rijn, 1984a. According to Bagnold (1954), the movement of bed load particles was dominated by particle saltation, caused by a combination of hydrodynamic and gravity forces, which means that the motion of bed load particles is assumed to be dominated by gravity forces, while the effect of turbulence on the overall trajectory is of minor importance. In this present analysis, the bed load transport is defined as the transport of particles by rolling and saltation along the bed surface. The transport rate (q_b) of the bed load is defined as the product of the particle velocity (u_b), the saltation height (δ_b) and the bed load concentration (C_b).

$$q_b = u_b \delta_b C_b$$ (3.6.12)

where $u_b = 1.5[(s' - 1)gD]^{0.5} T^{0.6}$ (3.6.13)

$\delta_b = 0.3 D D_*^{0.3} T^{0.5}$ (3.6.14)

$C_b = 0.18 S_0 \dfrac{T}{D_*}$ (3.6.15)

The basic assumption of the bed load transport rate can be described adequately by two dimensional parameters which are (a) dimensionless particle diameter D_*, described in equation (3.6.6) and transport stage parameter (T). The D_* parameter can be derived by eliminating the shear velocity from the particle mobility parameter and the particle Reynold's number, while the T parameter express the mobility of the particle in terms of the stage of movement relative to the critical stage for initiation of motion.

Transport stage parameter, $\quad T = \dfrac{(u_*')^2 - (u_{*cr})^2}{(u_{*cr})^2}$ (3.6.16)

where $\quad u_*' = (g^{0.5} / C') \bar{u} \quad = \quad$ bed shear velocity related to grains

$\quad C' = 18 \log(\dfrac{12h}{3D_{10}}) \quad = \quad$ Chezy coefficient related to grains

$\quad \bar{u} \quad = \quad$ mean flow velocity

$\quad u_{*cr} = [\theta_{cr}(s - 1)gD_{50}]^{0.5} = $ critical bed shear velocity   (3.6.17)

where $\quad \theta_{cr} \quad = $ critical mobility parameter given by Shield's

By substituting equation (3.6.13), (3.6.14) and (3.6.15) into equation (3.6.12), the bed load transport (in m^3/sec) for particles in the range 200-2000 μm can be computed as:

$$\dfrac{q_b}{[(s - 1)g]^{0.5} D_{50}^{1.5}} = 0.053 \dfrac{T^{2.1}}{D_*^{0.3}}$$ (3.6.18)

or $q_b = 0.053(s - 1)^{0.5} g^{0.5} D_{50}^{1.5} D_*^{-0.3} T^{2.1}$ (3.6.19)

Equation (3.6.19) was found to overpredict the transport rates for T>3 (Van Rijn, 1984a) and modifying expressions have suggested for the range as:

$$q_b = 0.1(s-1)^{0.5} g^{0.5} D_*^{-0.3} T^{1.5} , for T \geq 3 \qquad (3.6.20)$$

The assumptions considered to derive equations (3.6.19) and (3.6.20) are as follows:

(i)   particle diameter (D_{50}) ranges from 200 to 2000 m.

(ii)   water depth larger than 0.1 meters.

(iii)   Influence of side wall roughness was eliminated

(iv)   Form roughness was eliminated by using a bedform factor, $\tau_b' = \dfrac{C}{C'} \tau_b$

(ii)   Suspended-load transport (Van Rijn, 1984b)

This is a complex formulation to calculate the depth integrated sediment flux per unit width. The particle diameter is calculated by equation (3.6.6). The critical bed shear velocity U has been calculated from Shield's diagram (Figure 3.6.1), where

$$D_* \leq 4 \quad ; \theta_{cr} = 0.24(D_*)^{-1}$$

$$4 < D_* \leq 10 \quad ; \theta_{cr} = 0.14(D_*)^{-0.64}$$

$$10 < D_* \leq 20 \quad ; \theta_{cr} = 0.04(D_*)^{-0.10}$$

$$20 < D_* \leq 150 \quad ; \theta_{cr} = 0.013(D_*)^{0.29}$$

$$150 < D_* \quad ; \theta_{cr} = 0.055$$

From equation (3.6.17) we can find U*cr and from which

$$\theta_{cr} = \frac{(U_{*cr})^2}{(s-1)g D_{50}} \qquad (3.6.21)$$

The Chezy coefficient is calculated from $C' = 18 \log \left[\dfrac{12 R_b}{3 D_{90}} \right]$ $\qquad (3.6.22)$

The effective bed shear velocity is given as: $U_*' = \dfrac{18 U_s}{C'}$ $\qquad (3.6.23)$

where R_b = hydraulic radius related to bed

U_s = depth average fluid speed

The transport stage parameter T can be calculated from equation (3.6.16). The reference level 'a' for the elevation of the boundary transition from bed load to suspended load transport is defined by: $a = 0.5\Delta$

where $\dfrac{\Delta}{H} = 0.11 \left[\dfrac{D_{50}}{H} \right]^{0.3} \left(1 - e^{-0.5T}\right)\left(25 - T\right)$ $\qquad$ (3.6.24)

The reference concentration S_a is calculated by:

$$S_a = 0.015 \frac{D_{50} T^{1.5}}{a D_*^{0.3}}$$ $\qquad$ (3.6.25)

The representative particle diameter D_S of the suspended sediment is calculated by:

$$\frac{D_S}{D_{50}} 1 + 0.011 \left(\sigma_s - 1\right)\left(T - 25\right)$$ $\qquad$ (3.6.26)

where σ = geometric standard deviation of bed material, defined as:

$$\sigma_s = \frac{1}{2} \left[\frac{D_{84}}{D_{50}} + \frac{D_{50}}{D_{16}} \right]$$ $\qquad$ (3.6.27)

Fall velocity, w_s can be calculated from equation (3.6.3) and a factor ϕ is defined as:

$$\phi = 2.5 \left[\frac{W_f}{U_*} \right]^{0.8} \left[\frac{S_a}{S_o} \right]^{0.4}$$ $\qquad$ (3.6.28)

where S_o = maximum bed concentration (=0.65)

The suspension parameters Z and Z' are calculated as:

$$Z = \frac{W_f}{\beta \kappa U_*} \quad \text{and } Z' = Z + \phi$$ $\qquad$ (3.6.29)

Finally the factor 'F' is calculated by

$$F = \frac{\left[\dfrac{a}{H} \right]^{Z'} - \left[\dfrac{a}{H} \right]^{1.2}}{\left[1 - \dfrac{a}{H} \right]^{Z'} \left(1.2 - Z'\right)}$$ $\qquad$ (3.6.30)

The depth integrated suspended load per unit width, q_s is

$q_s = F U_s H S_a$ $\qquad$ (3.6.31)

The equilibrium depth averaged sediment concentration S_e can be calculated and will be used in equation (3.6.11) $S_e = \dfrac{q_s}{q}$.

3.6.3   Nearshore Sediment Transport

The sediment transport in the nearshore zone is influenced by the wave and wave breaking in the area. When waves propagate into shallow waters near coasts they may encounter relatively strong currents which affect the wave characteristics, the current velocities and the bed shear stress. In order to evaluate the sediment transport equations for combined waves and currents, it is necessary to know the wave height, the water motion in the wave, the bed shear stress, the turbulence level and the current which are introduced in the surf zone. The energy dissipation in this area is one of the important factors to consider to calculate the wave height decay and also is a measure of the production of turbulence in the surf zone.

The flux of the wave energy and the radiation stress decreases in the shoreward direction and vanishes in the shoreline. The change in the wave momentum can not be balanced by a pressure gradient, it needs shear stresses as well, which can only be associated with mean current. Breaking waves can drive strong currents in the surf zone, and this wave driven currents are important for the sediment transport and morphological development in the coastal region.

The method described by Van Rijn (1993) to yield the bed load transport and the suspended load transport due to the combined affect of currents and waves were used in this study (detail in Appendix A). An instantaneous approach is used to compute the instantaneous bed-load transport from the equation

$$q_{b,c} = 0.25 d_{50} u'_{*,c} D_*^{-0.3} T^{1.5} \qquad (3.6.32)$$

in which $u'_{*,c} = \left(\tau'_{b,c} / \rho \right)^{0.5} = g^{0.5} \overline{u} / C' = $ *effective* bed shear velocity (m/s)

The time-averaged value is obtained by averaging over the wave period. The instantaneous bed load transport can be expressed as:

$$q_b(t) = 0.25 \alpha d_{50} D_*^{-0.3} \left[\tau'_{b,cw} / \rho \right]^{0.5} \left[\left(\tau'_{b,cw} - \tau_{b,cr} \right) / \tau_{b,cr} \right]^{1.5} \qquad (3.6.33)$$

where

$q_b (t)$: instantaneous bed load transport

α : calibration factor $= 1 - (H_s /h)^{1.5}$

$\tau'_{b,cw}$: grain related instantaneous bed shear stress due to combined current

and wave (N/m^2)

$\tau_{b,cr}$: critical bed shear stress according to Shields (N/m^2)

A time-averaged approach is used to compute the suspended load transport integration over the depth of the product of velocity and concentration, as follows:

Current direction : $q_s = \int\limits_{a}^{h} ucdz$ (3.6.34)

Wave direction : $q_s = \int\limits_{a}^{h} vcdz$ (3.6.35)

where

q_s : suspended load transport (m^2/s)

u : current velocity at height z above bed in the direction of velocity vector (m/s)

v : wave-induced velocity (m/s) at height z above the bed in the wave direction

c : sediment concentration (volume) at height z above the bed computed numerically from the convection-diffusion equation

a : reference level (m)

h : water depth (m)

Based on the sediment transport rate the coastal profile evaluation can be obtained. The coastal profile can vary considerably during a year or even a single storm event. The cross-shore sediment transport plays an important role in the development of the coastal profile. The coastal model formulating the morphological development is two-dimensional that means the net discharge in the direction parallel to coastline is zero. The morphological development can be computed numerically. The onshore/offshore and longshore sediment transport rates are calculated with the variation of transport across the profile. From the sediment transport field, the development of the coastal profile is calculated by the continuity equation for the sediment

$$\frac{\partial z}{\partial t} = -\frac{1}{1-n}\frac{\partial q_{sx}}{\partial x}$$ (3.6.36)

where z is the bed level, n is the porosity of the bed and q_{sx} is the sediment transport rate in the cross-shore direction. In practise, the sediment transport model and the continuity equation will have to be solved numerically. Normally a finite difference scheme is used, so that the hydrodynamic conditions and sediment transport rates are calculated at each grid point at time t. By use of equation (3.6.36) the bed topography after a morphological time step $(t+\Delta t)$ is determined. It is not trivial to select the numerical scheme for solving the continuity equation.

3.7 Summary

The governing equations of fluid flow and sediment transport in estuarine and coastal waters have been given in this chapter. This chapter was divided into three parts. Firstly, from the general form of conservation and momentum law, the two-dimensional depth integrated fluid flow has been obtained. Also the corresponding boundary conditions and shear stresses are discussed. Secondly, the mild slope parabolic wave equations have been derived in a Cartesian co-ordinate system. The different stresses occurred for wave-current interactions have been discussed. Finally, the sediment transport rate due to estuarine and nearshore wave effects have been obtained. Also, the depth integrated mass balance equation for predicting bed level changes was reviewed.

CHAPTER 4

NUMERICAL MODELLING

4.1 Introduction

The basic governing equations for the hydrodynamics, nearshore wave induced flow patterns, sediment transport rates due to tidal currents and wave action have been derived in the previous chapter [Chapter 3]. The principles of mass, momentum, energy, wave motion and sediment transport mechanisms have been established, which can be used for any suitable solution scheme. A suitable numerical procedure now has to be selected to solve the set of equations, both accurately and economically.

Numerical methods are used to convert any differential equation into an algebraic difference form, which can then be solved for the unknown values at incremental finite points, both in space and time. An intensive amount of work has been done on the numerical solution of a set of partial differential equation. The most common type of numerical methods used in the field of hydraulics are the finite difference method, the finite element method and the finite volume method.

All of the methods have advantages and disadvantage when compared to one another. The finite difference method of solution, either explicit or implicit, is more efficient than the finite element method and also the approximations of the

differential equation are relatively straightforward. However, the treatment of the boundary condition is not so simple. The finite element method requires less nodal points and is more suitable for modelling irregular boundaries. The finite difference method uses less computer time for the same set solution than the finite element method. On the other hand the finite volume method is the integral formulation of the governing equations, which can be discretised directly and transformed to an algebraic system of equations (Roache, 1998).

The numerical modelling of coastal and estuarine waters generally covers a large domain in space and also for unlimited time as this is a long-term process. The main objective of this study is to model the estuarine process for both tidal and wave action for long term sediment transport process, so the accuracy of the model boundaries was not the main focus of attention. In this study the governing differential equations have been discretised and approximated using the finite difference method, which has been successfully applied in many numerical model such as DIVAST (Depth Integrated Velocity and Sediment Transport), TRIVAST (Three Dimensional Layer Integrated Velocity and Sediment Transport), PARAB (Parabolic Wave Model), WRAY (Wave Ray Model) etc.

4.2 Finite Difference Method

In the field of computational hydraulics there are many problems which require the numerical solution of differential equations. One of the classical ways to approach these computational problems is through the method of finite differences. The finite difference method is generally regarded as the oldest and simplest method for numerically solving differential equations. This method uses the Taylor series expansion to approximate the derivatives of the differential equation. The differential terms are then replaced by discrete spatial or temporal differences.

The method consists of the approximate estimation of the values of one or more functions at characteristic locations (nodes) of the solution domain. This numerical estimation is achieved by discretisating the domain through a one-, two- or three-dimensional grid, and the approximation of the differential by a difference equation.

The Taylor's series expansion states that the value of a continuous function $f(x)$ can be calculated at point $(x+\Delta x)$ by stating (Sokolnikoff and Redheffer, 1966):

$$f(x+\Delta x) = f(x) + \Delta x \frac{\partial f(x)}{\partial x} + \frac{\Delta x^2}{2!} \frac{\partial^2 f(x)}{\partial x^2} + \frac{\Delta x^3}{3!} \frac{\partial^3 f(x)}{\partial x^3} + H.O.T. \qquad (4.2.1)$$

where Δx is taken as increment of x and H.O.T. = higher order terms.

Similarly the value of function $f(x)$ at the point $(x-\Delta x)$ can be approximated by

$$f(x-\Delta x) = f(x) - \Delta x \frac{\partial f(x)}{\partial x} + \frac{\Delta x^2}{2!} \frac{\partial^2 f(x)}{\partial x^2} - \frac{\Delta x^3}{3!} \frac{\partial^3 f(x)}{\partial x^3} + H.O.T. \qquad (4.2.2)$$
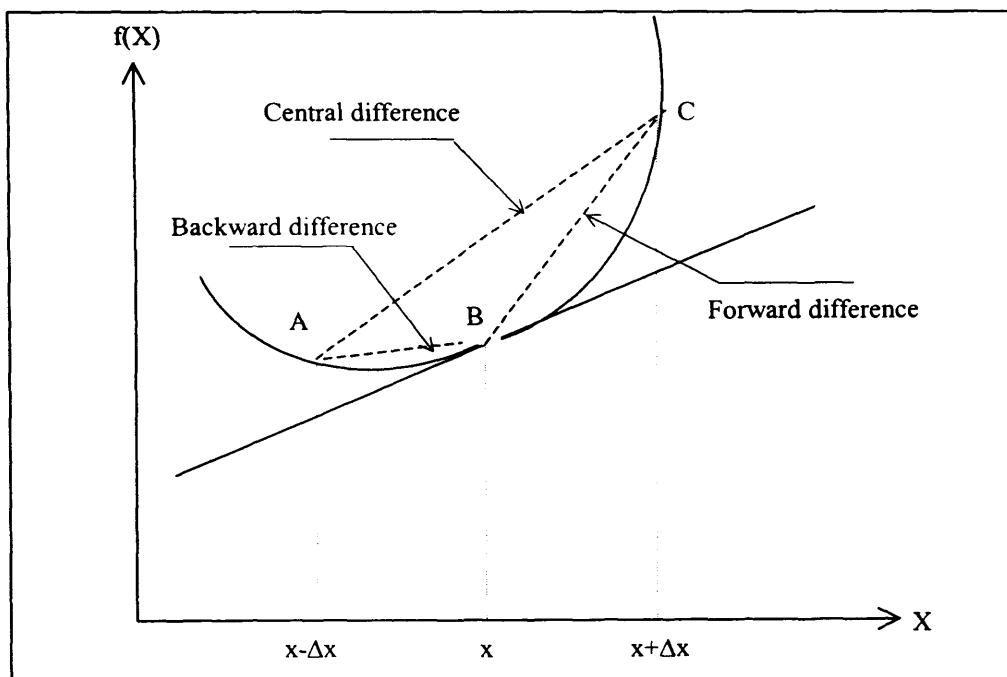

Figure 4.2.1 Comparisons of Finite Difference Approximation

The details of Taylor's expansion series are described in Smith (1985). From equation (4.2.1), we can obtain a second order finite difference representation of the form:

$$\frac{\partial f(x)}{\partial x} = \frac{f(x+\Delta x) - f(x-\Delta x)}{2\Delta x} + O(\Delta x^2) \qquad (4.2.3)$$

Which is called the central difference scheme with a leading truncation error of order (Δx^2). In any finite difference scheme the central difference are preferable due to the associated small function error. The accuracy of any scheme depends on the size of the distance Δx and also on the spatial variations of the function involved (Hirsch, 1988). The three schemes are illustrated graphically in Figure 4.2.1.

An approximation to the second derivative can be obtained by summing equation (4.2.1) and (4.2.2) to give:

$$\frac{\partial^2 f(x)}{\partial x^2} = \frac{f(x+\Delta x) - 2f(x) + f(x-\Delta x)}{\Delta x^2} + O(\Delta x^2) \qquad (4.2.4)$$

which is also second order accurate having a truncation error $O(\Delta x^2)$. Approximations of higher order accuracy are possible by including Taylor series expansions for $f(x+2\Delta x)$, $f(x-2\Delta x)$ etc. (for further details see Smith, 1985). These will usually result in more complex equations whose solutions require greater computational effort.

The difference equations can be solved either explicitly or implicitly. Explicit solutions of these equations are obtained at each mesh point, depending only on previously calculated or boundary values. Implicit solutions are obtained when the set of equations is solved simultaneously at each time step. The differential equations from equation 4.2.1 to equation 4.2.4 can be represented in a number of different finite difference forms. The approximation and substitution of differential operators by difference operators and the numerical integration over the discretised solution domain is not simple. In order to obtain an appropriate numerical scheme, it

is necessary to check the quality of the finite differences numerical schemes (Koutitas, 1981), which includes the criteria of: stability, accuracy, consistency and convergence.

A finite difference numerical scheme will be stable if the error introduced by the numerical scheme remains bounded. The measure of the accuracy of a scheme can be made by calculating the ratio of the numerical and physical wave speeds.

Each finite difference scheme is said to be consistent if in the limit as Δx, $\Delta t \rightarrow 0$, the difference equation tends to the original differential equation, i.e. the truncation error term disappears as the incremental step is reduced. If this requirement is satisfied, then the difference scheme is said to be consistent with the differential equation.

Convergence exists if the numerical solution tends to the analytical when $\Delta x \rightarrow 0$. The solution of a finite difference scheme should always converge to the true solution after a certain number of time steps. Analytical investigations of convergence tend to be complex. So a good finite difference scheme should satisfy the criteria of stability, consistency and convergence and maintain a high order of accuracy. Further details of these properties are given in Roache (1998).

The various numerical properties of finite difference schemes will now be considered for the hydrodynamic, sediment transport and wave equations in order to establish suitable finite difference representation for the above equations.

4.3   ADI Finite Difference Scheme

The particular type of finite difference scheme used in this model is based upon the Alternating Direction Implicit [ADI] technique, which involves the sub-division of each time step into two half time steps. Thus a two-dimensional implicit scheme can

be applied, but considering only one dimension implicitly for each half time step, without the solution of a full two-dimensional matrix.

On the first half time step the water elevation (η), the U velocity component in the x-direction, and the solute concentration are solved implicitly in the x-direction, while the other variables are represented explicitly. Similarly for the second half
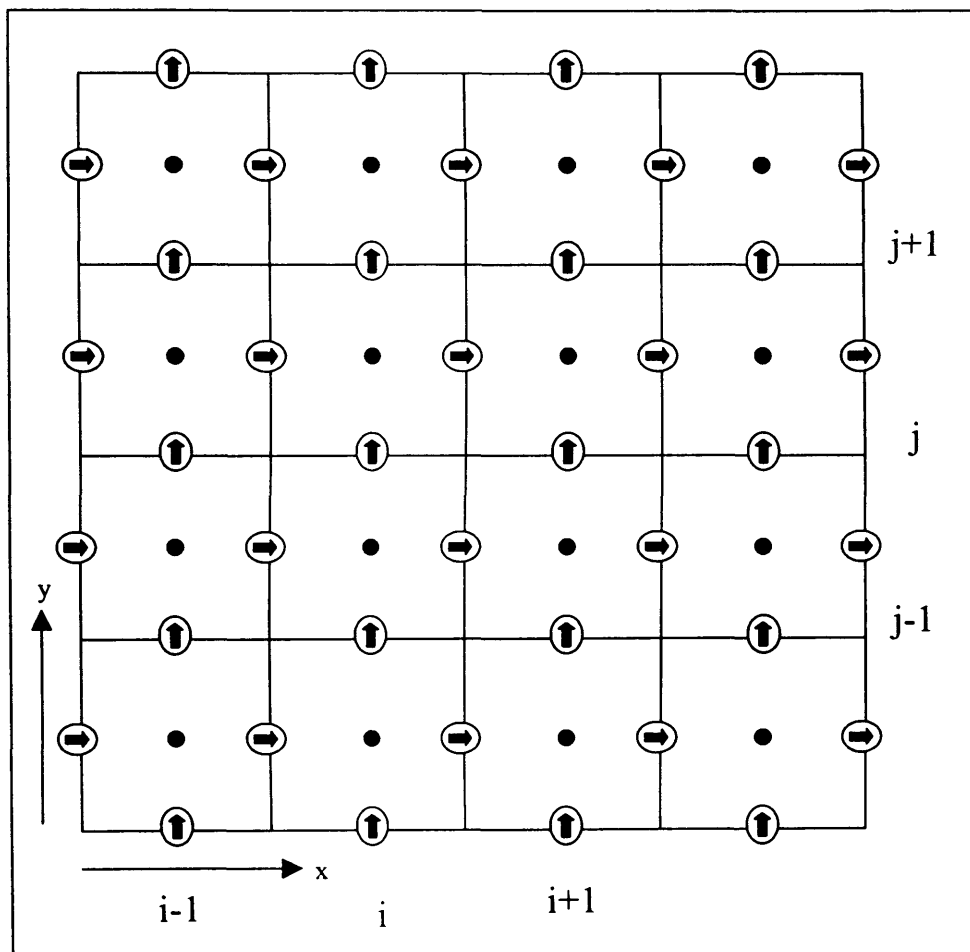
Notation:

●   Water elevation above datum (η) and Solute concentration (S)

➡   x - component discharge per unit width (p = UH)

⬆   y – component discharge per unit width (q = VH)

◯   Depth below datum (h)

Figure 4.3.1: Space staggered grid scheme

time step, the water elevation (η), the V velocity component in the y-direction and the solute concentration are solved implicitly in the y-direction, with the other variables represented explicitly. The resulting finite difference equations for each half time step are solved using the method of Gauss elimination and back substitution, with the inclusion of initial and boundary conditions.

A space staggered grid system is used, with the variables η (elevation) and S (concentration) being located at the grid centre and with the U and V velocity components at the centre of grid sides as shown in Figure 4.3.1. The use of a staggered grid system prevents the appearance of oscillatory solutions, which tend to occur in non-staggered grids for space centred differences. The depths are specified directly at the centre of the grid sides so that twice as much bathymetric detail can be included as in the traditional way, which gives depths at the corners. This method also allows the bed topography to be represented more accurately. The advantage of using a staggered grid for the wave equations is that for each velocity point there is a spatially centred approximation for the water elevation derivative and for each elevation point there are spatially centred differences for both velocity components. Variables required at other grid locations are calculated by linear interpolation.

4.4   Solution Formulation

4.4.1 General Outline

The finite difference transformation of the mass and momentum equations, following Falconer et al. (1999), and the energy equations presented by Lilly (1965), Holland and Liu (1975), Blumberg (1977) and Dalrymple and Ebersole (1980), need to be solved to give the current and wave field.

A rectangular grid mesh was established over the area of interest as shown in Figure 4.4.1. The method of Gauss elimination and back substitution can be applied if there are only three unknowns in each equation. To solve the simplified advective
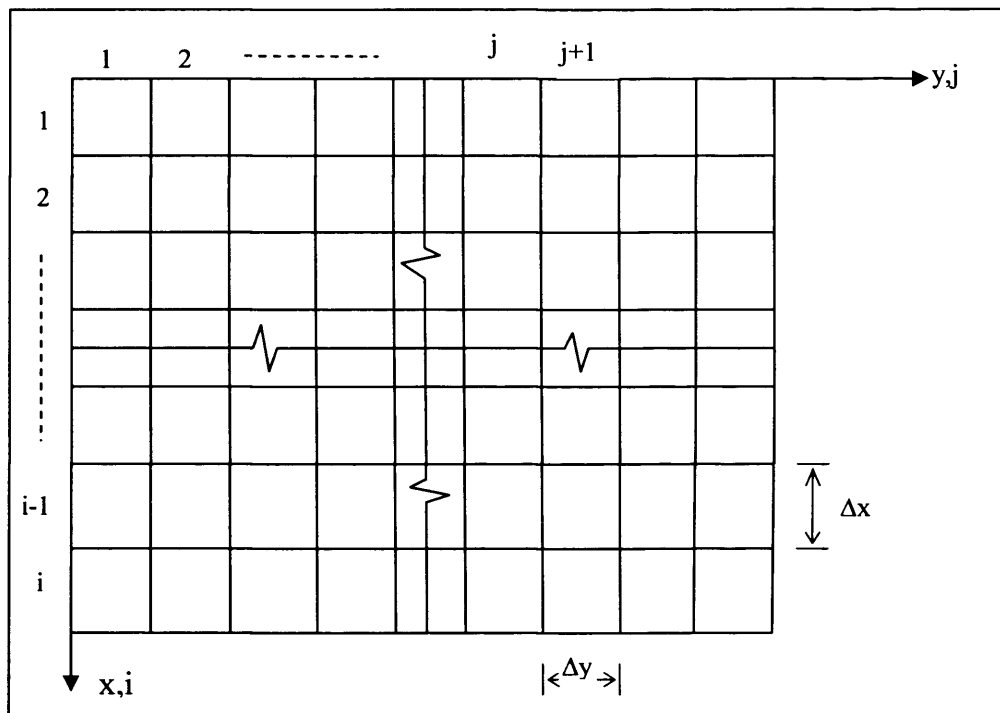
Figure 4.4.1 Grid mesh representation

diffusion equation, the Gauss elimination technique can be extended to two dimensions using the alternating direction implicit technique. The time step is split into two halves; from n to $(n+1/2)$, the derivatives in the x-direction are expressed implicitly, whilst those in the y-direction are expressed explicitly. The equations along each row of grid squares throughout the computational domain can then be solved by the Gauss elimination technique. During the second half time step the derivatives in the y-direction are expressed implicitly and the solution proceeds via the columns in the same manner as for first half time step.

4.4.2 Solution Procedure

The hydrodynamic models are based on different flow parameters which continuously changes with time. These different parameters have been taken care of in different sub-models at the same time step. When the system is not in equilibrium all the variables belonging to the hydrodynamic, wave and sediment transport sub-models are continuously changing with time. In an estuary the fluid motion causes the sediment particles to move along the bed in an unsteady manner. The water level

and velocity changes throughout the tidal period make the sediment motion a continuous short term process. The same happens in nearshore flow fields, where the incoming wave motion changes the sediment movement all times. This type of morphological change is a very important factor in coupling the governing equations of flow, nearshore wave field and sediment transport.

For tidal model it is assumed that the flow and sediment transport field is periodic over several tidal periods, which affects the sediment transport pattern and also the direction of flow. For one tidal period the total sediment transport flux can be calculated in each direction from

$$T_x = \int_0^T \left(q_{s,x} + q_{b,x} \right) dt \qquad\qquad (4.4.1)$$

$$T_y = \int_0^T \left(q_{s,y} + q_{b,y} \right) dt \qquad\qquad (4.4.2)$$

where T_x and T_y are the total sediment transport fluxes in the x and y direction respectively. The estuarine flow field can be expressed by the following flow diagram (Figure 4.4.2).

According to de Vriend (1987) the water discharge and elevation at each point across the domain are the same as for the previous tidal period and the velocity and water depth only changes if there is any change in the depth below datum. With all of the appropriate boundary conditions being included, then the finite difference equations for momentum and continuity are solved for each half time step. After establishing the hydrodynamic field within the model domain, including the water surface elevations, the flow depths and velocity distributions, the solute or sediment transport parameters are then computed for each half time step.

The boundary condition plays an important part in the solution procedure. Depending upon the different combination of boundary conditions the unknowns for the momentum equation change. The solution of the equation change according to

the boundary conditions for each half time step and the computation proceeds to the next time step until the solution reaches the prescribed simulation time.

For the wave model, the general structure is described in Figure 4.4.2. The wave period (T), wave height (H) and the incident wave angle (θ) are provided at the start of the simulation period. The wave height given is the offshore deep water wave height. The wave number (k) for each initial point is evaluated using the dispersion relationship from the given wave period and angle. These calculations are mainly based on the fact that the current is present in the calculation procedure. Based on the presence or non-presence of the current in the calculation then the procedure changes.

For the tidal model, at the start of the simulation period, the initial velocities are usually set to zero across the domain, the sediment concentration is set to a constant value if the sediment distribution is uniform initially, and the water elevations are set horizontally, usually near high or low water level. During the simulation period, the velocities, elevations and sediment concentrations are set to conditions at the end of a previous run, so that eventually equilibrium is achieved.

4.5 Depth Integrated Finite Difference Equations

The two dimensional hydrodynamic model DIVAST [Depth Integrated Velocity and Solute Transport] has been chosen in this study for the hydrodynamic modelling of the shallow water flows. DIVAST has been extensively tested and used for a wide range of problem. For the wave part the two-dimensional wave model [Parabolic Mild Slope Numerical Model] has been developed for predicting the nearshore wave circulation and its resulting effects on nearshore sediment transport. The main objective is to observe the effect of tide and wave currents on shallow water flows.
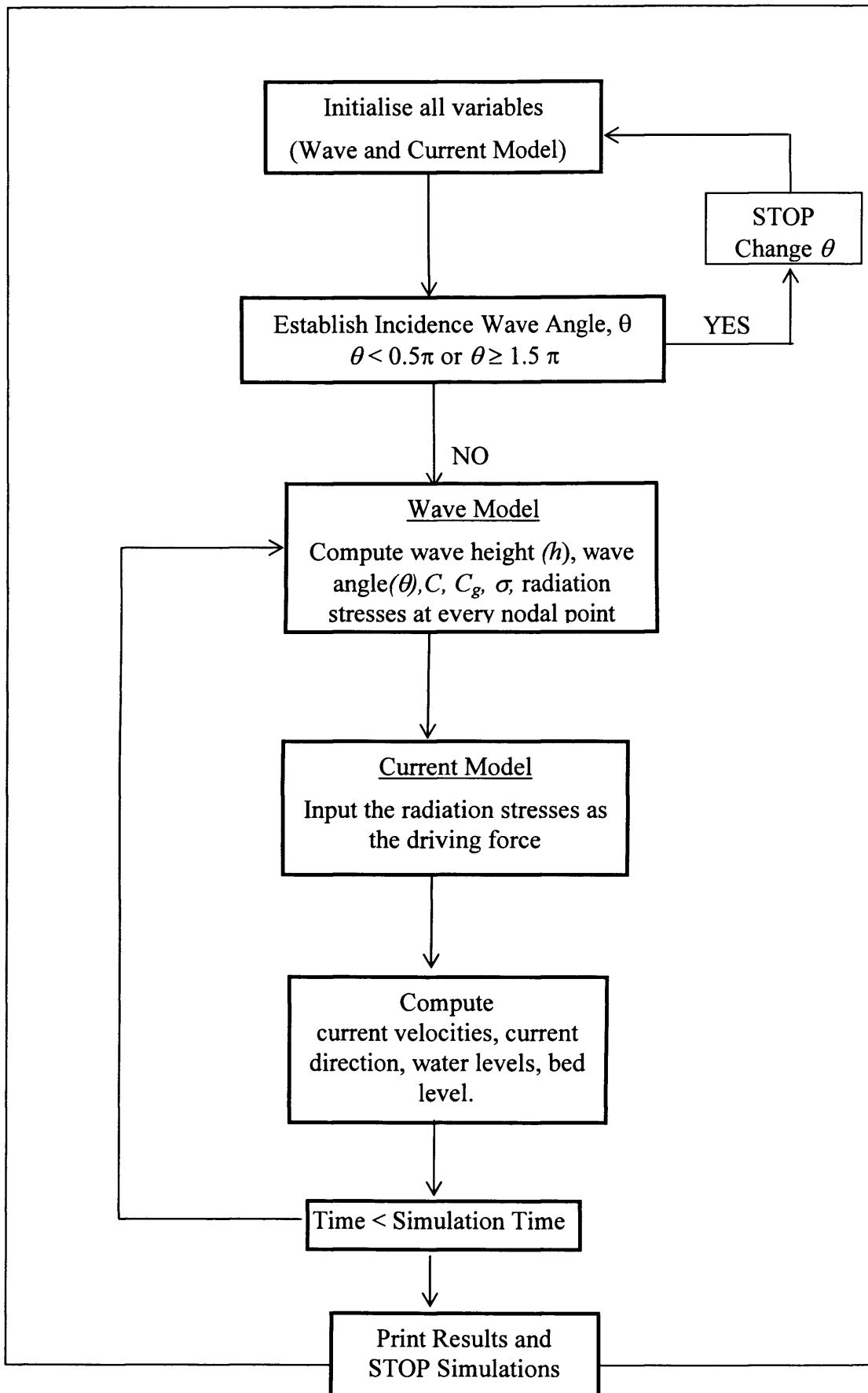
```
┌─────────────────────────────────────────────────────────────────────┐
│                                                                       │
│              ┌────────────────────────────┐                           │
│              │   Initialise all variables │◄──────────┐               │
│              │ (Wave and Current Model)   │           │               │
│              └────────────────────────────┘           │               │
│                           │              ┌──────────────────┐         │
│                           │              │     STOP         │         │
│                           │              │   Change θ       │         │
│                           ▼              └──────────────────┘         │
│              ┌────────────────────────────┐          ▲                │
│              │ Establish Incidence Wave   │   YES     │                │
│              │      Angle, θ              │───────────┘                │
│              │ θ < 0.5π or θ ≥ 1.5 π      │                            │
│              └────────────────────────────┘                           │
│                           │ NO                                         │
│                           ▼                                            │
│              ┌────────────────────────────┐                           │
│     ┌───────►│       Wave Model           │                           │
│     │        │ Compute wave height (h),   │                           │
│     │        │  wave angle(θ),C, Cg, σ,   │                           │
│     │        │  radiation stresses at     │                           │
│     │        │     every nodal point      │                           │
│     │        └────────────────────────────┘                           │
│     │                     │                                            │
│     │                     ▼                                            │
│     │        ┌────────────────────────────┐                           │
│     │        │      Current Model         │                           │
│     │        │ Input the radiation        │                           │
│     │        │  stresses as the driving   │                           │
│     │        │         force              │                           │
│     │        └────────────────────────────┘                           │
│     │                     │                                            │
│     │                     ▼                                            │
│     │        ┌────────────────────────────┐                           │
│     │        │         Compute            │                           │
│     │        │ current velocities, current│                           │
│     │        │ direction, water levels,   │                           │
│     │        │       bed level.           │                           │
│     │        └────────────────────────────┘                           │
│     │                     │                                            │
│     │                     ▼                                            │
│     └────────┤ Time < Simulation Time │                                │
│                           │                                            │
│                           ▼                                            │
│              ┌────────────────────────────┐                           │
│              │     Print Results and      │                           │
│              │    STOP Simulations        │                           │
│              └────────────────────────────┘                           │
└─────────────────────────────────────────────────────────────────────┘
```

Figure 4.4.2 : Flow diagram for wave-current model

4.5.1   Hydrodynamic Equations

The two dimensional depth integrated mass and momentum equation for an incompressible flow can be stated as (from chapter 3)

$$\frac{\partial \eta}{\partial t} + \frac{\partial}{\partial x}(UH) + \frac{\partial}{\partial y}(VH) = 0 \qquad (4.5.1)$$

$$\frac{\partial UH}{\partial t} + \frac{\partial \beta U^2 H}{\partial x} + \frac{\partial \beta UVH}{\partial y} = fVH - gH\frac{\partial \eta}{\partial x} + \frac{\rho_a}{\rho} C_W W_x \sqrt{W_x^2 + W_y^2}$$
$$- \frac{gU\sqrt{U^2 + V^2}}{C^2} + \varepsilon H \left(2\frac{\partial^2 U}{\partial x^2} + \frac{\partial^2 U}{\partial y^2} + \frac{\partial^2 V}{\partial x \partial y} \right) - \frac{\partial S_{xx}}{\partial x} - \frac{\partial S_{xy}}{\partial y} \qquad (4.5.2)$$

$$\frac{\partial VH}{\partial t} + \frac{\partial \beta UVH}{\partial x} + \frac{\partial \beta V^2 H}{\partial y} = fUH - gH\frac{\partial \eta}{\partial x} + \frac{\rho_a}{\rho} C_W W_y \sqrt{W_x^2 + W_y^2}$$
$$- \frac{gV\sqrt{U^2 + V^2}}{C^2} + \varepsilon H \left(2\frac{\partial^2 V}{\partial x^2} + \frac{\partial^2 V}{\partial y^2} + \frac{\partial^2 U}{\partial x \partial y} \right) - \frac{\partial S_{yy}}{\partial y} - \frac{\partial S_{xy}}{\partial x} \qquad (4.5.3)$$

The discrete values of variables (η, U, V, h) are represented by a space staggered grid system (Figure 4.2.2) in which the water elevation (η) is described at the centre of the grid square, while the velocity components (U, V) and the depths below datum (h) in both x and y directions are described at centre of the sides of the grid squares. Each time step is divided into two half time steps, i.e. from time (n) to time ($n+1/2$), values of water elevation (η) and velocity in x direction (U) are solved implicitly. Here the velocity component in the y-direction is expressed explicitly. The second half time step is from time ($n+1/2$) to ($n+1$). Here water elevation (η) and velocity (V) solved implicitly while U is expressed explicitly.

For simplicity the equations can be written in terms of the discharge per unit width or depth and the integrated velocity components defined as

$$p = HU \qquad (4.5.4)$$

$$q = HV \qquad (4.5.5)$$

The continuity equation (4.5.1) can be expressed for the first time step in the *x*-direction as:

$$\frac{2}{\Delta t}\left(\eta_{i,j}^{n+\frac{1}{2}} - \eta_{i,j}^{n}\right) + \frac{1}{\Delta x}\left(p_{i+\frac{1}{2},j}^{n+\frac{1}{2}} - p_{i-\frac{1}{2},j}^{n+\frac{1}{2}}\right) + \frac{1}{\Delta y}\left(q_{i,j+\frac{1}{2}}^{n} - q_{i,j-\frac{1}{2}}^{n}\right) = 0 \qquad (4.5.6)$$

and for the second half time step in the y-direction the continuity equation (4.5.1) gives:

$$\frac{2}{\Delta t}\left(\eta_{i,j}^{n+1} - \eta_{i,j}^{n+\frac{1}{2}}\right) + \frac{1}{\Delta x}\left(p_{i+\frac{1}{2},j}^{n+\frac{1}{2}} - p_{i-\frac{1}{2},j}^{n+\frac{1}{2}}\right) + \frac{1}{\Delta y}\left(q_{i,j+\frac{1}{2}}^{n+1} - q_{i,j-\frac{1}{2}}^{n+1}\right) = 0 \qquad (4.5.7)$$

where i, j = grid point location in the x and y direction respectively. Subscript n, (n+1/2) and (n+1) represents variables evaluated at time $t = n\Delta t$, $t = (n$+1/2)Δt and $t = (n$+1)Δt time levels respectively. Δt represents the time step for computations and n is the timestep number. Equation (4.5.6) and (4.5.7) are first order accurate. But when these two equations are add together then the representation can be summed in both time and space over the whole time step, thereby giving second order accuracy.

In the first half time step the momentum equation is also solved for in the x-direction. The advective acceleration and the Reynolds stress terms are expressed explicitly to avoid having more than three unknown values in the equation, which involves a more complicated and computationally expensive solution procedure. According to Weare (1976) the non-linear terms in the momentum equation can give rise to instabilities, even though an implicit scheme has been used. The instability can be overcome by time centering differences using three time levels, or a velocity smoothing algorithm (Ponce and Yabusaki, 1981). An alternative approach has been for the non-linear advective accelerations and the eddy viscosity terms to be time centred iteration (Roache, 1998), except for the cross product advective acceleration terms which are represented using a first order upwind method, thereby including sufficient artificial diffusion to eliminate grid scale oscillation in regions of high velocity gradients (Owens, 1986).

The x-direction momentum equation (4.5.2) can be written in the following manner for the first half time step:

$$\frac{p_{i+\frac{1}{2},j}^{n+\frac{1}{2}} - p_{i+\frac{1}{2},j}^{n-\frac{1}{2}}}{\Delta t} + \beta \left[\frac{(\hat{U}\hat{p})_{i+\frac{3}{2},j}^{n} - (\hat{U}\hat{p})_{i-\frac{1}{2},j}^{n}}{2\Delta x} + \frac{(\overrightarrow{Vp})_{i+\frac{3}{2},j+\frac{1}{2}}^{n} - (\overrightarrow{Vp})_{i+\frac{3}{2},j-\frac{1}{2}}^{n}}{\Delta y} \right]$$

$$= \lambda q_{i+\frac{1}{2},j}^{-n} - \frac{gH_{i+\frac{1}{2},j}^{n}}{2\Delta x} \left(\eta_{i+1,j}^{n+\frac{1}{2}} + \eta_{i+1,j}^{n-\frac{1}{2}} - \eta_{i,j}^{n+\frac{1}{2}} \eta_{i,j}^{n-\frac{1}{2}} \right) + \frac{\rho_a}{\rho} C_* W^2 \cos \psi$$

$$- \frac{g \left(p_{i+\frac{1}{2},j}^{n+\frac{1}{2}} - p_{i+\frac{1}{2},j}^{n-\frac{1}{2}} \right) \sqrt{\left(\hat{p}_{i+\frac{1}{2},j}^{n} \right)^2 + \left(\hat{q}_{i+\frac{1}{2},j}^{n} \right)^2}}{2 \left(H_{i+\frac{1}{2},j}^{n} C_{i+\frac{1}{2},j}^{n} \right)^2}$$

$$+ \frac{\varepsilon H_{i+\frac{1}{2},j}^{n}}{\Delta x^2} \left[2 \left(\hat{U}_{i+\frac{3}{2},j}^{n} + \hat{U}_{i-\frac{1}{2},j}^{n} \right) + \hat{U}_{i+\frac{1}{2},j+1}^{n} + \hat{U}_{i+\frac{1}{2},j-1}^{n} - 6\hat{U}_{i+\frac{1}{2},j}^{n} + \right.$$

$$\left. + \hat{V}_{i,j-\frac{1}{2}}^{n} - \hat{V}_{i,j+\frac{1}{2}}^{n} - \hat{V}_{i+1,j+\frac{1}{2}}^{n} + \hat{V}_{i+1,j+\frac{1}{2}}^{n} \right]$$

$$- \frac{1}{\Delta x} \left[(S_{xx})_{i+\frac{1}{2},j}^{n} - (S_{xx})_{i-\frac{1}{2},j}^{n} \right] - \frac{1}{\Delta y} \left[(S_{xy})_{i,j+\frac{1}{2}}^{n} - (S_{xy})_{i,j-\frac{1}{2}}^{n} \right] \tag{4.5.8}$$

where $\overline{U}$ denotes the value corrected by iteration by setting:

$$\hat{U}^{n} = \begin{cases} U^{n-\frac{1}{2}} \\ \frac{1}{2} \left(U^{n-\frac{1}{2}} + U^{n+\frac{1}{2}} \right) \end{cases} \tag{4.5.9}$$

$\overline{V}$ denotes a value obtained by averaging the corresponding values at surrounding grid points:

$$\overline{V}_{i+\frac{1}{2},j+\frac{1}{2}}^{n} = \left(V_{i,j+\frac{1}{2}}^{n} + V_{i+1,j+\frac{1}{2}}^{n} \right) \tag{4.5.10}$$

and $\overline{p}$ denotes a value obtained from the upwind algorithm where

$$\vec{p}^{\,n}_{i+\frac{1}{2},j} = \begin{cases} p^n_{i+\frac{1}{2},j-1} \\ \\ p^n_{i+\frac{1}{2},j+1} \end{cases} \qquad\qquad (4.5.11)$$

Similarly, the y-direction momentum equation (4.5.3) can be written for the second half time step as:

$$\frac{q^{n+\frac{1}{2}}_{i,j+\frac{1}{2}} - q^n_{i,j+\frac{1}{2}}}{\Delta t} + \beta\left[\frac{\left(\hat{V}\hat{q}\right)^{n+\frac{1}{2}}_{i,j+\frac{3}{2}} - \left(\hat{V}\hat{q}\right)^{n+\frac{1}{2}}_{i,j-\frac{1}{2}}}{2\Delta y} + \frac{\left(\overline{U}\vec{q}\right)^{n+\frac{1}{2}}_{i+\frac{1}{2},j+\frac{1}{2}} - \left(\overline{U}\vec{q}\right)^{n+\frac{1}{2}}_{i-\frac{1}{2},j+\frac{1}{2}}}{\Delta y}\right]$$

$$= \lambda p^{n+\frac{1}{2}}_{i,j+\frac{1}{2}} - \frac{gH^{n+\frac{1}{2}}_{i+\frac{1}{2},j}}{2\Delta y}\left(\eta^{n+1}_{i,j+1} + \eta^{n-\frac{1}{2}}_{i,j+1} - \eta^{n+1}_{i,j} - \eta^n_{i,j}\right) + \frac{\rho_a}{\rho}C_*W^2\sin\psi$$

$$- \frac{g\left(q^{n+1}_{i,j+\frac{1}{2}} + q^n_{i,j+\frac{1}{2}}\right)\sqrt{\left(q^{n+\frac{1}{2}}_{i,j+\frac{1}{2}}\right)^2 + \left(\vec{p}^{\,n+\frac{1}{2}}_{i,j+\frac{1}{2}}\right)^2}}{2\left(H^{n+\frac{1}{2}}_{i,j+\frac{1}{2}}C^{n+\frac{1}{2}}_{i,j+\frac{1}{2}}\right)^2}$$

$$+ \frac{\varepsilon H^{n+\frac{1}{2}}_{i,j+\frac{1}{2}}}{\Delta x^2}\left[2\left(\hat{V}^{n+\frac{1}{2}}_{i,j+\frac{3}{2}} + \hat{V}^{n+\frac{1}{2}}_{i,j-\frac{1}{2}}\right) + \hat{V}^{n+\frac{1}{2}}_{i+1,j+\frac{1}{2}} + \hat{V}^{n+\frac{1}{2}}_{i-1,j+\frac{1}{2}} - 6\hat{V}^{n+\frac{1}{2}}_{i,j+\frac{1}{2}} + \right.$$

$$\left. + U^{n+\frac{1}{2}}_{i-\frac{1}{2},j} - U^{n+\frac{1}{2}}_{i-\frac{1}{2},j} - U^{n+\frac{1}{2}}_{i-\frac{1}{2},j+1} + U^{n+\frac{1}{2}}_{i+\frac{1}{2},j+1}\right] \qquad (4.4.12)$$

$$- \frac{1}{\Delta x}\left[\left(S_{xy}\right)^n_{i+\frac{1}{2},j} - \left(S_{xy}\right)^n_{i-\frac{1}{2},j}\right] - \frac{1}{\Delta y}\left[\left(S_{yy}\right)^n_{i,j+\frac{1}{2}} - \left(S_{yy}\right)^n_{i,j-\frac{1}{2}}\right]$$

with the V, $\overline{U}$ and q being similar to those expressions listed in equations (4.5.9) to (4.5.11) at the time level $(n+1/2)$ instead of n.

4.5.2 Wave-Current Equations

The higher order approximation of Booij's (1981) parabolic method for the wave equation has been derived from the Helmholz equation using operator splitting technique. The parabolic model equation takes the form as given below (equation 3.4.66):

$$2iKA_u + [2K(K - K_0)A + i(K)_u]A + \left[\frac{3}{2} - \frac{1}{2}\left(\frac{K_0}{K}\right)^{1/2} - \frac{3i}{4K^2}(K)_u\right]A_{vv} = 0$$

The above equation can be re-written as

$$f_1 A_{vv} + f_2 A + f_3 A_u = 0 \qquad\qquad (4.5.13)$$

where

$$\left. \begin{array}{l} f_1 = \left[\dfrac{3}{2} - \dfrac{1}{2}\left(\dfrac{K_0}{K}\right)^{1/2}\right] - \dfrac{3i}{4K^2}(K)_u \\[4mm] f_2 = 2K(K - K_0) + i(K)_u \\[4mm] f_3 = 2iK \end{array} \right\} \qquad\qquad (4.5.14)$$

Equation (4.5.13) can now be written in finite difference form as

$$A = \frac{A_j^{n+1} - A_j^n}{2} \qquad\qquad (4.5.15)$$

$$A_u = \frac{A_j^{n+1} - A_j^n}{\Delta u} \qquad\qquad (4.5.16)$$

$$A_{vv} = \frac{\left(A_{j+1}^{n+1} - 2A_j^{n+1} + A_{j-1}^{n+1}\right) - \left(A_{j+1}^n - 2A_j^n + A_{j-1}^n\right)}{\Delta v^2} \qquad\qquad (4.5.17)$$

By substituting the values of A_{vv}, A_u and A in equation (4.5.13), we get

$$f_1\left[\frac{\left(A_{j+1}^{n+1} - 2A_j^{n+1} + A_{j-1}^{n+1}\right) - \left(A_{j+1}^n - 2A_j^n + A_{j-1}^n\right)}{\Delta v^2}\right] + f_2\left[\frac{A_j^{n+1} - A_j^n}{2}\right] + f_3\left[\frac{A_j^{n+1} - A_j^n}{\Delta u}\right] = 0$$

$$\dots\dots\dots\dots(4.5.18)$$

$$\Rightarrow F_1 A_{j+1}^{n+1} + (F_2 + F_3 - 2F_1)A_j^{n+1} + F_1 A_{j-1}^{n+1} = -F_1 A_{j+1}^n + (F_2 + F_3 + 2F_1)A_j^n - F_1 A_{j-1}^n$$

$$\Rightarrow F_1 A_{j+1}^{n+1} + P_1 A_j^{n+1} + F_1 A_{j-1}^{n+1} = (-F_1)A_{j+1}^n + P_2 A_j^n + (-F_1)A_{j-1}^n$$

$$\Rightarrow F_1 A_{j+1}^{n+1} + P_1 A_j^{n+1} + F_1 A_{j-1}^{n+1} = Q_j^n \qquad\qquad (4.5.19)$$

where

$$F_1 = \frac{f_1}{2\Delta v^2}; \qquad F_2 = \frac{f_2}{2}; \qquad F_3 = \frac{f_3}{\Delta u}$$

$$P_1 = F_2 + F_3 - 2F_1$$

$$P_2 = F_2 + F_3 + 2F_1$$

$$Q_j^n = (-F_1)A_{j+1}^n + P_2 A_j^n + (-F_1)A_{j-1}^n$$

Equation (4.5.19) is an implicit finite difference scheme, which can be solved by knowing all of the coefficients at each time step.

For the wave model, by using a forward difference scheme in the x-direction and backward difference in the y-direction to approximate equation (3.4.82), Noda et al., 1974 (see Lima, 1981), he found the following equation for incidence wave angle θ.

$$\theta_{i,j} = \frac{1}{B_{i,j}} [\frac{1}{k}\frac{\partial k}{\partial y}\cos\theta_{i,j} - \frac{1}{k}\frac{\partial k}{\partial x}\sin\theta_{i,j} + \frac{\theta_{i,j-1}}{\Delta y}\{\sin\theta_{i,j} - \frac{\cos\theta_{i,j}}{A_{i,j}}(W_{i,j}\sin\theta_{i,j} - $$

$$Y_{i,j}\cos\theta_{i,j})\} - \frac{\theta_{i+1,j}}{\Delta x}\{\cos\theta_{i,j} + \frac{\sin\theta_{i,j}}{A_{i,j}}(W_{i,j}\sin\theta_{i,j} - Y_{i,j}\cos\theta_{i,j})\}] \qquad (4.5.20)$$

where

$$\left. \begin{array}{l} W_{i,j} = \frac{1}{2}(U_{i,j} + U_{i+1,j}) \\[2mm] Y_{i,j} = \frac{1}{2}(V_{i,j} + V_{i,j+1}) \end{array} \right\} \qquad (4.5.21)$$

$$B_{i,j} = \frac{\sin\theta_{i,j}}{\Delta y} - \frac{\cos\theta_{i,j}}{\Delta x} - \frac{1}{A_{i,j}}(W_{i,j}\sin\theta_{i,j} - Y_{i,j}\cos\theta_{i,j})\left(\frac{\cos\theta_{i,j}}{\Delta y} + \frac{\sin\theta_{i,j}}{\Delta x}\right) \qquad (4.5.22)$$

and are defined by equation (3.4.79) to (3.4.81).

To approximate the derivatives within equation (3.4.80) and (3.4.81), the central difference method was used. Values of $sin\theta_{i,j}$ and $cos\theta_{i,j}$ are determined by using a

first order Taylor series expression for the four neighbouring grid blocks, summing the results and taking the average value to give:

$$\sin\theta_{i,j} = \frac{1}{4}\left(\sin\theta_{i+1,j} + \sin\theta_{i-1,j} + \sin\theta_{i,j+1} + \sin\theta_{i,j-1}\right)$$

$$+\frac{1}{8}\left(\frac{\theta_{i+1,j} - \theta_{i-1,j}}{\Delta x}\right)\left(\cos\theta_{i-1,j} - \cos\theta_{i+1,j}\right) \qquad (4.5.23)$$

$$+\frac{1}{8}\left(\frac{\theta_{i,j+1} - \theta_{i,j-1}}{\Delta y}\right)\left(\cos\theta_{i,j-1} - \cos\theta_{i,j+1}\right)$$

and likewise:

$$\cos\theta_{i,j} = \frac{1}{4}\left(\cos\theta_{i+1,j} + \cos\theta_{i-1,j} + \cos\theta_{i,j+1} + \cos\theta_{i,j-1}\right)$$

$$+\frac{1}{8}\left(\frac{\theta_{i+1,j} - \theta_{i-1,j}}{\Delta x}\right)\left(\sin\theta_{i+1,j} - \sin\theta_{i-1,j}\right) \qquad (4.5.24)$$

$$+\frac{1}{8}\left(\frac{\theta_{i,j+1} - \theta_{i,j-1}}{\Delta y}\right)\left(\sin\theta_{i,j+1} - \sin\theta_{i,j-1}\right)$$

The wave height equation for the steady state form of equation (3.4.85) is translated into finite difference formulation in the same way as the wave angle equation which is written in a forward difference form in the x-direction and a backward difference form in the y-direction to give:

$$H_{i,j} = \frac{\dfrac{\left(Y_{i,j} + C_{g_{i,j}}\sin\theta_{i,j}\right)}{\Delta y}H_{i,j-1} - \dfrac{\left(W_{i,j} + C_{g_{i,j}}\cos\theta_{i,j}\right)}{\Delta x}H_{i+1,j}}{\dfrac{\left(Y_{i,j} + C_{g_{i,j}}\sin\theta_{i,j}\right)}{\Delta y} - \dfrac{\left(W_{i,j} + C_{g_{i,j}}\cos\theta_{i,j}\right)}{\Delta x} - \dfrac{R_{i,j}}{2}} \qquad (4.5.25)$$

with central velocities $W_{i,j}$ and $Y_{i,j}$ being defined in equation (4.5.19) and with $R_{i,j}$ being:

$$R_{i,j} = \left\{ C_{g_{i,j}} \sin\theta_{i,j} \left(\frac{\theta_{i+1,j} - \theta_{i-1,j}}{2\Delta x} \right) - C_{g_{i,j}} \cos\theta_{i,j} \left(\frac{\theta_{i,j+1} - \theta_{i,j-1}}{2\Delta y} \right) \right\}$$

$$-\left\{ \left(\frac{U_{i+1,j} - U_{1,j}}{\Delta x} \right) + \left(\frac{i_{1,j+1} - V_{i,j}}{\Delta y} \right) \right\} - \cos\theta_{i,j} \frac{\partial C_g}{\partial x} - \sin\theta_{i,j} \frac{\partial C_g}{\partial y}$$

$$-\frac{1}{E_{i,j}} \left\{ S_{xx_{i,j}} \left(\frac{U_{i+1,j} - U_{1,j}}{\Delta x} \right) + S_{xy_{i,j}} \left(\frac{Y_{i+1,j} - Y_{1-1,j}}{2\Delta x} \right) + S_{yx_{i,j}} \left(\frac{W_{i,j+1} - W_{1,j-1}}{2\Delta y} \right) + S_{yy_{i,j}} \left(\frac{V_{i,j+1} - V_{1,j}}{\Delta y} \right) \right\}$$

$$\dots\dots\dots\dots\dots(4.5.26)$$

where $\dfrac{\partial C_g}{\partial x}$ and $\dfrac{\partial C_g}{\partial y}$ are calculated from equations (3.4.86) and (3.4.87)

respectively. By using the governing equations in their finite difference forms and by introducing proper boundary conditions with proper implementation for the stability criteria, a systematic solution method is obtained.

4.5.3   Sediment Transport Equations

The sediment transport computations associated with the tidal model are key to the calculations and predictions of the long term changes in the estuarine area. Also the wave related sediment transport (equation 3.6.32 to 3.6.35) affected the changes in nearshore zone. As already discussed in Chapter 3, the estuarine sediment transport module has two main parts namely: suspended load transport and bed load transport. The nearshore sediment transport has also gets this two parts suspended and bed load transport but which can be derived with the presence of wave. The finite difference method has been used to solve the transport of suspended load which is mainly governed by the solution of the advective-diffusion equation in depth integrated form.

The depth integrated two-dimensional sediment transport equation again uses the finite difference scheme to determine the suspended sediment concentration across the model domain. As before a space staggered grid is used (see Figure 4.3.1) in which the suspended sediment concentration is introduced at the centre of each grid square. The advective-diffusion equation (3.6.7) has been solved for each half time

step and the choice of this time step should include the stability criteria as well. Equation (3.6.8) consists of a combination of the different terms mainly: advection, diffusion, dispersion and a source or sink term. The finite difference formulation of this equation can be written in the following form for any arbitrary grid *(i,j)* as:

$$S_{i,j}^{n+\frac{1}{2}} = S_{i,j}^n + (advectionterms) + (dispersionterms) + (sourceterms) \qquad (4.5.27)$$

The two-dimensional suspended sediment transport [equation (3.6.7)] formulation can be written for the first half time step as:

$$
\left(SH \right)_{i,j}^{n+\frac{1}{2}} + \frac{\Delta t}{4\Delta x} \left[p_{i+\frac{1}{2},j}^{n+\frac{1}{2}} \left(S_{i+1,j}^{n+\frac{1}{2}} + S_{i,j}^{n+\frac{1}{2}} \right) - p_{i-\frac{1}{2},j}^{n+\frac{1}{2}} \left(S_{i,j}^{n+\frac{1}{2}} + S_{i-1,j}^{n+\frac{1}{2}} \right) \right]
$$

$$
- \frac{\Delta t}{2\Delta x^2} \left[\left(HD_{xx} \right)_{i+\frac{1}{2},j}^{n+\frac{1}{2}} \left(S_{i+1,j}^{n+\frac{1}{2}} + S_{i,j}^{n+\frac{1}{2}} \right) - \left(HD_{xx} \right)_{i-\frac{1}{2},j}^{n+\frac{1}{2}} \left(S_{i,j}^{n+\frac{1}{2}} + S_{i-1,j}^{n+\frac{1}{2}} \right) \right]
$$

$$
= \left(SH \right)_{i,j}^{n} - \frac{\Delta t}{4\Delta y} \left[q_{i,j+\frac{1}{2}}^n \left(S_{i,j+1}^n + S_{i,j}^n \right) - q_{i,j-\frac{1}{2}}^n \left(S_{i,j}^n + S_{i,j-1}^n \right) \right]
$$

$$
+ \frac{\Delta t}{2\Delta y^2} \left[\left(HD_{yy} \right)_{i,j+\frac{1}{2}}^n \left(S_{i,j+1}^n + S_{i,j}^n \right) - \left(HD_{yy} \right)_{i,j-\frac{1}{2}}^n \left(S_{i,j}^n + S_{i,j-1}^n \right) \right]
$$

$$
+ \frac{\Delta t}{2\Delta x \Delta y} \left[\left(HD_{xy} \right)_{i+\frac{1}{2},j}^n \left(S_{i+\frac{1}{2},j+\frac{1}{2}}^n - S_{i+\frac{1}{2},j-\frac{1}{2}}^n \right) - \left(HD_{xy} \right)_{i-\frac{1}{2},j}^n \left(S_{i-\frac{1}{2},j+\frac{1}{2}}^n - S_{i-\frac{1}{2},j-\frac{1}{2}}^n \right) \right]
$$

$$
+ \frac{\Delta t}{2\Delta x \Delta y} \left[\left(HD_{yx} \right)_{i,j+\frac{1}{2}}^n \left(S_{i+\frac{1}{2},j+\frac{1}{2}}^n - S_{i-\frac{1}{2},j+\frac{1}{2}}^n \right) - \left(HD_{xy} \right)_{i,j-\frac{1}{2}}^n \left(S_{i+\frac{1}{2},j-\frac{1}{2}}^n - S_{i-\frac{1}{2},j-\frac{1}{2}}^n \right) \right]
$$

$$
+ \frac{\beta^s \Delta t}{2\Delta x} \left[p_{i+\frac{1}{2},j}^{n+\frac{1}{2}} \nabla_{xx}^2 S_{i+\frac{1}{2},j}^n - p_{i-\frac{1}{2},j}^{n+\frac{1}{2}} \nabla_{xx}^2 S_{i-\frac{1}{2},j}^n \right]
$$

$$
+ \frac{\beta^s \Delta t}{2\Delta y} \left[q_{i,j+\frac{1}{2}}^n \nabla_{yy}^2 S_{i,j+\frac{1}{2}}^n - q_{i,j-\frac{1}{2}}^n \nabla_{yy}^2 S_{i,j-\frac{1}{2}}^n \right] + \frac{\Delta t}{2} \phi_s \delta(x_s, y_s) \qquad (4.5.28)
$$

and in a similar manner for the second half time step, except that the derivatives in the x and y-directions are written explicitly and then implicitly respectively.

where

$$
\nabla_{xx}^n S_{i+\frac{1}{2},j}^n = \begin{cases} S_{i+1,j}^n - 2S_{i,j}^n + S_{i-1,j}^n & if\left(U_{i+\frac{1}{2},j}^n \geq 0 \right) \\[2ex] S_{i+2,j}^n - 2S_{i+1,j}^n + S_{i,j}^n & if\left(U_{i+\frac{1}{2},j}^n \leq 0 \right) \end{cases} \qquad (4.5.29)
$$

$$\nabla_{yy}^n S_{i,j+\frac{1}{2}}^n = \begin{cases} S_{i,j+1}^n - 2S_{i,j}^n + S_{i,j-1}^n & if\left(V_{i,j+\frac{1}{2}}^n \geq 0 \right) \\ \\ S_{i+2,j}^n - 2S_{i+1,j}^n + S_{i,j}^n & if\left(U_{i+\frac{1}{2},j}^n \leq 0 \right) \end{cases} \qquad (4.5.30)$$

$$S_{i+\frac{1}{2},j+\frac{1}{2}}^n = \frac{1}{4}\left(S_{i+1,j+1}^n + S_{i+1,j}^n + S_{i,j+1}^n + S_{i,j}^n \right) \qquad (4.5.31)$$

The term $\delta(x_s, y_s)$ is a point unit pulse function used to introduce pollutants at an outfall cell. The function takes the value

$$\delta(x,y) = \begin{cases} 1 & if(x = x_s)and \ (y = y_s) \\ 0 & otherwise \end{cases} \qquad (4.5.32)$$

where are the co-ordinates location where a source or sink term may be allocated. Value for β of 1/6, 1/8 and 0 corresponds to the ADI-TOASOD, ADI-QUICK and second order central difference schemes respectively, where TOASOD stands for Third Order Advection and Second Order Diffusion and QUICK stands for Quadratic Upwind Interpolation for Convective Kinematics (Falconer et al., 1999).

4.6 Model Stability Criteria

The stability should be defined in terms of the sequence of solutions of the difference equations. It has been found that as Δt, Δx, $\Delta y \rightarrow 0$ the truncation error goes to zero. However, when the computation is stable the sequence of approximate solutions tends to the true solution as Δt, Δx, $\Delta y \rightarrow 0$. When the computation is unstable these solutions differ more and more as Δt, Δx, $\Delta y \rightarrow 0$, even though the truncation error tends to zero.

In order to establish an accurate and efficient model, the numerical scheme should be stable. The fluctuation or instability cannot be in the solution when the model will be verified against any controlled system. For the tidal model (DIVAST), the scheme is

basically second order accurate both in time and space with no stability constraints due to the time centred implicit character of the ADI technique. However, for the case of computational time step provided in the input file, it should be restricted in such a way that a reasonable computational accuracy can be achieved (Chen (1992), see Falconer et al. (1999)). A maximum Courant number (C_f) has been suggested by Stelling (1982) as:

$$C_f = 2\Delta t \sqrt{gH\left(\frac{1}{\Delta x^2} + \frac{1}{\Delta y^2}\right)} \leq 4\sqrt{2} \qquad (4.6.1)$$

For the case of two dimensional depth average sediment transport equations which is also solved in each half time step, then the choice of the time step should also consider the stability requirements for the solute transport equation. The stability constraint for the case of pure advection is expressed in equation (4.6.2) with less restrictive stability for the case of advection and diffusion. The DIVAST model used in this study has been third order accurate in space giving:

$$\frac{U\Delta t}{\Delta x} + \frac{V\Delta t}{\Delta y} \leq 2 \qquad (4.6.2)$$

For the wave model, the stability criteria can be expressed in the following manner, in that the speed of propagation of any disturbance in the model must be less than or equal to the speed it takes for the disturbance to cross a computational grid block in a time step. Hence the disturbance speed can be explained as the shallow water gravity wave celerity (C) plus some time independent mean current. The stability criteria can therefore be expressed as:

$$\frac{\sqrt{\Delta x^2 + \Delta y^2}}{\Delta t} \geq |u| + \sqrt{gh} \qquad (4.6.3)$$

At the time when the maximum shallow water wave celerity exceeds the right hand side of equation (4.6.3), the criteria used for the two dimensional depth average condition is:

$$\frac{\sqrt{\Delta x^2 + \Delta y^2}}{\Delta t} \geq \sqrt{gh_{max.}} \qquad\qquad (4.6.4)$$

The left hand side of the above equation can be described as the 'solution velocity'.

4.7   Model Boundary Conditions

Conditions within a computational domain can be solved numerically when initial and boundary condition data are provided accurately to find the unique solution of that particular set of partial differential equations. For a two dimensional depth integrated flow problem the lateral boundary conditions are provided, either as a solid wall or open boundary (inflow or outflow) conditions, which can be obtained from the flow characteristics.

The governing equations of the hydrodynamic, sediment transport and wave model have been discretised in section 4.5 of this chapter and are specified for grid cells within the computational domain. For grid cells near the boundaries, depending upon the type of boundary condition, the equations need to be modified. Generally the boundary conditions can be divided into four categories including: open boundaries, closed boundaries, surface boundaries and bed or bottom boundaries. Boundary conditions for the z-direction at the free surface and at the bed have already been introduced in chapter 3 in order to integrate the mass and momentum equations for the tidal hydrodynamic and wave motion.

4.7.1   Initial Conditions

The velocities, water elevations and sediment concentrations must be specified throughout the computational domain at the beginning of the simulation period in order to initialise the equations. It has to be noted that the higher the accuracy of the initial values provided, then the more rapid the model converges to the correct solution. At the start of the simulation period in a tidal flow model, it is convenient to start the model at high or low tide, with the water elevations being set at the

corresponding level throughout the domain. The velocity components are generally set to zero at the beginning of simulation period. Initial sediment concentrations can be estimated from appropriate field measurements or set to zero. For wave motion the deep water wave height, initial incidence wave angle and wave period are set to initialise the domain. From the deep water wave height etc, then the initial wave height is calculated.

4.7.2 Closed Boundary Conditions

Closed boundary conditions can be regarded as 'wall' boundaries, with no flow or sediment fluxes being permitted to cross these boundaries. This type of boundary occurs along a coastline or adjacent to structures. Values outside the modelling domain are obtained by assuming a 'no slip' condition (i.e. zero flow velocity at the wall) parallel to the boundary and zero flow perpendicular to the boundary. This representation is illustrated for the case in Fig. 4.7.1 using the equation:
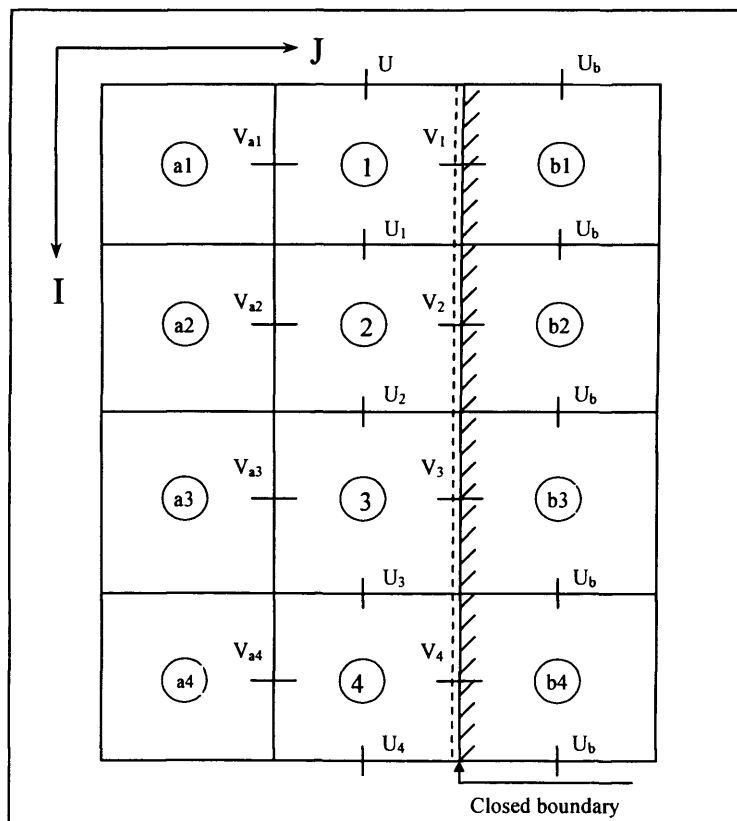
Figure 4.7.1: Wall Boundary

$V_1 = V_2 = V_3 = V_4 = 0$ (4.7.1a)

$U_{bi} = -U_{bi}$ (i = 0,1,2,3.....)   (4.7.1b)

All of the velocities parallel to the wall are set to zero, whereas the velocities outside of the boundary are assigned the same value as the corresponding velocity inside the domain, but with a negative sign. This is done to satisfy the condition across the boundary.

The closed boundary condition for the sediment concentration (equation 4.7.2) assumes that the concentration gradient does not change parallel to the boundary and that there is therefore no sediment flux across the solid boundary, with the subscript 'w' indicating wall boundary value in the following boundary equation, giving:

$$\left.\frac{\partial S}{\partial y}\right|_w = 0 \quad and \quad \left.\frac{\partial^2 S}{\partial y^2}\right|_w = 0 \qquad (4.7.2)$$

4.7.3   Open Boundary Condition

Flow and solutes are allowed to cross an open boundary, which is the opposite for a closed boundary. Appropriate hydrodynamic and solute boundary conditions need to be specified in order to acquire accurate predictions and open boundary values may include: water elevations, velocities and solute concentration level. A free slip boundary condition is used by assuming zero gradient of a variable perpendicular to the open boundary. If the open boundary is a flow boundary, then the velocities at the boundary can be defined as given in Figure 4.7.2 and the following boundary conditions can be obtained for the hydrodynamics parameters, which means that the V velocity at the boundary is given by:

$$\begin{cases} V_i = V_{bi} & (i = 1,2,3,4) \\ U_{bi} = U_i & (i = 0,1,....,4) \end{cases} \qquad (4.7.3)$$

With the corresponding U velocity values outside of the domain being set equal to the boundary value.
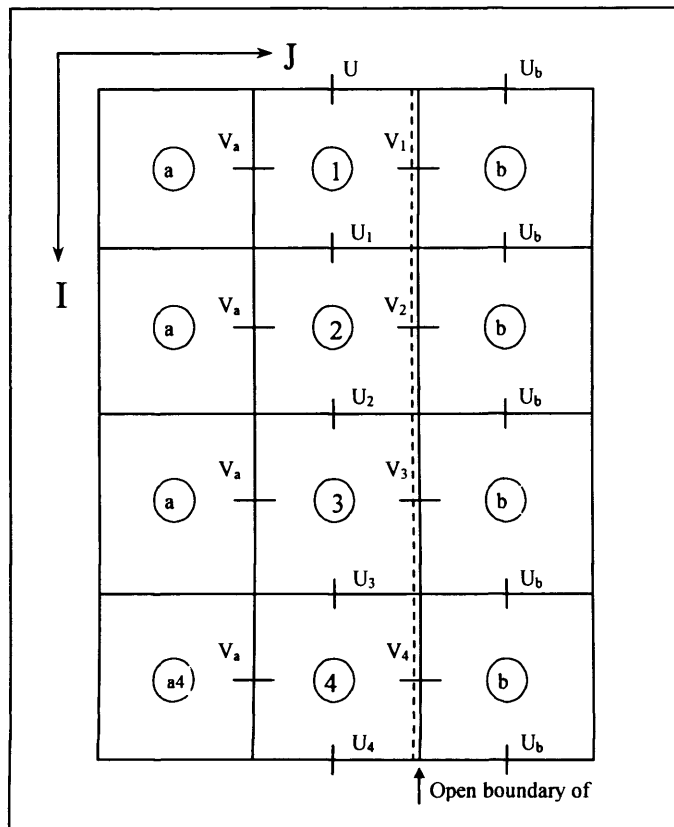
Figure 4.7.2: Flow boundary

Another type of open boundary condition is a water elevation type also shown in Figure 4.7.2, where the following boundary condition can be obtained for the hydrodynamic conditions:

$$
\begin{cases}
U_i = U_{Ai} & (i = 0,1,...,4) \\
V_i = V_{Ai} & (i = 1,........,4) \\
\eta_i = \eta_{Bi} & (i = 1,........,4)
\end{cases}
\qquad (4.7.4)
$$

If the value of the water elevation or velocity along an open boundary is unknown, then the best approximation for tl_s ca   is to prescribe the boundary condition in such a manner that there are no changes to the value of the flow parameters normal to the boundary. Hence, the variation o_ these parameters normal to the boundary can be assumed to be zero, giving:

$$\frac{\partial u}{\partial x}\bigg|_{\substack{open \\ boundary}} = 0 \; ; \quad \frac{\partial v}{\partial x}\bigg|_{\substack{open \\ boundary}} = 0 \quad \text{and} \quad \frac{\partial \eta}{\partial x}\bigg|_{\substack{open \\ boundary}} = 0 \qquad\qquad (4.7.5)$$

For the sediment transport model, the open boundary conditions can be divided into two parts including inflow and outflow boundaries. The sediment concentration at the open boundary is described by the known boundary values S_{Bi}.

$$S_i = S_{Bi} \qquad\qquad\qquad (4.7.6)$$

If the flow at the boundary is leaving the domain, then specification of the sediment concentration outside the boundary is not needed. For an outflow sediment boundary as for the hydrodynamic sub-model, it can be assumed that the variation in the sediment concentration normal to the boundary can be set to zero, giving:

$$\frac{\partial S}{\partial x}\bigg|_{\substack{open \\ boundary}} = 0 \qquad\qquad\qquad (4.7.7)$$

Similarly the boundary conditions along the y-direction can also be obtained in the same way as those described along the x direction.

4.8 Summary

The solution procedure for two-dimensional depth integrated nearshore flow has been discretised in this chapter. The alternating direction implicit scheme technique which is based on finite difference method were explained. The governing equations were discretised using an appropriate numerical scheme for the hydrodynamic equations. The wave-current equations were discretised in fully implicit scheme. And the sediment transport equations by advective-diffusion equations. The solution procedures for this model set-up were discussed. The model stability criteria and also the different boundary conditions effected the flow have been described.

CHAPTER 5

TIDAL MODEL APPLICATION

5.1 Introduction

Coastal processes form part of a continuous dynamic system, which responds to many natural forces and events. The mechanism and interaction of these natural forces such as tides, winds, currents and waves are of key interest in understanding the environmental and hydrodynamic processes in the shallow water regions, as well as the coastline geometry and the basin bathymetry. Without a sound knowledge and understanding of these complicated processes it is virtually impossible to respond to any coastal related problem.

Investigations of integrated tidal, wave and sediment transport mechanisms have been undertaken by many researchers (e.g. Sauvget, et al., 2000; Jakobsen, et al., 2002; Cugier and Hir, 2002) with many different results and conclusions being obtained, based on the theory included in the studies. Sediment transport processes in shallow water regions (e.g. Vos, et al., 2000; Orten and Kineke, 2001; Bai, et al., 2003) form much complex dynamic process that one universal solution is not generally possible. So the predictions are mainly dependent upon accurate investigations carried out for natural phenomena to reproduce the best suitable solution or results.

Numerical models are the tools generally used to study, analyse or compare the physical processes on a long-term basis. To study the combined effects of tidal, wave and sediment transport mechanisms, numerical models have been used to simulate the principal physical processes and to examine their interaction with other features in the estuarine system.

The objectives of this part of the research study were to carry out the above investigations to acquire a better understanding of estuarine sediment transport systems and also to predict the coastline sediment fluxes. The two dimensional numerical model DIVAST was refined and used in this research study to get a better understanding of estuarine transport. The hydrodynamic part of this computational model can simulate tidally induced flows, which in turn drives the sediment transport and wave modules.

The application of this programme has been performed for a natural estuary known as the 'Bristol Channel'. The numerical model has been set up for this site for model calibration and verification. The Bristol Channel has been chosen for this study due its complexity in nature and especially for its high tidal range. The establishment of satisfactory comparisons between the field data and the model results will enable us to use DIVAST for any future application to this site more confidently.

5.2   The Bristol Channel

5.2.1   Location

The Bristol Channel is located along the south-western coastline of the Great Britain (Figure 5.2.1). The channel is open to the west, where it is exposed to the North Atlantic Ocean, and narrows towards the east. The easternmost part of the channel is known separately as the Severn Estuary (Harris and Collins, 1985). The tidal ranges reach an upchannel maximum of 13m (Admiralty, 1993).

Figure 5.2.1 Location of study area (from Miles, 1982)
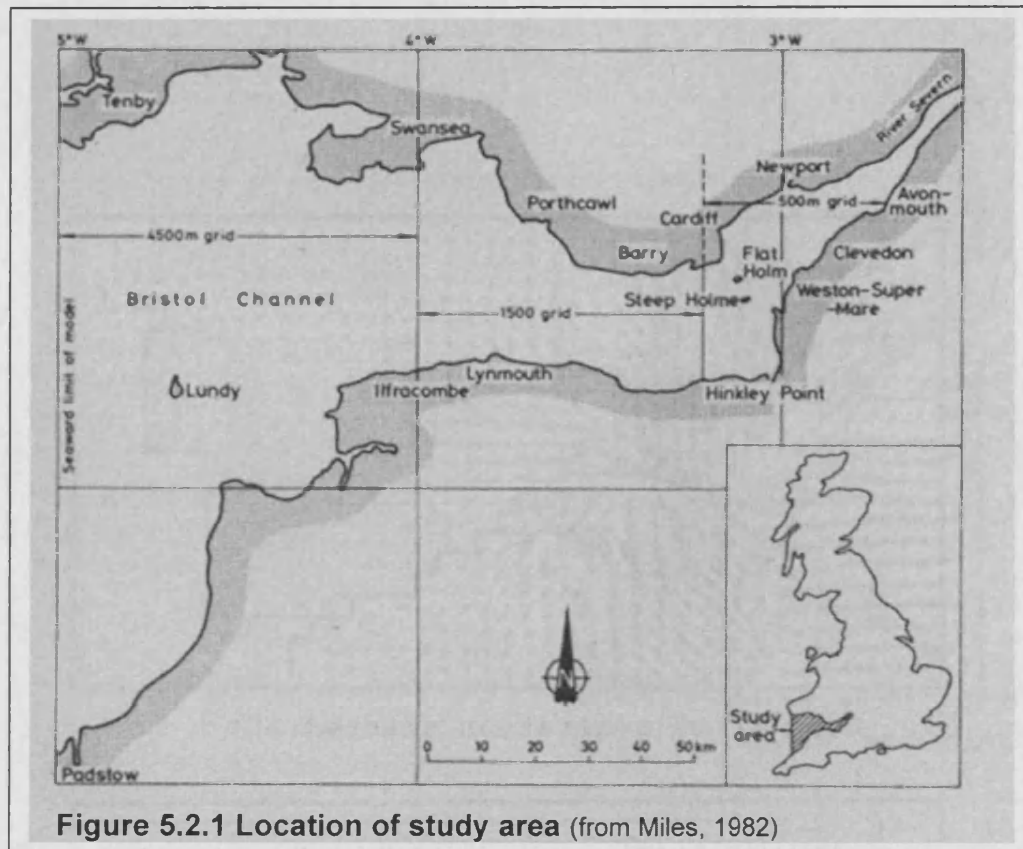
5.2.2   Estuary Features

The Bristol Channel is a macro tidal (i.e tidal range 4m<TR<6m) estuary, which is renown for its strong currents and high tidal range, and also its complex hydrodynamic environment. The upper reaches of the Bristol Channel and the lower Severn Estuary contain a large areas of intertidal and subtidal mud deposits, which can be found particularly in areas between Cardiff and Newport. Also the presence of mudflat are visible around in the Bridgwater Bay, near English coastal site.

5.2.3   Bathymetric Characteristics

The bathymetry of the Bristol Channel shows (see Figure 5.2.2) that the most of the areas within the study area have relatively shallow depths (h<20m). The main channel consists of a series of embayments, separated by sections of cliffed coastlines often enclosing submarine valleys. The Severn Estuary and the majority of the embayments scattered around the channel periphery are generally less than

Figure 5.2.2 : Bathymetry of the Bristol Channel

LEGEND

LAND

Depth below datum (m)

< 5
5 - 10
10 - 15
15 - 20
20 - 25
25 - 30
30 - 35
35 - 40
40 - 45
45 - 50
50 - 55
55 - 60

7.5 km

Grid Size   600m x 600m

SCALE   1 : 750,000

Stackpole Quay

Swansea

Newport

Cardiff

Ilfracombe

Avonmouth

Physiography of the study area (From ABP Report, 2000)

Scale 1:80000   Figure 5.2.3
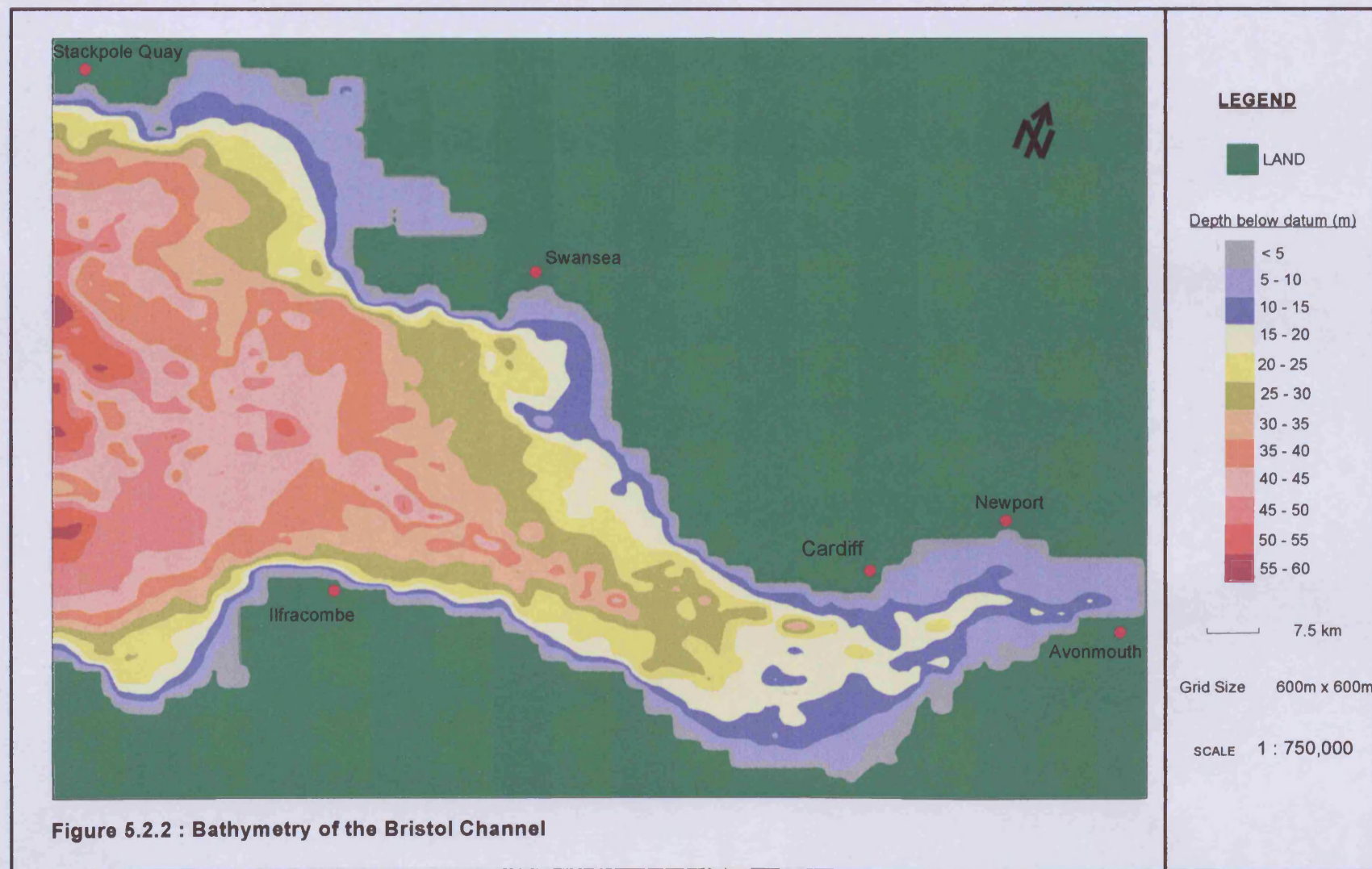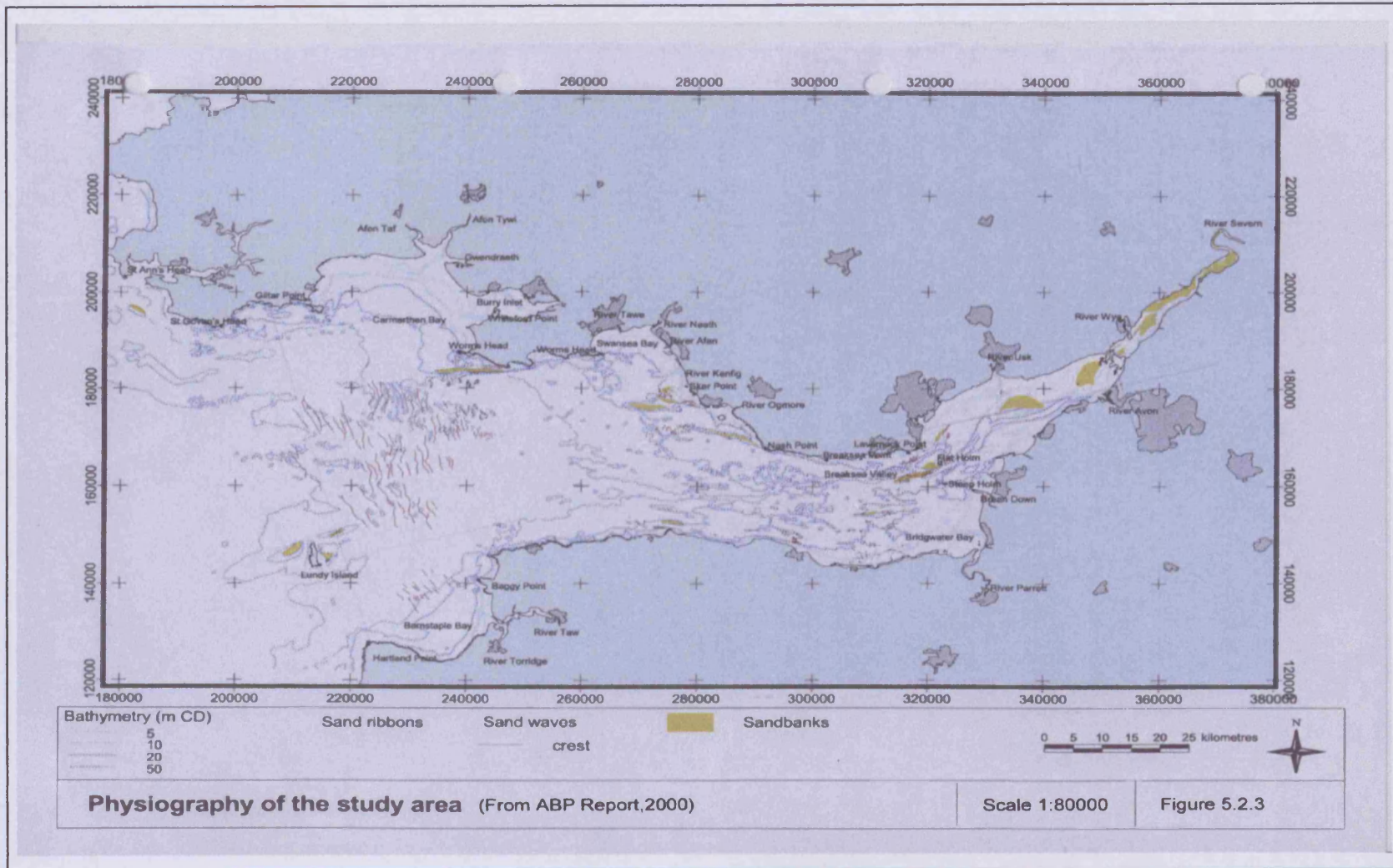
10m deep. The area of the Bristol Channel is divisible geologically into three parts (Evans, 1982). The inner Bristol Channel forms the western part, with the bed consisting of gently folded strata. The central consists of complex folding with carboniferous limestone (Flat Holm, Figure 5.2.3) and the eastern part consists of gently folded Trias Strata.

The water depth reaches typically 60m in the outer Bristol Channel and becomes shallower in an easterly direction over a distance of 120 km and to depths of less than 30m in the Inner Bristol Channel. From this area a large estuary system runs upstream in a north-east direction, known as Severn Estuary, over a distance of around 65 km (Figure 5.2.3). There are four major bays situated in the study area, including; Carmarthen Bay and Swansea Bay along the South Wales Coast and Barnstaple Bay and Bridgwater Bay along the English Coast. These bays originated as drowned portions of the tributary system.

Normally sandbanks are found in the shallow waters (i,e, for depths < 20m), with several bank crests being exposed at extreme low water. The banks include Turbot, Helwick (Outer Bristol Channel), Nash and Scarweather Sands (Central Bristol Channel), Culver Sand and One Fathom Bank (i.e. Inner Bristol Channel) and the west middle ground, namely Chaston Sands, in the Severn Estuary. These sandbanks are tidally generated and rise from a predominantly flat adjacent sea bed, they remain submerged at all states of the tide except spring low waters, when the crests of Scareweather and Nash are exposed.

5.2.4 Hydrodynamic and Environmental Regime

The relevant hydrodynamic processes considered in this study are tidal, fluvial and wave driven mechanisms. The direct effect of winds has not been considered, although the wind has a great influence on wave and tidal currents. From the west to east across the study area the hydrodynamic regime changes in character from a coastal to an estuarine environment. Coastal erosion and accretion and sediment transport are all governed by the hydrodynamic processes.

The direction and strength of tidal currents sometimes explains how sedimentary material are supplied and transported from one area to another, but this is not the only factor responsible for the direction and rate of sediment movement (Owen, 1980; Uncles, 1982; Uncles, 1984). Wave induced currents along with fluvial flows (Collins et al., 1980) also contribute to the movement of sediments. The main hydrodynamic factors which govern the behaviour of the study are therefore mainly the periodic tidal conditions, waves, wind and freshwater flows, all of which are discussed below.

Tides: Tidal currents are one of the most influential transport mechanisms in the Bristol Channel hydrodynamic regime. The tidal current peak increases up the channel with speeds from about 0.7 m/s at Lundy Island to 2.4 m/s within the Severn Estuary, for a mean spring tidal range (Admiralty 1993). The direction of the tidal stream shows that the current regime is one of strong rectilinear flows. The flow direction is reversed between the flood and ebb stages of the tide and runs parallel to the coastline (Figure 5.2.5).

Freshwater Flow: The significance of freshwater discharges is in relation to the hydraulic capacity. Freshwater flow has an effect on the salinity and temperature distribution and also on the intrusion of the sediment load. The freshwater discharges into the Bristol Channel are relatively small when compared to the tidal flows and hence the fluvial flows give rise only to very localised effects, which are close to the various river confluences (Heathershaw et al., 1981) and where salinity gradients can influence sediment movement (Uncles, 1984). Figure 5.2.4 shows the average river discharge in a part of the Bristol Channel. The average fresh water flow into the estuary is about 300 m^3/s (Severn Estuary Report, 1997) and the average water volumes in the estuary are as follows (RCL Report, 1986):

Chart Datum	5,869,500,000 m^3
Mean Neap Tidal Level	10,707,800,000 m^3
Mean Spring Tidal Level	10,835,000,000 m^3

Wind: Wind is one of the principle forces governing the hydrodynamic features of the Bristol Channel. Sustained wind conditions induce surface flows, waves and swell. The onset of atmospheric depression can cause tidal surges. Wind and surges are two important processes in the development of a hydrodynamic regime, but in this study these effects were not directly considered.

Waves: Waves are an important process in the development of the shoreline, also influencing the mobility and transportation of the sediment load through the system. Waves propagating from the North Atlantic through the Celtic Sea are responsible for the majority of severe wave events in the Bristol Channel (Coastline Response Study, 1993). Waves entering from the Celtic Sea normally enter the Bristol Channel and penetrate further upstream along the estuary. One of the important features of wave distribution patterns relates to the sheltering effects of the inner estuary near Hartland Point. There is variability within the wave climate for various areas in the channel. Waves coming from the Celtic Sea and moving eastward along the main axis of the channel penetrate into the system as far as the Severn Estuary (ABP Report, 2000). It is this force of the offshore waves which drives the sediment material back into the system.

Within the Bristol Channel fetch distances are large enough to allow high waves to develop. But within the Severn Estuary the fetch length is limited by the geometry of the estuary and is dependent on state of the tide. At high water the maximum fetch distance is about 60 km. These limited fetches lead to locally generated waves of shorter period and a maximum wave height of approximately 2m. The dissipation of wave energy as the waves propagate in shallow water or over underwater features (i.e. linear sandbanks) can result in large quantities of sediment being mobilised through the effects of turbulent entrainment. According to Collins, et al. (1980) the average wave period in the Bristol Channel is about 7.5s with H_{sig} = 0.5m. Storm and oceanic wave periods are about 8.5s and 12.5s respectively, with corresponding significant wave heights of H_{sig} = 2.7m and H_{sig} =2.3m.

RIVER LOUGHOR
36.18 M³/S

RIVER TAWE
221.6 M³/S

RIVER NEATH
164.5 M³/S

RIVER AFAN
69.4 M³/S

RIVER KENFIG
8.0 M³/S est

RIVER OGMORE
132.7 M³/S

RIVER TAFF
397.1 M³/S

RIVER ELY
60.18 M³/S

N
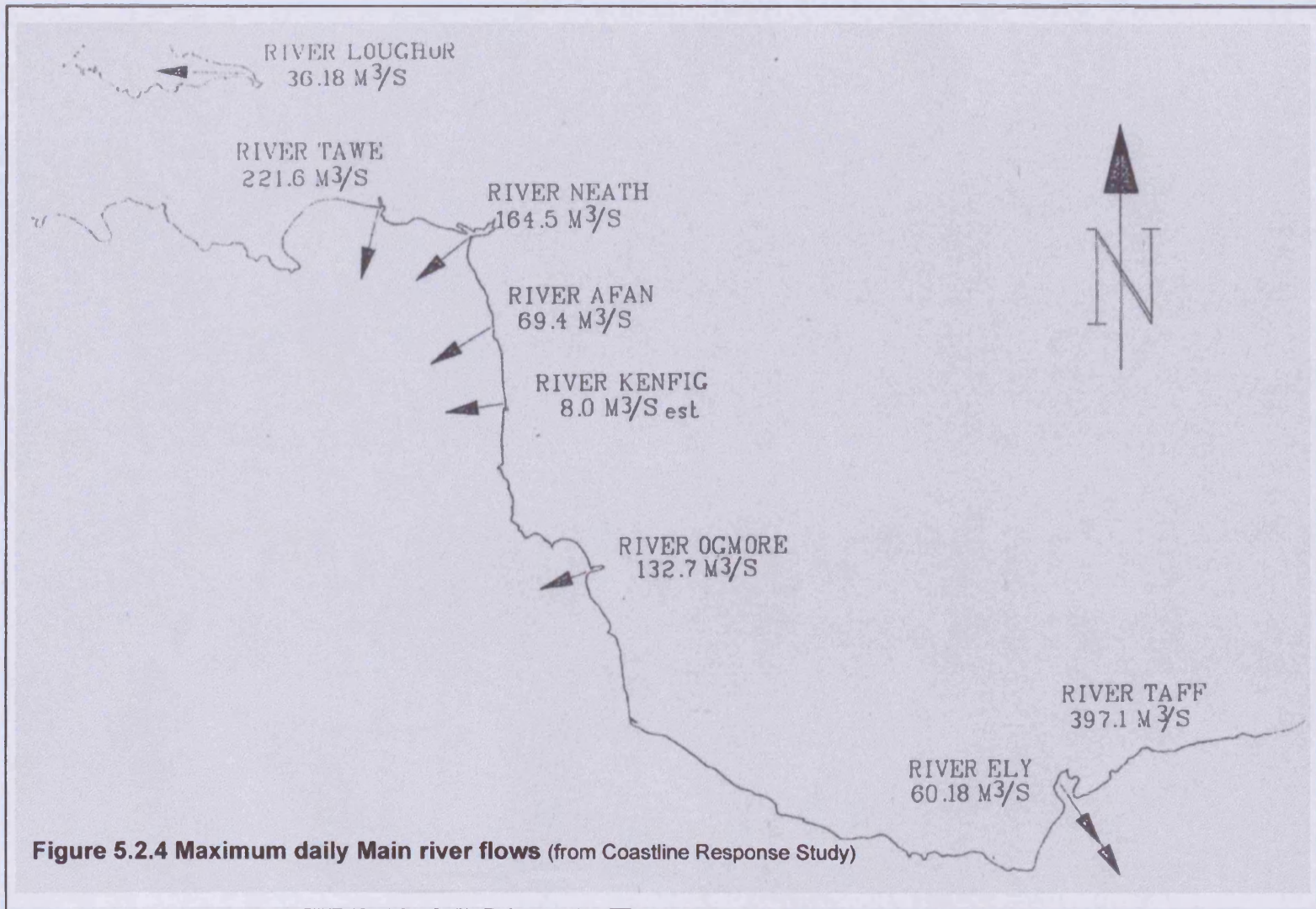
Figure 5.2.4 Maximum daily Main river flows (from Coastline Response Study)

Co-range (m) (mean spring tide range)
Co-phase (hrs) (high water interval)

0 5 10 15 20 25 kilometres

N

Co-tidal chart (From ABP Report, 2000)

| Scale 1:800000 | Figure 5.2.5 |
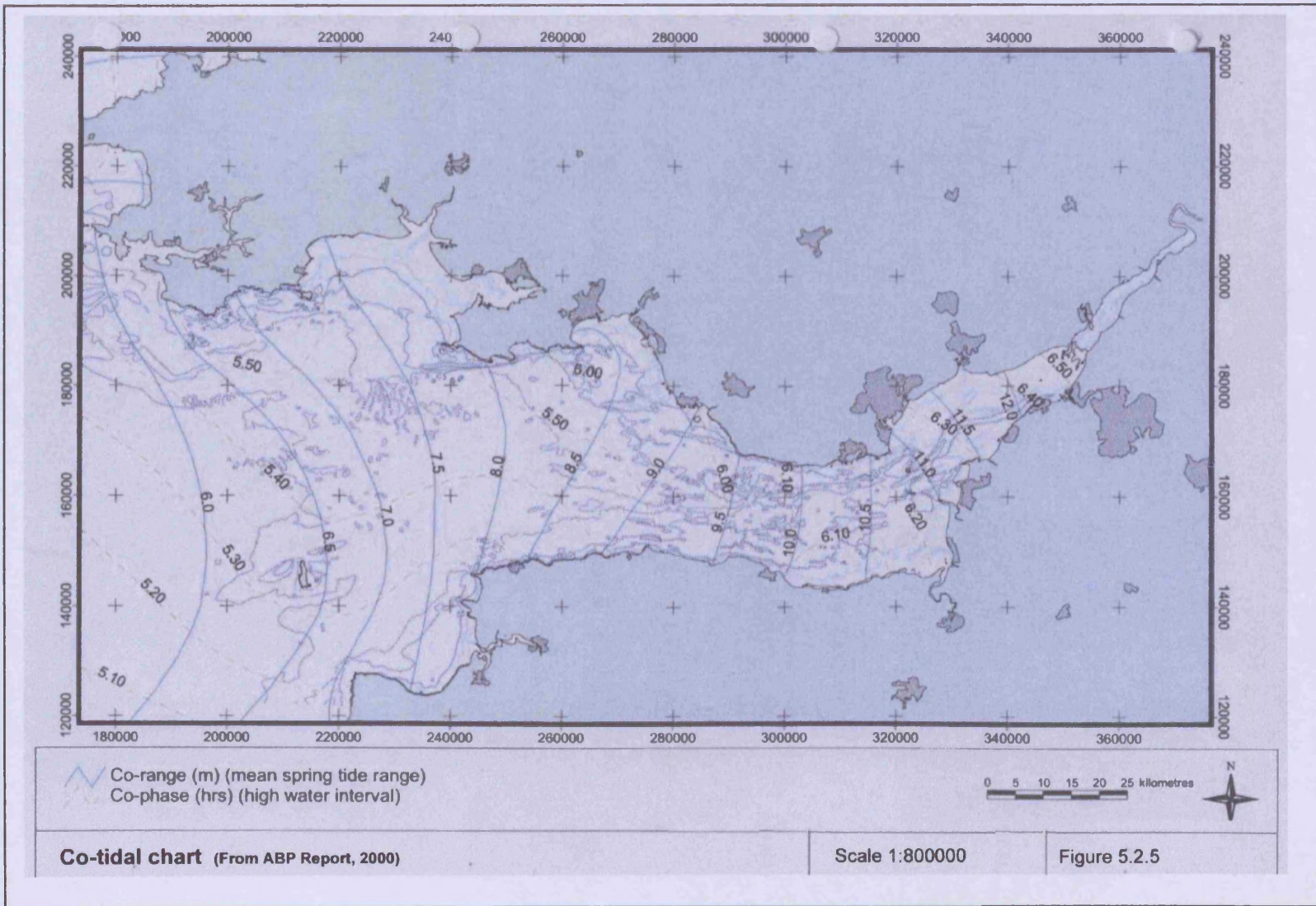
Other than the above mentioned factors there are many natural changes, as well as human interference, which lead to changes in hydrodynamic regime. The major effect is the sea-level rise due to global climatic change. The hydrodynamic changes can be seen to effect tide level changes, wave and wind pattern changes, changes in freshwater flows and surge effects. The rate and magnitude of such changes can be found by continued long term monitoring, with numerical models playing a key role in predicting future conditions.

5.2.5 Tidal Condition

The tidal regime of the Bristol Channel system is extremely dynamic, exhibiting one of the largest tidal ranges in the world. The mean spring range varies from 6.0m in the outer Bristol Channel to greater than 12.0m within the Severn Estuary. The tidal regime is strongly semi diurnal in character, with a progressive tidal wave. The semi diurnal tide typically produces two high and two low waters each day, which leads to a large volume of water and sediment exchange twice daily.

The tidal wave is amplified in the landward direction as a result of the reduction in the channel width and depth. The mean spring tidal range at Lundy Island [Lat $51°10'$, Lon $4°40'$] is around 5.0m, increasing to 8.6m at Swansea [Lat $51°37'$, Lon $3°55'$] and 12.3m at Avonmouth [Lat $51°20'$, Lon $2°43'$]. Similarly the corresponding mean neap tidal ranges are 3.2m at Lundy, 4.0m at Swansea and 6.0m at Avonmouth. The phase lag is approximately 1 hour 24 minutes for a mean spring tidal condition, between high water at Lundy and that at Avonmouth (Figure 5.4.4). This phase lag reduces to approximately 1 hour 12 minutes for mean neap tidal conditions (Figure 5.4.3). This phase lag is the result of the progressive nature of the propagation of the tidal wave. This can be justified by the nature of the Co-tidal chart (Figure 5.2.5), which shows the uniform progression of the tidal wave.

5.2.6 Sediment Transport Regime

The sediment regime responds directly to the hydrodynamic influences, which initiate sediment movement, determine sediment transport rates, direction and mode of transport and also the deposition environment for the material. The periodic tidal forces are the principal sediment moving mechanisms, where waves have a short term effect on the system. Sediments are present as gravel and sand and mud deposits, with the later being generally divided into grain size fractions by tidal sorting to form discrete deposits rather than a mixture of different types (Evans, 1982). The thickness of the surficial deposits are generally less than 10m and rarely exceed 5m (Dyer, 1984).

The coarser material is formed among parallel flow structures like linear sandbanks and sandwaves (Harris and Collins, 1985), but the finer grades tend to reside within sheltered embayments. Sand is present in large volumes in the form of linear sandbanks. These sandbanks can be found in Nash, Scarweather and Huge Sandbanks and the Helwick Sandbank at Gower Peninsula. The main sediment sources within the Bristol Channel are from the rivers and coastal erosion (e.g. from beaches, cliffs and saltmarsh), human activity, beach recharge and dredge material disposal. Sediment sinks include: sub-estuaries, shoreline accretion, marine aggregate mining and locally at the sandbanks. According to McLaren, et. al. (1993) deposition occurs in the Severn Estuary, Bridgwater Bay, Swansea Bay and the Outer Bristol Channel and areas of erosion occur in the Inner Bristol Channel, which exposes the bedrock floor.

5.3 Numerical Model DIVAST

The numerical model DIVAST (Depth Integrated Velocities And Solute Transport) is a two-dimensional, depth integrated, time variant model, which has been developed for estuarine and coastal modelling. It is suitable for water bodies that are dominated by horizontal unsteady flows, and where significant vertical stratification

does not occur. The model simulates the two-dimensional distribution of currents, water surface elevations and various water quality parameters within the modelling domain as function of time. The hydraulic characteristics are governed by the bed topography and the boundary conditions. DIVAST has been developed using FORTRAN 77 further details are given in Falconer (1993).

DIVAST is based on finite difference model. Details of the governing equations and their discretisation have been given in Chapter 3 and Chapter 4. The original model has subsequently been developed and refined with particular emphasis being given to the advective accelerations (Falconer, 1991), wind effects, bottom friction, turbulence, high concentration gradients (Lin and Chandler-Wilde, 1996), dispersion, water quality indicators (Lin and Falconer, 2001), sediment transport processes (Falconer and Chen, 1996) and flooding and drying (Lin and Falconer, 1997). The model is structured into one main program, which includes a hydrodynamic module and a water quality and a sediment transport module, solved for each half time step. The main program is supported by more than 20 sub-routines.

The program first lists the key variables, such as grid size, time step, open boundary specifications, coefficient values for the governing hydrodynamic equations, followed by the dispersion and decay rates etc. for the water quality and sediment transport equations. In this study water quality modelling has not been included and hence specific coefficients have not been used. One of the key features in the current study has been inclusion of the open boundary conditions, particularly since the model results are significantly dependent upon the accuracy of the boundary values. These values are given either in the form of water elevations or depth averaged velocities for the hydrodynamic module, and initial concentration levels for the sediment transport equations.

The model domain has been specified in terms of a prescribed integer code, where zero (0) represents dry land and unity (1) represents an active wet or interior grid square. The depth below datum for each grid square has been obtained from the

relevant Admiralty Chart. A constant roughness coefficient has been specified across the domain, primarily due to a lack of relevant field data. The eddy viscosity and the dispersion-diffusion terms were specified in a spatially varying manner, as related to the shear velocity and water column depth.

The hydrodynamic module is based on the solution of the depth-integrated Navier-Stokes equations (as given in Chapter 3) for shallow water flows and including the effects, such as: (a) Local and advective accelerations, (b) Earth's rotation (Coriolis force), (c) Barotropic and free surface pressure gradients, (d) Wind action, (e) Bed resistance and (f) Refined mixing length turbulent model.

The sediment transport module used two widely used formulae for predicting both the suspended and bed load sediment fluxes. These formulations were based on theories proposed by Engelund-Hansen (see Graf, 1971) and Van Rijn (1984).

The output files enable numerical and graphical output to be produced with user defined flags for water elevation, velocity fields, wet and dry cells, shear stresses, residual velocities and erosion and sediment quantities. The results can be plotted graphically either as map based graphics or as time series plots.

5.4   Model Calibration and Verification

When numerical models are applied to field or laboratory studies, they first need to be calibrated and verified to ensure that the results obtained from the model are accurate enough to predict future scenarios.

To investigate the hydrodynamic and sedimentary mechanisms within the Bristol Channel, the numerical model DIVAST was first set up in this region to reliably predict the hydrodynamic characteristics in the area. The results from the tidal model predictions for this study area were then compared with actual recorded field data. The first set of data were obtained from Admiralty Charts for water levels, current speed and directions, as specified at the tidal diamond sites (Figure 5.4.2). The

second set of data were obtained from a field study carried out in 2001 (from CREH, 2001).

Calibration: Calibration is the process of establishing the most suitable model schematisation, time step, roughness coefficients, eddy viscosity and other numerical coefficients by comparing the results of the model simulations against actual observations.

Calibration is achieved through a process of optimising the bed resistance friction coefficient, eddy viscosity coefficient, small modifications to the bathymetry, boundary conditions and specification of an appropriate time step.

Verification: Verification involves no adjustment of the model parameters and is a straight forward comparison of the model simulations with observations for a different set of events from those used for model calibration.

Tidal Model Performance: For the calibration and verification procedure predicted results from the model were compared with actual field data and the difference between the corresponding values was then obtained. The difference between the observed and model results were calculated as both a Percentage Absolute Difference (PAD) and as the Root Mean Square (RMS) differences. Target values were set based on previous studies (e.g. ABP Report, 2000 and Dun, 1995) and the accuracy reported by Falconer (1988). The RMS values were considered to compare with the target values, which will be described in subsequent sections (section 5.4.2 and 5.4.3).

5.4.1 Bristol Channel Model Details

The western open boundary extended from a line between Hartland Point and Stackpole Head (Fig 5.4.1). The grid orientation of the x-axis was $+76^0$ from true North and was specified at this angle to create as close as normal a flow to the open boundaries as possible. The grid size of the model was taken as 600m. The cell size

of the model was determined by the limits of PC computational power and the maximum calculation time step defined by the Courant condition (Dun, 1995). The present 600m square cell enabled the complex bathymtery of the Bristol Channel to be adequately represented, while maintaining an acceptable run time. The resulting dimensions of the coarse model yielded grid dimension of 231 cells in the X-direction and 168 cells in the Y-direction.

TABLE 5.4.1 : <u>Bathymetric information for Bristol Cahnnel</u>

Model	Admiralty Chart Nos.	Other Bathymetric Information
Bristol Channel	1165 1169 1179	(1) Coastline Response Study – Final Report, (1993) (2) Bristol Channel Marine Aggregates– Resources and Constrains: Final Report. (ABP Report, 2000)

The bathymetric data sources used building the Bristol Channel model are shown in Table 5.4.1. The bed levels for each of the grid squares were specified at the corner of each grid square, with these data being obtained from the irregularly spaced chart data by means of the Digital Ground Model DGM3. The majority of the bathymetric data for the Bristol Channel tidal model were taken from Admiralty Chart No. 1179. The updated and corrected bathymetry were used in this study so that correction needed (Dun, 1995) for local Chart Data and that of Ordnance Datum Newlyn (OD(N)) have already been completed.

The water elevations at the open boundaries used as the boundary conditions, were functions of the amplitude and phase relationship of the principal tidal harmonic components M2, S2, K1 and O1. They were calculated by the Simple Harmonic Method of Tidal Predictions, which included shallow water corrections with reference to Admiralty Tide Tables (ATT): Volume 1. The tidal elevation curve for

Outer Bristol Channel

Central Bristol Channel

Inner Bristol Channel

Severn Estuary

Celtic Sea

200000

150000

200000

250000

300000

350000

Overall Extent of the Study Area

0 5 10 15 20 25 kilometres

N

Divisions within the Bristol Channel and Severn Estuary (from ABP Report, 2000)

Scale 1:800000
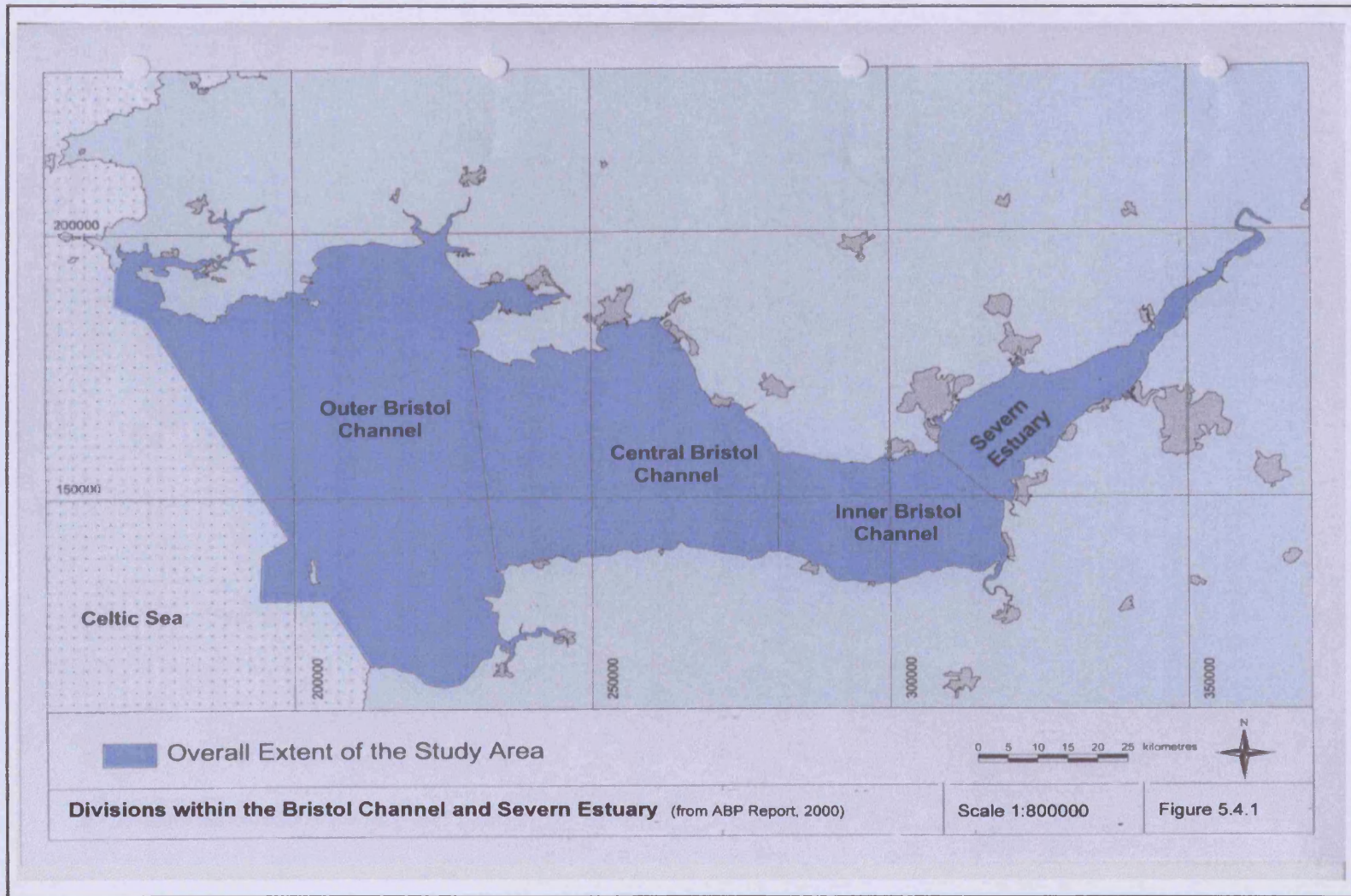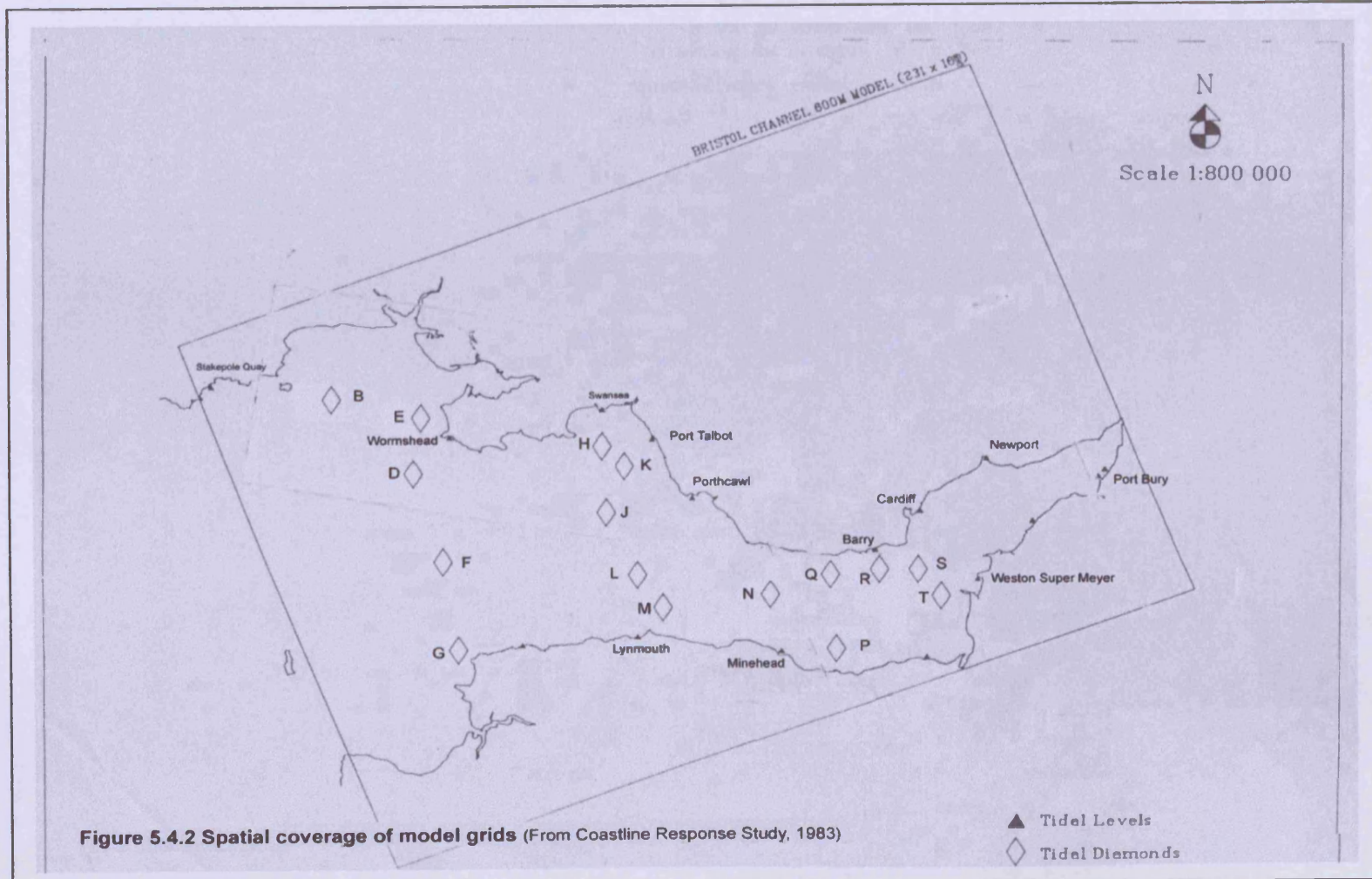
Figure 5.4.1

Figure 5.4.2 Spatial coverage of model grids (From Coastline Response Study, 1983)

the eastern boundary was defined by using the Standard Port at Avonmouth, and the western boundary defined using the secondary port of Stackpole Quay. The mean neap tide, mean spring tide, and extreme spring tidal events (i.e. Highest Astronomical Tide, HAT and Lowest Astronomical Tide, LAT) were generated by defining the proper amplitude.

Table 5.4.2 : Table for tidal constituents (from Macmillan, 1966)

Symbol of Constituent	Speed Number	Description and Function
M_2	$28^0 .98$	Lunar semi-diurnal constituent for distortation of progressive wave
S_2	30^0	Solar semi-diurnal constituent
K_1	$15^0 .041$	Diurnal oscillation due to the moon's declination.
O_1	$13^0 .943$	They balance each other

5.4.2 Calibration

In order for the predicts of the 2-D hydrodynamic model, DIVAST, to be used with confidence for future predictions, it was first necessary to calibrate the model. To ensure good calibration, the model was compared against a range of data, including: water levels and tidal diamond velocities and speed at different locations as given by Admiralty Chart (1993). In this study the 'Bristol Channel model' was calibrated against mean neap tide conditions with no applied wind stresses. The calibration process involved tuning various empirical coefficients until the optimal agreement was obtained between measured and simulated values. In this case the current speed and directions and water levels at selected sites across the domain (Figure 5.4.2) of the model were compared with observation station data. Although the Admiralty Chart data provided average data for the estuary, but to calibrate the model it was taken as the necessary data as bathymetric data obtained from the same chart.

The following sections present comparisons of the model with these data sets. The position of the sites used for calibration and verification of the model are shown in

Figure 5.4.2. The mean neap tidal conditions without wind were simulated using the following water level amplitudes shown in Table 5.4.3.

TABLE 5.4.3 : Water level amplitudes for neap tides

Port	MHWN	MLWN	Range (m)
Avonmouth	9.8	3.8	6.0
Stackpole Quay	5.9	2.7	3.2

A semi-diurnal tidal cycle of 12 hours and 24 minutes (12.4 hours) was specified, with a phase lag of 1.2 hours between the occurrence of high water (HW) at the western model boundary and that of high water (HW) at Avonmouth. Calibration was achieved by optimising the bed resistant coefficient, along with small modifications to the model bathymetry and boundary conditions. The model was run for an M2 tide applied at open seaward Western boundary, with zero run-off from the minor tributaries flowing into the estuary. To run the Bristol Channel the wave was not included as the domain is large enough where tidal fluctuation has pronounced effcet on flow than the wave itself.

The calibration required the determination of the most appropriate Nikaradse roughness length and the depth averaged eddy viscosity. The eddy viscosity $\bar{\varepsilon}$ value responsible for horizontal mixing was taken using the equation $\bar{\varepsilon} = 0.15 U_* H$, after Fischer (1979); where U_* is the shear velocity and H is the total depth of flow. The bottom friction coefficient (k_s) was taken to be 40mm for calibration.

The results obtained from the model analysis were based on a quantitative analysis. The distribution of observed data for calibration and verification of the hydrodynamic tidal conditions were chosen at twelve water level stations and sixteen Admiralty Tidal Diamonds (Figure 5.4.2). The accuracy of the model was expressed in terms of RMS error with respect to amplitude and phase differences. The "Target Values" to achieve for water level data were ±0.01m for the height and

±5 minutes in phase. The limits for the velocities were ± 5 cm/s in magnitude, ±1⁰ in direction and ±30 minutes in phase (Coastal Response Study, 1993).

The tidal model analysis was based on the assumption that all times were expressed relative to high water at the Western Boundary. The water level stations referenced in Figure 5.4.2. were monitored by HR Wallingford Ltd. (previously Hydraulics Research Ltd.). Figure 5.4.3 shows the neap conditions on 14 May 1980 as reported by Hydraulics Research (1980b), which confirmed that wind and wave conditions were mild on that day. The maximum tidal diamonds were located mainly in deep water and only a few can represent the shallow water flow.

Figures 5.4.5 to 5.4.8 shows the water surface elevations as determined from the model against the measured data for different locations along the estuary with the results being summarised in Table 5.4.4. The trend in the predicted water level variations matches closely with the field data. The differences in the peak water level were higher at sites such as Newport and Port Bury, which might be due to the high tidal range. The table shows that the overall RMS error was 0.11m and 4.9% for peak amplitudes, i.e. at times of high water (HW) and low water (LW), and with a 9 minute phase lag, which was within the calibration targets.

The results from the tidal velocities and directions prediction for calibration purposes are summarised in Table 5.4.5 and are illustrated in Figures 5.4.9 to 5.4.12. From the table it can be seen that the range of difference in the peak velocities (at times of mid ebb and mid flood) was within 0.08m/s, which corresponds to an error of 11.9 %. The difference in direction was typically 4⁰, and the phase difference was generally about 11 minutes. The model performance was therefore quiet good. The higher difference in the peak amplitude and direction was thought to be due to the relatively coarse grid size of 600m, which could not represent the complex bathymetry accurately on the coastline geometry. The results obtained in this study were comparable with the results of the Coastal Response Study (1991) and Dun (1995) and it can be seen that the trend in the water level variations, the current speed and direction were relatively similar in terms of accuracy.

5.4.3 Verification

According to the definition of the verification procedure, the 'Bristol Channel Model' has been verified by using the spring tide condition without the application of wind, but other than the tidal values all other principal empirical coefficients were the same as those used for calibration. The mean spring tidal condition without the application of wind has been simulated using the water level amplitudes given in Table 5.4.4.

TABLE 5.4.4 : Water level amplitudes for spring tides

Port	MHWS	MLWS	Range (m)
Avonmouth	13.3	1.1	12.2
Stackpole Quay	7.9	1.0	6.9

Spring tides occur for two days following a new or full moon at the Avonmouth site. Representative tidal curves have been generated using the data of 21 May 1980 (Figure 5.4.4). The time expressed in the verification procedure is with respect to the Western open seaward boundary. The semi-diurnal tidal period of 12 hours and 24 minutes has again been specified, with a phase lag of 1.4 hours for spring tides between the occurrence of high water (HW) at the Stackpole Quay point along the western boundary and HW at Avonmouth (Admiralty, 1993).

The comparison of Bristol Channel water level model results with the field data of corresponding points are illustrated in Figures 5.4.13 to 5.4.16 and the overall results and comparisons are summarised in Table 5.4.7. The RMS error for the peak water level were around 0.10m, which corresponds to a 2.1% error and 8 minutes in phase, and the values are within the target levels. The tidal velocities and direction at the sixteen tidal diamonds are summarised in Table 5.4.8 and illustrated in Figures 5.4.17 to 5.4.20. The overall RMS values were 0.08 m/s and 1.08% for peak velocities, 5^0 in direction and 7 minutes in phase. Again all values are within the target verification level.

Table 5.4.5 : Bristol Channel Model : calibration of water levels, neap tide

Water Level Station	Tidal State	Water Level (m)				Time (h:min) (relative to Western Boundary)		
		Observed	Predicted	Difference	Error(%)	Observed	Predicted	Difference
Stackpole Quay	HW	1.56	1.58	-0.02	-1.266	00:22	00:30	-00:08
	LW	-1.57	-1.51	-0.06	3.974	-05:30	-05:32	00:02
Wormshead	HW	1.9	1.81	0.09	4.972	00:22	00:24	-00:02
	LW	-1.8	-1.65	-0.15	9.091	-05:20	-05:24	00:04
Lynmouth	HW	2.23	2.21	0.02	0.905	00:12	00:24	-00:12
	LW	-2.1	-1.98	-0.12	6.061	-05:00	-05:10	00:10
Minehead	HW	2.52	2.53	-0.01	-0.395	00:22	00:36	-00:12
	LW	-2.41	-2.33	-0.08	3.433	-05:10	-05:12	00:02
Swansea	HW	2.08	2.07	0.01	0.483	00:22	00:24	-00:02
	LW	-2.01	-1.93	-0.08	4.145	-05:30	-05:36	00:06
Port Talbot	HW	2.15	2.09	0.06	2.871	00:22	00:24	-00:02
	LW	-1.94	-1.84	-0.1	5.435	-05:30	-05:36	00:06
Porthcawl	HW	2.18	2.17	0.01	0.461	00:22	00:36	-00:14
	LW	-2.07	-1.96	-0.11	5.612	-05:20	-05:24	00:04
Barry	HW	2.72	2.7	0.02	0.741	00:52	01:00	-00:08
	LW	-2.62	-2.55	-0.07	2.745	-05:30	-05:24	-00:06
Cardiff	HW	2.9	2.85	0.05	1.754	00:52	01:00	-00:08
	LW	-2.85	-2.8	-0.05	1.786	-05:30	-05:30	00:00
Newport	HW	3.06	3.01	0.05	1.661	01:02	01:10	-00:08
	LW	-3.12	-2.68	-0.44	16.418	-06:00	-05:30	-00:30
W-Super-Mare	HW	2.94	2.91	0.03	1.031	00:52	01:00	-00:08
	LW	-2.81	-2.76	-0.05	1.812	-05:30	-05:36	00:06
Portbury	HW	3.29	3.18	0.11	3.459	00:00	00:12	-00:12
	LW	-3.32	-3.19	-0.13	4.075	-06:00	-06:00	00:00
RMS Value				0.1167	4.919			00:09

Difference = Observed-Predicted
Error(%) = [(Observed-Predicted)/Observed]*100

Table 5.4.6 : Bristol Channel Model : calibration of tidal velocities, neap tide

Tidal Diamond	Tidal State	Peak Tidal Velocity (m/s)				Direction (°)			Time (h:min) (relative to Western Boundary)		
		Observed	Predicted	Difference	Error(%)	Observed	Predicted	Difference	Observed	Predicted	Difference
B	ME	0.36	0.45	-0.09	-20.000	235	236	-1	02:30	02:18	00:12
	MF	0.36	0.4	-0.04	-10.000	52	52	0	-04:36	-04:24	-00:12
D	ME	0.668	0.5	0.168	33.600	296	288	8	02:00	02:06	-00:06
	MF	0.617	0.42	0.197	46.905	116	107	9	-04:36	-04:12	-00:24
E	ME	0.36	0.26	0.1	38.462	328	316	12	02:00	02:00	00:00
	MF	0.206	0.27	-0.064	-23.704	122	116	6	-05:06	-05:00	-00:06
F	ME	0.668	0.58	0.088	15.172	250	255	-5	02:00	02:10	-00:10
	MF	0.617	0.54	0.077	14.259	85	84	1	-04:36	-04:30	-00:06
G	ME	0.771	0.74	0.031	4.189	231	238	-7	02:00	02:00	00:00
	MF	0.72	0.71	0.01	1.408	44	45	-1	-05:06	-05:00	-00:06
H	ME	0.36	0.38	-0.02	-5.263	246	241	5	02:30	02:40	-00:10
	MF	0.36	0.39	-0.03	-7.692	57	57	0	-03:36	-03:30	-00:06
J	ME	0.711	0.69	0.021	3.043	285	288	-3	02:00	02:06	-00:06
	MF	0.72	0.64	0.08	12.500	106	107	-1	-04:36	-04:30	-00:06
K	ME	0.36	0.37	-0.01	-2.703	253	253	0	02:00	02:00	00:00
	MF	0.308	0.34	-0.032	-9.412	80	78	2	-04:06	-04:00	-00:06
L	ME	0.72	0.85	-0.13	-15.294	283	284	-1	02:30	02:40	-00:10
	MF	0.771	0.82	-0.049	-5.976	97	97	0	-03:36	-03:48	00:12
M	ME	1.079	1.06	0.019	1.792	276	276	0	02:00	02:00	00:00
	MF	0.977	1.04	-0.063	-6.058	93	95	-2	-04:36	-04:30	-00:06
N	ME	0.771	0.9	-0.129	-14.333	271	271	0	03:00	03:00	00:00
	MF	0.771	0.93	-0.159	-17.097	96	100	-4	-03:36	-03:00	-00:36
P	ME	0.822	0.86	-0.038	-4.419	283	289	-6	03:00	03:00	00:00
	MF	0.771	0.82	-0.049	-5.976	108	103	5	-04:12	-04:00	-00:12
Q	ME	1.234	1.18	0.054	4.576	274	275	-1	03:00	03:00	00:00
	MF	1.182	1.24	-0.058	-4.677	94	93	1	-04:36	-04:20	-00:16
R	ME	0.822	0.84	-0.018	-2.143	252	257	-5	01:30	01:40	-00:10
	MF	0.771	0.82	-0.049	-5.976	73	73	0	-03:36	-03:30	00:06
S	ME	0.822	0.89	-0.068	-7.640	253	250	3	02:00	02:10	-00:10
	MF	0.977	1.01	-0.033	-3.267	75	73	2	-03:36	-03:10	-00:26
T	ME	0.822	0.78	0.042	5.385	222	227	-5	03:00	03:00	00:00
	MF	0.874	0.79	0.084	10.633	51	51	0	-04:12	-04:00	-00:12
				0.081				4.29			00:11

Table 5.4.7 : Bristol Channel Model : calibration of water levels, spring tide

Water Level Station	Tidal State	Water Level (m)				Time (h:min) (relative to Western Boundary)		
		Observed	Predicted	Difference	Error(%)	Observed	Predicted	Difference
Stackpole Quay	HW	3.91	3.79	0.12	3.166	00:24	00:24	00:00
	LW	-3.67	-3.59	-0.08	2.228	-05:10	-05:12	00:02
Wormshead	HW	4.4	4.24	0.16	3.774	00:04	00:12	-00:08
	LW	-3.97	-3.86	-0.11	2.850	-05:00	-05:12	00:12
Lynmouth	HW	5.05	4.99	0.06	1.202	00:14	00:24	-00:10
	LW	-4.78	-4.68	-0.1	2.137	-04:50	-05:00	00:10
Minehead	HW	5.69	5.65	0.04	0.708	00:44	00:48	-00:04
	LW	-5.22	-5.2	-0.02	0.385	-05:30	-05:30	00:00
Swansea	HW	4.82	4.8	0.02	0.417	00:24	00:30	-00:06
	LW	-4.53	-4.39	-0.14	3.189	-05:00	-05:10	00:10
Port Talbot	HW	4.92	4.85	0.07	1.443	00:24	00:28	-00:04
	LW	-4.4	-4.32	-0.08	1.852	-05:00	-05:00	00:00
Porthcawl	HW	4.92	4.84	0.08	1.653	00:24	00:30	-00:06
	LW	-4.65	-4.55	-0.1	2.198	-05:00	-05:05	00:05
Barry	HW	6.01	6.05	-0.04	-0.661	00:54	01:00	-00:06
	LW	-5.34	-5.21	-0.13	2.495	-05:50	-05:48	00:02
Cardiff	HW	6.32	6.26	0.06	0.958	01:04	01:12	-00:08
	LW	-5.79	-5.63	-0.16	2.842	-05:50	-05:48	-00:02
Newport	HW	6.77	6.63	0.14	2.112	01:04	01:12	-00:08
	LW	-5.97	-5.9	-0.07	1.186	-04:50	-05:00	00:10
W-Super-Mare	HW	6.46	6.36	0.1	1.572	01:04	01:12	-00:08
	LW	-5.72	-5.8	0.08	-1.379	-05:50	-05:38	-00:12
Portbury	HW	7.13	6.99	0.14	2.003	01:24	01:30	-00:06
	LW	-6.13	-5.94	-0.19	3.199	-04:50	-04:40	-00:10
				0.105	2.117			00:08

Table 5.4.8 : Bristol Channel Model : verification of tidal velocities, spring tide

Tidal Diamond	Tidal State	Peak Tidal Velocity (m/s)				Direction (^{0})			Time (h:min) (relative to Western Boundary)		
		Observed	Predicted	Difference	Error(%)	Observed	Predicted	Difference	Observed	Predicted	Difference
B	ME	0.822	0.92	-0.098	-10.652	233	233	0	02:30	02:18	00:12
	MF	0.874	0.89	-0.016	-1.798	52	54	-2	-04:36	-04:30	-00:06
D	ME	1.234	1.09	0.144	13.211	296	287	9	02:00	02:00	00:00
	MF	1.131	1.01	0.121	11.980	116	107	9	-04:36	-04:24	-00:12
E	ME	0.771	0.64	0.131	20.469	328	320	8	02:00	02:00	00:00
	MF	0.463	0.43	0.033	7.674	123	113	10	-05:36	-05:30	-00:06
F	ME	1.439	1.36	0.079	5.809	250	255	-5	02:00	02:00	00:00
	MF	1.285	1.21	0.075	6.198	85	84	1	-04:36	-04:30	-00:06
G	ME	1.645	1.57	0.075	4.777	231	237	-6	02:00	02:00	00:00
	MF	1.497	1.42	0.077	5.423	43	47	-4	-05:06	-05:00	-00:06
H	ME	0.771	0.74	0.031	4.189	248	240	8	02:30	02:36	-00:06
	MF	0.72	0.74	-0.02	-2.703	57	54	3	-03:36	-03:30	-00:06
J	ME	1.439	1.39	0.049	3.525	285	287	-2	02:00	02:06	-00:06
	MF	1.336	1.27	0.066	5.197	106	105	1	-04:36	-04:30	-00:06
K	ME	0.771	0.7	0.071	10.143	253	260	-7	02:00	02:00	00:00
	MF	0.668	0.68	-0.012	-1.765	80	88	-8	-04:06	-04:00	-00:06
L	ME	1.696	1.77	-0.074	-4.181	283	283	0	02:30	02:36	-00:06
	MF	1.748	1.66	0.088	5.301	97	102	-5	-03:36	-03:30	-00:06
M	ME	2.364	2.22	0.144	6.486	276	282	-6	02:00	02:00	00:00
	MF	2.056	2.01	0.046	2.289	93	99	-6	-04:36	-04:24	-00:12
N	ME	1.645	1.69	-0.045	-2.663	271	277	-6	03:00	03:10	00:10
	MF	1.645	1.77	-0.125	-7.062	96	102	-6	-03:36	-03:30	-00:06
P	ME	1.542	1.51	0.032	2.119	283	289	-6	03:00	03:00	00:00
	MF	1.491	1.53	-0.039	-2.549	112	111	1	-03:36	-03:24	-00:12
Q	ME	2.262	2.18	0.082	3.761	274	276	-2	03:00	03:00	00:00
	MF	2.21	2.26	-0.05	-2.212	94	93	1	-04:36	-04:24	-00:12
R	ME	1.645	1.51	0.135	8.940	252	256	-4	01:24	01:30	-00:06
	MF	1.491	1.42	0.071	5.000	73	76	-3	-03:36	-03:24	-00:12
S	ME	1.593	1.56	0.033	2.115	253	248	5	02:00	02:00	00:00
	MF	1.85	1.83	0.02	1.093	75	74	1	-03:36	-03:48	00:12
T	ME	1.542	1.39	0.152	10.935	222	226	-4	03:00	03:00	00:00
	MF	1.645	1.48	0.165	11.149	51	52	-1	-04:06	-04:00	-00:06
				0.0867	1.090			5.238			00:07
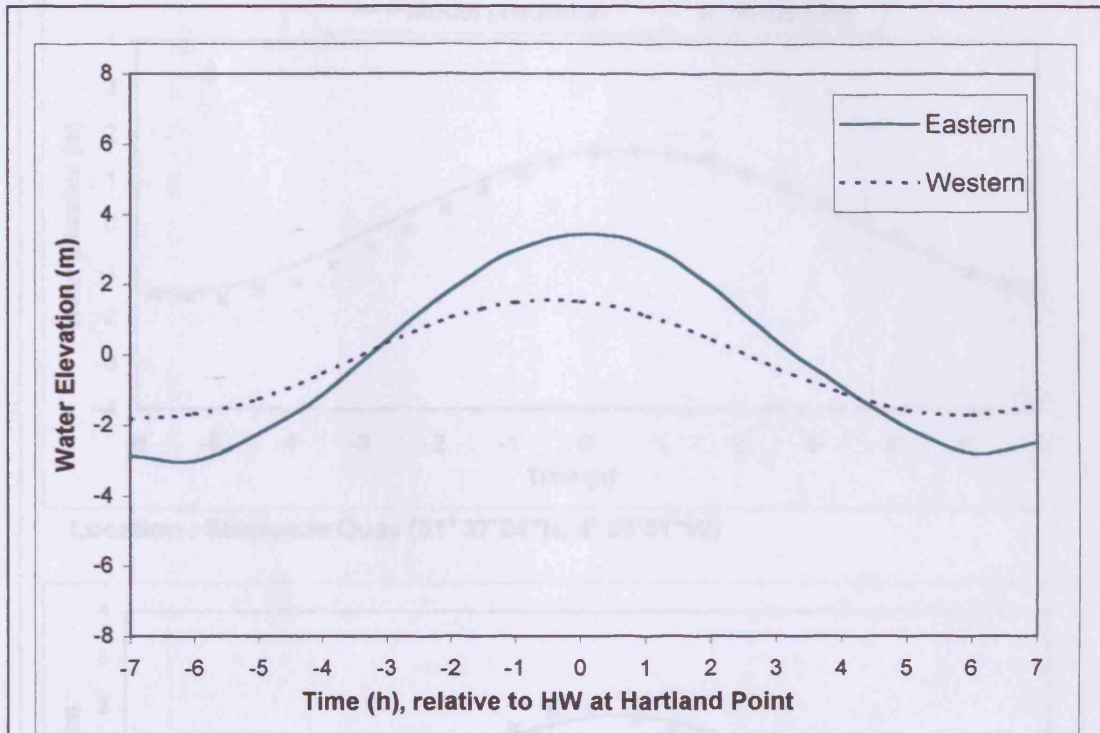
Figure 5.4.3: Water levels at open boundary locations for mean neap tides
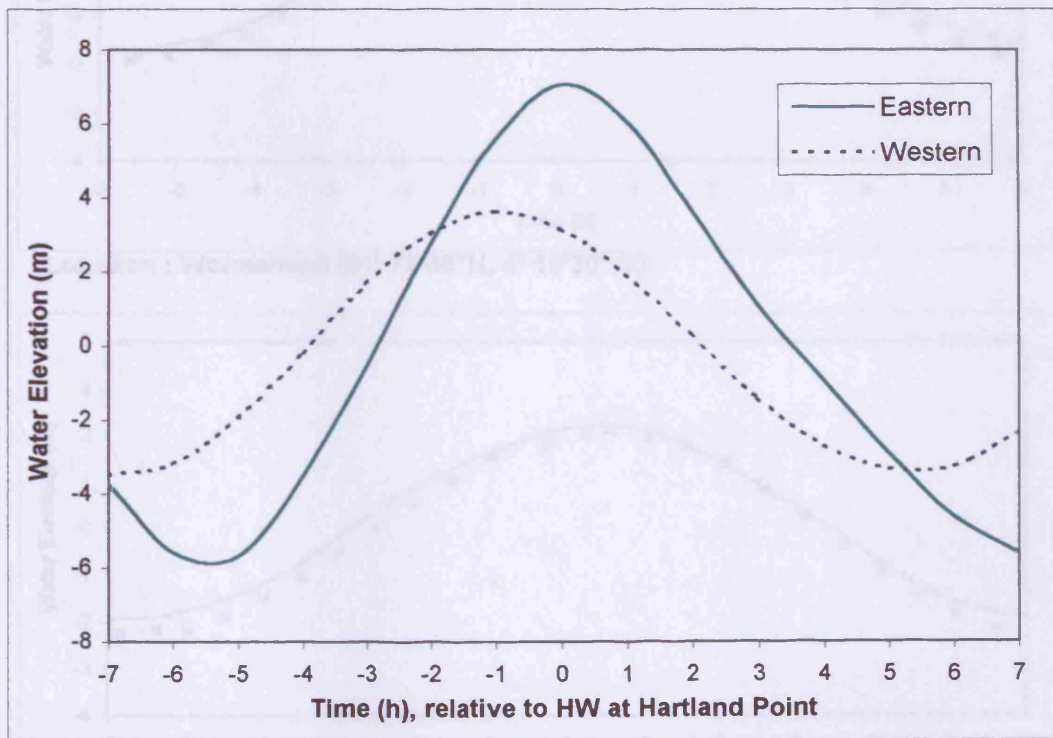
Figure 5.4.4: Water levels at open boundary locations for mean spring tides
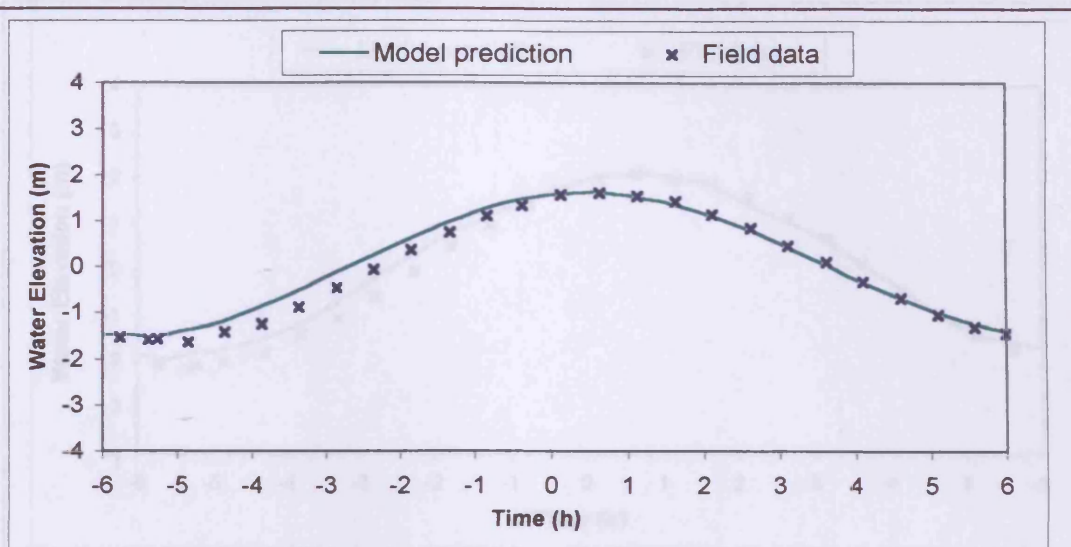
Location : Stackpole Quay (51⁰ 37'24"N, 4⁰ 53'51"W)
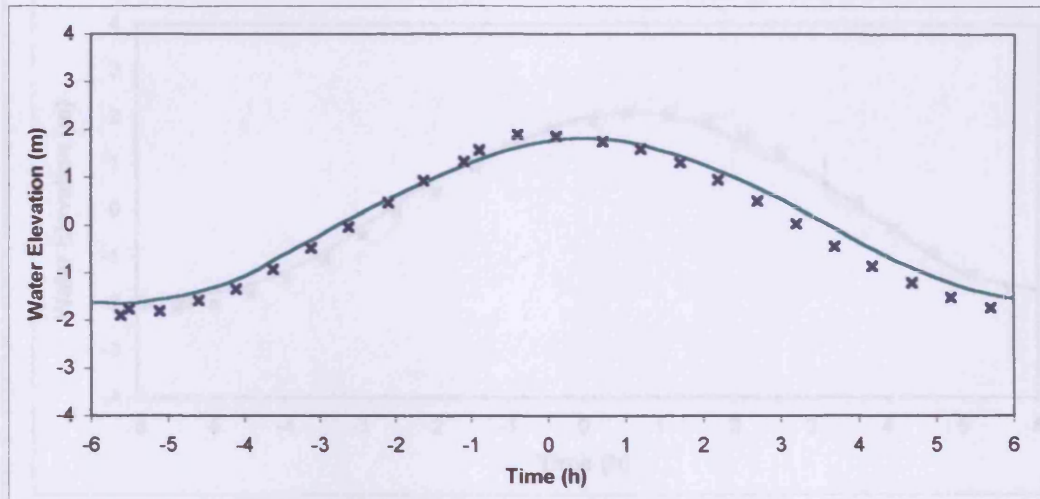
Location : Wormshead (51⁰ 33'48"N, 4⁰ 18'30"W)
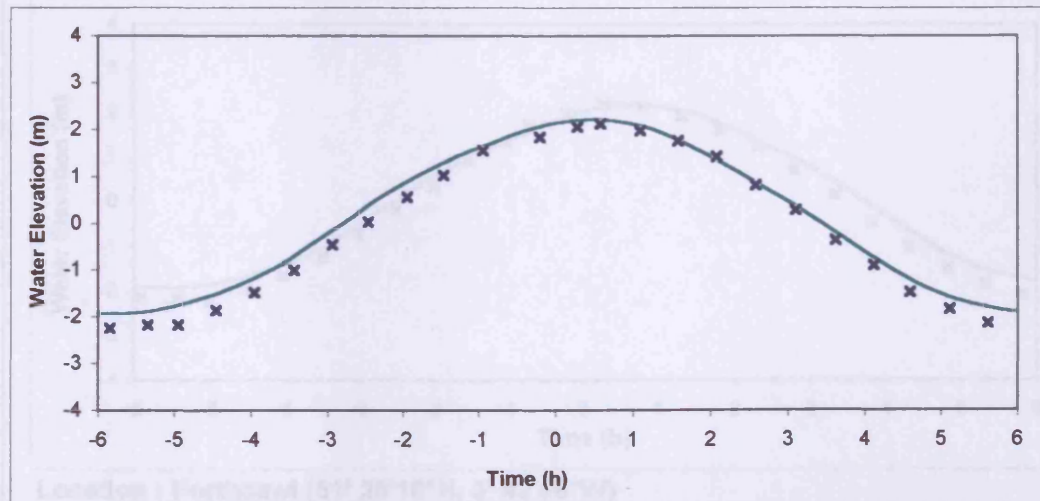
Location : Lynmouth (51⁰ 14'04"N, 3⁰ 49'44"W)

FIGURE 5.4.5: Comparison of water elevations for mean neap tides
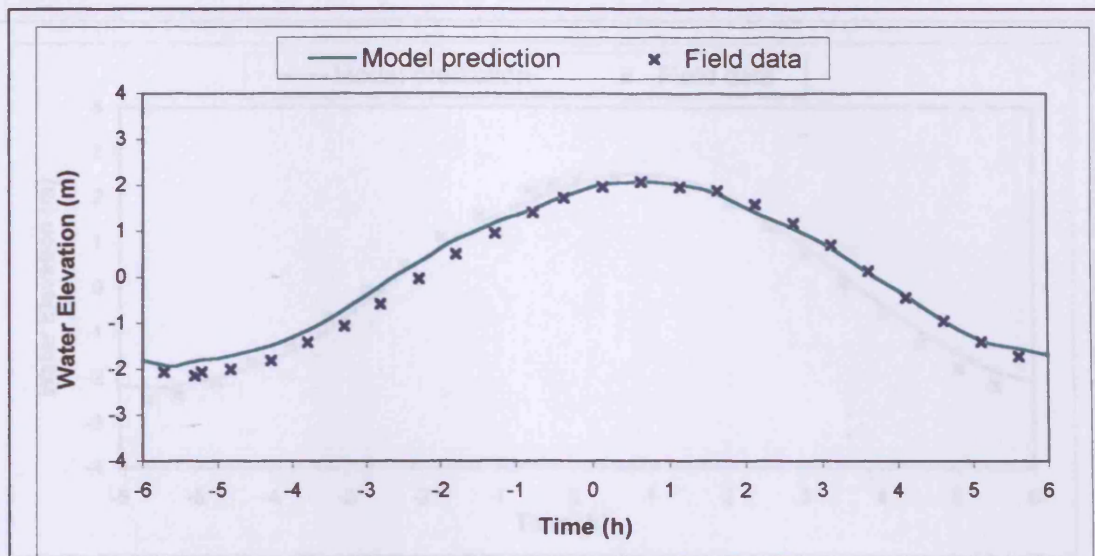
Location : Swansea (51⁰ 36'38"N, 3⁰ 55'26"W)
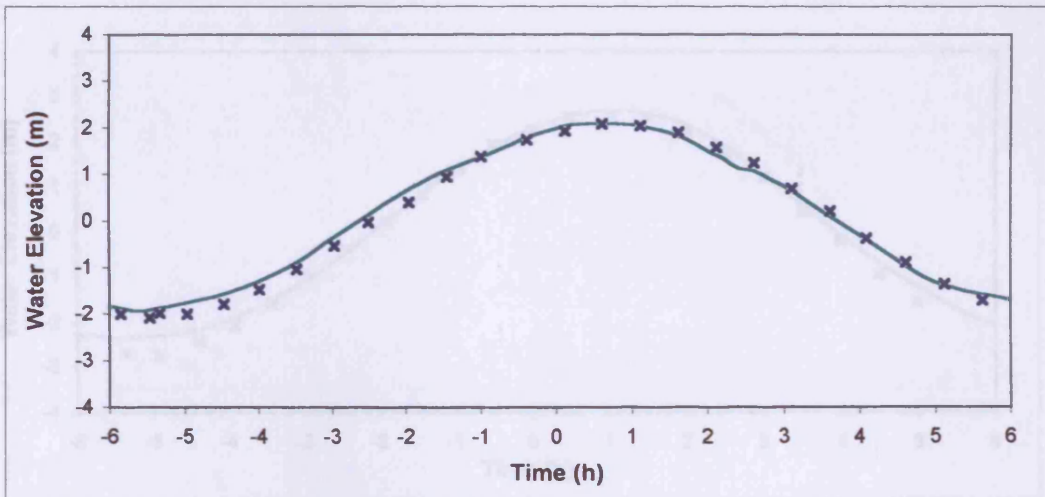
Location : Port Talbot (51⁰ 34'24"N, 3⁰ 48'06"W)
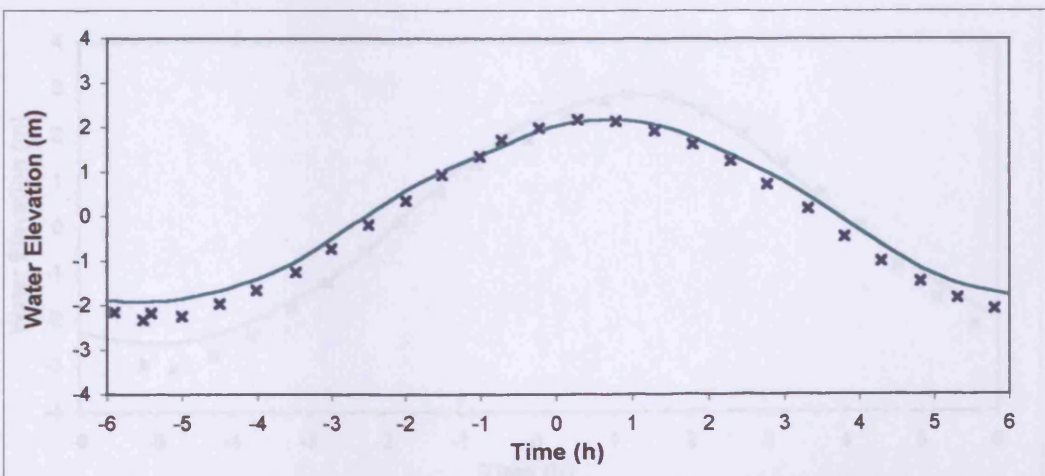
Location : Porthcawl (51⁰ 28'18"N, 3⁰ 42'06"W)

FIGURE 5.4.6: Comparison of water elevations for mean neap tides
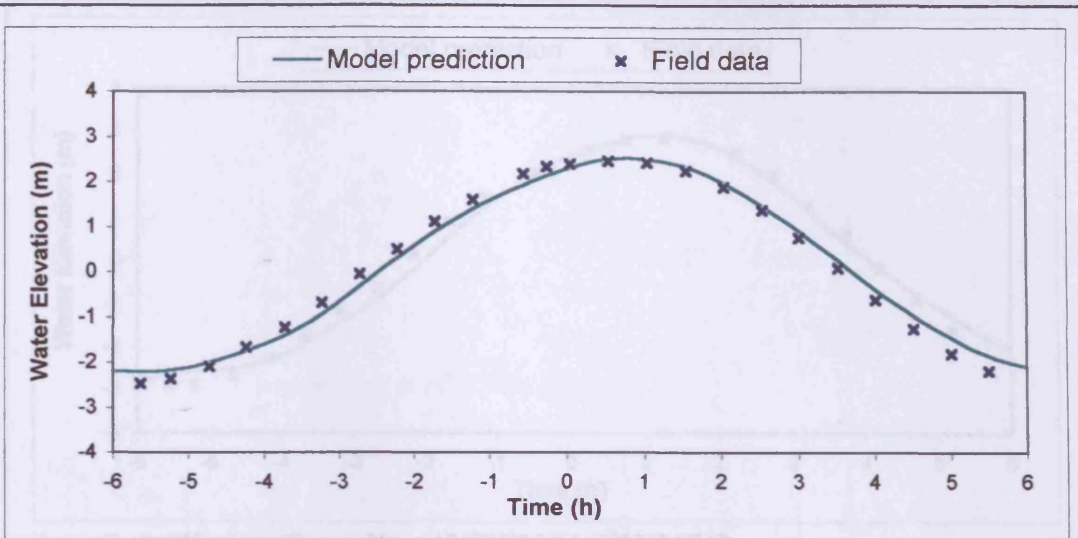
Location : Minehead (51°12'55"N, 3°28'22"W)
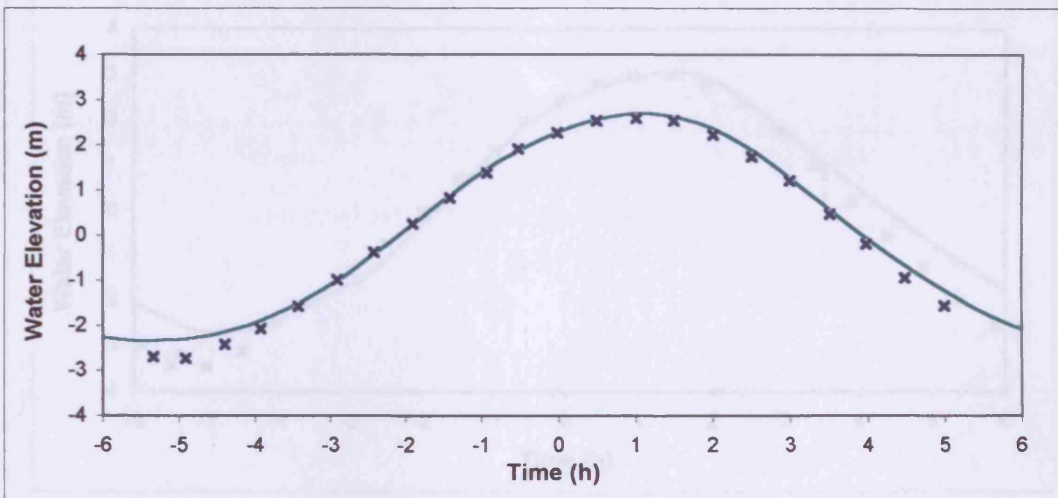
Location : Barry (51°23'27"N, 3°15'26"W)
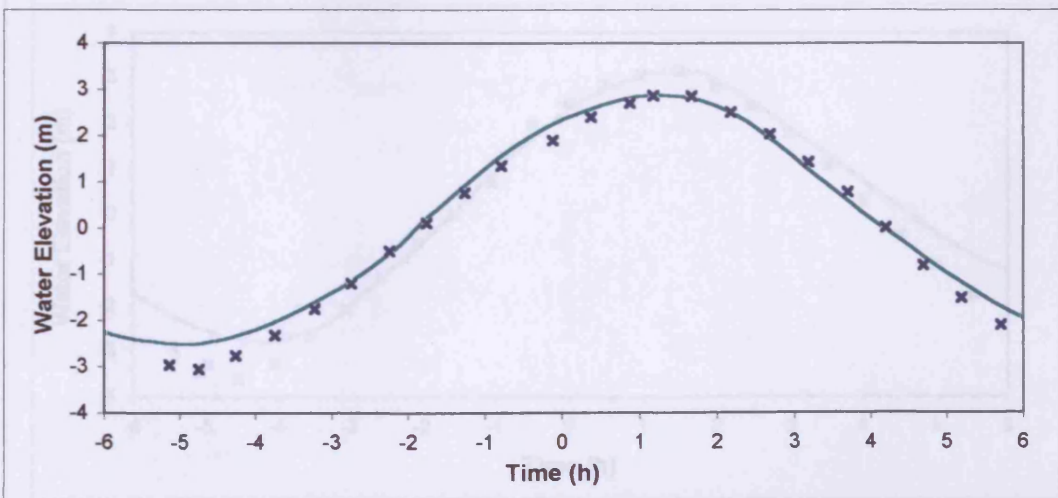
Location : Cardiff (51°27'08"N, 3°09'32"W)

FIGURE 5.4.7: Comparison of water elevations for mean neap tides
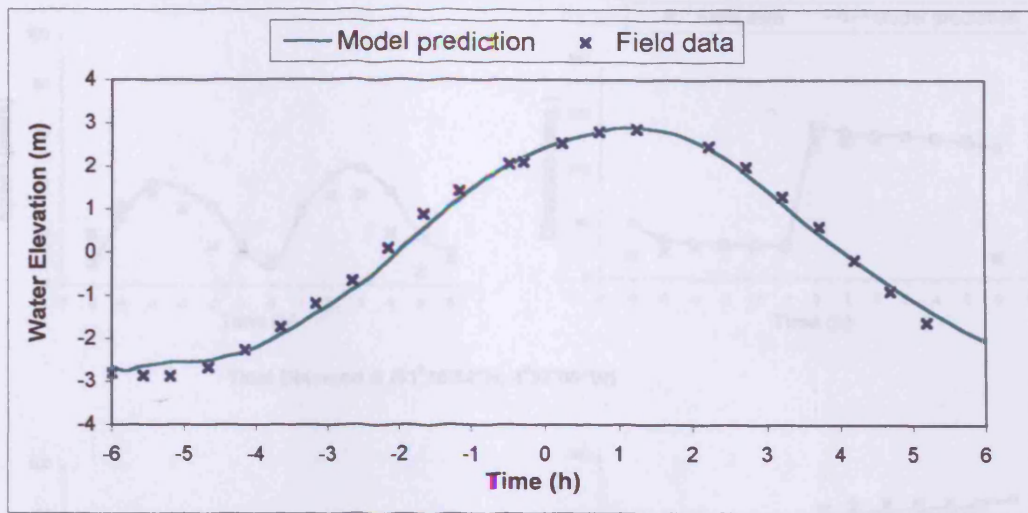
Location : Western Super Mare (51⁰21'28"N, 3⁰00'01"W)
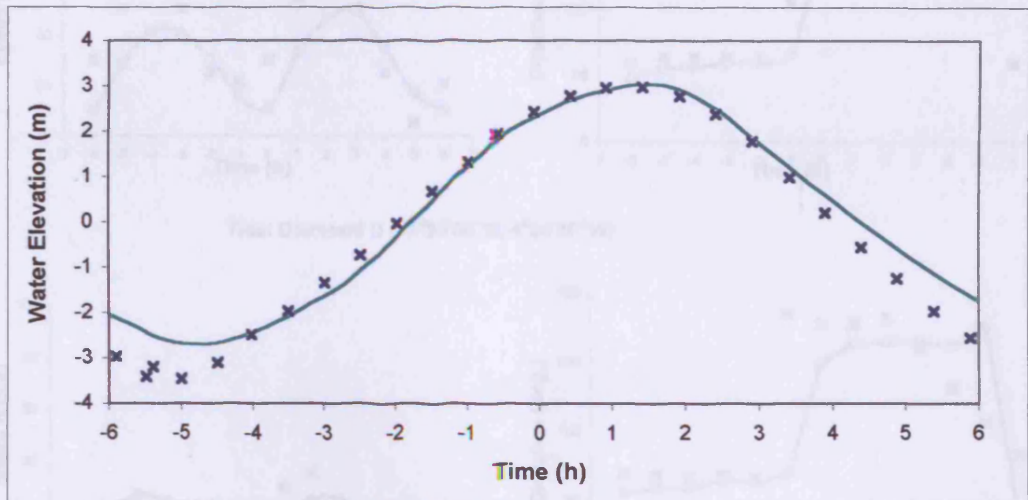
Location : Newport (51⁰32'59"N, 2⁰59'10"W)
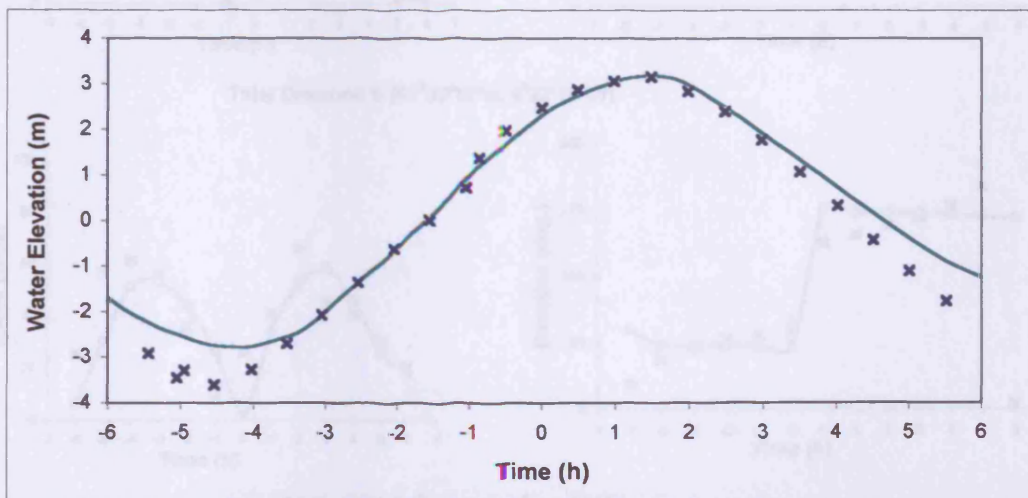
Location : Portbury (51⁰29'58"N, 2⁰43'37"W)

FIGURE 5.4.8 : Comparison of water elevations for mean neap tides
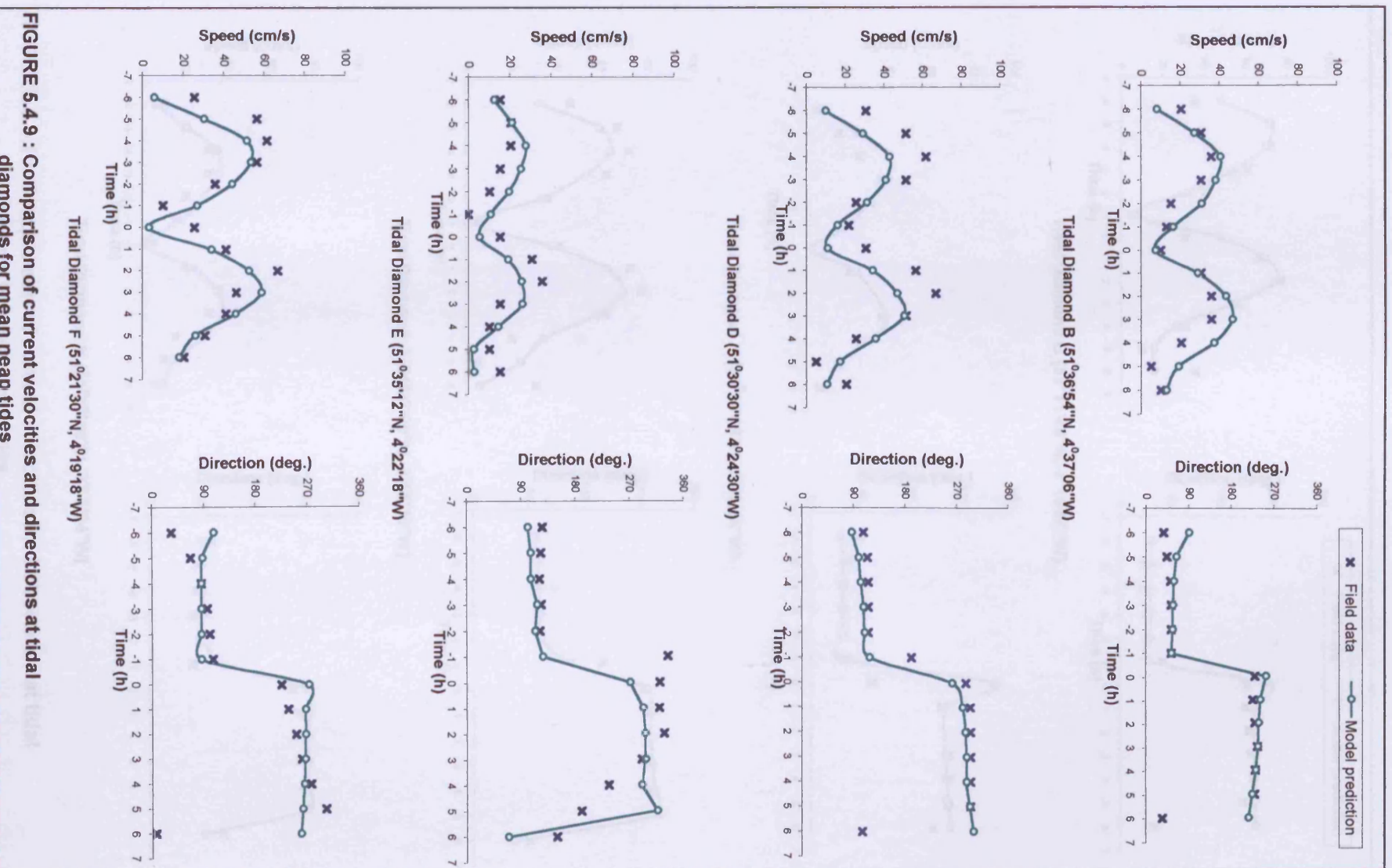
FIGURE 5.4.9 : Comparison of current velocities and directions at tidal diamonds for mean neap tides

Tidal Diamond G (51°11'48"N, 4°16'00"W)

Tidal Diamond H (51°33'18"N, 3°56'48"W)

Tidal Diamond J (51°27'00"N, 3°55'30"W)

Tidal Diamond K (51°32'30"N, 3°53'24"W)

FIGURE 5.4.10: Comparison of current velocities and directions at tidal diamonds for mean neap tides
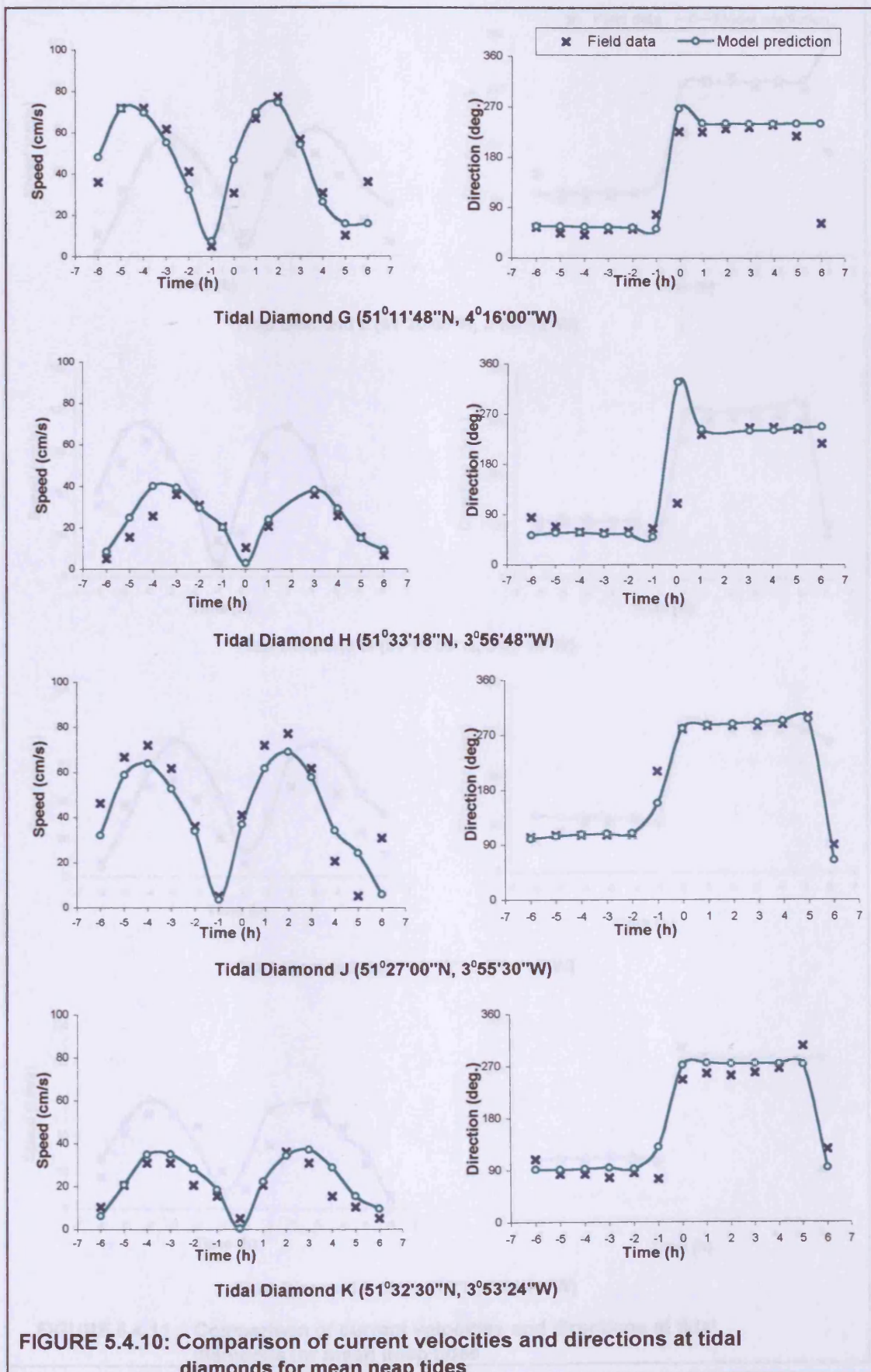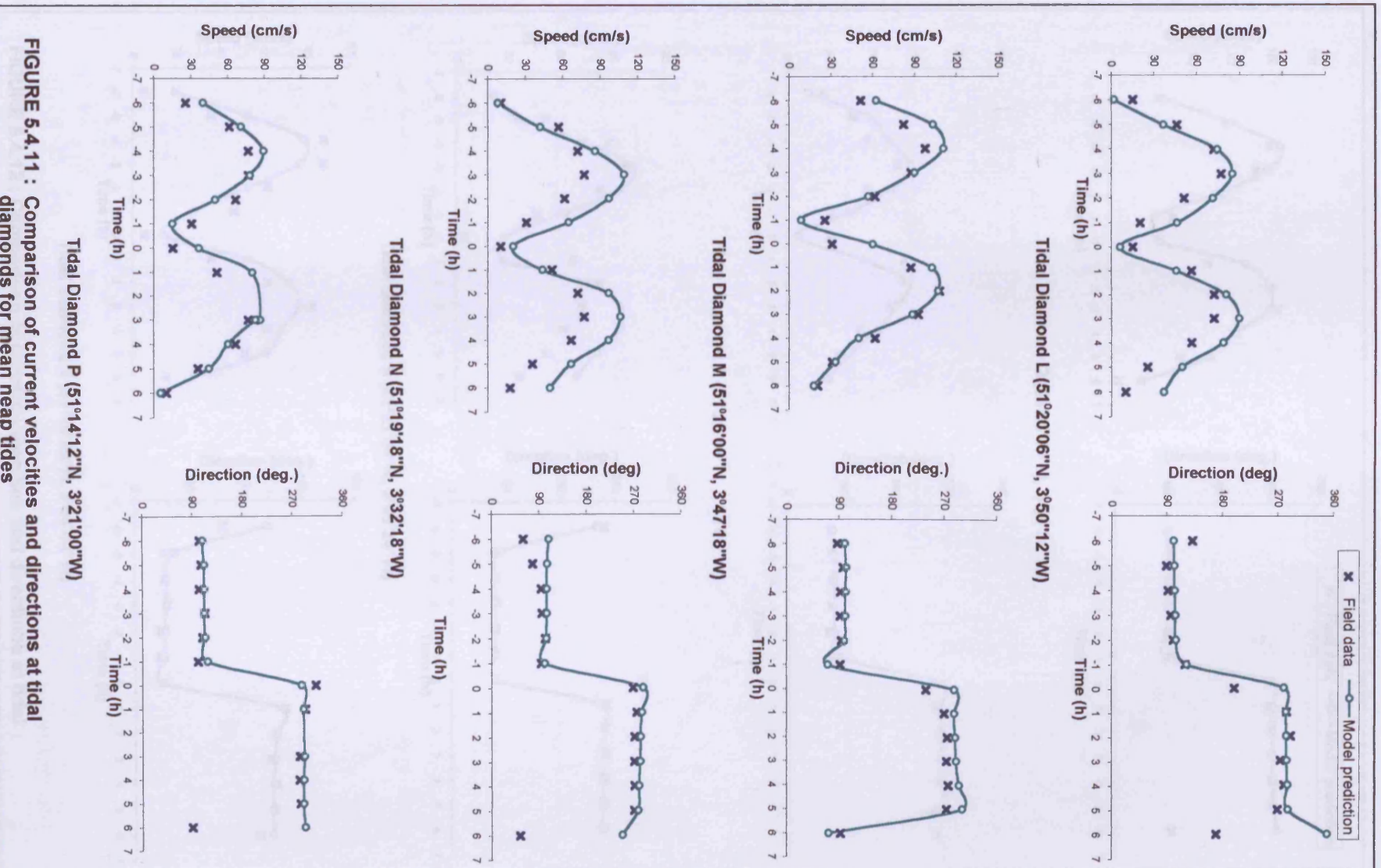
FIGURE 5.4.11 : Comparison of current velocities and directions at tidal diamonds for mean neap tides
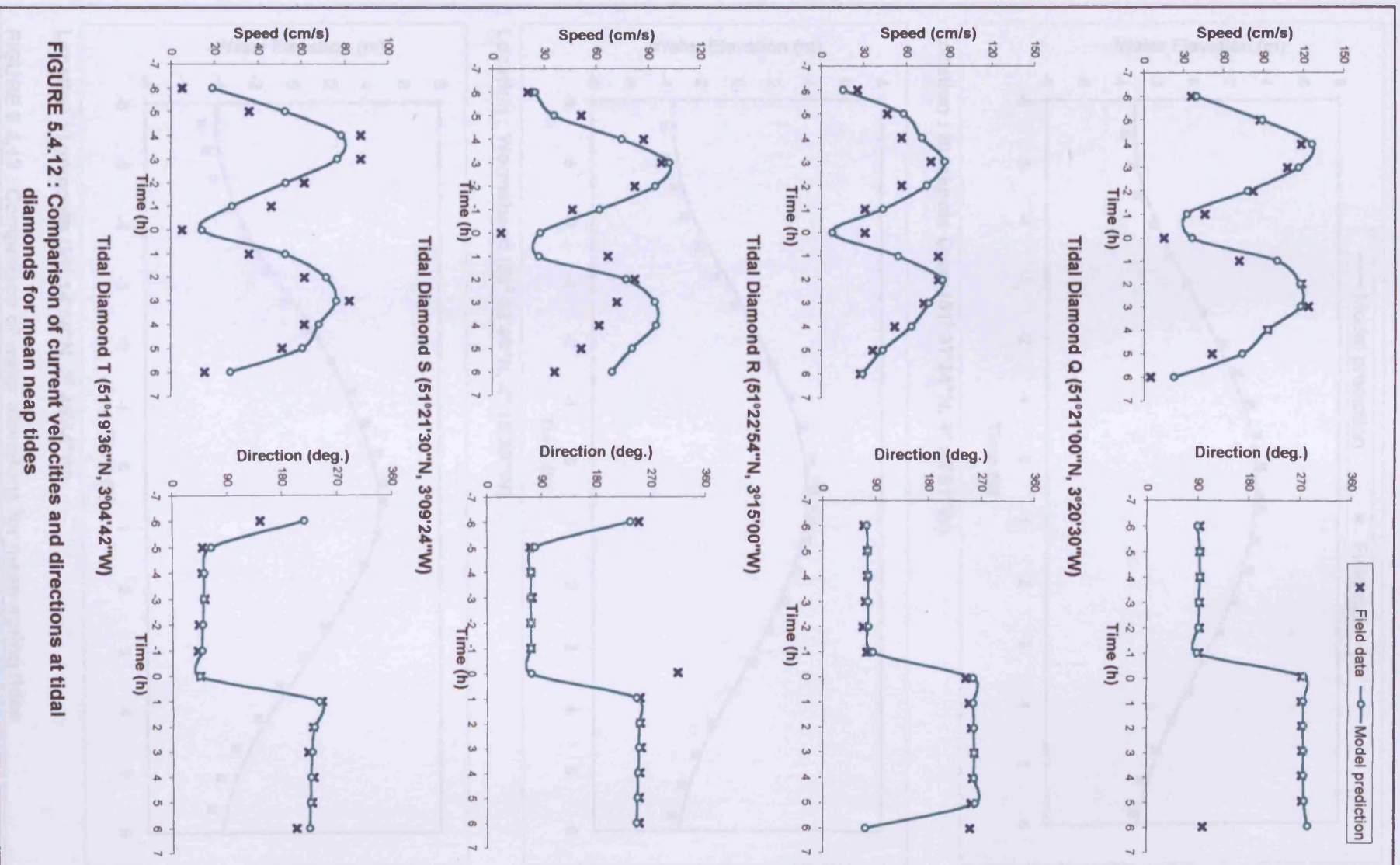
FIGURE 5.4.12 : Comparison of current velocities and directions at tidal diamonds for mean neap tides
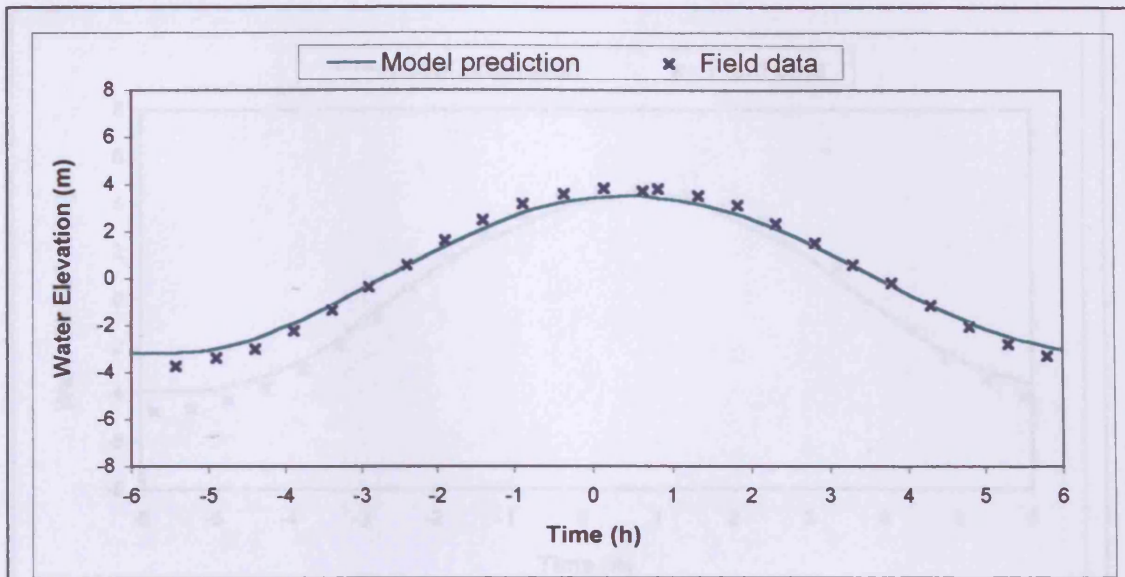
Location : Stackpole Quay (51⁰ 37'24"N, 4⁰ 53'51"W)
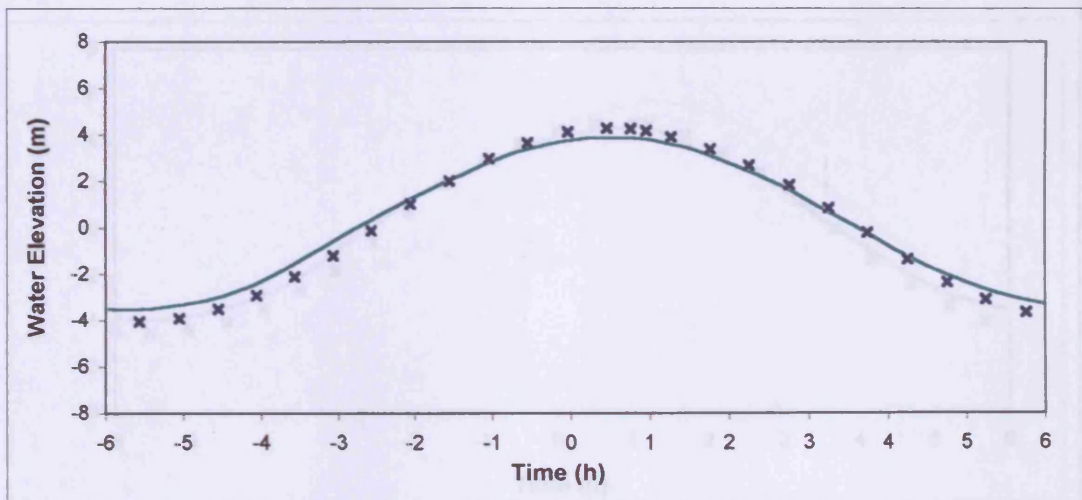
Location : Wormshead (51⁰ 33'48"N, 4⁰ 18'30"W)
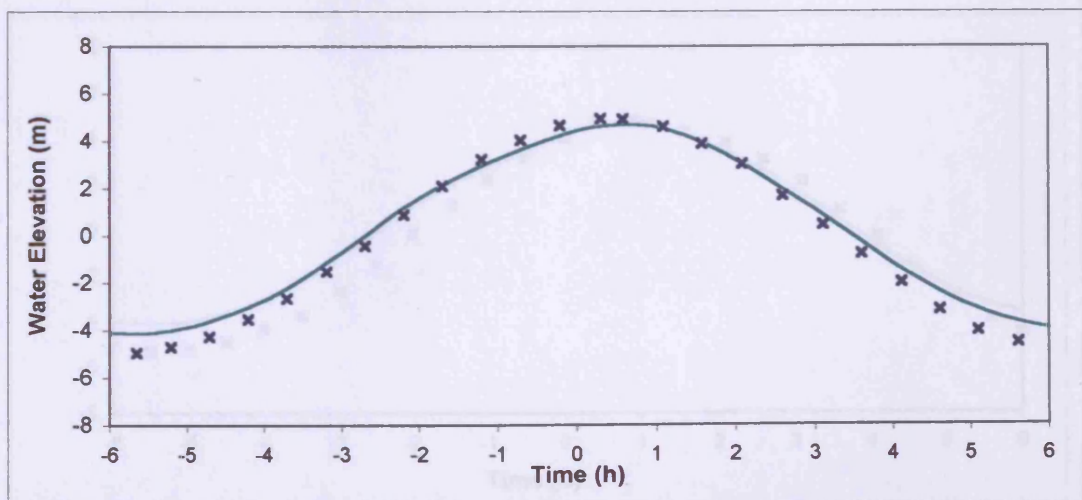
Location : Lynmouth (51⁰ 14'04"N, 3⁰ 49'44"W)

FIGURE 5.4.13 : Comparison of water elevations for mean spring tides
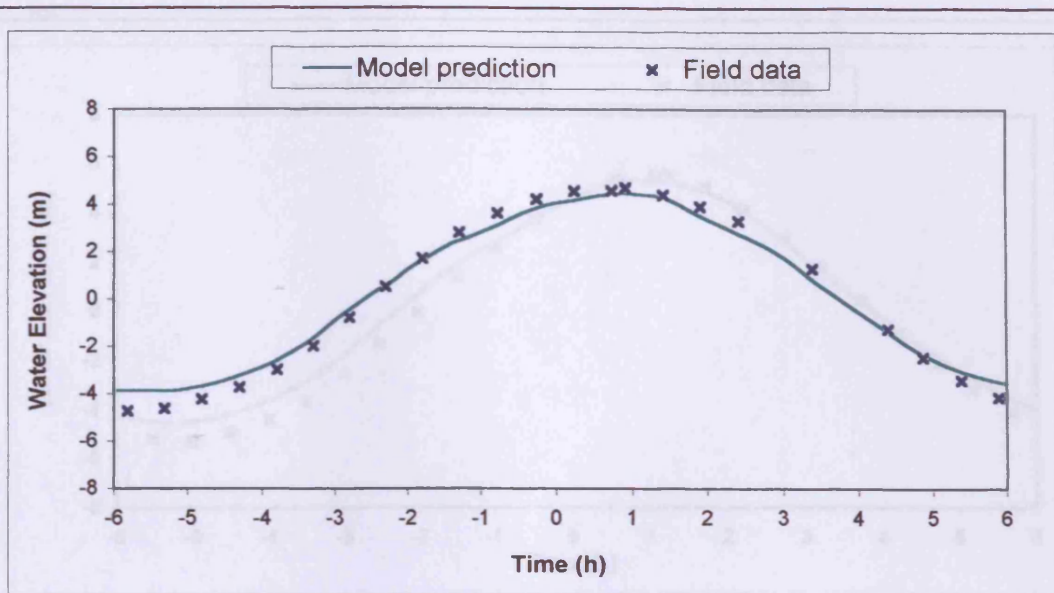
Location : Swansea (51⁰ 36'38"N, 3⁰ 55'26"W)
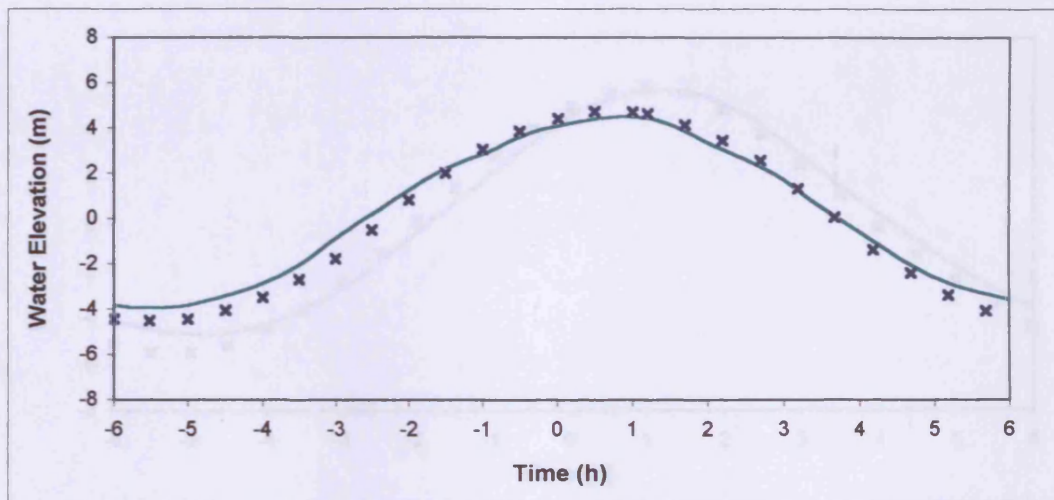
Location : Port Talbot (51⁰ 34'24"N, 3⁰ 48'06"W)
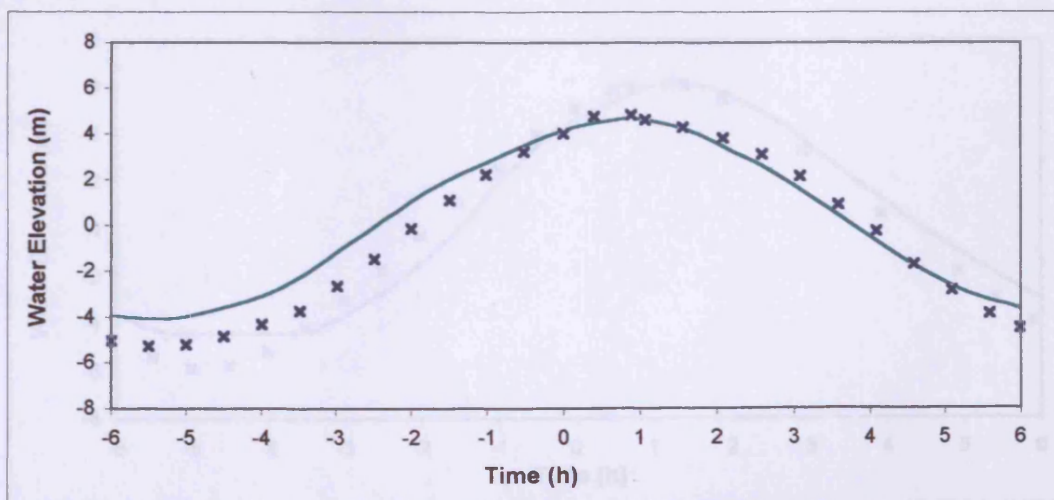
Location : Porthcawl (51⁰ 28'18"N, 3⁰ 42'06"W)

FIGURE 5.4.14: Comparison of water elevations for mean spring tides

Location : Minehead (51⁰12'55"N, 3⁰28'22"W)

Location : Barry (51⁰23'27"N, 3⁰15'26"W)

Location : Cardiff (51⁰27'08"N, 3⁰09'32"W)

FIGURE 5.4.15 : Comparison of water elevations for mean spring tides
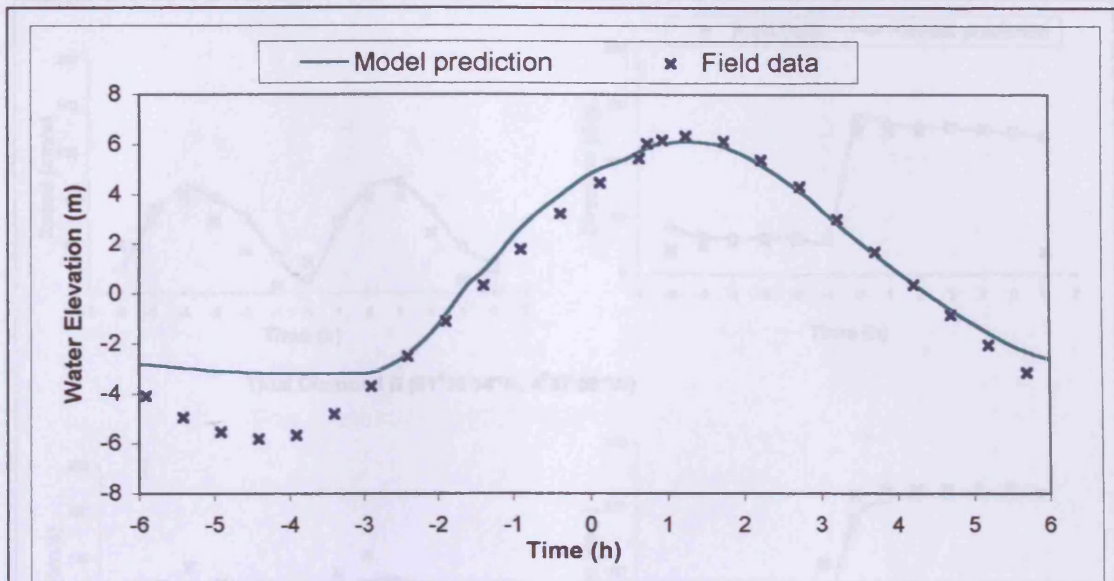
Location : Western Super Mare (51⁰21'28"N, 3⁰00'01"W)
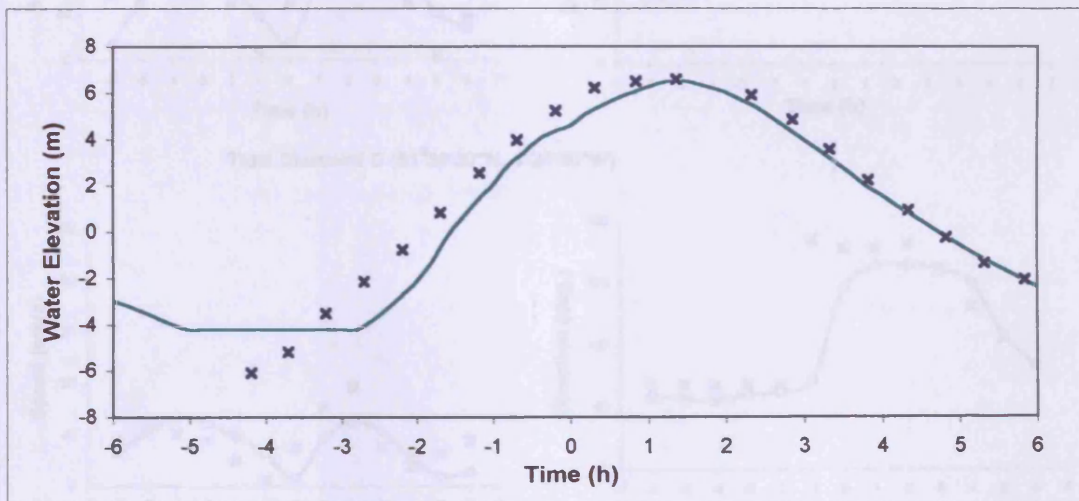
Location : Newport (51⁰32'59"N, 2⁰59'10"W)
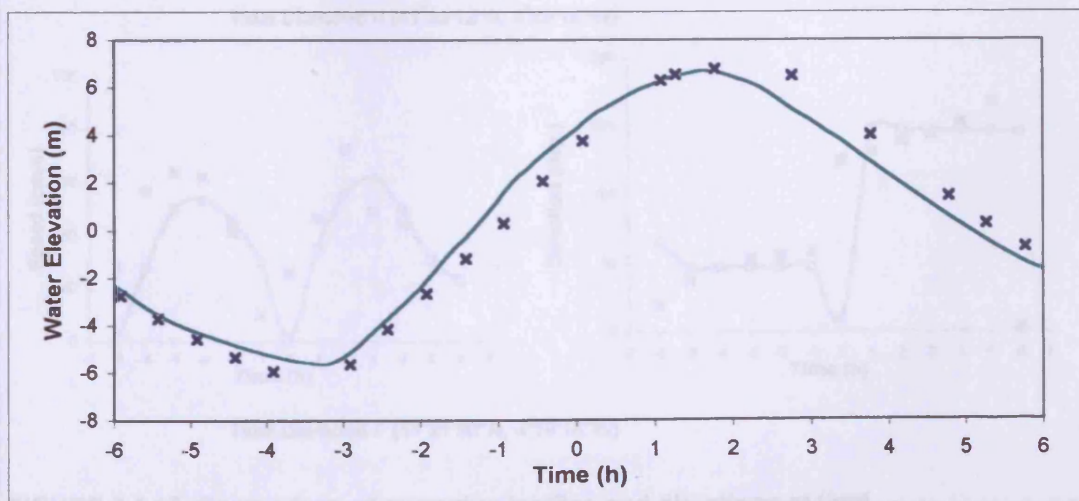
Location : Portbury (51⁰29'58"N, 2⁰43'37"W)

FIGURE 5.4.16 : Comparison of water elevations for mean spring tides
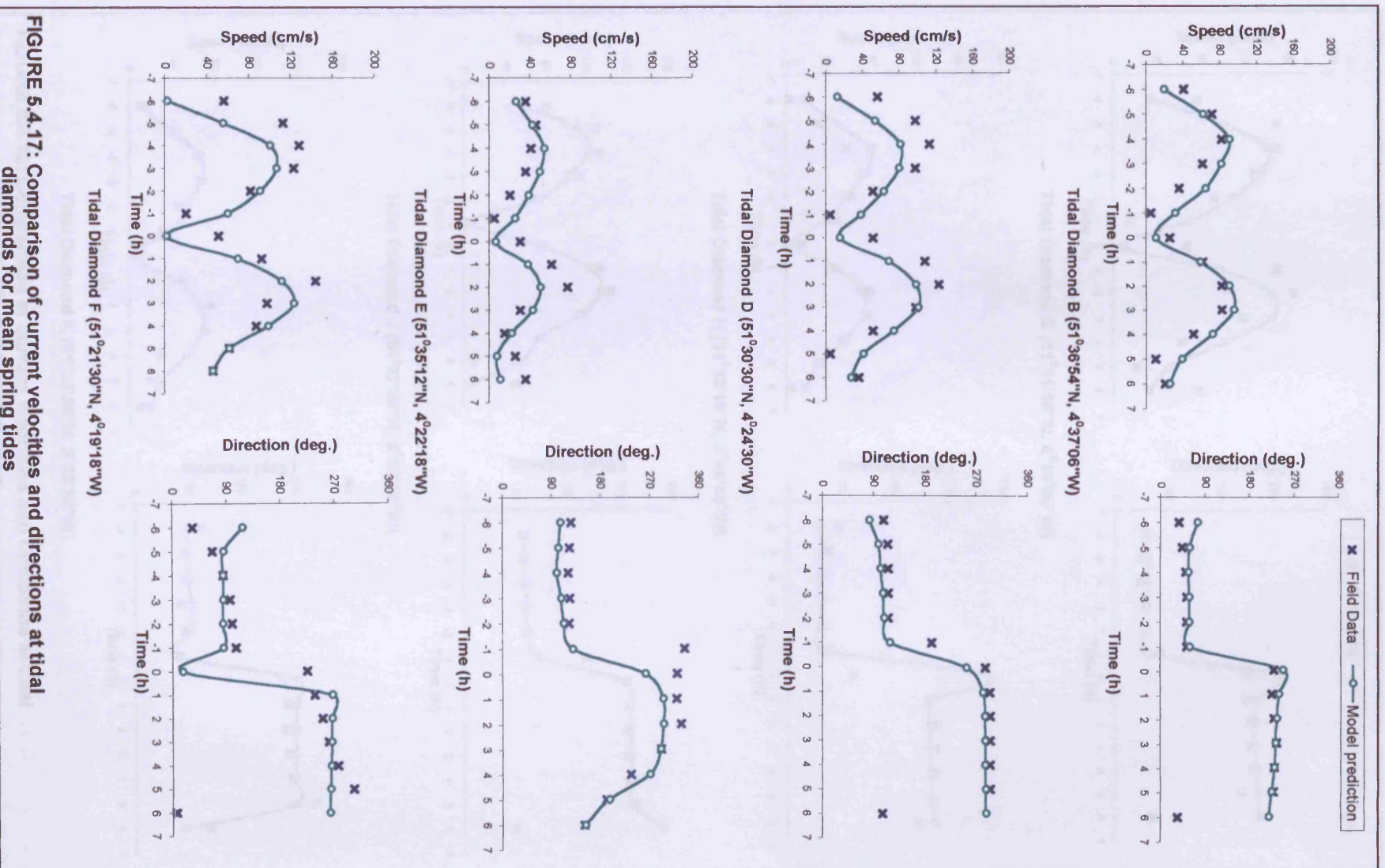
FIGURE 5.4.17: Comparison of current velocities and directions at tidal diamonds for mean spring tides
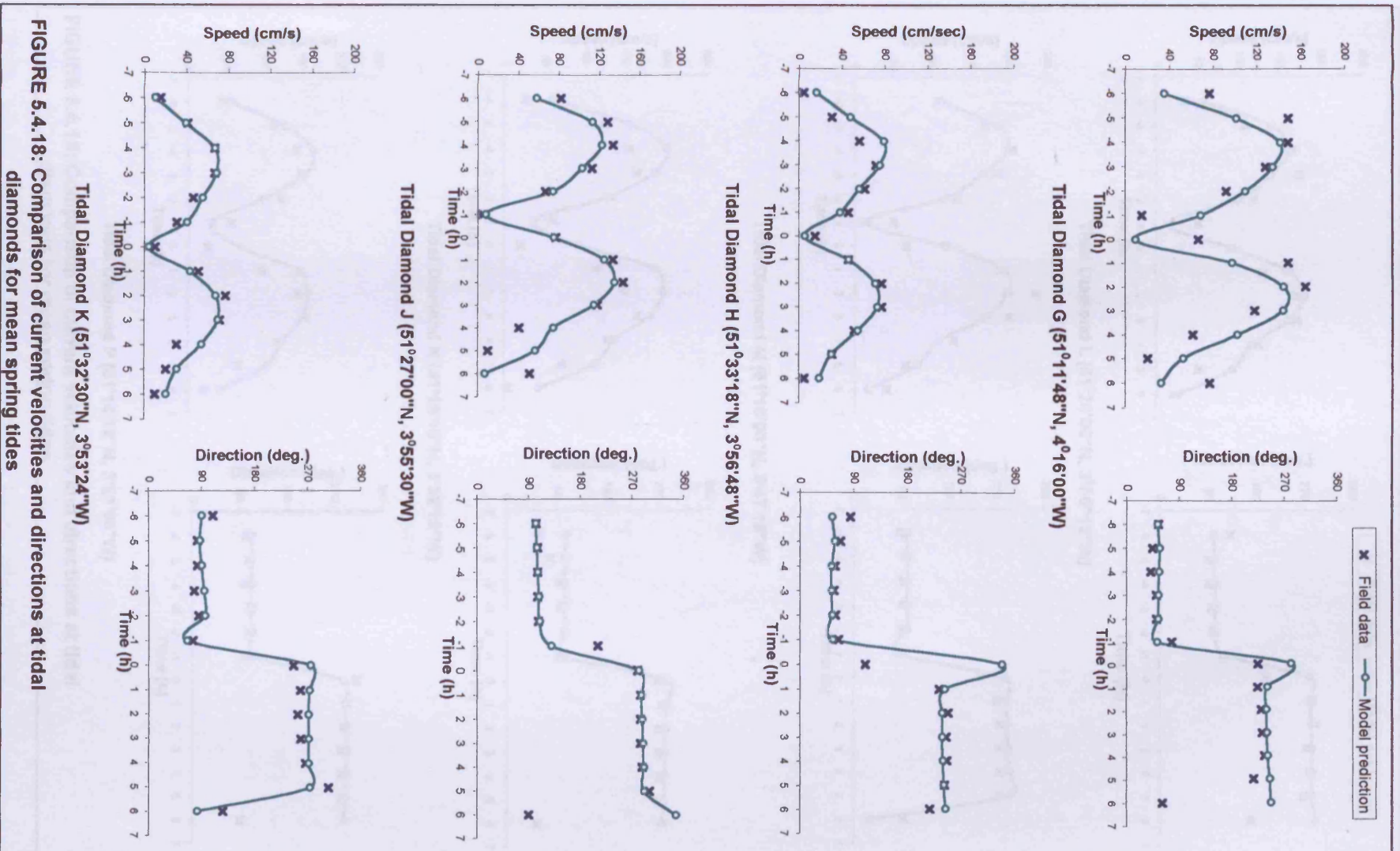
FIGURE 5.4.18: Comparison of current velocities and directions at tidal diamonds for mean spring tides
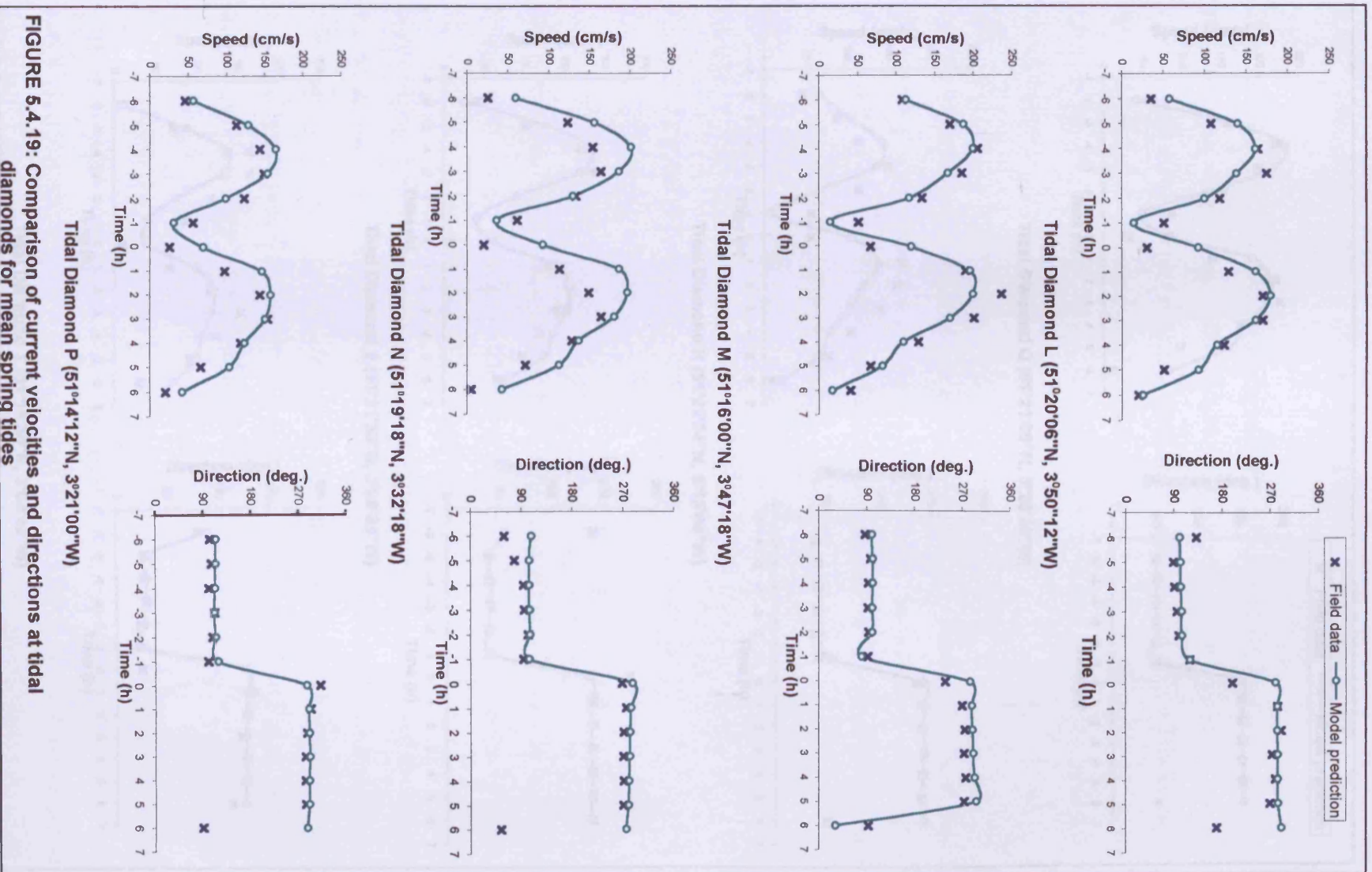
FIGURE 5.4.19: Comparison of current velocities and directions at tidal diamonds for mean spring tides
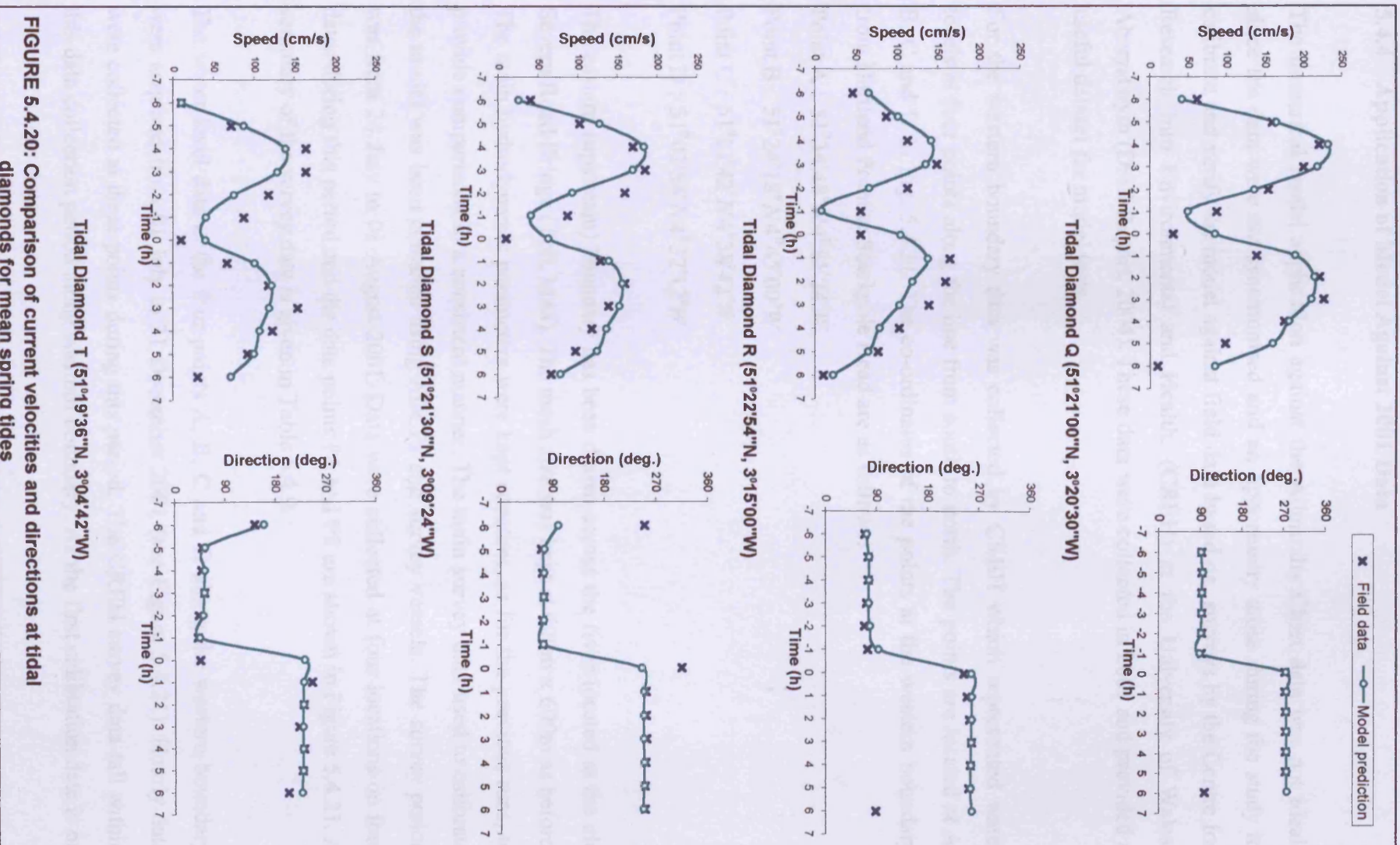
FIGURE 5.4.20: Comparison of current velocities and directions at tidal diamonds for mean spring tides

5.4.4   Application of Model Against 2001 Data

The numerical model application against the Admiralty Chart data was not ideal, since the data were not synchronised and an opportunity arose during the study to calibrate and verify the model against field data based on surveys by the Centre for Research into Environmental and Health, (CREH) at the University of Wales, Aberystwyth (Draft Report, 2004). These data were collected in 2001 and provided a useful dataset for model tests.

For the western boundary data was collected by CREH which represented water levels at four points along the line from south to north. The points are located at A, B, C and D in Fig. 5.4.21. The co-ordinates of the points at the western boundary from Hartland Point to Stackpole Head are as follows:

Point A : $51^{0}34'48''N4^{0}51'24''W$

Point B : $51^{0}24'18''N4^{0}45'00''W$

Point C : $51^{0}13'42'N4^{0}38'42''W$

Point D : $51^{0}02'54'N4^{0}32'12''W$

The eastern (upstream) boundary has been drawn across the river located at the old Severn Road Bridge (Toll, M48). The mesh size was kept at 600m x 600m as before. The main hydrodynamic parameters were kept constant, as for the previous runs, to provide comparisons in a consistent manner. The main survey data used to calibrate the model was been collected using ADCPs and survey vessels. The survey period was from 24 July to 01 August 2001. Data were collected at four locations on four dates during this period and the data points P1 and P2 are shown in Figure 5.4.21. A summary of the survey data is given in Table 5.4.9.

The water level data at the four points A, B, C and D along the western boundary were acquired from 01 July to 31 December 2001 (see Figure 5.4.21). Hourly data were collected at these points during this period. The CREH survey data fall within this data collection period along western boundary. As the first calibration date is on

24 July 2001, the simulation time of the model starts three days before 24 July 2001 to provide more steady flow result. The simulation starts at 20 July 2001 and simulation time was considered to be 310 hours (25 tidal cycle), which can cover all the four survey data for calibration and ended in 02 August 2001.

TABLE 5.4.9: Timetable for 2001 data set

Survey	Location	Co-ordinate	Start Time	End time
Survey-01	South Wales (point P1)	$51^\circ26.102'N3^\circ38.414'W$	04:58:06am 24.07.01	17:30:06pm 24.07.01
Survey-02	South Wales (point P1)	$51^\circ26.103'N3^\circ38.375'W$	04:20:57am 26.07.01	17:45:14pm 26.07.01
Survey-03	Minehead (point P2)	$51^\circ12.820'N3^\circ23.30'W$	04:58:16am 30.07.01	17:34:17pm 30.07.01
Survey-04	Minehead (point P2)	$51^\circ12.820'N3^\circ23.30'W$	06:49:48am 01.08.01	17:25:50pm 01.08.01

The model prediction for the above simulation and field survey data have been compared and the results are shown in Figures 5.4.22 to 5.4.33. The results showed very good agreement between the survey data and model results during the simulation times. The comparisons of the current speed at the four surveys times (Surveys 01 – 04) showed that for survey- 01 (Figure 5.4.22) and survey-02 (Figure 5.4.25) the comparison were very close. For survey-03 (Figure 5.4.28) and survey-04 (Figure 5.4.31) the field data showed higher peaks at high tide than the model results but at other times the data matched well. The corresponding directions (expressed in degrees) are shown in Figures 5.4.23, 5.4.26, 5.4.29 and 5.4.32. Again very good comparisons were obtained between the field data and model results for each of the survey results. The point of reversal in direction matches almost exactly in all of the surveys, with this being an important feature with the changing flow direction from flood to ebb tide and vice versa. The water level are shown for survey-01 in Figure 5.4.24 and for survey-02 in Figure 5.4.27 with the trend in the water level variation between the survey data and model results agreeing very closely. For survey-03 in

Figure 5.4.30 and survey-04 in Figure 5.4.33, the agreement between the water level variations was again good. The magnitude of the field data matches well with the model result throughout the total calibration time. The bed level data being used here is from Chart 1179 (1993), whereas the collected survey data were from 2001. The bed level might have changed during the period with the new bathymetric data not being considered in this study so minor differences were found in results.

This calibration based on the recently collected data (Draft Report, 2004) from the Bristol Channel confirmed that the current numerical model was performing accurately and could now be used for predicting the sediment transport rates or any other hydrodynamic parameters for the estuary.

5.5. Tidal Velocity and Sediment Transport Predictions

The tidal model for the Bristol Channel was then run for both neap and spring tidal conditions to predict the sediment concentration distributions. The predictions were reproduced at high water (HW) and eight other times during the tidal cycle. The times cited are relative to conditions at Hartland Point, at the western boundary. The tidal residuals, which consist of the tidal velocity, net erosion (in $g/m^2/s$), suspended sediment load (in mg/l) and residual erosion (in kg/m^2) are reproduced after successive tidal cycle.

Much research has been undertaken on sediment transport fluxes (Dyer, 1984; Mclaren, et al., 1993) within the Bristol Channel, based on different model values for the grain size and sediment mineralogy etc. Collins and Ferentinos (1984) analysed data available at the time and proposed a laterally varying transport model, describing conditions along the coastal margins as flood dominant and with the central channel being ebb dominant. A sediment budget for the Bristol Channel was undertaken by Collins, et al. (1980) which lacks verification against comprehensive field measurements, but some characteristics of sediment budget can be found in Bryant and Williams (1983). Validation of the numerical models was difficult due to the lack of reliable long-term data. The model predictions were compared with RCL,

Figure 5.4.21: Location of 2001 survey points in Bristol Channel

| Outer Bristol Channel | Central Bristol Channel | Inner Bristol Channel | Severn Estuary |
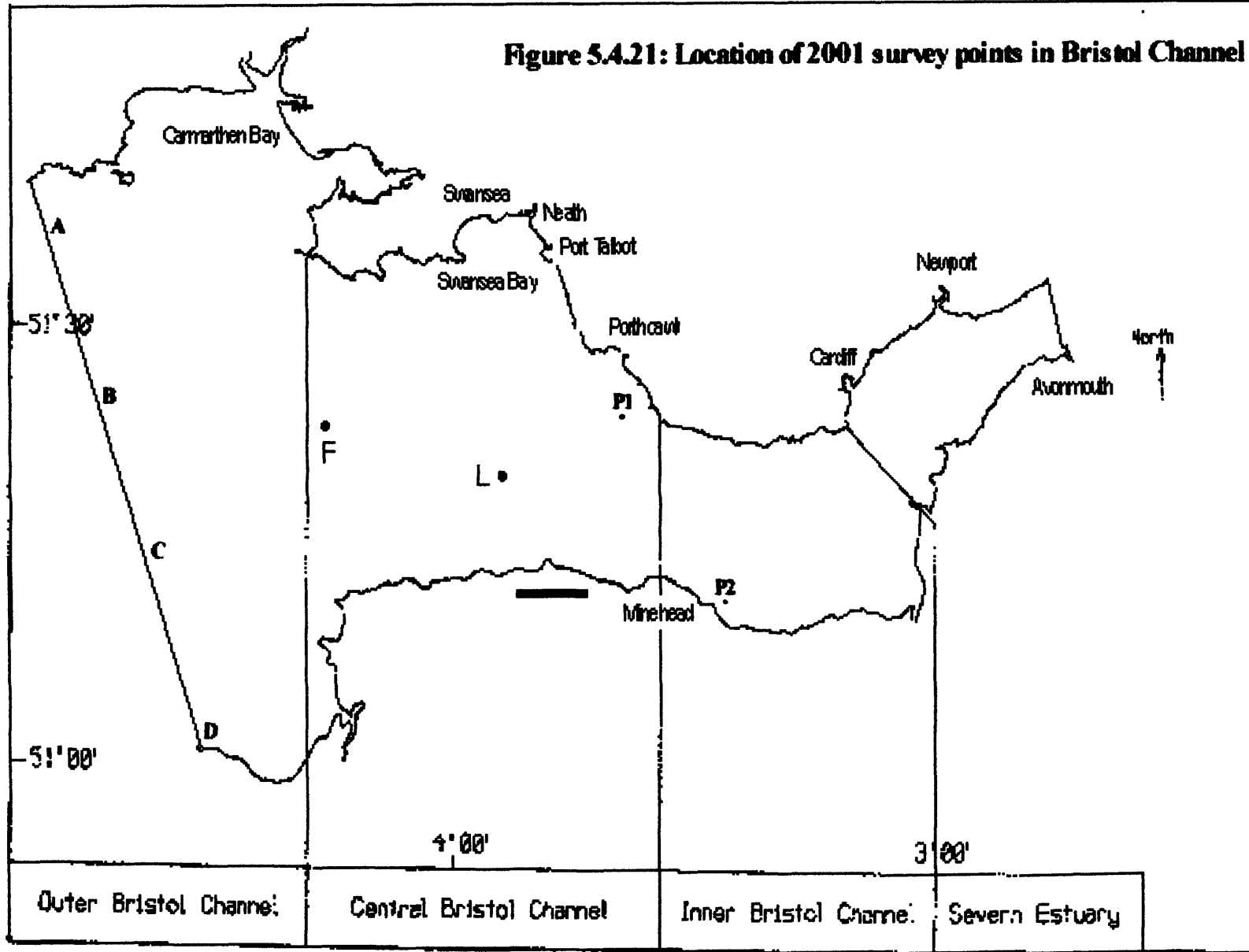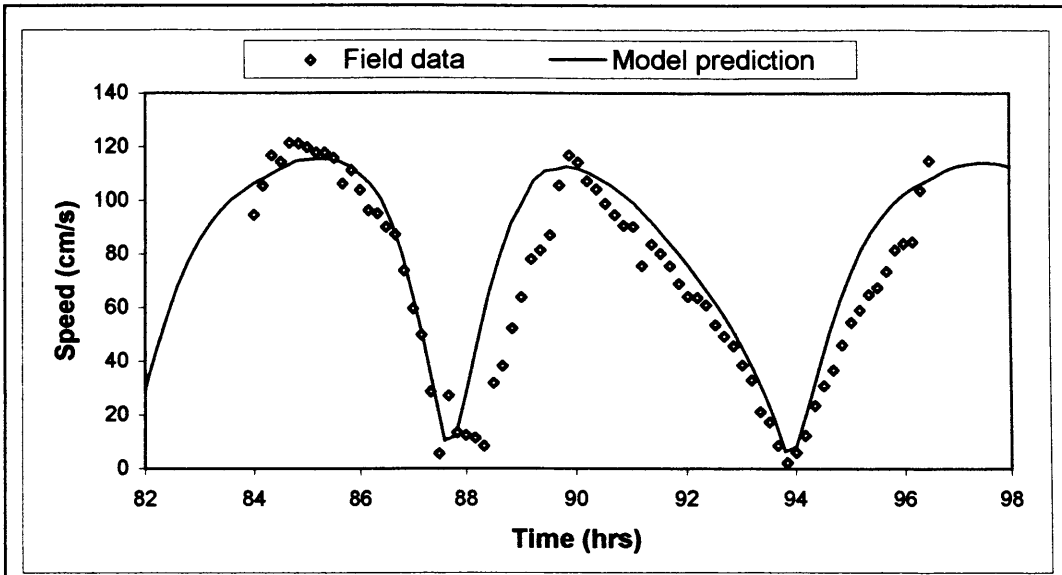
Figure 5.4.22 : Comparison of current speed for survey-01 at point P1
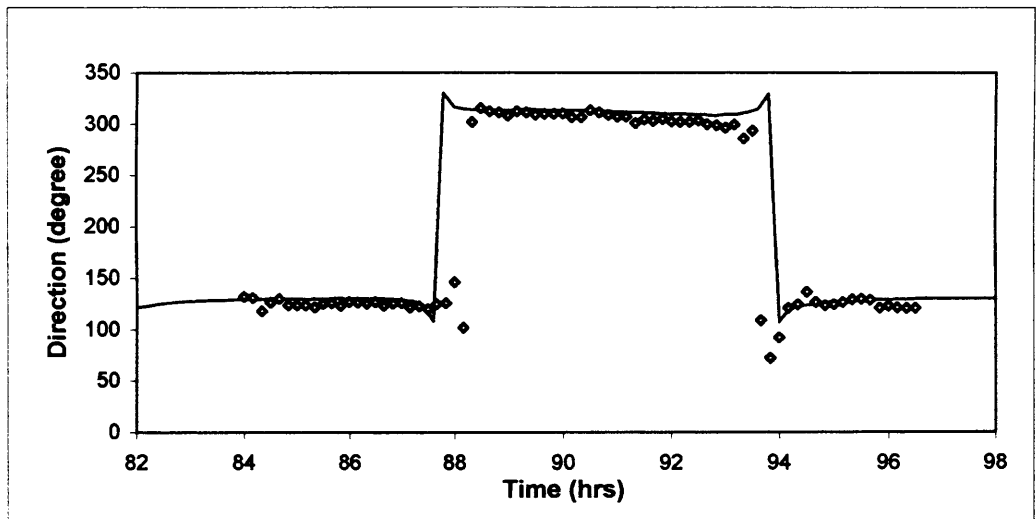
Figure 5.4.23 : Comparison of current direction for survey-01 at point P1
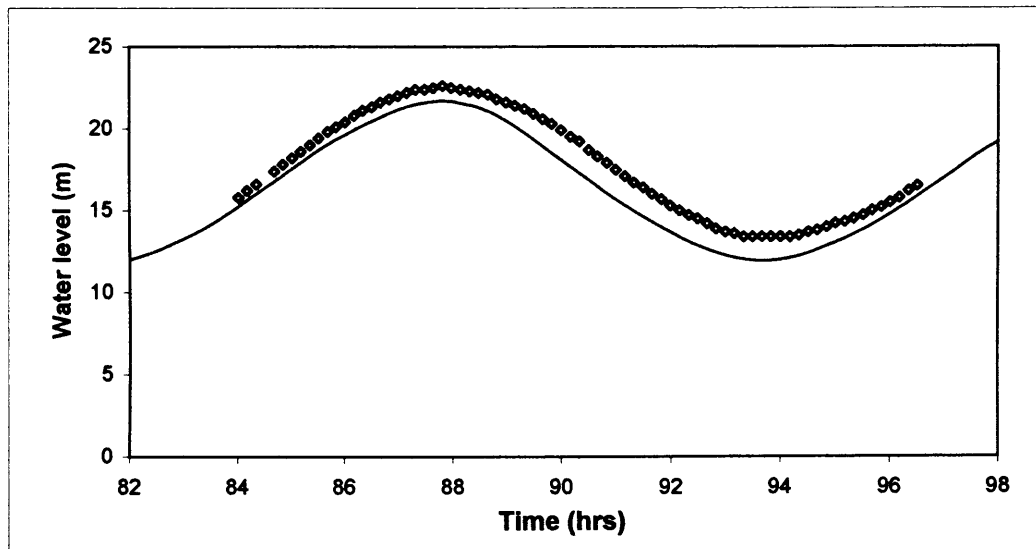
Figure 5.4.24 : Comparison of water levels for survey-01 at point P1
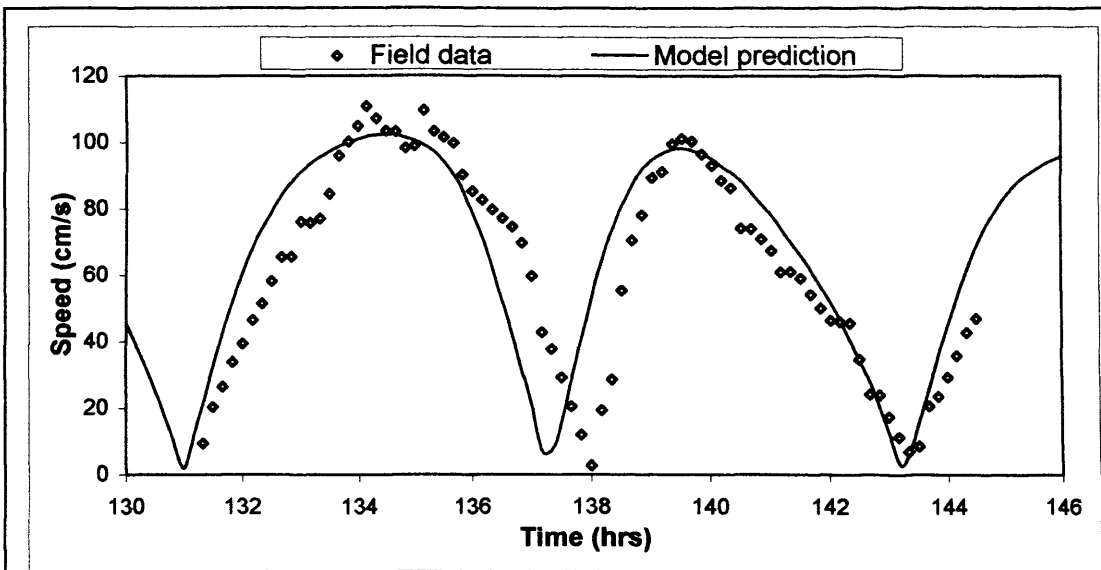
Figure 5.4.25 : Comparison of current speed for survey-02 at point P1
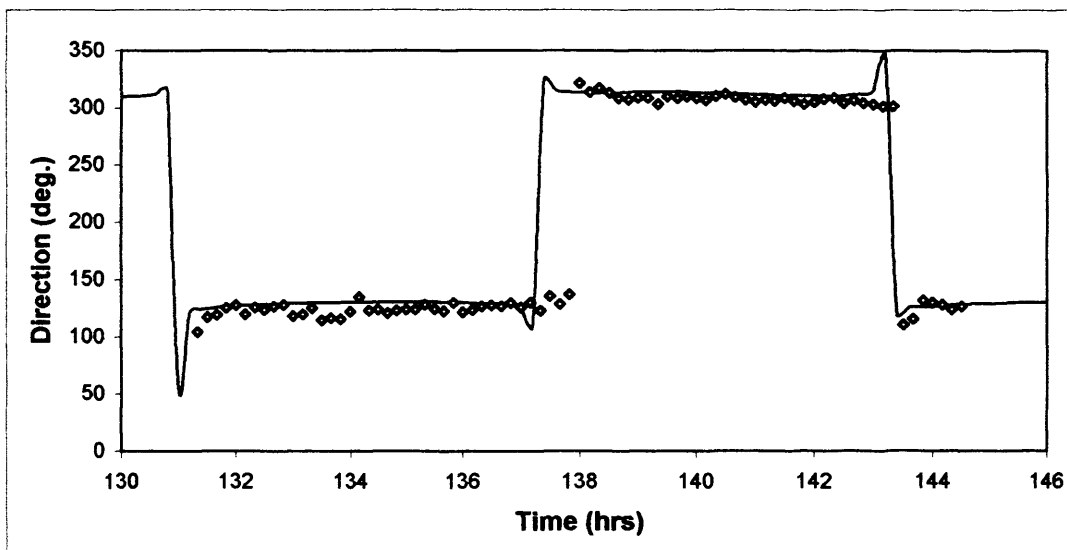
Figure 5.4.26 : Comparison of current direction for survey-02 at point P1
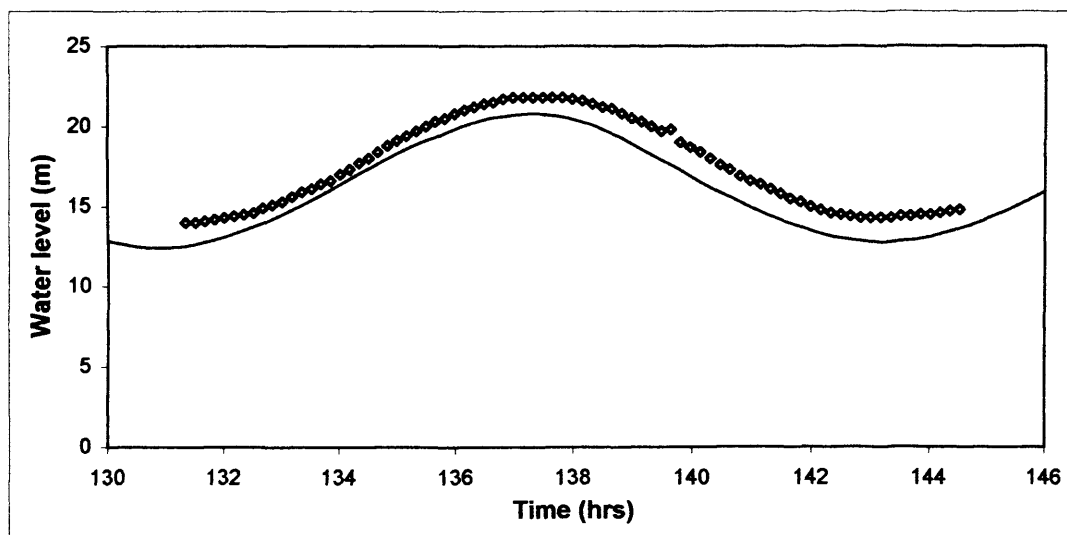
Figure 5.4.27 : Comparison of water levels for survey-02 at point P1
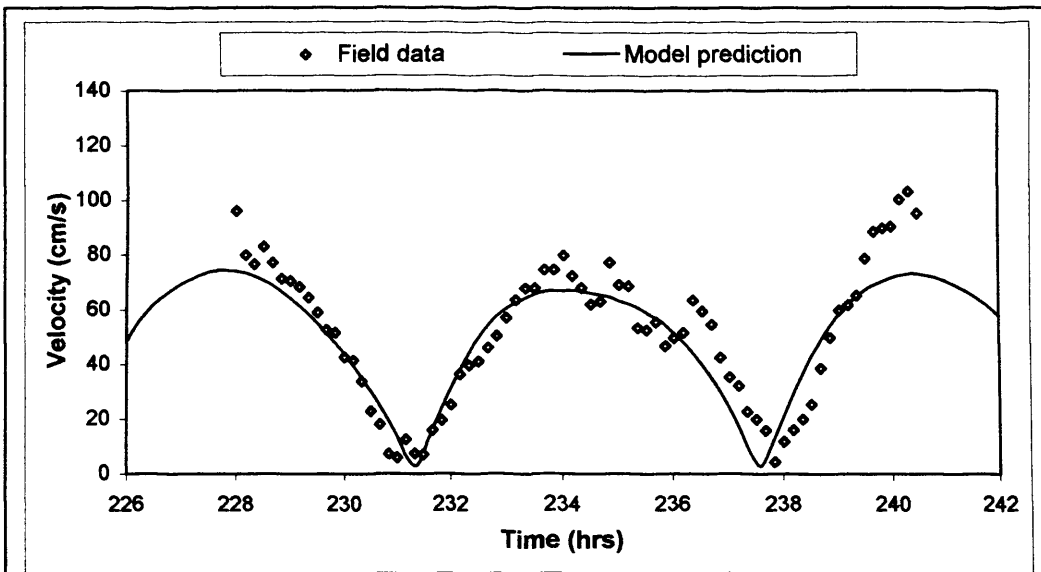
Figure 5.4.28 : Comparison of current speed for survey-03 at point P2
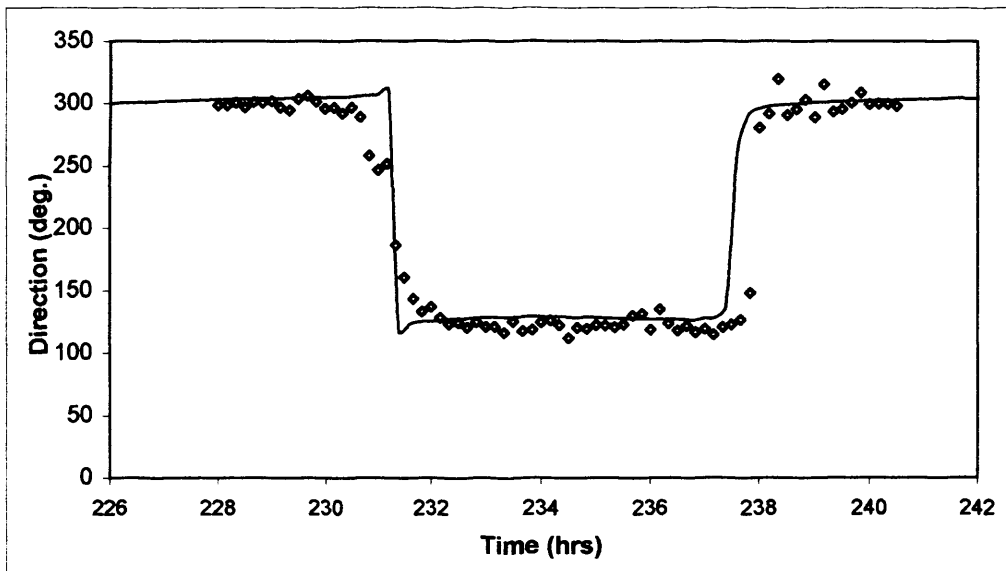
Figure 5.4.29 : Comparison of current direction for survey-03 at point P2
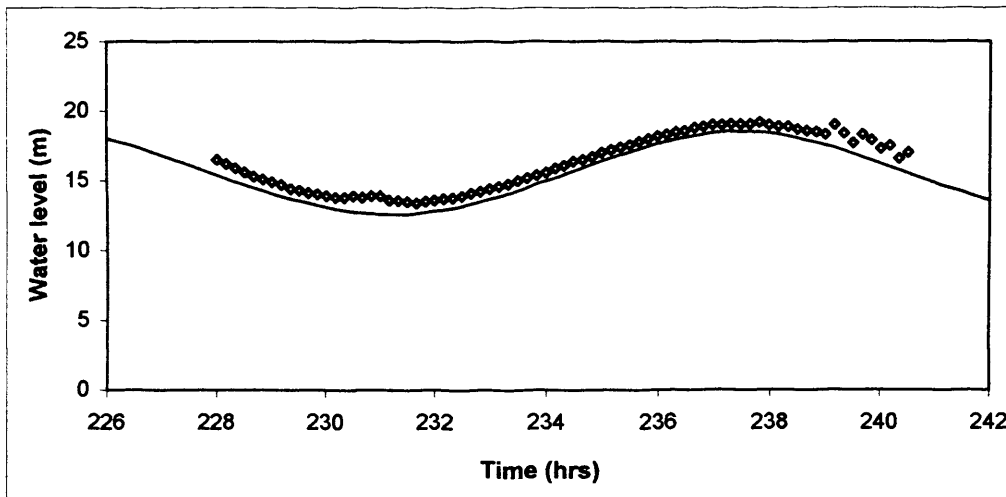
Figure 5.4.30 : Comparison of water levels for survey-03 at point P2
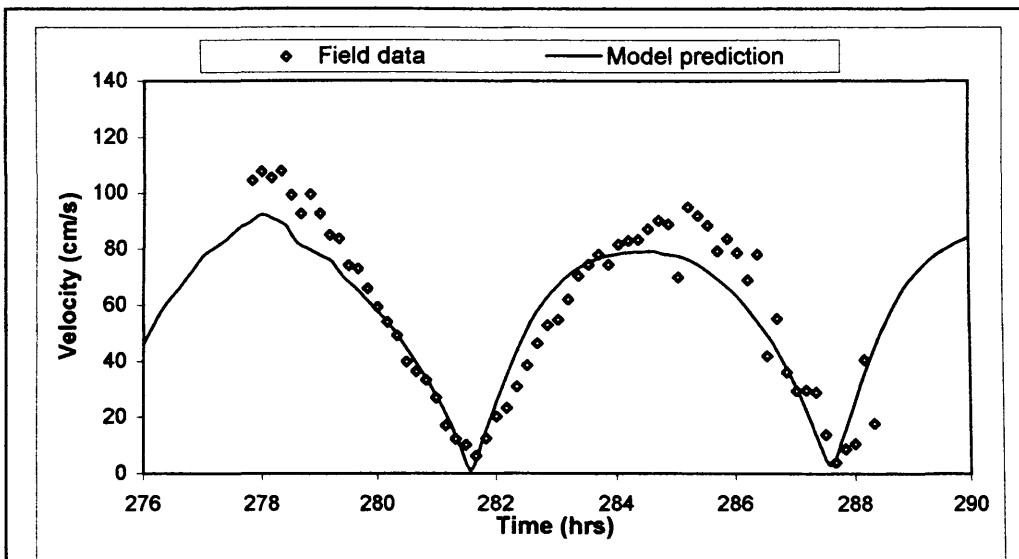
Figure 5.4.31 : Comparison of current speed for survey-04 at point P2
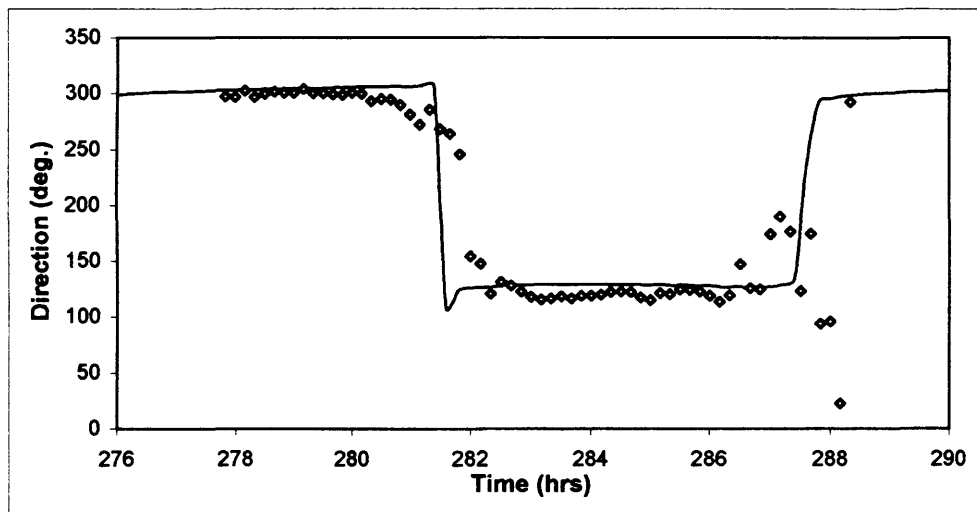
Figure 5.4.32 : Comparison of current direction for survey-04 at point P2
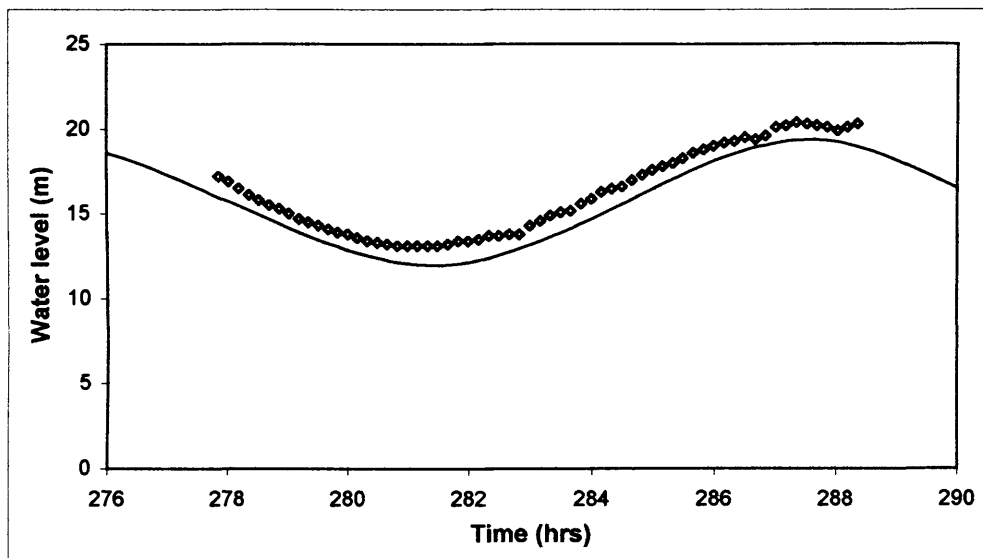
Figure 5.4.33 : Comparison of water levels for survey-04 at point P2

1986 report as they compared their model predictions with some field data. The sediment transport patterns for the whole estuary were described, but it was regarded as difficult to assess the grain size for the model simulations. The accuracy of the model predictions mainly depended upon the parameters chosen in the simulations. These parameters were mainly taken from previous laboratory experiments (ABP Report, 2000; RCL Report, 1986), field data or based on relevant theory.

Some field data were available for sediment transport fluxes for the Bristol Channel (Harris, et al., 1986). Samples of suspended sediments from a variety of locations within the estuary showed consistency with tidal mixing in the basin. The samples showed a spatial uniformity of mineralogy, with average suspended sediment composition was found to be illite (44%), quartz (23%), chlorite (19%), calcium carbonate (5%), kaolinite (4%) and organic carbon (3%) (by weight) (Bryant and Williams, 1983). The grain size of the sediment investigated also shows limited variation throughout the area, and for cohesive sediment it was found in Bryant and Williams, 1983 that the average floc diameter was about 140μm. The sediment grain size chosen for the study was 0.0004m (median size), as non-cohesive sediment part was considered in this study as the main source of suspended sediment load and the value was taken from a previous study of Bristol Channel by Falconer (1996).

The predictions confirms that suspended sediments are clearly visible during the semi-diurnal tidal cycle of 12.4 hours. There is a small hysteresis between the turn of the tide (between flood and ebb tide) and the sediment concentration level reaching the surface and, on the other hand, settling out at the end of each tidal cycle. The model prediction for suspended sediment transport for both neap and spring tide were compared with results from RCL, 1986 with good comparisons. The RCL report showed that their model predictions were compared with field data (which are not accessible) and obtained good comparison with field values. Figures 5.5.1 to 5.5.12 represent the different stages of the velocity profile and the suspended sediment concentration level for neap tides and Figures 5.5.17 to 5.5.28 represents similar conditions for spring tidal conditions. Details of the different stages of the sediment fluxes are given below.

5.5.1. Neap Tide Profiles

For the neap tide concentrations, the suspended solid front is not well defined at all times, mainly due to the frequent low concentrations. The 1000mg/l contour is rarely present and even the 500mg/l contour is not present over the main period of the neap tidal cycle. From Figures 5.5.1 to 5.5.12 the pattern of suspended settling, movement of sediment, their concentration and advection can be observed throughout a tidal cycle. The tidal flow pattern changes from flood tide to ebb tide and vice versa, but the settling process continues after the high water occurs over much of the area. The results obtained in this study were compared with the RCL Report (1986) and it was found that both sets of results were in good agreement.

HW+1.55hrs. : Three or four locations (very small area) were predicted where the suspended concentration exceeded 100mg/l, which indicates that the settling process continues well after high water or the turn of the tide. For neap tides effects are much less than for spring tides, which means that sediments settling for a longer time and may therefore delay entrainment.

HW+3.10hrs. : An evenly developed velocity field occurs (Figure 5.5.1), which gives rise to a larger area of entrainment of suspended solid (>100mg/l). The middle part of the Bristol Channel shows the entrainment of suspended solid (Figure 5.5.2). This is indicative of entrainment, resulting in sediment mixing to the surface on a regional pattern. A small part of area near to Cardiff shows higher concentrations, which reflect entrainment from the bed of the shallower water near land.

HW+4.65hrs. : Higher velocities occur in the Severn Estuary (Figure 5.5.3) relative to the rest of the Channel, thereby highlighting a progressive expansion of the area occupied by sediment concentrations in the range 100mg/l to 250mg/l and a general regional increase in concentration at areas near to Avonmouth. At this phase, concentrations >500mg/l are not visible (Figure 5.5.4), which might be due to the sediment still in a state of settlement.

HW+6.20hrs. : During this phase Figure 5.5.6 showed a decrease in the concentration in area wise but an increase in the concentrations in the region of the mouth of the Severn. This result showed that settlement occurred in the mid-estuary and at a regional scale.

HW+7.65hrs. : At this time, after low water exhibited a relatively low velocity throughout the estuary, except in the upper part of the Severn. A small area of suspended solids over the whole estuary which is at Avonmouth. The 500 mg/l concentration was limited in extent, occurring just at the entrance of the Severn Estuary. The rest of the estuary showed no entrainment of any significance.

HW+9.30hrs. : Larger areas of suspended sediments are visible (Fig. 5.5.8), with a well developed velocity field being established after low tide. There are some regions of high concentration, which highlight the continuing settlement and up-estuary advection.

HW+10.85hrs. : The average concentration of 100mg/l spreads across half of the channel, with a small area near Cardiff reducing a concentration level of 250mg/l (Figure 5.5.10). For this phase of neap tide 1000mg/l concentration level never occurs. This is primarily due to the lower entrainment of suspended solid and the settlement due to the low velocity patterns.

HW+12.4hrs. : At this stage where tidal reversal occurs the area of sediment concentration is reduced (Fig. 5.5.12). The concentration level become low (<100 mg/l) and nowhere across the estuary are any high concentration patches to be seen.

5.5.2. Spring Tidal Profiles

HW+1.55hrs. : It is the period just after high water and after the turn of the tide. The velocity direction has just changed its direction and the maximum velocity is about 0.7 m/s. Due to slack water at high tide the sediment continues to settle and the sediment concentration is very low.

HW+3.10hrs. : Figure 5.5.17 shows an increase in the ebb tide velocity, especially in the area from Cardiff to Swansea direction. The estuary reach from Avonmouth has a lower concentration than in the middle part of the channel, with this period also indicating settling or entrainment of sediment, which has not yet reached the upper surface region. The suspended solid front starts to develop at this phase.

HW+4.65hrs. : At this phase the whole of the Bristol Channel is well developed (Figures 5.5.19 and 5.5.20). Entrainment occurs especially around the middle part of the estuary, resulting in an increasing area occupied by the >500mg/l contour increasing further. The concentration around Cardiff increases even further, and a north-westerly spread is shown of the contours in the main channel and Bridgwater Bay. This indicates a cross-channel movement of the suspended sediment front.

HW+6.20hrs. : Figure 5.5.21 highlights the maximum velocity path around Cardiff and Bridgwater Bay. The sediment contours shows that the highest concentration areas are to the south east of Bridgwater Bay, where the load exceeds 1000mg/l. This high concentration is thought to be due to the highest sediment concentration levels in the upper part of the water column. After this period the lower currents reduce the sediment load and the 1000mg/l contour diminishes in area, indicating sediment settling in most of the low velocity areas. At this period advection is small and the sediment front is well defined.

HW+7.75hrs. : The concentration in the Severn Estuary is relatively low at this phase. The main suspended concentration is only visible near to Newport Deep and around Avonmouth. The highest concentration contour of 250mg/l occurs at the banks of the estuary, where the high velocity patterns are still visible. This is thought to be due to settling or entrainment in the shallower waters at low tide.

HW+9.30hrs. : The suspended sediment concentration front is clearly visible and well defined at this phase. A high velocity flow occurs (Figure 5.5.23) from the outer Bristol Channel towards the Severn Estuary, with high concentrations (>1000mg/l) areas near to Cardiff, along Bristol Deep and around Bridgwater Bay (Figure 5.5.24).

This phase of the tidal cycle clearly shows when sediment is entrained from the bed and reaches the water surface.

HW+10.85hrs. : At this phase the maximum flood tide velocities occur (i.e. 2.5m/s) as shown in Figure 5.5.25. The velocity front has a maximum drag to the west of the Cardiff zone. The suspended solids front is well defined and shows that entrainment has increased and that the area of high concentration are wider in between Bristol Deep and Bridgwater Bay. There is no clear evidence of advection but this phase coincides with the increase in the surface concentration.

HW+12.4hrs. : At this phase, where slack water occurs, a more or less uniform velocity distribution (Figure 5.5.27) is seen together with widespread evidence of regional settlement. The high concentration contour (i.e. 1000mg/l) has disappeared, with settling continuing to occur before the high water stage is reached. This process is exaggerated by the low velocities at the seaward side of the estuary.

5.5.3. Residual Velocities and Erosion

Tidal simulations for residual velocities and erosion have been undertaken for both spring and neap tides. The residual sediment concentration or net erosion or residual circulation is one of the important characteristic of tidal flows (Fischer, 1979), for establishing the long term estuarine behaviour. This characteristic of most tidal flows, is that superimposed on the back-and-forth flow is a net, steady circulation, often called the 'residual circulation'. The residual circulation is generally said to be velocity field obtained by averaging the velocity at each point in the estuary over the tidal cycle. One of the causes of the residual circulation is the earth's rotation; another cause is the interaction of the tidal flow with the irregular bathymetry found in most estuaries. In this study, the residual values after 5 and 10 tidal cycle were evaluated for both neap and spring tides.

Figure 5.5.13 shows the residual velocities after 5 tidal cycle, highlighting the localised high velocity sediment volume movement. Figure 5.5.14 shows that the outer estuary is more or less uniformly eroded for values between 0 and 50 kg/m^2.
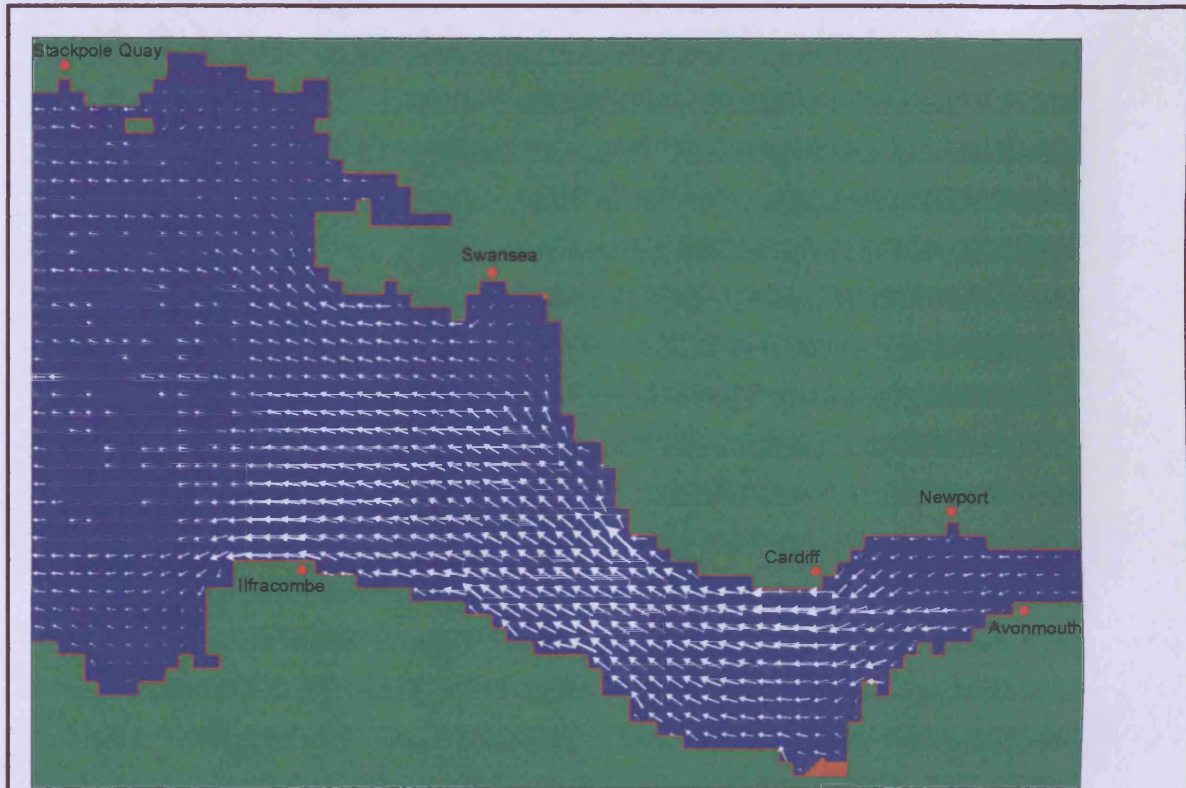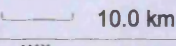
Figure 5.5.1 : Velocities and wet and dry cells
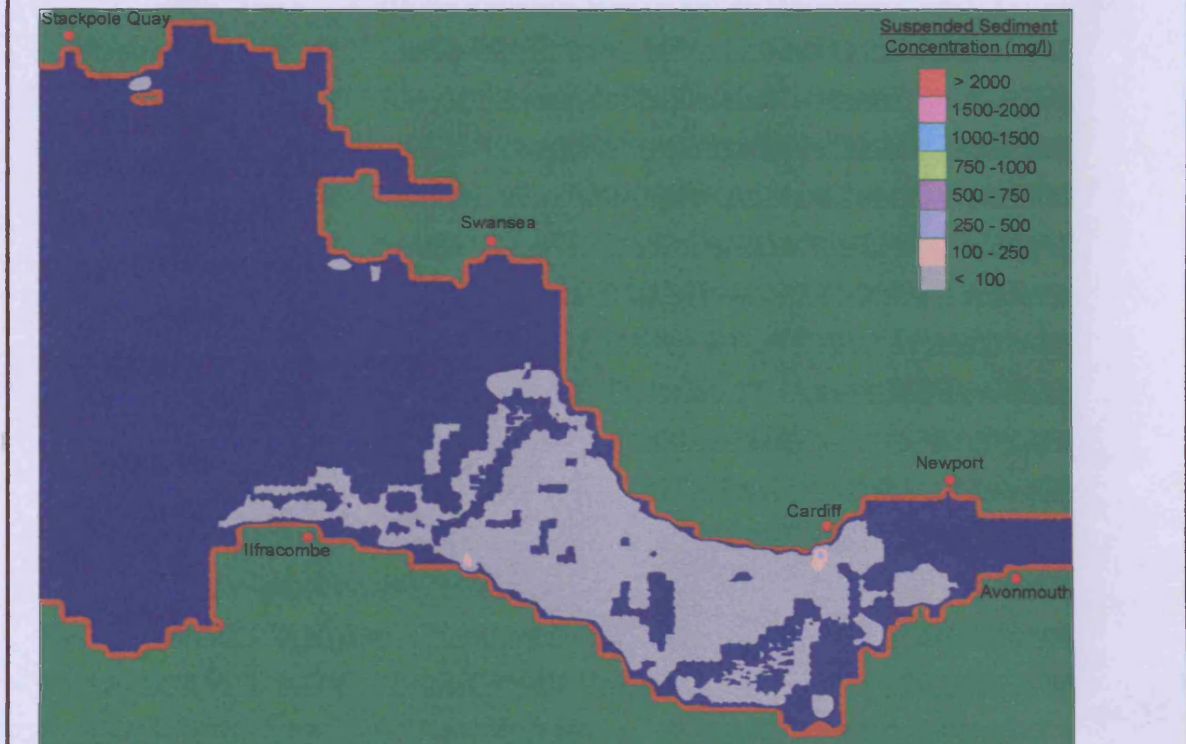
Figure 5.5.2 : Suspended sediment concentrations

				Grid size	Scale	Tidal data	Time of presentation
	Wet Cell	———	10.0 km				
	Dry Cell	MAX V = 1.30 m/s		600m x 600m	1 : 1,000,000	Mean Neap Tide	HW + 3.10 hrs.
	Land	—→ 2.00 m/s					

Figure 5.5.3 : Velocities and wet and dry cells

Suspended Sediment
Concentration (mg/l)

	> 2000
	1500-2000
	1000-1500
	750 -1000
	500 - 750
	250 - 500
	100 - 250
	< 100
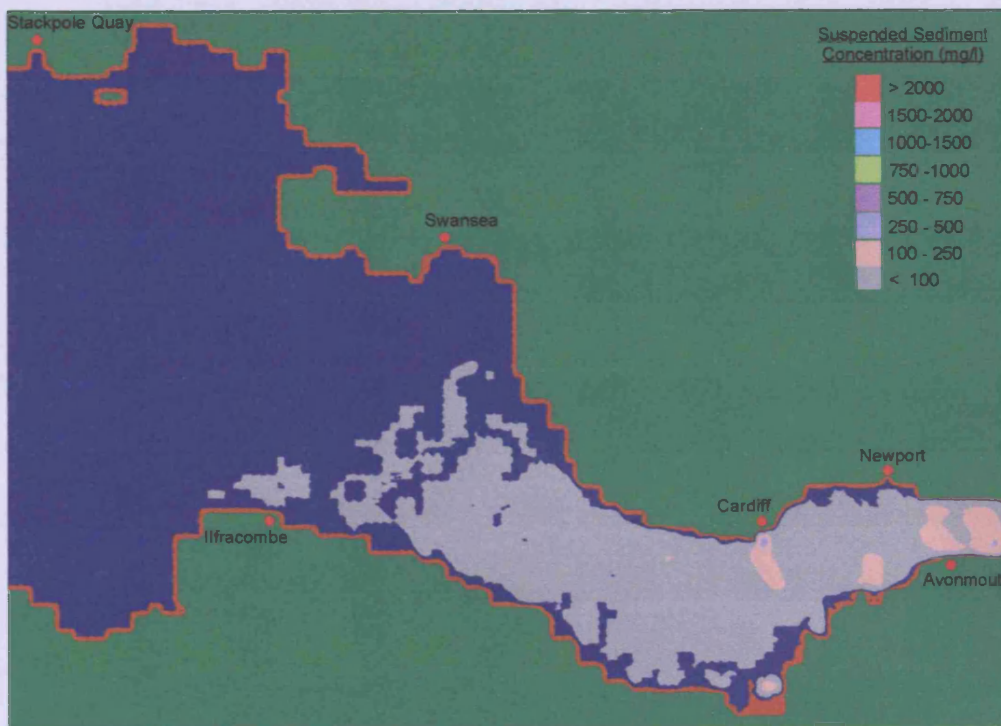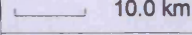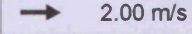
Figure 5.5.4 : Suspended sediment concentrations

	Wet Cell	⌐_____⌐	10.0 km	Grid size	Scale	Tidal data	Time of presentation
	Dry Cell	V^{MAX} = 1.33 m/s					
	Land	⟶	2.00 m/s	600m x 600m	1 : 1,000,000	Mean Neap Tide	HW + 4.65 hrs.

Figure 5.5.5 :   Velocities and wet and dry cells

Figure 5.5.6 : Suspended sediment concentrations

			Grid size	Scale	Tidal data	Time of presentation
■	Wet Cell	⊢————⊣ 10.0 km				
■	Dry Cell	V MAX = 1.41 m/s				
■	Land	→ 2.00 m/s	600m x 600m	1 : 1,000,000	Mean Neap Tide	HW + 6.20 hrs.

Figure 5.5.7 : Velocities and wet and dry cells
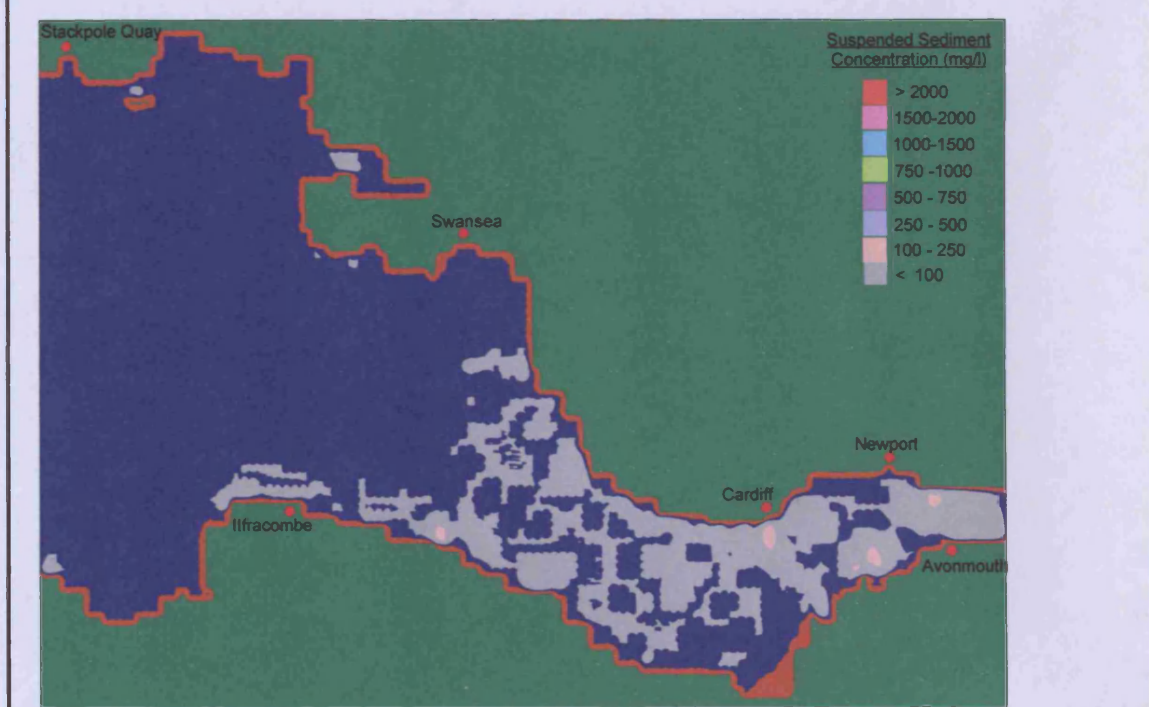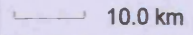
Figure 5.5.8 : Suspended sediment concentrations

				Grid size	Scale	Tidal data	Time of presentation
	Wet Cell	⊢——⊣	10.0 km				
	Dry Cell	V MAX	= 1.10 m/s	**600m x 600m**	**1 : 1,000,000**	**Mean Neap Tide**	**HW + 9.30 hrs.**
	Land	——→	2.00 m/s				

Figure 5.5.9 : Velocities and wet and dry cells
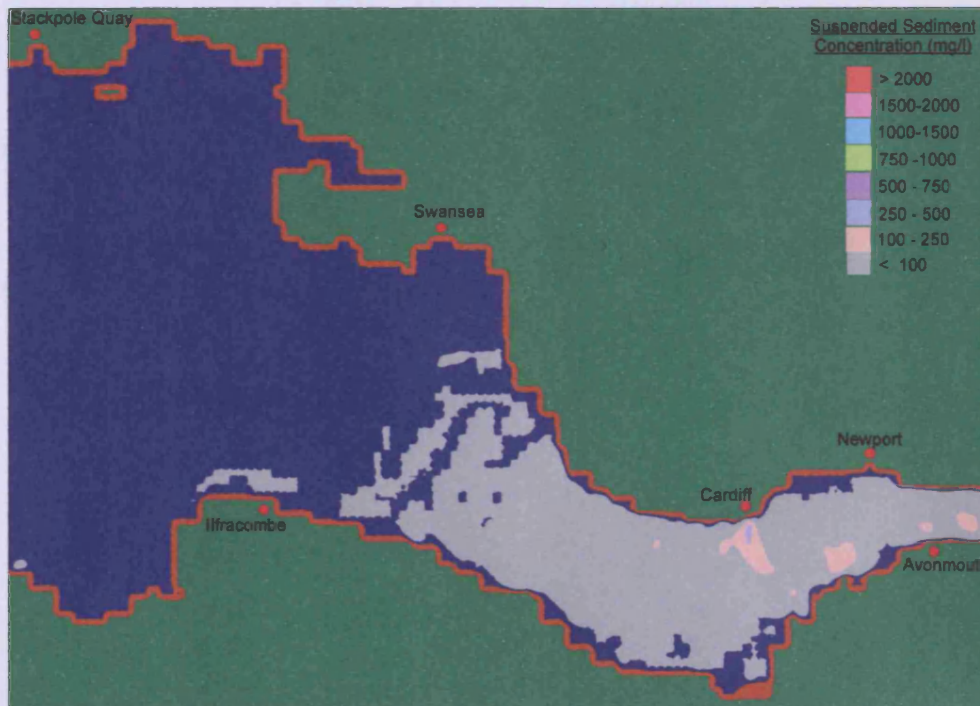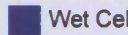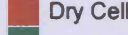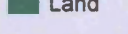
Figure 5.5.10 : Suspended sediment concentrations

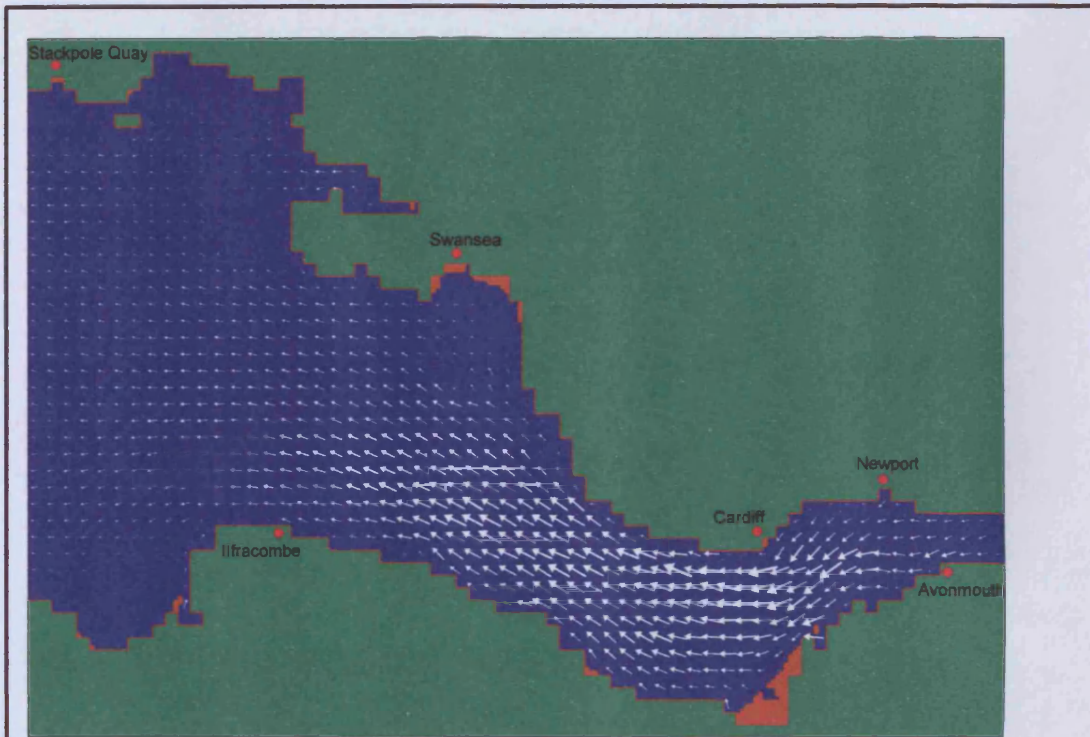|	Wet Cell	⊢——⊣ 10.0 km	Grid size	Scale	Tidal data	Time of presentation
	Dry Cell	V^MAX = 1.39 m/s				
	Land	→ 2.00 m/s	600m x 600m	1 : 1,000,000	Mean Neap Tide	HW + 10.85 hrs.

Figure 5.5.11 : Velocities and wet and dry cells

Suspended Sediment
Concentration (mg/l)

	> 2000
	1500-2000
	1000-1500
	750 -1000
	500 - 750
	250 - 500
	100 - 250
	< 100
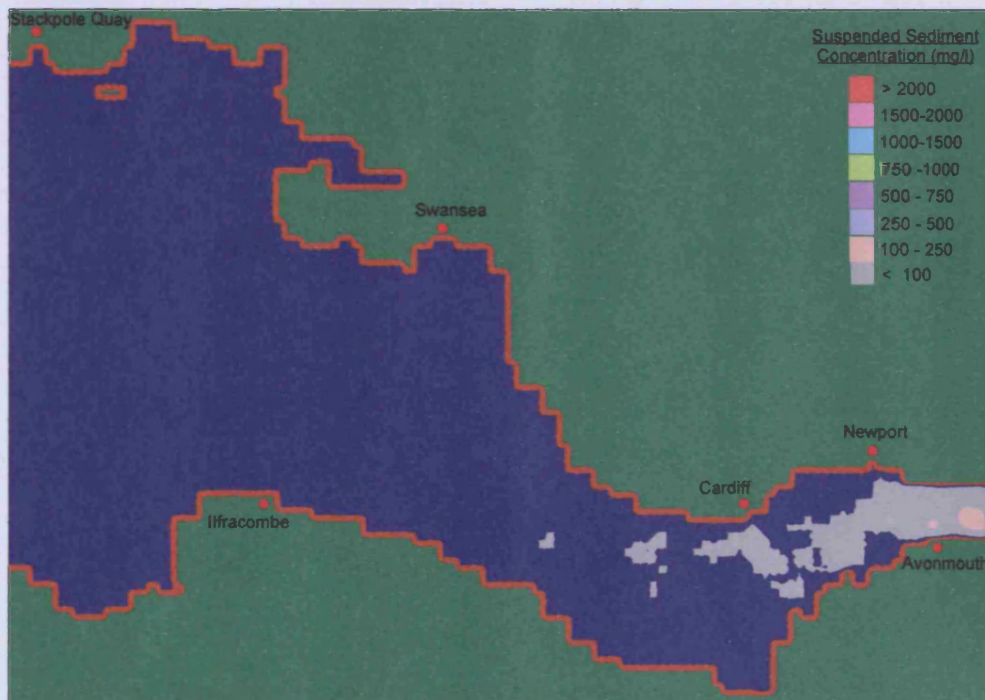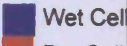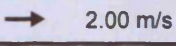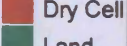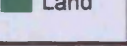
Figure 5.5.12 : Suspended sediment concentrations

Wet Cell	10.0 km	**Grid size**	**Scale**	**Tidal data**	**Time of presentation**	
Dry Cell	V^MAX = 1.17 m/s					
Land	→ 2.00 m/s	**600m x 600m**	**1 : 1,000,000**	**Mean Neap Tide**	**HW + 12.40 hrs.**	

Figure 5.5.13 : Residual velocities and wet and dry cells

Residual Erosion
in kg/m²

	< (-200)
	(-200) - (-100)
	(-100) - (-50)
	(-50) - 0
	0 - 50
	50 - 100
	100 - 200
	> 200
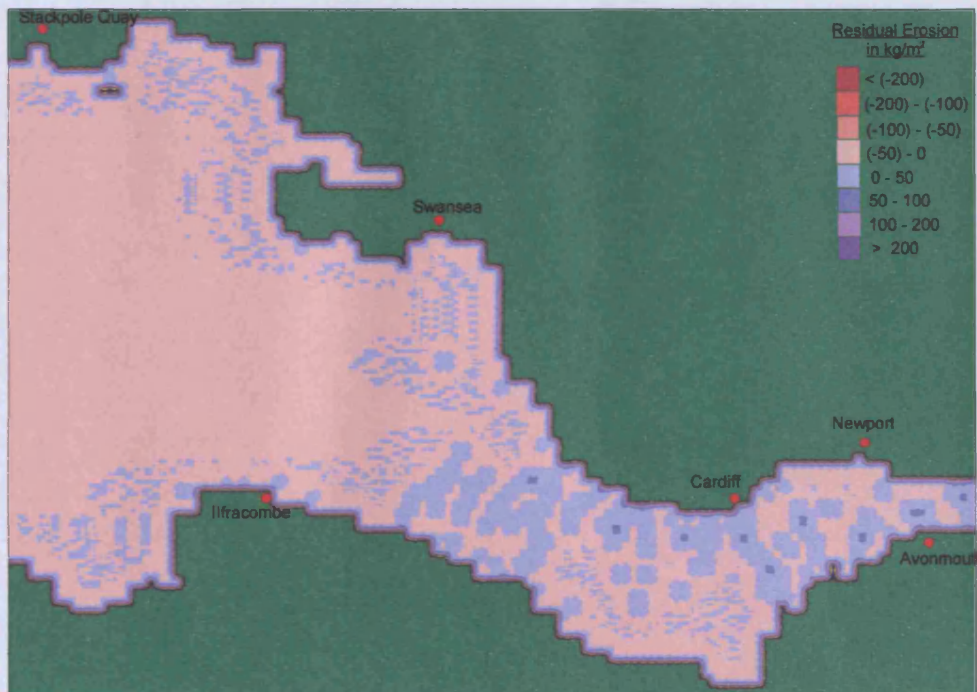
Figure 5.5.14 : Residual erosion after 5 tidal cycles

Dry Eroded	10.0 km	Grid Size	Scale	Tidal Data	Time of Presentation
Dry Accreted	MAX				
Dry Cell	V = 0.25 m/s	600m X 600m	1 : 1,000,000	Mean Neap Tide	HW + 62.00 hrs.
Land	→ 2.00 m/s				

Figure 5.5.15 : Residual velocities and wet and dry cells
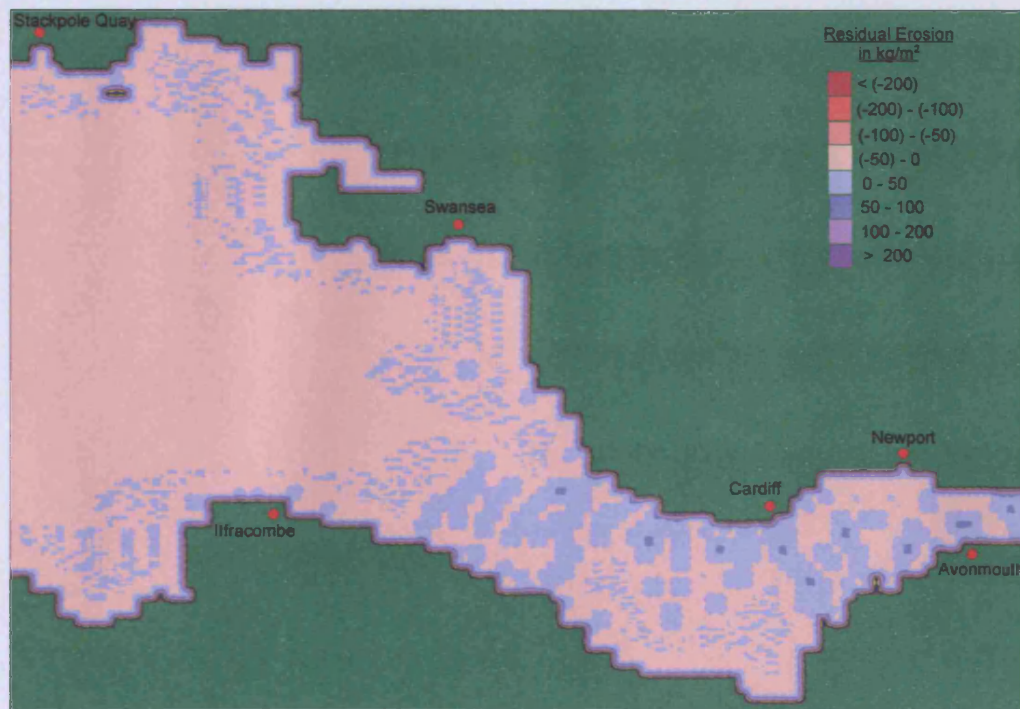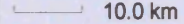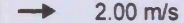
Figure 5.5.16 : Residual erosion after 10 tidal cycles

				Grid Size	Scale	Tidal Data	Time of Presentation
	Dry Eroded	⟍⟍ 10.0 km					
	Dry Accreted	V MAX = 0.40 m/s		600m X 600m	1 : 1,000,000	Mean Neap Tide	HW + 124.00 h.
	Dry Cell						
	Land	→ 2.00 m/s					

Figure 5.5.17 : Velocities and wet and dry cells
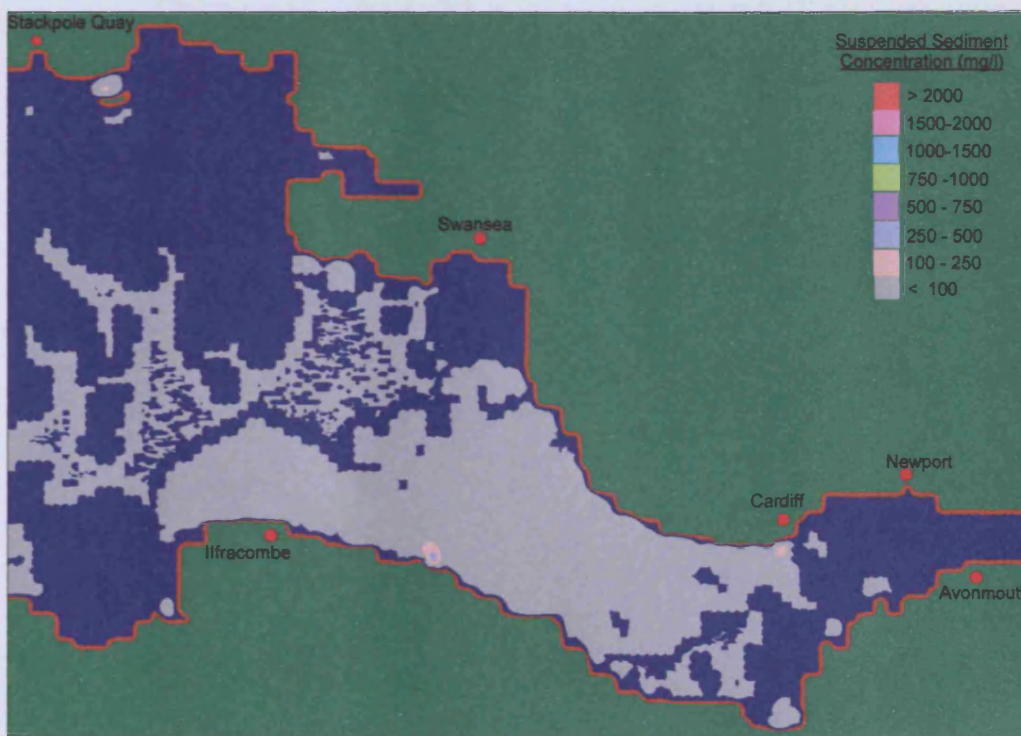
Figure 5.5.18 : Suspended sediment concentrations

			Grid Size	Scale	Tidal Data	Time of Presentation
Wet Cell	———	10.0 km				
Dry Cell	V^MAX = 1.38 m/s		600m X 600m	1 : 1,000,000	Mean Spring Tide	HW + 3.10 hrs.
Land	→ 2.00 m/s					

Suspended Sediment Concentration (mg/l)

> 2000
1500-2000
1000-1500
750 -1000
500 - 750
250 - 500
100 - 250
< 100

Figure 5.5.19 : Velocities and wet and dry cells

Suspended Sediment
Concentration (mg/l)

	> 2000
	1500-2000
	1000-1500
	750 -1000
	500 - 750
	250 - 500
	100 - 250
	< 100
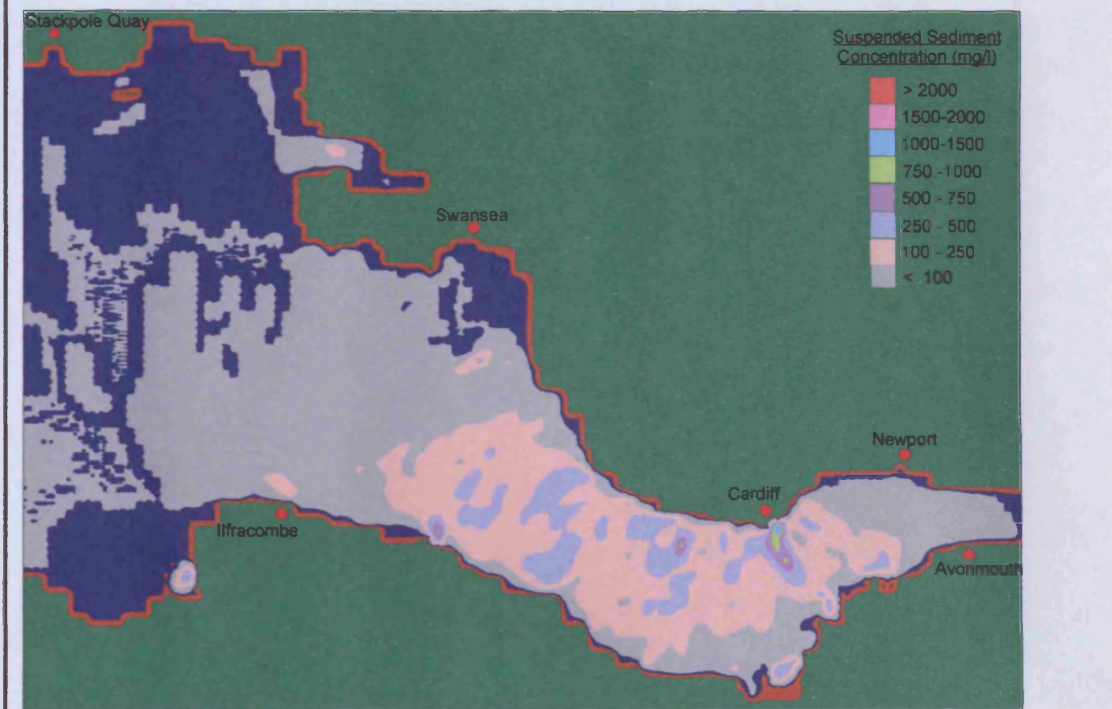
Figure 5.5.20 : Suspended sediment concentrations

Wet Cell	⊢——— 10.0 km	Grid Size	Scale	Tidal Data	Time of Presentation
Dry Cell	V^MAX = 2.05 m/s				
Land	⟶ 2.00 m/s	600m X 600m	1 : 1,000,000	Mean Spring Tide	HW + 4.65 hrs.

Figure 5.5.21 : Velocities and wet and dry cells
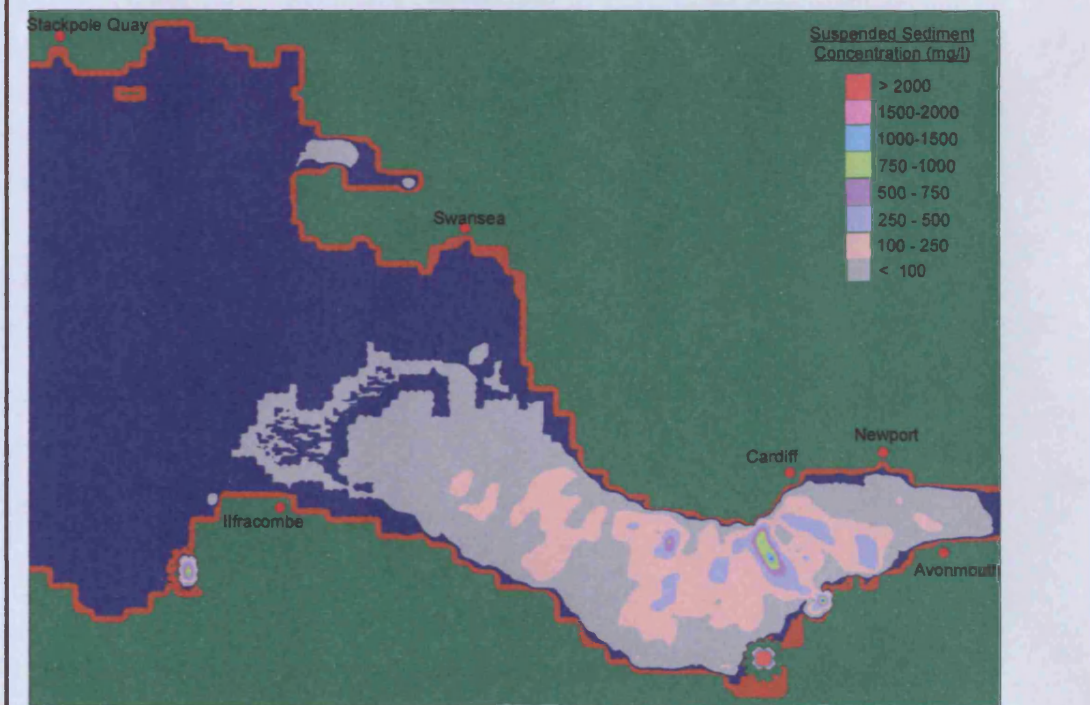
Figure 5.5.22 : Suspended sediment concentrations

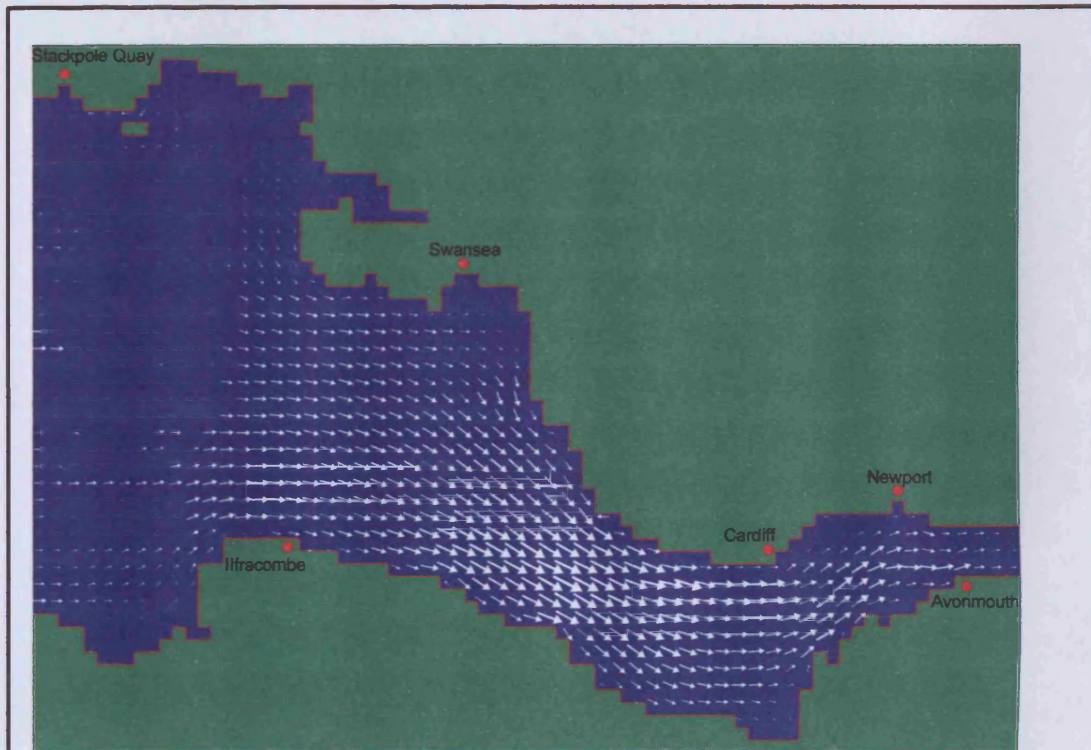|			Grid Size	Scale	Tidal Data	Time of Presentation
Wet Cell	⊢——⊣ 10.0 km					
Dry Cell	MAX V = 1.91 m/s					
Land	——→ 2.00 m/s		600m X 600m	1 : 1,000,000	Mean Spring Tide	HW + 6.20 hrs.

Figure 5.5.23 : Velocities and wet and dry cells

Suspended Sediment
Concentration (mg/l)

	> 2000
	1500-2000
	1000-1500
	750 -1000
	500 - 750
	250 - 500
	100 - 250
	< 100
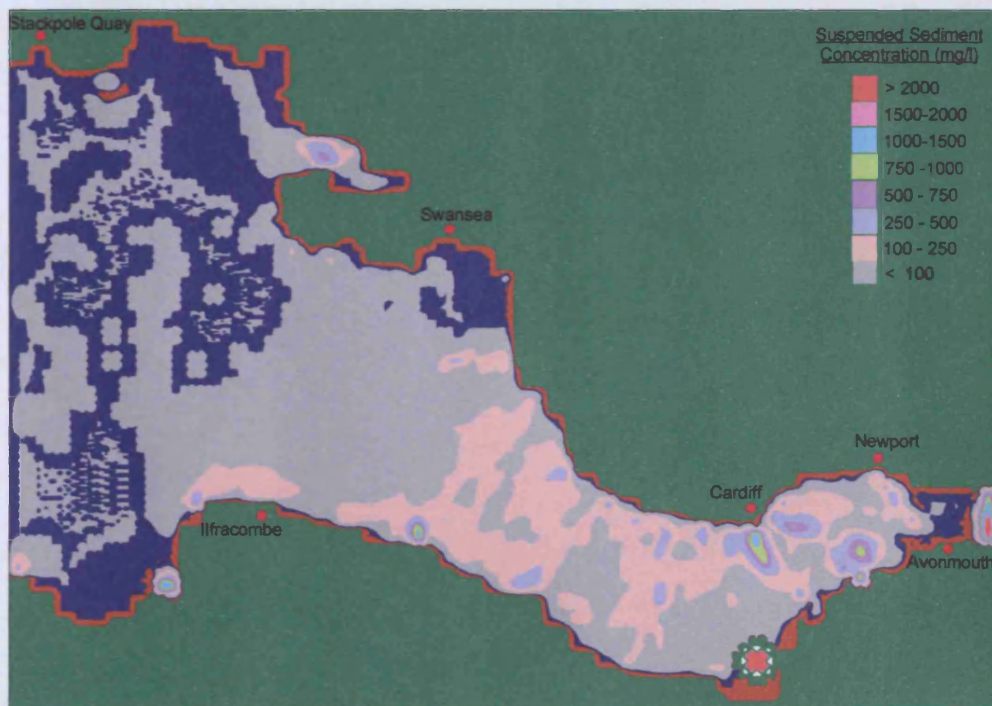
Figure 5.5.24 : Suspended sediment concentrations

	Wet Cell	⊢──── 10.0 km	Grid Size	Scale	Tidal Data	Time of Presentation
	Dry Cell	V MAX = 1.82 m/s				
	Land	⟶ 2.00 m/s	600m X 600m	1 : 1,000,000	Mean Spring Tide	HW + 9.30 hrs.

Figure 5.5.25 : Velocities and wet and dry cells
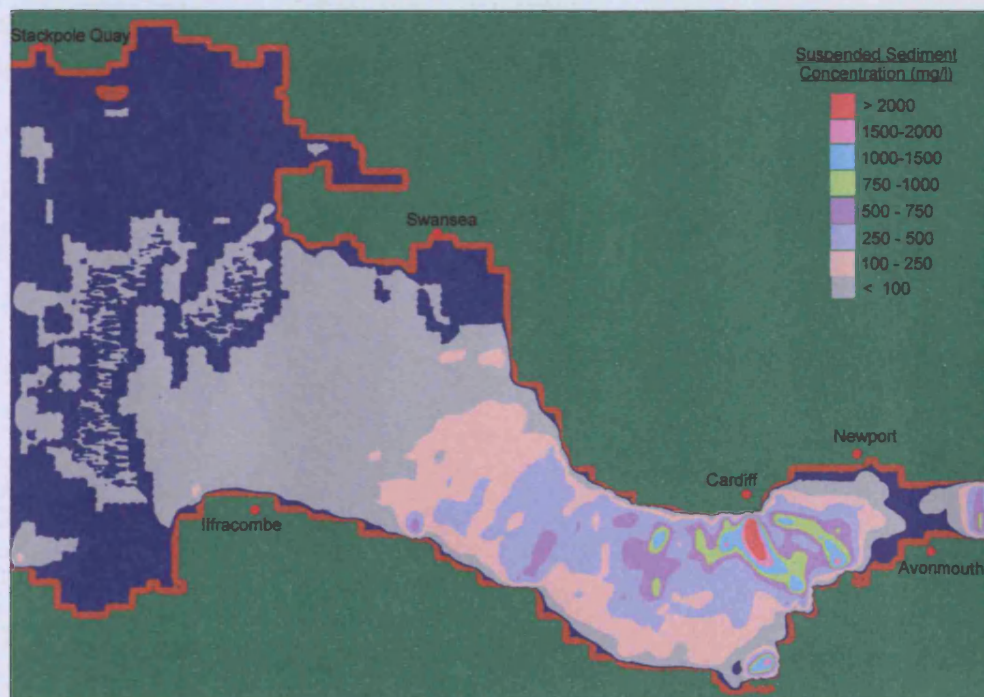
Figure 5.5.26 : Suspended sediment concentrations

		10.0 km				
■ Wet Cell			Grid Size	Scale	Tidal Data	Time of Presentation
■ Dry Cell	V MAX = 2.55 m/s		600m X 600m	1 : 1,000,000	Mean Spring Tide	HW + 10.85 hrs.
■ Land	→ 2.00 m/s					

Figure 5.5.27 : Velocities and wet and dry cells
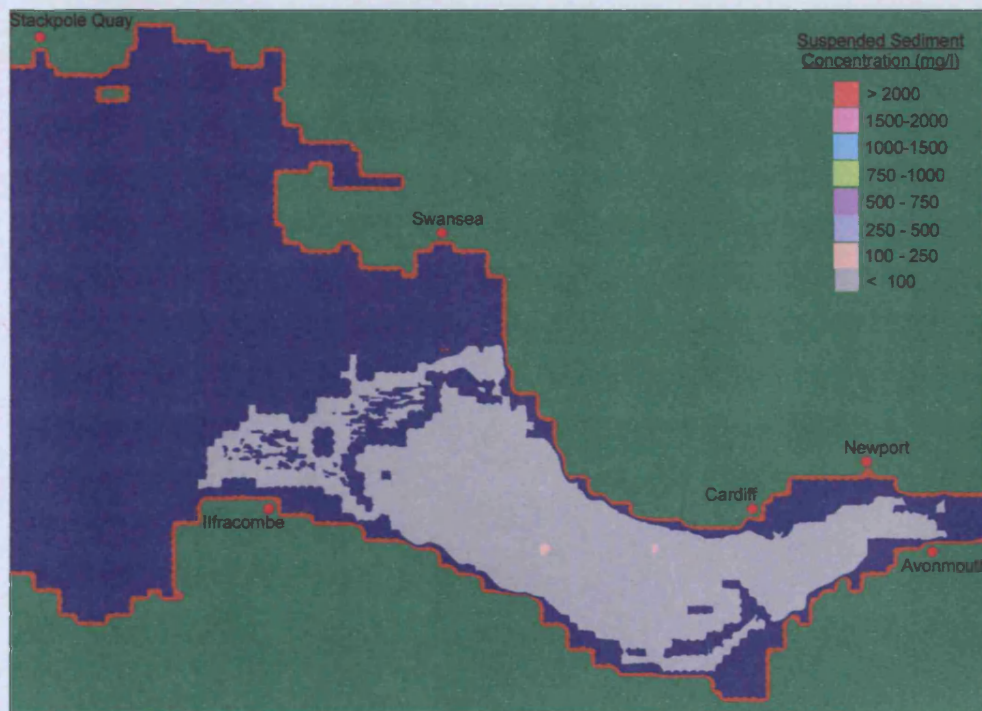
Figure 5.5.28 : Suspended sediment concentrations

			Grid Size	Scale	Tidal Data	Time of Presentation
■	Wet Cell	10.0 km				
■	Dry Cell	MAX V = 1.53 m/s				
■	Land	→ 2.00 m/s	600m X 600m	1 : 1,000,000	Mean Spring Tide	HW + 12.40 hrs.

Figure 5.5.29 : Residual velocities and wet and dry cells

Residual Erosion
in kg/m²

< (-200)
(-200) - (-100)
(-100) - (-50)
(-50) - 0
0 - 50
50 - 100
100 - 200
> 200
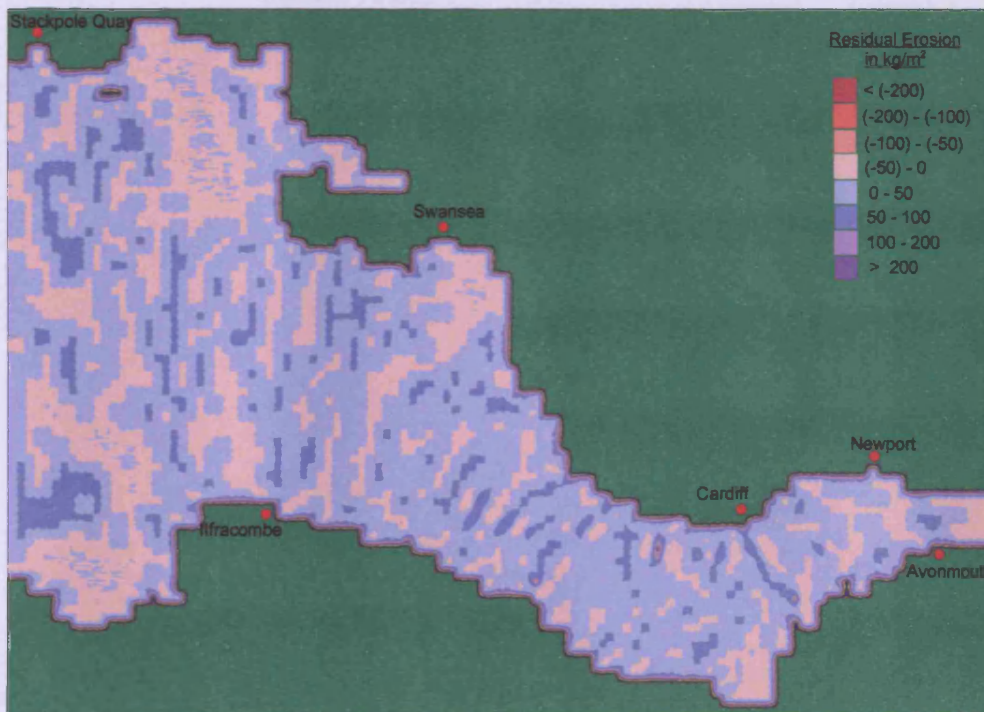
Figure 5.5.30 : Residual erosion after 5 tidal cycles

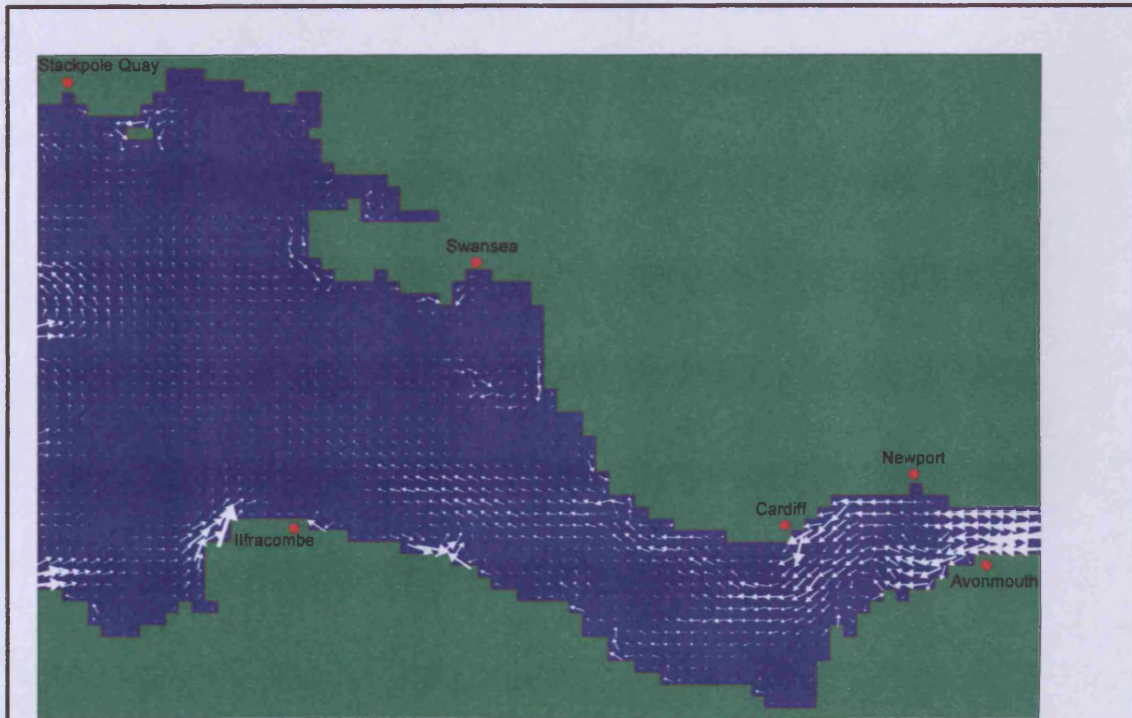|			10.0 km				
	Dry Eroded			Grid Size	Scale	Tidal Data	Time of Presentation
	Dry Accreted	MAX					
	Dry Cell	V = 0.49 m/s		600m X 600m	1 : 1,000,000	Mean Spring Tide	HW + 62.00 hrs.
	Land	→ 2.00 m/s					

Figure 5.5.31 : Residual velocities and wet and dry cells
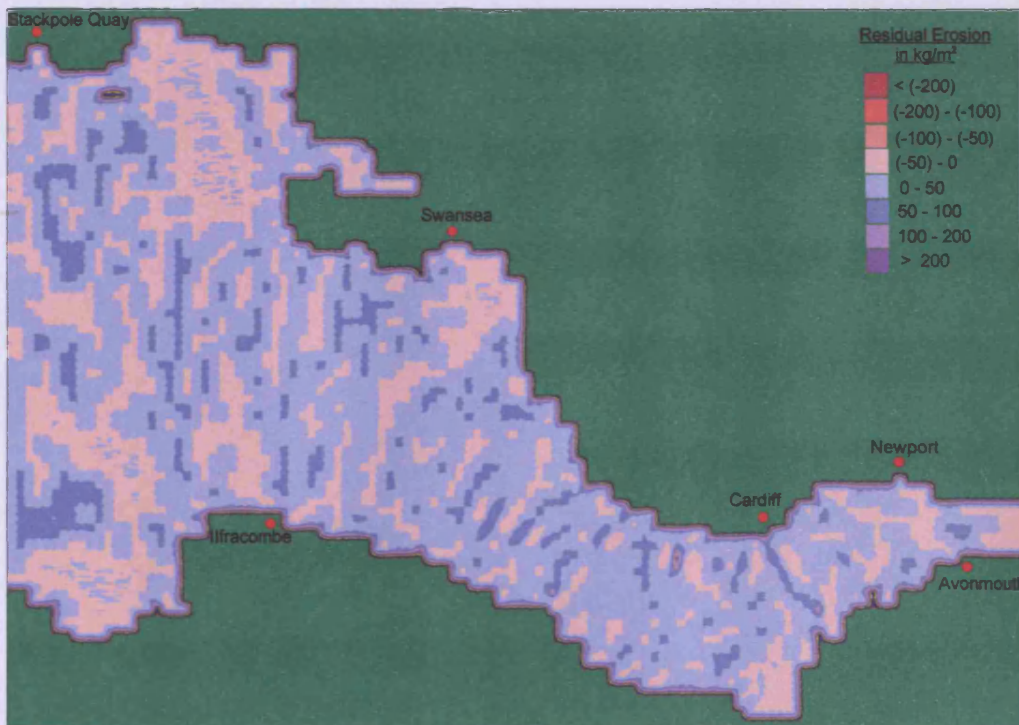
Figure 5.5.32 : Residual erosion after 10 tidal cycles

	Dry Eroded		10.0 km	Grid Size	Scale	Tidal Data	Time of Presentation
	Dry Accreted	MAX V = 0.47 m/s					
	Dry Cell	→ 2.00 m/s	600m X 600m	1 : 1,000,000	Mean Spring Tide	HW + 124.00 hrs.
	Land						

The Severn Estuary shows the dynamic behaviour in terms of both erosion and deposition. The residual velocity after 10 tidal cycle increases and especially by the Avonmouth area. However, the sediment distribution patterns do not change much after 5 tidal cycle (Figure 5.5.16). Similarly for the spring tidal period the residual velocities showed localised high values (Figures 5.5.29 and 5.5.31), which effect the sediment behaviour in the nearshore area. The residual erosion and deposition shows (Figures 5.5.30 and 5.5.32) a fairly uniform pattern of concentration. The whole estuary is in a state of instability as the regions of erosion and deposition are throughout the channel.

5.6   Summary

The model has been set-up to investigate the physical processes occurring in the Bristol Channel, which will enable the visualisation and prediction of long term sediment transport patterns and erosional behaviour. Results from simulation of the model with the field data have generally shown good agreement. The reproduction of water levels is shown to be very consistent with the specified calibration and verification targets, with questions remaining over the reliability of the tidal diamonds observed data. The application of the model to a data set for the year 2001 proved to be particularly reliable.

The suspended sediment concentrations for the Bristol Channel has been elaborately presented through a cycle for neap and spring tides. The pattern of concentration shows that this is a regular estuary with a periodic change in the sediment concentration with tidal wave changes. The spring tidal range is very high in the Bristol Channel, with a large volume of water being exchanged twice daily, enabling extensive exchange of sediments. The report from RCL, 1986 suggested that they attained good comaprable results with field data though for this study that field data was not accessible. So the indirect comaprison was done between model prediction of this study with RCL, 1986. The suspended concentration profiles and patterns are also compared with the report from RCL (1986), which indicated that the sediment concentration values and patterns of movement were comparable for both studies.

CHAPTER 6

WAVE MODEL ANALYSIS

6.1 Introduction

Wave induced transport processes are related to the velocities generated by high and low frequency wave phenomenon. Wave induced nearshore circulations generally arise from complex processes driven by gravity water waves (Yoo and O'connor, 1986). When waves approach shoreline or man-made coastal structures, then processes such as: shoaling, refraction, diffraction, dissipation and wave-current interactions can all occur at these locations. At relative water depth h/L_0 becomes smaller than 0.1, the wave height becomes greater than H_0 and it continues to increase due to shoaling until the waves become unstable and break. When waves propagate closer to the shoreline, or diffract behind a breakwater, then nearshore currents are produced through the excess momentum flux of the waves, as the radiation stresses (Longuet-Higgins and Stewart, 1964). The nearshore currents are then modified by bottom friction and mixing processes, particularly in the surf zone (Longuet-Higgins, 1972). An additional effect produced by the presence of the waves can lead to a change in the mean water level, called set-up and set-down.

There have been many developments in recent years in the study of nearshore circulation induced by waves, with the establishment of various wave models

(Dalrymple, 1988, Li, 1994). The availability of different wave models highlight that the particular need of any study should be identified at the beginning of the study to ensure the wave model used can serve the best purpose. For this study the wave model is to be used to calculate the wave height and direction due to wave breaking. The wave models become more realistic by including the bottom friction and different mixing processes (e.g. advection, turbulence, diffusion and dissipation). In this study a wave model has been integrated within the main DIVAST model and then studied for different beach patterns. The angle of wave incidence is another important parameter, which affects the nearshore velocity pattern and the resulting longshore sediment transport (Komar and Inman, 1970; Longuet-Higgins, 1970), that are to be studied for different test cases in this chapter.

It is first important to understand the physical processes that occur continuously in the nearshore zone. The fluid velocity is subjected to two non-linear boundary conditions at the initially unknown free surface, including: a pressure condition and a kinemetic flow condition. The waves are generated normally in deep water in an ocean and have gone through different physical processes of change by the time that they come near to the coastline. At the end of the propagation path, waves arrive at a shallow water region (or beach), which is referred to the surf zone, and is where the waves break and dissipate their energy. A theoretical and experimental analysis of the rate of energy dissipation as a function of bottom slope and the convergence of wave orthogonals were presented by Divoky et al., 1970. The factors which affect these changes (refraction, diffraction and shoaling of waves) in waves propagating from deep water to the shoreline are mainly the bed topography, tidal currents and wind generated currents.

Waves have two unique characteristics with regard to sediment movement and which differs from the characteristics of unidirectional flow (Chien and Wan, 1998). First, waves cause periodic oscillations of velocity and pressure. These forces and velocities act on sediment particles on the bed and are near their maximum value for
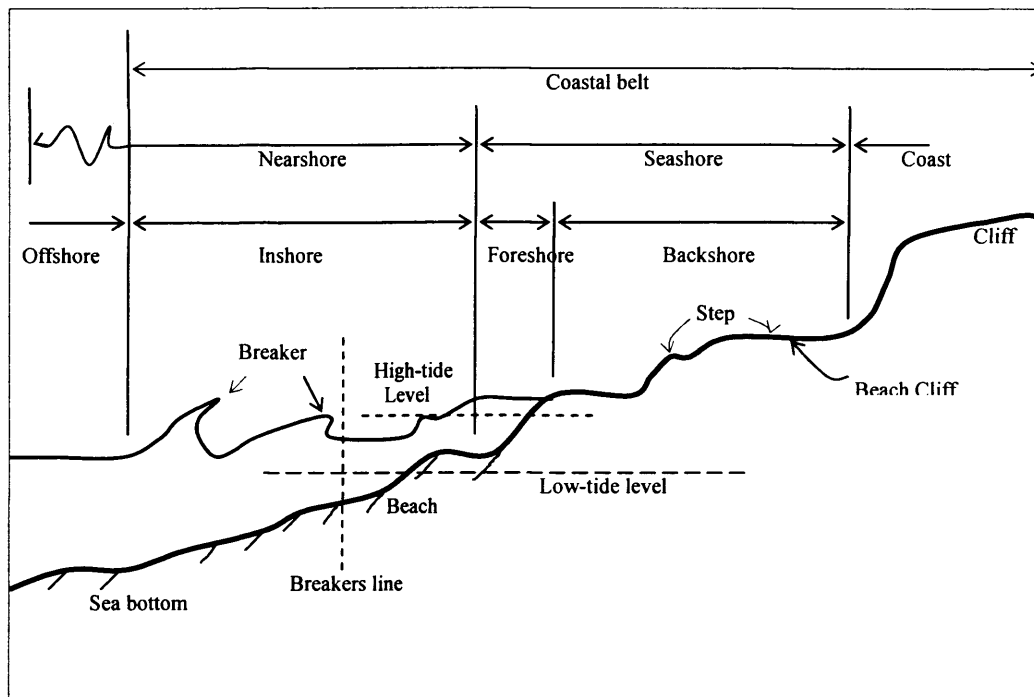
Figure 6.1.1: Typical profile for waves near the coast (from Chien and Wan, 1998)

only short periods. Their values at all other time are much smaller and so large accelerations occur. Consequently, the inertia of sediment particles plays a more important role with waves. Second, the shear stress on the bed affects the entire velocity field in open channel flows, whereas wave motion is primarily an exchange mechanism between potential energy and kinetic energy.

6.2 The Wave Model

The primary objective of any numerical model based research or investigation is to ensure that the model has the ability to predict fundamental physical effects occurring in the system. The establishment of a numerical model for nearshore waves should be able to analyse all of the shallow water processes affecting waves as they travel from offshore to where they break in the surf zone. These processes include: (i) depth refraction, (ii) current refraction, (iii) wave breaking in shallow water and (iv) bottom friction and shoaling.

Waves are generally the dominating factor affecting beach (along the coastline) and coastal processes and therefore need to be analysed closely. At the nearshore area waves are more dominating hydrodynamic factor than the tide. Tides are generated by astronomical forces affecting the oceanic and estuarine flows. At the nearshore zone, the effects of tide are considered indirectly, the nearshore wave height is calculated from offshore wave height where tidal effect occurs. There are many physical parameters interacting in the wave-current environment in the nearshore zone such as: wave breaking, bottom friction etc each of which may influence the longshore and cross-shore sediment movement. Wave breaking occurs as the wave steepness becomes sharp and when the depth becomes shallower. The forward wave orbital velocity at the crest becomes large and ultimately unstable (Fredsøoe and Deigaard, 1995). Wave breaking is associated with a large loss of wave energy and due to this strong energy dissipation the wave height decreases in the surf zone. One of the main aims of wave analysis is therefore to improve our understanding of the wave regime nearshore and its effect on longshore sediment transport.

Linear wave theory can be applied to both shallow and deep water waves. Shallow water waves deviate more from the basic assumptions of linear wave theory than deep water waves (Martin et al., 1996). Since in the surf zone waves undergo strong turbulent motion, then the linear wave theory cannot predict the complexity of wave motion for breaking and shoaling (Booij, 1983). A breaking criterion (Weggel, 1972) is applied to predict wave heights within shallow waters to overcome the limitations of adopted wave theories in such regions (Yoo and O'Connor, 1986).

The mild slope equation is the vertically integrated refraction-defraction (Berkhoff, 1972) equation used to predict wave propagation in a region with an uneven bed topography. As the name indicates it is based on the assumptions of a mild bottom slope. The parabolic approximation provides a feasible way to obtain numerical solutions to the mild-slope wave equation and this equation is very useful for calculating wave characters at places where only transmitted wave can considered, with the simple approximation that the reflected waves can be neglected (Booij, 1981). The wave model developed in this current study is based on parabolic wave theory for the mild slope equations. The model solves the governing equation of

wave propagation using the finite difference method. The formulation of the model and the corresponding equations are given in Chapters 3 and 4, with the model being based on Booij's (1981) parabolic approximation of the mild slope equation.

The original parabolic equation (i.e. equation 3.4.42) does not include non-linear effects such as bed friction and wave breaking. These effects have been included in present wave-current model using the following methods. An empirical formula has been used to calculate the wave height change due to seabed friction at each grid point. The values of the wave height (equation 3.4.85), wave length and wave direction (equation 3.4.76) are determined at regular grid positions. Then by equation 3.4.66 the final wave height can be obtained and these predicted values are then readily utilised to estimate the radiation stresses. The spatial gradients of the radiation stresses are regarded as the primary agents in the generation of wave induced currents (Noda, 1972).

To test for the accuracy, consistency and efficiency of the numerical model it was first tested against approved classical numerical and laboratory model test cases and also against field data. The objective of this chapter is to verify the newly developed numerical model by applying the model to published test cases which can also enable a better understanding of the physical processes involved.

6.3   Test Case I : Model Application to Sinusoidal Beach

The first test case used to analyse the numerical wave model was the transformation of waves on a sinusoidal beach. The beach included one full sinusoidal curve for different sizes to accommodate the incident waves (Figure 6.3.1). The numerical domain consisted of 50 rows and 50 columns, with grid size being 20m (Figure 6.3.3) in each direction. The waves were either in the normal direction or inclined to the shoreline. The response of a sinusoidal beach during wave attack was the main focus. The change in different hydrodynamic parameters and their corresponding changes in the velocity and wave fields observed in this test case provided the

necessary information to construct the beach for the experimental work to be described in Chapter 7.

The main challenge in aiming to acquire accurate results was to select appropriate boundary conditions. For this case (test case 1) the offshore boundary condition taken as an open water elevation boundary (Figure 6.3.2) from where the waves propagate from deep water. The model was set-up in such a manner that the north-direction coincides with the offshore direction (Figure 6.3.2). In that way, the left side along north-direction will be treated as western boundary, and the right side along north-direction will be treated as eastern boundary. Both of the western and eastern boundaries have been treated here as the flow or velocity boundaries, see equations 4.7.3 to 4.7.5 (Chapter 4). That means that their numerical domain is part of a continuous long beach which is uninterrupted.

The nearshore region was affected by wave action, with wave breaking and maximum energy dissipation occurring here. The source of the wave did not have any significant effect at the breaking zone because the characteristics of shallow water waves (H, T) are different from deep water waves (H_0, T_0). The bed slope and bottom friction were the dominating factors in the wave breaking area. The oscillatory wave caused the sediments to move either perpendicular or parallel to the beach. The normal incident waves produce on-offshore velocity and oblique incident waves produce both on-offshore and longshore velocity components. The movement of sediments can be predicted using the velocity field.

Test case 1 was run for wave action only, the interaction of waves and currents was not considered as a constant water level was assumed in this case. The model domain was kept in such a way that the positive x-axis and the North direction coincided (Figure 6.3.2), which simplified the solution. The initial wave height, wave period and incident wave angle were taken as 0.5 m, 4.0s and 0^0 (wave incidence normal to the shoreline) respectively. These values were taken based on the assumption that this chosen numerical domain represents a case in between field condition and experimental condition. The breaking index, γ_b, was taken as 0.78 from McCowan's formula (Weggel, 1972). Another important factor was to specify

the value of the bed friction coefficient, which in this case was taken as 0.01 (Borthwick, et al., 1997). The value of 0.01 represented the roughness of a nearly smooth bed.

The bathymetric information required was necessary, as is generally the case for wave models. The information required was twice in this case than that necessary for the DIVAST model (but for coarse hydrodynamic grid, the grid size for wave sub-model can be taken as 4-8 times of the hydrodynamic grid). The bathymetric data being given as the depth below the datum for each grid square. Tidal motion was not considered in this part, since it was decided that for the nearshore zone only wave motion would be tested first. Wind effects were also not considered in this case because the numerical domain in this study were not wide enough to develop a wind speed and wind fetch which can affect the wave spectral energy to grow. However, in the nearshore zone, then bottom topography and breaking wave energy are the two dominating factors to develop excess momentum flux resulting in radiation stresses which will cause nearshore sediment transport and beach erosion and accretion.

The bathymetry of the sinusoidal beach was given by:

$$h_i(x,y) = \frac{h_1 + (h_2 - h_1)}{(ny * dx - y_i) * (y_c - y_i)}$$

(6.3.1)

where

$$y_i = 0.0 \qquad\qquad \text{for } x \le 200 \text{ and } x \ge 800$$

$$y_i = 0.5\left[1.0 - \cos\left(\frac{2\pi(x_i - X_I * dx)}{(X_L - X_I)dx}\right)\right] \qquad \text{for } 200 \le x \le 800$$

here h_i = depth below datum at any location in the domain; h_1 = initial value of bed slope; h_2 = final value of bed slope; X_I = initial value of sinusoidal curve; X_L = final value of sinusoidal curve; dx = grid spacing; i = point location in the domain.

Figure 6.3.3 shows the velocity profile of the above domain for a normal incident wave. The minimum depth below datum was set at 0.2m. The model was run for

0.57 hours, with the maximum velocity occurring at the tip of the beach. The short period waves approached the shore in a perpendicular orientation, but the waves were refracted slightly and rip currents were numerous but relatively small. A clear pattern of rip currents was visible, which concentrated the offshore current. The rip current passed the line of breakers, spread out in a fan shape manner and gradually lost its identity in the surf zone (Noda, 1974; Sonu, 1972). Based on the steepness of the beach the main circulation was expected to be seaward for normal incident wave. The velocity distribution changed when the angle of wave incidence changed. The short period waves approached the shore obliquely (with an inclined angle of 20^0), and a continuous longshore current formed as shown in Figure 6.3.4.

Figure 6.3.5 and Figure 6.3.6 show the sinusoidal beach for a different coastline. The bathymetry was similar to that given in equation (6.3.1) except that the boundary was changed to give:

$$y_i = 0.0 \qquad\qquad \text{for } x \leq 400 \text{ and } x \geq 600$$

$$y_i = 0.5\left[1.0 - \cos\left(\frac{2\pi(x_i - X_I * dx)}{(X_L - X_I)dx}\right)\right] \qquad \text{for } 400 \leq x \leq 600 \qquad\qquad (6.3.2)$$

The minimum depth below datum was set to 0.1m with the minimum value for wet and dry cells being set to 0.2m. The offshore water depth was taken as 10m. The size of the domain was 1000m x 1000m. These parameters were set to make the beach clearly visible. The inclined wave showed that the longshore current pattern followed the direction of the wave direction (Figure 6.3.5). When wave propagated normal to the shoreline (Figure 6.3.6) the maximum velocities occurred at the tip of the sinusoidal beach. It circulated in a clockwise direction in western part and anticlockwise in eastern part of the shoreline. The landward velocity near the bottom of the oscillatory waves was larger than the seaward velocity, thereby making the rip currents asymmetric. The waves came from outside the breaker zone and were advected in the direction of wave propagation, to create rip currents. This

circulation pattern was obtained for a sinusoidal curve with the effect of continuous sine curves being covered later in section 6.4.

Figures 6.3.7 to 6.3.10 describe the different physical conditions when waves approach a shoreline at an inclined angle for different shaped sinusoidal beaches. The waves are approaching at 20^0 normal to the beach. It can be seen that the dominating flow velocity follows the direction of the wave component, which runs parallel to the shoreline. The longshore sediment transport will be expected to follow the same direction as the flow velocity. The grid size was first taken as 40m x 40m, but it was found that it was too coarse to represent the velocity field (maximum velocity = 0.88m/s). Then the grid size was reduced to 20m x 20m and the minimum depth was kept at 0.2m. The minimum value for wetting and drying of a grid cell was also kept at 0.2m. For this reason after a simulation time of 0.57 hr the sinusoidal shoreline was under water and behaved as a shallow water region within a straight shoreline. The grid size was reduced to a half in Figure 6.3.8 (i.e. 10m x 10m). The variation in the flow circulation showed that while all other parameters remained constant decrease in the cell size resulted in an increase in the longshore current component. Also another test run was performed with grid size 5m x 5m producing maximum velocity as 0.99m/s, similar to Figure 6.3.8 while the computational time was longer. In terms of computational efficiency these results show that engineers need to make a compromise between cell size and accuracy.

The bathymetry of the test run represented in Figures 6.3.9 and 6.3.10 was the same as for previous case (i.e. Figure 6.3.7). The parameters included the minimum depth below datum being kept at 0.1m and the value for the wetting and drying process was kept at 0.2m in Figure 6.3.9 and increased to 0.4m in Figure 6.3.10. The corresponding changes in shoreline flow field also affected the velocity pattern. The magnitude of the velocity was found to increase from the offshore zone to the inshore area. The maximum velocities were found to occur in the breaking area. The circulation at the tip of the sinusoidal part showed that there was a clockwise circulation, which made this part of the beach a dynamically changing region. This
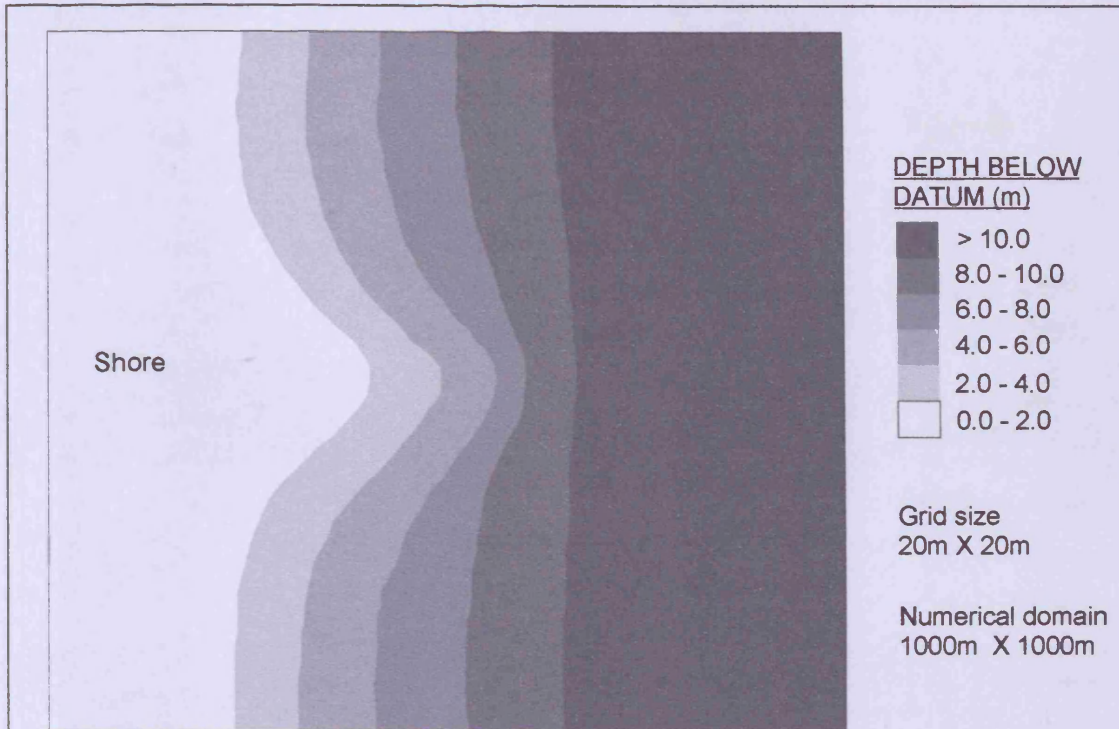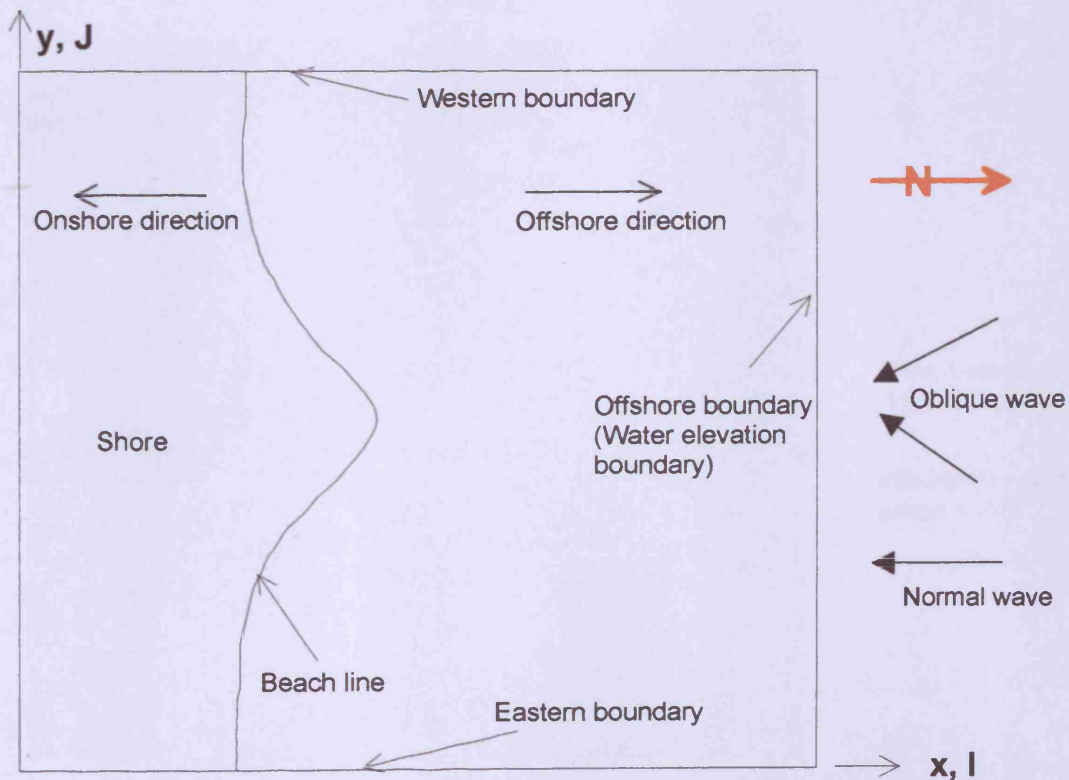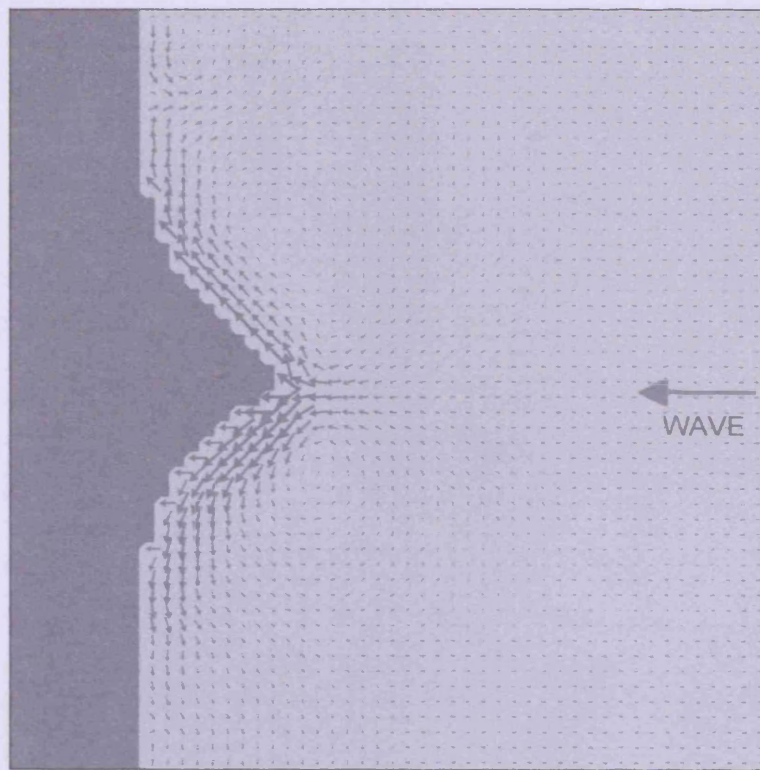
Figure 6.3.1 : Numerical domain of sinusoidal beach

DEPTH BELOW DATUM (m)

> 10.0
8.0 - 10.0
6.0 - 8.0
4.0 - 6.0
2.0 - 4.0
0.0 - 2.0

Grid size
20m X 20m

Numerical domain
1000m X 1000m

Shore

Figure 6.3.2 : Boundary notation and location for sinusoidal beach

Figure 6.3.3 : Wave induced velocity vectors after 0.5 h.
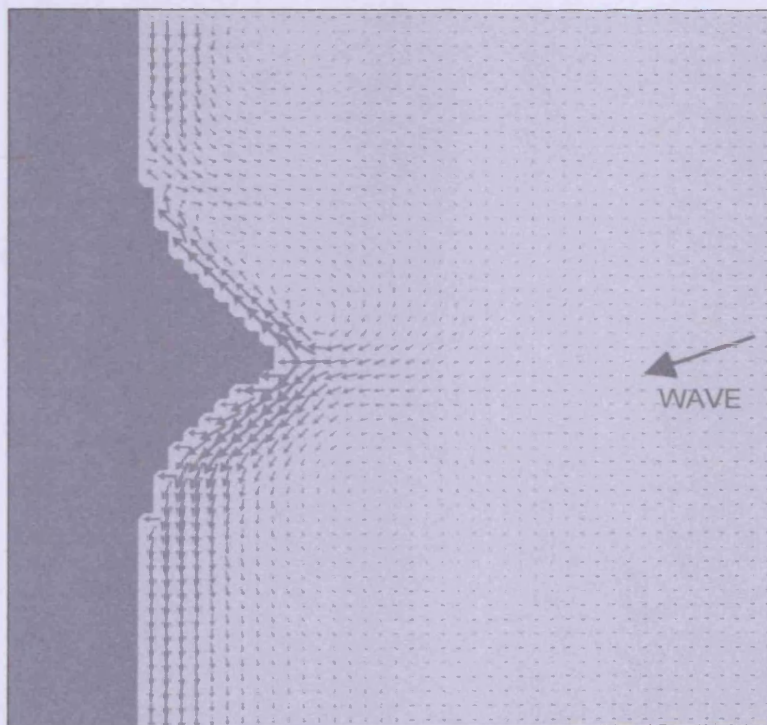
Figure 6.3.4 Wave induced velocity vectors after 0.5 h.

LEGEND

■ DRY CELL

  WET CELL

WAVE PARAMETER

Height, h = 0.5m
Period, T = 4.0 s
Incidence angle = -20^{0}
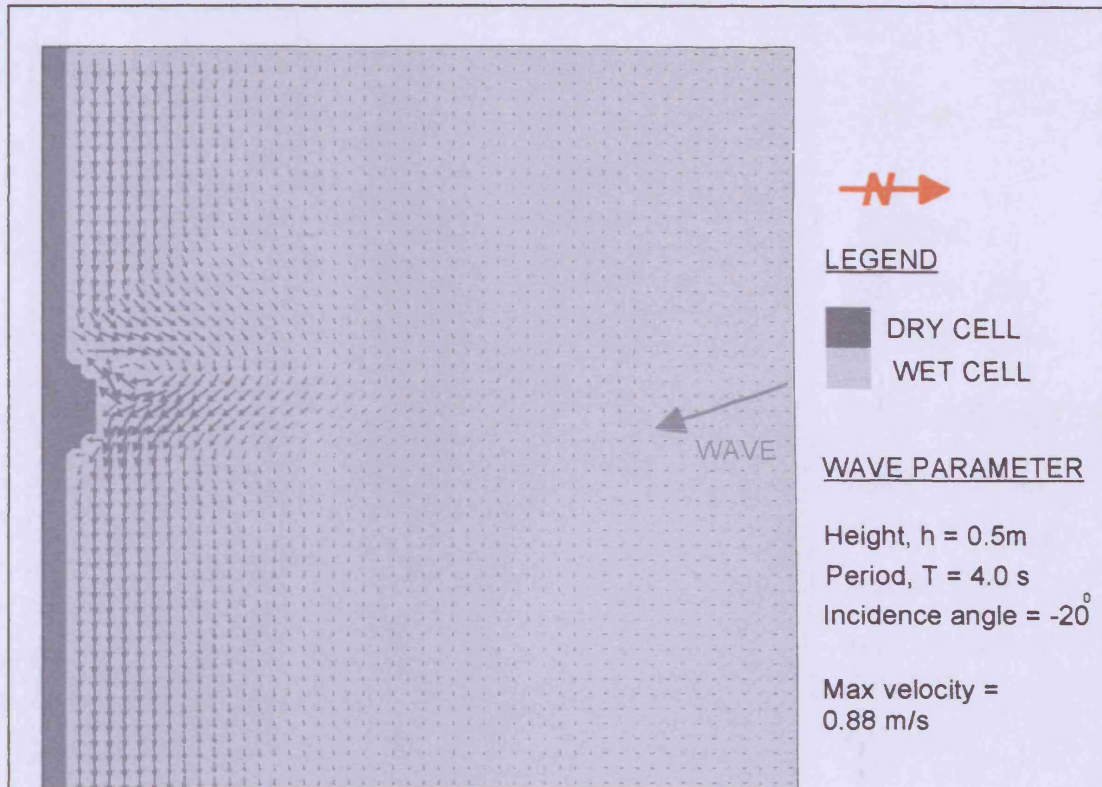
Max velocity =
0.88 m/s

Figure 6.3.5 : Wave induced velocity vectors after 0.50 h.

WAVE PARAMETER

Height, h = 0.5m
Period, T = 4.0 sec
Incidence angle = 0^{0}
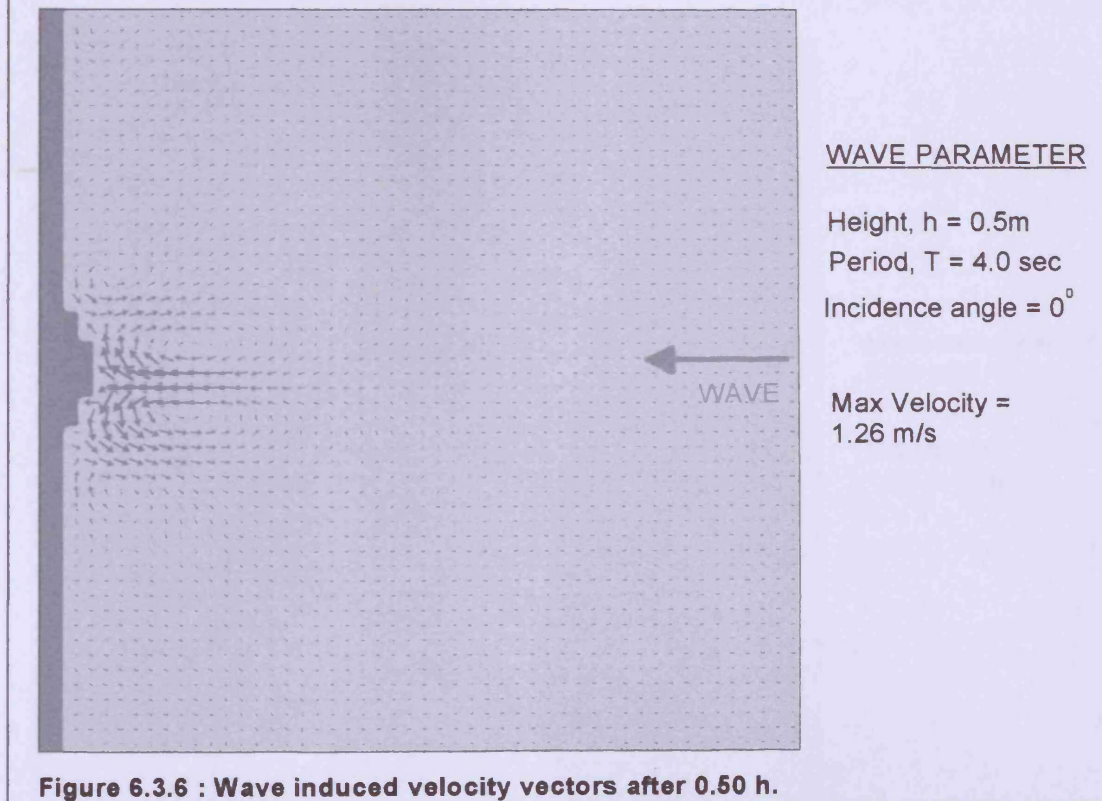
Max Velocity =
1.26 m/s

Figure 6.3.6 : Wave induced velocity vectors after 0.50 h.

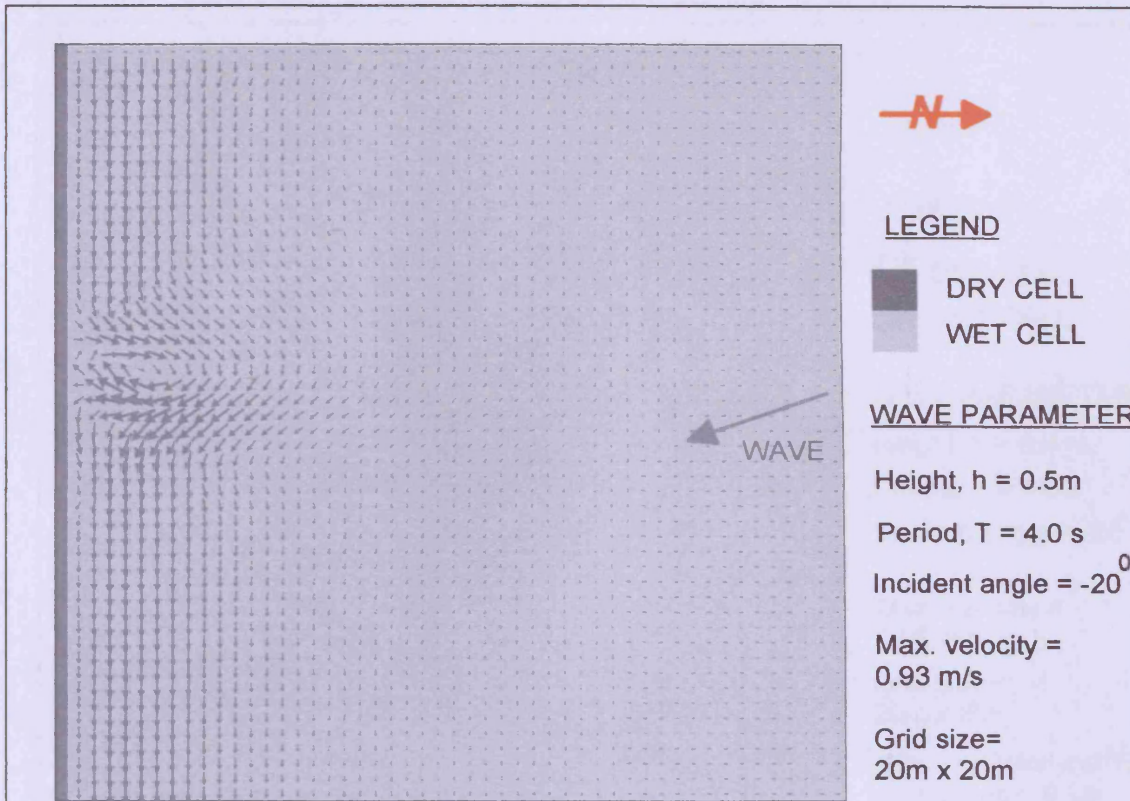**Figure 6.3.7 : Wave induced velocity vectors after 0.50 h.**

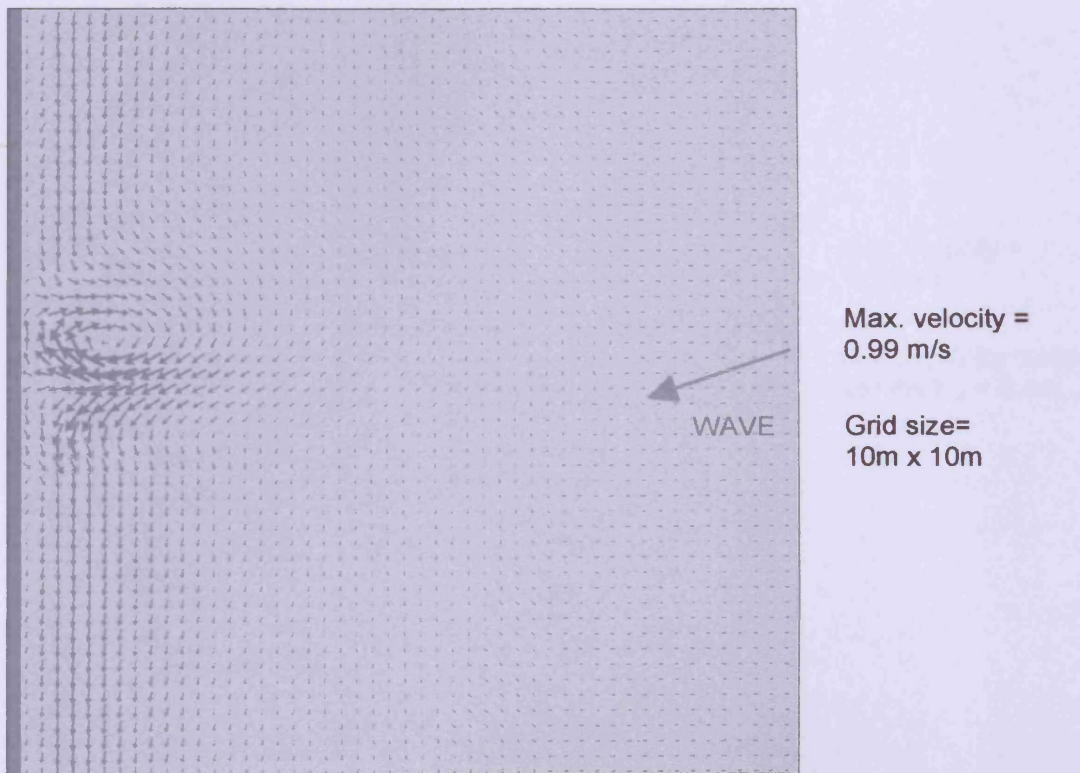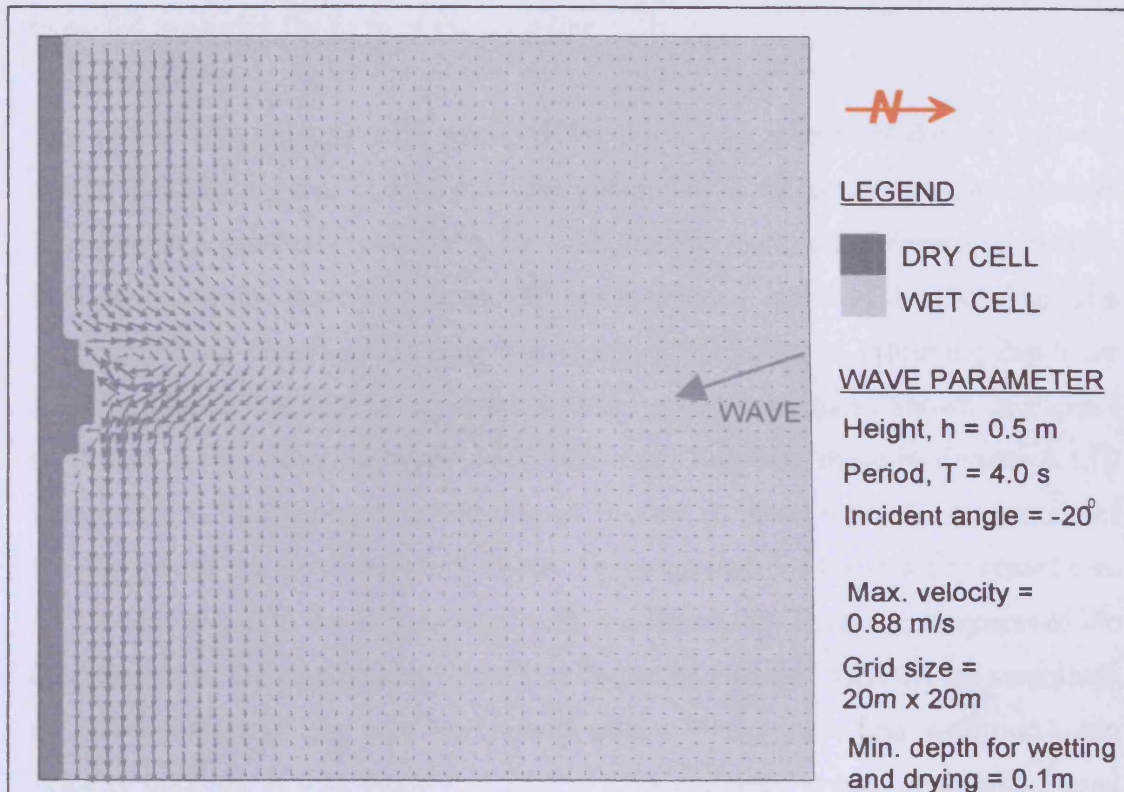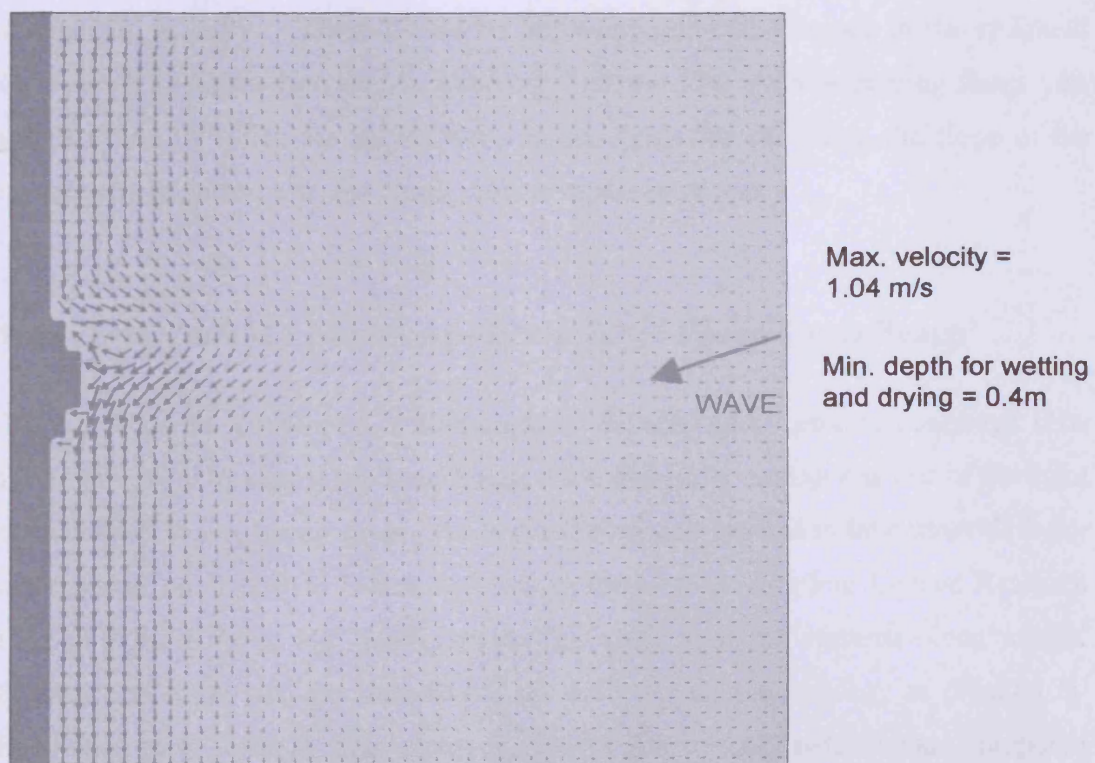LEGEND

DRY CELL
WET CELL

WAVE PARAMETER

Height, h = 0.5m

Period, T = 4.0 s

Incident angle = -20^0

Max. velocity = 0.93 m/s

Grid size= 20m x 20m

Max. velocity = 0.99 m/s

Grid size= 10m x 10m

Figure 6.3.8 : Wave induced velocity vectors after 0.50 h.

LEGEND

◼ DRY CELL

◻ WET CELL

WAVE PARAMETER

Height, h = 0.5 m

Period, T = 4.0 s

Incident angle = -20^{0}

Max. velocity =
0.88 m/s

Grid size =
20m x 20m

Min. depth for wetting
and drying = 0.1m

Figure 6.3.9 : Wave induced velocity vectors after 0.50 h.

Max. velocity =
1.04 m/s

Min. depth for wetting
and drying = 0.4m

Figure 6.3.10 : Wave induced velocity vectors after 0.50 h.

region was therefore expected to be highly mobile and this constant mobility was expected to change the form of the shoreline.

The physical parameters were changed for the above numerical domain and the effects can be observed. Though the wave parameters were constant, the bed friction was also kept constant. So it can be said that the nearshore circulation pattern depended upon the wave climate as well as the physical shape of the shoreline. The water depth for different test runs was changed according to minimum depth for flooding and drying. The water depth was 0.1m less than those shown in Figures 6.3.8 then 6.3.7. Also the water depth was 0.3m less than those in Figures 6.3.10 than in 6.3.9. The decrease in water level caused an increase in the magnitude of velocity and more dry areas were visible. The magnitude of the velocity component which contributed to the longshore current was dependent upon the steepness of the shoreline as well as the bottom slope. The choice of grid size affected the magnitude of velocity as well. The test was started with a 40m square grid with maximum velocity 0.88m/s. It was found that 20m x 20m and 10m x 10m grids still caused changes in the flow velocity, while further reduction to a 5m x 5m grid did not change the velocity. There would be however, periodic changes in the sediment concentration distribution due to wave oscillations. The main governing factor was the direction in which the waves were approaching the shoreline, the slope of the nearshore region and also the configuration of the shoreline.

6.4 Test Case II : Model Application to 'Three Cusp Beach'

The wave model developed in this study was required to predict nearshore flow fields generated by normal and incidence wave direction as this was one of the main objectives of this research study. The wave model was applied to laboratory data for a sinusoidal multi-cusped beach installed in the United Kingdom Coastal Research Facility (UKCRF), at HR Wallingford. The wave induced currents along cusped beaches are important for inducing large scale horizontal mixing, as detailed by Borthwick et al., (1997). The model results for the velocity pattern were compared with the experimental velocity profiles.

The model results were compared with the experimental data obtained by the UKCRF three cusp beach, with wave gauge data being giving in the form of field wave heights and wave induced currents with the latter being determined by digital image analysis of video film. At multi-cusped beaches, the excess mass and momentum was created by wave breaking non-uniformly and thereby producing nearshore currents. The patterns of nearshore currents are extremely important in the nearly horizontal advection and large scale mixing of suspended sand. For normally incident wave at a multi-cusp beach, longshore currents are generated parallel to the beach contours, and directed from cusp crest to trough

WAVE

1. Circulation under normal wave

WAVE
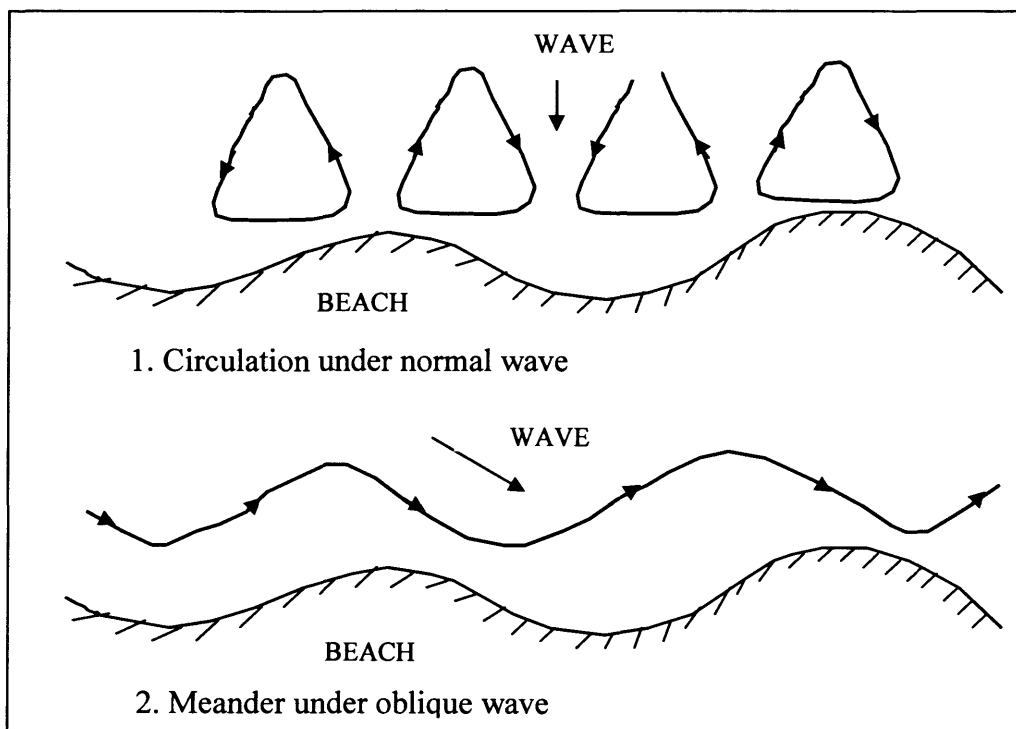
BEACH

2. Meander under oblique wave

Figure 6.4.1: Dependence of current pattern on wave incidence angles

(from Sonu, 1972)

where they feed into rapidly flowing offshore jets (rip currents). Inturns this are balanced by inflowing currents at the cusp crests. Thus a system of primary nearshore circulation cells is established at a multi-cusp beach by normally incident regular waves. For oblique incident waves, the excess fluxes predominate in one alongshore direction and so a meandering longshore current occurs instead of a primary nearshore circulation system (Borthwick et al., 1997).

Sonu (1972) obtained extensive field observations of wave-induced nearshore circulation patterns and meandering longshore currents due to attack by uniform wave systems (Noda, 1972). A schematic description of these two types of patterns is shown in Figure 6.4.1. From this data, Sonu suggests that these circulation patterns are strongly dependent on local bottom bathymetry. The interaction of the wave system with the non-uniform bottom topography produces variations in the wave height and direction field, which Sonu suggests is the driving mechanism for nearshore circulation. For this development of wave-current model, the current field was included in the wave sub-model with a change in the mean water level with time. This change in water level will generate the additional currents on top of wave field. When the water level changes, the wave sub-model will calculate the radiation stresses which will be used for calculation for the next time step.

6.4.1 UKCRF Multi-cusped Beach : Physical Setup and Numerical Model

The UKCRF had plan dimensions of 27 m (cross-shore) x 36 m (alongshore) with a working area of 20m x 15m. Waves were generated using a 72 paddle wave maker. The longshore currents were recirculated in the laboratory setup by using 4 pumps (Figure 6.4.2). The mean water level at the paddles was kept at 0.5 m at all times. The multi cusped beach had overall dimensions of 12 m alongshore and 5 m across-shore. It consisted of three sinusoidal cusps situated on a 1:20 plane beach, with the still water depth being given by:

$$h(x,y) = S\left[(x_L - x) - A\sin\left(\frac{\pi(x_L - x)}{x_L}\right)\left(1 + \sin\left(\phi - \frac{2\pi y}{R}\right)\right)\right]$$

(6.4.1)

where x = distance measured onshore from the cusp's toe (located 5 m onshore from the toe of an underlying plane beach, of slope S=0.05); y = distance measured alongshore from the edge of a cusp; x_L = cross-shore length of the cusps (= 5m); A = amplitude of the sine wave used to generate the cusped profile above the plane beach (= 0.75); R = longshore wave length of a single cusp (= 4 m) and ϕ = phase

angle (= 3π/2). The three cusps were located within 0≤ x ≤ 5 m and –12m≤ y ≤ 0 m (Figure 6.4.2).

The product of A and S represented the maximum height of a cusp for the above configuration. The choice of formula was based on the earlier laboratory based work by Lima (1981), Test case III in this study and Borthwick and Joynes (1989) who modelled a single circulation cell in the vicinity of a half-sinusoidal beach. Figure 6.4.2 shows the still water depth contours and outline of the multi cusped beach within the UKCRF basin. The constructed multi-cusped beach profile was accurate to within ±0.1 cm. The final surface of the cusps was smooth, although the surrounding plane beach had an average roughness height of 1.7 cm.

The numerical model was set up for the multicusp beach. The model domain was setup as for the three-cusp part of the laboratory setup. The length of the cross shore direction was 16m (x-axis) and the length of the alongshore direction was 12m. The grid spacing for the wave model was taken as 0.25m x 0.25m and for the hydrodynamic part the spacing was 0.5m in both the x and y directions. The formula for the still water depth followed equation 6.4.1, the water level was kept at 0.5m and the numerical setup was as shown in Figure 6.4.3. The wave maker paddle which created the waves for the cusp beach was considered as a water elevation boundary for the numerical setup.

The other parameters considered in the numerical model were taken to be identical to those of the laboratory setup. The preset value for wetting and drying of the cell was kept at 0.01m. The selection of the eastern boundary and the western boundary depended on the laboratory set up. According to the figures (Figure 1) presented in the paper by Borthwick et al., 1997, it was found that both boundaries acted as water elevation boundaries (equation 4.7.4). The boundary conditions affected the circulation of flow along the boundary, so to obtain physical similarity with the laboratory set-up the boundaries were projected as water elevation boundaries which means that the variation of the flow values normal to the boundary can be assumed to be zero (equation 4.7.5).

6.4.2 Experimental and Numerical Results

During the experiments, two overhead cameras were used to record the movement of 10 cm diameter neutrally buoyant markers distributed throughout the test zone. The video image was digitised and after enhancement by thresholding and lens distortion calibration, the images were processed wave-by-wave to give the spatial distribution of velocity vectors corresponding to the depth averaged currents.

The numerical simulations were undertaken for 600 s. The wave height, wave angle, the water level, the velocity vectors and longshore sediment components were output for the desired simulation time. A FORTRAN program was written to convert the output results into a suitable format for the Surfer or Tecplot graphical packages.

Four wave conditions were considered for the experimental setup and three-wave conditions for the numerical model predictions. The mean water level (the highest water depth) at the wave maker was fixed at 0.5 m and the wave parameters were as follows:

Table 6.4.1: Different test run for three cusp beach

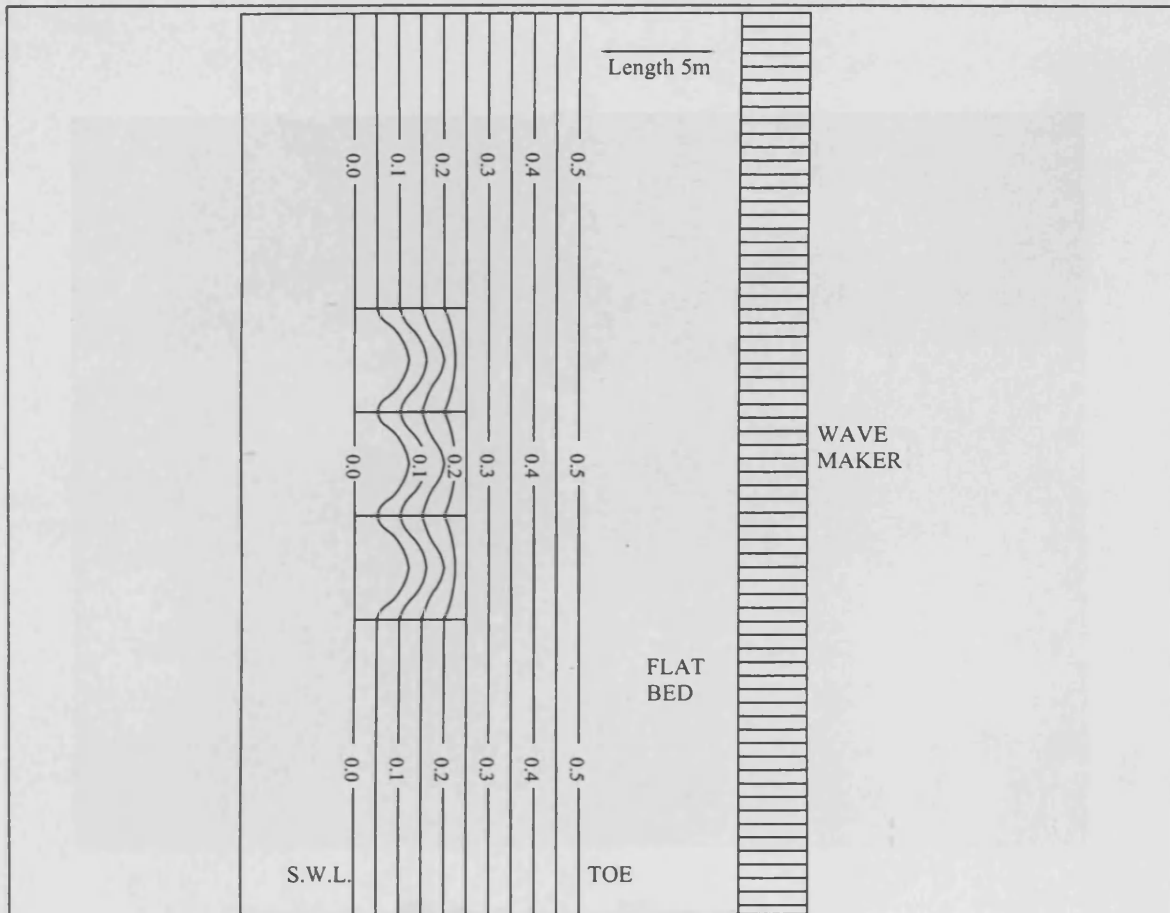|	Wave Type	Wave Period T (sec)	Wave Height H (m)	Incident wave angle (degree)
Case A	Normal regular	1.0	0.1	180^0
Case B	Normal regular	1.2	0.125	180^0
Case C	Incidence regular	1.2	0.125	160^0
Case C	Incidence regular	1.2	0.125	200^0

Figure 6.4.2 : Layout of UKCRF multi-cusp beach
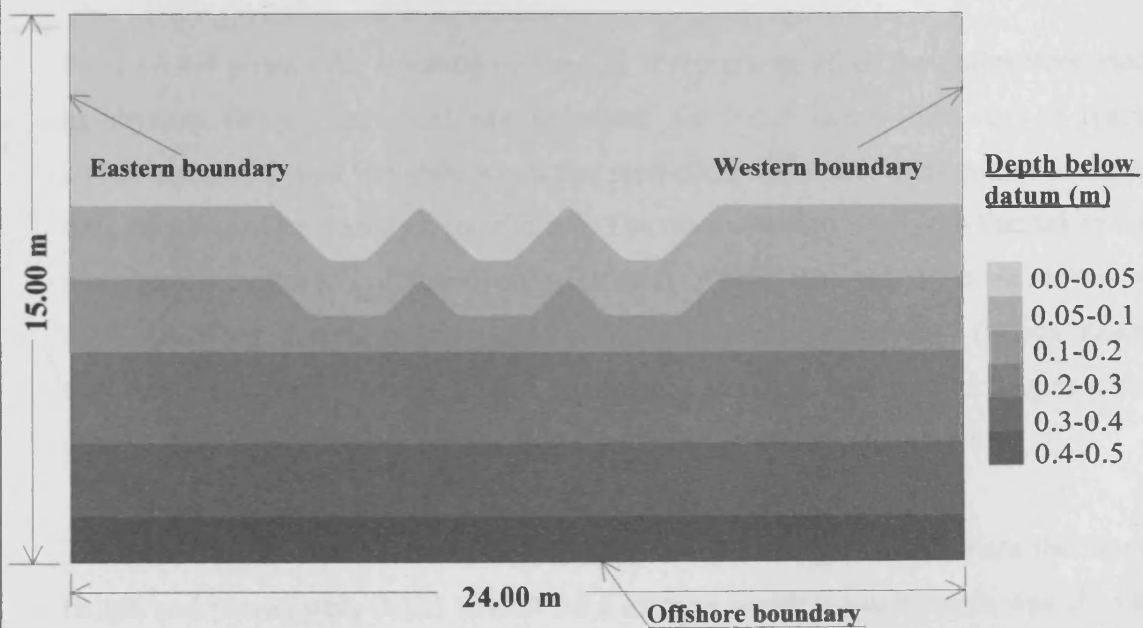
Figure 6.4.3 : Multi-cusp beach - numerical model set-up
(Grid size : 0.5m x 0.5m)
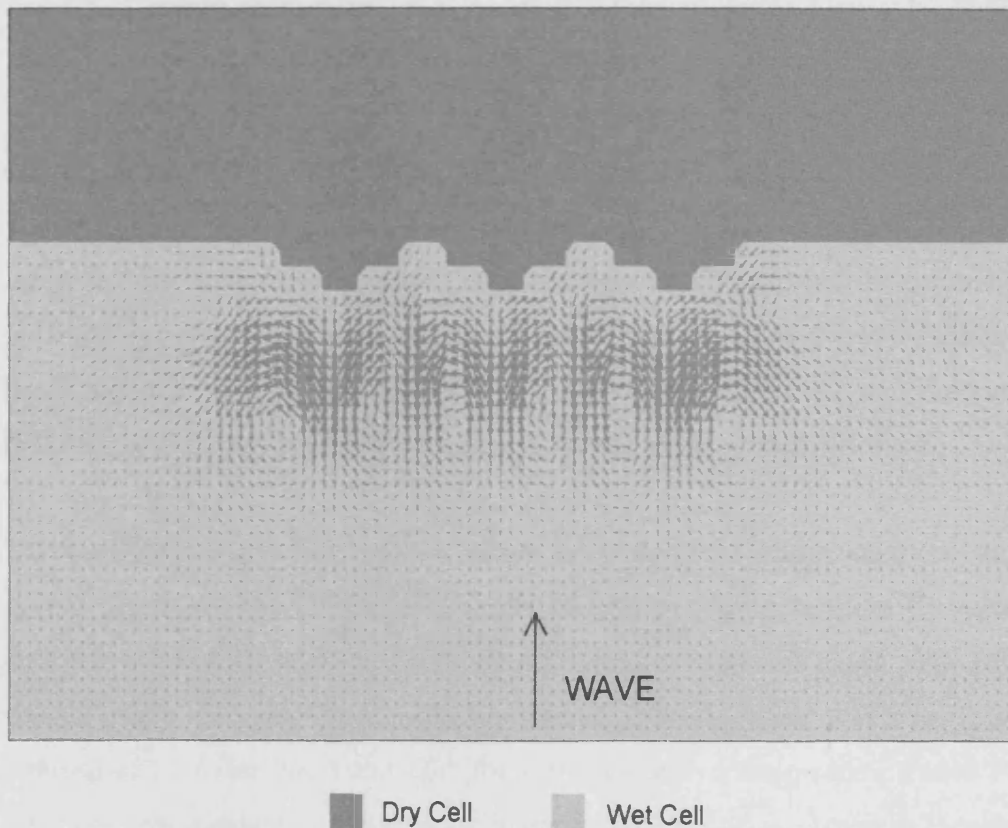
Dry Cell   Wet Cell

Figure 6.4.4 : Predicted velocity field for case A
(i.e. regular waves; wave period = 1.0s;
wave height = 0.1m; incident wave angle = 0^0)

Figure 6.4.4 present the situation of Case A. It represents all of the parameters used in physical setup. The model was simulated for 0.167 hours (600 sec) to reach steady state as it was the state when the prediction difference between successive time step is smaller than a given criterion. The time was also similar to that taken for the physical model to stabilise (Borthwick et al., 1999). The time step was taken as 0.1 s, which satisfied the stability criteria. The waves approached at 0^0 (which meant that they were normal to shore line), incident to the cusp and produced symmetric counter rotating primary and secondary circulation cells with rip currents.

The experimental condition for Case B (Borthwick, et al., 1997), where the wave height and period were 0.125 m and 1.2 s and the incident wave angle was 0^0, i.e. means normal to the cusped beach, is represented in Figure 6.4.5. Nearly, 5000 wave averaged velocity vectors were estimated for each point. The laboratory measured

interpolated vectors and depth averaged stream function contours are illustrated. The numerical model predictions for the same case are given in Figure 6.4.7, with the predictions showing similar results to the experimental data. The maximum measured velocity vector was 0.50 m/s from the experiments and 0.46 m/s from the numerical model computations. Both of these velocity distribution showed common features, such as the nearshore circulation patterns which formed a fan-shaped inflowing current structure running up the peaks of each cusp and the narrow jet-like outflowing rip currents, which extend a short distance beyond wave breakers. The predicted wave distribution for this case is shown in Figure 6.4.8 and it agrees with the basic principle that the wave angle is effected by the bottom friction.

The results from the experimental setup for an incident wave angle are shown in Figure 6.4.6. For the numerical simulations corresponding to Case C, wave from both the left and the right hand directions, with an incidence angle of ± 20° to the normal wave direction have been considered. This incident wave angle will be referred as +20° (for 200°) and -20° (for 160°) relative to the positive x axis. For this two cases, the circulation patterns are in opposite direction as shown in Figures 6.4.9 and 6.4.11 respectively. The current velocity showed the trend of travelling parallel to the beach profile, along the dominating wave direction. This profile strongly illustrated the presence of meandering nearshore currents which give rise to longshore sediment transport. The wave direction distribution is shown in Figures 6.4.10 and 6.4.12 for the respective angles of approach. The presence of beach cusps and bottom friction modified the incident wave angle from their original orientations as shown in the figures.

The distributions of wave height along the middle line of the cusp beach for normal and oblique incident wave angles (i.e. Case B and Case C) showed a distinct difference based only on the wave direction. Also the wave angles at 3 locations showed a clear pattern of wave distribution due to the incident angle. The shape of the beach profile changed according to the meandering current magnitude and direction. In nature, the dominant wave direction changes at different seasons and also at different times of the year. For example, during one year if a wave approaches from a N-E direction for one season and approaches from a N-W
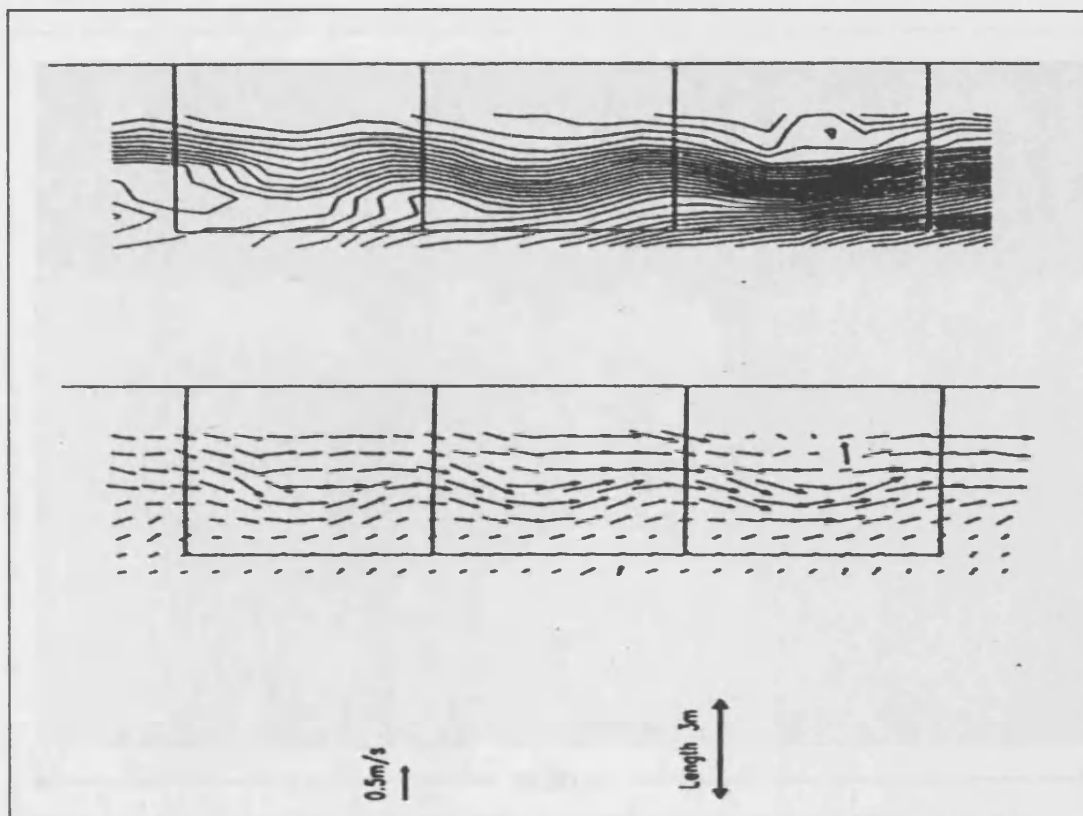
Figure 6.4.5 : Experimental results for case B (interpolated current vectors
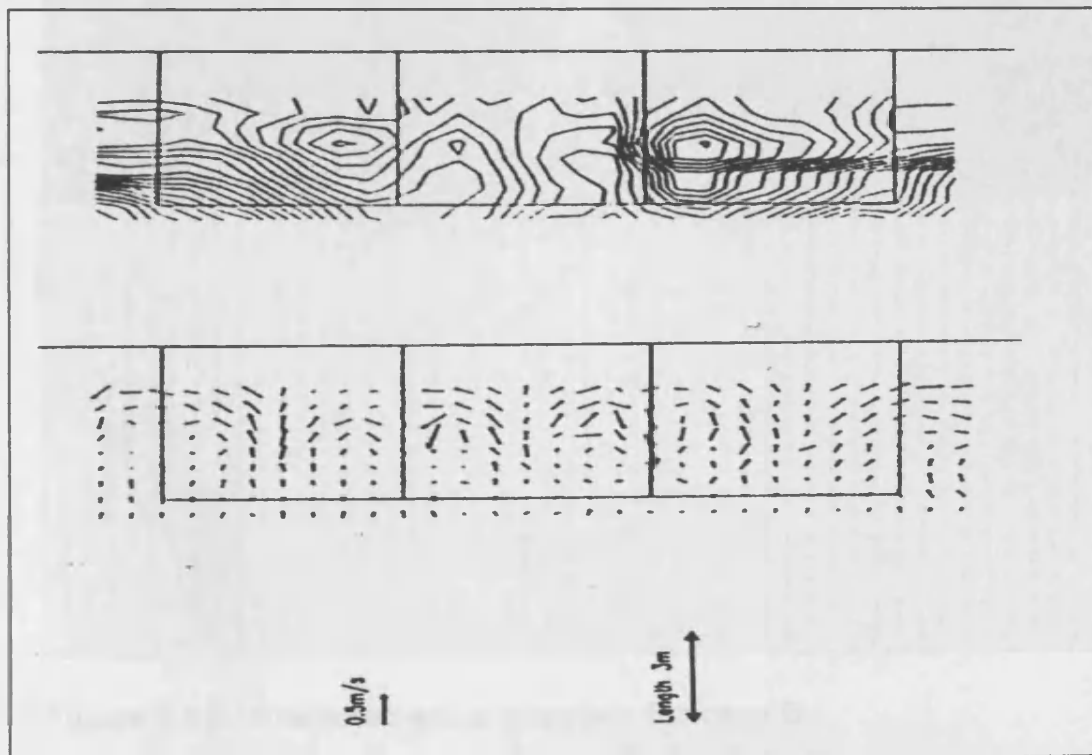   and stream contours)

Figure 6.4.6 : Experimental results for case C (interpolated current vectors
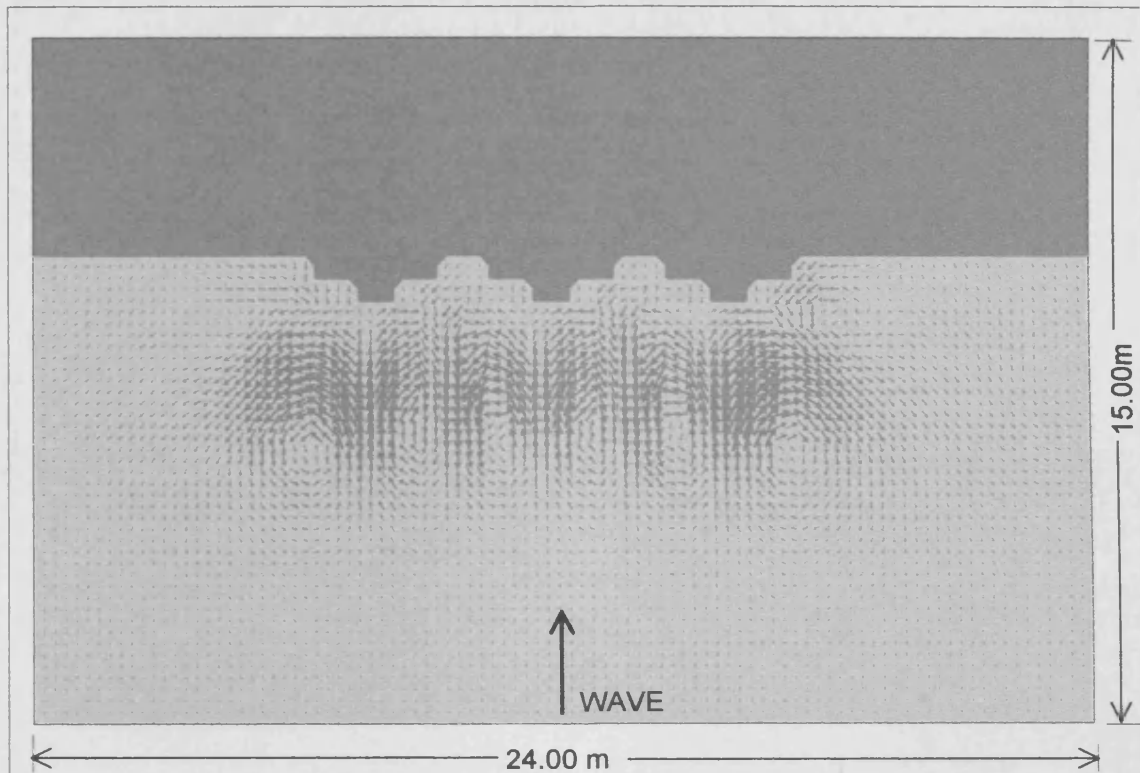   and stream contours)
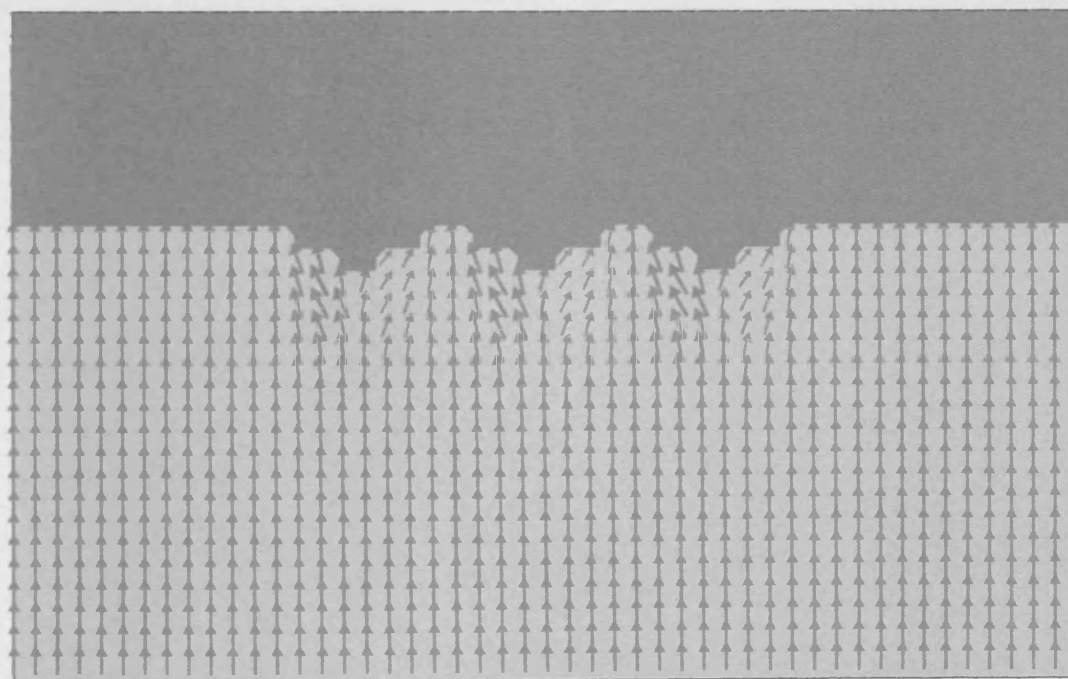
Figure 6.4.7 : Predicted velocity field for case B

Figure 6.4.8 : Predicted wave direction for case B

(i.e. regular wave; wave height = 0.125 m;
wave period = 1.2s; incident wave angle = 0°)

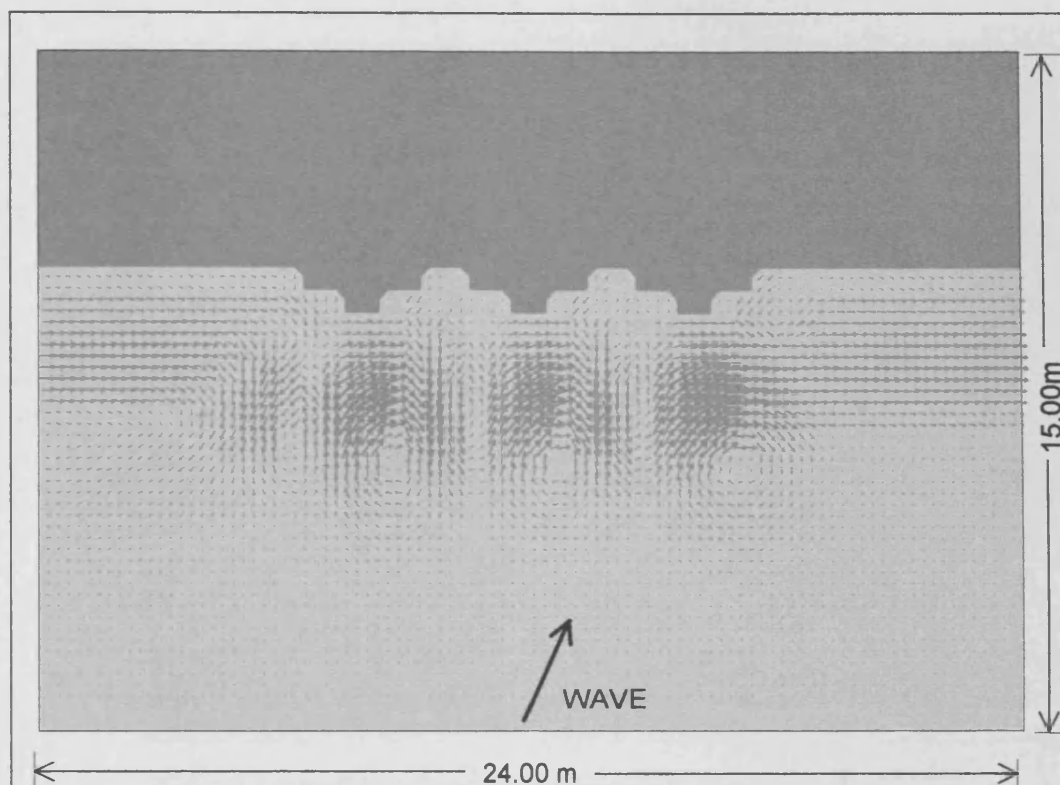■ Dry cell   ■ Wet cell

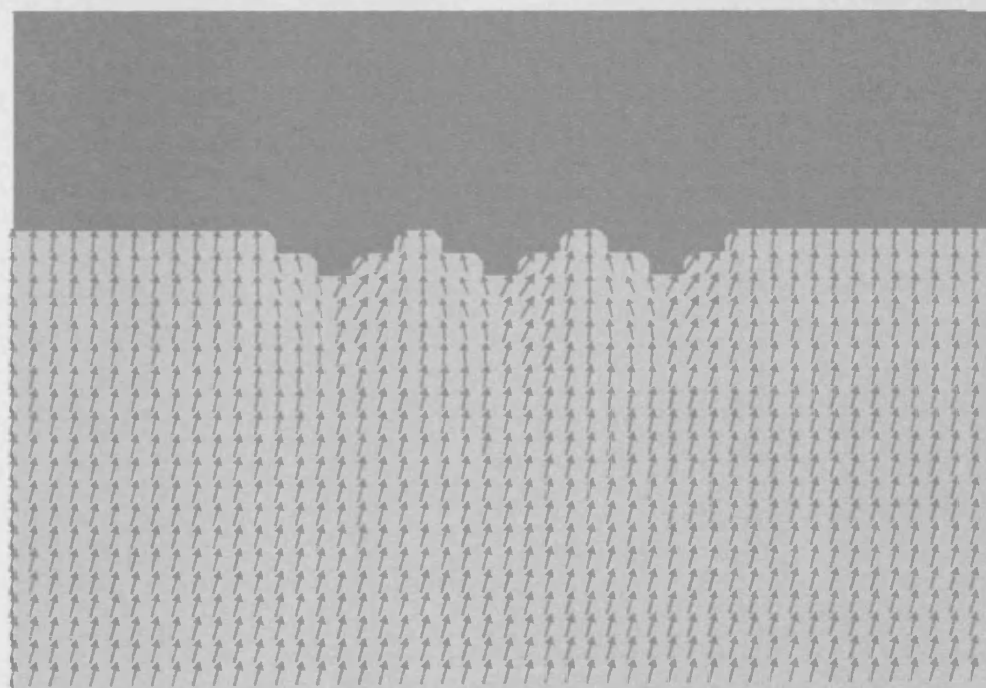**Figure 6.4.9 : Predicted velocity vectors for case C**

Figure 6.4.10 : Predicted wave direction for case C

(i.e. regular wave; wave height = 0.125 m;
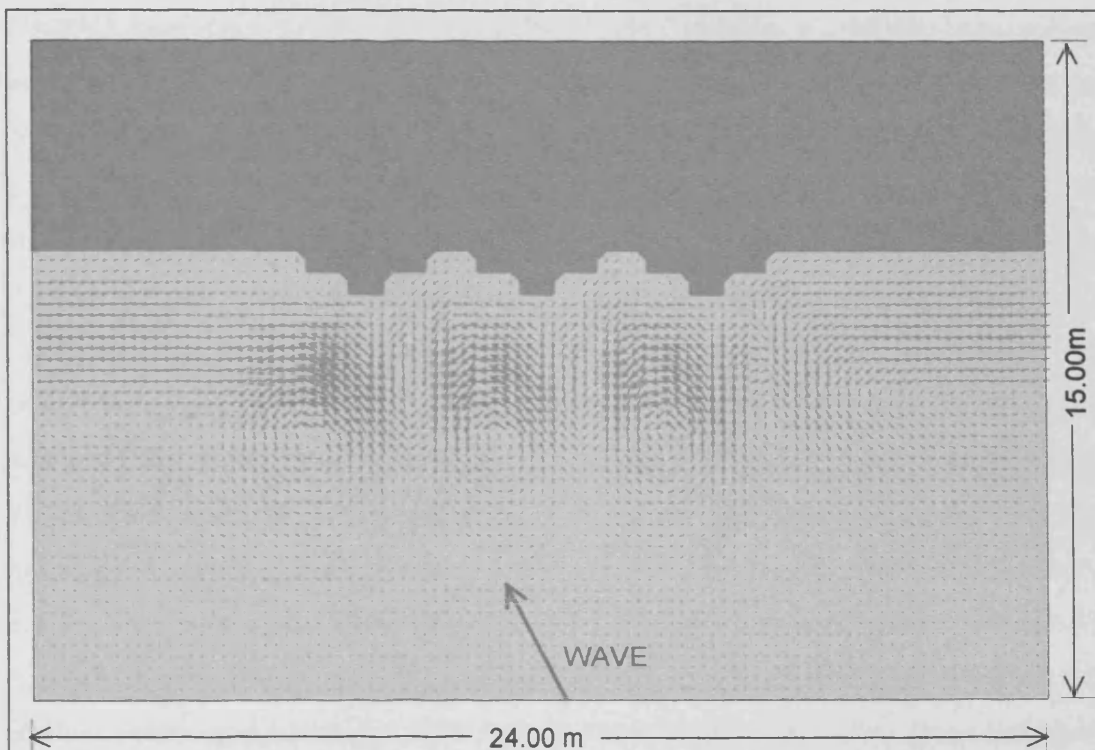wave period = 1.2s; incident wave angle = + 20°)

Dry cell   Wet cell
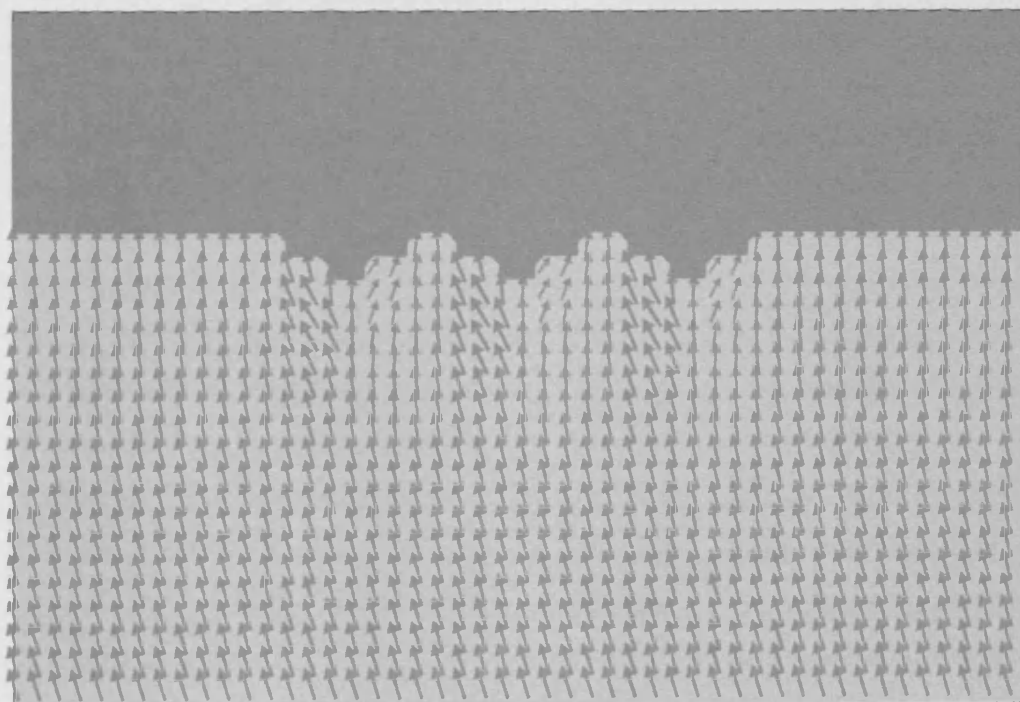
Figure 6.4.11 : Predicted velocity vectors for case C

Figure 6.4.12 : Predicted wave direction for case C

(regular wave; wave height = 0.125 m;
wave period = 1.2s; incident wave angle = -20^0)

■ Dry cell   ■ Wet cell

direction in another season, then this effect might produce a meandering current in opposite directions. The resultant longshore sediment transport will therefore be the combined effect of the above and the shoreline profile will be in a stable condition physically. Clearly from an engineering view point, it is desirable to have a stable shoreline, but in nature such conditions are very rare. But with model predictions, the change in net longshore sediment transport rate could have been calculated.

In this set up, the results of the wave model were also compared with the laboratory results for the three-cusp beach and it was found that for normally incident regular waves, the combination of rip and longshore currents gave rise to a steady system of multiple circulation cells, whereas oblique incident waves generated a stable meandering longshore current. To estimate the longshore velocity component with changing wave direction and water level is one of the challenging conditions to predict. Such calculations for different times will produce the net or gross longshore sediment transport rate over an annual cycle. The shoreline changes due to erosion or accretion can then be evaluated to give the net/gross beach profile.

6.5 Test Case III : Model Application to Half Sinusoidal Beach

The understanding of complex wave-current interactions and the resulting longshore sediment transport processes has been the subject of extensive research for many years. A proper understanding of the process of nearshore circulation provides a breakthrough for coastal engineers, as this provides information on beach nourishment, wave-current interaction with nearshore structures and so on. Research in this field has been going on in three categories: firstly, with regard to field measurements; secondly, with regard to experimental measurements, and thirdly with regard to numerical modelling. Sonu, 1972; Harikawa and Sasaki, 1978 and Bayram, 2000 have performed a range of successful field investigations, with complex and sophisticated techniques being used to acquire data correctly from field sites. Numerical models have been validated for nearshore circulation by comparing predictions with controlled laboratory or experimental data. Typical controlled

laboratory experimental studies in nearshore circulation pattern have been documented by Visser (1991), Hamilton and Ebersole (2001), Doering and Baryla (2002) and Suh, et al. (2002). The wave model in this study will be compared with the experimental results of Lima (1981), with different data sets for the controlled experiment being compared with numerical predictions. The numerical modelling of waves and currents and also for combined wave-current interactions, have developed extensively in recent years, e.g. Baumert, et al. (2000), Pan et al. (2001), Guo (2002) and Grasmeijer and Ruesrink (2003).

The interaction between waves and currents in the nearshore zone or, more precisely, in the surf zone is a matter of immense complexity. Within the surf zone many physical processes occur at the same time, such as excess energy dissipation, excessive mass and momentum flux and non-equilibrium sediment flux, with all of these conditions associated with wave breaking. The generation of longshore and the rip currents (O'Donoghue and Clubb, 2002), which run parallel and perpendicular to the shoreline respectively, are the result of wave-current interactions. These co-directional currents produce nearshore circulation cells, resulting in sediment transport fluxes. To observe the different wave induced parameters such as: wave height, wave angle, longshore and cross-shore velocity component, an experimental set-up is considered in this section for detailed analysis.

6.5.1 Experimental Set-up

The experiment for a half-sinusoidal beach (Lima, 1981) were performed in a glass walled basin approximately 760 cm long x 300 cm wide x 50 cm deep. The horizontal bed of the basin together with both end walls was made of plywood. The bed was horizontal and waves were generated along the flume, with the help of a paddle type wavemaker. A beach with a slope of 0.667 was placed behind the paddle and the basin end, and made from hairlock foam to absorb the energy in that region. Figure 6.5.1 schematically shows the layout of the wave basin. The smooth plywood beach was plane in the region above the still water line. It was sinusoidally, slowly varying in both directions offshore from this line (for details see Lima, 1981). A

half-sinusoidal beach was modelled in the longshore direction. The beach can be expressed in the following way:

$$h(x, y) = sx \qquad \text{for } -70\text{cm} \leq x < 0 \qquad (6.5.1)$$

$$h(x, y) = s\left[x - a\sin\left(\frac{2\pi y}{\lambda}\right)\right] \qquad \text{for } 0 \leq x < 436\text{cm} \qquad (6.5.2)$$

where,   s = slope = 0.05

a = amplitude of the periodic contour in cm = 75 sin (πx/436)

λ= bottom contour wavelength in the longshore direction (rip current

spacing) = 600 cm; and

150 cm $\leq$ y $\leq$ 450 cm

The still water depth was constant at 21.80 cm in the horizontal part of the basin. Figure 6.5.2 shows the contour of the basin with respect to still water level. The rectangular grid mesh had 26 rows of 20 cm each and 8 columns each of 37.5 cm. Water surfaces variations were measured using Churchill wave equipment. Piezometers made of 4.75 mm ID perspex tubing were positioned at the grid centres of the lateral lines (Figure 6.5.3) to measure the pressure at bottom boundary layer.

The wave heights and periods were measured near the toe of the beach after the passage of the first three to seven waves. The true wave heights at each wave gauge (4 in number) were averaged to find the input wave height H_n. This wave height was projected back by linear wave theory to obtain the deep water wave height H_o' without reflection, which was the numerical model input wave height. The wave period was determined by dividing the distance of 10 wavelengths (mm) by the product of integer and velocity (250 mm/s). After the attainment of steady state conditions, wave height obtained by averaging recorded heights of twenty or more successive waves passing through each gauge, the water level was determined at grid centre. The accuracy of the water elevation results were of the order of 0.1 mm and velocities were then obtained from cassette recordings by timing the travel of weighted floats. All waves were generated normally to the still water shoreline, with
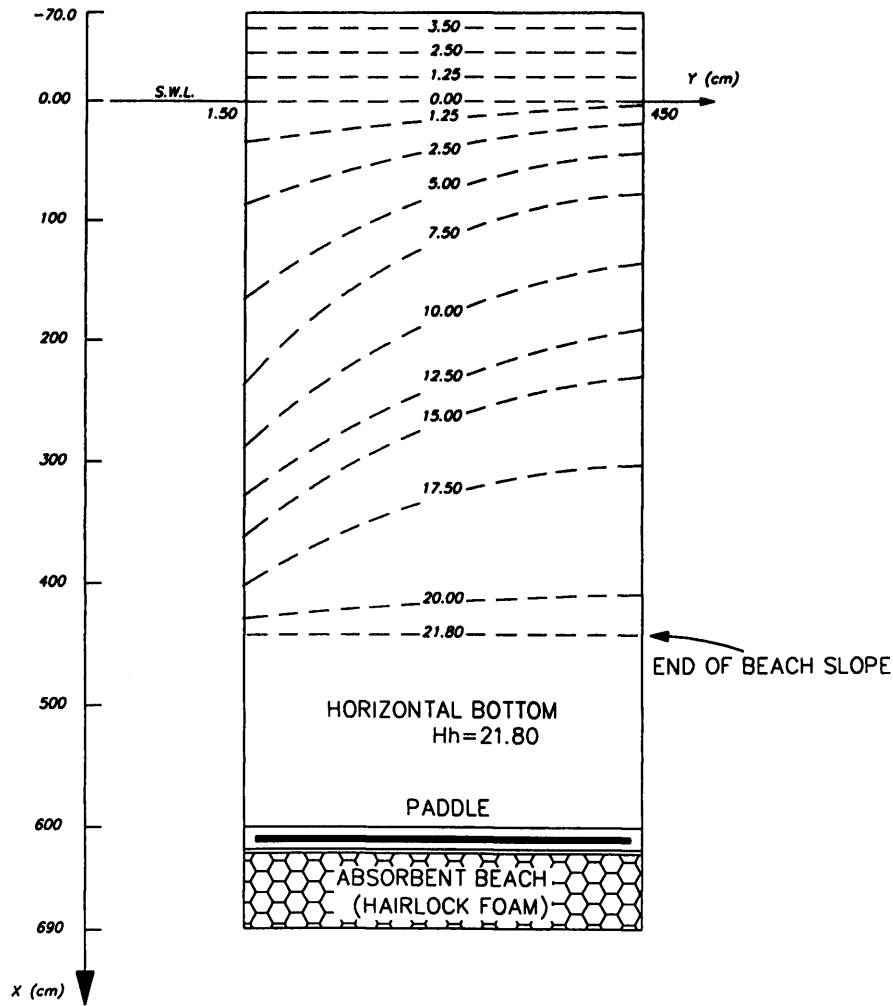
Figure 6.5.1: Still Water Depth Contour in Lima's (1981) half-sinusoidal beach
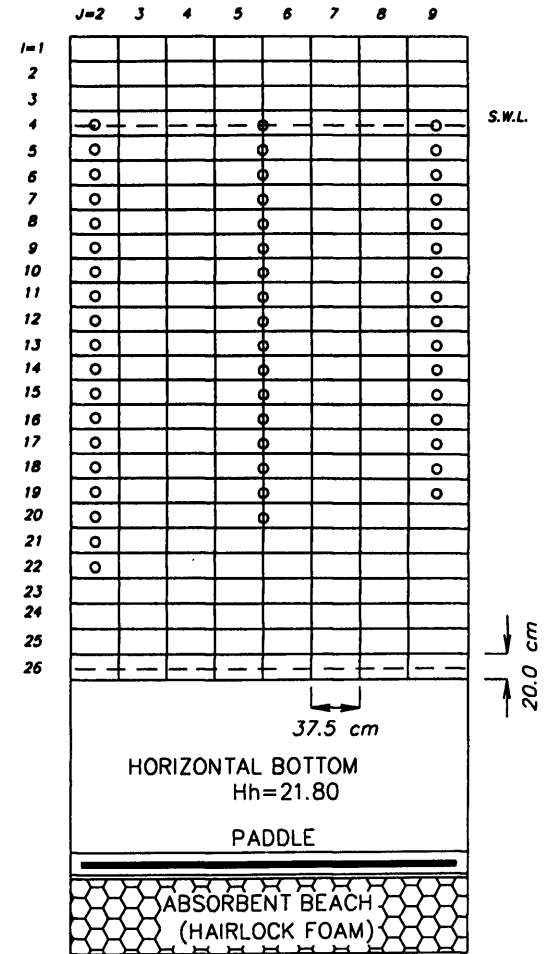

Figure 6.5.2: Positions of the Piezometer Conduits and Grid Mesh Utilised in Wave Basin, Lima's (1981)
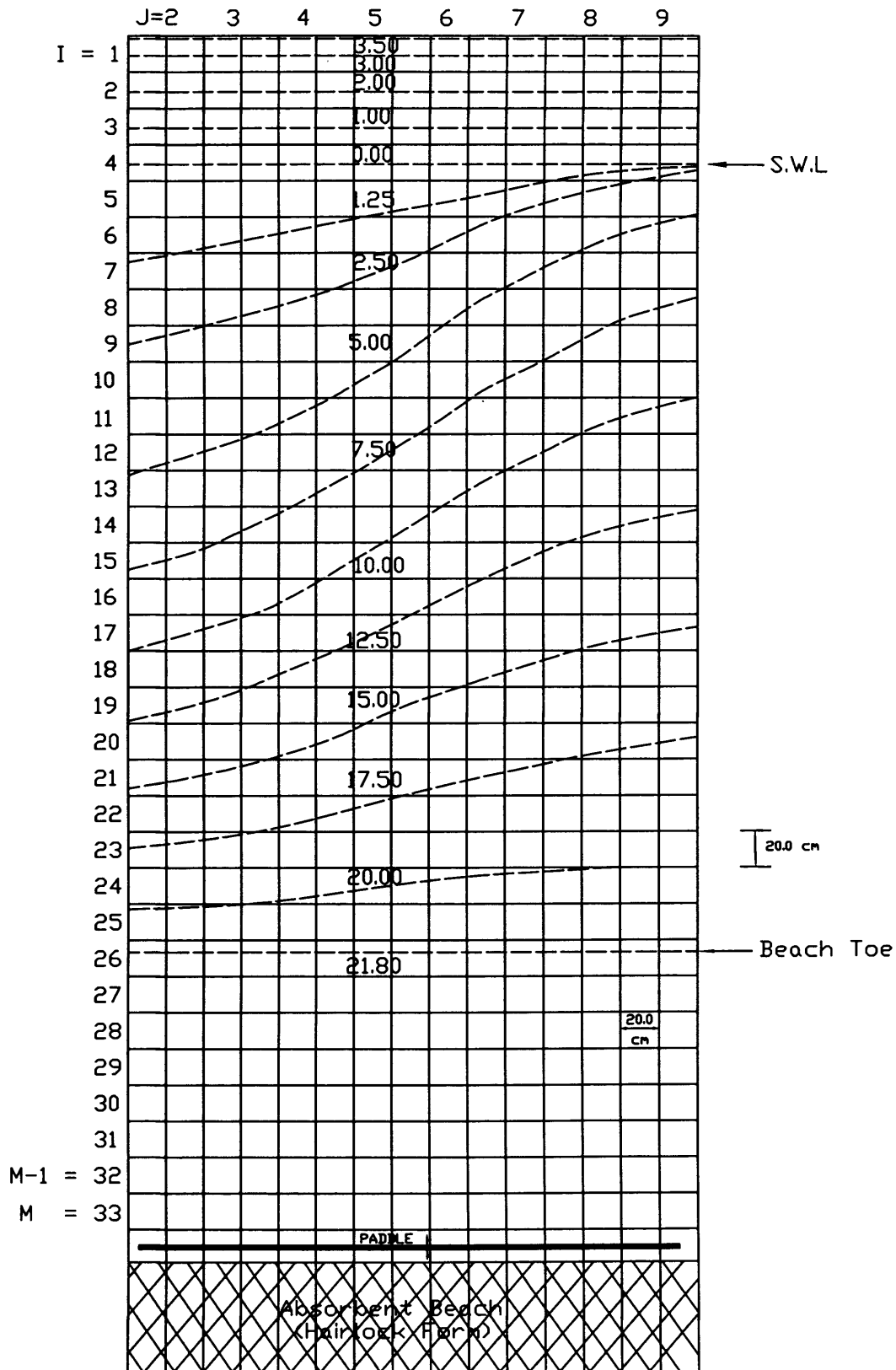
Figure 6.5.3: Grid scheme for half-sinusoidal
beach applications by Lima (1981)

the results from the laboratory experiments then being compared with those obtained from the results of the numerical model predictions.

6.5.2 Numerical Model Set-up

The numerical wave model was then applied to the periodic beach outlined above (Lima, 1981 and also described in Borthwick and Joynes, 1989 and Park and Borthwick, 2001) for incident waves normal to the sinusoidal beach.The numerical model domain consisted of 33 rows (20 cm each) in the x-direction (cross-shore) and 15 columns (20 cm each) in the y-direction (alongshore). In the experimental set-up there were 8 columns (37.5 cm each) but in the wave model analysis grids needed to be square, with Δx equal to Δy. Hence a column width of 20cm was chosen. The data for the middle of any column for the experimental tests was calculated by taking the weighted average of the corresponding columns (Fig 6.5.3).

The boundary conditions were described as water elevation boundary at the end of the beach, where the waves were generated. The wave model runs along with DIVAST are works in two stages. In the first stage the data input consists of bathymetric data being inserted at twice the fequency as for DIVAST. The subroutine 'wave' calculated the initial wave height, wave period and wave angle from the input parameters. The calculation was then based through the mild slope parabolic wave equation (see Chapter 3) to predict the final wave height, angle and period at each grid point and after the designated time of simulation. Also the radiation stresses and bed stresses were calculated at each grid point to give the longshore current, with this current values then being transferred to main hydrodynamic model. The hydrodynamic part of the model was then used to predict the magnitude and direction of the flow velocity and water level. The still water level was kept constant at 21.80 cm and the frictional resistance coefficient was taken as 0.06 (Lima, 1981) for the first trial.

6.5.3 Comparison of Model Results with Experimental Measurements

This section describes the variation between the wave model and experimental results. The data sets, which were used for running the wave model, were taken from the data used in the experimental set up. The numerical model had 33 rows and 15 columns which was 660 cm in the x-direction and 300 cm in y-direction to fit the experimental set-up (Figure 6.5.3), but 26 rows were utilised in the experimental work (Figure 6.5.2). The alternate vertical lines show the position of the columns in the physical model and all the vertical lines show the position of columns in the numerical model (Figure 6.5.3). The half time step was taken to be 0.025s and was found adequate to ensure stability of the numerical simulation. The stability index was 20% of the value required for the van Newmann stability criterion, given as:

$$\frac{\sqrt{\Delta x^2 + \Delta y^2}}{\Delta t} \geq \sqrt{gh_{max}}$$ (6.5.3)

where h_{max} = maximum water elevation.

The condition for the model run consisted of a relatively high wave steepness, which was $H_0'/L_0 = 0.0686$, as found from laboratory model results. This wave condition emphasised some wave height differences found between the experimental and numerical results arising from the effect of currents. The variations in the set-up at the first wave grid for both side wall columns i.e. J=2 and J=15 showed that steady state conditions were obtained after 140 s (i.e. 2800 iterations). The model was then run for 180 s to ensure that steady state conditions had been attained.

Figure 6.5.4 shows the wave height variation at the basin centre. Sensitivity test was done to find the suitable model parameter. The bed friction coefficient was taken as 0.06 in the first trial. After checking for different values 0.01 was seen to give the better prediction. The figure also shows the effect of changing the breaking index γ_b (0.66, 0.72, 0.78, 0.83 and 0.90). The roughness coefficient was also varied for these sensitivity tests. When compared to the laboratory data it was found that $C_f = 0.01$,

$\gamma_b = 0.78$ and $k_s = 5\text{mm}$ provided the best results for most cases. So the rest of the figures will be presented based on these parameters.

Figures 6.5.5 to 6.5.12 illustrate the wave height variations with distance offshore from still water level for each experimental grid column, with its corresponding numerical column also being shown. It can be seen from all of the figures that the predicted and measured wave heights are in reasonable agreement at the beach toe side. It can be also seen from the figures that the measured wave height is much steeper than the predicted wave height in the area of wave breaking. The model predicted smooth changes through the breaking criteria, eventhough conditions were set the same as those in the experiments (Weggel, 1972). The results shown in Borthwick and Joynes (1989) and Park and Borthwick (2001) agreed with Lima (1981) with only exception being those given by Yoo and O'Connor (1986). The reason for this difference in peak wave height calculation is thought to be due to two reasons: (a) the non-linear effect of wave breaking, which was ignored in the linear wave model, and (b) the high shoaling effect, which causes an increase the dissipation of energy at breaker line. The main difference in wave heights are found close to the west boundary (Figures 6.5.11 and 6.5.12). Also it can be noted that the breaking criteria slightly under predicts and overpredict the wave height in the shallower and deeper basin sides respectively. The breaking index γ_b, played an important role in this computation. The effect of different parameters in the wave height calculations were described in Karjadi and Kobayashi (1996) and Kobayashi, et al. (1997) and can be summarised as the dispersion effects of the wave height and and set-up were minor. The dispersion effects on the longshore current were significant for regular waves. And for planer beaches, the alongshore current profile was insensitive to the small alongshore variation of obliquely incident wave.

The stronger concentrated offshore current in column J=16 (J=9, experimental) caused a retardation of the waves in that region, with the wave crests refracted towards the side wall slong this column. Figures 6.5.13 and 6.5.15 show the mean water level profiles for columns J=2 (J=2, experimental) and J=16 (J=9, experimental) and Figure 6.5.14 shows the mean water profile along the basin

centre. The maximum value for wave set down can be observed in near the breaker zones and this is thought to be one of the main reasons for difference in the predicted and measured value. The present wave model did not calculate the wave run-up beyond the mean water level.

Figures 6.5.16 and 6.5.17 represented the onshore-offshore velocities at rows I=14 and I=15, thereby giving some understanding of the longshore distribution of these velocities near the breaker line. The experimental velocity at the row centres was found by averaging linearly the neighbouring velocities. Because of the high turbulence near the breaker line the offshore current moved more towards the longshore direction. The offshore velocity increased at a steady rate from the surf zone to the toe. Figures 6.5.18 to 6.5.23 illustrate the longshore current profile for the experimental and numerical results for columns J=3 to J=15. The experimental values along the column centre were obtained by averaging linearly the neighbouring velocities. The predicted velocities were calculated as a weighted average from the corresponding columns. For column J=4 (exp.) and J=5 (exp.) it can be seen that both sets of results are in good agreement (Figures 6.5.19 and 6.5.20). The experimental maximum values of the longshore current for column J=6 (exp.) and J=7 (exp.) are closer to the shoreline than the predicted values (see Figures 6.5.21 and 6.5.22), with the reason for this difference thought to be due to the width of the surf zone which is narrowed here. A similar scenarios occurred for column J= 3 (exp.) and J=8 (exp.) for the surf zone width, although the results were in good agreement (Figures 6.5.18 to 6.5.23). The results were also checked with those of Borthwick and Joynes, 1989. Another characteristic was found in the experimental data in that the measured profile exhibited a secondary longshore current peak near the breaking position, which was much higher than the predicted value. These peaks were thought to be be due to the difference in the breaking wave height and the surf zone width.

The experimental and numerical velocity profile for the half sinusoidal beach is presented in Figures 6.5.24 to 6.5.27 for the two test cases described by Lima (1981). The difference in the centre of mass can be seen in Figure 6.5.24 and 6.5.25. Figure 6.5.24 shows the experimental velocity profile for the 6.18 cm wave height

and 0.76 s wave period considered in the experimental set up and Figure 6.5.25 shows the numerical model prediction of the wave field for the same parameters. Figures 6.5.26 and 6.5.27 represents the experimental results and model predictions of the velocity field for a wave height of 4.17 cm and a wave period of 1.04 s. The same circulation pattern was observed for all of the velocity field. It can be seen from the figures that there was one counter-clockwise inner cell and one clockwise outer cell, which included the deeper basin side of the shore. It was also observed that the experimental inner cell was smaller than the predicted one, and this was thought to be due to the choice of friction factor, which might not represent the actual basin, and also the linearisation of the mixing term, which would exclude higher order interactions. The difference between the centres of mass between the experimental and model prediction might be arise due to the reason that, both the side boundaries were considered as no flow boundary (equation 4.7.1). There might be some reflected wave which was not considered in the model and that's why the centre of mass was working at the centre of basin. The experimental centre of circulation of the large cell is off-set from the predicted one, both being due to the velocity differences which could have resulted from the combination of such factors as the mixing and friction coefficients used were too high. The velocity field obtained by this model are in close comparison with the model prediction by Lima (1981) for the two test cases (Figure 6.5.25 with 6.5.28 for test run 2 and Figure 6.5.27 with 6.5.29 for test run 9). On the other hand, physical measurements the may also involve errors, as the velocity field shown in Figure ? would be difficult to satisfy the mass balance. The flow flux on the left hand side of the mass centre would be different from the right hand side, unless a very steep surface slope exists. The velocity field obtained using the model was comparable with the velocity field obtained for the explicit scheme and A.D.I. schemes reported by Borthwick and Joynes (1989). It was difficult to create the exact boundary condition in the numerical model of conditions in the experimental set up, with the boundary condition giving rise to some differences near the wall for the wave height and mean water level fluctuations.
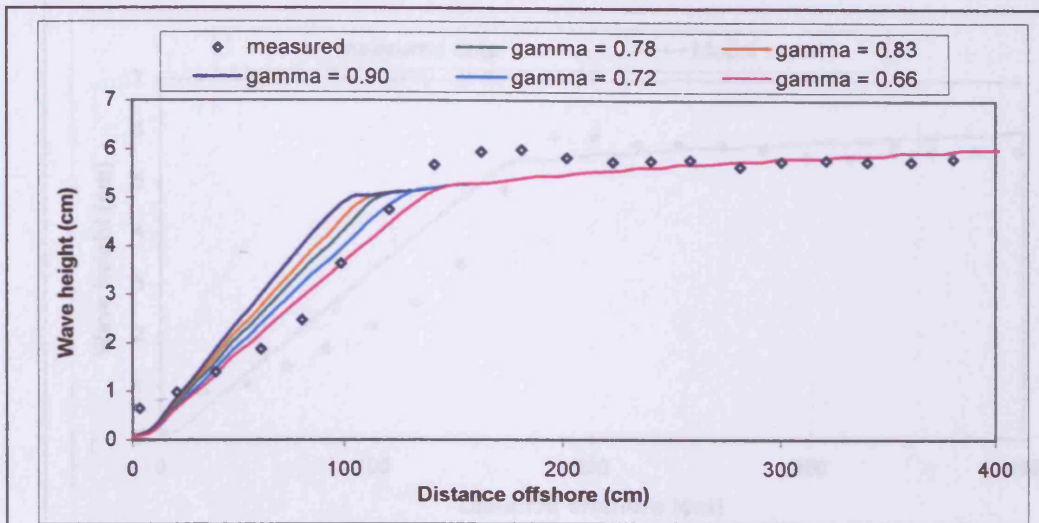
Figure 6.5.4 : Wave height profiles at basin centre for half-sinusoidal beach
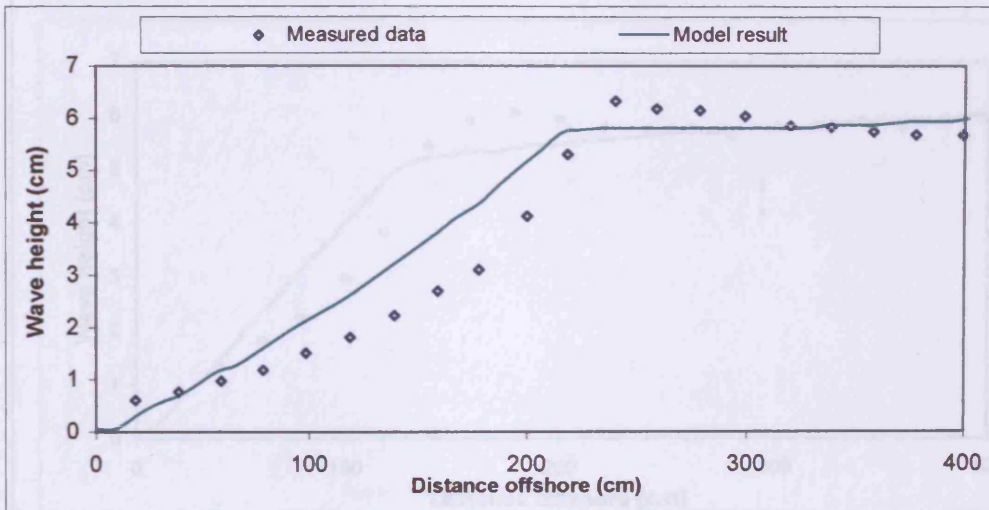

Figure 6.5.5 : Wave height profiles for line J=2 (expt.) for half-sinusoidal beach
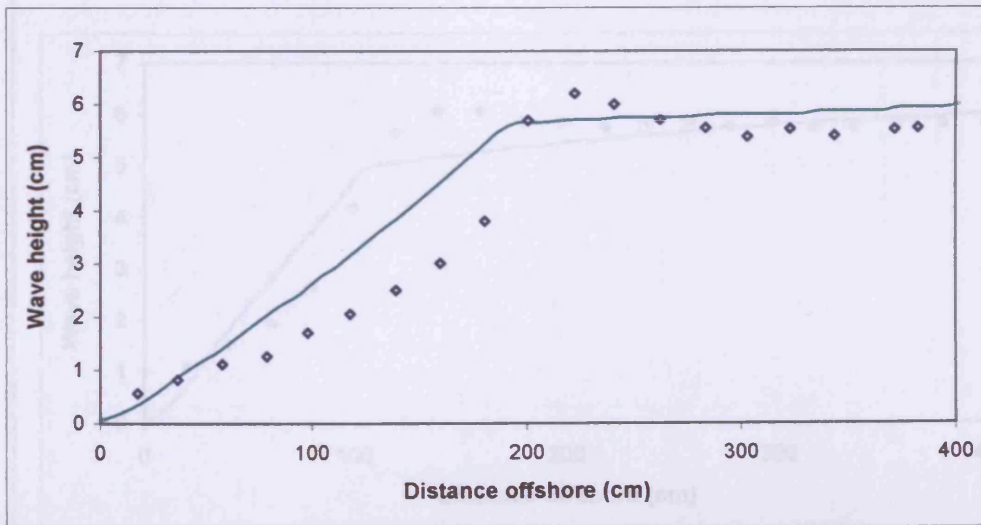

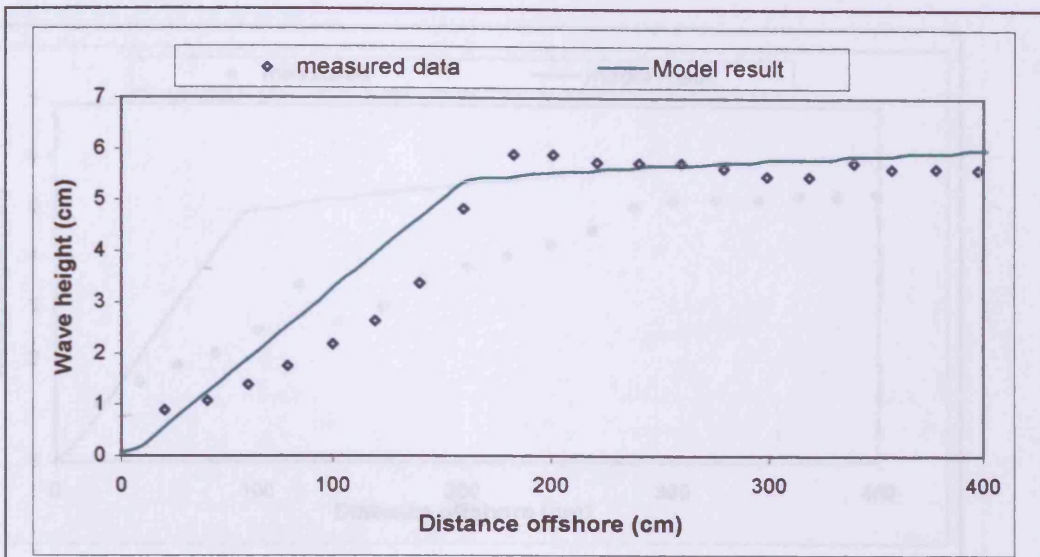Figure 6.5.6 : Wave height profiles for line J=3 (expt.) for half-sinusoidal beach

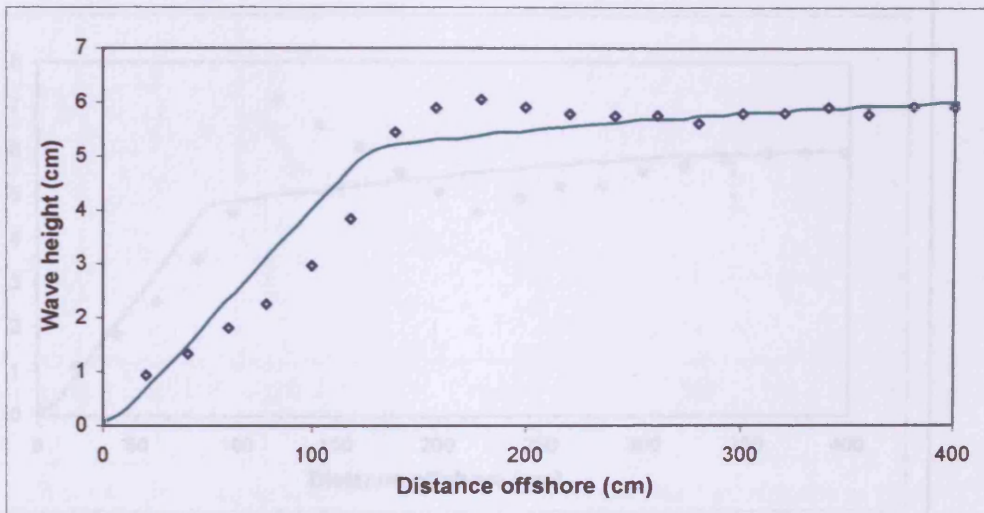Figure 6.5.7 : Wave height profiles at line J=4 (expt.) for half-sinusoidal beach

Figure 6.5.8 : Wave height profiles at line J=5 (expt.) for half-sinusoidal beach
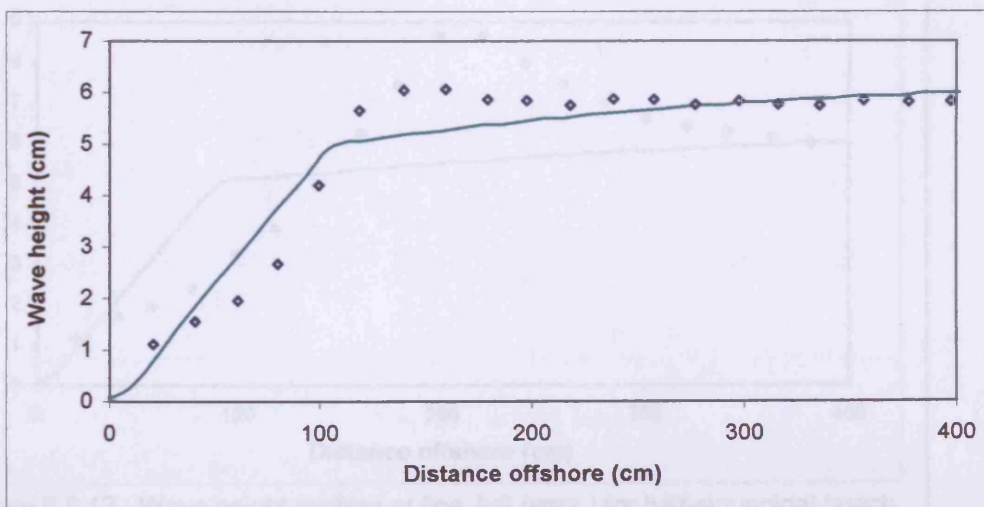

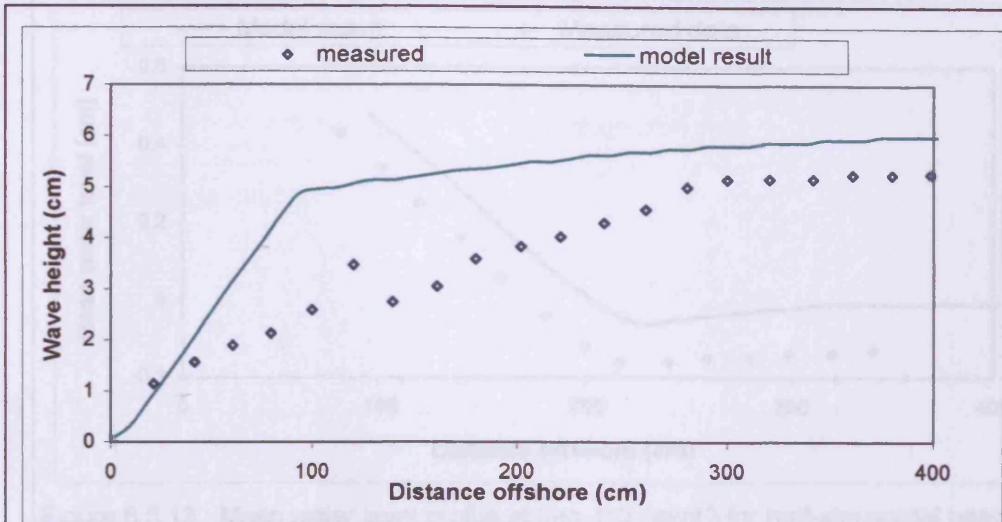Figure 6.5.9 : Wave height profiles at line J=6 (expt.) for half-sinusoidal beach

Figure 6.5.10 : Wave height profiles at line J=7 (expt.) for half-sinusoidal beach
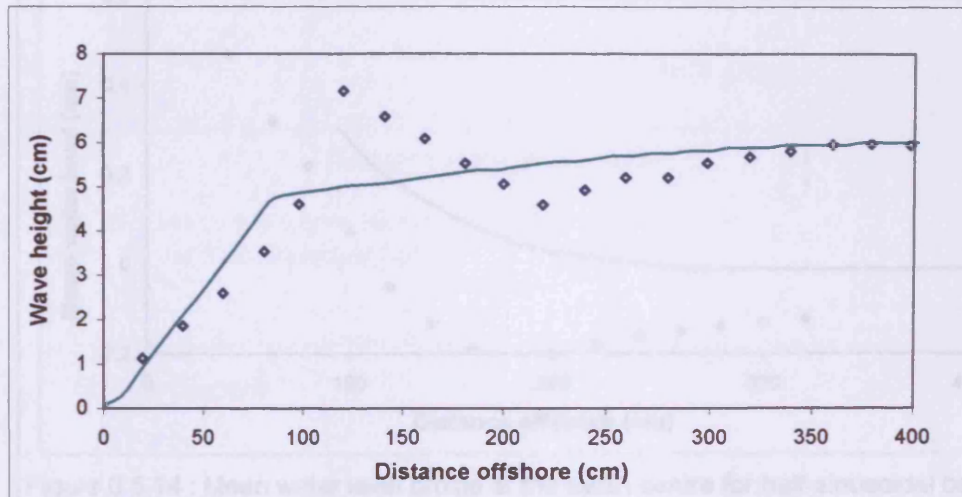

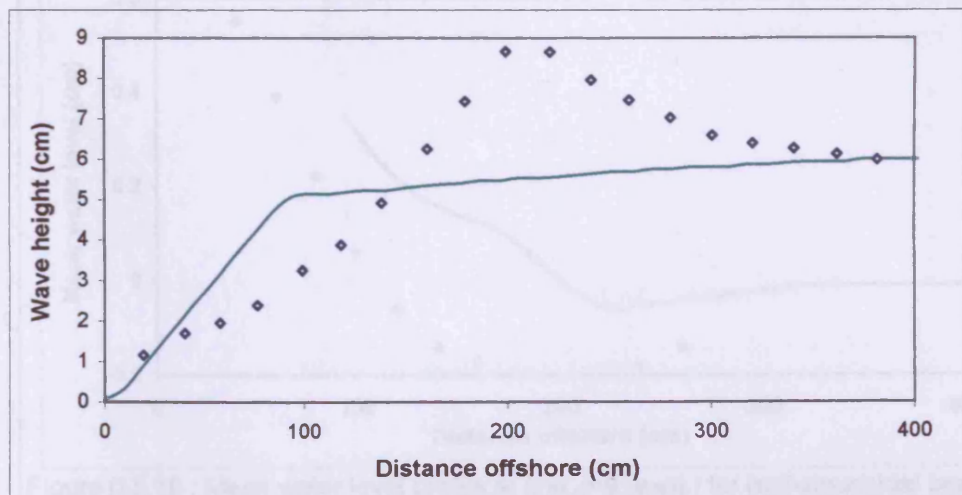Figure 6.5.11 : Wave height profiles at line J=8 (expt.) for half-sinusoidal beach

Figure 6.5.12 : Wave height profiles at line J=9 (expt.) for half-sinusoidal beach
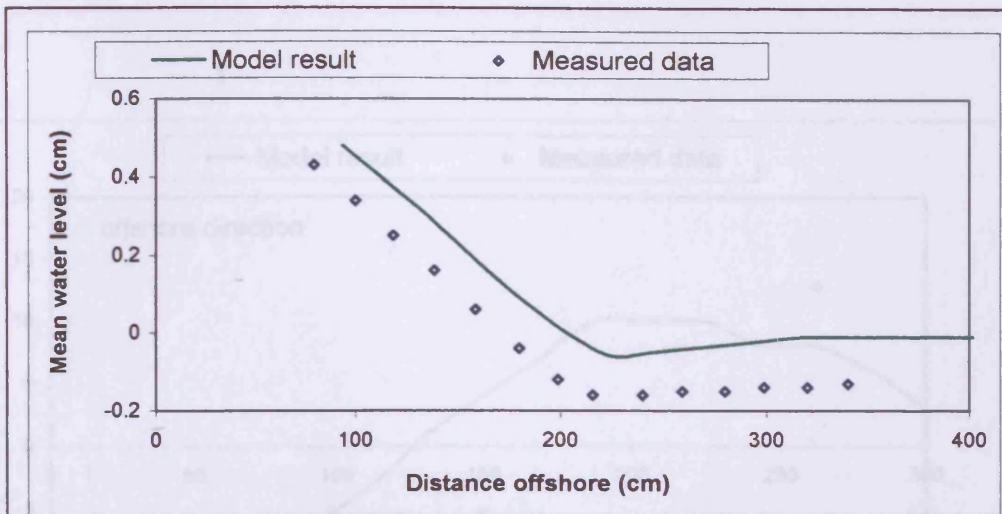
Figure 6.5.13 : Mean water level profile at line J=2 (expt.) for half-sinusoidal beach
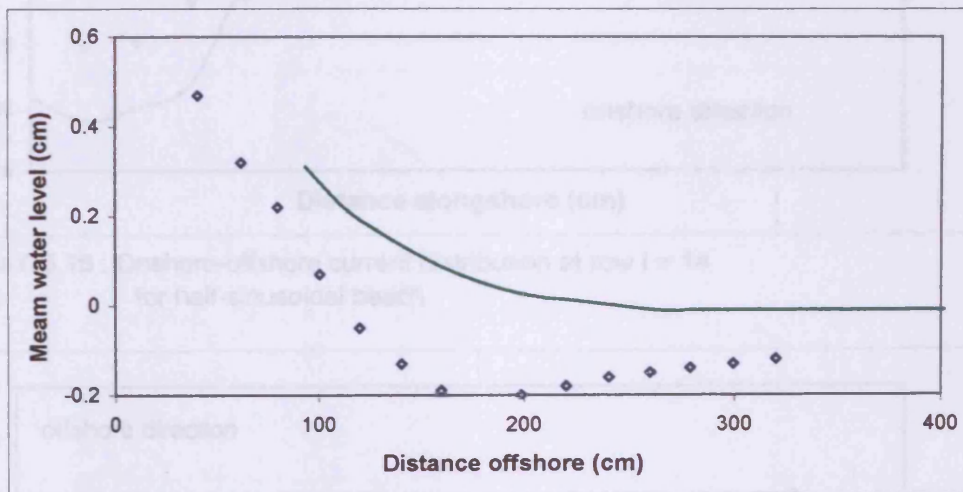

Figure 6.5.14 : Mean water level profile at the basin centre for half-sinusoidal beach
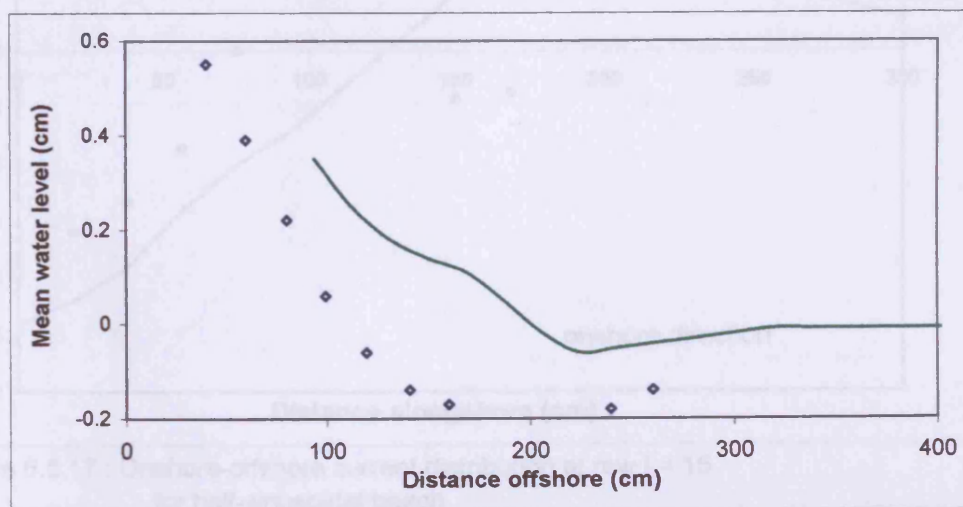
Figure 6.5.15 : Mean water level profile at line J=9 (expt.) for half-sinusoidal beach
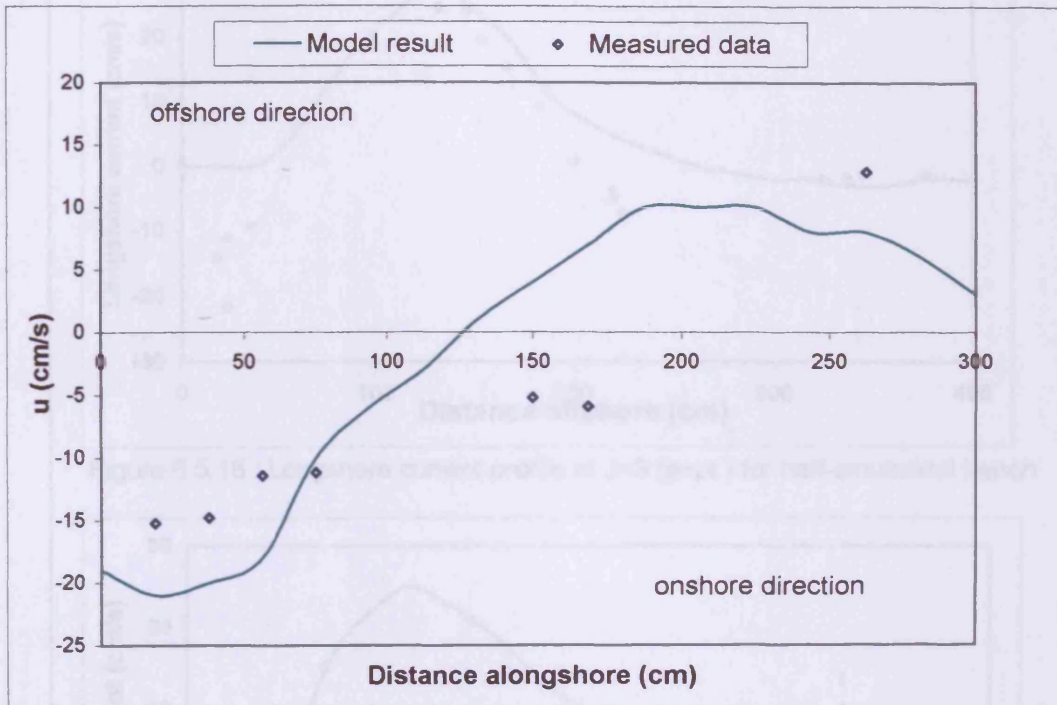
Figure 6.5.16 : Onshore-offshore current distribution at row I = 14
for half-sinusoidal beach
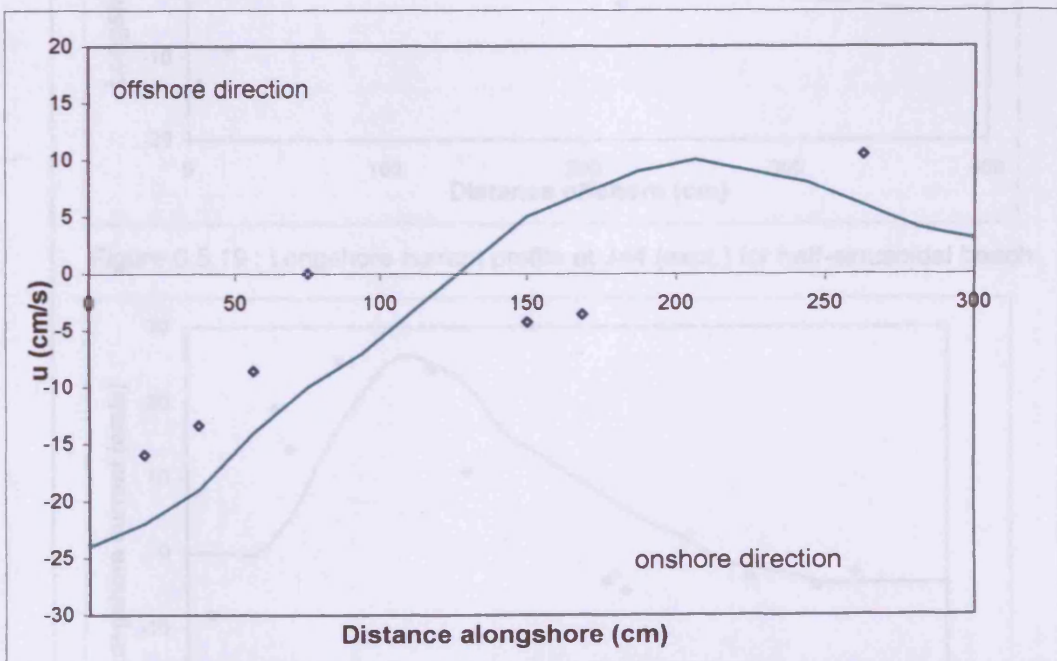
Figure 6.5.17 : Onshore-offshore current distribution at row I = 15
for half-sinusoidal beach
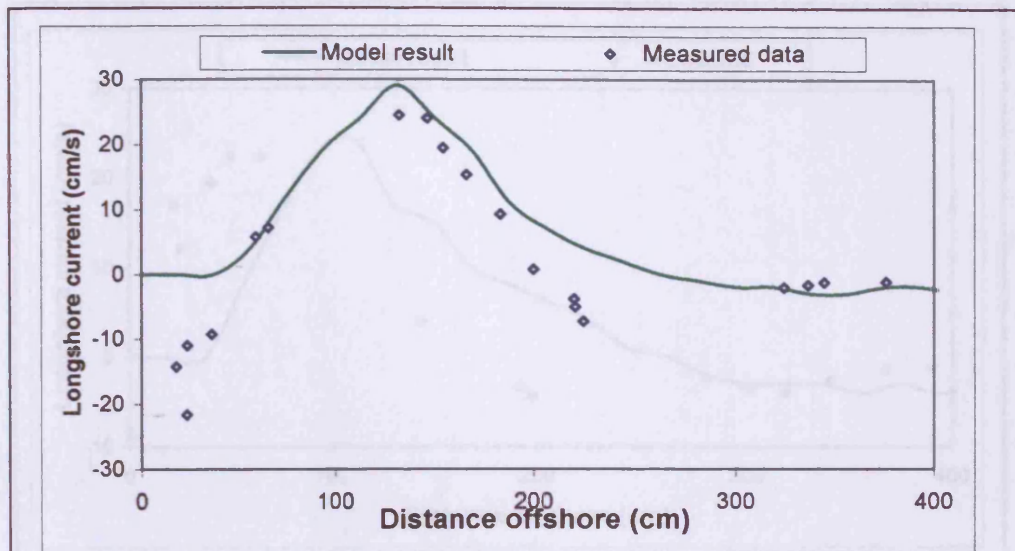
Figure 6.5.18 : Longshore current profile at J=3 (expt.) for half-sinusoidal beach
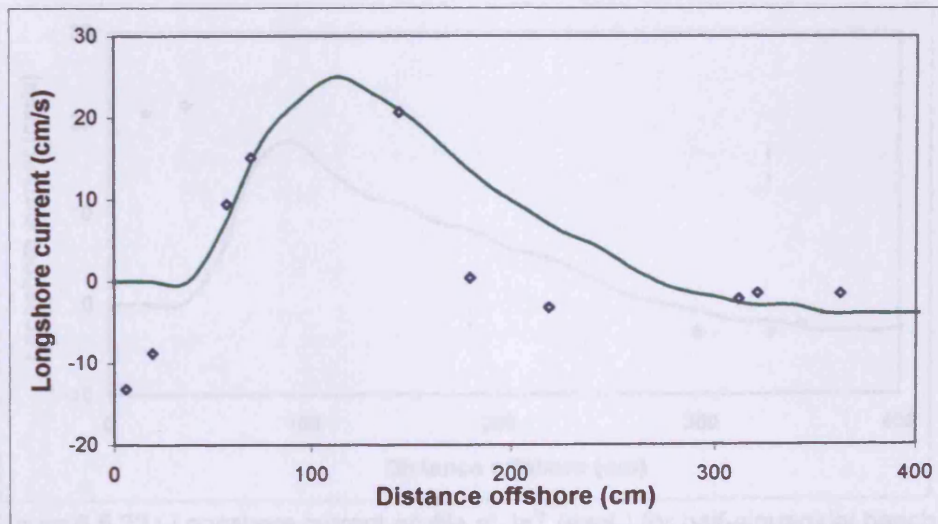
Figure 6.5.19 : Longshore current profile at J=4 (expt.) for half-sinusoidal beach
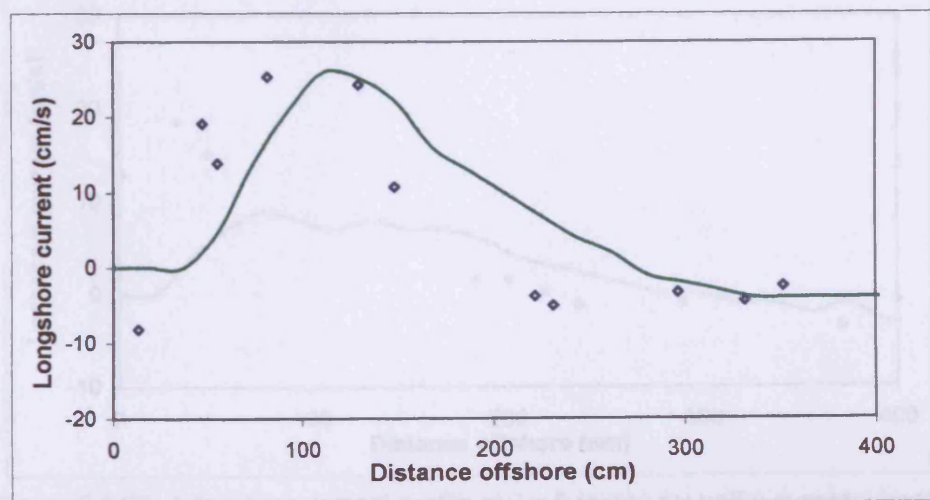
Figure 6.5.20 : Longshore current profile at J=5 (expt.) for half-sinusoidal beach
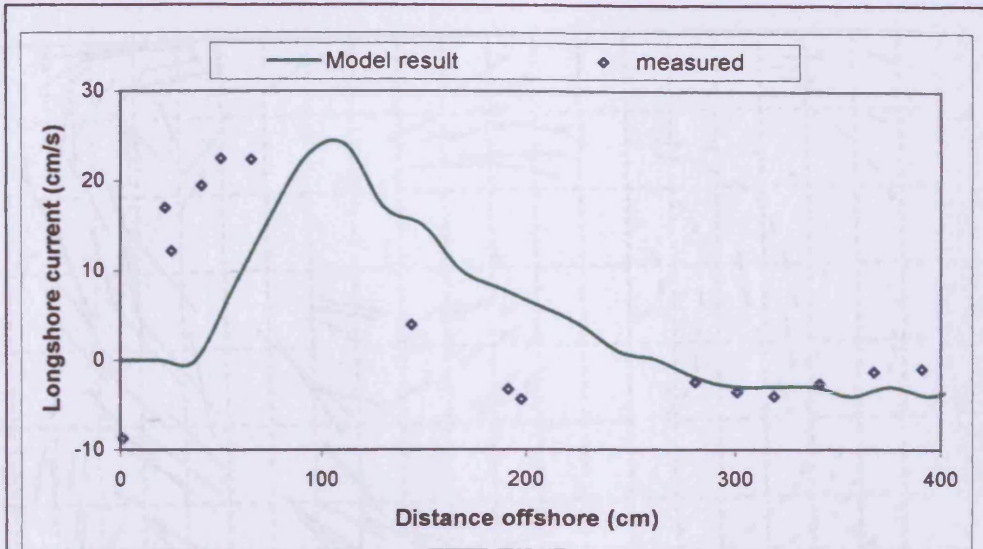
Figure 6.5.21 : Longshore current profile at J=6 (expt.) for half-sinusoidal beach
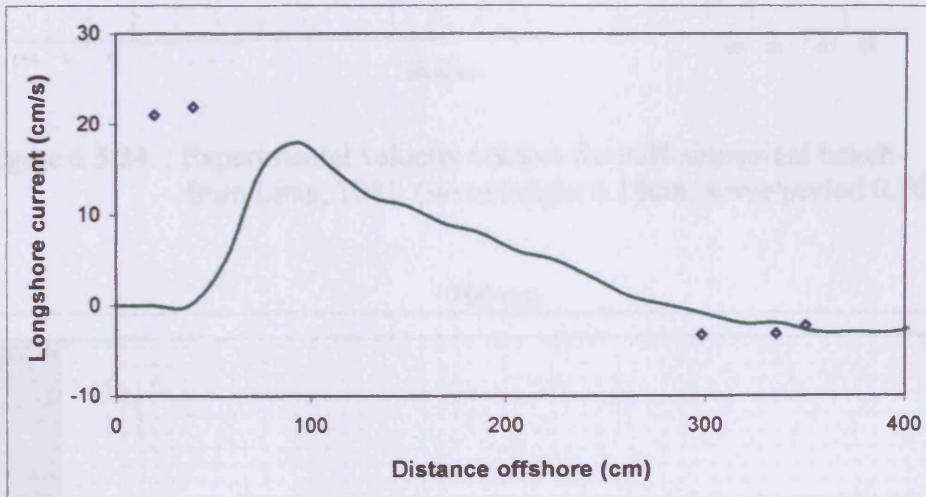
Figure 6.5.22 : Longshore current profile at J=7 (expt.) for half-sinusoidal beach
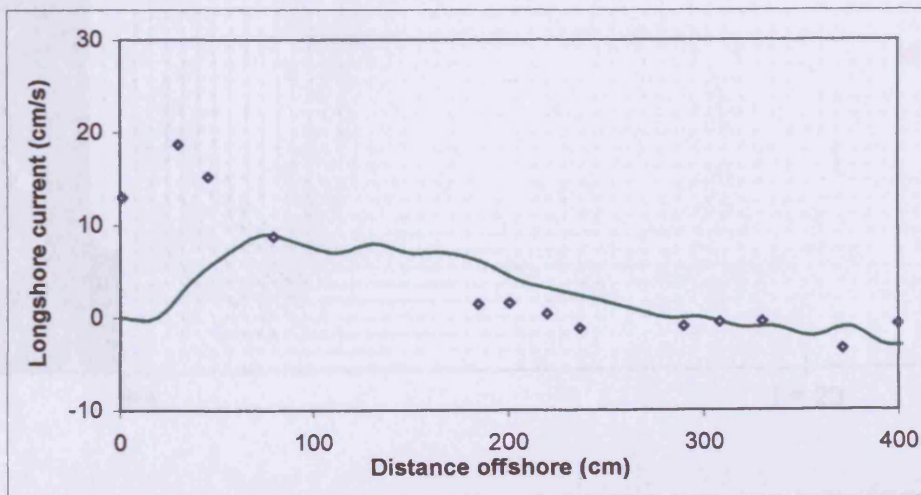
Figure 6.5.23 : Longshore current profile at J = 8 (expt.) for half-sinusoidal beach
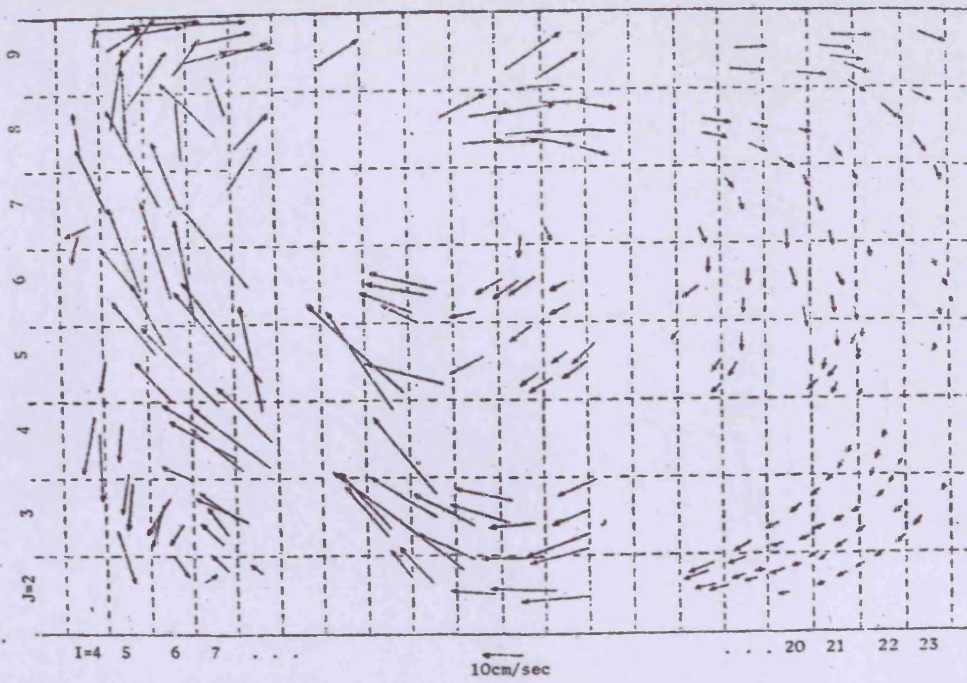
Figure 6.5.24. : Experimental velocity vectors for half-sinusoidal beach
from Lima, 1981. (wave height 6.18cm; wave period 0.76s)
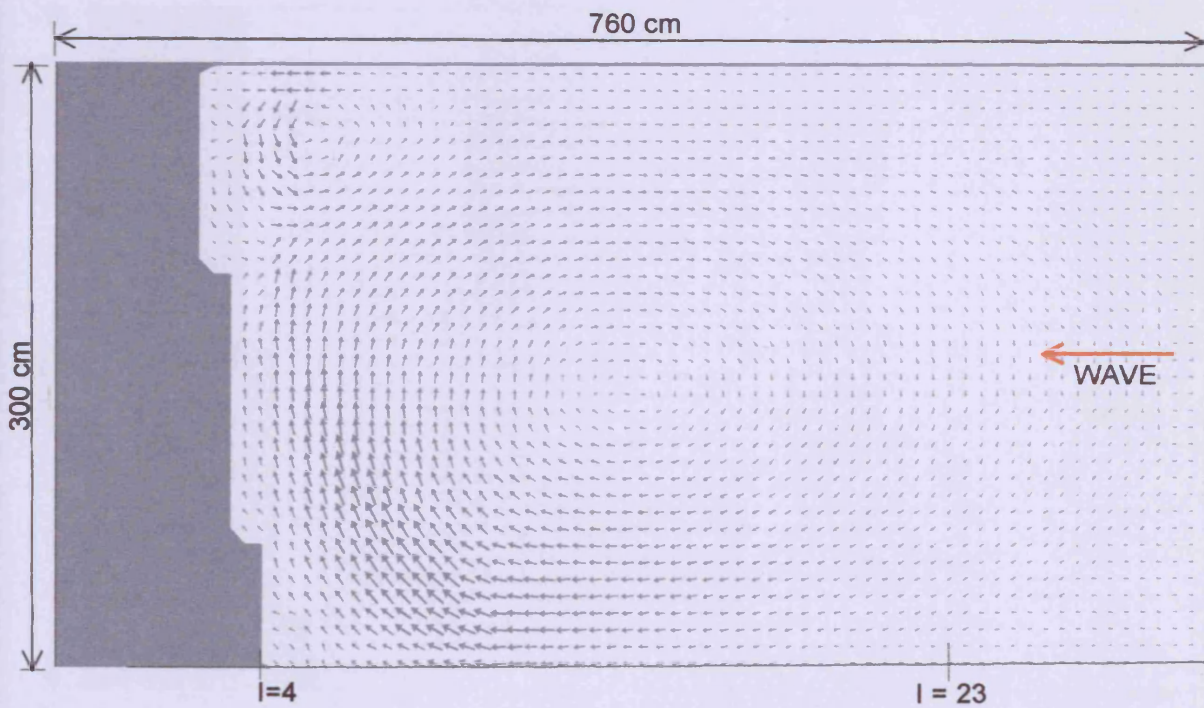
Figure 6.5.25 : Predicted velocity field for half-sinusoidal beach after 180s.
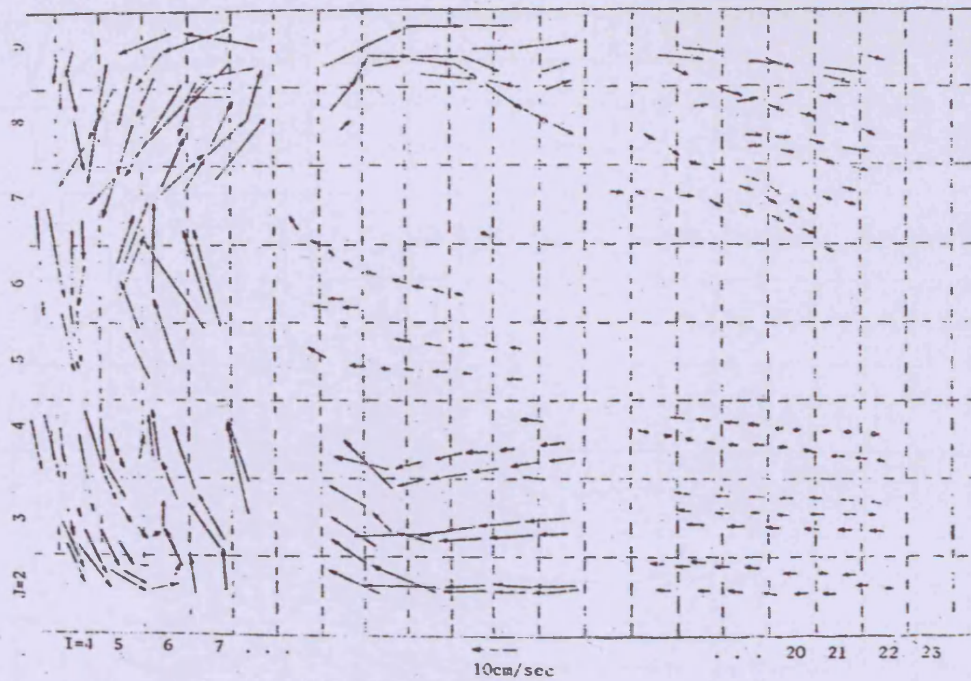
Figure 6.5.26 : Experimental velocity vectors for half-sinusoidal beach
from Lima, 1981. (wave height 4.17cm; wave period 1.04s)
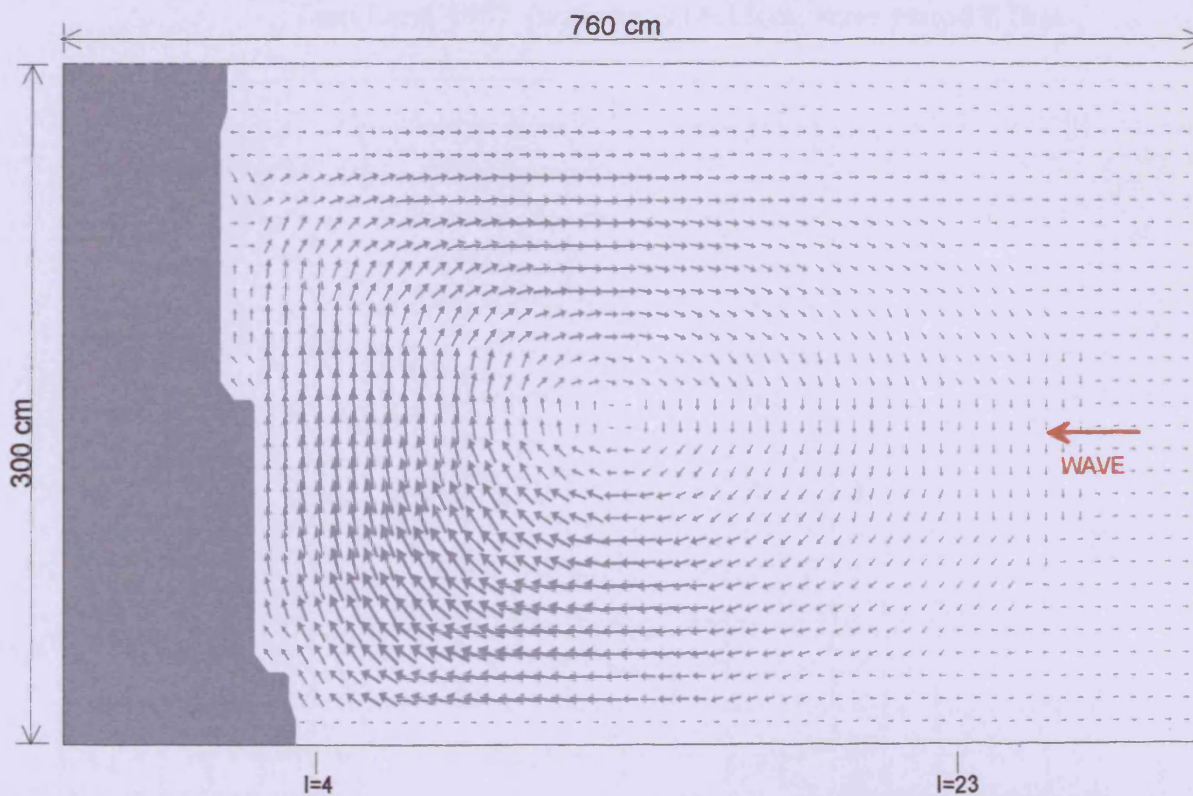
Figure 6.5.27 : Predicted velocity field for half-sinusoidal beach after 180s.
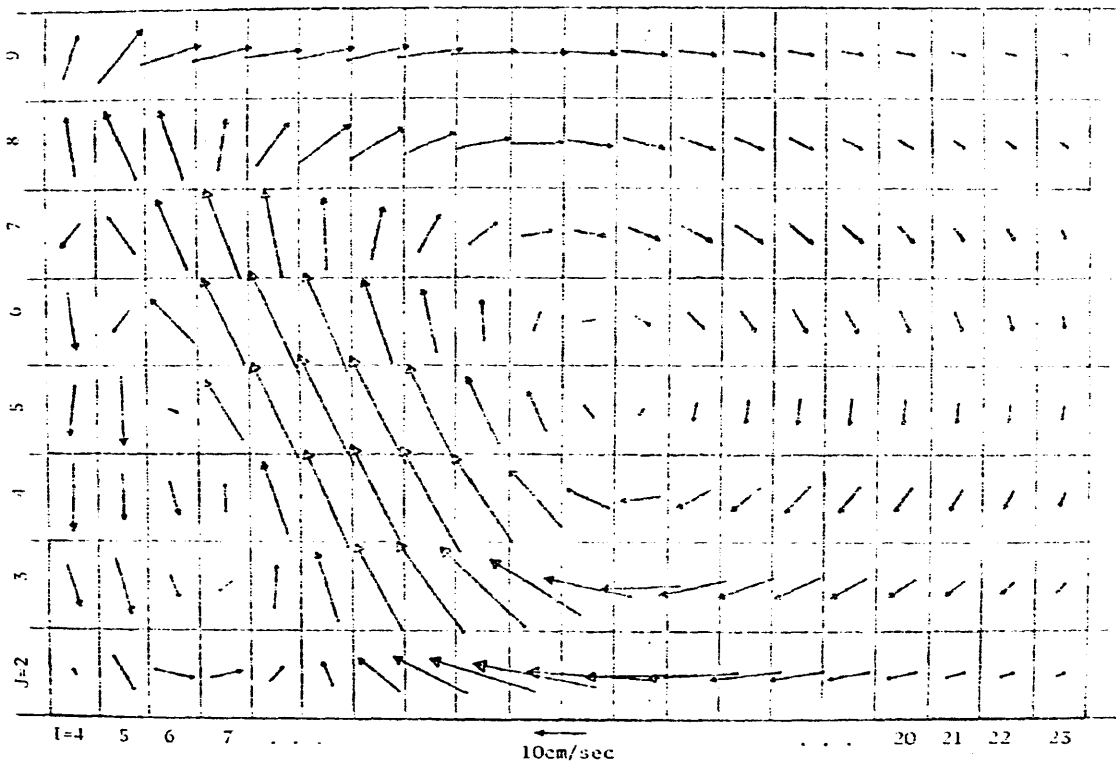
Figure 6.5.28 : Predicted velocity vectors for half-sinusoidal beach
from Lima, 1981. (wave height 6.18cm; wave period 0.76s)
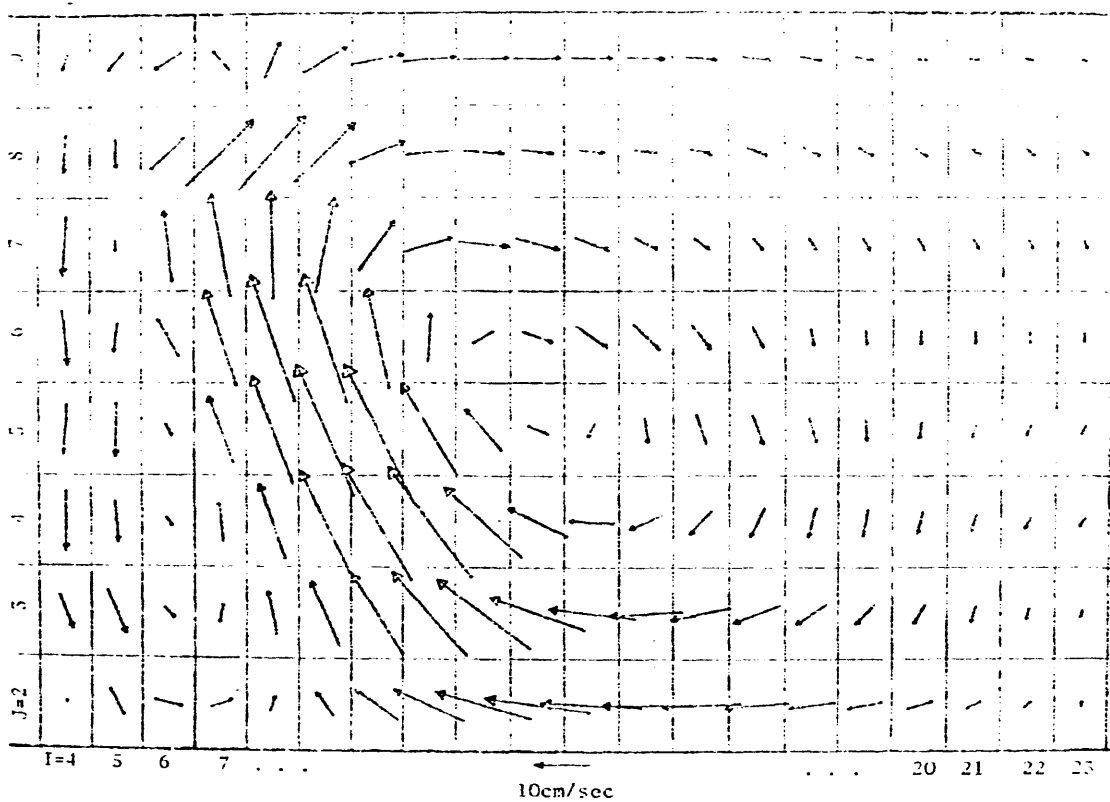
Figure 6.5.29 : Predicted velocity vectors for half-sinusoidal beach
from Lima, 1981. (wave height 4.17cm; wave period 1.04s)

6.6 Summary

This Chapter highlights the application of the wave-current model. The theoretically developed wave-current model based on the mild slope parabolic wave equation has been tested against published laboratory results. The behaviour and predictive accuracy of the wave model is generally satisfactory, but there is scope for improvement. Despite some of the discrepancies in the results, between the experimental and numerically predicted values in wave height, it can be said that the numerical model has predicted the nearshore flow circulation in a realistic manner. Detailed analysis of the cause for the discrepancies and the limitation of the parabolic wave model are given. The model could now be applied to laboratory or field experimental set-up, with all of these comparisons providing the necessary support to confirm the credibility of the wave-current model.

CHAPTER 7

WAVE MODEL APPLICATION

7.1   Introduction

The numerical model developed in this study for wave-current interaction (where wave and current interact at the same point with same or different directions) to evaluate the nearshore circulation processes (i.e. the velocity field and wave field) has been tested against the well-established documented data as reported in the previous chapter. Various types of model beach were considered, such as a flat plane beach, a sinusoidal beach, a three-cusp beach and a half-sinusoidal beach, but some of them was not in good agreement specially in the last case. In this chapter a new type of beach profile is numerically modelled and the predicted model results are compared with the corresponding experimental data set. The beach has a sinusoidal curve which is exposed as an inverse sinusoidal curve for wave attacks , as shown in Figure 7.1.2, at the face of the incident wave and the circulation pattern and resulting sediment transport rates were observed and reported in this chapter.

The advantages of laboratory experiments are many, and in particular they give rise to controlled conditions. Accurate measurements can be undertaken as accurately as possible with the development of highly sensitive equipment and more importantly, for the case of nearshore circulation, laboratory experiments reduce the cost in comparison with field investigations, which are relatively expensive. However, for nearshore investigations the laboratory experiments have some negative attributes

too. The perfect field conditions such as the beach orientation, the incoming wave impact, the boundary conditions and the sediment distribution etc. are all very difficult to generate precisely in a laboratory flume. Thus, it is very important that extensive care is taken when constructing the basin geometry and the boundaries, so that the designed wave current system is not significantly effected by scaling.

Much research has been undertaken in the past to develop theoretical models for nearshore circulation and those model results have often been compared with laboratory data, where the laboratory environment can simulates natural nearshore field conditions. The focus of each individual study has been different, however it is still difficult to find inclusive solutions for particular nearshore circulation field. The theoretical model developed in this study has been based on a parabolic mild slope equation for large angle incident waves (Booij, 1981). The wave parameters, including the wave height, period and angle, were determined at every grid point specified in the model, and with the magnitude and direction of the longshore and cross-shore currents also being calculated. The net sediment transport can also be predicted using this model. Bed level changes and comparisons of the model and laboratory bed level changes are also reported in this chapter. The laboratory experiments, considered in this study provided data of bed level changes with time, with the longshore and cross-shore velocities at specific locations (see Figure 7.1.2) and changes in the wave height also being predicted at specific sites.

7.2   Experimental Set-Up

To validate the wave-current model developed in this study for nearshore circulation, experimental data were obtained from laboratory work undertaken in Hannover University, Germany. An extensive experimental programme was performed (Anastioanis, 2003) on an inversely sinusoidal beach, for different wave conditions and beach material. In this study only one type of beach condition will be
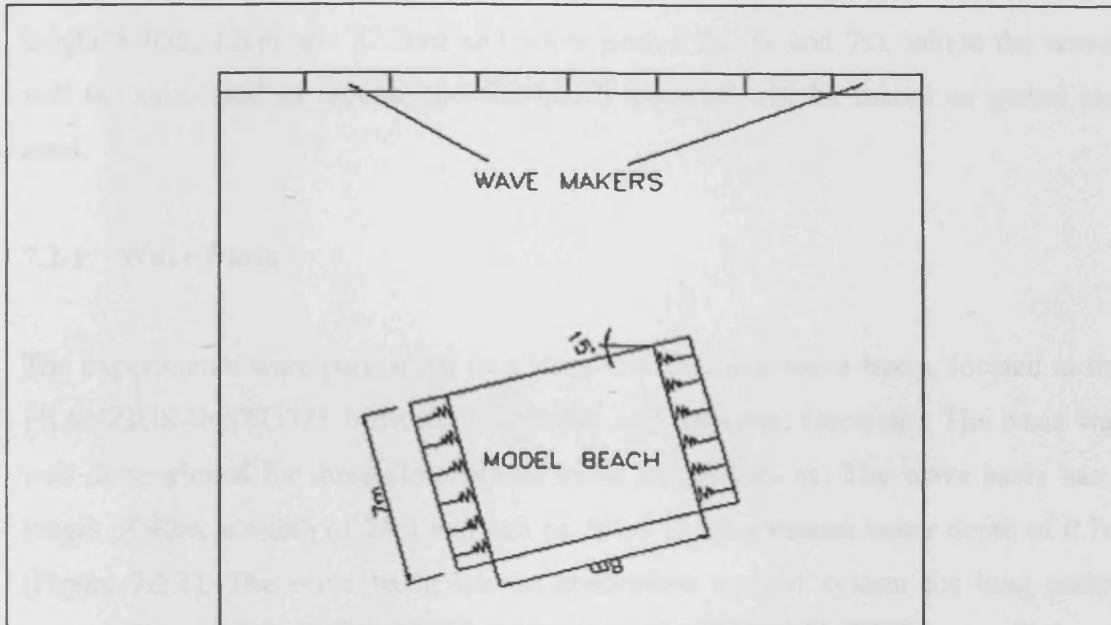
Figure 7.1.1. Experimental set up of the wave basin
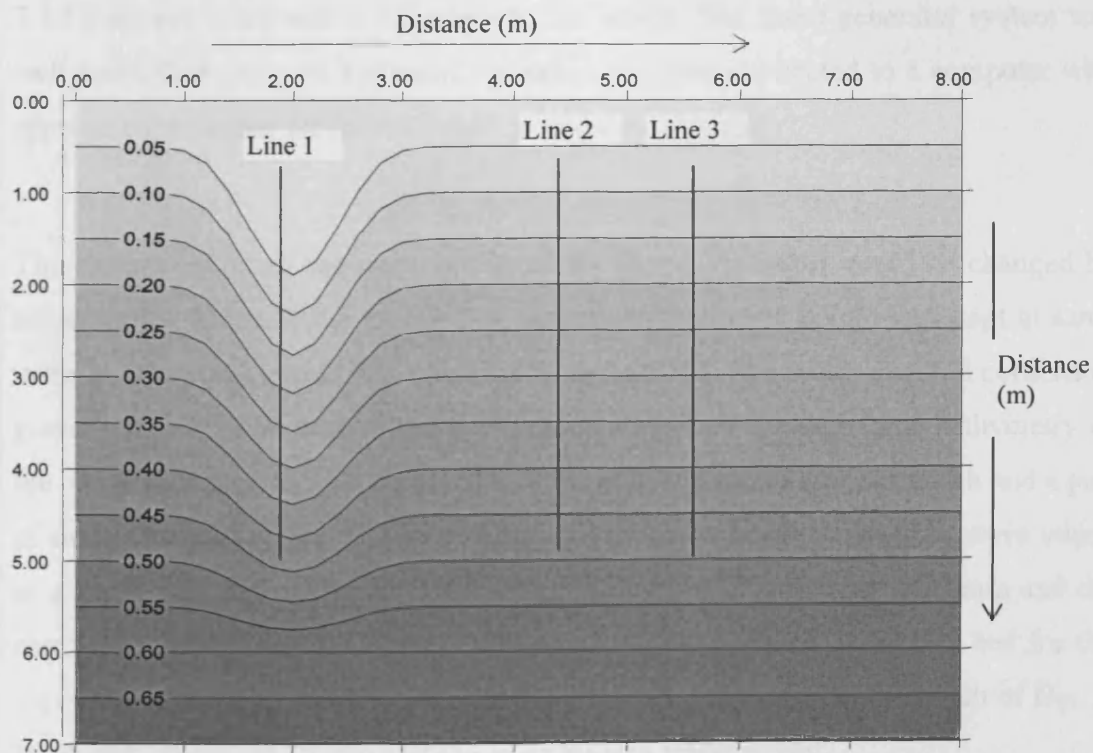
Figure 7.1.2: Bed levels of the experimental beach

compared (experiment was undertaken for regular and irregular waves, for wave height 8.4cm, 12cm and 22.2cm and wave period 2s, 3s and 7s), where the waves will be considered as regular and the beach material will be mixed as gravel and sand.

7.2.1 Wave Basin

The experiments were performed in a three-dimensional wave basin, located at the FRANZIUS-INSTITUT Institute, University of Hannover, Germany. The basin was well dimensioned for three-dimensional swell investigations. The wave basin has a length of 40m, a width of 24m and can be filled to a maximum water depth of 0.7m (Figure 7.2.1). The wave basin has an absorption control system for long period waves. The wave machine can generate waves with wave heights varying upto 0.45m, with an approximate wave period of 2.2 s, and for a water level of 0.7m. The beach was oriented in such a way that waves generated by the wave maker (Figure 7.1.1), always came with a 15^0 angle to the beach. The wave generator system was well controlled using oil hydraulic cylinders and was connected to a computer with appropriate software for data acquisition and data storage.

The characteristics of the wave produced by the wave maker could be changed by adjusting the speed of the motor. For this study, the wave height was kept at same value but the wave period was changed by the paddle. The beach material consists of gravel and sand, which gave the appearance of a natural beach. The bathymetry of the beach (Figure 7.1.2) consisted of a straight-line parallel contour beach and a part of sinusoidal curved beach. The sloping curved section was exposed to wave attack as a depressed section (Figure 7.4.3). The size of the gravel was 10-30 mm and the size of the sand was 0.1 – 0.5 mm. The bed was considered as mobile bed for the experiments. A sieve analysis produced a value for the mixed mode beach of D_{15} = 16.66mm, D_{50} = 22.76 mm and D_{85} = 28.86 mm respectively.
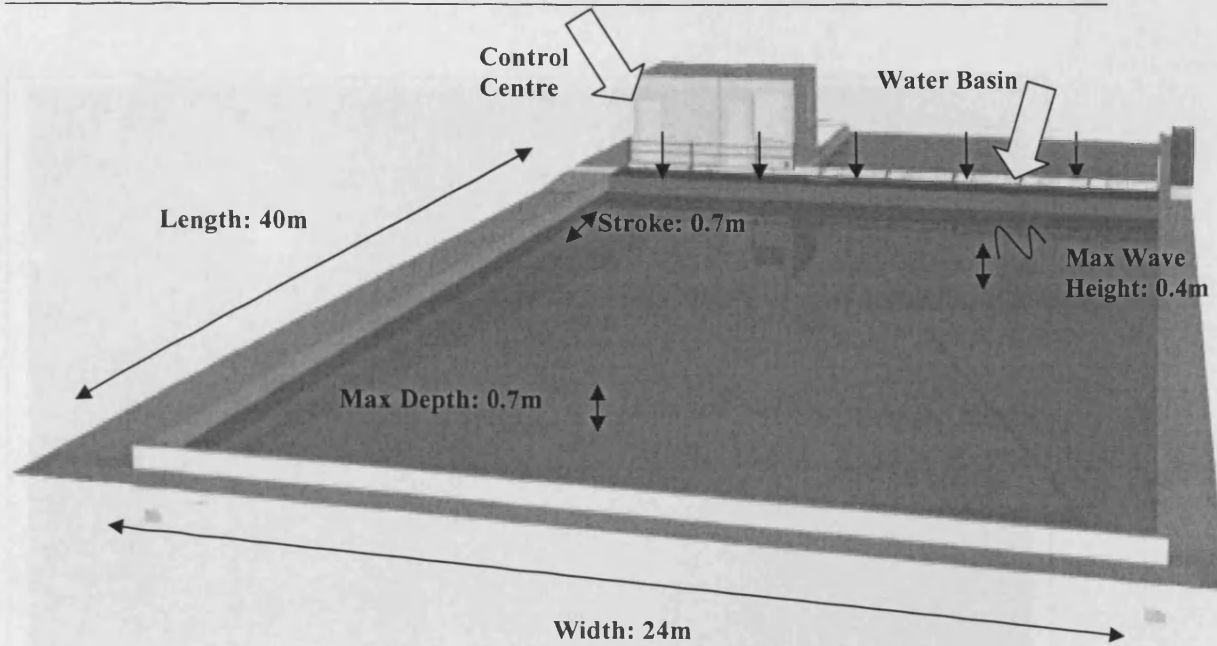
Figure 7.2.1: Dimensions of the wave basin

The model beach was constructed in the middle of the wave basin. The model beach was open to the site from which the generated waves were coming, was treated as an open flow boundary (mathemaical expression given in equation 4.7.3 and 4.7.4). The other three sides of the beach were considered differently. When the generated waves approaches shoreline and wave breaking occurred in the breaker zone, then a large amount of energy was dissipated. Both the bed material and the sides of the model beach were able to withstand the impact of wave breaking. Due to this reason the three sides of the model beach (left, right and rear side) were reinforced. The rear site was constructed so that wave run up could not pass the boundary (i.e. Figure 7.2.2 and Figure 7.2.3). There was some wave reflection generated from this area. For the other two sides (i.e. left and right) the reinforcement was done in three (3) layers, in step wise fashion, to provide a solid boundary with free movement of water across the boundary (water elevation boundary, eqn 4.7.4). After different test runs the reinforcement pattern was chosen which would provide the stability of the model beach during the smooth running of the experiment. Some additional structures were built outside the model beach, and within the wave basin, to make the whole system more stable and a pathway was made through the basin to access the data and observe wave breaking and sediment movement.

Figure 7.2.2: Details of the boundary in the rear side of the experimental beach

Figure 7.2.3: Details of boundary at side of the experimental beach

After construction of the model beach, with the stable wave generating system, the specific generation of waves was started with well defined parameters. Different instruments were used to take the various measurements. An ADV (Acoustic Doppler Velocimeter) was used to collect velocity data and 6 GHM (Wave Height Meter) was used to collect wave height data. Six wave gauges were set up in the wave basin (Figure 7.2.1) to measure the wave height and period. The ADV was used to measure wave driven currents and bed levels at line 1, line 2 and line 3 at specified times.

The wave height meter (GHM) was designed to measure the dynamic fluid level at any instant, so it was used to measure wave heights for this experiment. The probe of the GHM was attached to a point gauge for calibration and to get a fixed position for measurements. The water depth should be chosen in such a way that during calibration and also at the measuring time the top of the reference electrode would be at least 4cm below the water surface. While several wave height meters (GHM) were placed close to each other, some influence occurred on the measurements of each other. But for this study the distances were more than 20cm, and so the imposed influences were neglected.

The ADV current meter was developed to measure accurately three-dimensional dynamic fluid flow in physical models and practical field applications. An ADV is a simple measuring device, which can provide a continuous digital record of the velocity at specified sampling rates. The ADV consists of four specific parts: the ADV sensor which consists of two/three acoustic receivers and transmitters, the ADV probe, which is connected to the ADV signal, the ADV signal conditioning module held by the receiver, and the ADV processor connected to the ADV signal processor by high frequency cable and also a PC card.

The measurements of the water level and bed profile were done at the middle part of the model beach. The measurements were not taken near the side boundaries, as it was thought that some reflective waves might effect the measuring technique. Another important issue was to achieve stable and steady state of flow to take the measurements. When the wave generator was first switched on, it took some time to

obtain steady state conditions. So the measurements were not taken until after 5 minutes of wave simulation.

7.3   Numerical Model Set Up

The experimental set-up described in the previous section provided detailed data for different wave heights, wave periods and bed material combinations. A numerical model was set-up to replicate these experiments with the aim being to evaluate the accuracy of the model. The bed material considered as one of mixed gravel and sand. Regular wave conditions were considered and the wave height was taken to be 8.4cm, which corresponded the case of the experimental set up. Two test cases have been considered for wave period, the first one referred to as 'test case I' was for a wave period of 3 s and the later referred to as 'test case II' for a period of 2 s.

By considering the bathymetry used in the experimental beach, the numerical domain was set up to replicate this profile as accurate as possible. To avoid reflection (as the numerical model is based on mild slope equation which do not include wave reflection) of wave along the beach the model was extended 4m in the numerical model (Figure 7.3.1). Also along the cross-shore direction the plane beach was extended a further 3m on the offshore side to provide smooth conditions for the numerical incident wave. The slope of the beach was adjusted so that propagation and wave breaking were smooth and a parabolic wave equation could be utilised properly. The beach profile can be summarised as follows:

$$h(x, y) = sx \qquad \text{for } 0 \leq x \leq 5 \text{ m and } 7\text{m} \leq x \leq 12\text{m}$$

$$(7.3.1)$$

$$h(x, y) = s\left[1.0 - \cos\left(\frac{2\pi(x(i) - (10 * dx))}{(20 * dx)}\right)\right] * 1.5 \qquad \text{for } 5\text{m} \leq x \leq 7 \text{ m}$$

$$(7.3.2)$$

where, s = slope = 0.01

$x(i)$ = distance from origin for longshore distance

dx = 0.1m, grid spacing

Longshore Distance (m)

1   2   3   4   5   6   7   8   9   10   11   12

Cross-shore Distance (m)

1

2

Line 3   Line2   Line 1

3   Line 4

4

5   Line 5

6

0.45

0.35

0.25

0.15

0.05

7

Experimental Beach Boundary

8

9

10
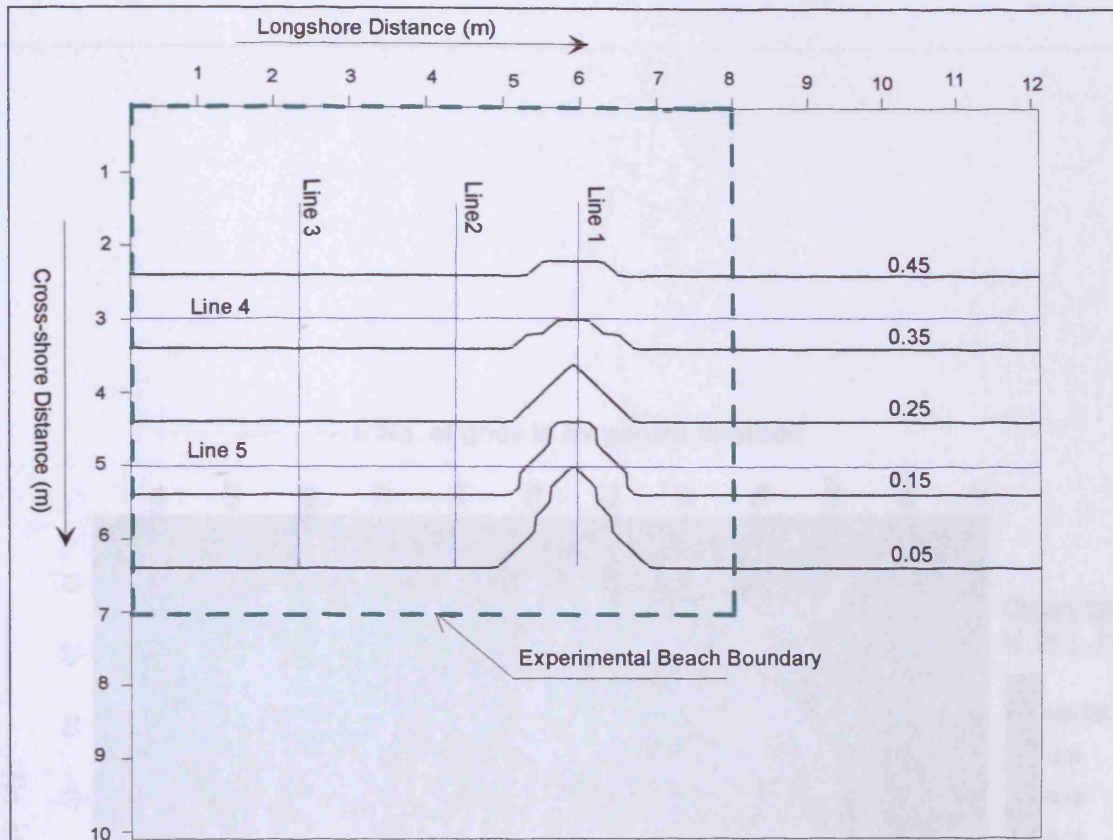
Figure 7.3.1: Numerical model set-up with experimental beach

No of Grids in Longshore Direction

10   20   30   40   50   60   70   80   90   100   110   120

x, I

Grid size: 0.1m x 0.1m

10

20

0.45

30

0.35

40

0.25

50

0.15

60

0.05

70

No of Grids in Cross-shore Direction

80   Water Elevation Boundary

90

100   Open Boundary
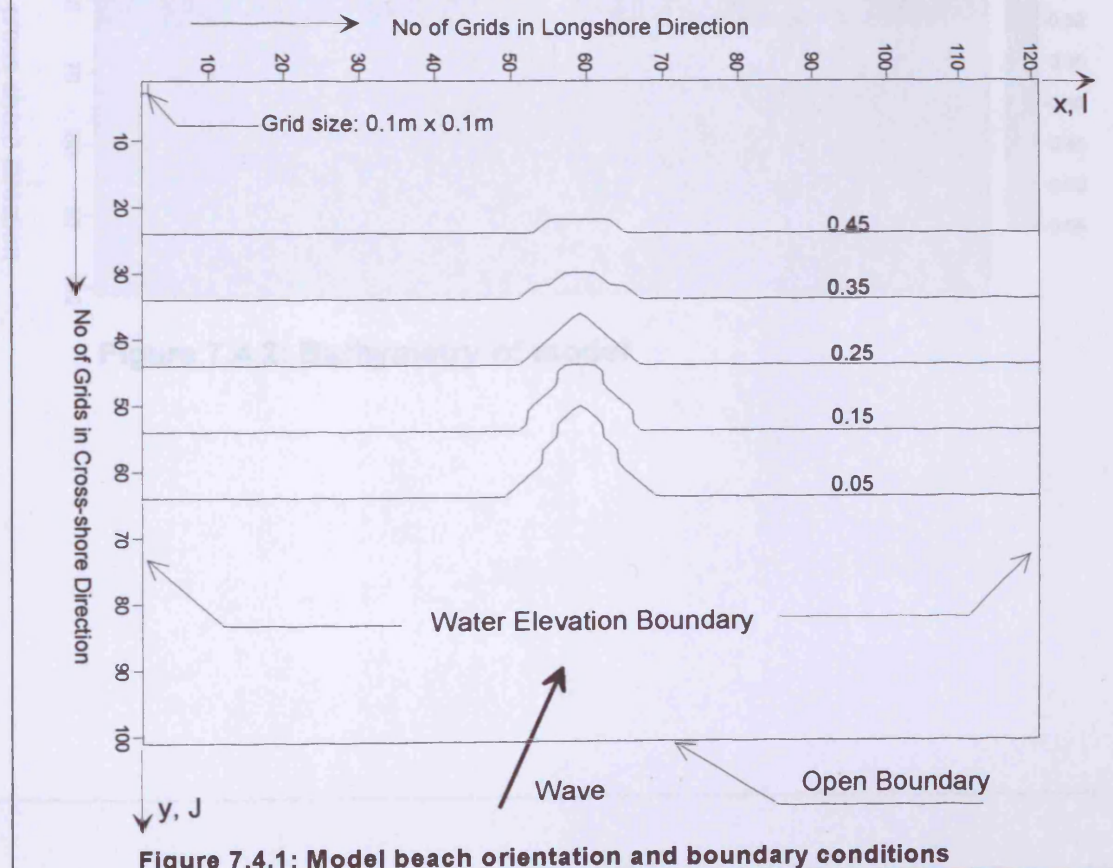
y, J   Wave

Figure 7.4.1: Model beach orientation and boundary conditions
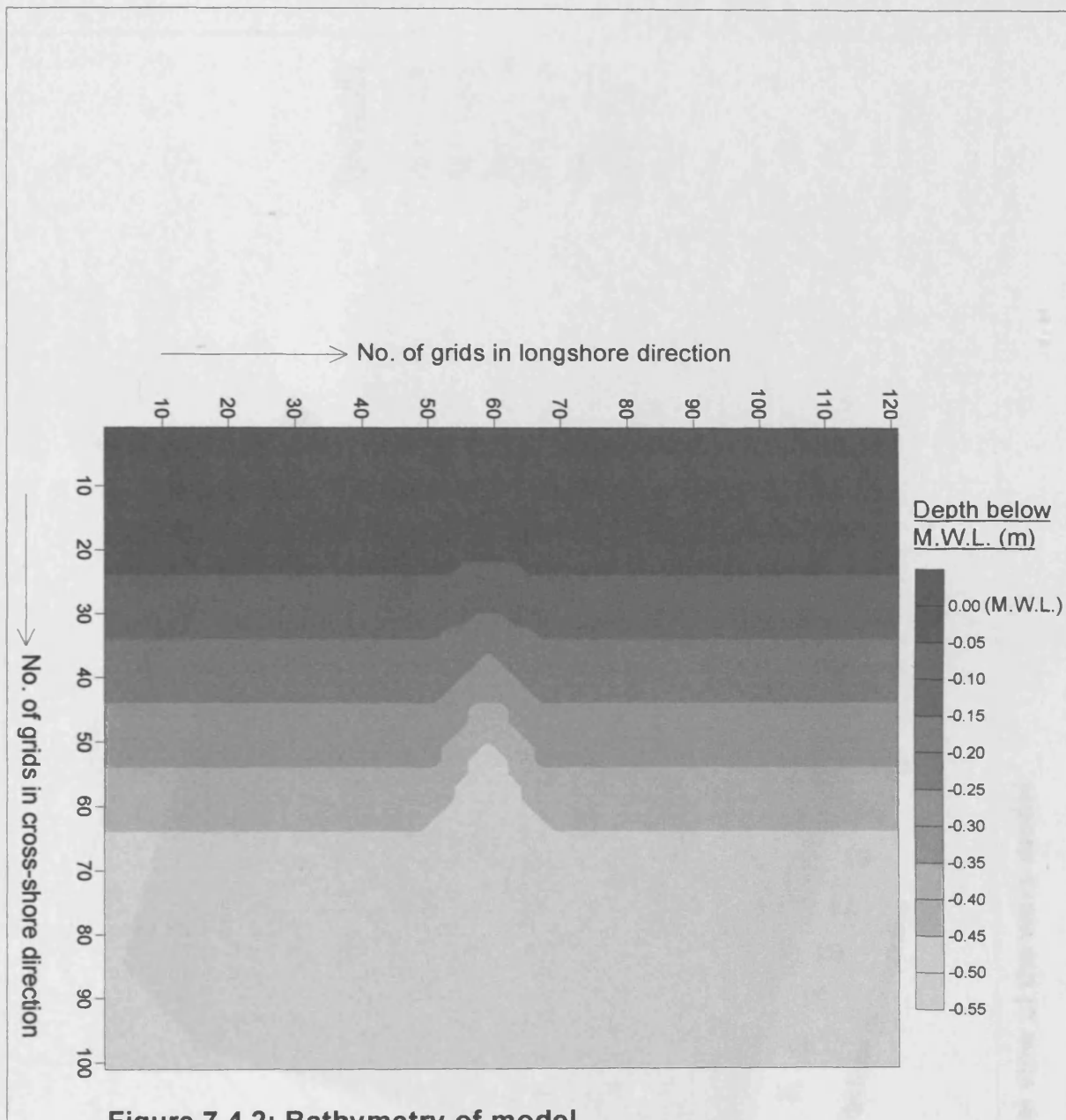
Figure 7.4.2: Bathymetry of model
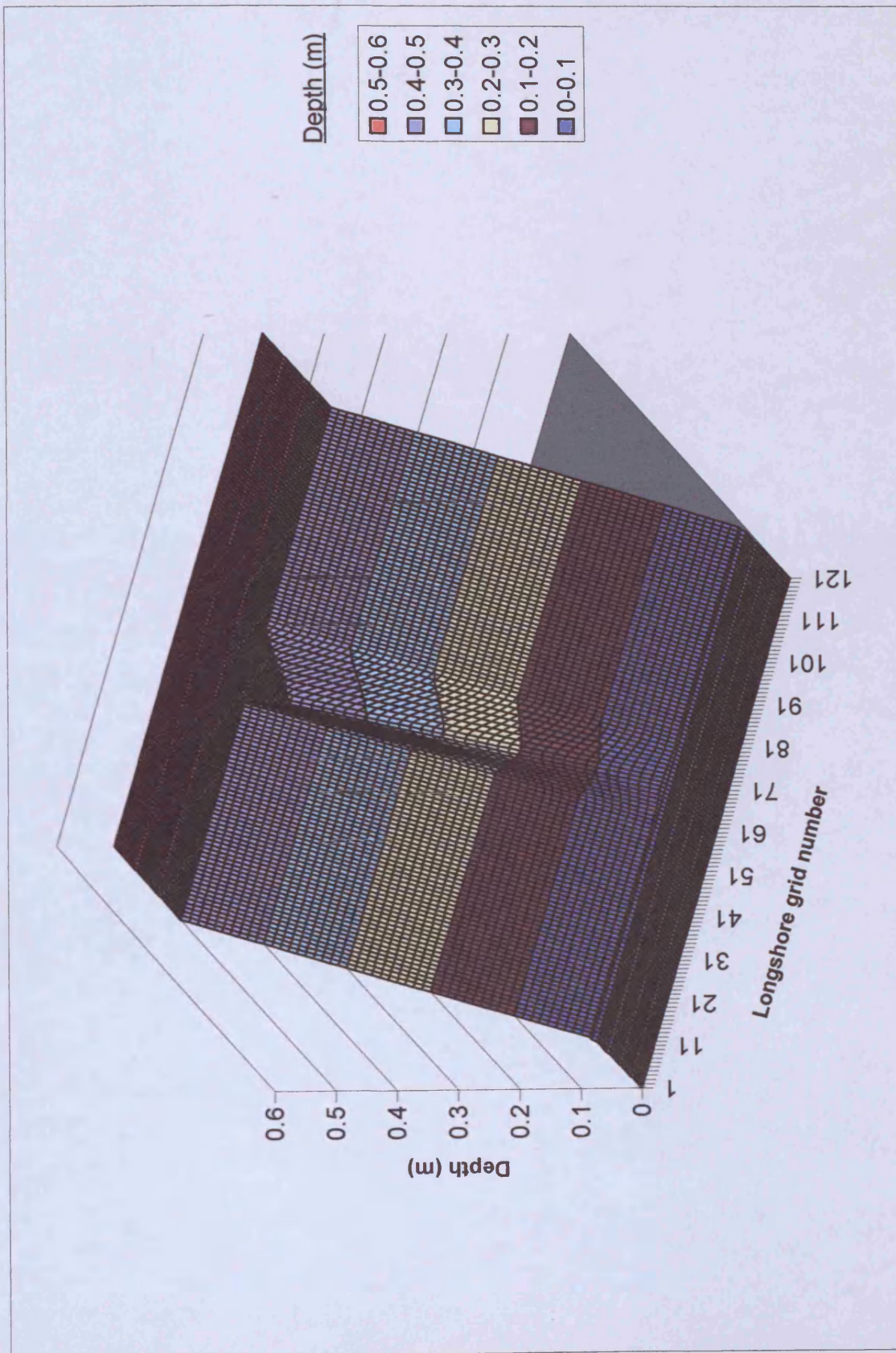
Figure 7.4.3: Three-dimensional view of the wave model

The still water depth was kept constant at 0.5 m giving enough space for wave run up and energy dissipation. The mesh size was considered in such a way that the experimental measurement lines coincided with the model grid and without the need to super impose adjacent grid results. The numerical model domain covered 120 columns and 100 rows and had a mesh size of 0.1m x 0.1m. The grid mesh size was independent of the bed slope and was tested against the stability criteria (Figure 7.4.1).

The numerical model was based on mild slope parabolic wave equation (which can take care of large wave incidence angle). The numerical scheme was based on an implicit finite difference scheme, which meant that the scheme would be unconditionally stable with mesh size and time step increment. The case for regular waves approaching the beach at an angle was considered in this part of study, with the wave input data being: deep water wave height of 0.084m, incident wave angle of 195^0, wave period for test case I of 3 s and for test case II of 2 s. The time increment used to run the model was 0.25 s and the grid size was 0.1 m for wave parameter determination, and 0.2m for the hydrodynamic part.

7.4   Results

The numerical model was run for the input data used in the experimental procedure. There were different parameters to run the experiments, and the parameters were changed to provide distinct test cases, such as: regular waves, irregular waves, gravel bed, sand and gravel bed, different wave heights etc. However, for this research study, two test cases were selected to evaluate the numerical model. The wave height was set to 8.4 cm since this wave height gave sediment movement in the experiments. The wave angle was fixed at 195^0 as the model basin was oriented by 15^0 to the wave generator. For test case I, the wave period was selected as T = 3 s and for test case II it was T = 2 s, based on the maximum wave period the generator could produce. The slope of the basin and the straight part was 0.01 and this was considered to be a mild slope for wave breaking.

Table 7.4.1 : Test cases run for model simulation

	Wave height (cm)	Wave period (sec)	Wave angle (deg)
Test Case I	8.4	3	195
Test Case II	8.4	2	195

The wave induced velocity generated by the incoming waves was measured in the experimental set-up at three specific locations, and identified as line 1, line 2 and line 3. The position and location of these lines in the laboratory wave basin are illustrated in Figure 7.3.1. The orientation of the grid cell, boundary location and grid size are illustrated in Figure 7.4.1, with the dotted lines representing the experimental set-up boundary. The numerical set up was extended in the direction of the longshore current to avoid the reflection of waves from near to the boundary of the depressed bathymetry.

The rear boundary was closed, as wave run up cannot reach the end point, and the concrete wall acted effectively as a solid boundary. The left and right side boundaries of the numerical basin were treated as water elevation boundaries (equation 4.7.4 and 4.7.5), which meant that the water level was kept the same at both sides of the boundary and the current velocity also had the same value. Figure 7.4.2 described the bathymetry of the model beach for numerical computation. The bed height was a maximum of 0.5m above the model beach as the mean water level was set to 0.5m. Enough cross-shore space was provided for the experimental set up and the numerical model to release the breaking energy and to observe the wave breaking phenomenon completely.

For test case I, the experimental set up was run for 23,700 s, i.e. nearly 6.58 hr. The data were not recorded just after starting the wave generator, at least 5 minutes of lapse time was assumed to ensure steady state conditions of the mild slope wave generation. The experimental data were collected throughout the run time and averaged of every 60s before comparison. The depth averaged velocities were evaluated at each measuring point. Comparisons were undertaken for horizontal

velocities for the longshore and cross-shore current directions. For test case II, the experimental set up was run for 24,000s, corresponding to nearly 6.67 hr and a similar test procedure was adopted to that for test case I.

7.4.1 Sensitivity Test for Velocity Field

There are various hydrodynamic parameters responsible for the sensitivity of the numerical model predictions. The model results obtained with specific parameters (e.g. eddy viscosity co-efficient, friction co-efficient, breaking index) were compared with the laboratory results or field data, and the parameter values which produced the closest agreement with the data were treated as the 'model parameters' for that specific laboratory or field study comparison. The laboratory results considered in this study were compared with the model predictions by changing the various hydrodynamic parameters. For the hydrodynamic part of the model, the changing parameters for the sensitivity tests were the friction coefficient, bed roughness and breaking index, which all affects the velocity and sediment concentration distributions. There was no means of measuring directly the friction coefficient in the laboratory experiments, but values were assumed based on empirical relationships and also on the bed material characteristics. For the numerical model simulations, there was a scope for establishing the effect of changing the friction coefficient, C_f (for wave related shear stress) on the velocity and wave-breaking phenomena by considering different friction values within the bounds of those values most closely related to the field conditions. Another important parameter is the bottom roughness height, k_s (for hydrodynamic calculations) which effects the velocity distribution and the water depth. The roughness coefficient was changed in the model runs, and the value, which gave the closest agreement with the field or experimental data was used in subsequent simulations. The other parameter taken into consideration in this study was the breaking index, γ_b for breaking waves. The effect of different values of γ_b (equation 3.4.82 in chapter 3) was studied in the model predictions.

The model predictions were commenced for T = 3 s (test case I) data, and the other parameters were chosen as: γ_b = 0.78 (according to Weggel, 1972), the bottom roughness height k_s = 30mm (based on sand gravel mean diameter), and the friction coefficient as C_f = 0.01 (based on Lima, 1981). The results for line 2 are presented in Figures 7.4.4 and 7.4.5. It was observed from the longshore and cross-shore current profiles that the model results predicted higher values than those measured in the laboratory, but the velocity directions matched the field conditions. At the breaking point the model peak was higher than laboratory observations, although the location of the wave breaking was compatible with both sets of data. So further tests run were therefore needed to acquire better comparisons between the magnitude of the velocities.

The next model run was made by changing the bed roughness height. The value was changed to k_s = 20mm (D_{50} =22.26mm) (the value is taken as $k_s \cong D_{50}$ not k_s = 2.5D_{50} as it was found that with this wave height and period only the sand has the movement, the gravel did not move with time) and the effect is shown in Figures 7.4.6 and 7.4.7. The velocity magnitude reduced and a clear wave breaking location was observed with higher peak. Subsequently, the friction coefficient was increased to C_f = 0.06 and the results are shown in Figures 7.4.8 and 7.4.9. The velocity magnitude produced better correlation, but after wave breaking a higher magnitude was predicted as the location of wave breaking was close. After changing the frictional and roughness coefficients and observing their effects on the current magnitude, it was then appropriate to change the breaking index. The value γ_b was then changed to 0.64 and the effect is illustrated in Figures 7.4.10 and 7.4.11. A comparison of velocities gave much better results and also showed that the location of wave breaking gave better agreement. The parameter, γ_b was then changed to a value of 0.5 and the model re-run. This run was found to be giving the best comparisons between the model predictions and laboratory measurements. Figures 7.4.12 –7.4.13 showed results for this case.

After changing the model parameters, the velocity profiles, both magnitude and direction, and the location of wave breaking were all observed. The model was run

Figure 7.4.4 : Cross-shore velocity for test case I, line 2

Figure 7.4.5 : Longshore velocity for test case I, line 2
(k_s = 30mm; C_f = 0.01; γ_b = 0.78)

Figure 7.4.6 : Cross-shore velocity for test case I, line 2

Figure 7.4.7 : Longshore velocity for test case I, line 2
(k_s = 20mm; C_f = 0.01; γ_b = 0.78)

Figure 7.4.8 : Cross-shore velocity for test case I, line 2

Figure 7.4.9 : Longshore velocity for test case I, line 2
$(k_s = 20\text{mm}; C_f = 0.06; \gamma_b = 0.78)$

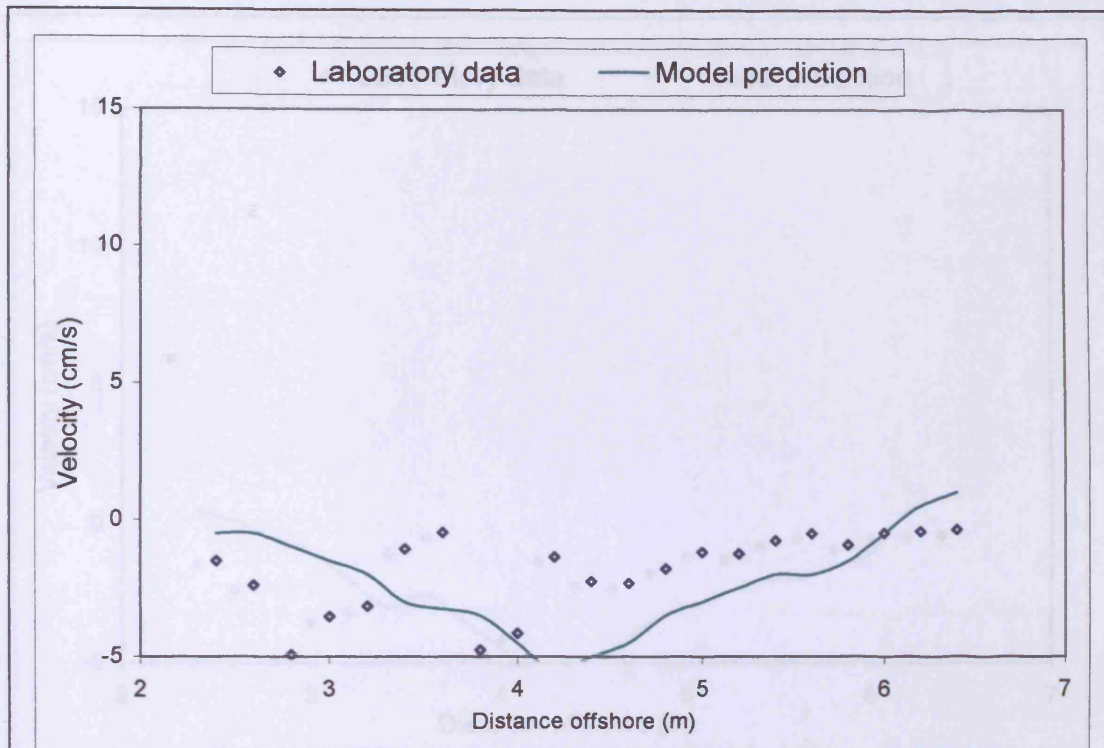Figure 7.4.10 : Cross-shore velocity for test case I, line 2
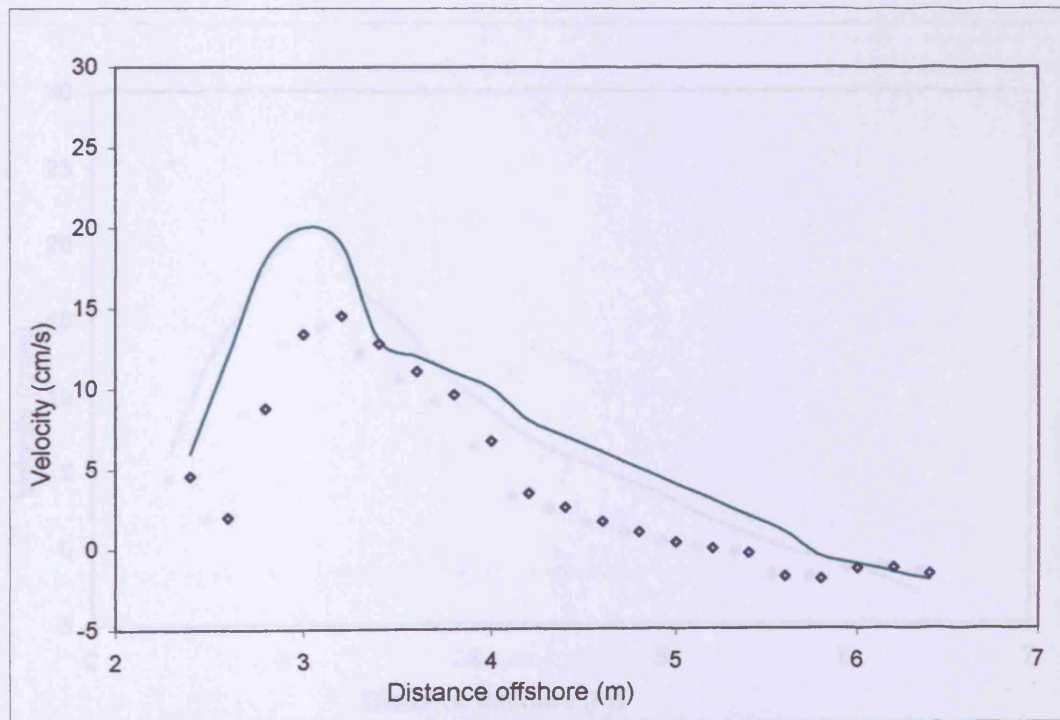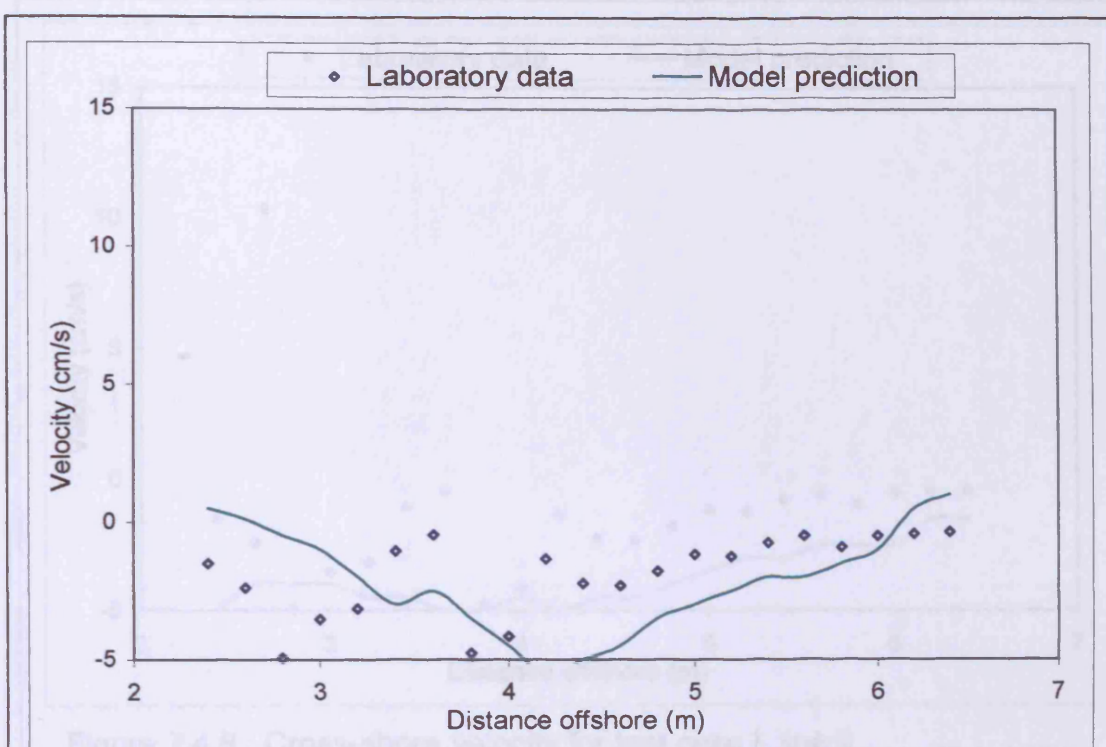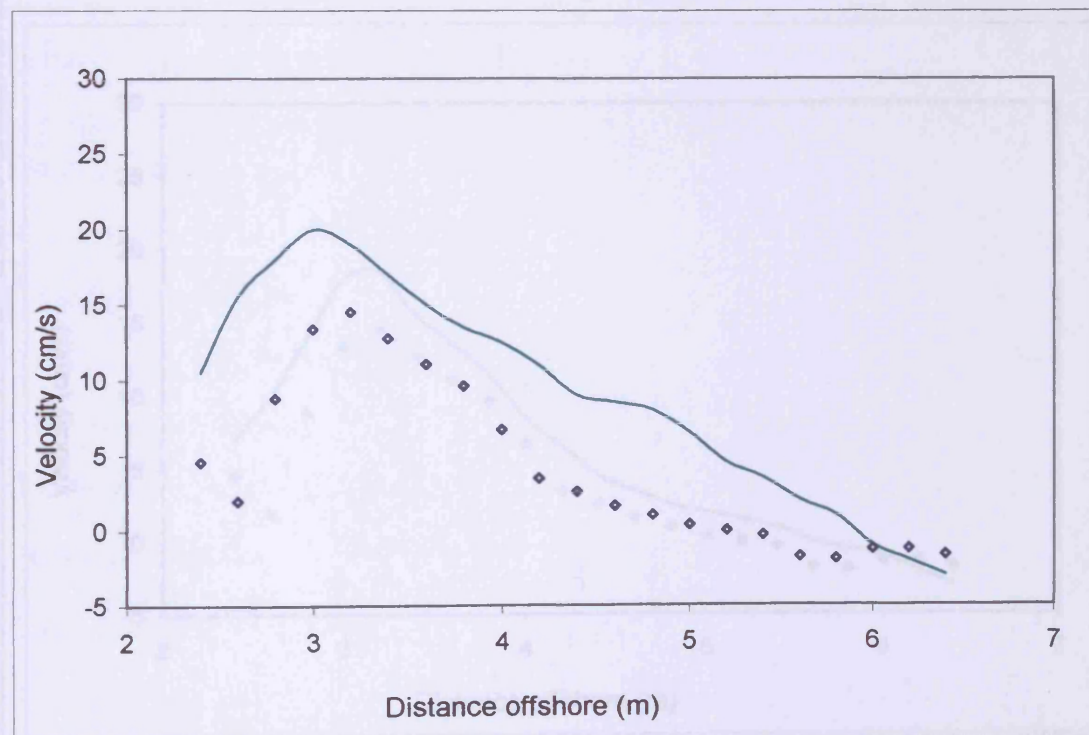

Figure 7.4.11 : Longshore velocity for test case I, line 2
$(k_s = 20mm; C_f = 0.06; \gamma_b = 0.64)$
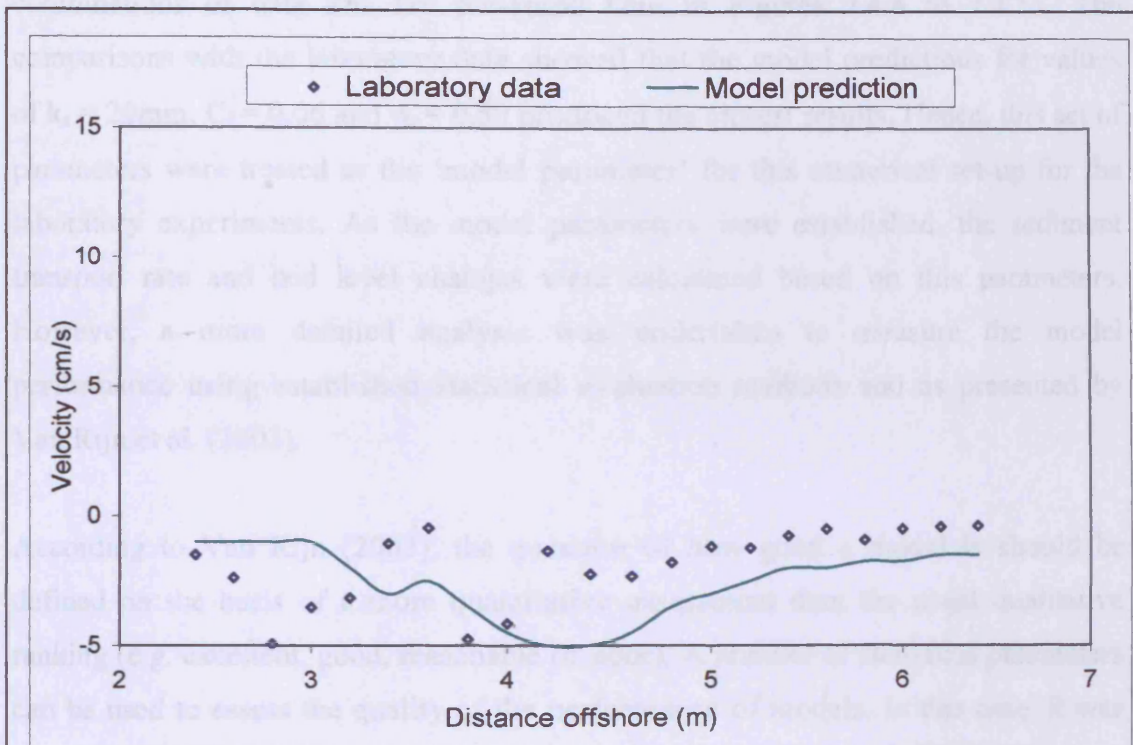
Figure 7.4.12 : Cross-shore velocity for test case I, line 2

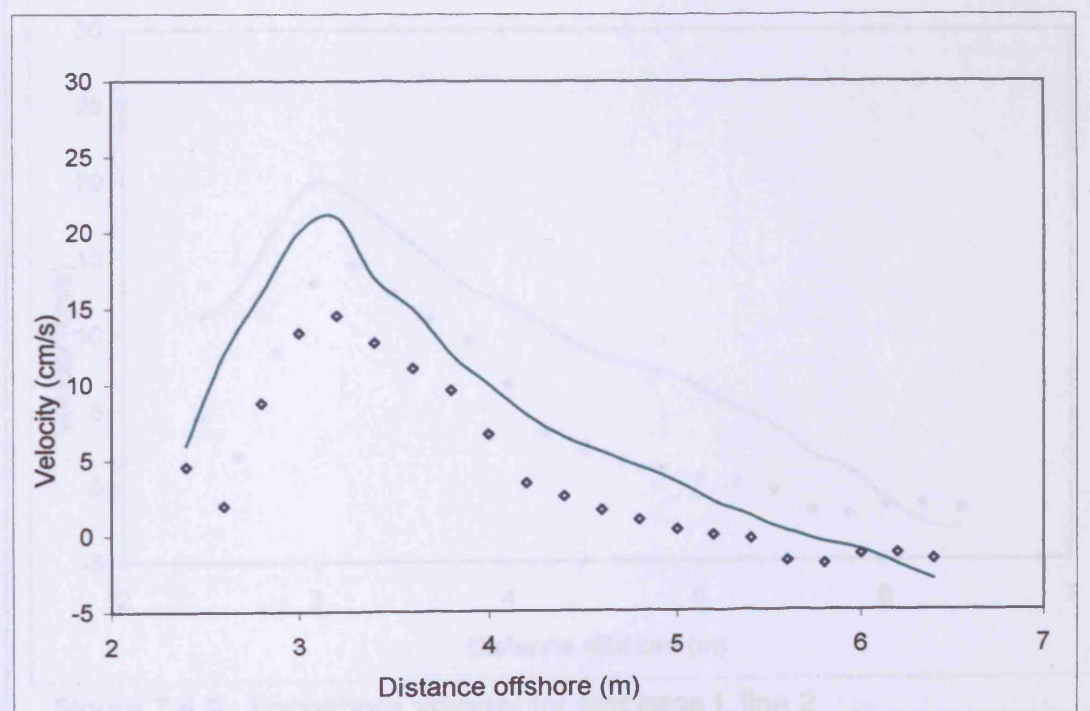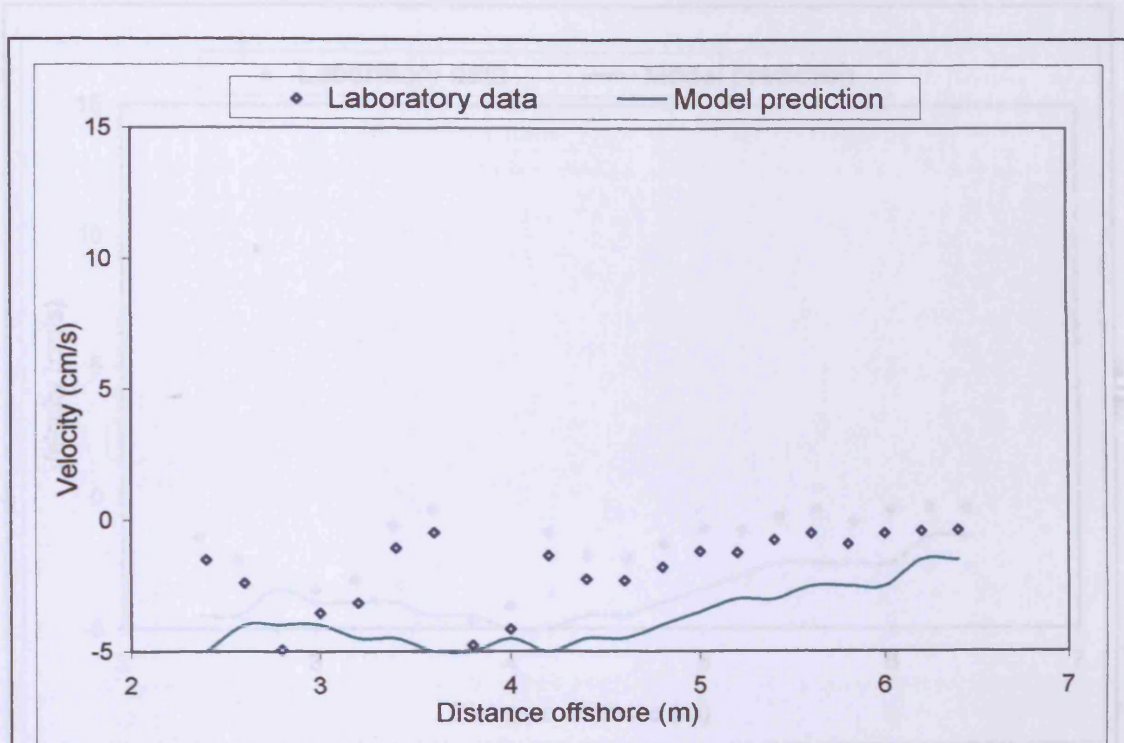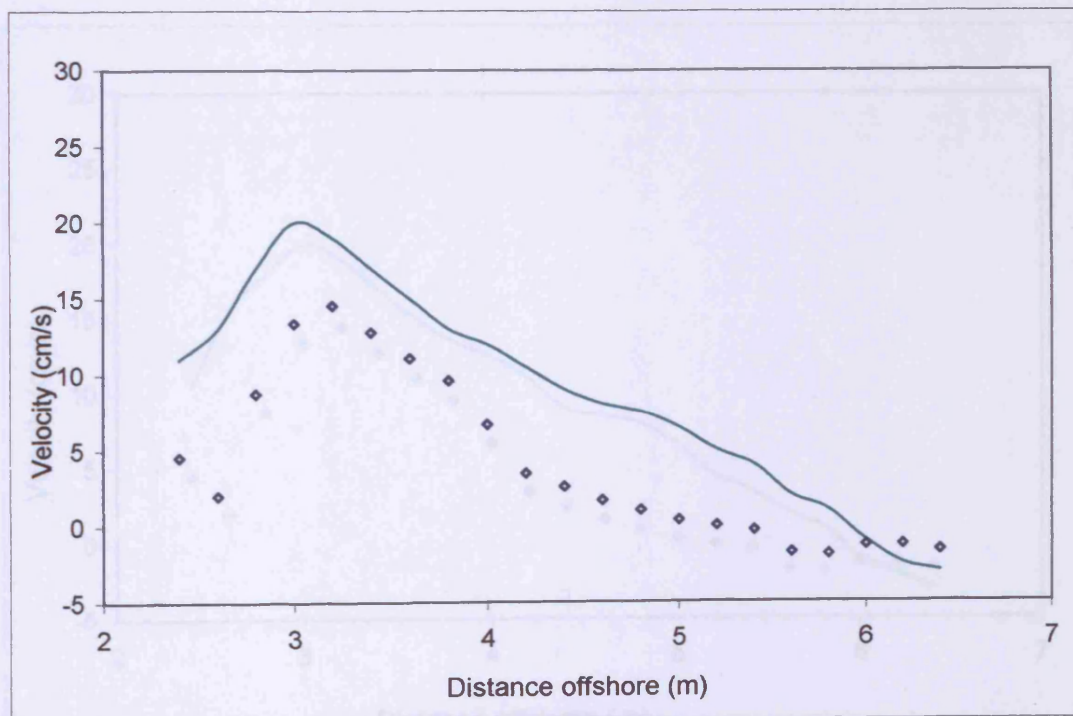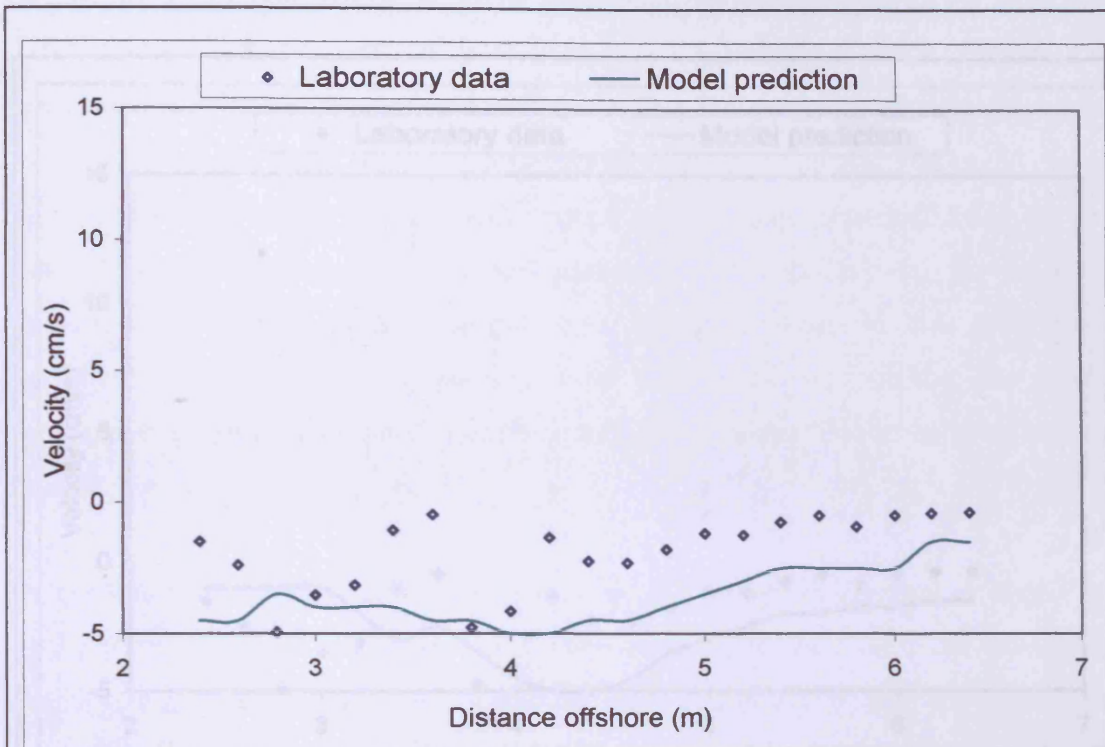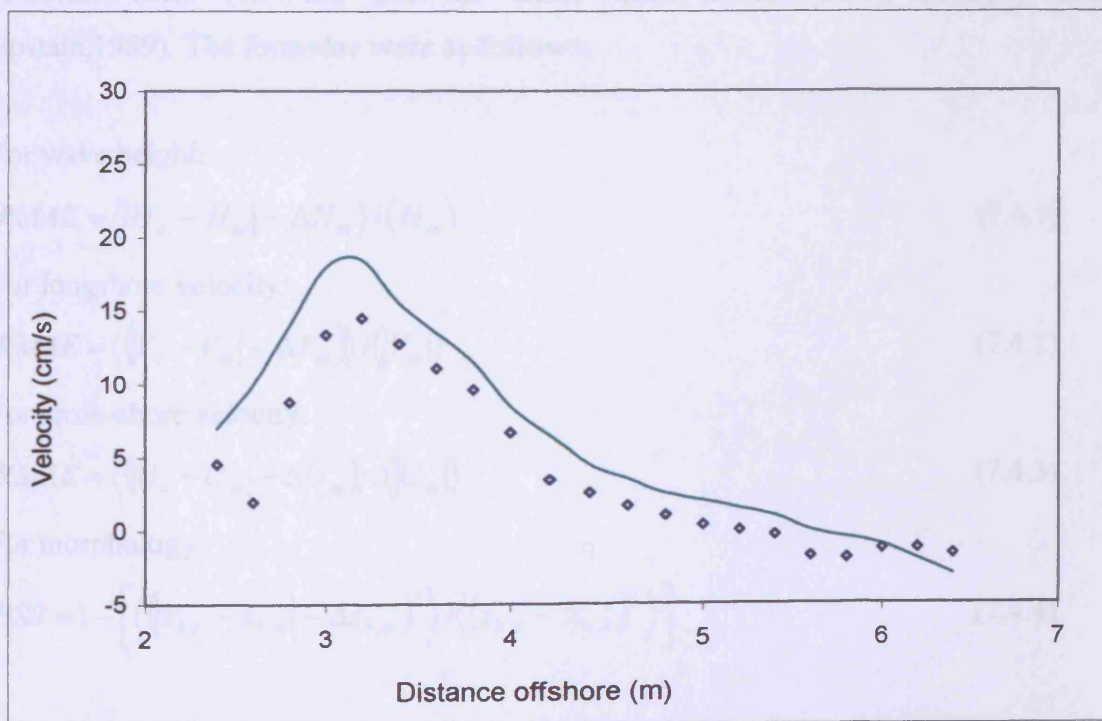Figure 7.4.13 : Longshore velocity for test case I, line 2
(k_s = 20mm; C_f = 0.06; γ_b = 0.50)

for different combinations of the above mentioned parameters, and among them five combinations of data sets are presented here in Figures 7.4.4 to 7.4.13. The comparisons with the laboratory data showed that the model predictions for values of $k_s = 20$mm, $C_f = 0.06$ and $\gamma_b = 0.50$ produced the closest results. Hence, this set of parameters were treated as the 'model parameter' for this numerical set-up for the laboratory experiments. As the model parameters were established, the sediment transport rate and bed level changes were calculated based on this parameters. However, a more detailed analysis was undertaken to measure the model performance using established statistical evaluation methods and as presented by Van Rijn et al. (2003).

According to Van Rijn (2003), the question of how good a model is should be defined on the basis of a more quantitative assessment than the usual qualitative ranking (e.g. excellent, good, reasonable or poor). A number of statistical parameters can be used to assess the quality of the performance of models. In this case, it was proposed to evaluate the performance of the model on the basis of Relative Mean Absolute Error (RMAE) and the Brier Skill Score (BSS), (Murphy and Epstain,1989). The formulae were as follows:

For wave height:

$$RMAE = \left\langle \left| H_c - H_m \right| - \Delta H_m \right\rangle / \left\langle H_m \right\rangle \tag{7.4.1}$$

For longshore velocity:

$$RMAE = \left\langle \left(\left| V_c - V_m \right| - \Delta V_m \right) \right\rangle / \left\langle \left| V_m \right| \right\rangle \tag{7.4.2}$$

For cross-shore velocity:

$$RMAE = \left\langle \left(\left| U_c - U_m \right| - \Delta U_m \right) \right\rangle / \left\langle \left| U_m \right| \right\rangle \tag{7.4.3}$$

For morphology:

$$BSS = 1 - \left[\left\langle \left(\left| z_{b,c} - z_{b,m} \right| - \Delta z_{b,m} \right)^2 \right\rangle / \left\langle \left(z_{b,0} - z_{b,m} \right)^2 \right\rangle \right] \tag{7.4.4}$$

where H = wave height, ΔH_m = error of measured wave height, V = longshore velocity, ΔV_m = error of measured longshore velocity, U = cross-shore velocity,

ΔU_m = error of measured cross-shore velocity, Δz_m = bed-level, $\Delta z_{b,m}$ = error of measured bed level, $\langle ..... \rangle$ = averaging procedure over time series.

It was noted that the statistical parameters (ΔH_m, ΔU_m, ΔV_m, Δz_m) of wave height, current velocity and bed level were corrected for the measurement errors. For the laboratory experiments, the values were computed based on the equipment used, and the values considered as $\Delta H_m = 0.01m$ for wave height, $\Delta U_m = \Delta V_m = 1cm/s$ for the current velocity and $\Delta z_m = 0.02m$ for the bed level of the laboratory data measured in this test.

The RMAE value is preferred above the RMSE (relative mean square error) value because the presence of a few outliers will have a greater influence on the RMSE visa-vis on the RMAE value. The data from the laboratory experiments and the model results were used to compute the RMAE and BSS values for the different hydrodynamic components. It was found from the statistical analysis for the model predictions that values were: RMAE (wave height) = 0.085, RMAE (longshore current) = 0.29, RMAE (cross-shore current) = 0.24 and BSS = 0.68 and this calculation was based on the model parameters k_s = 20mm, C_f = 0.06 and γ_b = 0.50.

Table 7.4.2: Calculation for the RMAE values

H_c	H_m	U_c	U_m	V_c	V_m	$Z_{b,0}$	$Z_{b,c}$	$Z_{b,m}$
8.4	8.578	2.520	2.3	3.497	3.5	42.92	41.84	39.88
8.41	8.47	5.099	4.9	6.668	6.5	41.84	40.64	39.05
8.4	8.44	6.83	6.7	9.19	9.0	38.15	39.64	38.46
8.39	8.35	4.528	4.5	13.141	12.9	37.99	39.64	38.26
8.4	8.49	2.511	2.7	10.45	10	37.99	38.28	37.89
8.412	8.378	-.523	-1	6.47	6.5	37.02	37.59	36.97
8.39	8.398	-.648	-.5	2.33	2.3	36.7	36.64	36.09
		-.541	-.5	-.33	-.4	35.02	35.64	34.89
		-.3168	-.3	-1.59	-1.6	34.25	34.64	34.52
		-2.22	-2	-2.03	-2	33.18	32.68	32.88
		-3.68	-3.5	-2.11	-2	31.55	31.64	30.99

Table 7.4.3: Qualification of the process parameters (from Van Rijn et al., 2003)

Qualification	Wave height; RMAE	Velocity; RMAE	Morphology; BSS
Excellent	<0.05	<0.01	1.0-0.08
Good	0.05-0.1	0.1-0.3	0.8-0.6
Reasonable/fair	0.1-.0.2	0.3-0.5	0.6-0.3
Poor	0.2-0.3	0.5-0.7	0.3-0.0
Bad	>0.3	>0.7	<0

Table 7.4.3 highlights the model performance as described by Van Rijn et al., (2003). According to the standard set of tests it was found that the present model could be treated as a reasonably accurate in predicting the nearshore wave and current field and bed level changes. The parameters for this wave-current model for the laboratory experiments have been checked with qualitative model performance indicators. The comparison results for velocity (for lines 1 and 3) will be represented for both test cases I and II with the assigned model parameters.

Figures 7.4.14 to 7.4.17 represent the current velocity for test case I, where T = 3s and the parameters were k_s = 20mm, C_f = 0.06 and γ_b = 0.5. The cross-shore current for line 1 has been represented in Figure 7.4.14. It showed that the model results were in good agreement with the experimental results along the offshore distance. The longshore current distribution along line 1 (Figure 7.4.15) matched well, particularly as this is the centre line for the model beach and the shallowest point of the depression. The magnitude of the highest current showed a higher peak in the model result (Figure 7.4.15 and 7.4.17), there was no difference in location of wave breaking, which represented the good predictive capacity of the model.

Figure 7.4.12 shows the cross-shore current distribution for line 2. The trend in current velocity matches well along this line (magnitude being 0 to −5 cm/s). The velocity changed direction along the offshore distance (Figure 7.4.13, after 5m from shoreline), which showed the characteristics of a circulatory flow along this area. The longshore current profile (Figure 7.4.13) showed good agreement between the

measured and predicted data. The point of wave breaking showed the same location with a similar magnitude. The slope of the curve from breaking towards offshore also match well. It was very difficult to measure the wave height just before breaking, so the value of γ_b could not be established fully at breaking in the experimental settings.

Figure 7.4.16 illustrates the cross-shore velocity for line 3, which is near to the boundary along the right hand side. The results were comparable and the experimental results showed higher values than the model results for the longshore current. Flow reversal occurred along this line, but occurred further offshore than for line 2. Figure 7.4.17 illustrates the longshore current profile for line 3. For this case the location of wave breaking matched both sets of results. The model results gave higher current velocities at breaking then the experimental measurements. As this line was near to the boundary, some reflected wave components were thought to affect the velocities. Also the flat bed level for the model beach imposed less friction at this site.

Good comparisons were obtained with the parameter values mentioned above (k_s = 20mm, C_f = 0.06 and γ_b = 0.50) for test case II (T = 2 s) by considering the same parameters as before, and it was found that the results were in good agreement. The results for Figure 7.4.18 represented the cross-shore velocity along line 1 for test case I. The observed and predicted data matched well and along this line it was seen that the current remained in one direction along the offshore distance. The longshore current profile for line 1 (Figure 7.4.19), for experimental data, it did not show the peak velocity was similar in magnitude. However, the location of wave breaking did not match at this location. The wave breaks at (4-5m) offshore which is not similar to case I, and it did not present the similar nature of breaking points of other lines. The breaking point in (Fig. 7.4.19) did not match with test case I for the same line in the laboratory. Figures 7.4.20 and 7.4.22 showed the cross-shore velocity profiles for line 2 and line 3 respectively. In both cases, the results were in good agreement with laboratory measurements. Line 2 showed flow reversal at half way but line 3 showed that the current direction changed at the end of the sloping part. Figures
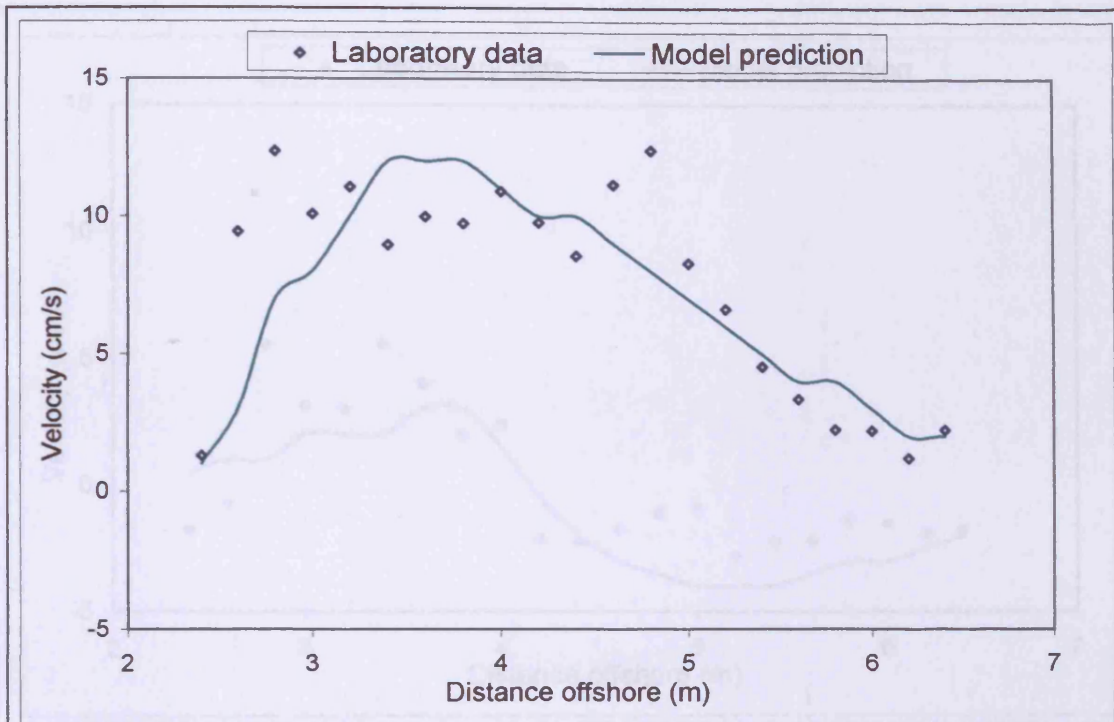
Figure 7.4.14: Cross-shore velocity for test case I, line 1
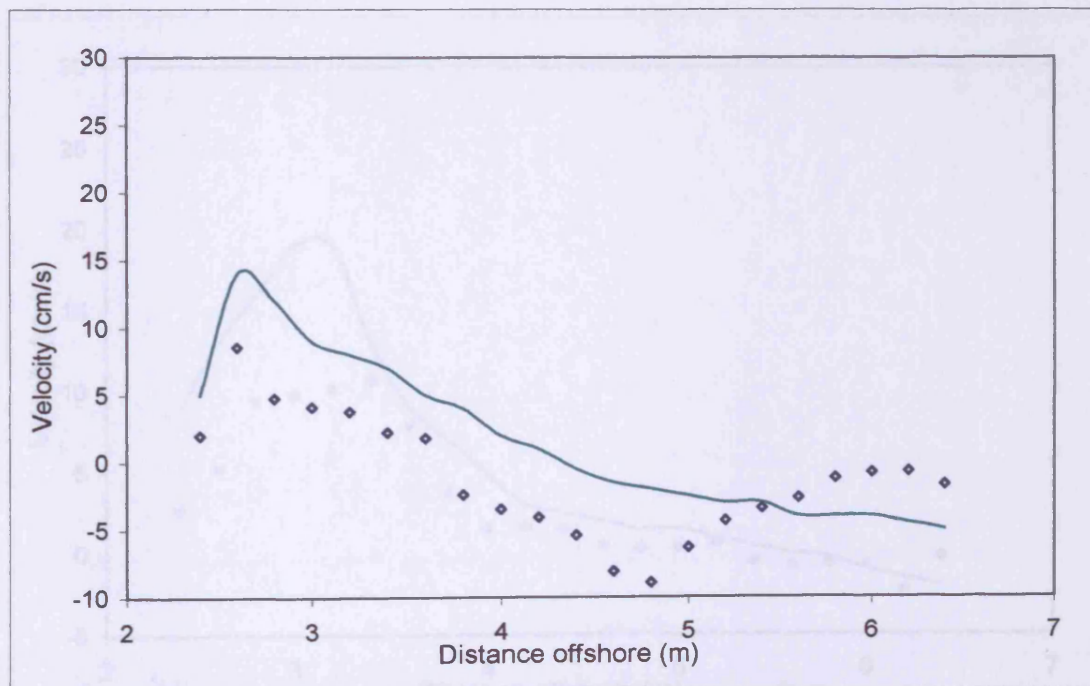
Figure 7.4.15: Longshore velocity for test case I, line 1
(k_s = 20mm; C_f = 0.06; γ_b = 0.50)
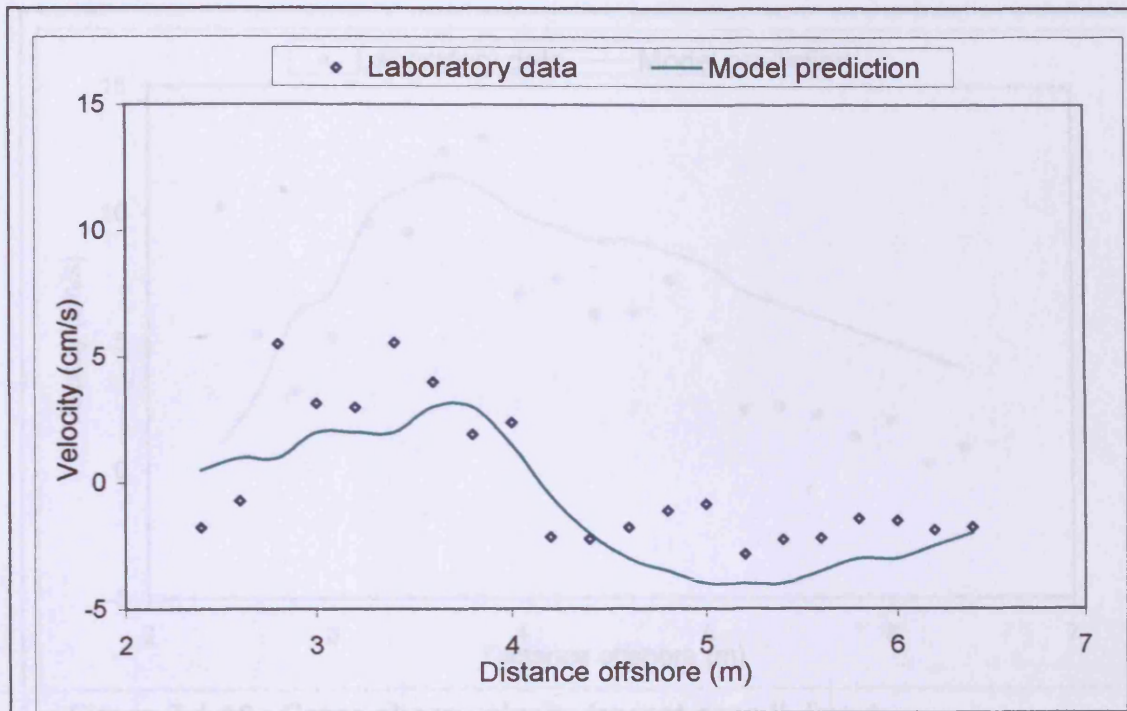
Figure 7.4.16 : Cross-shore velocity for test case I, line 3
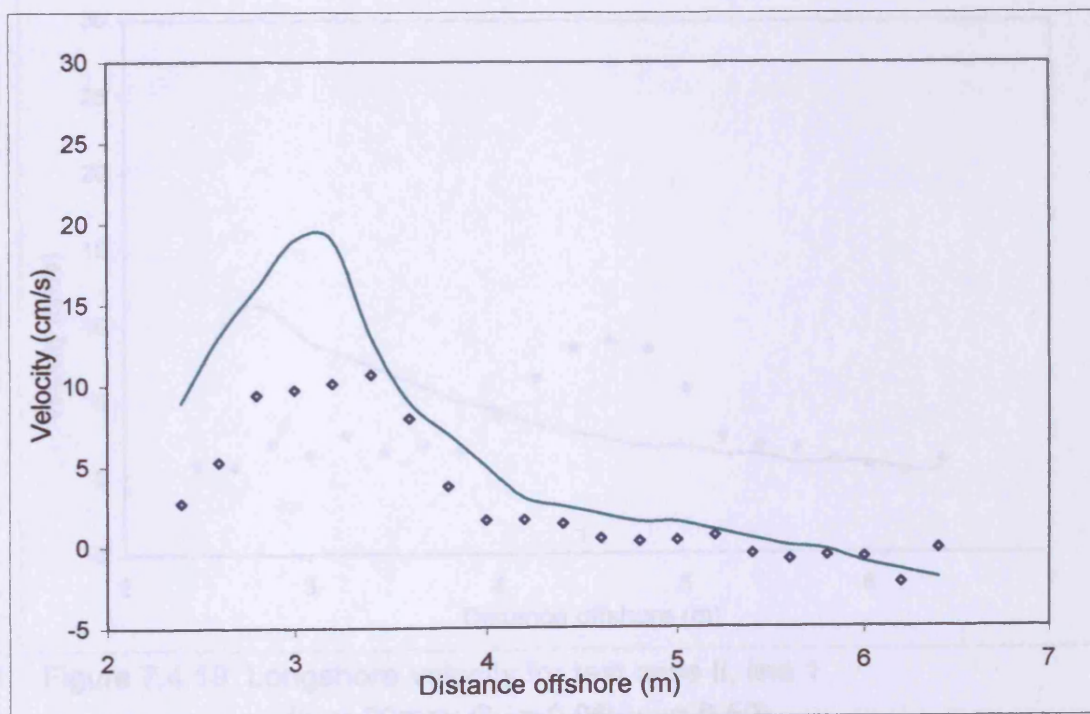
Figure 7.4.17: Longshore velocity for test case I, line 3
(k_s = 20mm; C_f = 0.06; γ_b = 0.50)
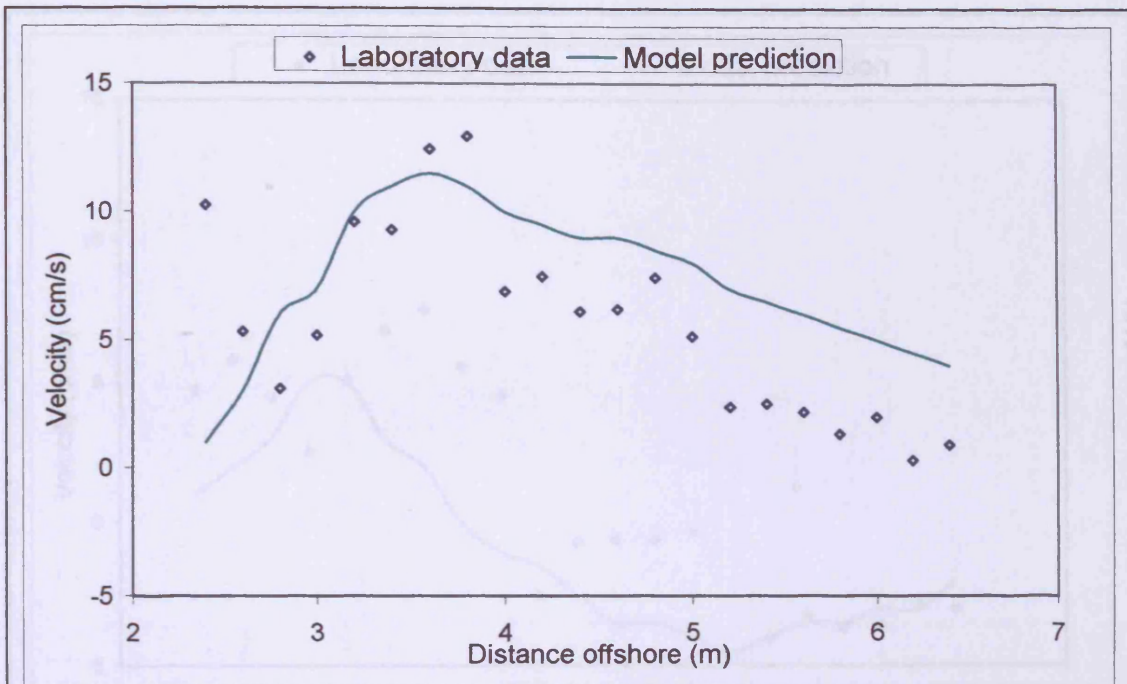
Figure 7.4.18 : Cross-shore velocity for test case II, line 1

Figure 7.4.19: Longshore velocity for test case II, line 1
(k_s = 20mm; C_f = 0.06; γ_b = 0.50)
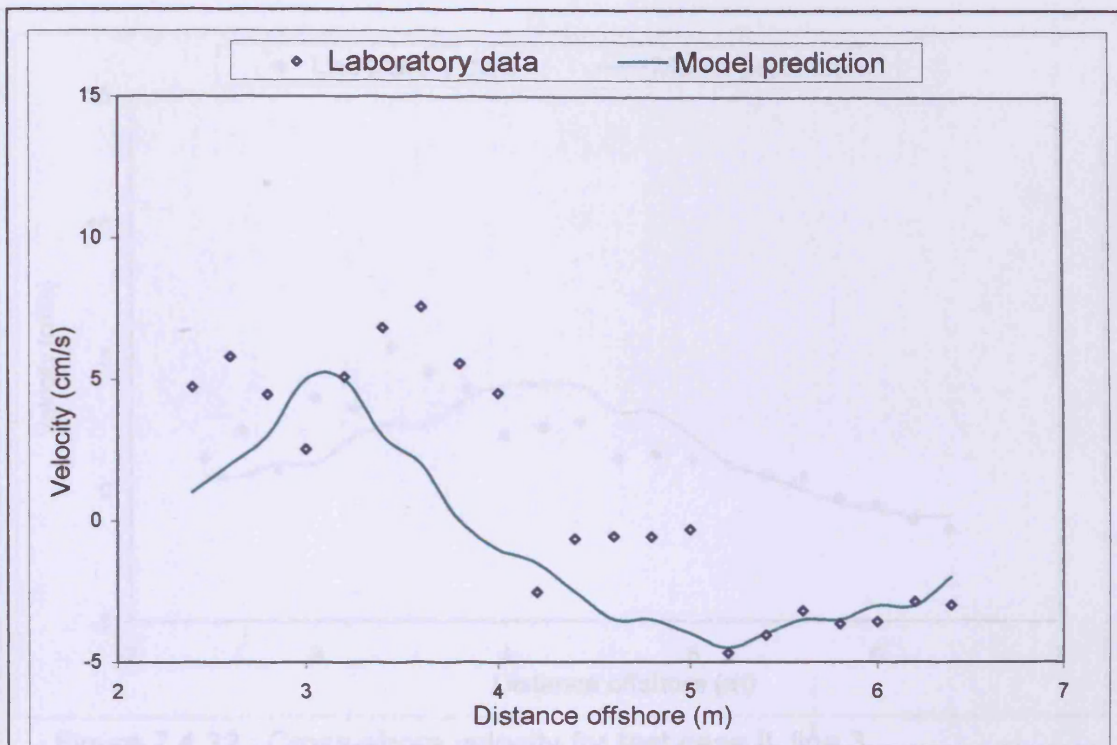
Figure 7.4.20: Cross-shore velocity for test case II, line 2
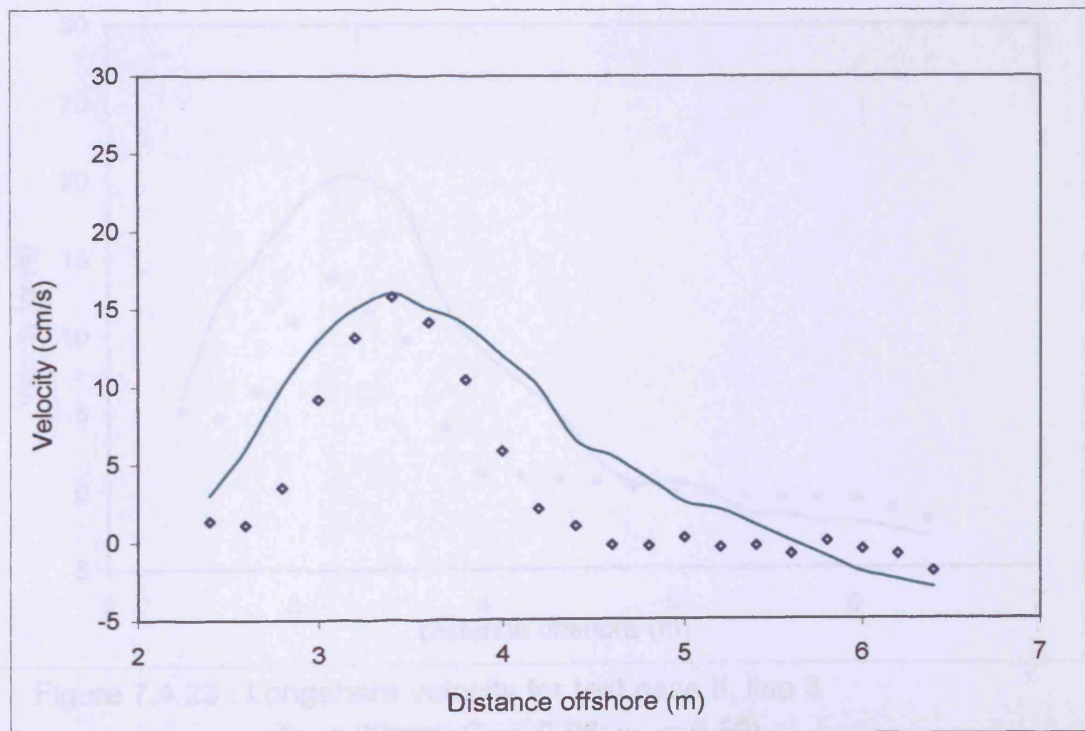
Figure 7.4.21 : Longshore velocity for test case II, line 2
$(k_s = 20mm; C_f = 0.06; \gamma_b = 0.50)$
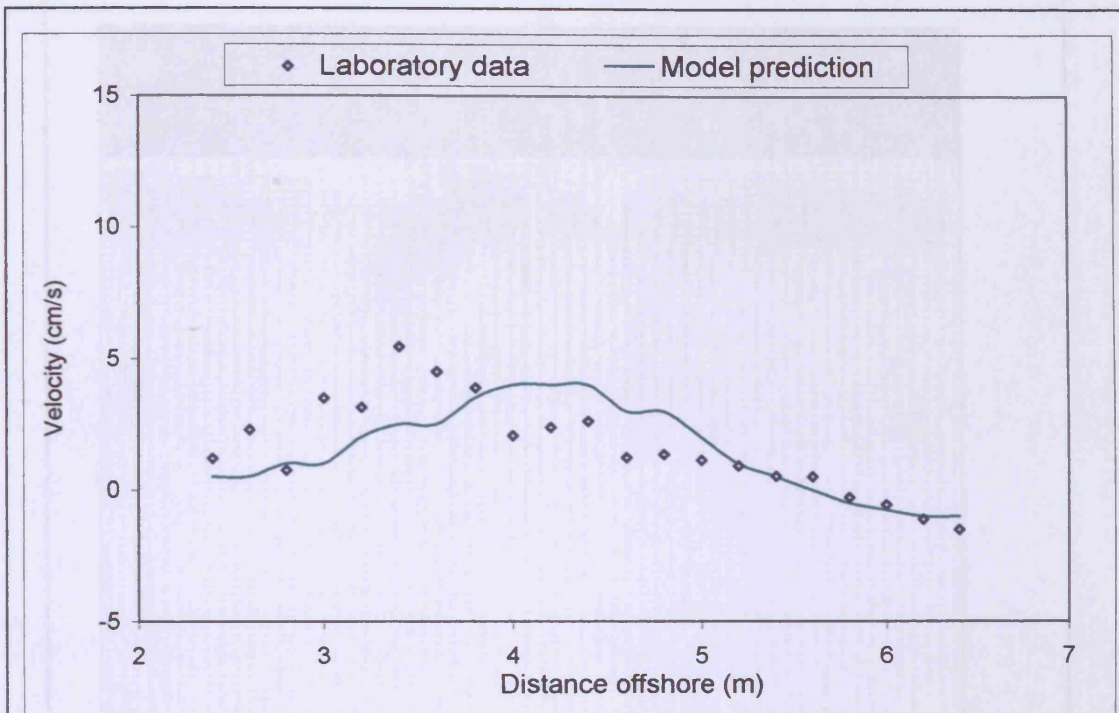
Figure 7.4.22 : Cross-shore velocity for test case II, line 3
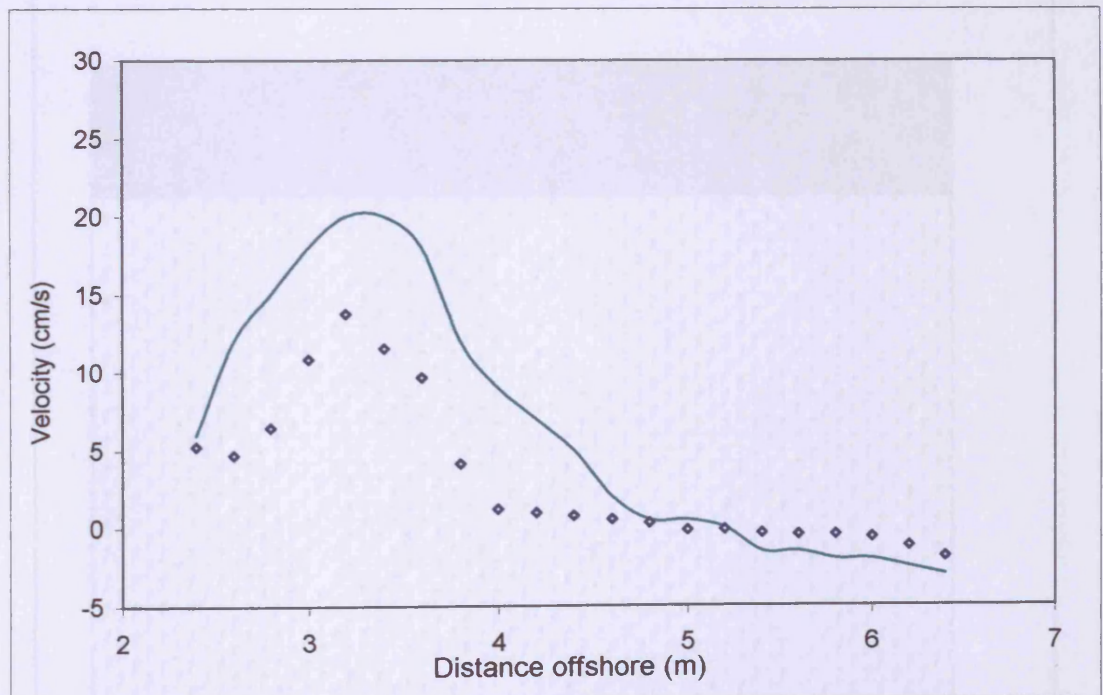
Figure 7.4.23 : Longshore velocity for test case II, line 3
(k_s = 20mm; C_f = 0.06; γ_b = 0.50)
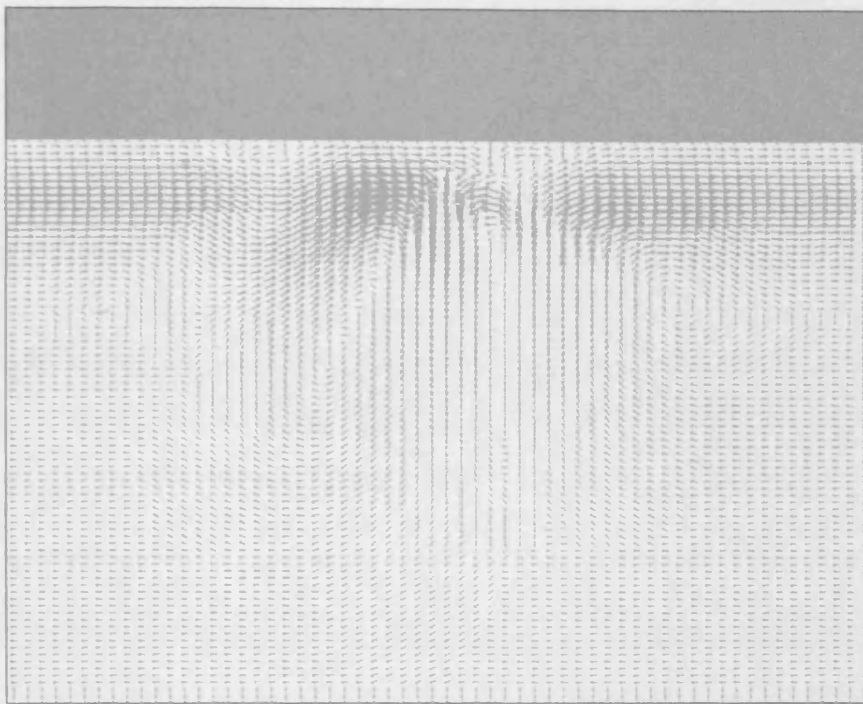
Figure 7.4.24 : Predicted velocity field for test case I (T = 3s)
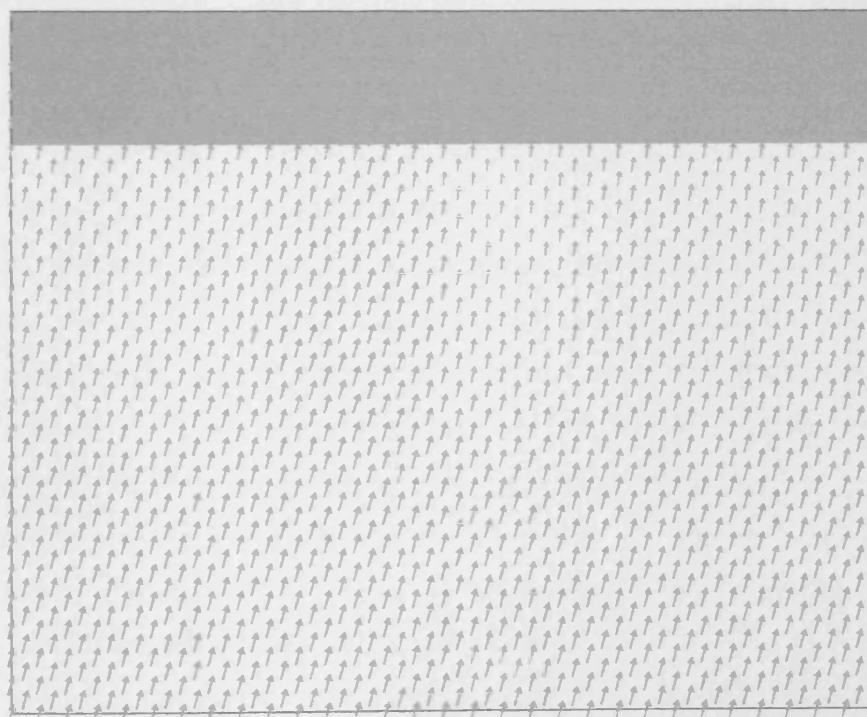
Figure 7.4.25 : Predicted wave direction for test case I (T = 3s)
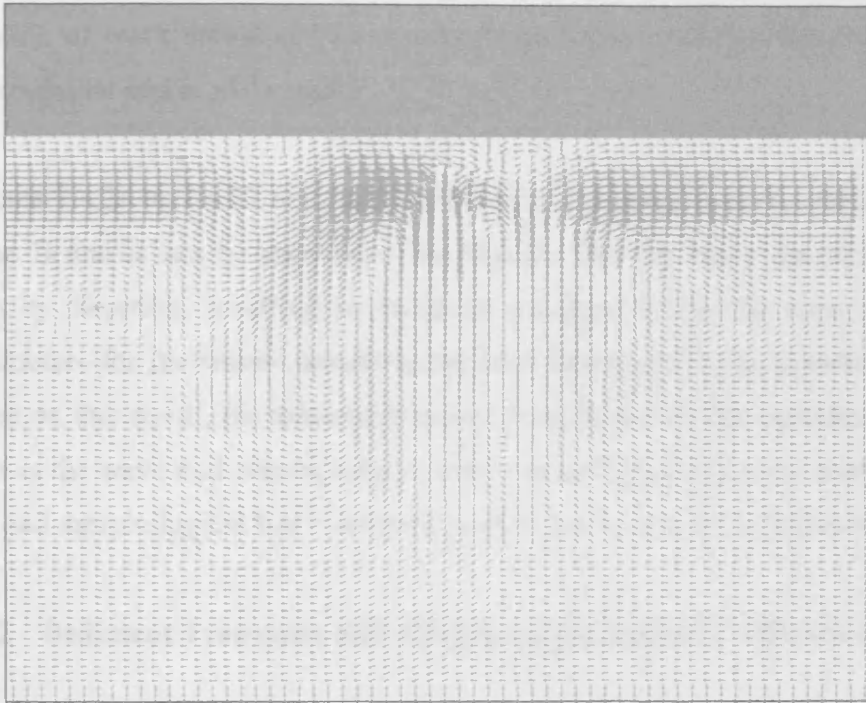
Figure 7.4.26 : Predicted velocity field for test case II (T = 2s)
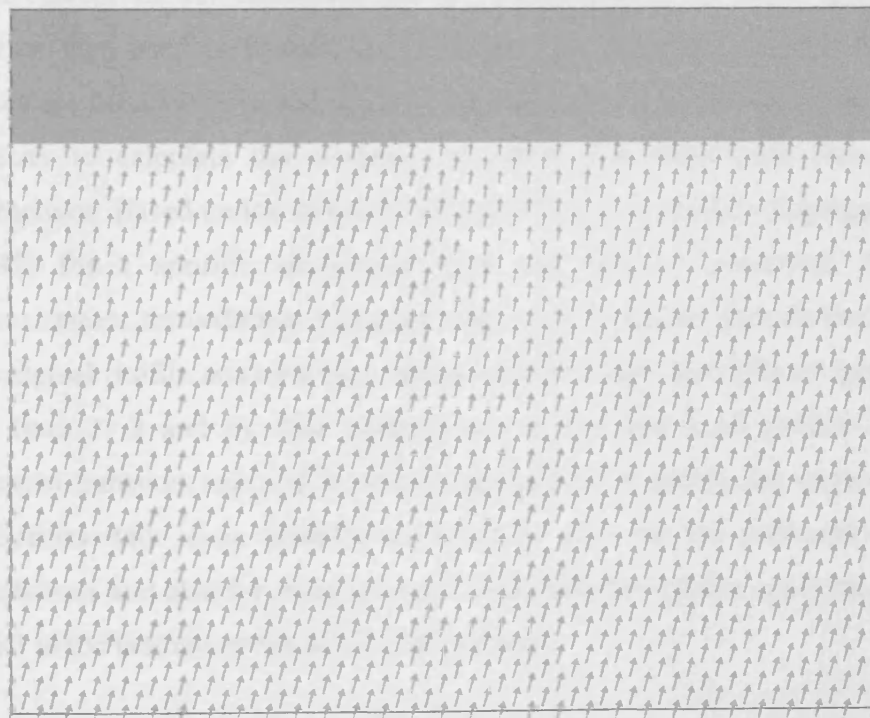
Figure 7.4.27 : Predicted wave direction for test case II (T = 2s)

7.4.21 and 7.4.23 represents the longshore velocity for lines 2 and 3 respectively. Both the profiles showed similar agreement with the experimental results. The location of wave breaking best matches line 2 and condition the distinct point for experimental and model results.

Figures 7.4.24 to 7.4.27 represent the velocity field and the wave field for test cases I and II and it can be seen from the figures that the wave direction controls the velocity direction, resulting in sediment transport along the same direction. The parameters for the wave-current model have been set for the laboratory set up and based on this result, the numerical model predictions for the nearshore circulations, such as the wave and current related sediment transport rate, total sediment transport rate and morphological bed evolution, will be presented in the following sections.

7.4.2 Sediment Transport and Morphological Model Verification

The sensitivity test for the velocity field showed that the model was now capable of predicting the nearshore velocity field to the expected limit. The newly developed wave-current model calculates the radiation stresses at every grid point, these stresses then used in hydrodynamic module to calculate velocity field. Then the values are transferred in sediment module and the new sediment sub-model has the capacity to calculate the sediment transport rate from both wave and current interactions. Based on the sediment transport rate, the bed level change (i.e. equation 3.6.45) for a specific simulation time can also be predicted. No laboratory measurements for sediment transport rates were available, but the bed level data for the original profile and after the simulation time were available at specific locations (i.e. lines 1, 2 and 3). The computation of the bed level profile was based on sediment transport rate and therefore appropriate to verify the wave-current model predictions with some established literature data for the sediment transport rate calculations and also for morphological computations before applying the numerical model to the laboratory result for comparisons.

The conditions in the surf zone are characterised by the strong energy dissipation and production of turbulence caused by wave breaking. Energy dissipation is a

significant mechanism, which contributes to the surf zone sediment transport (Fredsøe and Deigaard, 1984). In order to obtain the force balance, the shear stress is important when the energy loss takes place near the surface of the velocity distribution. The distribution of the shear stresses, together with the continuity equation, give the mean velocity profile, with a strong offshore directed undertow near the bed and an onshore mean flow near the surface. The suspended sediment concentration profiles are influenced by the high turbulence level due to wave breaking. The sediment transport rate for the nearshore areas is governed by wave breaking in the surf zone. The calculation of wave-induced sediment transport rate has been presented in chapter 3, and which is based on the method of Van Rijn (1993) for sediment particle size 200-2000μm. The wave-current model sediment transport rate predictions are verified against established literature data (Davies et al., 2002), and under given conditions, to provide more confidence in the model application. According to Davies et al. (2002) the quantification of sand transport rates in the nearshore zone was a key element to predicting seabed changes and coastal or morphological evolution. However, large gaps remain in our knowledge of sediment transport processes and a continuing need exists for the development of reliable, well-validated, and practical modelling system.

It is always important to be able to develop local sediment transport predictors, suitable for use in coastal sediment transport and morphological models. The sediment transport rates predicted in this model were compared with seven research models, incorporating a wide range of wave and current conditions, including both plane and rough beds. The research models can determine both the 'wave-related' and 'current-related' components of the suspended load transport. The essential need of these comparisons were to give potential evaluation of sediment transport rate formulae, and to quantitatively assess the variability in the predictions of different formulations.

The parameter settings for this task were same as those used by Van Rijn (1993). In this case additional current are considered with wave to be similar with the test cases. The comparison involved a current alone case and two waves combined co-linearly with these currents in a water depth of 5m. The waves were treated as being

purely sinusoidal and the near bed wave velocity amplitudes (U_w) were calculated using linear wave theory. Table 7.4.2 describes the different parameters used for the comparisons, based on Davies, et al., 2002. Figures 7.4.28 to 7.4.30 showed the results for the various model scenarios, including the present model. The first column is for the current only case, with then the two columns being for wave-current cases. The calculated sediment transport rate (ST) has been plotted as a function of the depth-averaged velocity U_c on log-linear axis.

Table 7.4.4: Parameters used in calculating sediment transport rate:

Current alone		Current + Wave 1		Current + Wave 3	
Wave height, H_s = 0.0m		Wave height, H_s = 0.5m		Wave height, H_s = 2.0m	
Wave period, T_p = 0.0		Wave period, T_p = 5s		Wave period, T_p = 7s	
Near bed wave velocity, U_w = 0.0 m/s		Near bed wave velocity, U_w = 0.255 m/s		Near bed wave velocity, U_w = 1.207 m/s	
Depth-mean current velocity,U_C (m/s)	Bed roughness, k_S (m)	Depth-mean current velocity,U_C (m/s)	Bed roughness, k_S (m)	Depth-mean current velocity,U_C (m/s)	Bed roughness, k_S (m) = $2.5D_{50}$
0.1	0.1	0.1	0.1	0.1	Flat bed
0.3	0.1	0.3	0.1	0.3	Flat bed
0.5	0.1	0.5	0.1	0.5	Flat bed
0.6	0.1	0.6	0.1	0.6	Flat bed
0.7	0.1	0.7	0.1	0.7	Flat bed
0.8	0.1	0.8	0.1	0.8	Flat bed
1.0	0.1	1.0	0.1	1.0	Flat bed
1.2	0.08	1.2	0.08	1.2	Flat bed
1.5	0.06	1.5	0.06	1.5	Flat bed
1.8	0.03	1.8	0.03	1.8	Flat bed
2.0	Flat bed	2.0	Flat bed	2.0	Flat bed

The model considered for comparison was that established and described by Davies et al., (2002). The 'K-L', 'TKE' and 'Mixing Length' models could be used for all of the test cases. The STP model was considered for wave-current cases. The 'K-ε' model was considered for: (i) the current alone and (ii) wave 1 and current cases. The 'two-phase model' was run for current alone test. The variability between the different model results was considerable, as all of the models treated the near-bed
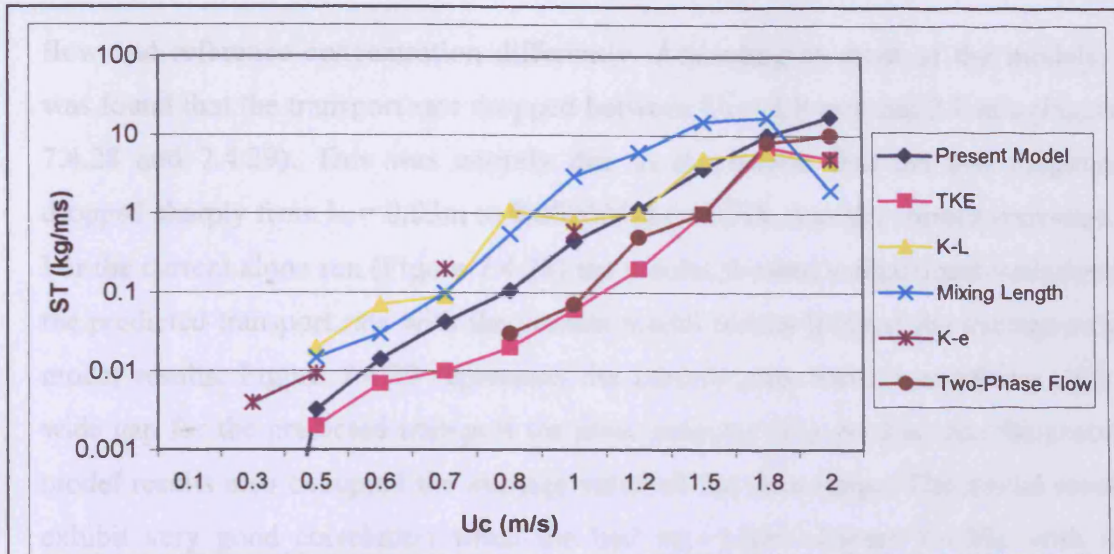
Figure 7.4.28 : Test case 1- only current considered
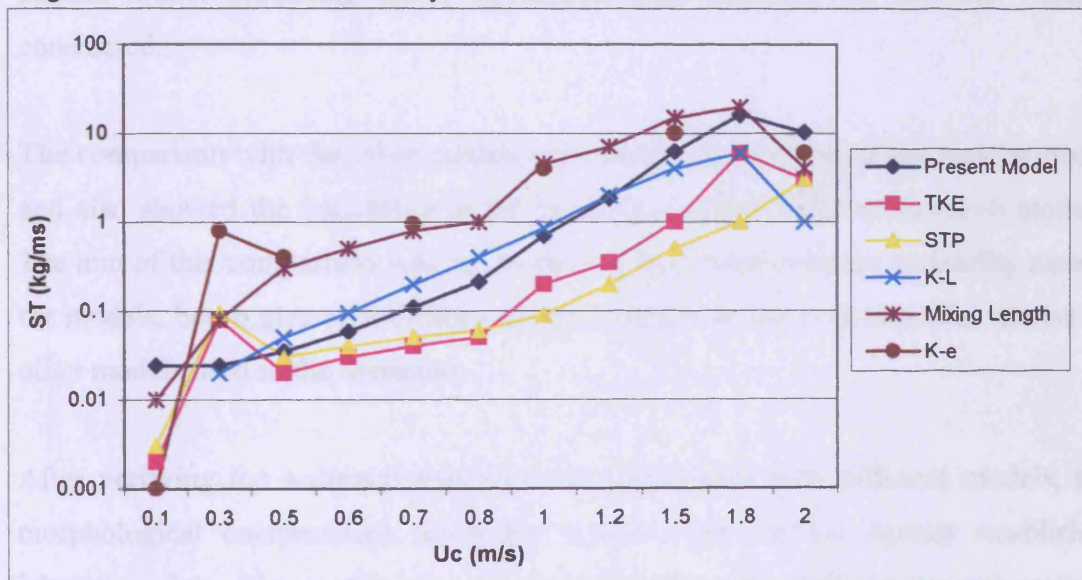
Figure 7.4.29 : Test case 2 - current + wave 1
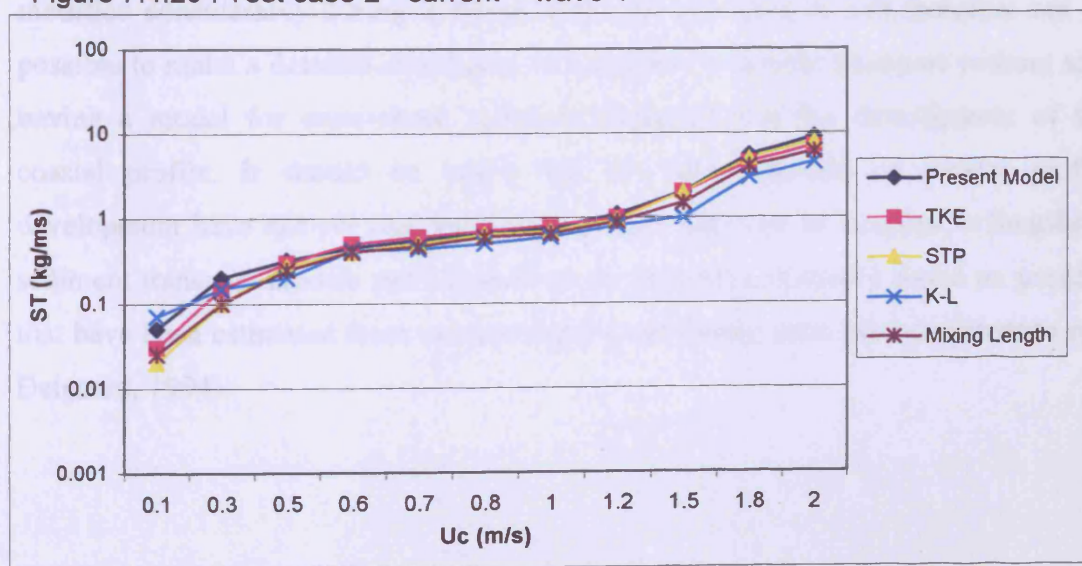
Figure 7.4.30 : Test case 3 - current + wave 3

flow and reference concentration differently. According to most of the models, it was found that the transport rate dropped between U_c = 1.8 m/s and 2.0 m/s (Figures 7.4.28 and 7.4.29). This was entirely due to the reason that the bed roughness dropped sharply from k_s = 0.03m to 0.000625m (= $2.5D_{50}$) as the current increased. For the current alone run (Figure 7.4.28) the results showed a significant variation in the predicted transport rate with the present model results lying at the average of all model results. Figure 7.4.29 represents the current plus wave 1 condition with a wide gap for the predicted transport for same velocity (U_c). In this case the present model results also occupied the average value of the data range. The model results exhibit very good correlation when the bed was plane (Figure 7.4.30), with the present model producing closer agreement with harmony of the other models considered.

The comparison with the other models provided an assessment of the present model and also showed the variability in the prediction of the different research models. The aim of this comparison was not to discuss the reasons for the variability among the models, but to give an indication of the accuracy of the present model relative to other models used in the literature.

After verifying the sediment transport rate predictions with different models, the morphological computations using the model were verified against established laboratory data. The profile of a sandy beach changes continuously and may be modified considerably during a single storm. In principle, it will therefore not be possible to make a detailed simulation of longshore sediment transport without also having a model for cross-shore sediment transport and the development of the coastal profile. It should be noted that in reality models of coastal profile development have not yet reached a stage where they can be coupled to longshore sediment transport models and simulations are therefore normally based on profiles that have been estimated from surveys carried out during calm periods (Fredsoe and Deigaard, 1994).

The coastal profile evaluation model will be applied to the laboratory experimental data obtained from the Delta Flume'93 experiments undertaken by Archilla et al. (1994). The model bed evolution predictions were compared with the simulation of the test case for test code 2b, with a wave height of 1.4m and a period 5s. The Delta Flume'93 experiment was undertaken in a large scale wave flume at Delft Hydraulics and details of the experimental procedure to generate the morphodynamic data are given in Archilla et al., 1994. For the numerical model, the geometry and the wave conditions were taken as the same from the experimental set-up. The boundary conditions were designated to closely resemble the flume condition. The wave-current model was applied to predict the sediment transport rate as well as the bed level, for the above mentioned test case, with simulations given in Figure 7.4.31.
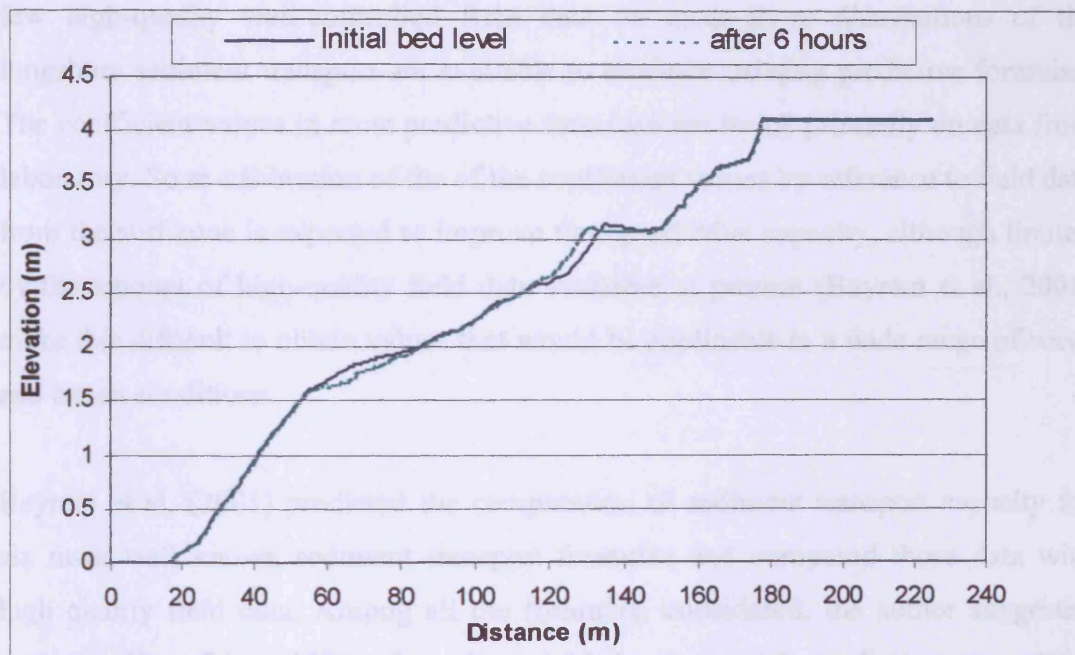
Figure 7.4.31: Bed profiles obtained in the numerical simulation

7.4.3   Sediment Transport and Morphological Model Prediction

The calculation of sediment transport rate by wave and currents can be calculated independently by this model, but is not possible to be measured in the laboratory. Figures 7.4.32 to 7.4.36 represented the rate of transport by waves and currents at

three cross-shore, sections namely line 1 to line 3 in Figure (7.3.1) and two longshore sections along line 4 and line 5 in Figure (7.3.1). It was found that the sediment transport by the nearshore currents were much higher than the transport by waves. The dominating factor for nearshore transport was the strong current, which was developed by wave breaking. Along the cross-shore distances the results (i.e. Figures 7.4.35 and 7.4.36) also showed that the currents related to the sediment transport were much higher than wave related transport. The magnitude of the sediment transport was much higher in the breaking area than the offshore line, which was as expected.

The ability to predict the surf zone hydrodynamics is based on reliable formulae to evaluate the sediment transport rate. Numerous formulae and models for computing the sediment transport rate by waves and currents have been proposed, but relatively few high-quality well-controlled field data on cross-shore distributions of the longshore sediment transport are available to evaluate existing predictive formulae. The coefficient values in most predictive formulae are based primarily on data from laboratory. So re-calibration of the of the coefficient values by reference to field data from the surf zone is expected to improve their predictive capacity, although limited by the amount of high-quality field data available at present (Bayram et al., 2001) make this difficult to obtain values that would be applicable to a wide range of wave and beach conditions.

Bayram et al. (2001) predicted the computation of sediment transport capacity for six most well known sediment transport formulae and compared those data with high quality field data. Among all the formulae, considered, the author suggested that the Van Rijn (1984) formulae yielded very good prediction as $q_p/q_m=$ $q_{predicted}/q_{measured}$, yielded the least scatter around the line of perfect agreement. It was found by different researchers (Bayram et al., 2001; Davies and Villaret, 2000; Saviolli, 1998 and Schonees and Theron, 1996) that the discrepancy between observed and predicted sediment transport rate upto 30-40% is considered as very good prediction by the corresponding respective formulae.
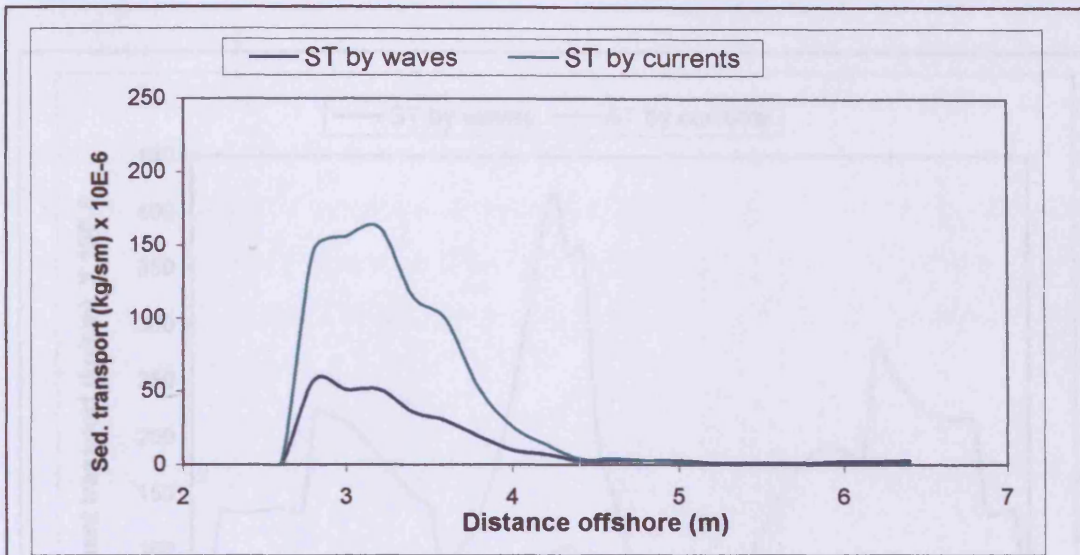
Figure 7.4.32 :Sediment transport by waves and currents (Line 1)
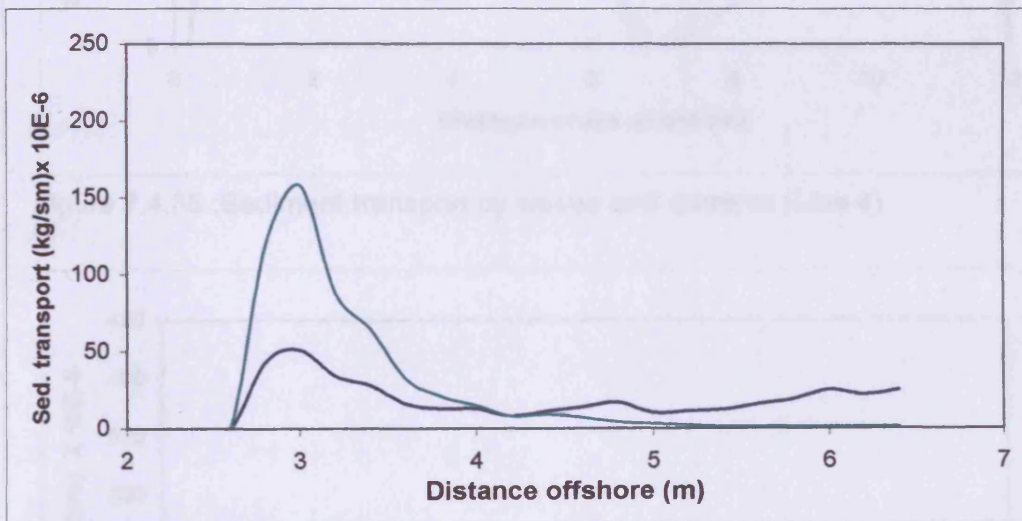
Figure 7.4.33 :Sediment transport by waves and currents (Line 2)
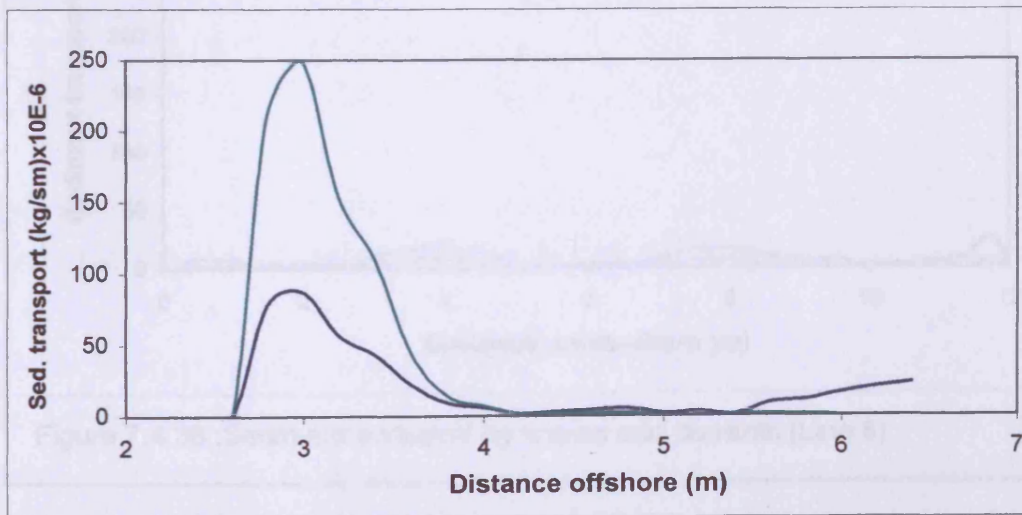
Figure 7.4.34 :Sediment transport by waves and currents (Line 3)
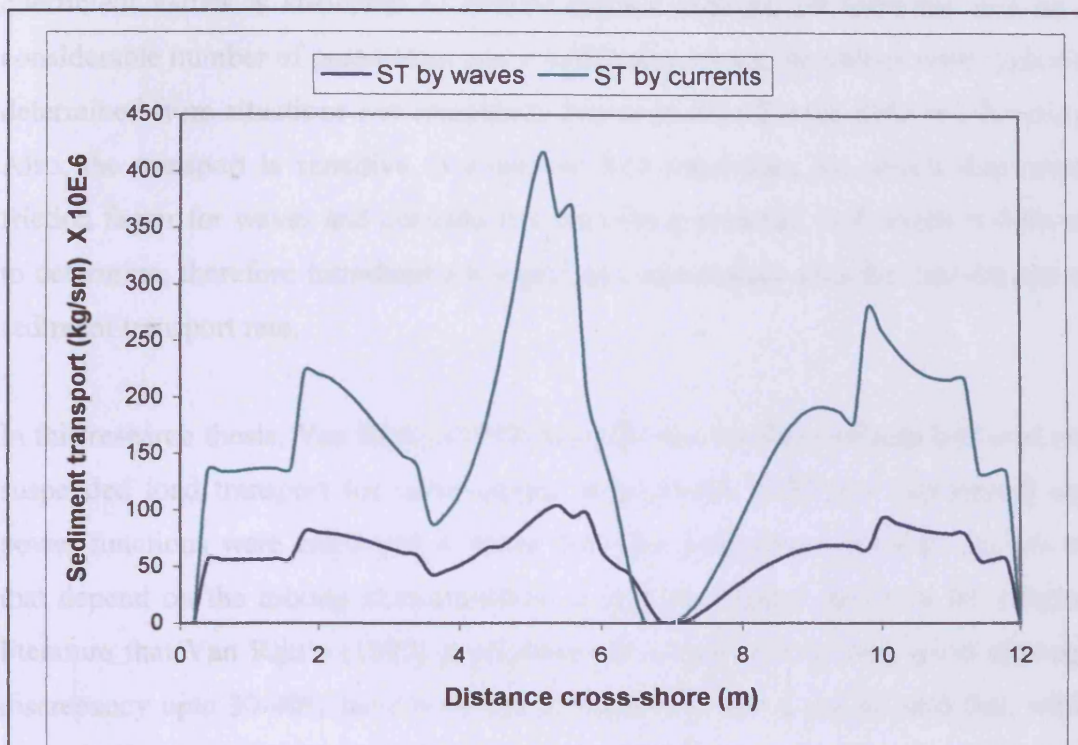
Figure 7.4.35 :Sediment transport by waves and currents (Line 4)
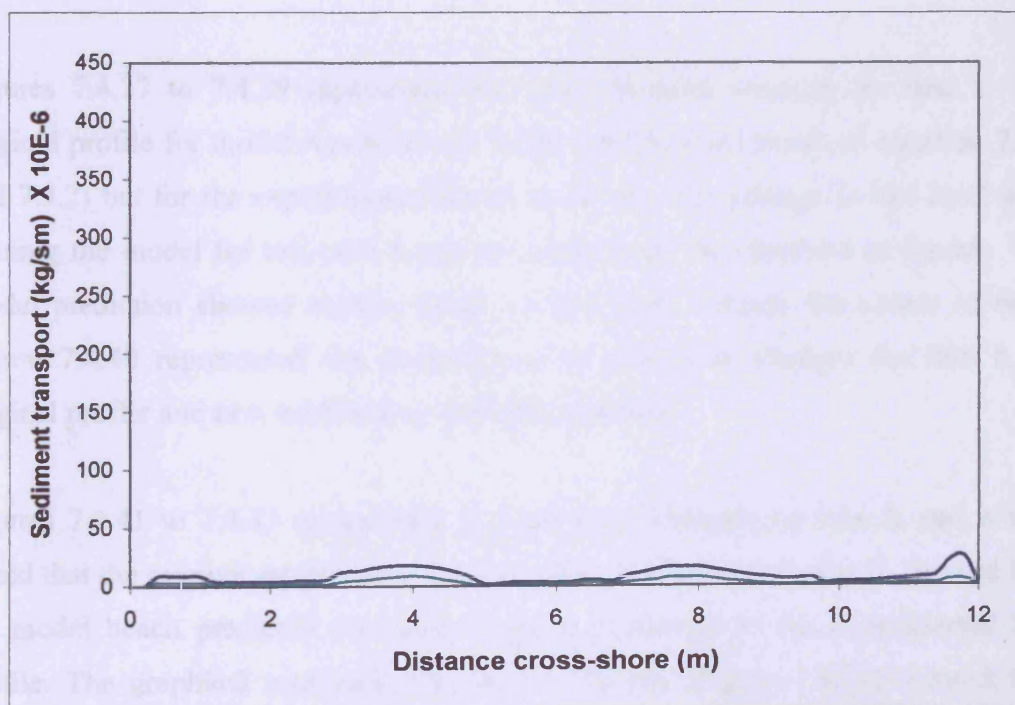
Figure 7.4.36 :Sediment transport by waves and currents (Line 5)

The observed discrepancy between the measurements and predictions using standard coefficient values is attributed to several factors such as, all formulae rely on a considerable number of parameters and coefficients, where the values were typically determined from situations not completely representative for the field or laboratory. Also, the transport is sensitive to estimated bed roughness, k_S, which determines friction factor for waves and currents in a decisive parameter, and which is difficult to determine, therefore introducing a significant uncertainty into the calculations of sediment transport rate.

In this research thesis, Van Rijn's (1993) formula was used to evaluate bed load and suspended load transport for wave-current interactions. Different exponential and power functions were employed in these formulae including empirical expressions that depend on the mixing characteristics. It was also found out from the existing literature that Van Rijn's (1993) predictions are considered as very good although discrepancy upto 30-40% have been found. Based, on this it can be said that, while computing the bed level changes, these discrepancies will also affect the computation.

Figures 7.4.37 to 7.4.39 represented the bed elevation changes for line 1. The original profile for model represented a fairly straight line (based on equation 7.3.1 and 7.3.2) but for the experimental set up it did not. The change in bed level after running the model for test case I and test case II can be observed in figures. The model prediction showed erosive nature of bed level through the course of time. Figure 7.4.40 represented the comparisons of bed level changes for line 1, as original profile and new profile after simulation period.

Figures 7.4.41 to 7.4.43 represented the bed level changes for line 2, and it was found that the original profile matched well. The profile for test case II, showed that the model beach predicted the similar nature of change as the experimental bed profile. The graphical representation for T = 2s run (Figure 7.4.21) showed that around the place of wave breaking (i.e. 2-3m from offshore), the maximum erosion could have taken place and bed level changes would be effected by these changes. Figure 7.4.44 shows a comparison between the original and simulated bed profiles
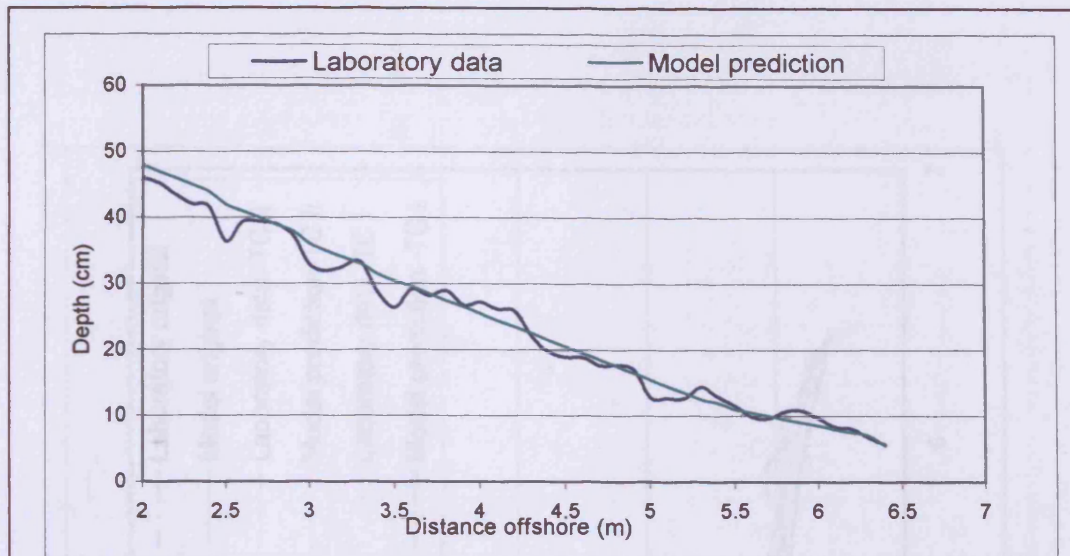
Figure 7.4.37 : Original profile, line 1
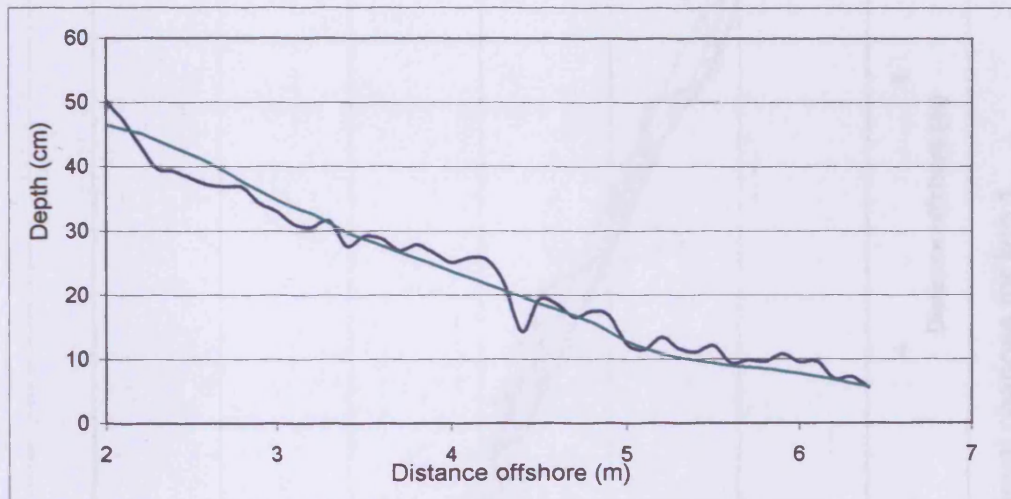
Figure 7.4.38: Bed profile after simulation for test case I
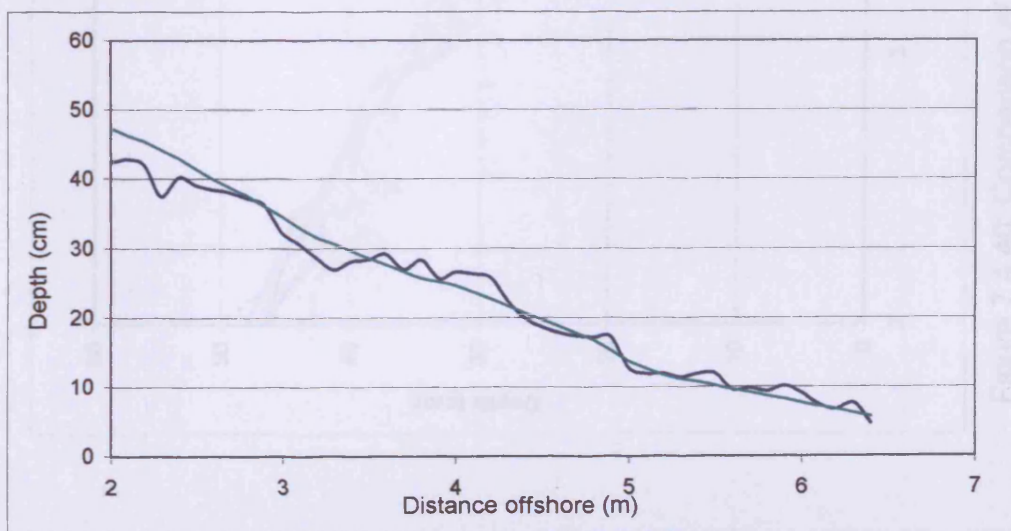
Figure 7.4.39: Bed profile after simulation for test case II.
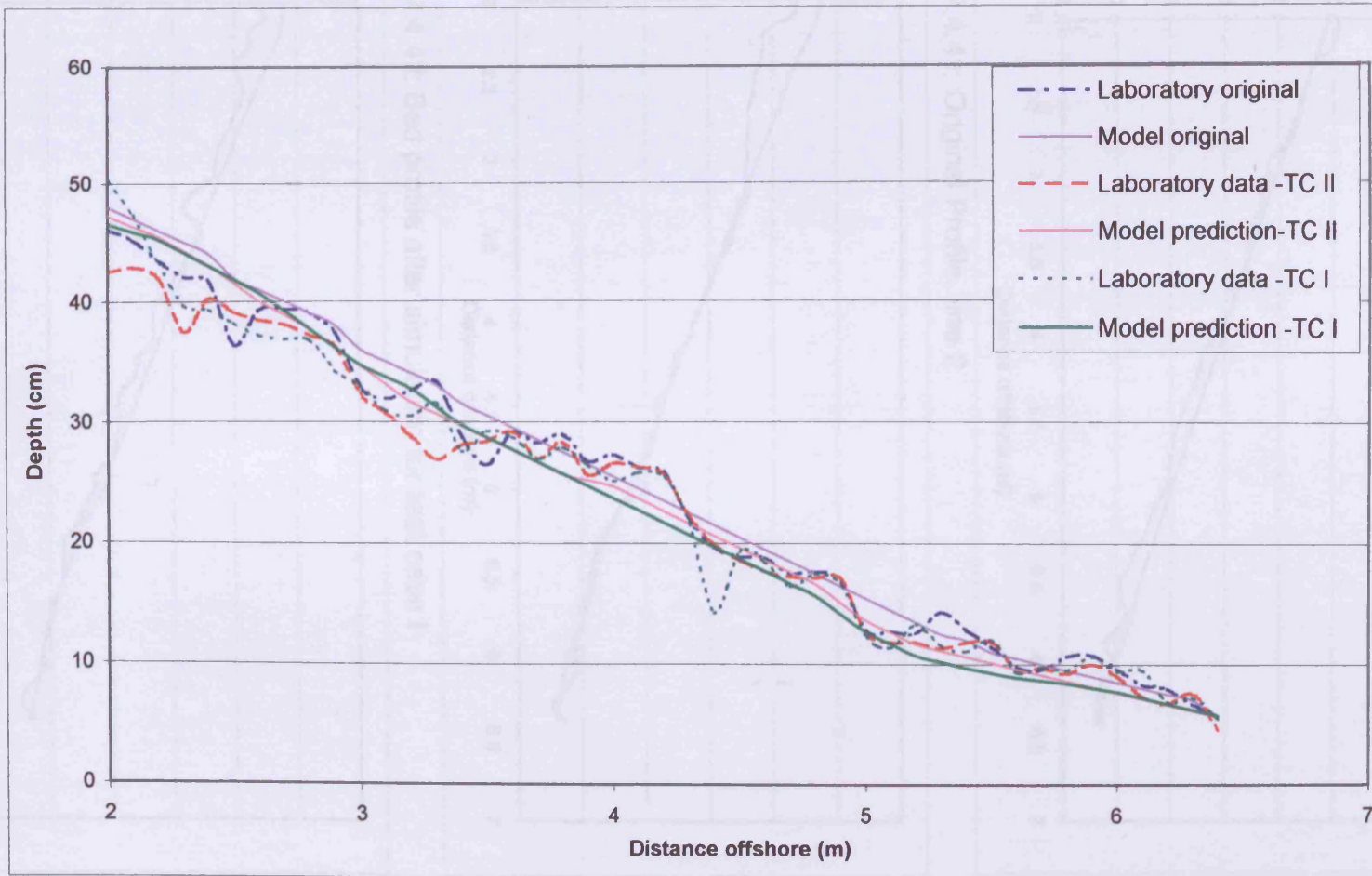
Figure 7.4.40: Comparison of bed level changes for line 1.
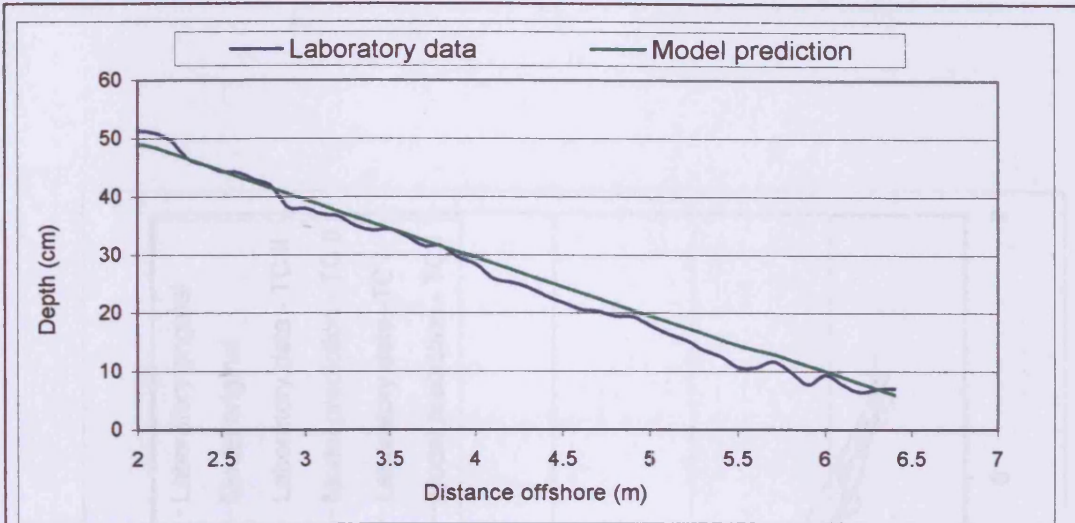
Figure 7.4.41: Original Profile, line 2
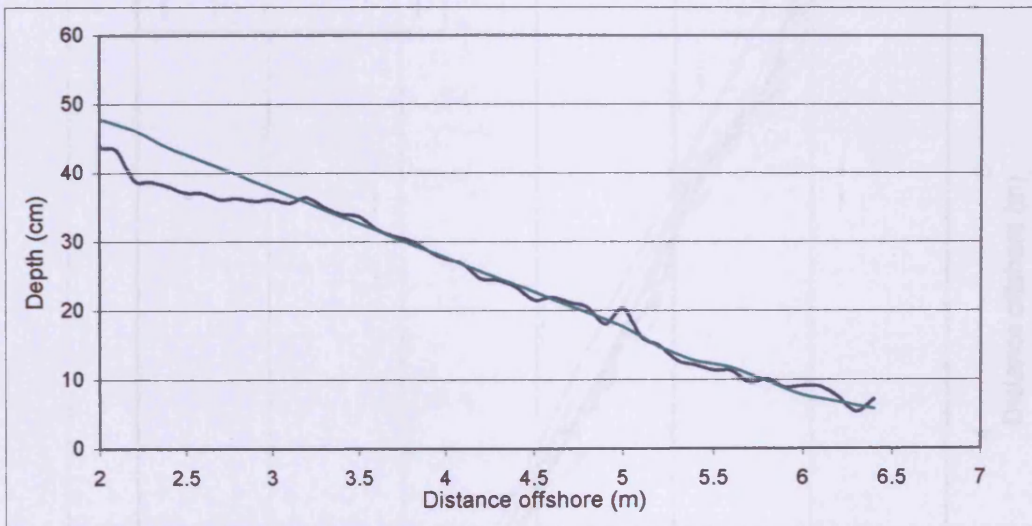
Figure 7.4.42: Bed profile after simulation for test case I
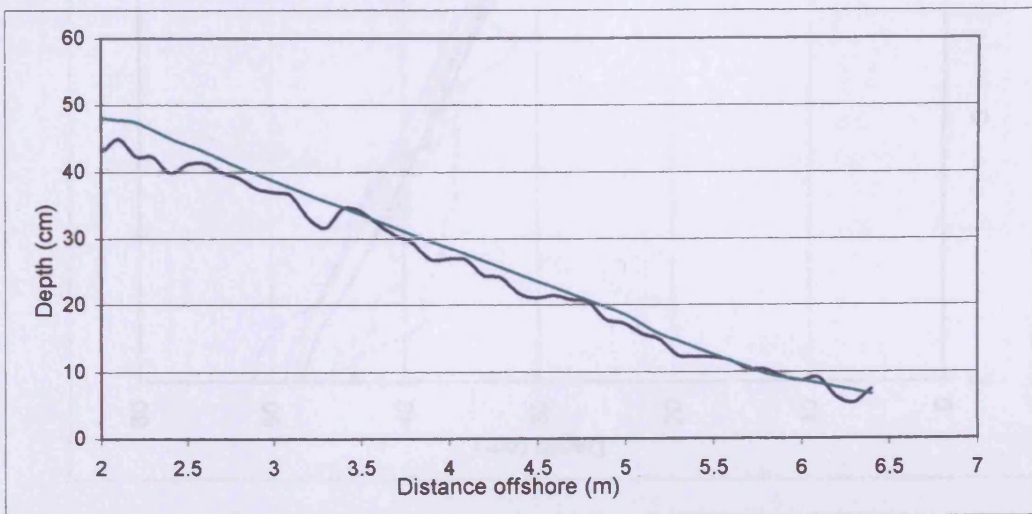
Figure 7.4.43 : Bed profile after simulatiom for test case II
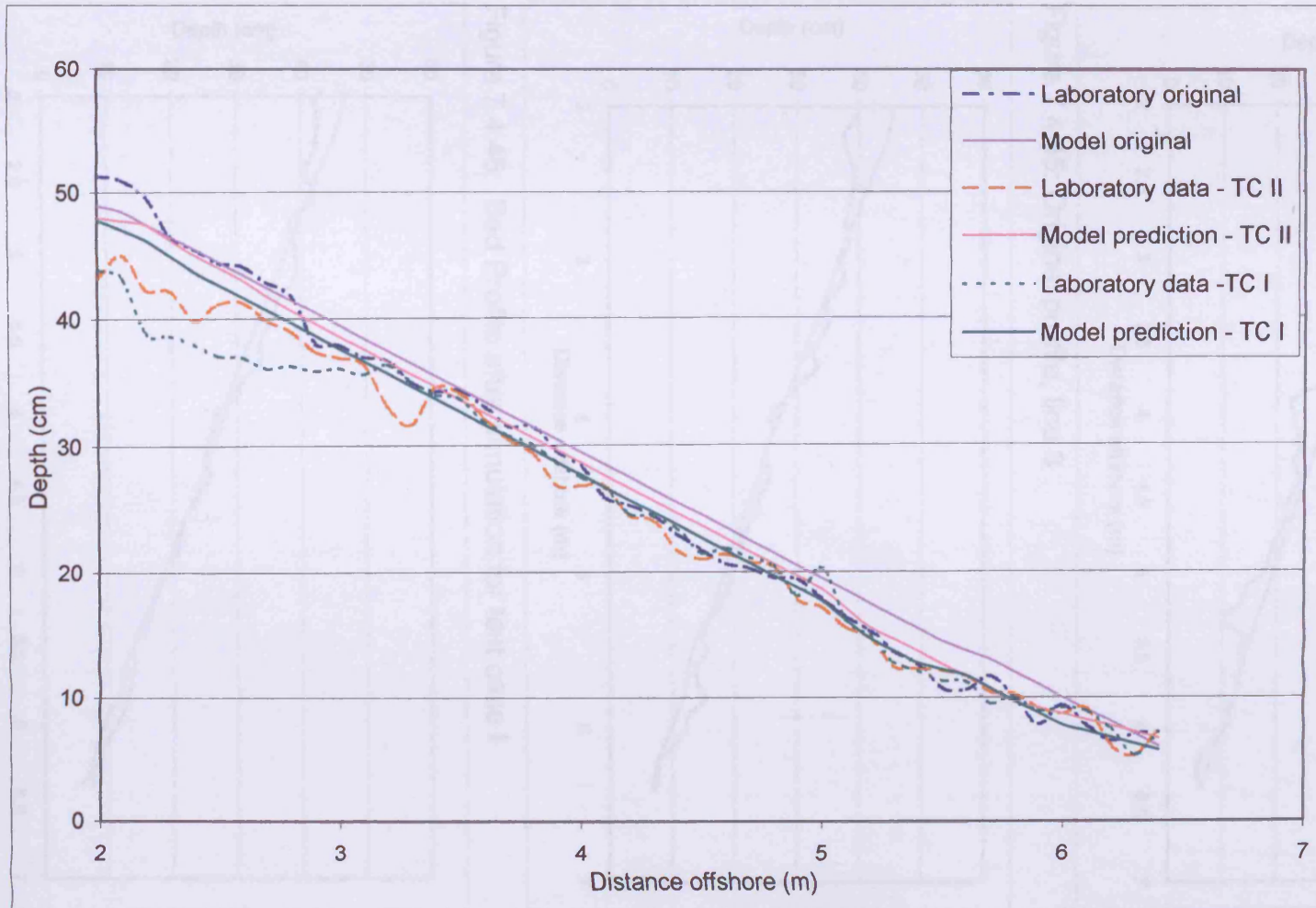
Figure 7.4.44: Comparison of bed level changes for line 2
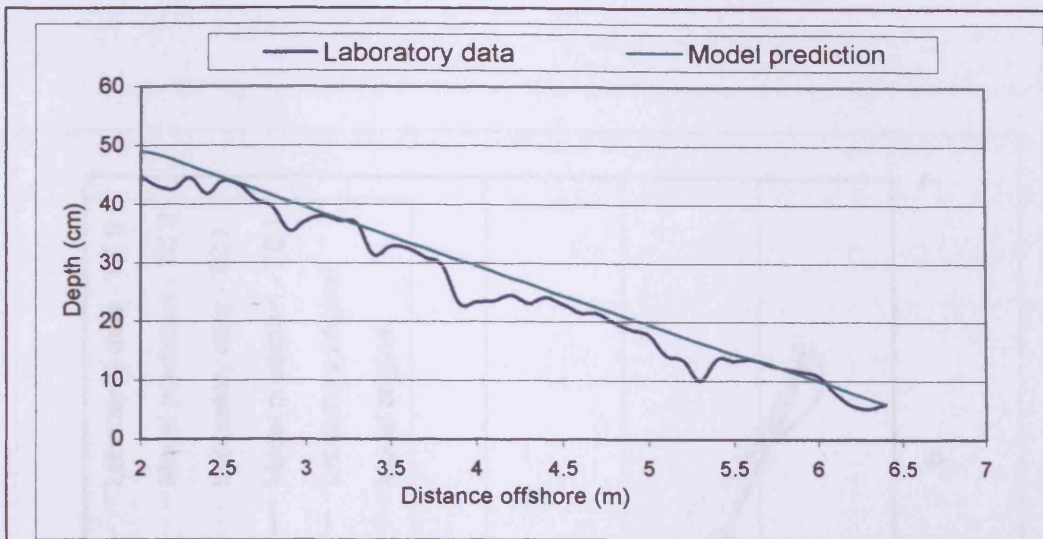
Figure 7.4.45: Original profile, line 3
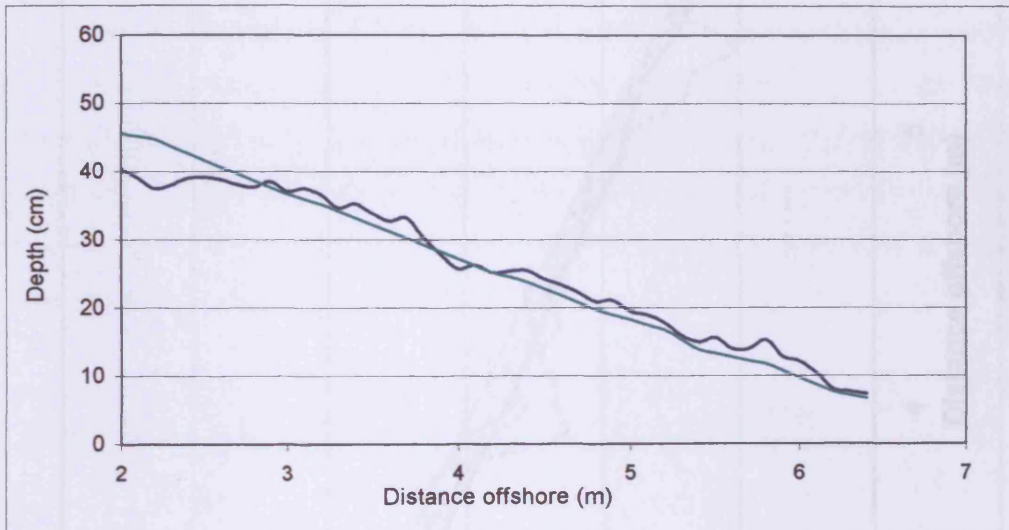
Figure 7.4.46: Bed Profile after simulation for test case I
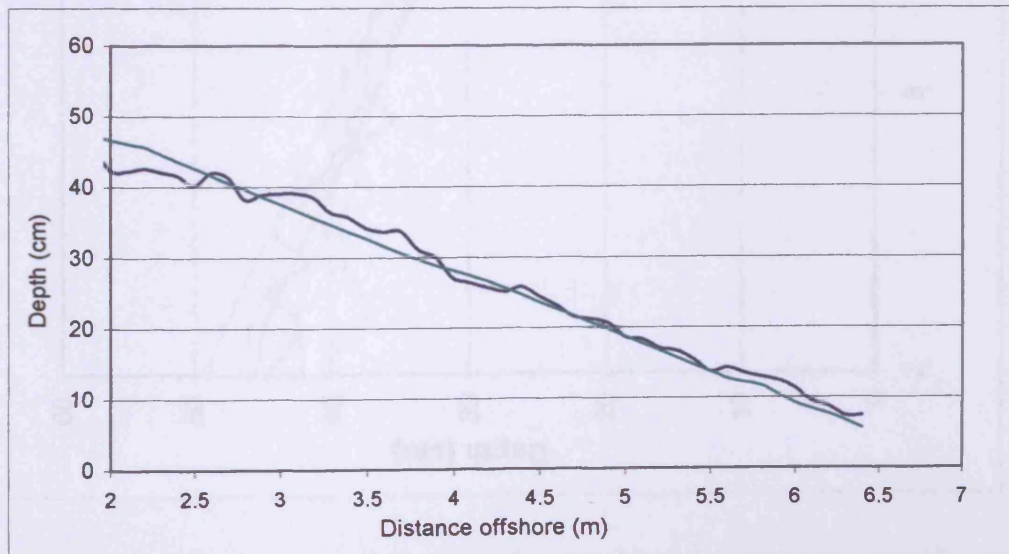
Figure 7.4.47: Bed Profile after simualtion for test case II
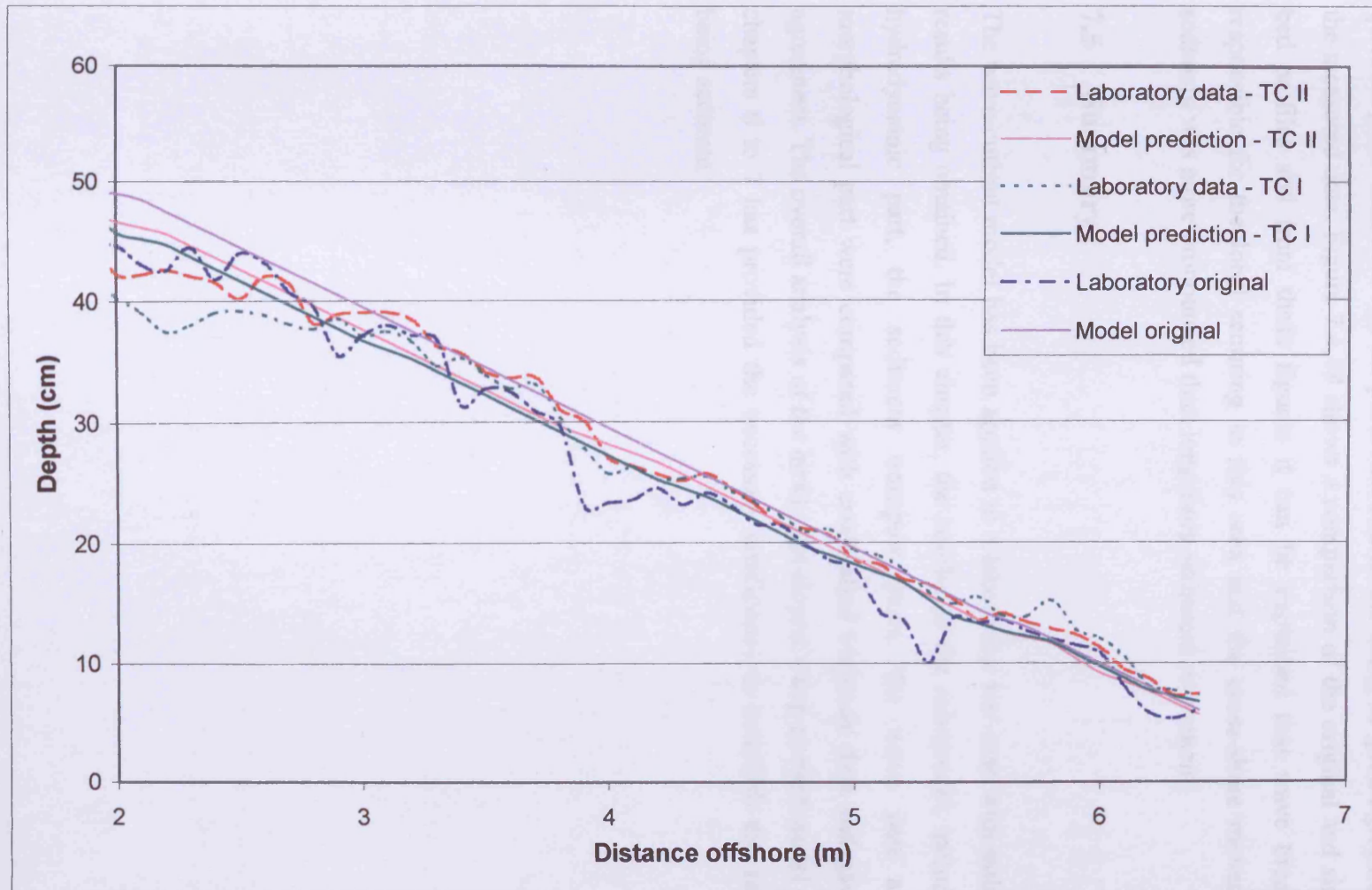
Figure 7.4.48: Comparison of bed level changes for line 3

and Figures 7.4.45 to 7.4.47 show the bed level changes for line 3 as the original profile, run for test cases I and II. The original experimental profile was found to be quite irregular with both run the predicted bed levels being in good agreement with the measured data. Figure 7.4.48 shows a comparison of the original and simulated bed profiles and from these figures it can be explained that wave breaking is responsible for the local scouring in this area and the cross-shore movement of sediment was more pronounced than longshore sediment movement.

7.5 Summary

The wave-current model has been applied to a laboratory test case with satisfactory results being obtained. In this chapter, the results of the sub-model, including the hydrodynamic part, the sediment transport parts, the wave part and the morphological part were compared with established literature data and gave good agreement. The overall analysis of the newly developed wave-current model through chapters 6 to 7 has provided the necessary confidence to establish this model as being accurate.

CHAPTER 8

CONCLUSIONS AND RECOMMENDATIONS FOR FURTHER STUDY

8.1 Conclusions

A two-dimensional depth integrated numerical model has been refined in this research project to investigate two different aspects of sediment transport process. The wave-current model has been developed and then incorporated into the hydrodynamic model to obtain flow pattern for both estuarine flow and nearshore circulation. Firstly to observe the sediment transport patterns in estuaries where tidal current play a very significant role. Secondly, the parabolic mild slope equation was introduced to this model as a sub-program, which can model nearshore circulation patterns. The integrated wave-current model has been checked against published research results and laboratory experiments.

The concept in Chapter 2 has been to deliver a review idea of the different fields of study within estuarine sediment transport and the nearshore circulation processes. Previous work, which has been undertaken up to the present time has been described and the basic objectives have been to show the scope of further research in related branches of work. The literature review provided a background for the necessity of this research work. It was found from the literature review that, although numerical models are available that could predict estuarine sediment transport, most of those

models are separate from those that can predict nearshore circulation. Hence, the need to have a combined wave-current model which can take care of both estuarine and nearshore circulation came out of the literature review as one of the main research objectives of this project.

The time dependent continuity equation and momentum equation form the basis of the mathematical formulation of the hydrodynamic field in of coastal and estuarine waters. Chapter 3 was divided into three broad divisions. Firstly, the two dimensional depth averaged Navier-Stokes equations were developed as the governing equations for the tidal flow. Secondly, the parabolic mild slope equation was derived in a form such that it could take care of large incident wave angles for this study, based on Booij (1981). The mild slope equation is valid for beaches with a milder slope. The derivation of the governing equations for currents and waves was followed by the transport equation for sediment for both estuarine and nearshore waters. Thirdly, the sediment transport rate, under the effects of currents or waves and waves and currents together were developed based on Van Rijn (1984 and 1993).

Chapter 4 develops the discretisation into numerical form of all of the mathematical equations derived in Chapter 3. The finite difference method was used in this study and the ADI method was chosen to discretise the governing equations for hydrodynamic, wave and the sediment transport models. The parabolic wave model was discretised using a fully implicit scheme to find the unknowns such as wave height, wave period and wave angle after the simulation time. The most suitable criteria for stability, the boundary conditions and the solution procedure were also discussed.

The numerical model for tidal circulation has been refined and was then calibrated and verified using field data available for the Bristol Channel. The first part of the study was to calibrate the model against neap tidal data. The parameters were chosen based on previous studies on this area. The eddy viscosity constant was calibrated and was set to as 0.15. The results of the water level comparisons at different locations with the tidal diamonds provided good agreement between the field data

and model results. The predictions of the magnitude and direction of the velocities at different locations in the Bristol Channel showed very good agreement and the 'Target Values' were achieved in terms of RMS errors. Only a few points did not give rise to good agreement. The reasons behind these discrepancies were primarily thought to be due to the bathymetry not being represented properly at several locations (especially in very complex regions using a 600m x 600m mesh size). Thus the tidal circulation pattern did not always accurately replicate the field condition. A smaller mesh size would probably have given better agreement. Also, at the eastern boundary where the tidal range was large (i.e. at Newport and Port Bury location) some differences were found in the range. The results obtained in this study were compared with the results from Coastal Response Study (1993) and Dun (1995) and it was found that there were similarities in terms of model behaviour.

The tidal model was then verified for the spring tide with all the parameters (coefficients) remaining the same. The difference between the neap and spring tidal range varied considerably in the Bristol Channel and was reflected in the respective figures of water level and velocity comparisons. The comparison results for a spring tidal cycle showed very good agreement between the field data and predicted results by the model. The discrepancy in the results at a few points was mainly due to the high tidal range and the average data for tidal diamonds. After calibration and verification of the estuarine model, it could be used with more confidence to test the model response to other field conditions. The model was applied for 10 day period simulations during which data were available at two locations (i.e. P1 and P2 in Figure 5.4.21) in South Wales and at Minehead. Also data were collected at locations of A, B, C and D shown in Figure 5.4.21 for the Bristol Channel, and were taken from July to December 2001. The model run covering these survey days for P1 and P2 showed that the predicting and measured comparisons were in very good agreement. The parameters were kept the same as for the previous calibrated model. The estuarine model was run for parameters which were carefully chosen based on the various laboratory and field experimental comparisons and were found to be in agreement with studies (Falconer et al., 2001; Falconer and Chen, 1996; Falconer and Owens, 1990; Fischer, 1979). These parameters greatly influenced the model behaviour. A uniform sediment size was assumed over the whole estuary in the

absence of geological data and this assumption was thought to be questionable. However, since little data existed it was difficult to justify any other assumption.

The velocity fields and the corresponding suspended sediment transport patterns for the Bristol Channel illustrated a clear picture of the changes in the estuary during neap and spring tides. During the neap tidal cycle the tidal velocity did not attain a very high value, and less sediment was entrained or advected for. The sediments were generally settled for a long time and entrainment was delayed as the average velocity was too small to transport large quantities of sediments. The spring tidal period represented a highly mobile estuary especially in the reach from Newport to Swansea. This was particularly marked from 4 hours after HW up to 10 hours after HW. The velocity field showed large velocity and the effects on the suspended sediment concentration were pronounced. The mechanism of sediment transport is still not fully understood but the basic equations developed by researchers like Bagnold (1966), England and Hansen (1976), Fredosoe (1984), Van Rijn (1984, 1993) have provided the basic understanding to estimate estuarine transport rates. The prediction of residual erosion for the model after different tidal cycles also gave an opportunity to visualise the morphological status of the estuary, which dominated the long-term changes. The results for the sediment transport patterns and residual erosion were compared with RCL Report (1986) and provided encouraging outcomes and the pattern of comparison has been discussed in Chapter 5.

The newly developed wave-current model was integrated within the existing estuarine model as a sub-program. At first it was necessary to verify the extended model against results from published literature. Different beach shapes were chosen to show that the circulation pattern changed with changes in the hydrodynamic and wave parameters. It was found from the model runs that the finer grid spacing provided a clearer resolution of the velocity patterns, but the sub-model needed more computational time. The minimum depth (preset) for wetting and drying criteria also effected the circulation pattern, although it did not have a major influence on the large estuarine circulation, although near to the coastline it was occasionally visible.

The wave model was then applied to the experimental data of Borthwick et al. (1997). The experimental set for three-cusp beach in the UKCRF provided a useful result for the wave simulation. The wave model was run for regular waves only. The circulation patterns for waves propagating at different incident angles produced corresponding circulation patterns. The wave angle distribution agreed with the fact that near the shoreline the friction force dominated as the water depth decreased. This made the wave angle more inclined towards the normal direction. The velocity patterns showed that the main circulation occurred in the presence of cusps. The bathymetry and the incoming wave direction were the main factors influencing the velocity circulation patterns, which caused the sediment movement to be either longshore or cross-shore. The laboratory data and the model results again showed good agreement.

After that the wave-current model was applied to the laboratory experimental configuration and results of Borthwick and Joynes (1989), which was based on a detailed laboratory experimental set-up first used by Lima (1981). The model was simulated against different wave conditions described by Lima. The velocity circulation pattern for the whole wave field showed satisfactory agreement between the laboratory data and the model predictions. The magnitude and direction of the predicted velocities matched up well with the laboratory measurements. The wave height distributions for different lines along in the onshore-offshore direction produced reasonably good agreement. For some points the results were not so good in comparison with the breaking points. This was thought to be due to the numerical model being based on linear wave theory whereas the higher order approximation of non-linear wave theory would possibly provide better result at these points. The water level variations in the offshore direction, and the onshore-offshore velocity distributions gave satisfactory results.

The application of the wave-current model in Chapter 6 to different published literature studies paved the way for applying the model to a new set of laboratory data. The objective of chapter 7 was to establish that the wave-current, sediment transport and morphodynamic part of the model had the ability to predict the laboratory results to a high level of accuracy. The sensitivity tests were performed

by changing various parameters, such as the bed roughness, friction coefficient and breaking index, in the wave-current part of the model. The effects in the nearshore circulation prediction were observed for changing values of these parameters. The parameters which gave the best comparisons between both sets of results were chosen as the model parameters. The sensitivity tests led to a detailed statistical performance analysis, based on Van Rijn et al. (2003), which provided the model with a qualitative ranking as 'reasonably good'.

The sediment transport predictions of the model were compared with different model results and were found to be satisfactory. Hence, the wave-current model has the capacity to calculate nearshore sediment transport rates for wave-currents or for current only scenarios. The uncertainties in the sediment transport predictions have been highlighted in this research study and the need to calculate bed level changes based on the corresponding sediment transport rates. The status of modelling sand transport can be summarised according to Davies et al. (1997) where in comparisons were found to be encouraging where the longshore component of suspended sand transport yielded agreement with a factor of 2, where a factor of 2 means between 2 and 0.5 times the actual level of transport. Hence, the resulting bed level changes can expect this level of variations as well. The model was capable of predicting bed level changes for a considerable time.

The objective of this research was to develop an intrigated wave-current model suitable to use in both large estuarine areas and also to predict nearshore circulation in relatively small areas. It can therefore be concluded that the objectives of developing a new wave-current model, which can account of both estuarine and nearshore circulation patterns, has been developed through this study. The prediction capacity of the model is generally satisfactory but there is scope for improvement. Laboratory experiments based on changing bed topography, different shoreline configuration, different hydrodynamic and wave climates have provided a better understanding of the nearshore circulation processes for various beach configurations.

8.2   Recommendations for Further Study

A parabolic wave model has been established and incorporated into an existing estuarine model, namely DIVAST. The combined model has been verified against different scenarios giving promising results, but the following points need to be considered in any future research studies.

The results obtained for the Bristol Channel using a grid size of 600m x 600m are satisfactory as the comparisons show good agreement. However, the Bristol Channel is a very complex estuarine system, and hence a new set up of the estuary, with a smaller grid size of say 200m x 200m, and particularly in the areas of complex bathymetry could provide more details of the complex hydrodynamic behaviour in the region. More data for the boundary conditions would also be invaluable. Further data would also be invaluable for the sediment transport fluxes, particularly in the shallow waters of the Bristol Channel, although the acquisition of sediment concentration for such a big estuary is often difficult to acquire.

The wave-current model developed in this research thesis is based on the parabolic wave equation for mild slope beaches. The comparisons of the model predictions with different laboratory conditions provides encouraging results. However, it would be appropriate to test this model again with more scenarios in the future. The smaller the mesh size the better the prediction for nearshore circulation as observed in this study. However, a smaller mesh size means more that a longer execution time would be required for each computer simulation. A balance between acceptable mesh size with computer storage capacity would need to be achieved.

The bed roughness considered in this model was based on sediment size used in the experimental beaches. The effects of vegetation on the nearshore circulation patterns can be observed both in laboratory and in the field. The effects of a mixed mode beach, such as shingle and sand mixture, could be checked in future, both in the laboratory and the corresponding prototype model predictions. The effects of different wave parameters on a mixed mode beach would also provide more

knowledge in this field. There is currently no standard at the present time for different the hydrodynamic and wave parameters used in various models. More laboratory, as well as field data, for different bathymetries in the nearshore zone, for different wave heights, wave periods, incidence wave angles and sediment sizes would assist in validating the model.

The combined wave-current model is suitable for predicting both estuarine and nearshore circulation patterns and sediment transport rates. However, this leads to a new dimension of work to be undertaken, which is to harmonise the mesh size for both estuarine and nearshore transport models. Normally estuarine grids are much bigger than those used in nearshore models as they are modelling processes at a different spatial scale. To make a balance between these two scenarios, research needs to be undertaken in developing refined numerical schemes.

It would be a good opportunity if the model were to be applied to field data for the whole estuary. At the same time wave climate data for different nearshore locations within the same estuary would also be appropriate. This type of investigation would provide any modeller with more confidence in representing tidal and wave interactions. Bed level changes could be calculated using this model, particularly when compared with establish data. Based on these data, integrated studies would provide a new dimension for the model if the shoreline changes could be predicted. Also, the wave-current model could be enhanced if water quality simulations were included in the future. Hence, valuable information could be attained about the nearshore beach water quality.

This section can be concluded by citing from Van Rijn et al. (2003), where he states that "the quality and use of process based models is still seriously affected by a number of limiting conditions such as: randomness and directionality of the wave, the wave-breaking processes, the wave induced cross-shore and longshore currents and wave induced sand transports, where a sand transport module is a key element and still requires a substantial input of information from empirical data sets and much more research is required to improve on this".

Appendix A

Wave and Current Induced Sediment Transport Rate

The method to calculate the wave induced or wave-current induced sediment transport rate has been derived by several reseacher. Among them the prediction by Van Rijn (1993) came out to be one of the accurate one. Though a unique solution for sediment transport rate is yet to be achieved in nearshore coastal waters. The derivation of bed load and suspended load tranport of wave induced sediment transport id described as follows:

The representative diameter of suspended material d_s can be espressed as:

$$d_s = 0.8 \, d_{50,bed} \qquad (A.1)$$

where d_{50} = median diameter of bed material (m)

$\quad\quad d_{90}$ = 90% diamter of bed material (m)

A reasonable guess is: $d_s = (0.6 \text{ to } 1.0) \, d_{50,bed}$

The wave-related bed roughness height in the ripple regime will be in the range $k_{s,w}$ = (1 to 3) Δ_r with values of Δ_r from 0.01 to 0.1. The wave-related bed roughnesss height in sheet flow regime will be: $k_{s,w}$ = 0.01m. The current-related bed roughnesss height will be in the range $k_{s,c}$ = 0.01 to 1m.

Chloridity can be defined as:

$$CL = (SA-0.03)/1.805 \qquad (A.2)$$

The fluid density (ρ), the kinematic viscosity (v) and the fall velocity (w_s) can be described as

$$\rho = 1000 + 1.455 \, CL \, 0.0065 \, (TE - 4 + 0.4 \, CL) \qquad (A.3)$$

$$v = (4/(20 + TE)) \, 10 \qquad (A.4)$$

$$w_s = \frac{(s-1)gd^2}{18v} \qquad \text{for } 1 < d < 100\mu m \qquad (A.5.a)$$

$$w_s = \frac{10v}{d}\left[\left(1 + \frac{0.01(s-1)gd^3}{v^2}\right)^{0.5} - 1\right] \qquad \text{for } 100 < d < 1000 \ \mu m \qquad (A.5.b)$$

$$w_s = 1.1[(s-1)gd]^{0.5} \qquad \text{for } d > 1000 \ \mu m \qquad (A.5.c)$$

where TE = fluid temperature (^{0}C)

SA= fluid salinity (%)
d = sieve diameter
s = specific gravity (=2.65)

The method of computing the critical Shield's parameter has been described in equation (3.6.6) in Chapter 3. The particle parameter, D can ve calculated as:

$$D = d\ [(s-1)g/\nu\ ] \tag{A.6}$$

Critical bed-shear stress, τ_{cr} and Critical depth-averaged velocity $\overline{u}_{cr}$ obtained as:

$$\tau_{cr} = (\rho_s - \rho)gd_{50}\theta_{cr} \tag{A.7}$$

$$\overline{u}_{cr} = 5.75[(s-1)gd_{50}]^{0.5}(\theta_{cr})^{0.5}\log(4h/d_{50}) \tag{A.8}$$

where the critical peak orbital velocity is:

$$d_{50} < 0.0005m \qquad\qquad : \hat{U}_{cr} = [0.12(s-1)g(d_{50})^{0.5}(T_p)^{0.5}]^{2./3} \tag{A.9}$$

$$d_{50} > 0.0005m \qquad\qquad : \hat{U}_{cr} = [1.09(s-1)g(d_{50})^{0.75}(T_p)^{0.25}]^{0.571} \tag{A.10}$$

The wave length (L')modified by currents as :

$$\left[\frac{L'}{T_p} - \overline{v}_R\cos\phi\right]^2 = \left[\frac{gL'}{2\pi}\right]\tanh\left[\frac{2\pi h}{L'}\right] \tag{A.11}$$

The relative wave period is:

$$T'_p = \frac{T_p}{1-(\overline{v}_R T_p\cos\phi)/L'} \tag{A.12}$$

The near-bed peak orbital velocity can be obtained from

$$\hat{U}_\delta = \frac{\pi H_s}{T'_p\sinh(2\pi h/L')} \tag{A.13}$$

The near-bed peak orbital velocity in forward direction:

$$h \geq 0.01g(T_p)^2 \qquad\qquad : \hat{U}_{\delta,f} = \hat{U}_\delta + \frac{3\pi^2(H_s)^2}{4(T'_p)(L')(\sinh(2\pi h/L'))^4} \tag{A.14}$$

$$h \leq 0.01g(T_p)^2 \qquad\qquad : \hat{U}_{\delta,f} = \alpha\hat{U}_\delta \text{(A.13)}$$

where $\alpha = 1 + 0.3(H/h)$

Near-bed orbital velocirt in backward direction:

$$h \geq 0.01g(T_p)^2$$

$$: \hat{U}_{\delta,b} = \hat{U}_\delta - \frac{3\pi^2 (H_s)^2}{4(T_p')(L')(\sinh(2\pi h / L'))^4} \quad (A.15)$$

$$h \leq 0.01g(T_p)^2$$

$$: \hat{U}_{\delta,b} = (2 - \alpha)\hat{U}_\delta$$

Return velocity mass transport

$$: \bar{u}_r = -\frac{0.125g^{0.5}(H_s)^2}{h^{0.5}h_t} \quad (A.16)$$

$$h_t = (0.95 - 0.35(H_s / h))h$$

So the near-bed wave-induced velocity become

$$u_b = (0.05 - (\alpha - 0.5_s))\hat{U}_b \quad (A.17)$$

where $\quad \alpha_s = \hat{U}_{\delta,f} / (\hat{U}_{\delta,f} + \hat{U}_{\delta,b})$

The apparent bed roughness can be computed as:

$$k_s = k_{s,c} \exp\left[\gamma \hat{U}_b / ((\bar{v}_v)^2 + (\bar{v}_v)^2)^{0.5}\right] k_{s,max} = 10k_{s,c}$$

$$\gamma = 0.8 + \beta - 0.3\beta^2 \quad (A.18)$$

$$\beta = \left(\frac{\phi}{360^0}\right) 2\pi$$

The friction factors for currents and waves are dependent mainly on water depth (h) and roughness coefficint. They can be computed as:

For current   : $\quad C' = 18\log(12h / 3d_{90})$

$$C = 18\log(12h / k_{s,c})$$

$$f_c' = 0.24\log^{-2}(12h / 3d_{90})$$

$$f_a = 0.24\log^{-2}(12h / k_s)$$

$$f_a = 0.24\log^{-2}(12h / k_a)$$

For waves $\quad : f_w' = \exp\left[-6 + 5.2(\hat{A}_b / 3d_{90})^{-0.19}\right]$

$$f_w = \exp\left[-6 + 5.2(\hat{A}_b / k_{s,w})^{-0.19}\right]$$

$$f_{w,max} = 0.3$$

In order to calculate the effective time-averaged bed-shear strees, it is first necessary to obtain the parameters.

Efficiency factor current $\quad : \mu_c = f_c' / f_c$

Efficiency factor wave $\quad : \mu_w = f_w' / f_w$

$$\mu_{w,a} = 0.6 / D_*$$

Wave-current interaction coefficient :

$$\alpha_{cw} = \left[\frac{\ln(90\delta_w / k_s)}{\ln(90\delta_w / k_{s,c})}\right]^2 \left[\frac{-1 + \ln(90h / k_{s,c})}{-1 + \ln(90h / k_s)}\right]^2 \qquad (A.19)$$

$$\alpha_{cw,\max} = 1$$

So the bed shear stresses for wave, current and both wave-current can be obtained through equation (A.20) to (A.22).

Bed-shear stress current $\qquad : \tau_c = \frac{1}{8}\rho f_c\left[(\bar{v}_R)^2 + (\bar{u}_r)^2\right]^{0.5} \qquad (A.20)$

Bed-shear stress waves $\qquad : \tau_w = \frac{1}{4}\rho f_w(\hat{U}_\delta)^2 \qquad (A.21)$

Bed-shear stress current-waves $\quad : \tau_{cw} = \tau_x + \tau_w \qquad (A.22)$

From this above the effective bed-shear velocity current becomes:

$$u'_{*,c} = [(\alpha_{cw}\mu_c\tau_c)/\rho]^{0.5} \qquad (A.23)$$

Dimensionless bed-shear stress for bed load transport :

$$T = \frac{(\alpha_{cw}\mu_c\tau_c + \mu_w\tau_w) - \tau_{cr}}{\tau_{cr}} \qquad (A.24)$$

Dimensionless bed-shear stress for reference concentration z=a

$$T_a = \frac{(\alpha_{cw}\mu_c\tau_c + \mu_{w,a}\tau_w) - \tau_{cr}}{\tau_{cr}} \qquad (T = 0 \text{ if } T<0) \qquad (A.25)$$

After calculating the shear stresses, the wave induced velocity and the roughness coefficients. The velocity distribution over the water depth can be calculated. The velocity component inside and outside the wave boundary layer is:

Outside wave-boundary layer, $\qquad z \geq 3\delta_w : v_{R,A} = \dfrac{\bar{v}_R \ln(30z/k_a)}{-1 + \ln(30h/k_a)}$

Inside wave-boundary layer, $\qquad z < 3\delta_w : v_{R,A} = \dfrac{\bar{v}_R \ln(30z/k_{s,c})}{-1 + \ln(90\delta_w/k_{s,c})}$

$$v_\delta = \frac{\bar{v}_R \ln(90\delta_w/k_a)}{-1 + \ln(30h/k_a)}$$

The coefficient for obtaining sediment mixing coefficient over the depth for wave and current can be expressed as:

For current $z < 0.5h$: $\varepsilon_{s,c} = \kappa\beta u_{*,c}z(1 - z/h)$

$z \geq 0.5h$: $\varepsilon_{s,c} = 0.25\kappa\beta u_{*,c}h$

where: $u_{*,c} = (g^{0.5}/C)[(\bar{v}_R)^2 + (\bar{u}_r)^2]^{0.5}$

$\beta = 1 + 2(w_s/u_{*,c})^2$

$\beta_{max} = 1.5$

for waves $z \leq \delta_s$: $\varepsilon_{s,w} = \varepsilon_{s,bed} = 0.004D_*\delta_s\hat{U}_\delta$

$z \geq 0.5h$: $\varepsilon_{s,w} = \varepsilon_{s,max} = 0.035hH_s/T_p$

where:

$\delta_s < z < 0.5h : \varepsilon_{s,w} = \varepsilon_{s,bed} + [\varepsilon_{s,max} - \varepsilon_{s,bed}]\left[\dfrac{z - \delta_s}{0.5h - \delta_s}\right]$

$\delta_s = 0.3h(H_s/h)^{0.5}$

$\delta_{s,min} = 0.05m, \delta_{s,max} = 0.2m$

At the time where both wave and current occurs simultaneously, the coefficient can be expressed as:

$$\varepsilon_{s,cw} = [(\varepsilon_{s,c})^2 + (\varepsilon_{s,w})^2]^{0.5} \qquad (A.26)$$

The reference concentration at the reference level z=a, can be taken as maximum of $(k_{s,c}, k_{s,w})$. The concentratio,c when expressed as gradient of depth becomes:

Concentration gradient $(z>a)$: $\dfrac{dc}{dz} = -\dfrac{(1-c)^5 cw_s}{\varepsilon_{s,cw}\left(1 + (c/c_0)^{0.8} - 2(c/c_0)^{0.4}\right)}$ (A.27)

Bed concentration $(z < a)$: $c_a = 0.015\dfrac{d_{50}}{a}\dfrac{T_a^{1.5}}{D_*^{0.3}}$ (A.28)

where $c_0 = 0.65$ = maximum volume concentration

The time averaged suspended load transport rates, q_s now can be obtained as:

Current direction $\qquad$: $\quad q_s = \rho_s \int_a^h v_R c\, dz$ $\qquad\qquad$ *(A.29)*

Wave direction $\qquad$: $\quad q_s = \rho_s \int_a^h u_r c\, dz$ $\qquad\qquad$ *(A.30)*

The time averaged bed load transport can be obtained through the following way, the current velocities at z=δ is:

Above bed $\qquad$: $\qquad \delta = \max imum(3\delta_w, k_{s,c})$

$$v_{R,\delta} = \frac{\bar{v}_R \ln(30\delta / k_s)}{-1 + \ln(30h / k_s)} \quad \text{and} \quad u_{r,\delta} = (\bar{u}_r / \bar{v}_R) v_{R,\delta}$$

Orbital velocities (asymm.) : $U_{\delta,f} \, and \, U_{\delta,b}$

Instantaneous velocity x $\qquad$: $\sum U_{\delta,x} = U_\delta \cos\phi + v_{R,\delta} + (u_b + u_{r,\delta})\cos\phi$

Instantaneous velocity y $\qquad$: $\sum U_{\delta,y} = U_\delta \sin\phi + (u_b + u_{r,\delta})\sin\phi$

Instantaneous velocity x $\qquad$: $U_{\delta,R} = \left[\left(\sum U_{\delta,x}\right)^2 + \left(\sum U_{\delta,y}\right)^2\right]^{0.5}$

Instantaneous friction coefficient : $\alpha = \dfrac{|v_{R,\delta}|}{|v_{R,\delta}| + |\hat{U}_\delta|}$

$$\beta = 0.25\left[\frac{-1 + \ln(30h / k_{s,c})}{\ln(30\delta / k_{s,c})}\right]^2$$

$$f'_{cw} = \alpha\beta f'_c + (1 - \alpha)f'_w$$

Instantaneous bed-shear stress $\quad$: $\quad \tau'_{b,cw} = 0.5\rho f'_{cw}(U_{\delta,R})^2$

Instantaneous bed-shear transport : $\gamma = 1 - (H_s / h)^{0.5}, \gamma_{min} = 0.3$

Current velocities at

$$q_b = 0.25\gamma\rho_s d_{50} D_*^{-0.3}\left[\frac{\tau'_{b,cw}}{\rho}\right]^{0.5}\left[\frac{\tau'_{b,cw} - \tau_{b,cr}}{\tau_{b,cr}}\right]^{1.5}$$

$$q_{b,x} = \left(\sum U_{\delta,x} / U_{\delta,R}\right)q_b$$

$$q_{b,y} = \left(\sum U_{\delta,y} / U_{\delta,R}\right)q_b$$

Time-averaged values are obtained by averaging over the wave period.

REFERENCES

Abbott, M.B., Peterson, H.M. and Skovgaard, O., 1978. "On the Numerical Modelling of Short Waves in Shallow Water." Journal of Hydraulic Research, Vol. 16, No. 3, pp. 173-204.

ABP Report, 2000. "Bristol Channel Marine Aggregates: Resources and Constraints Research Project." Final Report, Vol. 1-2, August 2000.

Ackers, P. and White, W.R., 1973. "Sediment Transport : New Approach and Analysis." Journal of Hydraulic Engineering, vol. 99, no. 1, pp 2041-2060.

Antia, E., 1989. "Beach Cusps and Beach Dynamics: A Quantitative Field Appraisal." Coastal Engineering, Vol. 13, pp. 263-272.

Antoniadis, C., 2003. "Draft Report on Experimental Procedure and Data Collection for an Inverse Sinusoidal Beach." School of Engineering, Cardiff University.

Archilla, A.S., Roelvink, J.A., O'Connor, B.A., Reniers, A. and Jiménez, J.A., 1994. "The Delta Flume'93 Experiment." Proceedings of the Coastal Dynamics Conference. Barcelona. pp. 488-502.

ASCE,. 1988. ASCE Turbulence Modelling of Surface Water Flow and Transport, part I – V, Journal of Hydraulic Engineering, ASCE, Vol. 114, no. 9, pp 970-1073.

Bagnold, R. A., 1954. "Experiments on a Gravity-free Dispersion of Large Solid Spheres in a Newtonian Fluid under Shear." Proceedings Royal Society, London, UK. Vol. 225A, pp. 49-63.

Bai, Y., Wang, Z. and Shen, H., 2003. "Three Dimensional Modelling of Sediment Transport and the Effects of Dredging in the Haihe Estuary." Estuarine Coastal and Shelf Science, Vol. 56, No. 1, pp 175-186.

Balzano, A., 1998. "Evolution of Methods for Numerical Simulation of Wetting and Drying in Shallow Water Flow Model." J. of Coastal Engineering, Vol. 34, No. 1-2, pp. 83-107.

Bao, X. W., Yan, J. and Sun, W. X., 2000. "A Three Dimensional Tidal Model in Boundary Fitted Curvilinear Grids." Journal of Estuarine, Coastal and Shelf Science, Vol. 50, No. 6, pp. 775-788.

Basco, D.R., 1985. "A Qualitative Description of Wave Breaking." J. of Waterway, Port, Coastal and Ocean Engineering, Vol. 111, No. 2, pp. 171-189.

Batchelor, G.K., 1967. "An Introduction to Fluid Mechanics." Cambridge University Press. Bently House, London.

Baumert, H., Chapalain, G., Smaoui, H., McManus, J.P., Yagi, H., Regener, M., Sundermann, J. and Szilagy, B., 2000. "Modelling and Numerical Simulation of Turbulance, Waves and Suspended Sediments for Pre-operational Use in Coastal Seas." Coastal Engineering, Vol. 41, pp 63-94.

Bayram, A., Larson, M., Miller, H.C. and Kraus, N.C., 2001. "Performance of Longshore Sediment Transport Formula's Evaluated with Field Data." Proc. of the 27th International Conference on Coastal Engineering, ASCE, pp. 3114-3127.

Berg, V.J.H. and Van. G., 1993. "Prediction of Suspended Bed Material Transport in Flow Over Silt and Very Fine Sand." Water Resources Research, Vol. 29, No. 5, pp. 1393-1404.

Berkhoff, J.C.W., 1972. "Computation of Combined Refraction-Diffraction." Proc. of the 13th Coastal Engineering Conference. ASCE, Vol. 1, pp. 471-490.

Berkhoff, J.C.W., Booy, N. and Radder, A.C., 1982. "Verification of Numerical Wave Propagation Models for Simple Harmonic Linear Water Waves." Coastal Engineering, Vol. 6, pp. 255-279.

Bishop, C.G., Donelan, M. A. and Kahma, K. K., 1992. "Shore Protection Manuals Wave Prediction Reviewed." Coastal Engineering, Vol. 17, pp. 25-48.

Blumberg, A. F., 1977. "Numerical Tidal Model for Chesapeake Bay." Journal of the Hydraulics Division, Vol. 103, No. HY, pp 1-17.

Booij, N., 1981, "Gravity Waves on Water with Non-Uniform Depth and Current." Communications of Hydraulics, Dept. of Civil Engg., Delft University of Technology, Report No. 81-1.

Booij, N., 1983, "A Note on the Accuracy of the Mild Slope Equation." Coastal Engineering, Vol. 7, pp. 191-203.

Borthwick, A.G.L. and Joynes, S.A., 1989. "Nearshore Circulation in the Vicinity of a Sinusoidal Beach." Hydrosoft, Vol. 2, No. 3, pp. 106-117.

Borthwick, A.G.L., Foote, Y.L.M. and Ridehalgh, A., 1997. "Measurements at a Cusped Beach in the UKCRF." Coastal Dynamics'97, Plymouth, UK, pp. 953-962.

Briand, M-H, G. and Kamphuis, J. W., 1993. "Waves and Currents on Natural Beaches:A Quasi 3-d Numerical Model." Coastal Engineering, Vol. 20, pp. 101-134.

Briand, M-H, G. and Kamphuis, J. W., 1993. "Sediment Transport in Surf Zone: A Quasi 3-d Numerical Model." Coastal Engineering, Vol. 20, pp. 135-156.

Bryant, R. and Williams, D. J. A., 1983. "Characteristics of Suspended Cohesive Sediments in the Severn Estuary, UK." Canadian J. Fish Aquatic Science, Vol. 40, Supp. 1, pp 96-101.

Cayocca, F., 2001. "Long Term Morphological Modelling of a Tidal Inlet, The Archachon Basin, France." Coastal Engineering, Vol. 42, No. 2, pp. 115-142.

Chadwick, A. and Morfett, J. 1998. "Hydraulics and Civil and Environmental Engineering." 3rd Edition, E&FNSPON, 11 Fetter Lane, London, E4P 4EE.

Chapalain, G. and Thais, L., 2000. "Tide, Turbulence and Suspended Sediment Modelling in an Eastern English Channel." Coastal Engineering, Vol. 41, No. 1-3, pp. 295-316.

Chapalain, G. and Thais, L., 2001. "A system for Measuring Horizontal Sand Transport by Currents." Journal of Coastal Research, Vol. 17, No. 1, pp. 162-172.

Chen, Y. and Liu, P. L-F., 1995. "Modified Boussinesq Equations and Associated Parabolic Models for Water Wave Propagation." Journal of Fluid Mechanics, Vol. 288, pp. 351-381.

Cheong, H-F., Shankar, N. J., Radhakrisnan, R. and Toh, A-C., 1993. "Estimation of Sand Transport by use of Tracers Along a Reclaimed Shoreline at Singapore Changi Airport." Coastal Engineering, Vol. 19, pp. 311-325.

Chien, N. and Wan, Z., 1998. "Mechanics of Sediment Transport." ASCE Press, USA. 922p.

Church, J. C. and Thornton, E. B., 1992. "Bottom Stress Modification by Breaking Waves Within a Longshore Current Model." Proc. of the 23rd International Conference on Coastal Engineering, Italy, pp. 314-327.

Coastline Response Study, 1993. "Coastline Response Study: Worms Head to Penarth Head." Final Report, Vol-3. October, 1993.

Collins, M. B., Pattiachari, C. B., Banner, F. T. and Ferrentinos, G.K., 1980. "The Supply of Sand to Swansea Bay." Industrialised Embayments and Their Environmental Problems, Pergamon Press, Oxford, pp 193-213.

Collins, M. B. and Ferrentinos, G.K., 1984. "Residual Circulation in the Bristol Channel as Suggested by Woodhead Seabed Drifter Recovery Patterns." Oceanographic Acta, Vol-7 (1), pp 33-42.

Copeland, G.J.M. and Bayne, G.L.S., 1998. "Tidal Flow Modelling Using a Minimisation Method." J. of Coastal Engineering, Vol. 34, No. 1-2, pp. 129-161.

Cougier, P. and Hir, P. L., 2002. "Development of a 3D Hydrodynamic Model for Coastal Ecosystem Modelling: Application to the Plume of the Seine River, France." Estuarine Coastal and Shelf Science, Vol. 55, No. 5, pp 673-695.

Dalrymple, R.A., 1988. "Model of Refraction of Water Waves." J. of Waterway, Port, Coastal and Ocean Engineering, Vol. 114, No. 4, pp. 423-435.

Dalrymple, R. A., 1994. "The Theory of Short Period Waves." Coastal, Estuarial and Harbour Engineers' Ref. Book, edited by Abbott, M. B., and Price, W. A., E & FN SPON, London, Chap 3, pp 37-44.

Dalrymple, R.A., Kirby, J.T. and Hwang, P.A., 1984. "Wave Diffraction due to Areas of Energy Dissipation", Journal of Waterway, Port, Coastal and Ocean Engineering, Vol. 110, No. 1, pp. 67-79.

Dalrymple, R.A. and Kirby, J.T., 1988. "Models for Very Wide-Angle Water Waves and Wave Diffraction." Journal of Fluid Mechanics, Vol. 192, pp. 33-50.

Dalrymple, R.A. and Kirby, J.T., 1994. "Waves in an Annular Entrance Channel." Proc. of the 24th Coastal Engineering Conference, Vol. 1, pp. 128-141.

Damgaard, J.S. and Soulsby, R.L., 1996. "Longshore Bed Load Transport." Proc. of the 25th International Conference on Coastal Engineering, ASCE, pp. 3615-3627.

Davies, R. A., 1964. "What is a Wave Dominated Coast?." Marine Geology, Vol. 60, pp. 313-329.

Davies, A.G., Ribberink., J.S., Temperville, A. and Zyserman, J.A., 1997. "Comparisons Between Sediment Transport Models and Observation Made in Wave and Current Flows Above Plane Beds." Coastal Engineering, Vol. 31, pp. 163-198.

Davies, A.G. and Villaret, C., 2000. "Sand Transport by Waves and Currents: Predictions of Research and Engineering models." Proc. of the 27th International Conference on Coastal Engineering, ASCE, Australia, pp. 2480-2494.

Davies, A.G., Van Rijn, L. C., Damgaard, J. S., Graaf, J. V. E. and Ribberink, J. S., 2002. "Intercomparison of Research and Practical Sand Transport Models." Coastal Engineering, Vol. 46, pp. 1-23.

Dean, R. G. and Dalrymple, R. A., 1994. "Water Waves Mechanics for Engineers Scientists, Advanced Series on Ocean Engineering-Vol 2, World Scientific Publishers Co. Ple Ltd. Singapore.

de Vriend, H. J., 1987. "2DH Mathematical Modelling of Morphological Evolution in Shallow Water." Coastal Engineering, Vol 11, pp. 1-27.

de Vriend, H. J., Capobianco, M., Chesher, T., de Swart, H. E., Latteau, B. and Strive, M. J. F., 1993. "Approaches to Longterm Modelling of Coast Morphology: A Review." Coastal Engineering, Vol. 21, pp. 225-269.

Dingemans, M.W., Stive, M.J.F., Kuik, A.J., Radder, A.C. and Booji, N., 1984. "Field and Laboratory Verification of the Wave Propagation Model Crediz." Proc. of the 19th Coastal Engineering Conference, Vol. 2, pp. 1178-1191.

Divoky, D., LeMehaute, B. and Lin, A., 1970. "Breaking Waves on Gentle Slopes." Journal of Geophysical Research, Vol. 75, no. 9, pp 1681 – 1692.

Doering, J.C. and Baryla, A.J., 2002. "An Investigation of the Velocity Field Under Regular and Irregular Waves Over a Sand Beach." Coastal Engineering, Vol. 44, pp 275-300.

Draft Report,., 2004. "Fate and Transport of Particles in Estuaries." Vol-4, Draft Report, School of Civil Engineering, Cardiff University.

Dronkers, J. J., 1964. "Tidal Computations in Rivers and Coastal Waters." North Holland Publishing Co. Amsterdam.

Dulou, C., Belzons, M. and Reys, V., 2002. "Bar Formation under Breaking Wave Condition: A Laboratory Study." J. of Coastal Research, Vol. 18, pp. 802-809.

Dun, R. W. A., 1995. "Some Aspects of the Hydrodynamics and Sedimentology of Swansea Bay, Central Bristol Channel." PhD Thesis, University of Wales, Cardiff.

Dyer, K. R., 1984. "Sedimentation Process in the Bristol Channel/Severn Estuary." Marine Pollution Bulletin, Vol. 15, pp 53-57.

Dyer, K. R., 1986. "Coastal and Estuarine Sediment Dynamics." John Wiley and Sons Ltd., NY, 342 pp.

Dyer, K. R., 1987. "Estuaries : A Physical Introduction." 2nd. Edition, John Wiley and Sons Ltd., NY, 195p.

Ebersole, B. A., 1985. "Refraction-Diffraction Model for Linear Water Waves." J. of Waterway, Port, Coastal and Ocean Engineering, Vol. 111, No. 6, pp. 939-953.

Ebersole, B. A. and Dalrymple, R. A., 1980. "Numerical Modelling for Nearshore Circulation." Proc. of the 17th Coastal Engineering Conf. Australia, pp 2710-2725.

Elder, J. W., 1959. "The Dispersion of Marked Fluid in Turbulant Shear Flow." Journal of Fluid Mechanics, Vol. 5, pp. 544 – 560.

Elfrink, B., Broker, I. and Deiggard, R., 2000. "Beach Profile Evolution due to Oblique Wave Attack." Proc. of the 27th Coastal Engineering Conference, ASCE, Australia, pp. 3021-3034.

Evans, C. D. R., 1982. "The Geology and Surficial Sediments of the Inner Bristol Channel and Severn Estuary." In Severn Barrage Project, Proc. of a Symposium Organised by Inst. of Civil Engg., 8-9 October, Thomas Telford, London, pp 35-42.

Falconer, R. A., 1980. "Numerical Modelling of Tidal Circulations in Harbours." Journal of Waterway, Port, Coastal and Ocean Division, ASCE, Vol. 106, No. WW1, pp. 31-48.

Falconer, R. A., 1988. "A Short Course on Flow and Water Quality Modelling of Coastal Waters, Estuaries, Rivers, Lakes and Reservoirs." University of Bradford, 20-22 Sep. 1988, Vol. 1.

Falconer, R. A., 1991. "Flow and Water Quality Modelling in the Coastal and Inland Water." Journal of Hydraulic Research, Vol. 30, No. 4, pp 437-452.

Falconer, R. A., 1993. "An Introduction to Nearly Horizontal Flows." Coastal, Estuarine and Harbor Engineering, Ref. Book, Edited by Abbott and Price, Chapter 2, pp 27-36.

Falconer, R. A. and Owens, P.H., 1990. "Numerical Modelling of Suspended Sedimnt Fluxes in Estuarine Waters." Estuarine, Coastal and Shelf Science, Academic Press Ltd., Vol. 31, pp. 745-762.

Falconer, R. A. and Chen, Y., 1996. "Modelling Sediment Transport and Water Quality Process on Tidal Flood Plains." In Floodplain Processes, Edited by M. J. Anderson, D. Walling and P.D. Bates, John Wiley and Sons, pp 361-398.

Falconer, R.A. and Chen, Y., 1996. "Three-Dimensional Modelling of Intermittent Effluent Discharges using Highly Accurate Schemes." Hydrodynamics-Theory and Practice, Proceedings of the 2nd International Conference on Hydrodynamics, Hongkong, 16-19 December, pp. 643-648.

Falconer, R.A., Lin, B., Wu, Y. and Harris, E., 1999. "DIVAST Model : Reference Manual." Draft Copy, Environmental Water Management Research Centre, Cardiff University.

Falconer, R.A., Lin, B. and Kashefipour, S.M., 2001. "Modelling Water Quality Processes in Riverine System." In Model Validation: Perspectives in Hydrological Science. Edited by M.G. Anderson and P.D. Bates. John Wiley and Sons, Ltd.

Fischer, H. B., 1979, "Mixing in Inland and Coastal Water." Academic Press, INC. Harcourt Brace Jovanovich, Publishers. California, USA.

Flick, R. E., Murray, J. F. and Ewing, L. C., 2003. "Trends in United States Tidal Datum Statistics and Tidal Range." Journal of Waterway, Port, Coastal and Ocean Engineering, Vol. 129, No. 4, pp. 155-164.

Fredsoe, J. and Deigaard, R., 1992. "Mechanics of Coastal Sediment Transport." Advance Series on Ocean Engineering. Vol. 3, World Scientific.

Frihy, O. E., Fanes, A. M., Khafazy, A. and Komar, P. D., 1991. "Patterns of Nearshore Sediment Transport Along the Nile Delta, Egypt." Coastal Engineering, Vol. 15, pp. 409-429.

Führböter, A., 1986. "Model and Prototype Tests for Wave Impact and Runup on a Uniform 1:4 slope." Coastal Engineering, Vol. 10, Issue. 1, pp. 49-84.

Gao, Q. and Radder, A.C., 1998. "A Refraction-Diffraction Model for Irregular Waves." Proc. of the 26th Coastal Engineering Conference, Vol. 1, pp. 366-379.

Goldstein, S., 1938, 1965. "Modern Developments in Fluid Dynamics, An Account of Theory and Experiment Related to Boundary Layers, Turbulent Motion and Wakes, Composed by the Fluid Motion Panel of the Aeronautical Research Committee and Others." Volume II, Oxford University Press.

Gorman, R.M. and Nielson, C., 1999. "Modelling Shallow Water Wave Generation in an Intertidal Estuary." Journal of Coastal Engineering, Vol. 36, No. 3, pp. 197-217.

Graf, W. H., 1971. "Hydraulics of Sediment Transport." Mc-Graw Hill Book Company.

Grasmeijer, B. T. and VanRijn, L. C., 1999. "Transport of Fine Sands by Currents and Waves III : Breaking Waves Over Barred Profile With Ripples." Journal of Waterway, Port, Coastal and Ocean Engineering, Vol. 125, No. 2, pp. 71-79.

Grasmeijer, B.T. and Ruessink, B.G., 2003. "Modelling of Waves and Currents in the Nearshore Parametric vs. Probabilistic Approach." Coastal Engineering, Vol. 49, pp 185-208.

Guo, J., 2002. "Simple and Explicit Solution of Wave Dispersion Equation." Coastal Engineering, Vol. 45, pp 71-74

Guza, R.T. and Thornton, E.B., 1985. "Velocity Moments in Nearshore." J. of Waterway, Port, Coastal and Ocean Engineering, Vol. 111, No. 2, pp. 235-257.

Hamilton, D.G. and Ebersole, B.A., 2001. "Establishing Uniform Longshore Currents in a Large-Scale Sediment Transport Facility." Coastal Engineering, Vol. 42, pp 199-218.

Harris, P.T and Collins, M.B., 1985. "Bedform Distributions and Sediment Transport Paths in the Bristol Channel Severn Estuary, UK", Marine Geology, Vol. 62, pp. 153-166.

Heathershaw, A. D., Carr, A. D. and Blackley, M.W.L., 1981. "Swansea (SKER) Project, Report 6: Final Report, Coastal Erosion and Nearshore Sedimentation Process." Institute of Oceanographic Science, Report no. 118.

Hirsch, C., 1988. "Numerical Computation of Internal and External Flow." Vol-1, John Wiley & Son's Ltd. Guildford, UK.

Holland, W. R. and Liu, L. B., 1975. "On the Generation of Mesoscale Eddies and their Contribution to the Oceanic General Circulation: A Preliminary Report." Journal of Physical Oceanography, Vol. 5, pp 642-657.

Hossain, S., Eyre, B. and McConchie, D., 2001. "Suspended Sediment Transport Dynamics in the Subtropical Micro-Tidal Richmond River Estuary, Australia", Journal of Estuarine, Coastal and Shelf Science, Vol. 53, No. 5, pp. 529-541.

Hu, C. and Hui, Y., 1996a. "Bed Load Transport I: Mechanical Characteristics", Journal of Hydraulic Engineering, ASCE, Vol. 122, No. 5, pp. 245-254.

Hu, C. and Hui, Y., 1996b. "Bed Load Transport II: Stochastic Characteristics", Journal of Hydraulic Engineering, ASCE, Vol. 122, No. 5, pp. 255-261.

Huntley, D.A., 1976. "Lateral and Bottom on Longshore Currents". Proc. of the 15th Coastal Engineering Conference, ASCE, Hawaii, pp. 645-659.

Hydraulics Research Station, 1980b. "The Severn Estuary Recording of Tidal Levels in 1980." Report No. Ex. 943. HR Wallingford, UK.

Isachsen, P.E. and Pond, S., 2000 "The Influence of Spring-Neap Tidal Cycle on Currents and Density in Burran Intel, British Columbia, Canada", Journal of Estuarine, Coastal and Shelf Science, Vol. 51, No. 3, pp. 317-330.

Ito, Y. and Tanimoto, K., 1972. "A Method of Numerical Analysis of Wave Propagation Application of Wave Refraction and Diffraction", Proc. of the 13th Coastal Engineering Conference., ASCE, pp. Chap 26, 503-522.

Jakobsen, F., Azam, M. H. and Kabir, M. M. U., 2002. "Residual Flow in Meghna Estuary on the Coastline of Bangladesh." Estuarine Coastal and Shelf Science, Vol. 55, No. 4, pp 587-597.

Jones, B., 2000. "A Numerical Study of Wave Refraction in Shallow Tidal Waters", Journal of Estuarine, Coastal and Shelf Science, Vol. 51, No. 3, pp. 331-347.

Jonsson, I.G., Skovgaard, C. and Wang, J.D., 1970. "Interaction Between Waves and Currents", Proc. of the 12th Coastal Engineering Conference., ASCE, pp. 489-507.

Johnson, H.K. and Poulin, S., 1998. "On the Accuracy of Parabolic Wave Models", Proc. of the 26th Coastal Engineering Conference, Vol. 1, pp. 352-365.

Kalkwijk, J.P.Th. and Booij, N., 1986. "Adaptation of Secondary Flow in Nearly Horizontal Flow." Journal of Hydraulic Research, Vol. 24, No. 1, pp. 19-27.

Karambas, T. V. and Koutitas, C., 1992. "A Breaking Wave Propagation Model Based on the Boussinesq Equations." Coastal Engineering, Vol. 18, pp. 1-19.

Karzadi, E.A. and Kobayashi, N., 1996. "Time Dependent Quasi-3D Modelling of Breaking Waves on Beaches." Proc. of the 25th Coastal Engineering Conference., ASCE, pp. 233-246.

Kasheifipour, S.M., Lin, B.L., Harris, E.L. and Falconer, R.A., 2002. "Hydro-environmental Modelling for Bathing Water Compliance of an Estuarine Basin." Water Research, Vol-36, pp. 1854-1868.

Katoh, K., 1994. "Difference Between Waves Acting on Steep and Gentle Beaches." Proc. of the 24th Coastal Engineering Conference, ASCE, Japan, pp. 315-329.

Kirby, J. T., 1984, "A Parabolic Equation for the Combined Refraction-Diffraction of Stokes Wave by Mildly Varying Topography." Journal of Fluid Mechanics, Vol. 136, pp 453-466.

Kirby, J.T., 1988. "Parabolic Wave Computations in Non-orthogonal Co-ordinate Systems." Journal of Waterway, Port, Coastal and Ocean Engineering, Vol. 114, No. 6, pp. 673-685.

Kirby, J.T., 1990. "Modelling Shoaling Directional Wave Spectra in Shallow Water." Proc. of the 22nd Coastal Engineering Conference, Vol. 1, pp. 109-122.

Kirby, J.T. and Dalrymple, R.A., 1984. "Verification of a Parabolic Equation for Propagation of Weakly Nonlinear Waves." Coastal Engineering, Vol. 8, pp. 219-232.

Kirby, J.T. and Dalrymple, R.A., 1986. "Modelling Waves in Surfzones and Around Island." Journal of Waterway, Port, Coastal and Ocean Engineering, Vol. 112, No. 1, pp. 78-93.

Kirby, J.T., Lee, C. and Rasmussen, C., 1992. "Time Dependent Solutions of the Mild Slope Wave Equation." Proc. of the 23rd Coastal Engineering Conference, ASCE, Italy, pp. 391-404.

Kirby, J.T., Dalrymple, R.A. and Kaku, H., 1994. "Parabolic Approximations for Water Waves in Conformal Co-ordinate Systems." Coastal Engineering, Vol. 23, pp. 185-213.

Kirk, R. M., 1992. "Experimental Beach Reconstruction-Renourishment on mixed Sand and Gravel Beaches, Washdyke Lagoon, South Cantey, New Zealand." Coastal Engineering, Vol. 17, pp. 253-277.

Kobayashi, N. and Karzadi, E.A., 1994. "Swash Dynamics under Obliquely Incident Waves." Proc. of the 24th Coastal Engineering Conference, ASCE, pp. 2155-2169.

Kobayashi, N., Karzadi, E.A. and Johnson, B.D., 1997. "Dispersion Effects on Longshore Currents in Surf Zones." Journal of Waterway, Port, Coastal and Ocean Engineering, ASCE, Vol. 123, Issue. 5, pp. 240-248.

Komar, P. D., 1971. "The Mechanics of Sand Transport on Beaches." J. of Geophysical Research,, Vol. 76, No. 3, pp. 713-721.

Komar, P. D. and Inman, D. J., 1970. "Longshore Sand Transport on Beaches." Journal of Geophysical Research, Vol. 75, no. 30, pp 5914 – 5927.

Koutitas, C. J., 1983, "Elements of Computation Hydraulics." London, Pentech, 1983.

Kumar, V.S., Kumar, K. A. and Raju, N. S. N., 2001. "Nearshore Processes Along Tikkavanipalem Beach, India." J. of Coastal Research, Vol. 17, No. 2, pp. 271-279.

Kuo, A. Y., Shen, J. and Hamrick, J. M., 1996. "Effect of Acceleration on Bottom Shear Stress in Tidal Estuaries." Journal of Waterway, Port, Coastal and Ocean Engineering, Vol. 122, No. 2, pp. 75-83.

Lee, J. L. and Wang, H., 1992. "Evaluation of Numerical Models on Wave-Current Interactions." Proc. of the 23rd Coastal Engg. Conference., ASCE, pp. 432-446.

Le Méhauté, B., 1976. "A Introduction to Hydrodynamics and Water Waves Fluid Mechanics." Springer-Verleg New York Inc.

Lessa, G. C., 2000. "Morphodynamic Controls on Tides and Tidal Currents in Macrotidal Shallow Estuaries, NE Australia." Journal of Coastal Research, Vol. 16, No. 4, pp. 976-989.

Li, B., 1994. "A Generalised Conjugate Gradient Model for the Mild Slope Equation." Coastal Engineering, Vol. 23, pp. 215-225.

Li, B. and Anastasiou, K., 1991. "Efficient Elliptic Solvers for the Mild-Slope Equation using the Multigrid Technique." Elsevier Science Publisher, B.V. Amsterdam, pp. 245-266.

Li, S. and Shibayama, T., 2000. "Calculation of Wave-Induced Longshore Current in Surf Zone by using Boussinesq Equation." Proc. of the 27th International Conference on Coastal Engineering, ASCE, Australia, pp. 334-345.

Lilly, D. K., 1965. "On the Computational Stability of Numerical Solutions of the Time Dependent Non-linear Geophysical Fluid Dynamics Problem." Monthly Weather Review, Vol, 93, Part 1, pp 11-26.

Lima, S.S.L.d.S., 1981. "Wave-induced Nearshore Circulation." PhD Thesis, University of Liverpool, UK. 193p.

Lin, B. and Falconer, R.A., 1995. "Modelling Sediment Fluxes in Estuarine Water Using a Curvilinear Co-ordinate Grid System." Estuarine, Coastal and Shelf Science, Vol. 41, pp. 413-428.

Lin, B. and Chandler-Wilde, S. N., 1996. "A Depth Integrated 2D Coastal and Estuarine Model with Conformal Boundary Fitted Mesh Generation." International Journal of Numerical Methods in Fluids, Vol. 23, pp 819-846.

Lin, B. and Falconer, R.A., 1996. "Numerical Modelling of Three-Dimensional Suspended Sediment for Estuarine and Coastal Waters." J. of Hydraulic Research, Vol. 34, No. 4, pp. 435-456.

Lin, B. and Falconer, R. A., 1997. "Three Dimensional Layer Integrated Modelling of Estuarine Flows with Flooding and Drying." Estuarine Coastal and Shelf Science, Vol. 44, pp 737-751.

Lin, B. and Falconer, R. A., 2001. "Numerical Modelling of 3-D Tidal Currents and Water Quality Indicators in the Bristol Channel." Proc. of the Institute of Civil Engineers, Water and Maritime Engg., Vol. 148, pp 737-751.

Liu, P. L-F. and Tsay, T-K., 1984. "Refraction-Diffraction Model for Weakly Nonlinear Water Waves." Journal of Fluid Mechanics, Vol. 141, pp. 265-274.

Liu, P. L-F. and Boisserain, P.L., 1988. "Wave Propagation Between Two Breakwaters." J. of Waterway, Port, Coastal and Ocean Engineering, Vol. 114, No. 2, pp. 237-247.

Longuet-Higgins, M.S., 1970. "Longshore Current Generated by Obliquely Incident Sea Waves-1." Journal of Geophysical Research, Vol. 75, no. 33, pp 6778 – 6789.

Longuet-Higgins, M.S., 1972. "The Mechanics of Surf Zone." Theoretical and Applied Mechanics, Proc. 13th International Congress, Moscow, pp 213-228.

Longuet-Higgins, M. S. and Stewart, R. W., 1960. "Changes in the Form of Short Gravity Waves on Long Waves and Tidal Currents." Journal of Fluid Mechanics, Vol 8, pp 565-583.

Longuet-Higgins, M. S. and Stewart, R. W., 1961. "The Changes in Amplitude of Short Gravity Waves on Steady Non-uniform Currents." Journal of Fluid Mechanics, Vol 10, pp 529 - 549.

Longuet-Higgins, M. S. and Stewart, R. W., 1962. "Radiation Stresses and Mass Transport in Gravity Waves with Application to Surf Beats." Journal of Fluid Mechanics, Vol 13, pp. 481-504.

Longuet-Higgins, M. S. and Stewart, R. W., 1964. "Radiation Stresses in Water Waves, A Physical Discussion with Application." Deep Sea Reasearch, Vol. 11, No. 4, pp 565-583.

Lozano, C. and Liu, P. L-F., 1980. "Refraction-Diffraction Model for Linear Surface Water Waves." Journal of Fluid Mechanics, Vol. 101, Part 4, pp. 705-720.

Madson, P.A. and Larsen, J., 1987. "An Efficient Finite-Difference Approach to the Mild Slope Equation." Coastal Engineering, Vol. 11, pp. 329-351.

Martin, P.A., Dalrymple, R.A. and Kirby, J.T., 1996. "Parabolic Modelling for Water Waves". In Gravity Waves in Water of Finite Depth, edited J. N. Hunt, Computational Mechanics Publications, Southampton, UK.

Mason, D.C., Amin, M., Devenport, I.J., Flather, R.A. and Robinson, S., 1999. "Measurement of Recent Intertidal Sediment Transport in Morecombe Bay using the

Waterline Method." Journal of Estuarine, Coastal and Shelf Science, Vol. 49, No. 3, pp. 427-456.

Mason, D.C. and Garg, P.K., 2001. "Morphodynamic Modelling of Intertidal Sediment Transport in Morecombe Bay." Journal of Estuarine, Coastal and Shelf Science, Vol. 53, No. 1, pp. 79-92.

Massey, B. S., 1990. "Mechanics of Fluids." 6th Edition, Chapman and Hall, London, 599p.

McAnally, W.H. and Mehta, A.J., 2002. "Significance of Aggregation Fine Sediment Particles in their Deposition." Journal of Estuarine, Coastal and Shelf Science, Vol. 54, No. 1, pp. 643-653.

McComb, W.D., 1992. "The Physics of Fluid Turbulance." Oxford Science Publications, N.Y. USA.

McLaren, P., Collins, M. B., Gao, S. and Powys, R.L., 1993. "Sediment Dynamics of the Severn Estuary and Inner Bristol Channel." Journal of the Geological Society, London, Vol. 150, pp 589-603.

Mei, C. C., 1983. "The Applied Dynamics of Ocean Surface waves." Advance Series on Ocean Engineering, Vol. 1, World Scientific.

Melo, E. and Gobbi, M. F., 1998. "Wave Propagation in Circular Jettied Channels." J. of Waterway, Port, Coastal and Ocean Engineering, Vol. 124, No. 1, pp. 7-15.

Meyers, E. P. and Baptista, A. M., 2001. "Conversion of Tides in the Eastern North Pacific Ocean." Advances in Water Resources, Vol. 24, pp. 505-519.

Miles, G. V., 1982. "Impact on Currents Transport Processes." In Severn Barrage Project, Proc. of a symposium organised by Inst. of Civil Engineers, 8-9 October, Thomas Telford, London, pp 59-64.

Misri, R.L., RangaRaju, K.G. and Garde, R.J., 1984. "Bed Load Transport of Coarse Uniform Sediments." J. of Hydraulic Engg., ASCE, Vol. 110, No. 3, pp. 312-328.

Mizuguchi, M. and Horikawa, K., 1976. "Physical Aspects of Wave-Induced Nearshore Current System." Proc. of the 15th Conference on Coastal Engineering, ASCE, Vol. 1, Hawaii, pp. 607-625.

Murphy, A.H. and Epstain, E.S., 1989. "Skill Scores and Correlation Coefficients in Model Verification." Monthly Weather Review, Vol. 117, pp. 572-581.

Naidu, V. S. and Sharma, R.V., 2001. "Numerical Modelling of Tide Induced Currents in Thane Creek, West Coast of India." Journal of Waterway, Port, Coastal and Ocean Engineering, Vol. 127, No. 4, pp. 241-244.

Nakumura, Y., Watanabe, A. and Isobe, M., 2000. "Cross-shore Distributions of Longshore Sand Transport Rate in Surf and Swash Zones." Proceedings of the 27th International Conference on Coastal Engineering, ASCE, Australia, pp. 3128-3138.

Nece, R. E., and Falconer, R. A., 1989. "Modelling of Tide Induced Depth Averaged Velocity Distribution in a Square Harbour." Hydraulic and Environmental Modelling of Coastal, Estuarine and River Waters, Paper 5, pp 56-66.

Nielson, P. and Zai-Jin, Y., 1996. "Eulerian Mean Velocities Under Non-breaking Waves on Horizontal Bottoms." Proc. of the 25th Coastal Engineering Conference, Vol. 4, pp. 4066-4077.

Noda, E. K., 1972. "Wave Induced Circulation and Longshore Current Patterns in the Coastal Zone." Technical Report, TC-149-3, Tetra Tech, Inc, Pasadena, California.

Noda, E. K., 1974. "Wave Induced Nearshore Circulation." Journal of Geophysical Research, Vol 79, No 27, pp 4097-4106.

Nordstorm , K. F., Jackson, N. L., Allen, J. R. and Sherman, D. J., 2003. "Longshore Sediment Transport Rates on a Microtidal Estuarine Beach." Journal of Waterway, Port, Coastal and Ocean Engineering, Vol. 129, No. 1, pp. 1-4.

ÓDonoghue, T. and Clubb, G.S., 2002. "Sand Ripples Generated by Regular Oscillatory Flow." Coastal Engineering, Vol. 44, pp 101-116.

Ono, M., Kim, K.H., Sawaragi, T. and Deguchi, I., 1994. "Suspended Sediment Caused by Waves and Currents." Proceedings of the 24th Intrnational Conference on Coastal Engineering, ASCE, Japan, pp. 2476-2487.

O'Reilly, W.C. and Guza, R.T., 1993. "A Comparison of Two Spectral Wave Models in the Southern California Bight." Coastal Engineering, Vol. 19, pp. 263-282.

Orten, P. M. and Kineke, G. C., 2001. "Comparing Calculated and Observed Vertical Suspended Sediment Distribution from a Hudson River Estuary Turbidity Maximum." Estuarine Coastal and Shelf Science, Vol. 52, No. 3, pp 401-410.

Owen, A., 1980. "A Three-Dimensional Model for Bristol Channel." Journal of Physical Oceanography, Vol. 10, pp 1290-1302.

Owen, A., 1980. "The Tidal Regime of Bristol Channel: A Numerical Model Approach." Geophysical Journal of Royal Astronomical Society, Vol. 62, pp. 59-75.

Owens, P. H., 1986. "Mathematical Modelling of Sediment Transport in Estuaries." PhD Thesis, Department of Civil Engg., University of Birmingham, UK.

Ozer, J., Padilka, R.A., Osuna, P. and Wolf, J., 2000. "A Coupling Module for Tides, Surges and Waves." Coastal Engineering, Vol. 41, No. 1, pp. 95-124.

Pan, S., O'Connor, B.A, Bell, P. and Williams, J.J., 2001. "Interactive numerical Modelling of the Hydrodynamics of Combined Waves and Tides in the Coastal Zone." In: H. Hanson and M. Larson, ed Coastal Dynamics'01, ASCE Lund, pp. 162-171.

Panchang, V.G., Cushman-Ruisin, B. and Pearce, B.R., 1988. "Combined Refraction-Diffraction of Short Waves in Large Coastal Regions." Coastal Engineering, Vol. 12, pp. 133-156.

Park, K.-Y. and Borthwick, A. G. L., 2001. "Quadtree Grid Numerical Model of Nearshore Wave Current Interaction." Coastal Engineering, Vol. 42, no.3, pp. 219-239.

Patel, P. L. and RanguRaju, K. G., 1996. "Fractionwise Calculation of Bed Load Transport." Journal of Hydraulic Research, Vol. 34, No. 3, pp. 363-380.

Pechon, P. and Teisson, C., 1994. "Numerical Modelling of Three-Dimensional Wave Driven Currents in the Surf zone." Proc. of the 24th Coastal Engineering Conference, ASCE, Japan, pp. 2503-2512.

Ponce and Yabushaki, (1981), "Modelling Circulation in Depth Averaged Flow", Journal of Hydraulic Division, ASCE, Vol. 107, pp. 1501 – 1518.

Prandtle, D., Hargreves, J.C., Campbell, A.R. and Wolf, J., 2000. "Tide, Wave and Suspended Sediment Modelling on an Open Coast, Holderness." Coastal Engineering, Vol. 41, No. 1-3, pp. 237-267.

Prasad, K.V.S.R. and Reddy, B.S.R., 1988. "Nearshore Sediment Dynamics Around Madras Port, India." J. of Waterway, Port, Coastal and Ocean Engineering, Vol. 114, No. 2, March, pp. 206-219.

Price, W. A., and Thorn, M. F. C., 1994. "Physical Model of Estuaries." Coastal, Estuarial and Harbour Engineers' Ref. Book, edited by Abbott, M. B., and Price, W. A., E & FN SPON, London, Chap 21, pp 275-288.

Pritchard, D. W., 1967. "What is an Estuary: Physical Viewpoint." From 'Estuaries', Edited by George H. Lauff, Publication No. 83., American Association for the Advancement of Science, pp. 3-5.

Radder, A. C., 1979. "On the Parabolic Equation Method for Water Wave Propagation." Journal of Fluid Mechanics, Vol. 95, Part. 1, pp. 159-176.

RCL Report, 1986. "Suspended Fine Cohesive Sediment in the Severn Estuary and Inner Bristol Channel, UK." By R. Kirby, Report to the UK Atomic Energy Authority, Revensrodd Consultants Limited, Somerset.

Roache, P. J., 1998. "Computational Fluid Dynamics." 2nd Ed., Albuquerque, N. M. : Hermosa Publishers, 1998.

Rodi, W., 1994. "Elements of the Theory of Turbulence." Coastal, Estuarial and Harbour Engineers' Ref. Book, edited by Abbott, M. B., and Price, W. A., E & FN SPON, London, Chap 4, pp 45-60.

Ruhl, C.A., Schoellhamer, D.H., Stumpf, R.P. and Lindsay, C.I., 2001. "Combined Use of Remote Sensing and Continuous Monitoring to Analyse the Variability of Suspended Sediment Transport in San Francisco Bay California." Journal of Estuarine, Coastal and Shelf Science, Vol. 53, No. 6, pp. 801 - 812.

Sanders, B. F., 2002. "Nonreflecting Boundary Flux Function for Finite Volume Shallow Water Models." Advances in Water Resources, Vol. 25, pp. 195-202.

Sankaranarayanan, S. and McCay, D. B., 2003. "Three Dimensional Modelling of Tidal Circulation in Bay of Fundy." Journal of Waterway, Port, Coastal and Ocean Engineering, Vol. 129, No. 3, pp. 114-123.

Sasaki, T., Harikawa, K. and Hotta, S., 1976. "Nearshore Current on a Gently Sloping Beach." Proc. of the 15th Coastal Engineering Conference., ASCE, pp. 627-644.

Sauvget, P., David, E. and Soares, C. G., 2000. "Modelling Tidal Current on the Coast of Portugal." Coastal Engineering, Vol. 40, No. 4, pp 393-410.

Savioli, J., 1998. "Numerical Investigation of Sediment Transport for Combined Waves and Current." Proceedings of the 26th International Conference on Coastal Engineering, ASCE, Denmark, pp. 2980-2991.

Scaffer, H. A., Madsen, P. A. and Deigaard, R., 1993. "A Boussinesq Model for Waves Breaking in Shallow Water." Coastal Engineering, Vol. 20, pp. 185-202.

Schilichting, H., 1987. "Boundary Layer Theory." 7th Edition, Mc-Graw Hill Book N.Y.

Schooness, J.S. and Theron, A.K., 1994. "Accuracy and Applicability of the SPM Longshore Transport Formula." Proceedings of the 24th International Conference on Coastal Engineering, ASCE, Japan, pp. 2595-2609.

Schooness, J.S. and Theron, A.K., 1996. "Improvement of the Most Accurate Longshore Transport Formula." Proceedings of the 25th International Conference on Coastal Engineering, ASCE, Florida, pp. 3652-3665.

Seymour, R.J. and Castel, D., 1985. "Episodicity in Longshore Sediment Transport." J. of Waterway, Port, Coastal and Ocean Engineering, Vol. 111, No. 3, pp. 542-551.

Shimiju, T., Ukai, A. and Isobe, M., 1992. "Field Verification of Numerical Models for Calculation of Nearshore Wave Field." Proc. of the 23rd Coastal Engineering Conference, Vol. 1, pp. 590-603.

Smith, G.D., 1985. "Numerical Solutions for Partial Differential Equations : Finite Difference Method." 3rd Edition Mc-Graw Hill Book, N.Y.

Sokolnikoff, I. S., and Redheffer, R. M., 1966. "Mathematics of Physics and Modern Engineering." 2nd Edition, Mc-Graw Hill Book, N.Y.

Sonu, C. J., 1972. "Field Observation of Nearshore Circulation and Meandering Currents." Journal of Geophysical Research, Vol. 77, No. 18, pp. 3232-3247.

Sorenson, R. M., 1978. "Basic Coastal Engineering." Wiley Interscience Publications.

Stelling, G. S., 1982. "Practical Aspects of Accuarte Tidal Measurements", Journal of Hydraulic Engineering, Vol. 112, pp. 802 – 817.

Suh, K.D., Lee, C., Park, Y.-H. and Lee, T.H., 2002. "Experimental Verification of Horizontal Two-Dimensional Modified Mild Slope Equation Model." Coastal Engineering, Vol. 44, pp 1-12.

Svendsen, I. J., 1984. "Maximum Flux and Undertow in Surf Zone." Coastal Engineering, Vol 8, pp 347-366.

Teisson, C., 1991. "Cohesive Suspended Sediment Transport: Feasibility and Limitations of Numerical Modelling." Journal of Hydraulic Research, Vol. 29, No. 6, pp. 755-769.

Thompson, E.F. and Hadley, L.L., 1996. "Validation of Numerical Method for Wind Waves and Swell in Harbours." Journal of Waterway, Port, Coastal and Ocean Engineering, Vol. 122, No. 5, pp. 245-257.

Tonis, I.E., Stam, J.M.T. and Van de graff, J., 2002. "Morphological Changes of the Harvingvliet Estuary After Closure in 1970." Coastal Engineering, Vol. 44, No. 3, pp. 191-203.

Tsay, T.-K., Ebersole, B.A. and Liu, P. L.-F., 1989. "Numerical Modelling of Wave Propagation Using Parabolic Approximation With a Boundary-fitted Co-ordinate System." International J. for Numerical Methods in Engineering, Vol. 27, pp. 37-55.

Uncles, R. J., 1982. "Computed and Observed Residual Currents in the Bristol Channel." Oceanographic Acta, Vol. 5, pp 11-20.

Uncles, R. J., 1982. "Residual Currents in the Severn Estuary and their Effects on Dispersion." Oceanographic Acta, Vol. 5, pp 403-410.

Uncles, R. J., 1984. "Hydrodynamics of the Bristol Channel." Marine Pollution Bulletin, Vol. 15, No. 2, pp 47-53.

Unrikrisnan, A. S., Gouveia, A. D. and Vethamory, P., 1999. "Tidal Regime in Gulf of Kutch, West Coast of India, by 2D model." Journal of Waterway, Port, Coastal and Ocean Engineering, Vol. 125, No. 6, pp. 276-284.

Van Dorn, W. G., 1953, "Wind Stress on an Artificial Pond." Journal of Marine Research, Vol. 13, No. 9, pp. 249-276.

Van Rijn, L. C., 1984a. "Sediment Transport Part I: Bed Load Transport." Journal of Hydraulic Engineering, ASCE, Vol. 110, No. 10, pp 1431- 1455.

Van Rijn, L. C., 1984b. "Sediment Transport Part II: Suspended Load Transport." Journal of Hydraulic Engineering, ASCE, Vol. 110, No. 11, pp 1613-1641.

Van Rijn, L. C., 1993. "Principles of Sediment Transport in Rivers, Estuaries and Coastal Seas." Aqua Publications, The Netharlands.

Van Rijn, L.C. and Kroon, A., 1992. "Sediment Transport by Currents and Waves." Proceedings of the 23rd International Conference on Coastal Engineering, ASCE, Italy, pp. 2613-2628.

Van Rijn, L.C. and Wijnberg, G., 1994. "One Dimensional Modelling of Individual Waves and Wave Induced Longshore Currents in the Surf zone." Coastal Engineering, Vol. 28, pp. 121-145.

Van Rijn, L.C., Walstra, D.J.R., Grasmeijer, B., Sutherland, J., Pan, S. and Sierra, J.P., 2003. "The Predictibility of Cross-Shore Bed Evolution of Sandy Beaches at the Time Scale of Storms and Seasons Using Process-Based Profile Models." Coastal Engineering, Vol. 47, pp. 295-327.

Visser, J.P., 1991. "Laboratory Measurements of Uniform Longshore Currents." Coastal Engineering, Vol. 15, pp. 563-593.

Vos, R. J., Brummelhuis, P. G. J. and Gerristen, H., 2000. "Integrated Data Modelling Approach for Suspended Sediment Transport on a Regional Scale." Coastal Engineering, Vol. 41, pp 177-200.

Vreugdenhil, C.B., 1998. "Numerical Methods for Shallow Water Flow." Dordrecht, Boston: Kluwer Academic Publishers. 261p.

Wang, Z. B., 1992a. "Theoretical Analysis of Depth Integrated Modelling of Suspended Sediment Transport." Journal of Hydraulic Research, Vol. 30, No. 3, pp. 403-421.

Wang, Z.B. and Ribberink, J.S, 1986. "The Validity of Depth Integrated Model for Suspended Sediment Transport." Journal of Hydraulic Research, Vol. 24, No. 1, pp. 53-66.

Wang, P. and Kraus, N. C., 1999. "Longshore Sediment Transport Rate Measured by Short Term Impoundment." Journal of Waterway, Port, Coastal and Ocean Engineering, Vol. 125, No. 3, pp. 118- 126.

Wang, P., Ebersole, B. A. and Smith, E.R., 2003. "Beach Profile Evolution under Spilling and Plunging Breakers." Journal of Waterway, Port, Coastal and Ocean Engineering, Vol. 129, No. 1, pp. 41-46.

Weare, T. J., 1976. "Instability in Tidal Flow Computational Schemes." Journal of the Hydraulics Division, Vol. 102, No. HY5, pp 569-580.

Weggel, J.R., 1972. "Maximum Breaker Height for Design." Proceedings of the 13th International Conference on Coastal Engineering, ASCE, Chap. 21, pp 419-732.

Weggel, J.R. and Perlin, M., 1988. "Statistical Description of Longshore Transport Environment." J. of Waterway, Port, Coastal and Ocean Engineering, Vol. 114, No. 2, pp. 125-145.

Westwater, D., 2001. "Modelling Hydrodynamic and Shallow Water Processes over Vegetated Floodplains." PhD Thesis, University of Wales, Cardiff, 269p.

White, T.E., 1994. "Field Test of Radiation Stress Estimators of Longshore Sediment Transport." Proceedings of the 24th International Conference on Coastal Engineering, ASCE, Japan, pp. 2799-2812.

White, T.E., 1998. "Status of Measurements for Coastal Sediment Transport." Journal of Coastal Engineering, Vol. 35, No. 1-2, pp. 17-45.

Wilson, B. W., 1960. "Note on the Surface Wind Strees Over Water at Low and High Wind Speed." Journal of Geophysical Research, Vol 65, no.10, pp 3372-3382

Wolanski, E., Imberger, J. and Heron, M. L., Thornton, E.B., 1984. "Islan wakes in the Shallow Coastal Waters." Journal of Geophysical Research, Vol 89, no.C6, pp. 10,553-10,569 .

Wu, C.-S. and Thornton, E.B., 1986. "Wave Numbers in Linear Progressive Waves." J. of Waterway, Port, Coastal and Ocean Engineering, Vol. 112, No. 4, pp. 536-540.

Wu, J. X. and Shen, H. T., 1999. "Estuarine Bottom Sediment Transport Based on the McLaren Model: A Case Study of the Huangmahoi Estuary, S. Chaina." Journal of Estuarine, Coastal and Shelf Science, Vol. 49, No. 2, pp. 265-279.

Yen, P-H., Jan, C-D., Lee, Y-P. and Lee, H-F., 1996. "Application of Kalman Filter to Short Term Tidal Level Prediction." Journal of Waterway, Port, Coastal and Ocean Engineering, Vol. 122, No. 5, pp. 226-231.

Yin, J., Falconer, R. A., Chen, Y. and Probert, S. D., 1996(2000). "Water and Sediment Movements in Harbours." Applied Energy, Vol. 67, pp 341-352.

Yoo, D. and O'Connor, B.A., 1986. "Mathematical Modelling of Wave Induced Nearshore Circulation." Proc. of the 20th Coastal Engineering Conference, pp. 1667-1681.

Yoon, S.B. and Liu, P. L-F., 1986. "Wave and Current Interactions in Shallow Water." Proc. of the 20th Coastal Engineering Conference. ASCE, Vol. 2, pp. 1682-1697.

Yoon, T.H. and Kim, M.K., 1995. "Quasi-3D Hydrodynamic Model and its Application to 3D Sediment Transport Model in Shallow Reservoirs." HYDRA-2000, Vol. 4, pp. 236-241.

Yoshiyuki, I. and Katsutoshi, T., 1972. "A Method of Numerical Analysis of Wave Propagation-Application of Wave Refraction and Diffraction." Proceedings of the 13th Coastal Engineering Conference. ASCE, Chap. 26, pp. 503-522.

Yu, X., Isobe, M. and Watanabe, A., 1992. "Finite Element Solution of Wave Field Around Structures in Nearshore Zone." Coastal Engineering in Japan, Vol. 35, No. 1, pp. 21-33.

Zhang, Q.Y. and Gin, K.Y.H., 2000. "Three Dimensional Numerical Simulation for Tidal Motion in Singapore's Coastal Water." Coastal Engineering, Vol. 39, No. 2-4, pp. 71-92.